Advances in Materials Science and Engineering

Hydraulic Engineering in Cold Regions: Materials, Structures, and Climate Impacts

Lead Guest Editor: Yanhu Mu
Guest Editors: Xiangtian Xu, Xiao Dong Zhao, Ying-hao Huang, and Hao Zheng

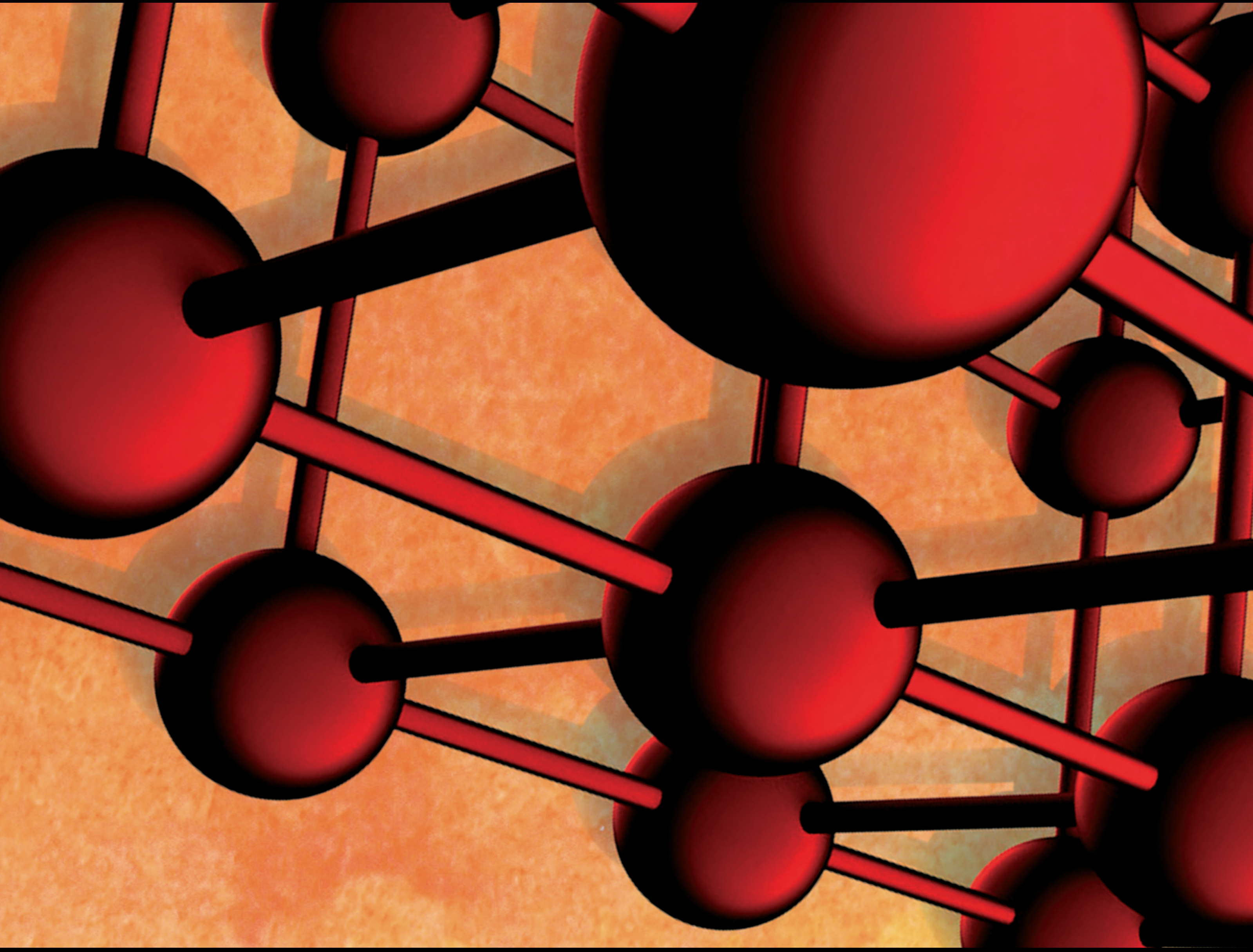

Hydraulic Engineering in Cold Regions: Materials, Structures, and Climate Impacts

Advances in Materials Science and Engineering

Hydraulic Engineering in Cold Regions: Materials, Structures, and Climate Impacts

Lead Guest Editor: Yanhu Mu
Guest Editors: Xiangtian Xu, Xiao Dong Zhao, Ying-hao Huang, and Hao Zheng

Claudio Pettinari, Italy
Giorgio Pia, Italy
Candido Fabrizio Pirri, Italy
Marinos Pitsikalis, Greece
Alain Portavoce, France
Simon C. Potter, Canada
Ulrich Prahl, Germany
Veena Ragupathi, India
Kawaljit singh Randhawa, India
Baskaran Rangasamy, Zambia
Paulo Reis, Portugal
Hilda E. Reynel-Avila, Mexico
Yuri Ribakov, Israel
Aniello Riccio, Italy
Anna Richelli, Italy
Antonio Riveiro, Spain
Marco Rossi, Italy
Fernando Rubio-Marcos, Spain
Francesco Ruffino, Italy
Giuseppe Ruta, Italy
Sachin Salunkhe, India
P Sangeetha, India
Carlo Santulli, Italy
Fabrizio Sarasini, Italy
Senthil Kumaran Selvaraj, India
Raffaele Sepe, Italy
Aabid H Shalla, India
Poorva Sharma, China
Mercedes Solla, Spain
Tushar Sonar, Russia
Donato Sorgente, Italy
Charles C. Sorrell, Australia
Damien Soulat, France
Adolfo Speghini, Italy
Antonino Squillace, Italy
Koichi Sugimoto, Japan
Jirapornchai Suksaeree, Thailand
Baozhong Sun, China
Sam-Shajing Sun, USA
Xiaolong Sun, China
Yongding Tian, China
Hao Tong, China
Achim Trampert, Germany
Tomasz Trzepieciński, Poland
Kavimani V, India
Matjaz Valant, Slovenia
Mostafa Vamegh, Iran
Lijing Wang, Australia
Jörg M. K. Wiezorek, USA
Guosong Wu, China
Junhui Xiao, China
Guoqiang Xie, China
YASHPAL YASHPAL, India
Anil Singh Yadav, India
Yee-wen Yen, Taiwan
Hao Yi, China
Wenbin Yi, China
Tetsu Yonezawa, Japan
Hiroshi Yoshihara, Japan
Bin Yu, China
Rahadian Zainul, Indonesia
Lenka Zaji#c#kova#, Czech Republic
Zhigang Zang, China
Michele Zappalorto, Italy
Gang Zhang, Singapore
Jinghuai Zhang, China
Zengping Zhang, China
You Zhou, Japan
Robert Černý, Czech Republic

Contents

Contents

Hindawi
Advances in Materials Science and Engineering
Volume 2021, Article ID 5541130, 13 pages
https://doi.org/10.1155/2021/5541130

Research Article

Influence of Dynamic Load on Soil Moisture Field in the Process of Freeze-Thaw Cycles

Yongting Huang,[1,2] Wei Ma ,[1,2] Donghui Xiao,[3] and Yuezhen Xu[1,2]

[1]*State Key Laboratory of Frozen Soil Engineering, Northwest Institute of Eco-Environment and Resources, Chinese Academy of Sciences, Lanzhou, Gansu 730000, China*
[2]*University of Chinese Academy of Science, Beijing 100049, China*
[3]*Poly Changda Engineering Company Limited, Guangzhou, Guangdong 510000, China*

Correspondence should be addressed to Wei Ma; mawei@lzb.ac.cn

Received 1 March 2021; Accepted 3 June 2021; Published 22 December 2021

Academic Editor: Xiao Dong Zhao

Due to climate warming and large-scale engineering activities, the embankment engineering risk in the permafrost and seasonally frozen regions caused by water content change in the soil has become more and more serious. To study the moisture migration law in the embankment under the vehicle load action and periodic variation of temperature, a series of temperature-controlled model tests under the dynamic load condition were carried out, the dynamic load was imposed by an air hammer connecting a vibration plate, which was installed on the top surface of the soil, and the variation law of the temperature and moisture fields in the model was analyzed. The test results show that the moisture field in the soil sample changes obviously with the increasing freeze-thaw cycles under the no-load condition, especially after nine freeze-thaw cycles, two moisture accumulation areas appear in the range of 8–15 cm from the soil surface; the dynamic load has an inhibitory effect on the moisture migration within 5 cm below the vibration plate and has a promoting effect on the range of 10–30 cm below the vibration plate. With the increase in the number of freeze-thaw cycles, three high-water content areas are gradually formed and approximately uniformly distributed within the 10–25 cm depth range of the soil, which has an important impact on the stability of the soil. The water content of the moisture accumulation areas during freezing is greater than that during thawing under the no-load condition, while the water content of the moisture accumulation areas during freezing is less than that during thawing under dynamic load. The research results can provide references for the embankment design and disease treatment in cold regions.

1. Introduction

In cold regions, the land surface will undergo repeated freezing and thawing due to periodic fluctuations in surface temperature [1]. As a process of intense weathering, the freeze-thaw cycle strongly changes the physical and mechanical properties of the soil, such as particle size, internal structure, and pore water distribution of the soil, which affects the stability of the engineering structure [2–6]. In the seasonally frozen regions, the freeze-thaw cycle causes repeated frost heave and thaw settlement of the surface soil, which is a crucial reason for engineering and natural diseases [7]. Frost heave and thaw settlement are closely related to the variation of moisture in the soil. During freezing, the moisture in the unfrozen area will migrate to the freezing front due to the thermal gradient and other driving forces. During thawing, the moisture flows down under the self-weight. However, the moisture cannot return to the original position after freezing and thawing due to some retarding force of soil particles, making the moisture redistribute [3, 8–10].

Konrad and Morgenstern [11] and Gilpin [12] studied moisture migration law in the soil through experiments. They found that the variation of the initial water content and temperature gradient are critical reasons for moisture migration in unsaturated soils. Hanks [13] conducted experiments on the moisture vapor migration in three sandy soils and found that the moisture vapor migration conforms to the simple diffusion theory. Chen and Liu [14] conducted many laboratory experiments to study the influence of different factors on moisture migration. The results showed that the moisture migration in frozen soil is related to the soil-water potential gradient, which is influenced by many parameters, such as physical and mechanical properties of the soil, test boundary conditions, freezing speed, temperature gradient, and other parameters. Zhang et al. [15] carried out large-scale laboratory model tests of moisture migration and explored the influence of soil density, freezing temperature, water content, freezing method, and other factors on the moisture migration of unsaturated soil, but they did not consider the influence of temperature gradient on moisture migration in the soil. Lu et al. [16] studied the variation of unfrozen water content and temperature of Qinghai-Tibet Plateau silty clay with different initial water content. The results showed that the supercooling phenomenon during the freeze-thaw process was strengthened significantly with the increase in initial water content of the soil samples, and the freezing rate was greatly increased. Wei et al. [17] conducted the freezing test of saturated soil under different temperature boundaries and sample heights. The results showed that freezing rate and frost heaving ratio were inversely proportional to the height of the soil sample and directly proportional to the temperature gradient.

The moisture migration rate for different soils is different, and the moisture migration rate decreases with the increase in dry density for the same soil [18]. Wang and Lu [19] studied the moisture migration of unsaturated soil under different temperature gradients. The results showed that the variation of the water content has a more significant correlation with the temperature gradient size and the dry density, and the water content of the soil near the warm end of the specimen decreased, while the water content of the soil near the cold end showed an increasing trend. Huang et al. [20] studied the frost heaving and deformation process of frozen soil under external loads. The results show that the external load has a great influence on the driving force of moisture migration, which causes changes in the amount of moisture migration, migration rate, and frost heaving ratio. Zhao et al. [21, 22] analyzed the moisture migration in soil samples under different freezing temperatures and thawing temperatures. The results showed that different freezing and thawing temperatures significantly affect the moisture migration in the soil samples, and the higher the freezing temperature of the top board of the test cases, the more the water content accumulation at the water accumulation layer. Zhang et al. [23] analyzed the moisture migration during the freeze-thaw cycle for sandy soil and silty clay and concluded that the water supply rate of silty clay is greater than that of sandy soil during the freeze-thaw cycle.

In seasonally frozen regions, the moisture in the embankment migrates during the freeze-thaw process. During freezing, the moisture migrates from the position with the high potential energy of the soil to the position with low potential energy, and the moisture near the frozen fringe migrates to the freezing front; during thawing, the moisture in the thawed area migrates to the frozen area. Therefore, the freeze-thaw cycle causes repeated moisture migration in the embankment, which results in moisture accumulation and changes the internal structure of the soil, thus changing the mechanical characteristics of the soil and leading to a decrease in the stability of the embankment [24]. When the moisture accumulates to a certain extent, the embankment will be damaged due to more significant frost heaving action during freezing. At the same time, under the combined actions of the vehicles and other upper loads, the road with excessively high-water content during thawing will produce pavement overturning and other phenomena, which has a huge impact on the performance and service life cycle of the roads [25]. This shows that moisture migration during the freeze-thaw cycle is highly crucial to the deformation of the soil and the stability of the embankment. However, the current research on moisture migration is mainly focused on model tests and small soil sample tests under unloaded conditions and few reports studies have been reported the influence of dynamic loads and freeze-thaw cycles on soil moisture migration based on large model tests. Therefore, this article carries out model tests under dynamic load and freeze-thaw cycles, measures the temperature and moisture in the soil during the tests, and analyses the moisture migration mechanism under dynamic loads. The research results can provide a scientific basis for the design, construction, and disease treatment of the embankment projects in seasonally frozen regions.

2. Experiment Materials and Methods

2.1. Soil Samples. The soil used in this model test is Lanzhou loess in Gansu Province (36°01′14″N 103° 50′15″E, altitude 1624 m), which belongs to the temperate continental climate and seasonal frozen regions [9]. The physical properties of the soil such as initial water content, natural dry density, specific gravity of soil particles, liquid limit, and plastic limit are tested according to the *Standard for Geotechnical Testing Method*, and results are shown in Table 1 [26]. Figure 1 shows the grain-size diameter distribution obtained by the laser diffraction method. The plasticity index of the soil is 8.6 less than 10, and the liquid limit of the soil is 27.3% less than 50%, so the soil is designated as a low liquid limit silt soil.

2.2. Model Testing Apparatus. The model test was carried out by a small temperature-controlled environmental chamber in the State Key Laboratory of Frozen Soil Engineering of the Chinese Academy of Sciences (Figure 2) [27]. The model test system includes an environmental chamber, a temperature control system, an insulation test chamber, a water supplement system, a vibration system, and an observation system (Figure 3). The internal space size of the environmental chamber is $1\,\mathrm{m} \times 1\,\mathrm{m} \times 1\mathrm{m}$, and its internal temperature is controlled by the temperature control system. The temperature control system is mainly composed of the compressor, the temperature controller, the liquid crystal control panel, the Freon liquid circulation pipeline, the evaporator, and the temperature sensor. The temperature control process is manually set on the liquid crystal control panel and automatically controlled by the instrument. The

Table 1: The physical properties of the soil.

Parameters	Initial water content (%)	Natural dry density ($g{\cdot}cm^{-3}$)	Particle density ($g{\cdot}cm^{-3}$)	Plastic limit (%)	Liquid limit (%)	Plasticity index
Test value	4.3	1.36	2.61	18.7	27.3	8.6

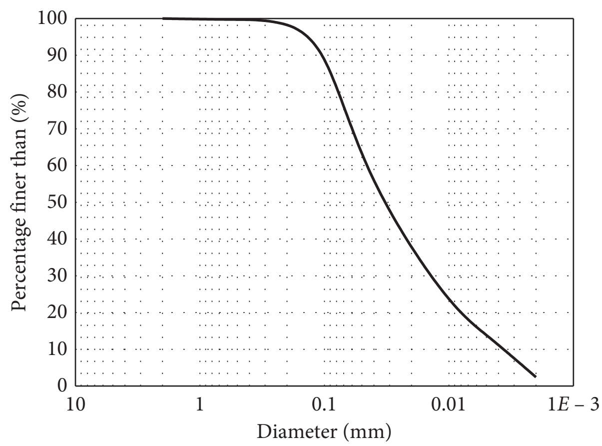

Figure 1: The grain-size diameter distribution.

Figure 2: Temperature-controlled environmental chamber.

temperature control range of the system is from −40°C to +100°C, and the temperature accuracy is about ±0.3°C. The insulation test chamber is used to fill the soil, and its internal dimension is $0.7\,m \times 0.7\,m \times 0.4\,m$. The insulation test chamber is placed in the environmental chamber, and its wall is made of insulation materials to ensure one-dimensional freezing and thawing of soil samples. The water supplement system mainly provides a water supply source for the soil in the insulation test chamber, which is equivalent to the groundwater level. The bottom water supplement system consists of a water inlet, water bin, and drainage port. The water inlet is located at the bottom of the side of the water bin, and the drainage port is located at the top of the side of the water bin, the purpose of which is to ensure that the water enters from the bottom up and gradually fills up the water bin. The vibration system consists of a vibration plate, air hammer, solenoid valve, relay, and air compressor. The vibration frequency of the dynamic load is mainly controlled by the air hammer fixed on the vibration plate; the maximum impact force of the air hammer is $9.6\,kg{\cdot}m{\cdot}s^{-1}$. The vibrating plate is a square of $0.18 \times 0.18\,m$, and the total mass of the vibrating plate, inner ring sleeve, and air hammer is about 16.2 kg. The observation system mainly consists of thermal sensors, moisture sensors, and a data acquisition instrument. The moisture sensors choose EC-5 soil moisture sensors (Figure 4), the range is 0~100%, and the accuracy is ±3%; the data are collected by the CR3000 data acquisition instrument.

2.3. Experiment Design. To study the influence of dynamic load on the moisture and temperature field in the soil, two model tests were designed: one is under the no-load condition on the sample surface and the other is to apply dynamic load on the sample surface. The vibration frequency of the dynamic load is 0.164 Hz, which is selected according to

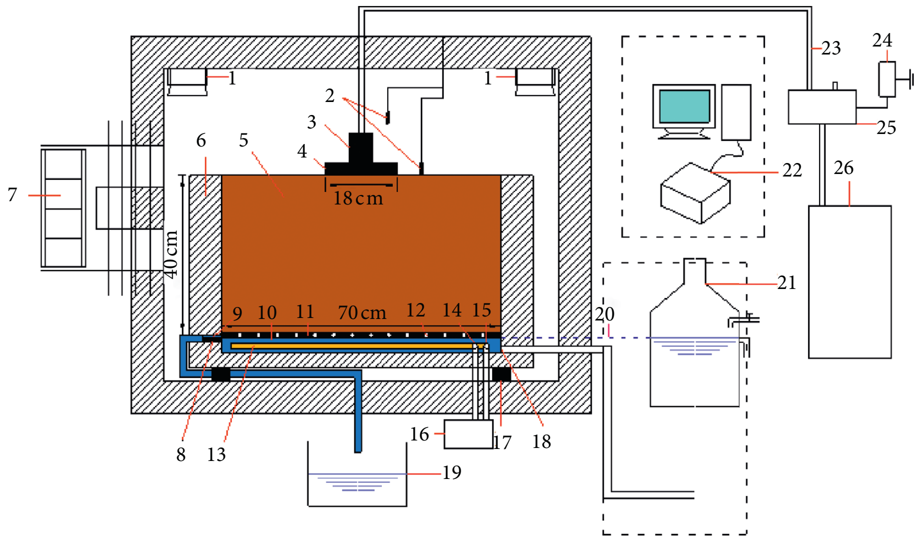

1 Cooling fan
2 Thermistors
3 Air hammer
4 Vibrating bottom plate
5 Soil sample
6 Insulation materimal
7 Compressor
8 Cork
9 Drain
10 Water supplement cabin
11 Bottom plate
12 Water supplement hole
13 Copper pipe
14 Copper pipe inlet
15 Copper pipe outlet
16 Cryostat
17 The base
18 Water inlet
19 Drainage system
20 Water level line
21 Water supply system
22 Data acquistion system
23 Intake pipe
24 Relay
25 Solenoid valve
26 Air compressor

FIGURE 3: System of the modelling test: 1: cooling fan, 2: thermistors, 3: air hammer, 4: vibrating bottom plate, 5: soil sample, 6: insulation material, 7: compressor, 8: cork, 9: drain, 10: water supplement cabin, 11: bottom plate, 12: water supplement plate, 13: copper pipe, 14: copper pipe inlet, 15: copper pipe outlet, 16: cryostat, 17: the base, 18: water inlet, 19: draining system, 20: water level inline, 21: water supply system, 22: data acquisition system, 23: intake pipe, 24: relay, 25: solenoid wave, and 26: air compressor.

FIGURE 4: EC-5 soil moisture sensors.

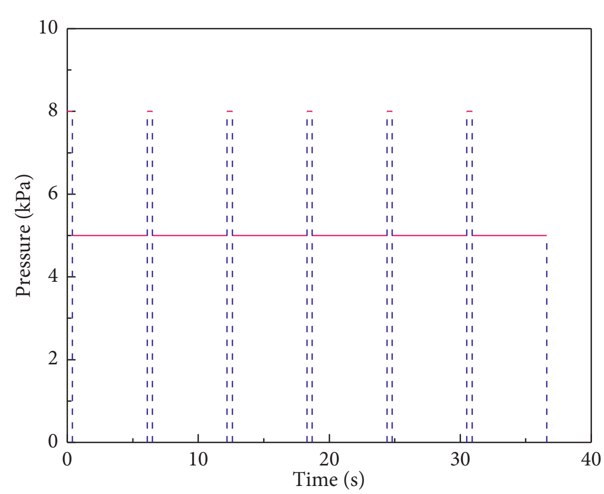

FIGURE 5: Dynamic load variations.

the high-speed traffic flow [28, 29]. The loading time is 0.4 s, the unloading time is 5.7 s, and the specific loading method is shown in Figure 5. The boundary temperature is controlled by an environmental test chamber, and the temperature data are referenced to the monthly average temperature in the loess area of Lanzhou City, which varies between −8.06 and 15.7°C in a sinusoidal function curve, and the freeze-thaw period is 24 h. The fitted curve based on the measured values of temperature is shown in Figure 6, and the fitted temperature equation is expressed as follows:

$$T = 3.82 + 11.88 \times \sin\left(\frac{2\pi t}{24} + \frac{\pi}{2}\right). \quad (1)$$

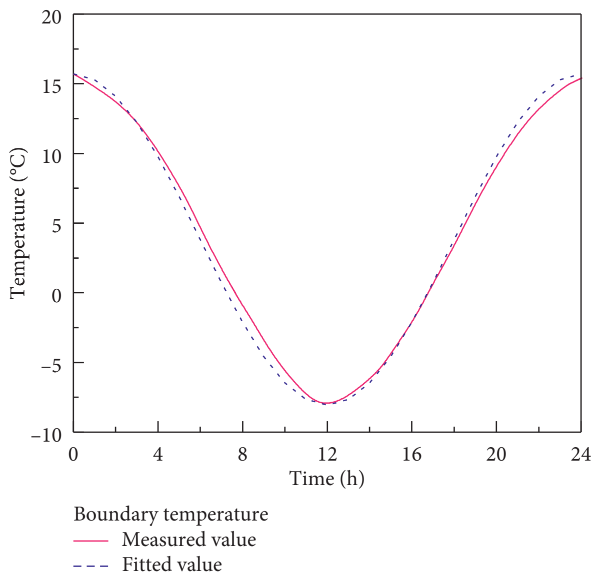

Figure 6: The boundary temperature change curve.

The test process is as follows. (1) *Soil*. The air-dried soil was added to a certain amount of distilled water, mixed well, and passed through a 2 mm sieve. And then, the water content measured by the drying method is 10.6% after 24 hours of sealed storage. (2) *Sample*. The prepared soil is weighed and compacted in layers in the insulation test chamber. The dry density of the sample was controlled at 1.6 g·cm^{-3}. After the soil sample is filled, a piece of plastic film was covered on the top of the soil sample to prevent the evaporation of water. (3) *Temperature*. The soil sample was kept at 20°C for at least 48 h, the purpose of which is to achieve a uniformly distributed initial temperature field. Then, the temperature of the environmental chamber was set to a sinusoidal mode (Figure 6) so that the soil is subjected to freeze-thaw cycles and simultaneously applied a dynamic load on the surface of the soil sample, where the variation of the dynamic load is shown in Figure 5. (4) *Testing*. During the test process, the temperature and moisture fields in the soil sample are measured by the thermal and moisture sensors arranged in layers, as shown in Figure 7. The thermal and moisture sensors are installed in the left half and right half, respectively, because the soil sample configuration, temperature, and load boundary are symmetrical.

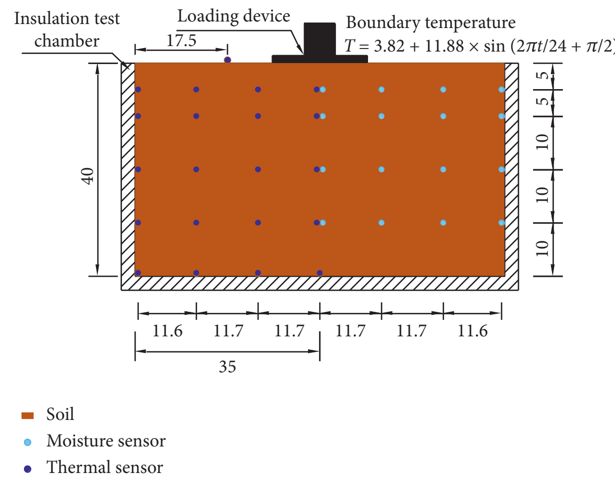

Figure 7: The location of moisture sensors and thermal sensors.

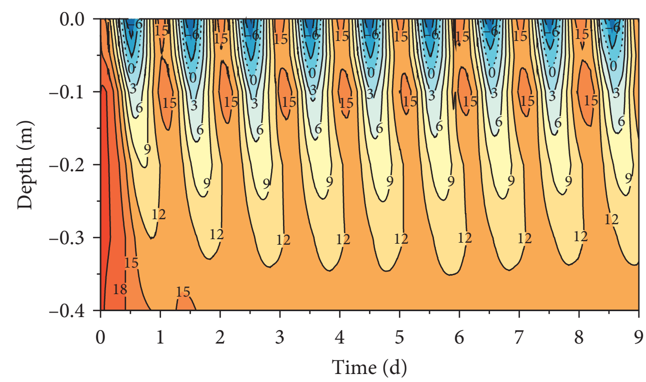

Figure 8: Variation of temperature in soil under dynamic load and freeze-thaw cycles.

3. Results and Analysis

3.1. Temperature Field in the Sample. Figure 8 shows the variation of temperature with time at different depths of the center of the soil sample under the combined action of dynamic load and freeze-thaw cycles. It can be seen that the soil temperature at different locations shows periodical variation with the boundary temperature. The amplitude variation of the temperature in the soil tends to decrease with increasing depth due to the thermal loss when heat is conducted downward from the surface of the soil. The variation of temperature in the soil sample lags behind the soil surface due to the time effect of thermal conduction. It is also seen that the maximum temperature in the soil sample is about 16°C, which occurs at the upper surface of the soil sample and a location of 10 cm from the upper surface of the soil during the freeze-thaw process, and the maximum depth of frost penetration is about 6.2 cm during the 1st freeze-thaw cycle and about 8 cm after nine freeze-thaw cycles. This indicates that the cold capacity gradually accumulates in the soil sample.

Figure 9 shows the contour map of the temperature during the 1st, 5th, 9th, 12th, and 15th freeze-thaw cycles under dynamic loading where 1 L, 5 L, 9 L, 12 L, and 15 L present the moments of the lowest ambient temperature (L) during the different freeze-thaw cycles (1, 5, 9, 15), and similarly 1 H, 5 H, 9 H, 12 H, and 15 H present the moments of the highest ambient temperature (H) during the different freeze-thaw cycles (1, 5, 9, 12, 15).

At the moment of the lowest ambient temperature during freeze-thaw cycles, the heat of soil is dissipated to the environment and the temperature of the soil sample gradually decreases and freezes from top to bottom. In the frozen area, the temperature of the soil sample under the vibration base plate is lower than that on both sides of the vibration plate at the same depth. Because the vibration base plate is

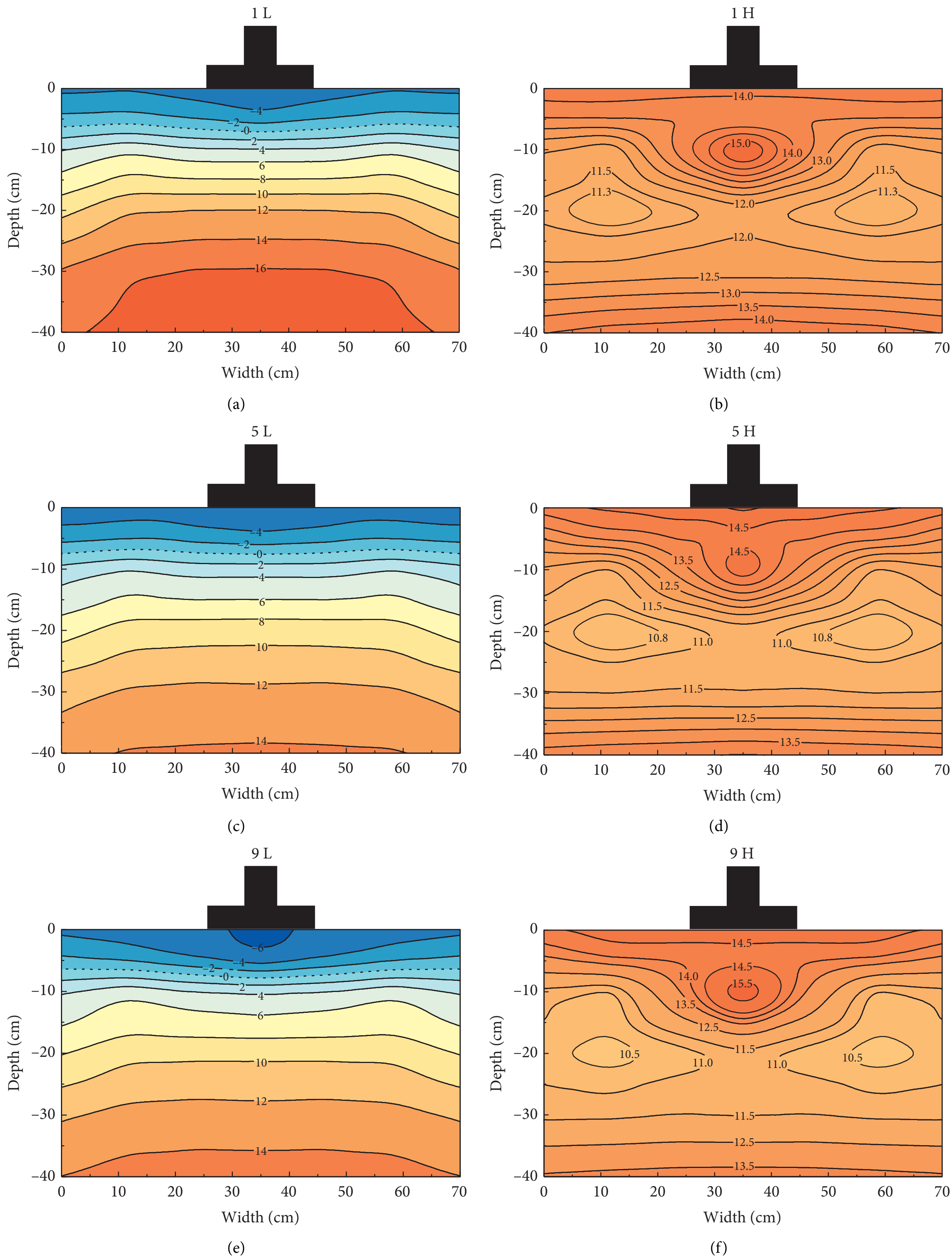

Figure 9: Continued.

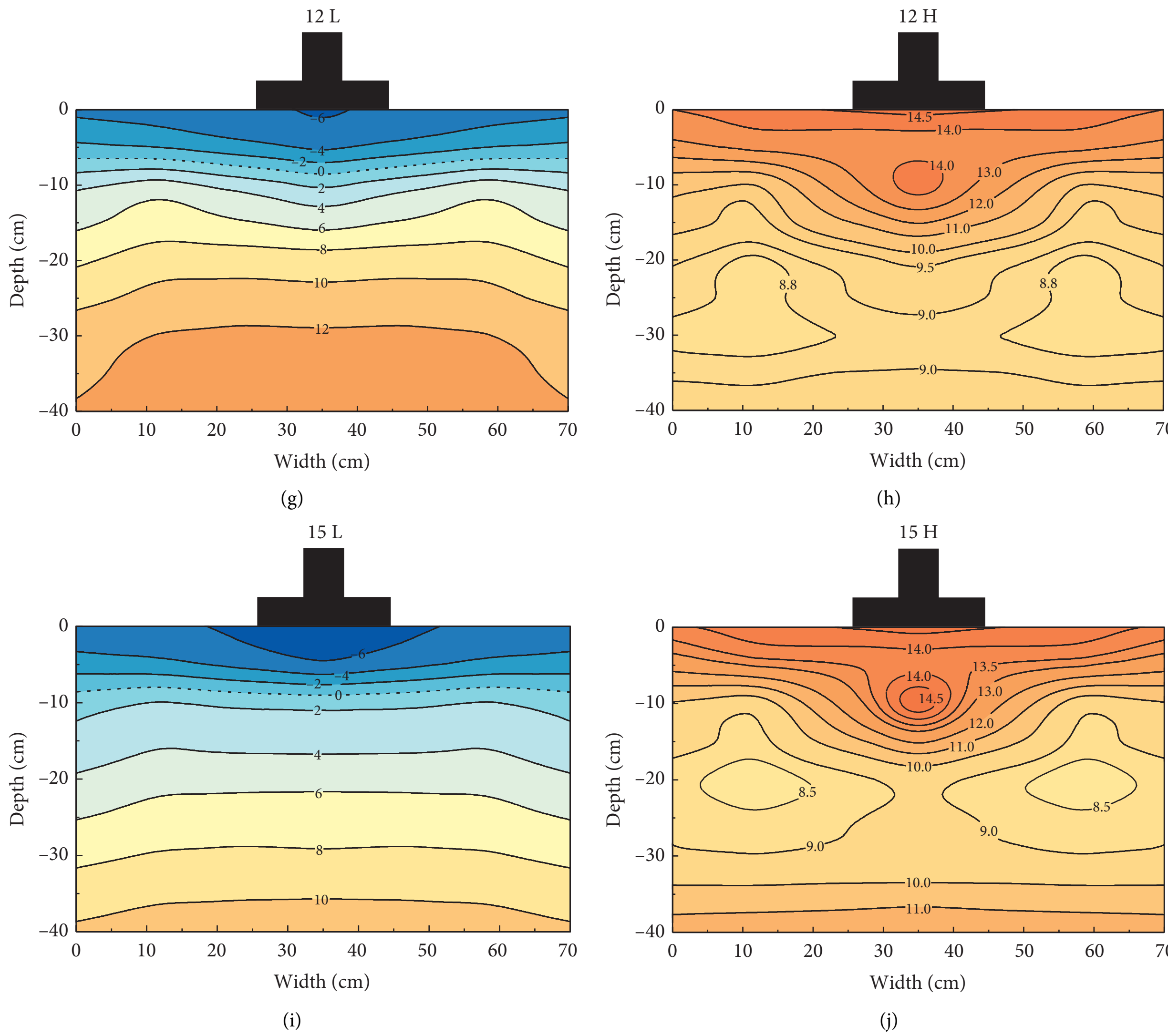

Figure 9: Variation of the temperature field at low and high temperature extremes at different freeze-thaw cycles.

made of steel with good thermal conductivity, which extrudes the soil surface during the loading process, thus it accelerates the release of heat from the surface soil to the environment, leading to the rate of temperature change of the soil under the vibration base plate greater than that on both sides. The results also show that the temperature under the vibration plate is gradually decreasing, and the low-temperature area is gradually expanding with the increase in the freeze-thaw cycle. This indicates that the cold capacity of the soil sample is slowly accumulated during freeze-thaw cycles.

At the moment of the highest ambient temperature during freeze-thaw cycles, in the range of 0–20 cm from the soil surface, the temperature of the soil sample under the vibration base plate is greater than that on both sides of the plate at the same depth, which is also caused by the larger thermal conductivity of the vibration plate, and the temperature gap gradually increases with the increase in the number of freeze-thaw cycles (Figure 9). The reasons are that, on the one hand, the dynamic load accelerates the migration of moisture which further affects the distribution of the temperature field; on the other hand, the thermal conductivity of the vibration base plate is larger than soil and affects the heat transfer and accumulation of the soil sample. For example, at a depth of 10 cm from the soil surface and time of 1H, the temperature at the center position is about 15.5°C, at 11.7 cm from the center position is about 13.6°C, and at 23.4 cm from the center position is about 11.8°C. At the time of 15H, the temperature at the center position is about 14.9°C, at 11.7 cm from the center position is about 12.1°C, and at 23.4 cm from the center position is about 9.4°C. The temperature distribution is more uniform at locations below 20 cm from the soil surface. Moreover, the temperature decreases at each position of the sample with the increase in freeze-thaw cycles, which is caused by the accumulation of cold capacity in the soil sample during the freeze-thaw cycles.

For whole freeze-thaw cycles, the accumulation of cold capacity occurs in the soil regardless of whether the ambient temperature is low or high. That is because the thermal

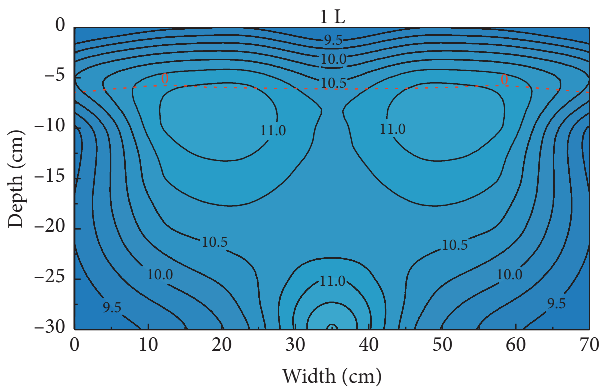

(a)

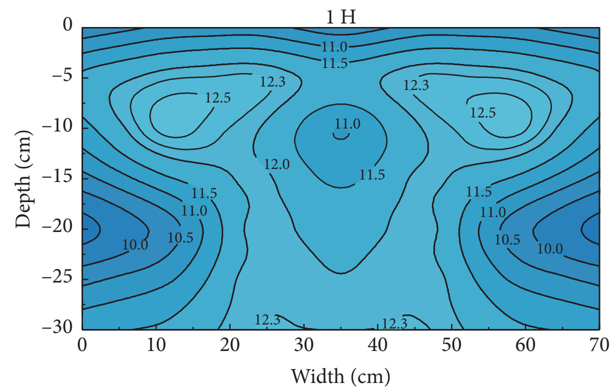

(b)

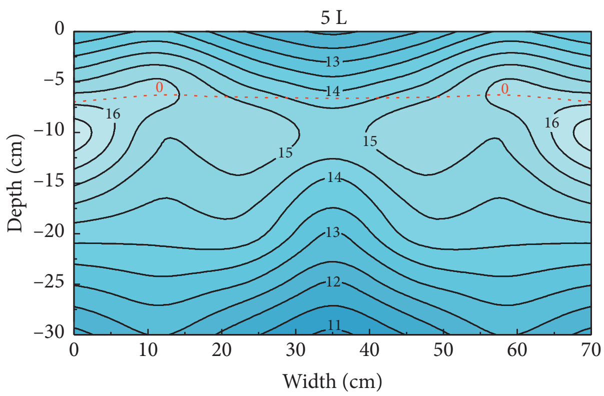

(c)

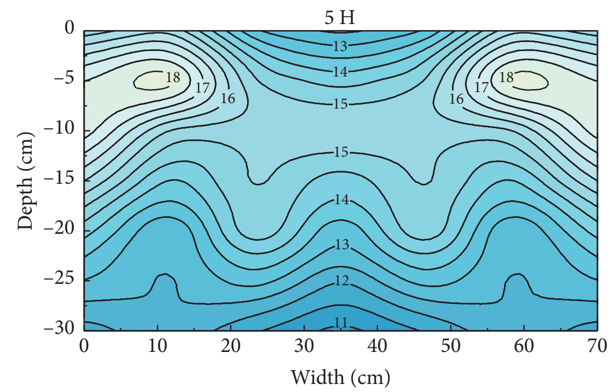

(d)

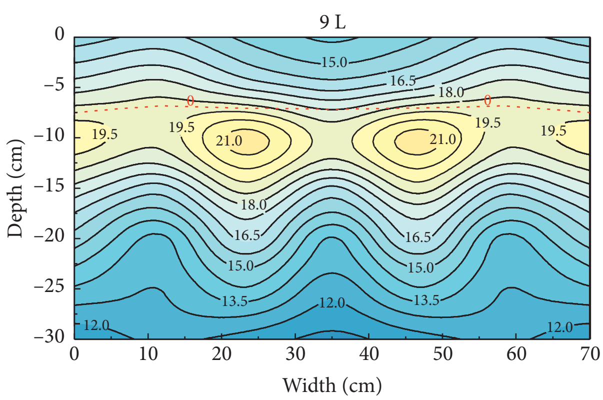

(e)

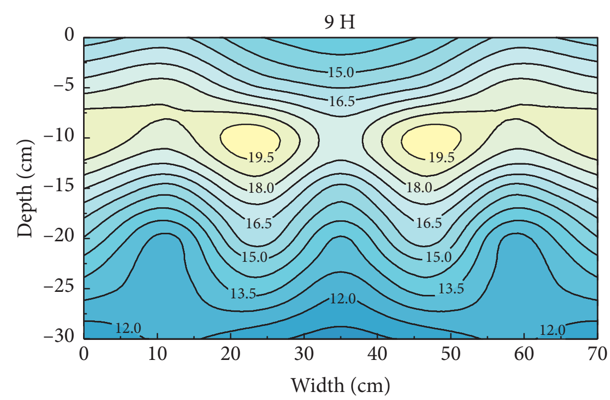

(f)

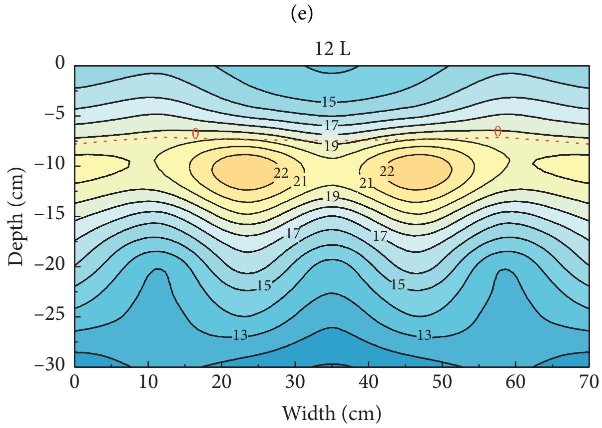

(g)

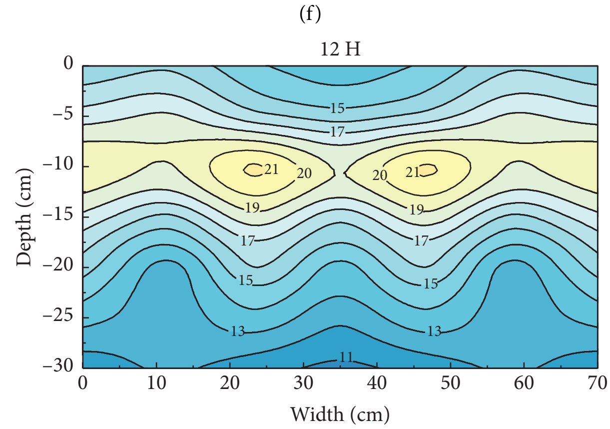

(h)

Figure 10: Continued.

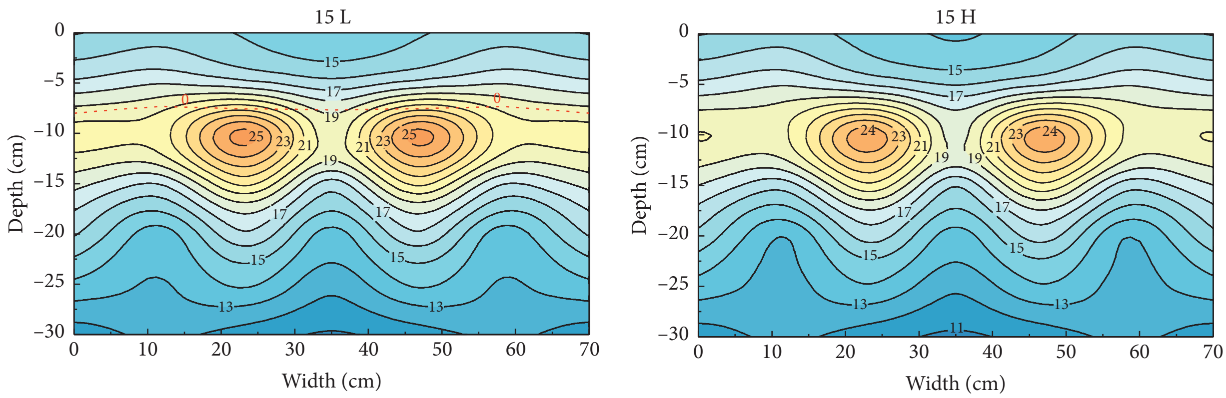

(i) (j)

Figure 10: Variation of the moisture field at low and high temperature extremes at different freeze-thaw cycles.

conductivity during freezing is greater than that during thawing, making the accumulated cold capacity during freezing more than the amount of cold capacity dissipated during thawing [30, 31].

3.2. Moisture Field in the Sample

3.2.1. Freeze-Thaw Cycles. Figure 10 shows the variation of moisture field at the H and L time in different freeze-thaw cycles under the no-load condition. It can be seen that the water content in the soil sample changes slightly during the first freeze-thaw cycle, and the water distribution is relatively uniform and close to the initial water content. The moisture field in the soil sample changes obviously with the increasing freeze-thaw cycles. Especially after nine freeze-thaw cycles, two areas of moisture accumulation appear in the soil sample which has distance from the surface of 8–15 cm and symmetric distribution. Additionally, there is little change in the moisture accumulation area but a continuous increase in water content with increasing freeze-thaw cycles. For example, the maximum water content in the moisture accumulation area at H and L time is 25.5% and 26.1% after 15 freeze-thaw cycles, which increased by 15.5% and 16.1% from the initial water content, respectively. The reason for this phenomenon is that the temperature gradient drives the moisture migrated to the freezing front during freezing [23, 25]. From Figure 10, it can be seen that the moisture accumulation area is close to the position of the 0°C line, which illustrates the relationship between the moisture migration area and temperature gradient. The moisture in the soil sample will flow downward under gravity during thawing, but the moisture flowing downwards is less than the migrating upward during the freezing due to the resistance effect of the soil; besides, since the soil is unsaturated in the model test, the moisture at the bottom of soil sample will also migrate upward under matric suction. By comparison, we found from Figure 10 that the moisture migrated upward during thawing is less than that during freezing. Therefore, during the freeze-thaw cycles, the moisture migrates towards the freezing front under various driving forces. Moreover, as the freeze-thaw cycles increase, the moisture migrating upward is more than that migrating downwards, which leads to the moisture gradually accumulating to form an accumulation area.

3.2.2. Freeze-Thaw Cycles under Dynamic Load. Figure 11 shows the variation of moisture field under dynamic load. It can be seen from the figure that the spatial distribution of water content in the soil sample is relatively uniform at the beginning of freeze-thaw. However, the water content significantly increases with the increasing freeze-thaw cycles, especially after nine freeze-thaw cycles. Three moisture accumulation areas appear in the soil sample: one is located below the vibration plate and the other two are located below the side of the vibration plate. Compared with Figure 10, it can be found that the locations of the moisture accumulation areas are lower under dynamic load than those under the no-load condition, which is mainly due to the soil near the vibration plate being compacted by the load, and the moisture-holding capacity is reduced. For example, during freezing of the 9th freeze-thaw cycles, the area with water content greater than 15% appeared in the range of 10–25 cm from the soil surface below the vibrating base plate and the area with water content greater than 15% appeared in the range of 10–30 cm from the soil surface below the side of the vibrating base plate. During the freezing process of the 15th freeze-thaw cycle, the area with water content greater than 19% appeared in the range of 10–22.5 cm from the soil surface below the vibrating base plate and the area with water content greater than 19% appeared in the range of 10–25 cm from the soil surface below the side of vibrating base plate. The variation in the water content and the range of the moisture accumulation area indicates that the moisture of the soil sample below the vibration plate tends to migrate upwards. The reason for this is that, on the one hand, the freeze-thaw cycle causes the moisture to migrate to the freezing front; on the other hand, the vibration load leads the adsorption force of the soil pores to increase [32, 33].

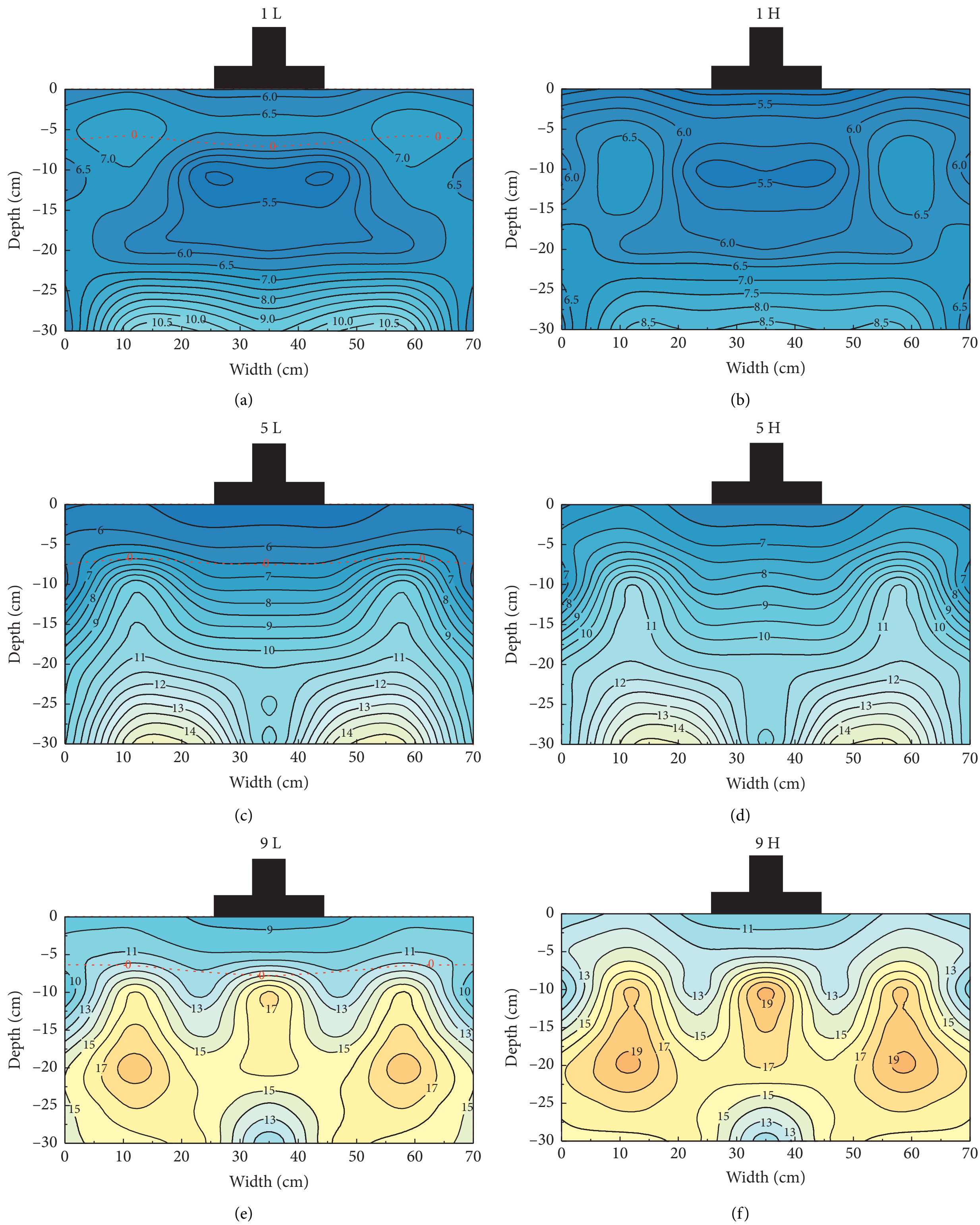

Figure 11: Continued.

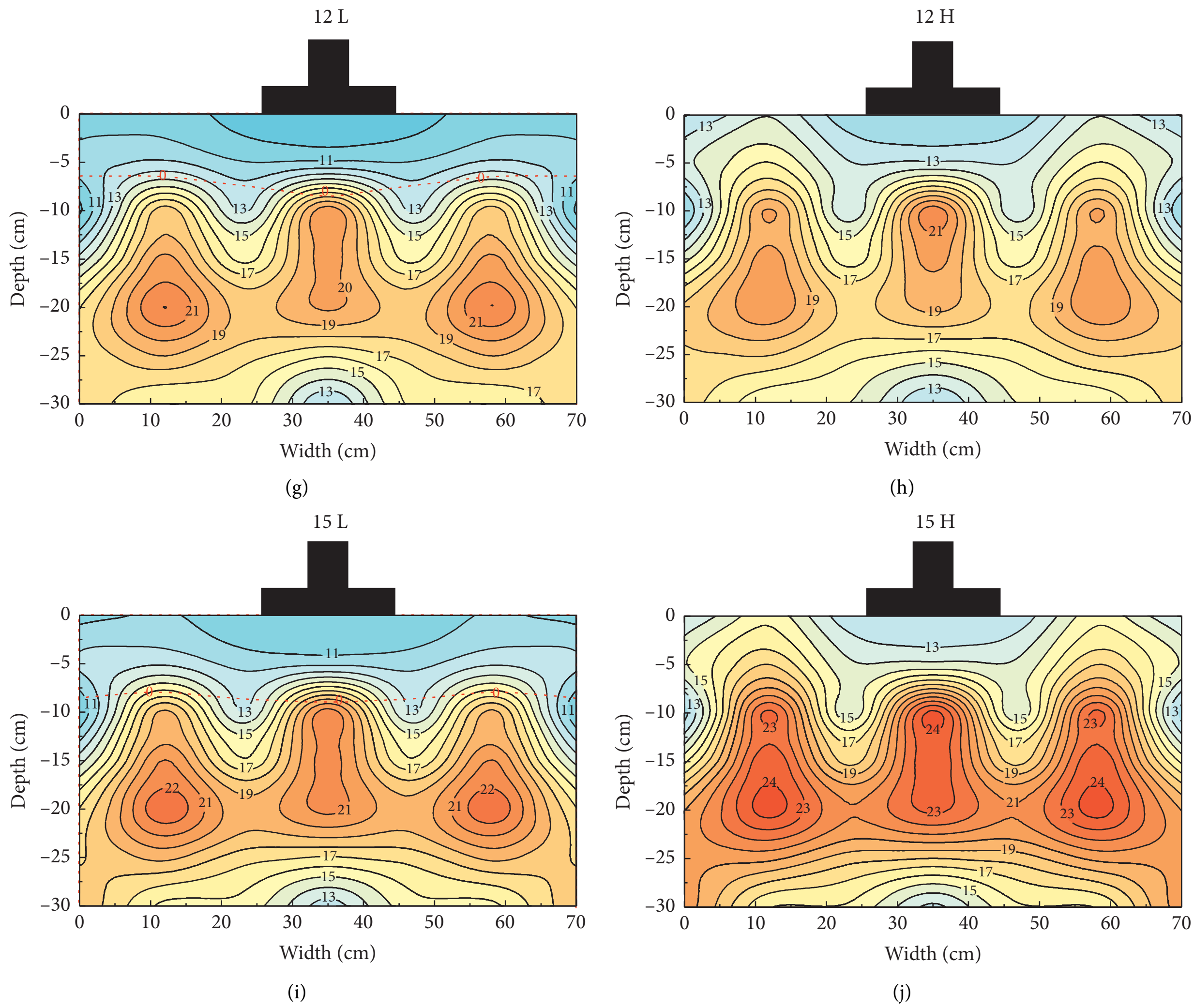

Figure 11: Variation of the moisture field at low and high temperature extremes under dynamic load and different freeze-thaw cycles.

Comparing the moisture field under the L and H time, Figure 11 shows that the difference of water content between freezing and thawing is slightly at the beginning of the freeze-thaw cycles. The difference gradually increases with the increase in freeze-thaw cycles. The reason for the variation is that when the ambient temperature is negative, the moisture in the soil migrates to the freezing front, leading to the reduction of water content in the middle of the soil sample. When the ambient temperature is positive temperature, the moisture in the soil under the vibration plate begins to move downwards and to both sides of the vibration plate due to the effect of dynamic load, which increases the water content in the middle of the sample. Besides, the dynamic load improves the adsorption force of the soil pores, which leads to the increase in the water content of the middle and upper parts of the soil sample. Compared with the moisture field under no load, it can be found that the water content of the moisture accumulation area during freezing is greater than that during thawing under the no-load condition and the water content of the moisture accumulation area during freezing is less than during thawing under dynamic load condition, which indicates that the dynamic load improves the adsorption potential energy of the soil pores and significantly enhances the capillary moisture migration during thawing [34].

4. Discussion

There are three moisture accumulation areas in the soil sample for the dynamic load test, which is different from the no-load test. The formation of the three water accumulation areas under dynamic load is closely related to the internal stress field in the soil sample. Figure 12 shows the internal stress distribution of the soil under dynamic load. It can be seen that both the longitudinal stress and transverse stress decrease with the increasing depth. The longitudinal stress is mainly concentrated under the vibration plate, and the curves bulge vertically downward, while the transverse stress is distributed as the symmetric saddle. It can be seen from Figure 12 that the soil on both sides of the vibration plate is subjected to higher stresses so that the soil here is compressed and the porosity is reduced; the moisture is squeezed and migrates to the place with less stress.

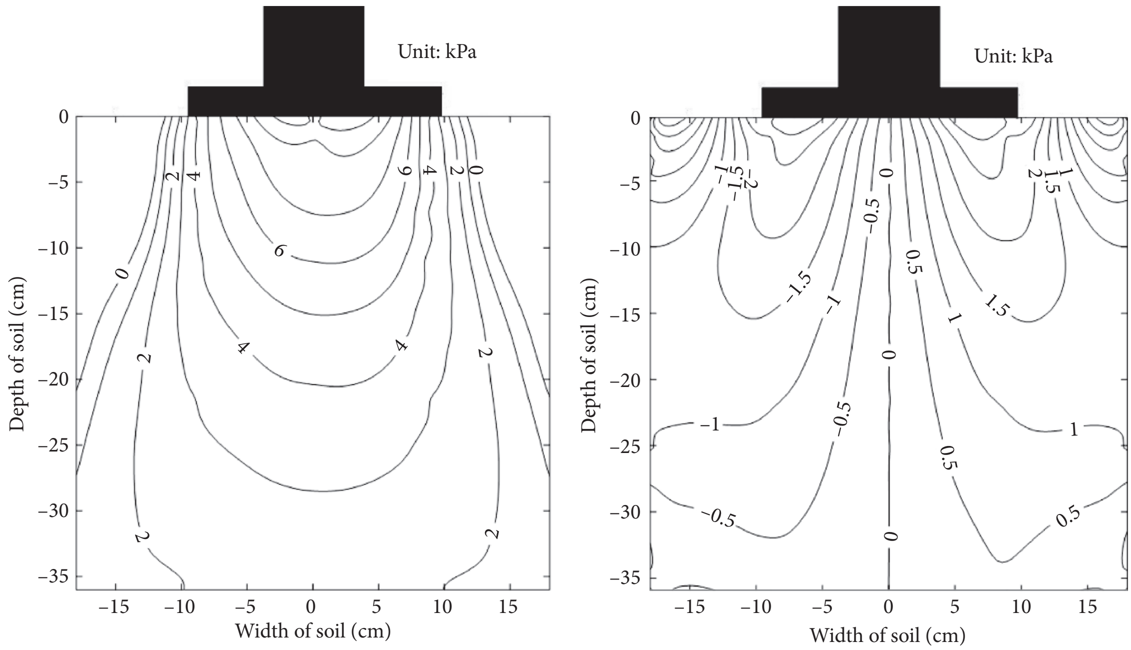

(a) (b)

Figure 12: Longitudinal stress fields (a) and transverse stress (b) in soil under the dynamic load.

In Figures 10 and 11, there are two moisture accumulation areas under the no-load condition. In comparison, there are three moisture accumulation areas under dynamic load, which is also caused by the variation of porosity due to load [31–33]. The stress compresses the soil, resulting in the extrusion of moisture from the soil and migrates to surrounding soil that creates moisture accumulation areas. This is the reason why the moisture accumulation area increases to three when the dynamic load is applied.

5. Conclusion

Two model tests were carried out to study the influence of dynamic load on the temperature and moisture fields of the soil during the freeze-thaw cycling and obtained the following conclusions:

(1) The temperature of the soil shows periodic change with the ambient temperature, and the closer to the surface of the soil, the greater the variation amplitude of temperature. The temperature in the soil sample gradually decreases with the increase in freeze-thaw cycles, which is caused by the accumulation of cold capacity in the soil sample during the freeze-thaw cycles.

(2) The moisture gradually migrates upward and accumulates near the freezing front to form moisture accumulation areas with the increasing freeze-thaw cycles.

(3) The dynamic load compacts the soil near the vibration plate that the position of moisture accumulation areas is lower than that under the no-load condition. Under the dynamic load, longitudinal and transverse stresses are generated in the soil sample, which causes three water aggregation areas to be formed, and the water content increases with the increase in freeze-thaw cycles in these areas.

(4) The water content of the moisture accumulation areas during freezing is greater than that during thawing under the no-load condition, while the water content of the moisture accumulation areas during the freezing period is less than that during thawing under dynamic load. This indicates that the dynamic load improves the adsorption potential energy of the soil pores and significantly enhances the capillary moisture migration during thawing.

Data Availability

The data used to support the findings of this study are included within the article.

Conflicts of Interest

The authors declare that they have no conflicts of interest.

Acknowledgments

This work was supported by the National Natural Science Foundation of China (No. 41630636).

References

[1] Y. Zhou, D. Guo, G. Qiu, G. Chen, and S. Shu, *Geocryology in China*, Science Press, Beijing, China, 2000.

[2] Z. Zhang, W. Ma, and J. Qi, "Structure evolution and mechanism of engineering properties change of soils under effect of freeze-thaw cycle," *Journal of Jilin University (Earth Science Edition)*, vol. 43, no. 6, pp. 1904–1914, 2013.

[3] J. Qi, P. A. Vermeer, and G. Cheng, "A review of the influence of freeze-thaw cycles on soil geotechnical properties," *Permafrost and Periglacial Processes*, vol. 17, no. 3, pp. 245–252, 2006.
[4] E. J. Chamberlain and A. J. Gow, "Effect of freezing and thawing on the permeability and structure of soils," *Developments in Geotechnical Engineering*, vol. 13, no. 1–4, pp. 73–92, 1979.
[5] D. R. Ingles, "Particle sorting and stone migration by freezing and thawing," *Science*, vol. 143, pp. 1616-1617, 1965.
[6] L. Fang, J. Qi, and W. Ma, "Freeze-thaw induced changes in soil structure and its relationship with variations in strength," *Journal of Glaciology and Geocryology*, vol. 34, no. 2, pp. 435–440, 2012.
[7] J. Qi, J. Zhang, and Y. Zhu, "Influence of freezing-thawing on soil structure and its soil mechanics significance," *Chinese Journal of Rock Mechanies and Engineering*, vol. 22, no. S2, pp. 2690–2694, 2003.
[8] N. Wang, Y. Mao, D. Zhang, G. Li, and Y. Mu, "Influence of freezing-thawing cycles on loess slope in seasonal frozen soil regions," *Highway traffic science and technology*, vol. 4, pp. 79–84, 2011.
[9] X. Xu, J. Wang, and L. Zhang, *Physics of Frozen Soils*, Science Press, Beijing, China, 2001.
[10] T. Zhang and P. Yang, "Effects of unilateralist freezing on the moisture migration of soil," *Journal of Nanjing Forestry University (Natural Science Edition)*, vol. 37, no. 1, pp. 117–121, 2013.
[11] J. M. Konrad and R. Morgenstern, "A mechanistic theory of ice lens formation in fine-grained soils," *Canadian Geotechnical Journal*, vol. 17, pp. 476–486, 1980.
[12] R. R. Gilpin, "A model for the prediction of ice tensing and frost heave in soils," *Water Resource Research*, vol. 21, pp. 281–296, 1985.
[13] R. J. Hanks, "Water vapor transfer in dry soil," *Soil Science Society of America Journal*, vol. 22, no. 5, pp. 372–374, 1958.
[14] X. Chen and J. Liu, *Frost Action of Soil and Foundation Engineering*, Science Press, Beijing, China, 2006.
[15] H. Zhang, T. Wang, and Y. Luo, "Experimental study on moisture migration of unsaturated loess under freezing effect," *Journal of Engineering Geology*, vol. 23, no. 1, pp. 72–77, 2015.
[16] J. Lu, M. Zhang, X. Zhang, and R. Yan, "Experimental study on the unfrozen water content and the freezing temperature during freezing and thawing processes," *Chinese Journal of Rock Mechanics and Engineering*, vol. 36, no. 7, pp. 1803–1812, 2017.
[17] H. Wei, J. Zhou, C. Wei, and P. Chen, "Experimental study of water migration in saturated freezing silty soil," *Rock and Soil Mechanics*, vol. 37, no. 9, pp. 2547–2552, 2016.
[18] F. Ming and D. Li, "Characteristics of moisture migration in freezing silty clay under the pressure," *Journal of Chang'an University (Natural Science Edition)*, vol. 35, no. 3, pp. 67–73, 2015.
[19] T. Wang and H. Lu, "Moisture migration in unsaturated loess considering temperature effect," *Rock and Soil Mechanics*, vol. 25, no. 7, pp. 1081–1084, 2004.
[20] L. Huang, Y. Shen, X. Huang, B. He, and X. Zhang, "Experimental study on force and deformation of soil during unidirectional frost heave under different paths," *Chinese Journal of Rock Mechanics and Engineering*, vol. 38, no. S2, pp. 3870–3882, 2019.
[21] G. Zhao, X. Tao, and B. Liu, "Experimental research on water migration in remolded soil during freezing and thawing process," *Journal of Central South University (Science and Technology)*, vol. 40, no. 2, pp. 519–525, 2009.
[22] G. Zhao, X. Tao, and B. Liu, "Experimental research on water migration in distributed soil during freezing and thawing process," *Chinese Journal of Geotechnical Engineering*, vol. 31, no. 12, pp. 1952–1957, 2009.
[23] L. Zhang, W. Ma, C. Yang, and C. Yuan, "Investigation of the pore water pressures of coarse-grained sandy soil during open-system step-freezing and thawing tests," *Engineering Geology*, vol. 181, pp. 233–248, 2014.
[24] Z. Zhou, W. Ma, S. Zhang, Y. Mu, and G. Li, "Effect of freeze-thaw cycles in mechanical behaviors of frozen loess," *Cold Regions Science and Technology*, vol. 146, pp. 9–18, 2018.
[25] F. Wang, S. Tang, and H. Wang, "Review of research on soil mobility in seasonally frozen area," *Journal of Irrigation and Drainage*, vol. 39, no. S1, pp. 51–55, 2020.
[26] GB/T50123-1999, *The Standard of Chinese Soil Test Method*, China Water & Power Press, Beijing, China, 2009.
[27] D. Xiao, W. Ma, S. Zhao, Z. Zhang, W. Feng, and L. Zhang, "Research on pore water pressure and moisture content in soil subjected to freeze-thaw cycles and loading action by model test," *Chinese Journal of Rock Mechanics and Engineering*, vol. 36, no. 4, pp. 977–986, 2017.
[28] M. Qiu, *Study on Post-Construction Settlement of Road under Traffic Load*, Zhejiang University, Hangzhou, China, 2011.
[29] M. Shen, Z. Zhou, and S. Zhang, "Effect of stress path on mechanical behaviours of frozen subgrade soil," *Road Materials and Pavement Design*, 2020.
[30] Z. Zhou, W. Ma, S. Zhang, Y. Mu, and G. Li, "Experimental investigation of the path-dependent strength and deformation behaviours of frozen loess," *Engineering Geology*, vol. 265, Article ID 105449, 2020.
[31] N. Li, B. Chen, and F. Chen, "Heat-moisture-deformation coupled for composite foundation in cold zone," *China Civil Engineering Journal*, vol. 36, no. 10, pp. 66–71, 2003.
[32] X. Xiao, X. Feng, L. Lin, B. Jiang, and Z. Feng, "An experimental research of vibration pore water pressure of remolded silt under low confining pressure: A case from Chengbei sea area," *Marine Geology & Quaternary Geology*, vol. 40, no. 4, pp. 214–222, 2020.
[33] D. Xiao, *Model Test Study on the Moisture, Pore Water Pressure Subjected to the Freeze-Thaw Cycle and Load Actions*, University of Chinese Academy of Sciences, Beijing, China, 2017.
[34] R. D. Jackson, "Water vapor diffusion in relatively dry soil: I. Theoretical considerations and sorption experiments," *Soil Science Society of America Journal*, vol. 28, no. 2, pp. 172–176, 1964.

Hindawi
Advances in Materials Science and Engineering
Volume 2021, Article ID 7723405, 16 pages
https://doi.org/10.1155/2021/7723405

Research Article

Effect of Freeze-Thaw Cycles on the Mechanical Properties of Polyacrylamide- and Lignocellulose-Stabilized Clay in Tibet

Haiping Shi,[1] Zhongyao Li,[1] Wenwei Li ,[2,3] Shaopeng Wang,[2,3] Baotian Wang,[1,2,3] and Peiqing Wang [1]

[1]*Water Conservancy Project and Civil Engineering College, Tibet Agricultural and Animal Husbandry University, Linzhi, China*
[2]*Key Laboratory of Ministry of Education for Geomechanics and Embankment Engineering, Hohai University, Nanjing, Jiangsu 210098, China*
[3]*Jiangsu Research Center for Geotechnical Engineering Technology, Hohai University, Nanjing, Jiangsu 210098, China*

Correspondence should be addressed to Peiqing Wang; 497450734@qq.com

Received 25 April 2021; Revised 17 August 2021; Accepted 8 September 2021; Published 28 September 2021

Academic Editor: Xiangtian Xu

Laboratory freezing experiments were conducted to evaluate the effect of polyacrylamide (PAM) and lignocellulose on the mechanical properties and microstructural characteristics of Tibetan clay. Direct shear and unconfined compressive tests and field emission scanning electron microscopy analyses were performed on clay samples with different contents of stabilizers. The test results show that the addition of PAM can improve the unconfined compressive strength and cohesion of Tibetan clay, but an excessive amount of PAM reduces the internal friction angle. After several freeze-thaw cycles, the unconfined compressive strength and cohesion of samples stabilized by PAM decrease significantly, while the internal friction angle increases. Samples stabilized by PAM and lignocellulose have higher internal friction angles, cohesion, and unconfined compressive strength and can retain about 80% of the original strength after 10 freeze-thaw cycles. PAM fills the pores between soil particles and provides adhesion. The addition of lignocellulose can form a network, restrict the expansion of pores caused by freeze-thaw cycles, and improve the integrity of PAM colloids. It is postulated that the addition of a composite stabilizer with a PAM content of 0.4% and a lignocellulose content of 2% may be a technically feasible method to increase the strength of Tibetan clay.

1. Introduction

Tibet is located in Southwest China, at a high altitude above sea level, with a dry and cold climate. In recent years, increasing state investment in infrastructure construction has led to increasing areas of Tibet being developed and utilized. This is particularly true for water conservancy projects, which have effectively alleviated energy shortage in the region. However, it should be noted that, compared with water conservancy construction in mild climate areas, water conservancy construction in cold regions should focus on the impact of climate, especially freezing and thawing.

Clay is widely distributed in Tibet and is often used as dam filling material or rockfill dam core material. However, clay is very sensitive to changes in temperature and moisture levels. Repeated freezing and thawing of clay soil affects its macrostructure and mechanical behavior. To reduce the adverse effects of freeze-thaw cycles and strengthen clay, many researchers have studied the effects of various additives to form geopolymers through chemical reactions. Ding et al. [1] studied the mechanical properties of fiber-cement composite-stabilized clay subjected to freeze-thaw cycles and proposed an empirical model for strength prediction accounting for the number of freeze-thaw cycles. Orakoglu et al. [2] studied the compressive strength of fly ash-lignin fiber-stabilized soil subjected to freeze-thaw cycles and found that the strength decreases as the blending ratio of lignin fiber increases. Hamza and Ali [3] discussed the effect of freeze-thaw cycles on the unconfined compressive strength of jute fiber, steel fiber, and lime-stabilized clay, and the results obtained from the study are fairly promising to employ jute fiber, steel fiber, and lime against freeze-thaw resistance. Due to the high cost of conventional additives and their adverse effects on the local environment, some researchers have proposed the use of nontraditional additives such as polymer materials to change the surface properties of soil particles and improve the strength of the soil. In recent years, polyacrylamide (PAM) has been widely used to improve the properties of clay because it is effective, nontoxic, and environmentally friendly.

PAM improves the resistance of soil to erosion, dispersion, collapse, and shearing. Since the 1950s, researchers [4–6] have established that PAM improves soil, reduces permeability, and improves durability. An increasing number of researchers have studied the applications of the chemical additive PAM in engineering. Lei et al. [7] studied the method of deep treatment of dredger fills with PAM, combined with vacuum preloading, by conducting indoor model tests. Gao et al. [8] discussed the mechanism of the effect of PAM on the compressibility of lime-stabilized soil. Different amounts of PAM were added to lime-stabilized soil, and the results showed that the addition of PAM to lime-stabilized soil reduces the mesopore volume and produces very large pores. Georgees et al. [9] assessed the benefits of using synthetic PAM additives to improve the performance-related properties of three pavement materials commonly used in Australian unsealed road construction. Jung and Jang [10] studied the soil-water characteristic curves for different concentrations of PAM. The results showed that PAM has a good irrigation effect with increasing water infiltration because of its ability to absorb and store a large amount of water. Zhang et al. [11] studied the consistency limit, compactness, microstructure, and cracking morphology of saline soil before and after PAM treatment. The results showed that PAM reduces the shrinkage strain and defects or pores in saline soil. Qi et al. [12] studied the cracking behavior of polyurethane (PU) and PAM-mixed clay soil for different polymer concentrations, using cracking tests for drying soil.

It is worth noting that Soltani-Jigheh et al. [13] studied the effects of water-soluble cationic PAM on the physical and mechanical properties of fine-grained soil under thawing and freeze-thaw conditions. The results showed that when soil undergoes a freeze-thaw process, the strength and durability of untreated and treated soil are greatly reduced, particularly after the first cycle. Hence, it is necessary to consider adding other modifiers to improve the applicability of environment-friendly polymer soil improvers such as PAM, to soil subjected to freeze-thaw cycles. In this study, clay samples were collected from Linzhi, Tibet, located 3500 m above sea level. The shear strength, unconfined compressive strength, and microstructure of the soil samples were studied for untreated soil and soil treated with PAM alone and with lignocellulose and PAM. A total of 10 types of stabilized soil samples with different proportions of modifiers were prepared. First, compaction and liquid-plastic limit tests were conducted on soil samples, and the compaction curves and liquid-plastic limits of the soil samples were determined. Next, changes in the mechanical properties of the samples after freeze-thaw cycles were studied by direct shear tests and unconfined compressive strength tests. Finally, the microstructures of the soil samples were studied using a scanning electron microscope.

2. Materials, Methods, and Testing Equipment

According to the standard of soil test method (GB/T 50123-2019) [14], the physical and mechanical properties of clay and stabilized clay in Tibet were studied per the standard of geotechnical tests, by laboratory tests including unconfined compression, direct shear, liquid-plastic limit, compaction, and scanning electron microscopy tests.

2.1. Materials

2.1.1. The Clay. In this paper, the test soil (as shown in Figure 1) is taken from Linzhi City, Tibet Autonomous Region, China, which is a kind of clay widely distributed in high-altitude areas of China. To purify the root systems existing in the soil, the obviously larger plant roots were picked out through the naked eye, and then the black plant root powder that is reunited in it after crushing was removed. In order to better understand its characteristics, the soil samples were crushed and passed through a sieve with a particle size of 2 mm for liquid-plastic limit, compaction, particle analysis, and specific gravity tests according to Test Methods of Soils for Highway Engineering (JTG E-2007) [15]. The basic property results are summarized in Table 1, the compaction curve is shown in Figure 2, and the gradation is shown in Figure 3.

2.1.2. Polyacrylamide. Polyacrylamide (PAM) (as shown in Figure 4) is mainly used in industry and is often used in soil stabilization. It is a high molecular weight synthetic waterborne polymer additive with low cost. It is adsorbed to the soil by an exchangeable cationic bridge through the connection between its ionic groups and negatively charged soil components. The polymer creates a long chain that binds soil particles together, improving soil resistance to erosion, dispersion, collapse, and shear. Table 2 shows the characteristic parameters of the PAM used in the test.

2.1.3. Lignocellulose. Lignocellulose (as shown in Figure 5) is an organic flocculent fiber material obtained from natural renewable wood by chemical treatment and mechanical processing. It is often used in road engineering; the material has a small specific gravity, large specific surface area, thermal insulation, sound insulation, insulation, and air permeability and can achieve resistance to low-temperature deformation and improve adhesion with minerals without adding any stabilizer. Table 3 shows the characteristic parameters of lignocellulose used in the experiment.

2.2. Testing Methods. Stabilized soil samples with different proportions of PAM were prepared. The amounts and proportions of different modifiers used to prepare the samples are listed in Table 4. Eighteen unconfined samples of stabilized soil with a height of 10 cm and a

Figure 1: The sampled clay.

Table 1: Basic properties of clay.

Natural dry density, ρ (g/cm^3)	Optimal moisture, content ω_{op} (%)	Maximum dry density, ρ_d (g/cm^3)	Plastic limit, ω_L (%)	Liquid limit, ω_P (%)	Plasticity index, I_L (%)	Specific gravity, G_s
1.52	14.3	1.605	19.8	27.4	7.6	2.74

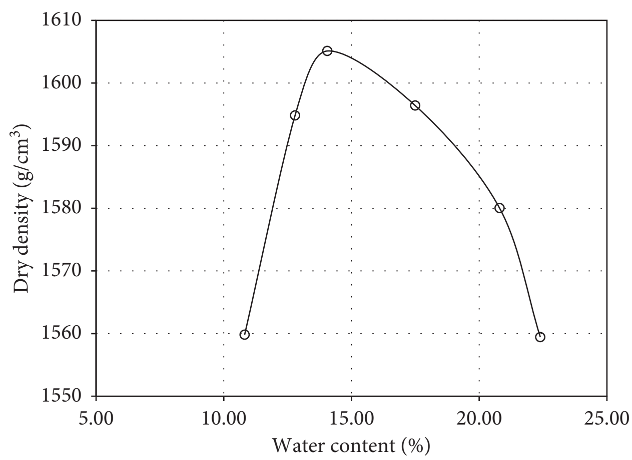

Figure 2: Compaction curve.

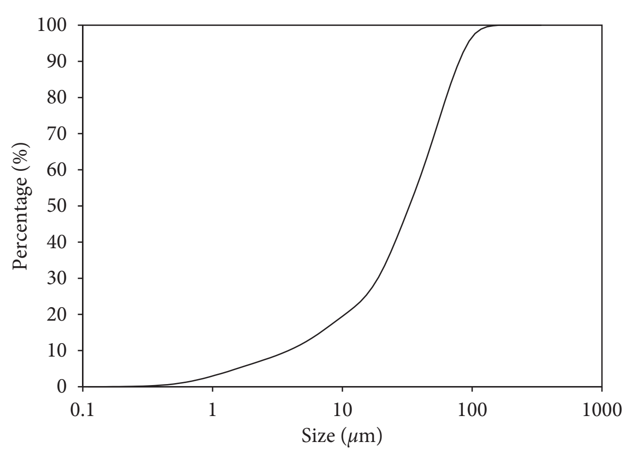

Figure 3: Gradation curve.

diameter of 5 cm were prepared based on optimal moisture content. Also, a quick shear of 72 samples with a height of 20 mm and a diameter of 61.8 mm was conducted. After curing for 7 days under standard curing conditions (as shown in Figure 6) following the Specification of Soil Test (JTGE51-2009) [16], the samples were subjected to freeze-thaw cycle tests of different durations. After a specified number of freeze-thaw cycles, follow-up direct shear, unconfined, and electron microscope scanning tests were conducted.

Figure 4: The PAM used in the test.

Table 2: Basic properties of PAM.

Average particle size (μm)	pH	Ion type	Molecular weight	Water solubility time (min)	Solid content
250~180	7.4	Cation ion	13 million	40	≥ 90%

Figure 5: The lignocellulose used in the test.

Table 3: The characteristic parameters of lignocellulose.

Fiber length (μm)	Density (g/cm^3)	Heat resistance (°C)	pH	Fiber content (%)	Color
200	1.76	260	6	99.5	White

Table 4: Sample preparation.

Test group	Sample number	PAM content (%)	Lignocellulose content (%)	Number of freeze-thaw cycles
Soil type A (nonstabilized soil)	1	0	0	0, 1, 3, 5, 7, and 10
Soil type B (PAM only)	2	0.1	0	
	3	0.2	0	
	4	0.4	0	
	5	0.6	0	
	6	0.8	0	
Soil type C (PAM and lignocellulose)	7	0.4	1	
	8	0.4	2	
	9	0.4	3	
	10	0.4	4	

Figure 6: Standard maintenance.

2.3. Freeze-Thaw Cycles. A self-made freeze-thaw cycle device, suitable for soil conditions in Tibet, tested freeze-thaw cycles. After the sample was prepared and cured for seven days, the sample was wrapped with plastic film and placed in a self-made closed test chamber with adjustable temperature for freeze-thaw cycle testing. For the freeze-thaw tests, the specimens were subjected to 1, 3, 5, 7, and 10 freeze-thaw cycles. According to meteorological data, summer temperatures in Tibet range between 18 and 24°C, and winter temperatures range from −13 to −22°C. To better simulate the freezing and thawing process of soil under local climatic conditions, during each freeze-thaw cycle, the samples were first frozen at −20°C for 12 hours and then thawed at 20°C for 12 hours. At the end of ten cycles, three unconfined samples and 12 quick shear samples were taken from each group, and follow-up experiments were conducted after determining the moisture content change.

2.4. Unconfined Compression Experiment. UCS tests have been conducted following the Specification of Soil Test (JTGE51-2009) [16]. The testing equipment used accurately and reliably measured a large data set (over 3000) for drawing the stress-strain curves for the tested specimens. The strain rate of this test was 1.5 mm/min, and the test stopped when axial deformation reached 25 mm. The peak load was determined according to the test data, and the unconfined compressive strength was calculated. Figure 7 shows the unconfined compression test samples, and Figure 8 shows the sample damaged during that test.

2.5. Direct Shear Test. The direct shear test is carried out in an electric quadruple shear apparatus according to soil test standard (GB/T 50123-2019) [14]; the test equipment and samples are shown in Figures 9 and 10. The effective consolidation pressures were 50, 100, 150, and 200 kPa. When the shear displacement reached 4 mm, the test stopped. Based on these data, the peak shear stresses under different vertical pressures were obtained, and linear fitting determined the cohesion and internal friction angle of the sample.

2.6. Scanning Electron Microscope Experiment. The microstructure of soil stabilized by different modifiers after the freeze-thaw cycle was analyzed by field emission scanning electron microscope (as shown in Figure 11). The sample destroyed by the unconfined compression test is dried in the oven. After the moisture is completely evaporated, the sample with a thickness of about 1 mm and a diameter of 5 mm is gilded to improve its electrical conductivity. Each sample was examined and imaged to depict its microstructure.

3. Results and Analysis

3.1. Effect of Freeze-Thaw Cycles on Shear Strength

3.1.1. Effect of Freeze-Thaw Cycles on the Shear Strength of PAM-Stabilized Soil Samples. Figures 12 and 13 show the variations of shear strength parameters of nonstabilized clay samples and PAM-stabilized clay samples with freeze-thaw cycles. As shown in Figure 14, when the number of freeze-thaw cycles is small, the internal friction angle of nonstabilized clay generally decreased as the number of freeze-thaw cycles increased, in agreement with previously reported results [17]. In this experiment, the internal friction angle decreased mainly in cycles 1–5, from 28.3° to 21.9° (22.6%), which was smaller than that of cohesion. The internal friction angle increased slightly after five freeze-thaw cycles and decreased only 17.6% after 10 freeze-thaw cycles. The phenomenon that the internal friction angle decreased slightly shows that the internal friction angle of soil is not significantly weakened by freeze-thaw cycles because the internal friction angle of soil relates primarily to the friction between soil particles. The first few cycles resulted in greater

Figure 7: Samples for unconfined compression test.

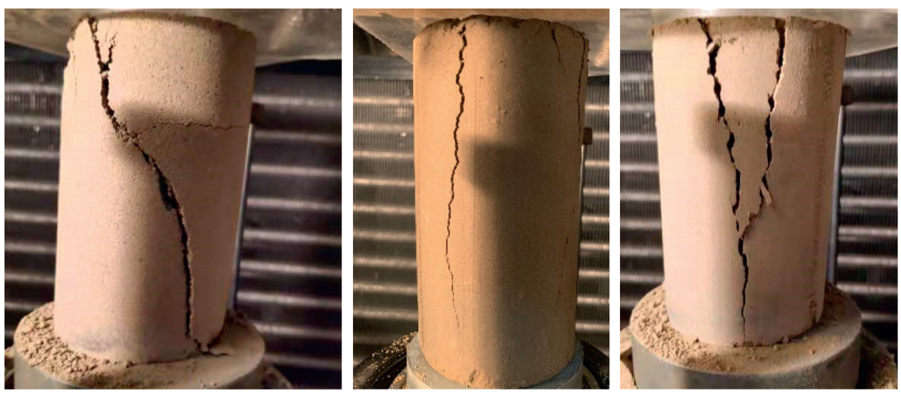

Figure 8: Samples damaged during unconfined compression test.

Figure 9: Ring cutter sample.

particle rearrangement caused by the freeze-thaw, so the angle of internal friction decreased and the rearrangement of soil particles gradually stabilized with additional cycles.

As shown in Figure 13, cohesion decreased for initial freeze-thaw cycles (<3). Soil specimens between 3–10 cycles yielded similar internal friction angles and ranged between 22.1 and 19.8 kPa. Compared with nonfreeze-thawed soil samples, cohesion decreased by 30% after three cycles and then stabilized. The total decrease in cohesion was as much as 41.2% after 10 cycles; hence, the effect of freeze-thaw cycles on the shear strength of soil cannot be ignored, and multiple freeze-thaw cycles can easily lead to slope landslides in practical engineering applications. For example, for the slope at K4213 + 50 of Sichuan-Tibet Highway 318 (as shown in Figure 14), due to shear strength decreases in the soil after multiple freeze-thaw cycles, the shallow soil becomes unstable and collapses along the slope direction due to gravity.

Freeze-thaw cycles can increase the internal friction angle of PAM-stabilized soil. Increasing the number of freeze-thaw cycles gradually increased the internal friction angle before stabilizing or decreasing slightly after seven cycles. However, the internal friction angle appeared to

Figure 10: Electric quadruple direct shear apparatus.

Figure 11: Field emission scanning electron microscope.

decrease for specimens with a large amount of PAM added (more than 0.6%), and the internal friction angle was lower for higher PAM content.

The reason for the above is that an excessive amount of added PAM affects the friction between soil particles and reduces the internal friction angle of soil. The internal friction angle gradually increased with more freeze-thaw cycles, which showed that the amount of PAM added should not be excessive. For example, when 0.8% of PAM was added, the internal friction angle of the unfrozen-thawed soil was 12.8°, which was 45% of that of nonstabilized soil.

The cohesion of PAM-stabilized samples decreased with an increase in the number of freeze-thaw cycles. The cohesion of samples with higher PAM levels decreased by more than 60% after three cycles and by more than 70% after 10 cycles. At a PAM level of 0.1%, cohesion decreased by 47% after ten freeze-thaw cycles due to the freezing of additional water in the pores of soil during the freeze-thaw cycles, which increased pore sizes after thawing and weakened the cementing effect of PAM on soil particles. The colloid produced by PAM also caused cracks, which led to changes in soil structure and decreased soil cohesion on a macroscopic level. Therefore, during construction processes, attention should be paid to the adverse effects of freeze-thaw cycles on PAM-stabilized clay.

3.1.2. Effect of Freeze-Thaw Cycles on the Shear Strength of PAM and Lignocellulose-Stabilized Specimens. Figures 15 and 16 depict the effect of freeze-thaw cycles on the shear strength parameters of composite-stabilized clay. Multiple freeze-thaw cycles had little effect on the internal friction

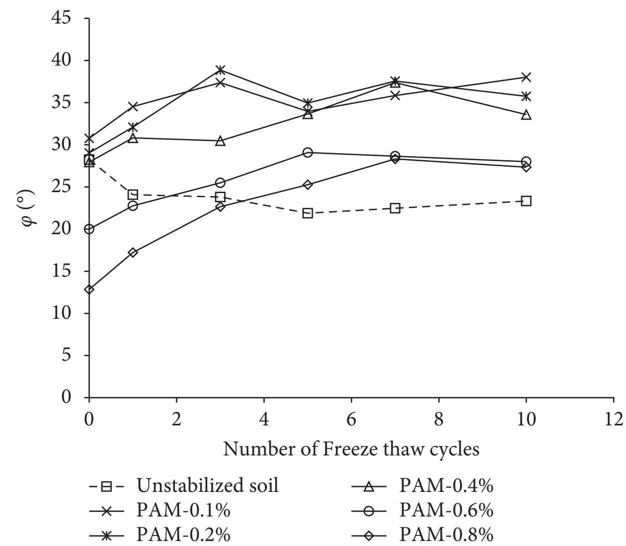

Figure 12: Changes of internal friction angle of PAM-stabilized samples with freeze-thaw cycles.

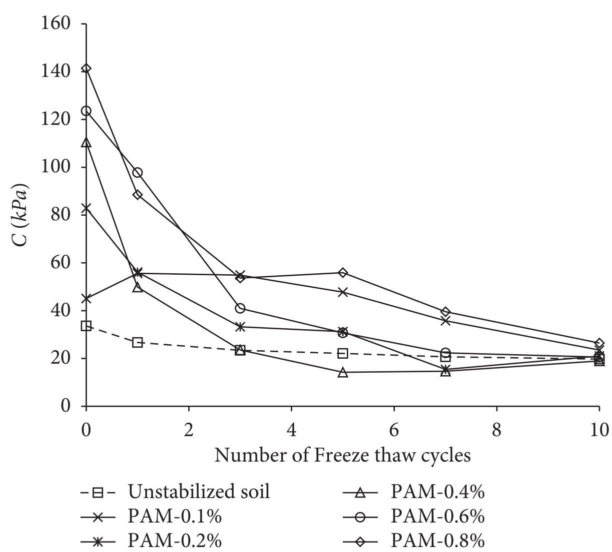

Figure 13: Changes of cohesion of PAM-stabilized samples with freeze-thaw cycles.

angle, even if the content of PAM added increased. As the number of freeze-thaw cycles increased, the shear strength parameters showed a fluctuating trend upward. The cohesion of stabilized PAM and lignocellulose samples decreased with additional freeze-thaw cycles. Only when the lignocellulose content was 2%, the cohesion of samples increased before three freeze-thaw cycles, after which it decreased. Cohesion decreased slightly after ten freeze-thaw cycles, in successive drops of 28.57%, 6.28%, 14.49%, and 21.66%. The change in cohesion was small when the amount of lignocellulose was 2%. Tibetan clay soils improved with the addition of composites such as PAM and lignocellulose and resulted in shear strength increases, stabilized soil, and maintained high cohesion after many freeze-thaw cycles. From a cost standpoint, 0.4% PAM and small amounts of lignocellulose (1%, 2%) are feasible for soil improvement. Such composite-based improvements not only increase the shear strength of Tibetan clay and prevent local slopes from being easily affected by freeze-thaw cycles but also provide a novel method for local soil improvement engineering and reduce environmental pollution.

3.2. Effect of Freeze-Thaw Cycles on Unconfined Compressive Strength

3.2.1. Effect of Freeze-Thaw Cycles on the Strength of Nonstabilized Specimens. Figure 17 shows the change in unconfined compressive strength of nonstabilized soil after freeze-thaw cycles. The results show that soil pores were enlarged due to interpore water freezing, but the increased pores could not be restored during the thawing process.

Figure 14: Shallow landslide due to multiple freeze-thaw cycles.

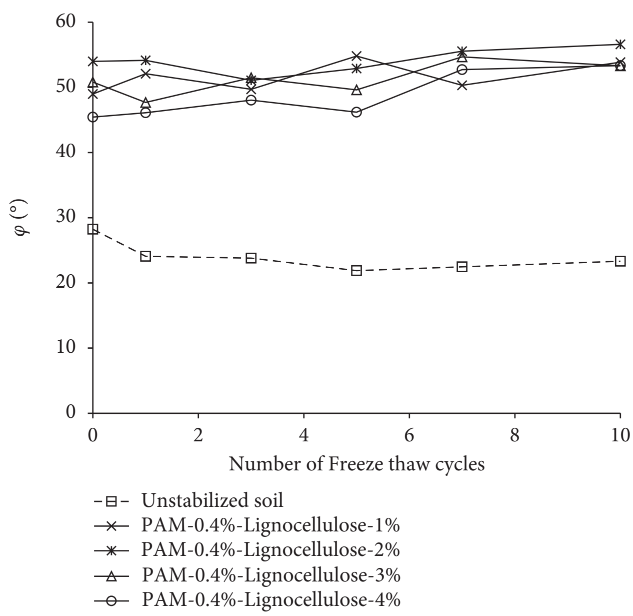

Figure 15: Changes of internal friction angle of stabilized PAM and lignocellulose samples with freeze-thaw cycles.

Hence, the spacing between soil particles increased, and the compressive strength of unstable clay decreased noticeably after the first freeze-thaw cycle from an initial value of 108.1 kPa to 61.6 kPa, representing a decrease of 43%. After the third freeze-thaw cycle, the strength increased slightly, which may be due to the low moisture content of the sample due to improper operation during sample preparation. After 5, 7, and 10 freeze-thaw cycles, the strength continued to decline. After 10 freeze-thaw cycles, the strength was only 42.4 kPa, less than 50% of the initial strength, indicating that the compressive strength of Tibetan clay is greatly affected by freeze-thaw cycles, and long-term freeze-thaw cycles decrease soil strength. Therefore, the improvement of this type of soil should be considered in engineering construction.

3.2.2. Effect of Freeze-Thaw Cycles on the Strength of PAM-Stabilized Samples. Figures 18 and 19 show the relationship between the unconfined compressive strength of PAM-stabilized samples and the number of freeze-thaw cycles. The characteristics of PAM help protect the local environment in Tibet and provide an alternative for soil from being contaminated by traditional modifiers such as cement and lime. The figures show that unconfined compressive strength increased significantly with additional PAM but decreased with an increasing number of freeze-thaw cycles. This observation indicated that PAM addition substantially improved the unconfined compression strength of clay in Tibet. This was attributed to the fact that the colloid formed by PAM wraps around the surface of soil

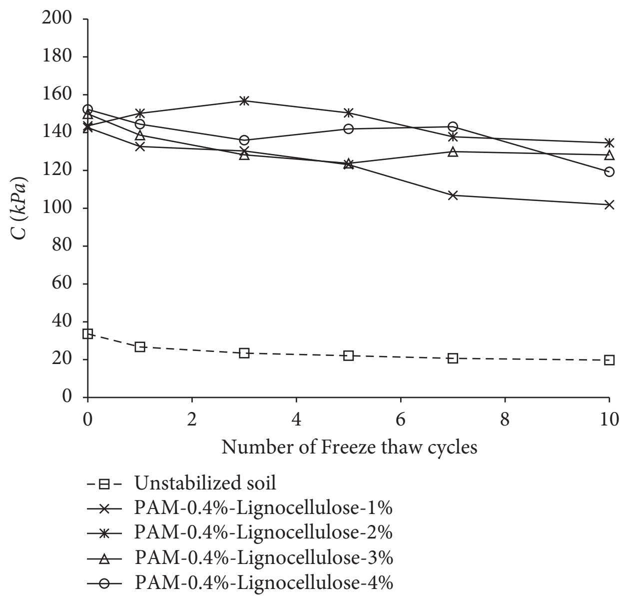

Figure 16: Changes of cohesion of stabilized PAM and lignocellulose samples with freeze-thaw cycles.

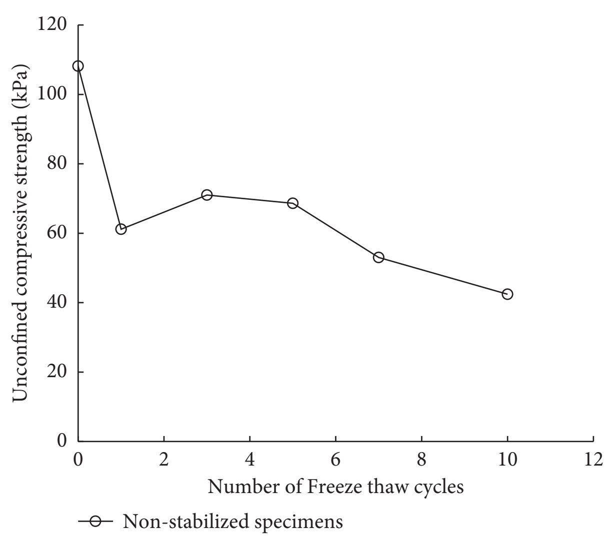

Figure 17: Changes of unconfined compressive strength of nonstabilized specimens with freeze-thaw cycles.

particles and provides adhesion between soil particles, fills soil pores, and forms a relatively stable spatial structure. This led to strength increases; however, subsequent freeze-thaw cycles weakened this filling and bonding effect.

As shown in Figures 18 and 19, after the addition of 0.1%, 0.2%, 0.4%, 0.6%, and 0.8% additives, the strength reached 245.3, 297.8, 343.4, 369.4, and 389.9 kPa, respectively, which was more than twice the strength of the nonstabilized samples. It is worth noting that when the added amount exceeded 0.4%, strength increases gradually decreased; this indicated that merely adding stabilizer was not cost-effective. As the number of freeze-thaw cycles increased, the strength of the stabilized samples with lower levels of added stabilizers increased slightly after the first freeze-thaw cycle because the initial freeze-thaw cycle played a role in healing the damaged structure [18], which resulted in a gradual soil strength increase. The first freeze-thaw cycle healed the soil structure and slightly increased the strength of the soil skeleton but was not observed in subsequent freeze-thaw cycles. When the added amount exceeded 0.4%, the strength of the samples decreased after the first freeze-thaw cycle, and the decrease was the most significant when the content was 0.8%. This indicated that excessive addition of PAM inhibited the healing of damaged structures by the initial freeze-thaw cycle.

To evaluate the magnitude of freeze-thaw weakening effects on degradation of unconfined compressive strength, the strength attenuation is defined as

$$\eta_i = \frac{q_i - q_0}{q_0}, \tag{1}$$

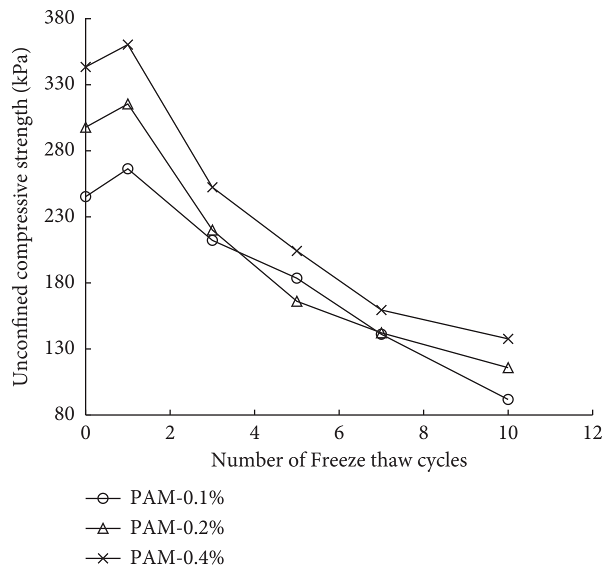

Figure 18: Changes of unconfined compressive strength of PAM (low content) stabilized specimens with freeze-thaw cycles.

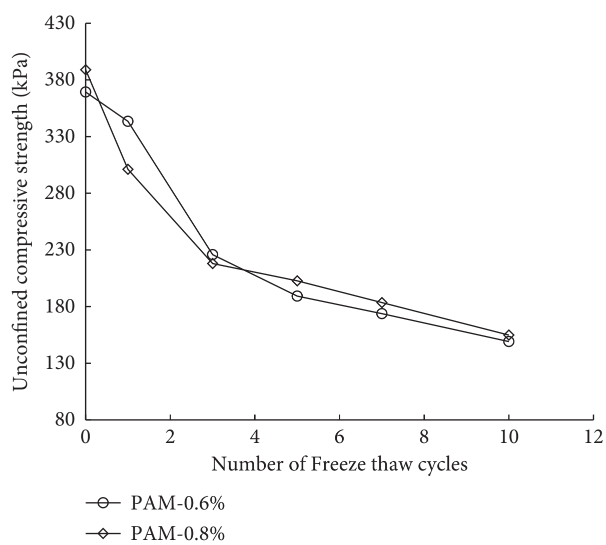

Figure 19: Changes of unconfined compressive strength of PAM (high content) stabilized specimens with freeze-thaw cycles.

where η_i is the strength decay rate after the i freeze-thaw cycle, q_i is the unconfined compressive strength after the i freeze-thaw cycle, and q_0 is the unconfined compressive strength before freeze-thaw cycles.

Figures 20 and 21 show the changes of strength decrease of PAM-stabilized specimens with freeze-thaw cycles. During freeze-thaw cycles, the strength of the samples stabilized with low amounts of stabilizers decreased significantly after three freeze-thaw cycles and continued to decrease after 5, 7, and 10 freeze-thaw cycles; however, the decrease was slightly less than previously observed. Among them, the strength attenuating trends of the samples stabilized, with 0.2% and 0.4% PAM content showing similar trends, but unconfined compressive strength trends differed slightly. The strength of high content samples decreased substantially after five freeze-thaw cycles but decreased slightly after each freeze-thaw cycle thereafter. The attenuating trend was linear overall. Although PAM effectively stabilized the sample strength initially, there was little difference between the strengths of the stabilized and non-stabilized soil samples after seven freeze-thaw cycles, and the strength was essentially the same after ten cycles. The strength attenuation reached 60%, indicating that freeze-thaw cycles had a significant effect on the cementation of PAM and that multiple freeze-thaw cycles greatly weakened the enhancing effect of the stabilizer. Although the PAM colloid filled the pores between soil particles and provided adhesion, it did not restrict soil particle displacement and limited the increase in the number of pores. After several freeze-thaw cycles, the cementation force of the colloid wrapped around the surface of the soil particles decreased. The strength of the PAM colloid between the pores

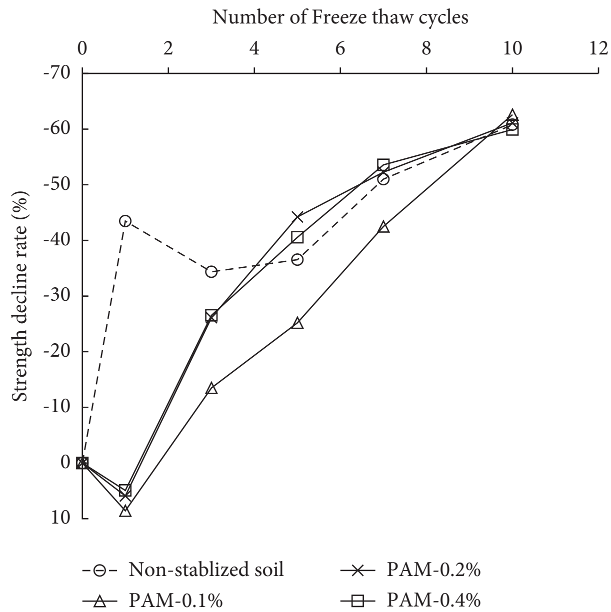

Figure 20: Changes of strength decrease of PAM (low content) stabilized specimens with freeze-thaw cycles.

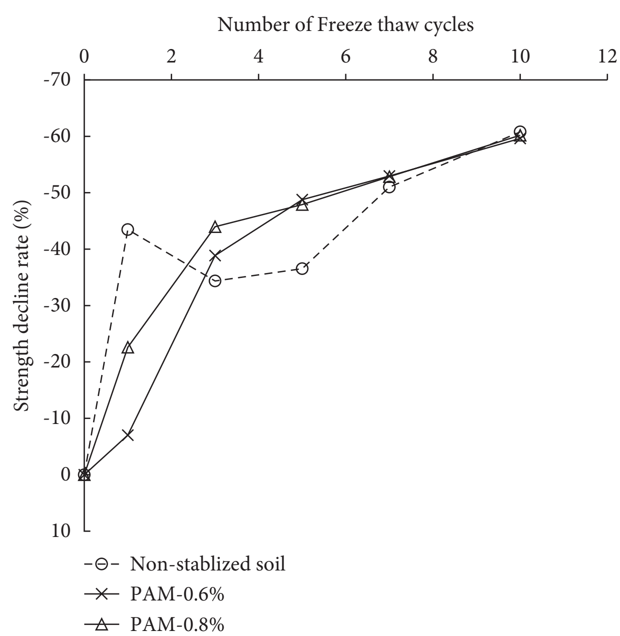

Figure 21: Changes of strength decrease of PAM (high content) stabilized specimens with freeze-thaw cycles.

decreased, and the soil readily fractured under an external load. The filling effect also decreased and a large stable structure did not form; hence, the adhesive force provided decreased significantly.

3.2.3. Effect of Freeze-Thaw Cycles on the Strength of PAM and Lignocellulose-Stabilized Samples. Figure 22 shows the relationship between the unconfined compressive strength of the samples stabilized with PAM and lignocellulose and the number of freeze-thaw cycles. Lignocellulose addition improved the frost resistance of the samples. The unconfined compressive strength increased significantly with lignocellulose addition. As shown, after adding 0.4% PAM and 1, 2, 3, and 4% lignocellulose, the strength of the unfreeze-thawed cyclic sample reached 493.8, 562.8, 594.9, and 615.1 kPa, respectively, and the strength was more than 1.5 times than when the level of PAM was 0.4%. Also, the strength of the sample increased gradually during the first three freeze-thaw cycles; this indicated that lignocellulose addition benefitted the aging of the freeze-thaw cycles and stabilized the soil skeleton strength. After the first three freeze-thaw cycles, the strength of the sample started decreasing, but the decrease was not significant and

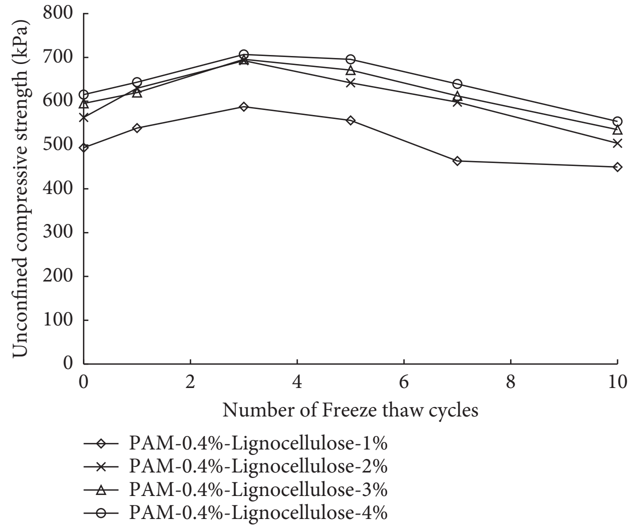

Figure 22: Changes of unconfined compressive strength of PAM and lignocellulose-stabilized specimens with freeze-thaw cycles.

much lower than that of each freeze-thaw cycle of the sample stabilized by PAM alone. This was due to wood fiber, which formed a network between the soil particles that partially limited dislocation between the particles, protected the colloid formed by PAM, and increased the energy needed to break the stable specimen.

When the content of lignocellulose exceeded 1%, strength increases decreased significantly and were seen in the strength change of the sample stabilized with a lignocellulose content of 2%, which remained the same after several freeze-thaw cycles. This indicated that a lignocellulose content of 2% (and a PAM level of 0.4%) significantly improved the frost resistance of the soil.

As shown in Figure 23, the attenuation of the strength of the composite-stabilized samples differed from that of nonstabilized soil and soil stabilized with PAM alone. Before three freeze-thaw cycles, the strength of the samples with 2% lignocellulose increased the most, and those increases were 23% and 14.9% after three cycles. In subsequent freeze-thaw cycles, the strength of all stabilized samples decreased continuously, but the rate of strength attenuation after ten freeze-thaw cycles was not high, ~10%, which was much smaller than nonstabilized soil and soil stabilized with PAM alone. This indicated that lignocellulose addition stabilized the frost resistance of the sample and helped maintain a high strength of PAM colloids with an optimal lignocellulose level of 2%.

3.3. Microscopic Analysis. To better understand the improvement due to different modifiers after freeze-thaw cycles, the microstructure of nonstabilized soil, PAM-stabilized soil, PAM, and lignocellulose composite-stabilized soil before and after a freeze-thaw cycle was analyzed by field emission scanning electron microscopy; the porosity and pore sizes of the sample cross-sections were calculated by Nano Measurer software and the MATLAB program.

Figure 24 shows the microstructural images of nonstabilized soil samples before and after freeze-thaw cycles. Due to the high degree of compaction, the soil particle samples without undergoing a freeze-thaw cycle were closely arranged and the pores were small. Among them, the maximum pore diameter was 17.2 μm, the average pore diameter was 6.43 μm, and the porosity was 0.12.

However, after many freeze-thaw cycles, the untreated samples had porous and discontinuous layered textures, and there were many pores (the maximum pore diameter was 32.4 μm, the average pore diameter was 13.7 μm, and the porosity was 0.26.) with many small particles on the surface. There were many pores between the particles due to pore enlargement after water freezing, which led to soil particle rearrangement; hence, the strength of the soil skeleton decreased after freeze-thaw cycles.

Figure 25 shows the microstructure of a PAM-stabilized soil sample before and after several freeze-thaw cycles. After adding PAM, a portion of the soil particles were coated with a colloid layer formed by PAM (as shown in Figure 25(a)), which resulted in a glue-like strong bond between particles. This led to tighter bonds between individual particles, the contact area between the adjacent particles increased and increased the energy needed for dislocating the soil particles. The inherent strength of the clay increased. Also, due to the high density of the samples, flake and needle-like PAM colloids were observed in the pores (as shown in Figure 25(b)), indicating that PAM colloids were filled with micropores during hydration; hence, the addition of PAM stabilized the strength of clay. After several freeze-thaw cycles, the PAM colloid was affected. As shown in Figure 25(c), the colloid wrapped around the surface layer of the soil particles was not smooth. Some pores between soil particles remained, and it was apparent that there were colloids in the pores, but most of the colloids were broken and did not form a good whole, indicating that the connection of the colloids was destroyed by repeated freeze-thaw cycles. Although the addition of PAM absorbed some

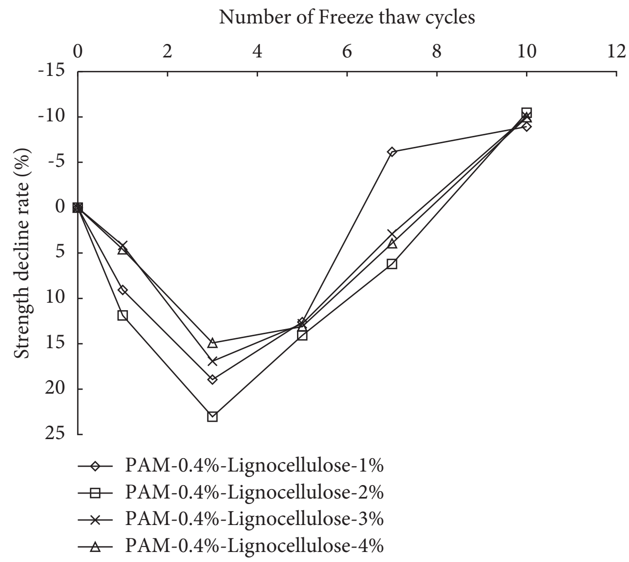

Figure 23: Changes of strength decrease of PAM and lignocellulose-stabilized specimens with freeze-thaw cycles.

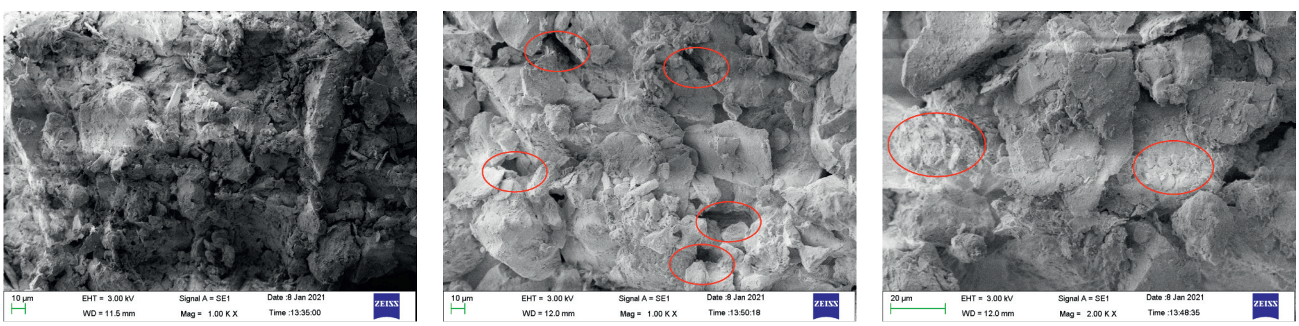

(a) (b) (c)

Figure 24: The microstructure of nonstabilized soil. (a) 0 cycles. (b) 7 cycles. (c) 10 cycles.

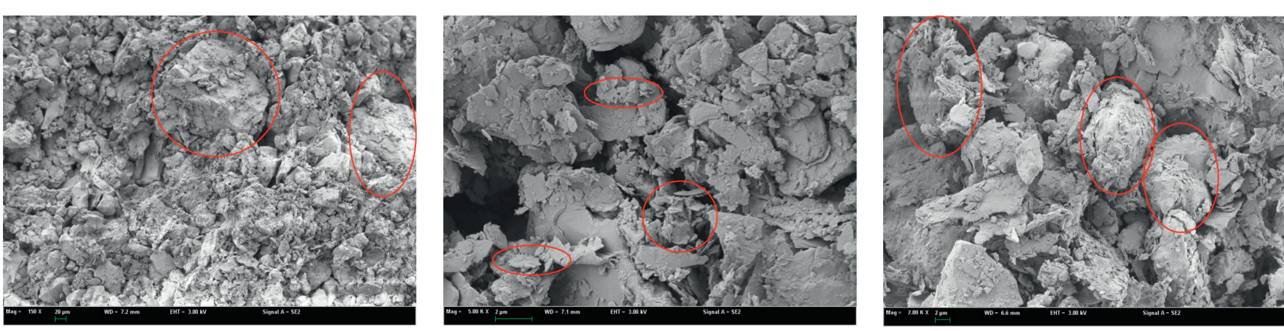

(a) (b) (c)

Figure 25: The microstructure of PAM-stabilized soil. (a) 0 cycles. (b) 0 cycles. (c) 10 cycles.

water in the pores and reduced pore increases during the freeze-thaw process, most of the colloids were fractured after repeated cycles, and the cohesion between soil particles decreased significantly. The effect of pore-filling was also poor; hence, the soil improvement effects of PAM after several cycles were limited.

Figure 26 shows the soil sample microstructures stabilized by PAM and lignocellulose before and after multiple freeze-thaw cycles. The gap between soil particles changed slightly before and after these cycles because the added fibers were intertwined with each other to form a network; hence, the gap between soil particles did not increase significantly after repeated cycles. Discrete fibers were intertwined with each other to form a spatial stress network between soil particles that contributed to maintaining its shear strength. Under external loads, when relative displacement between a

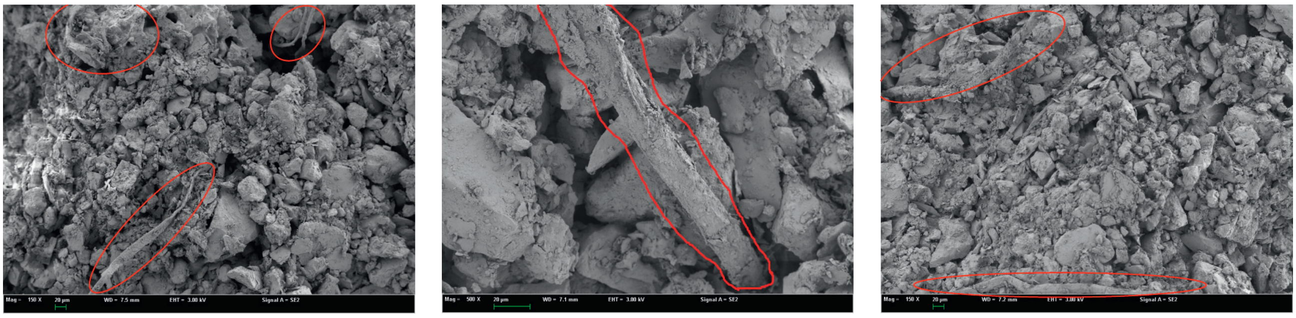

(a) (b) (c)

Figure 26: The microstructure of PAM and lignocellulose composite-stabilized soil. (a) 0 cycles. (b) 3 cycles. (c) 10 cycles.

fiber in the network and soil particles occurred, other adjacent fibers limited relative displacement and restricted the rearrangement of soil particles during the freeze-thaw cycle. Consequently, soil particles were not easy to move and the strength decreased by a smaller amount. Also, due to the constraint of the fiber network, increasing the number of pores was limited, the cement was not easily fractured, the colloid formed by PAM had good integrity, the effect of filling pores improved, and cohesion was conserved between the particles.

4. Conclusions

In this study, the change in the strength of clay samples stabilized by PAM, PAM and lignocellulose subjected to freeze-thaw cycles, and the mechanism of action of soil improvers were studied using unconfined compression and direct shear tests and scanning electron microscopy. The main conclusions of this study are as follows:

(1) The addition of PAM can improve the unconfined compressive strength and cohesion of Tibetan clay, but a large amount of PAM reduces the internal friction angle of soil. With an increase in the number of freeze-thaw cycles, the unconfined compressive strength and cohesion of clay samples stabilized by PAM decrease significantly, but the internal friction angle increases.

(2) Compared with nonstabilized clay, PAM and lignocellulose composite-stabilized clay has a higher internal friction angle, cohesion, and unconfined compressive strength and can retain about 80% of its original strength after 10 freeze-thaw cycles.

(3) PAM fills the pores between soil particles and provides adhesion. The adhesion between particles is higher, the contact area between the adjacent particles increases, and the strength of the sample increases. However, after several freeze-thaw cycles, the bonds between soil particles are destroyed and most of the colloids are fragmented. The addition of lignocellulose can form a network, restrict the expansion of pores caused by freeze-thaw cycles, and improve the integrity of PAM colloids.

(4) Based on test data and project cost considerations, it is recommended that a compound stabilizer consisting of 0.4% PAM and 2% lignocellulose be used to improve clay in Tibet, control local slopes, reduce landslide disasters caused by freeze-thaw cycles, improve roadbed strength, and reduce environmental pollution.

Data Availability

The results of the experiments used in this paper are available from the corresponding author by request.

Conflicts of Interest

The authors declare that they have no conflicts of interest regarding the publication of this paper.

Acknowledgments

The authors would like to acknowledge the financial support from the Key Projects of Natural Science Foundation of Tibet Autonomous Region (XZ 2019 ZR G-56(Z)) and the Fourth Batch of Flexible Talent Introduction Project of Tibet University of Agriculture and Animal Husbandry (Project No. 604419046).

References

[1] M. Ding, F. Zhang, X. Ling, and B. Lin, “Effects of freeze-thaw cycles on mechanical properties of polypropylene fiber and cement stabilized clay,” *Cold Regions Science and Technology*, vol. 154, pp. 155–165, 2018.

[2] M. E. Orakoglu, J. Liu, R. Lin, and Y. Tian, “Performance of clay soil reinforced with fly ash and lignin fiber subjected to freeze-thaw cycles,” *Journal of Cold Regions Engineering*, vol. 31, no. 4, pp. 1–18, Article ID 04017013, 2017.

[3] G. Hamza and K. Ali, “Effect of freeze–thaw cycles on unconfined compressive strength of fine-grained soil treated with jute fiber, steel fiber and lime,” *Cold Regions Science and Technology*, vol. 106, no. 1, pp. 55–65, 2014.

[4] R. A. Ruehrwein and D. W. Ward, “Mechanism of clay aggregation by polyelectrolytes,” *Soil Science*, vol. 73, no. 6, pp. 485–492, 1952.

[5] R. E. Terry and S. D. Nelson, “Effects of polyacrylamide and irrigation method on soil physical properties,” *Soil Science*, vol. 141, no. 5, pp. 317–320, 1986.

[6] T. Stutzmann and B. Siffert, “Contribution to the adsorption mechanism of acetamide and polyacrylamide on to clays,” *Clays and Clay Minerals*, vol. 25, no. 6, pp. 392–406, 1977.

[7] H. Lei, Y. Xu, X. Li, M. Jiang, and L. Liu, “Effect of polyacrylamide on improvement of dredger fill with vacuum preloading method,” *Journal of Materials in Civil Engineering*, vol. 31, no. 9, pp. 1–8, Article ID 04019193, 2019.

[8] M. Gao, F. Yuan, Y. Xue, and P. Guan, “Effect of polyacrylamide on compression rate of lime stabilized soil,” *Sains Malaysiana*, vol. 49, no. 8, pp. 1925–1934, 2020.

[9] R. N. Georgees, R. A. Hassan, R. P. Evans, and P. Jegatheesan, “An evaluation of performance-related properties for granular pavement materials using a polyacrylamide additive,” *International Journal of Pavement Engineering*, vol. 19, 2018.

[10] J. Jung and J. Jang, ““Soil–water characteristic curve of sediments containing a polyacrylamide solution,” *Géotechnique Letters*, vol. 6, no. 1, pp. 1–6, 2016.

[11] T. Zhang, Y. Deng, H. Lan et al., “Experimental investigation of the compactability and cracking behavior of polyacrylamide-treated saline soil in gansu province, China,” *Polymers*, vol. 11, no. 1, p. 90, 2019.

[12] C. Qi, Y. Bai, J. Liu et al., “Desiccation cracking behavior of polyurethane and polyacrylamide admixed clayey soils,” *Polymers*, vol. 12, no. 2398, p. 18, 2020.

[13] H. Soltani-Jigheh, M. Bagheri, and A. R. Amani-Ghadim, “Use of hydrophilic polymeric stabilizer to improve strength and durability of fine-grained soils,” *Cold Regions Science and Technology*, vol. 157, pp. 187–195, 2019.

[14] Ministry of Construction P.R. China, “Standard for Soil Test Method,” Tech. Rep. GB/T 50123-2019, Ministry of Construction P.R. China, Beijing, China, 2019.

[15] Ministry of Transport P.R. China, *Test Methods of Soils for Highway Engineering*, Ministry of Transport P.R. China, Beijing, China, 2007.

[16] Ministry of Transport P.R. China, *Test Methods of Materials Stabilized with Inorganic Binder for Highway Engineering*, Ministry of Transport P.R. China, Beijing, China, 2009.

[17] Y. Han, Q. Wang, N. Wang et al., “Effect of freeze-thaw cycles on shear strength of saline soil,” *Cold Regions Science and Technology*, vol. 154, pp. 42–53, 2018.

[18] G. Yan, H. Zhang, and X. Wang, “Study on freeze-thaw durability of Earth Building sites in Arid area,” *Rock and Soil Mechanics (Chinese)*, vol. 32, no. 8, pp. 2267–2273, 2011.

Hindawi
Advances in Materials Science and Engineering
Volume 2021, Article ID 7185616, 13 pages
https://doi.org/10.1155/2021/7185616

Research Article

Experimental and Numerical Analyses of the Thermal Regime of a Traditional Embankment in Permafrost Regions

Qihang Mei,[1,2] **Ji Chen**,[1,2] **Shouhong Zhang**,[3] **Xin Hou**,[1,2] **Jingyi Zhao**,[1,2] **Jinchang Wang**,[3] **Haiming Dang**,[3] **Guojun Liu**,[1] **and Guilong Wu**[1]

[1]*Beiluhe Observation and Research Station of Frozen Soil Engineering and Environment, State Key Laboratory of Frozen Soil Engineering, Northwest Institute of Eco-Environmental and Resources, Chinese Academy of Sciences, Lanzhou 730000, China*
[2]*University of Chinese Academy of Sciences, Beijing 100049, China*
[3]*China Railway Qinghai-Tibet Group Co., Ltd., Xining 810007, China*

Correspondence should be addressed to Ji Chen; chenji@lzb.ac.cn

Received 6 May 2021; Accepted 30 June 2021; Published 23 July 2021

Academic Editor: Xiangtian Xu

Traditional embankment is widely used in the permafrost regions along the Qinghai-Tibet Railway (QTR) because of its simple construction and lower cost. However, this form of embankment has insufficient ability to resist external thermal disturbance. To clarify the thermal characteristics of traditional embankment under climate warming, the ground temperature change process of section K1068 + 750 of the QTR was analysed in this study. Based on the field monitoring data from 2006 to 2019 and the established heat transfer model, the past and future changes of permafrost thermal regime under the embankment were analysed. The results show that the degradation of permafrost under the embankment is faster than that under the undisturbed site due to the combined of embankment construction and climate warming. The sunny-shady slope effect related to embankment orientation makes the distribution of permafrost temperature under embankment asymmetric. In the long term, permafrost degrades both under the undisturbed site and embankment. The continuous degradation of permafrost causes the settlement and deformation of embankment, especially the asymmetric degradation of permafrost on sunny side and shady side will cause longitudinal cracks on the embankment. Therefore, timely application of strengthening measures which can slow down the degradation of permafrost and adjust the uneven ground temperature on the sunny and shady sides under the embankment is of great significance to the safety of the traditional embankment.

1. Introduction

The Golmud-Lhasa section of the Qinghai-Tibet Railway (QTR) with a length of 1142 km was completed and started operation in 2006 [1]. It covers 550 km of continuous permafrost regions, 50% of which belong to warm permafrost areas with the mean annual ground temperature (MAGT) higher than −1°C [2]. The high thermal sensitivity of warm permafrost makes the stability of embankment in these areas significantly affected by changes in the external environment temperature [3]. Many studies based on field monitoring have shown that with the climate warming and the change of land-surface energy balance caused by the construction of embankment, the permafrost along the QTR has been extensively degraded, especially under the traditional embankment [4–7]. The degradation of permafrost has caused the settlement deformation of the embankment, which reduces the smoothness of the railway track and poses a threat to the safe operation of the train [8–11]. In addition, in the section of the QTR that is not in the north-south direction, there is a sunny and shady slope effect caused by different heat absorption on both sides of embankment that makes the ground temperature under two sides of the embankment slope different [12]. The asymmetry of the permafrost temperature distribution on the sunny and shady sides of the embankment causes asymmetrical settlement and eventually forms longitudinal cracks which may make the embankment fail [13, 14]. Considering the above problems faced by the embankment of the QTR under climate warming, it is necessary to timely evaluate the stability of the embankment that may be unstable.

The study on the embankment stability of the QTR is mainly carried out through field monitoring and numerical simulation. Most of the monitoring data of ground temperature and deformation of the embankment come from the long-term monitoring program of the QTR which started to work in October 2005. Based on ground temperature and deformation data, the researchers analysed the thermal response of permafrost under the embankment to climate and human activity [15–17]. Furthermore, by comparing the thermal stability and deformation stability of different embankment forms, the cooling ability of each structure is evaluated [5, 18–20]. However, due to the limitations of field conditions and the lack of enough monitoring data, methods such as numerical simulations other than field monitoring have also been used to study the embankment stability in permafrost regions. For example, for some new forms of embankment, the stability can be determined by establishing a suitable mathematical model before the embankment construction [21–24]. The numerical simulation can also be used to analyse the degradation progress of permafrost under the embankment and the embankment deformation in the future under climate change, so as to find the embankment that needs to be strengthened in time [25–27]. The simultaneous use of field monitoring and numerical simulation in the study not only helps to solve more engineering problems, but also improves the accuracy of the conclusions.

In this paper, the change process of ground temperature is analysed based on the ground temperature monitoring data of section K1068 + 750 from 2006 to 2019. In addition, a heat transfer model is established to predict the change of thermal regime of the section in the next few decades. The research includes the degradation characteristics of permafrost under the embankment and the difference of permafrost temperature distribution on both sides of the embankment caused by the sunny-shady slope effect. The analysis results can be used as the basis for the selection of strengthening measures for this section and provide reference for the stability evaluation of similar projects in the future.

2. Field Observations

2.1. Site Description. The study section, with the mileage of K1068 + 750 along the QTR, is located in the Chumaer River High Plain (Figure 1). The monitoring results of adjacent meteorological stations show that the mean annual air temperature in this region is −2.9°C [28]. As shown in Figure 2, the air temperature from 2007 to 2016 close to the ground shows that the temperature is between −28.9°C and 13.4°C, and it is higher than 0°C from June to September every year. The altitude of the study area is 4552 m, and the vegetation coverage is about between 30% and 50%. A borehole survey conducted in 2004 shows that the MAGT and the permafrost table (PT) under the study section is −0.5°C and 5 m, respectively, at undisturbed ground. In this paper, the PT is calculated by linear interpolation of adjacent depths of 0°C isotherm. The results of this survey also show that the permafrost in this region is mainly ice-rich permafrost (volume ice content less than 10% to 20%) and icy permafrost (volume ice content is between 10% and 20%). The embankment was built in the warm season of 2002 with a height of 2.8 m. This embankment is a traditional earthen embankment without any proactive cooling measures. The embankment orientation is 241.6°, which means that the intensity of the solar radiation on both sides of the slopes is different.

2.2. Ground Temperature Monitoring. In order to monitor the thermal stability of the embankment, a ground temperature monitoring system was built in this section and started operation at the end of 2005 as shown in Figure 3. The monitoring system consists of an undisturbed site monitoring borehole and two embankment monitoring boreholes. Since it is 20 m away from the slope toe of the embankment, it can be considered that the ground temperature of the undisturbed site monitoring borehole with a depth of 16 m is not affected by the embankment. Two embankment monitoring boreholes with a depth of 20 m are located on both sides of the embankment, which are used to monitor the temperature of the embankment and the soil on the sunny side and the shady side, respectively. In these boreholes, temperature sensors are distributed every 0.5 m from 0 m to 10 m depth and every 1 m below 10 m depth. These temperature sensors are made by the State Key Laboratory of Frozen Soil Engineering with an accuracy of ±0.05°C. The ground temperature data is automatically collected by the data logger (DT500) once a day. In the analysis of this paper, the ground temperature used is the monthly mean value obtained by averaging daily data.

2.3. Observational Results. Figure 4 shows the change process of ground temperature on the sunny side and shady side of the embankment from 2006 to 2019. It is found that there are differences in their thermal regimes between the two sides. First, since 2006, the ground temperature on the sunny side has been higher than that on the shady side at the same depth. The most representative one is the depth of PT on the sunny side that is more than 5 m, which is deeper than that on the shady side. Second, the depth variation of different isotherms indicates that the temperature variation rate of permafrost on both sides of the embankment is different. In Figure 4(a), the −0.1°C isotherm declined from 7.67 m in 2006 to 10.13 m in 2019, with a decrease of 2.46 m. And in Figure 4(b), the −0.2°C isotherm has increased from 6.75 m in 2006 to 6.40 m in 2019, which is only a change of 0.35 m. In addition, the 0°C isotherm on the sunny side declined from 7.69 m in 2006 to 9.18 m in 2019, while the 0°C isotherm on the shady side rose from 5.03 m in 2006 to 4.48 m in 2019. The change of 0°C isotherm indicates that the depth of the PT on the sunny side increases by 1.49 m while the depth of the PT on the shady side decreases by 0.55 m. The

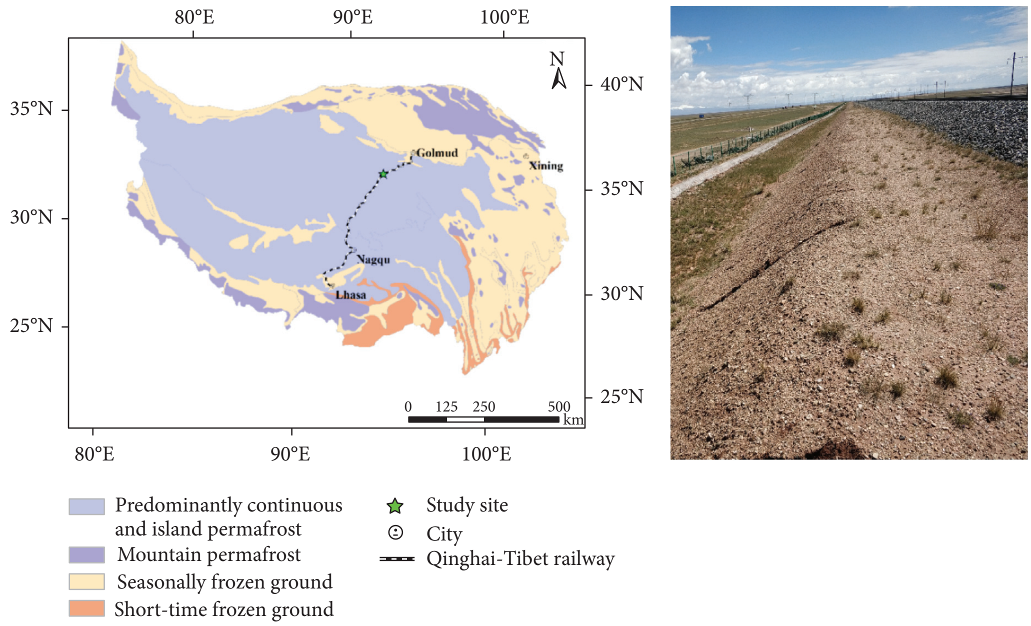

(a) (b)

Figure 1: Location (a) and image (b) at section K1068 + 750.

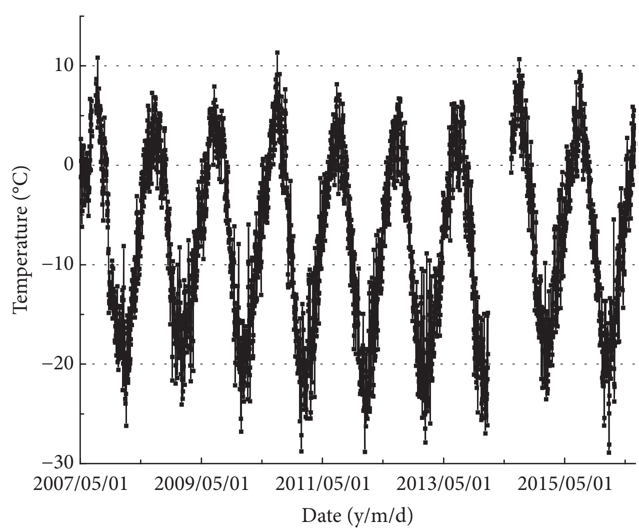

Figure 2: Air temperature changers of section K1068 + 750.

change of the above isotherms shows that the ground temperature in the shallow permafrost (with a depth of less than 10 m) on the sunny side increases significantly, while it decreases slightly on the shady side.

Figure 5 shows the ground temperature at different depths when the annual maximum melting depth occurs from 2006 to 2019, with an interval of three years. Affected by the drastically changing external environment temperature, the ground temperature in the active layer has no obvious regularity. The permafrost layers on the sunny and shady sides of the embankment showed different changes from 2006 to 2018. On the sunny side of the embankment, the permafrost is in the process of warming in both the shallow and deep layers (with a depth of greater than 10 m), and the warming range is between 0.05°C and 0.22°C (Figure 5(a)). Although the warming range decreases with the increase of depth, the temperature of permafrost above 18 m is warming up significantly, all of which are greater than 0.1°C. On the shady side of the embankment, the upper permafrost temperature decreases while the lower permafrost temperature increases (defined the upper and lower parts with a depth of 7 m) (Figure 5(b)). Both the increase and decrease of ground temperature are not greater than 0.1°C, which means that the thermal regime of permafrost is stable on the shady side of the embankment.

To further investigate the embankment thermal regime variation characteristics and the difference of ground temperature between the sunny and shady sides, the ground

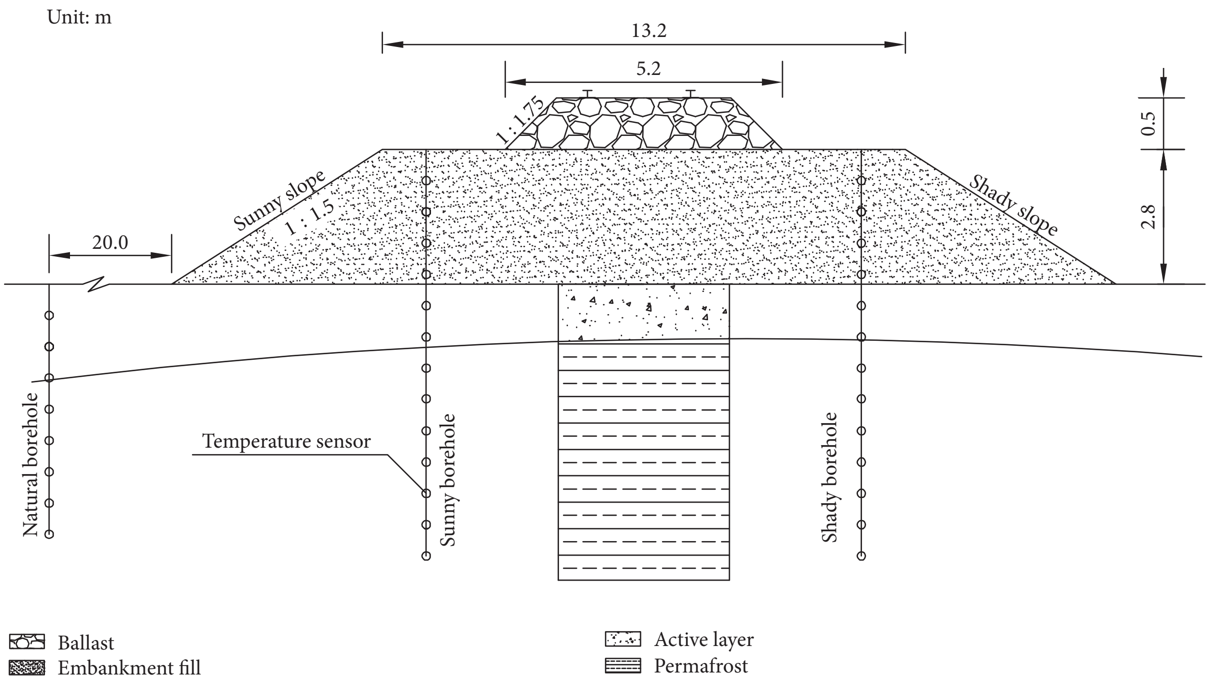

Figure 3: Monitoring system for the ground temperature at section K1068 + 750.

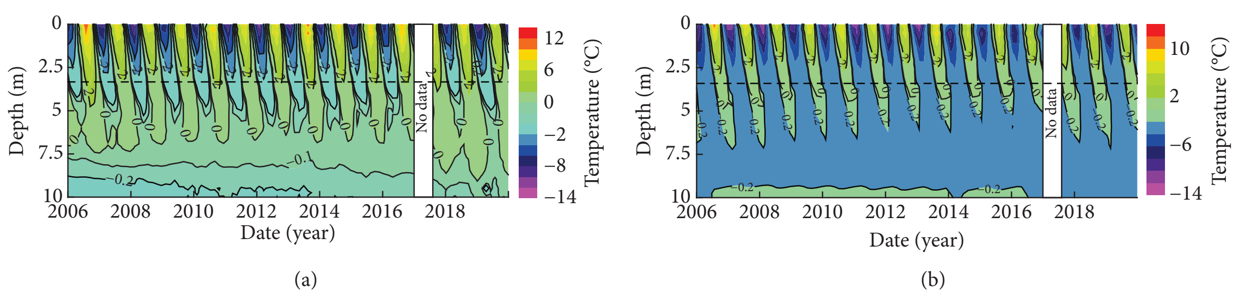

Figure 4: Ground temperature isotherms at the sunny shoulder (a) and the shady shoulder (b). The dotted line in the figure represents the original natural surface.

temperature of permafrost at depths of 8 m and 12 m was analysed, respectively, as shown in Figure 6. In 2006, there was permafrost at 8 m depth on the sunny and shady sides, and the ground temperature is −0.13°C and −0.25°C, respectively (Figure 6(a)). After 2006, the ground temperature on the sunny side has gradually increased and reached above 0°C in 2017, which means that the soil here has been degraded to seasonal permafrost. The mean annual temperature at 8 m depth on the sunny side increased from −0.12°C in 2006 to 0.01°C in 2019, with an increase of 0.13°C. However, the ground temperature at 8 m depth on the shady side changes in stages. In the first stage, the mean annual temperature decreased from −0.36°C in 2006 to −0.42°C in 2014. Then, in the second stage, the mean annual temperature increased from −0.42°C in 2014 to −0.3°C in 2019. From 2006 to 2019, the change of ground temperature on the sunny side is only 0.06°C, which is twice less than that on the sunny side. The variation trend of ground temperature at 12 m depth on the sunny side is similar to that at 8 m, which is continuously increasing (Figure 6(b)). The mean annual temperature on the sunny side increased from −0.37°C in 2006 to −0.22°C in 2019, increased by 0.15°C. The ground temperature on the shady side is basically stable, increased by 0.06°C from 2006 to 2019. The above analysis shows that from 2006 to 2019, the permafrost on the sunny side has undergone significant degradation, while the permafrost on the shady side is relatively stable.

3. Numerical Simulations

Obtaining long-term ground temperature data is conducive to further analyse the thermal performance of embankment in permafrost regions. Therefore, based on the reasonable simplification of K1068 + 750 embankment section of the QTR, a heat transfer model is established to investigate the thermal regime of the embankment under climate warming.

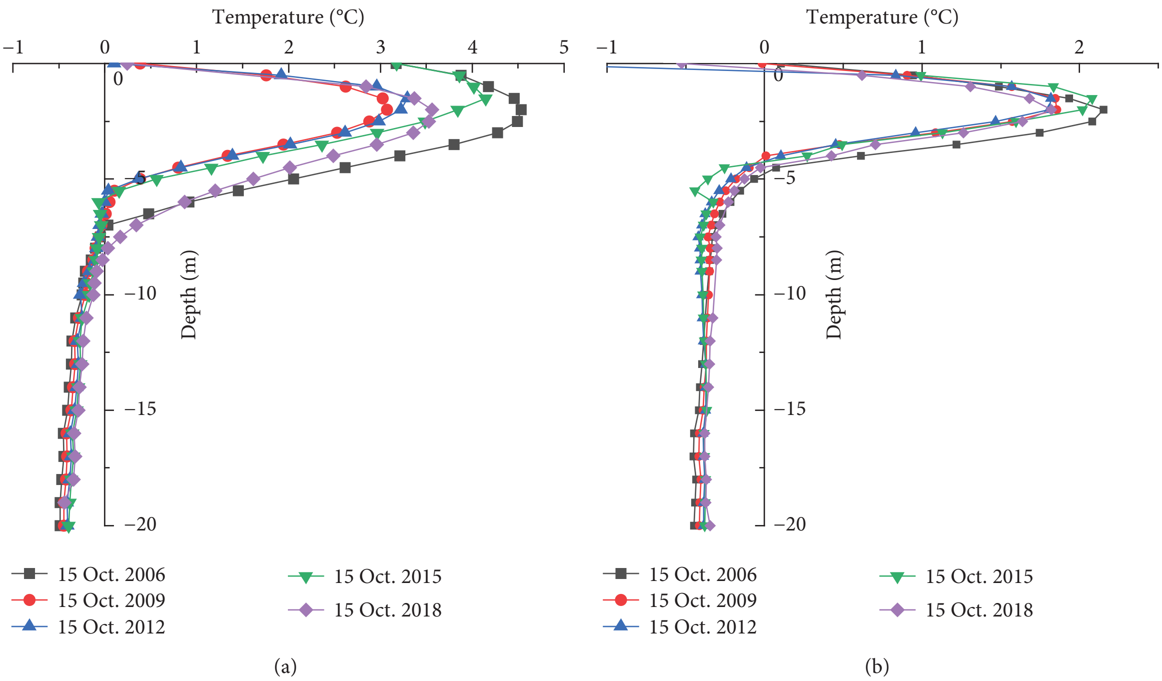

Figure 5: Ground temperature profiles on Oct. 15th at the sunny shoulder (a) and the shady shoulder (b) in different years.

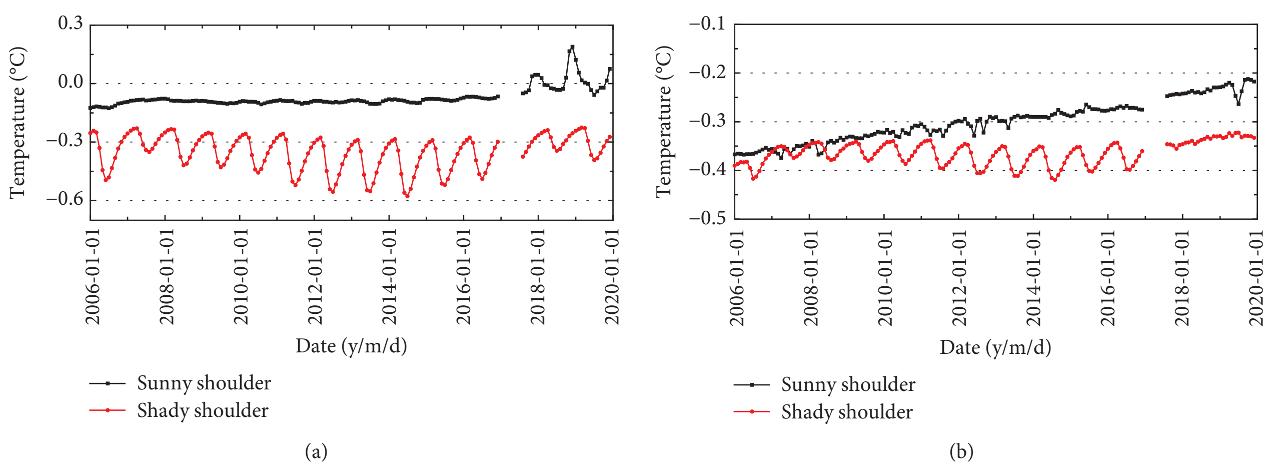

Figure 6: Variation of ground temperature at 8 m (a) and 12 m (b) on the sunny and shady sides of embankment.

3.1. Governing Equations. Previous study has shown heat transport by convective heat transfer was only 1/100 to 1/1000 of that by heat conduction in soil [29]. Therefore, in the heat transfer calculation, only the heat conduction of soil and latent heat of ice-water phase change are considered, and convection heat transfer is ignored. The governing equation of heat transfer calculation in embankment and soil layer is as follows [30, 31]:

$$C^e\frac{\partial T}{\partial t} = \frac{\partial}{\partial x}\left(\lambda^e\frac{\partial T}{\partial x}\right) + \frac{\partial}{\partial y}\left(\lambda^e\frac{\partial T}{\partial y}\right), \quad (1)$$

where C^e is the effective volumetric heat capacity of soil, λ^e is the thermal conductivity of soil, T is the temperature, and t is the time.

It is assumed that the heat capacity and thermal conductivity of the materials do not change with temperature outside the temperature range $T_m \pm \Delta T$ where the phase transition occurs. And within the temperature range of phase transition, the latent heat of phase transition of the water-bearing materials is simulated by the method of sensible heat capacity, as shown in the following equations [32]:

$$C^e = \begin{cases} C_f, & T < (T_m - \Delta T), \\ \dfrac{L}{2\Delta T} + \dfrac{C_f + C_u}{2}, & (T_m - \Delta T) < T < (T_m + \Delta T), \\ C_u, & (T_m + \Delta T) < T, \end{cases} \tag{2}$$

$$\lambda^e = \begin{cases} \lambda_f, & T < (T_m - \Delta T), \\ \lambda_f + \dfrac{\lambda_u - \lambda_f}{2\Delta T}\left[T - (T_m - \Delta T)\right], & (T_m - \Delta T) < T < (T_m + \Delta T), \\ \lambda_u, & (T_m + \Delta T) < T, \end{cases} \tag{3}$$

where C_f and C_u are the volumetric heat capacities of the materials in the frozen and the melting states, respectively; λ_f and λ_u are the thermal conductivity of the materials in the frozen and the melting states, respectively. L is the latent heat per unit volume. The influence of soil pores and solutes may make the freezing temperature below 0 °C, which means that the values of T_m and ΔT need to be determined in different situations. In this study, the values of T_m and ΔT in the calculation were 0°C and 0.5°C, respectively.

3.2. Physical Model. The physical model of the embankment is shown in Figure 7. Considering that the soil layer is considered to be infinite in the longitudinal direction and no heat transfer occurs, the 2D heat transfer model is established in this study [23]. Above the natural surface, the embankment can be divided into two parts: embankment fill and ballast. Referring to the field measurement, the heights of the two parts in the model are 2.8 m and 0.5 m, respectively. Based on the thermal disturbance range of embankment, the depth and horizontal width of the part under the embankment in the model are set as 30 m and 80 m, respectively. The borehole data show that there is sandy soil (0–3 m), gravel soil (3–13 m), and strongly weathered stone (13–30 m) under the natural surface. According to the existing experimental results and geological data, the thermal parameters of different materials in this model are determined as shown in Table 1 [23, 33].

3.3. Boundary and Initial Conditions. The upper thermal boundary of the model is affected by various factors such as external environmental temperature and solar radiation. The difference in thermal characteristics can divide the upper boundary conditions of the model into natural ground surface (AB and IJ), sunny slope surface (BCDE), shady slope surface (FGHI), and top surface of embankment (EF). The simplified ground temperature change process at the upper boundary can be described as follows [34]:

$$T = T_0 + A\sin\left(\frac{2\pi t}{8760} + \varphi\right) + R_0 t, \tag{4}$$

where T is the boundary surface temperature; T_0 is the mean annual temperature of the boundary surface; A is the annual amplitude temperature of the boundary surface; φ is the initial phase angle, which is $\pi/2$ in this model; R_0 is the rate of climate warming; and R_0 in this model is taken as 0.052°C/8760 h according to the conclusion of the temperature increase of 2.6°C in the next 50 years studied by Qin et al. [35]. Based on the adherent layer theory, the values of T_0 and A are determined by analysing field monitoring data and referring to previous studies as shown in Table 2 [13, 36].

This model also includes the wall boundaries on the left and right sides (AL and JK) that are considered adiabatic and the bottom boundary (LK) with a heat flow of 0.06 W/m^2 [37].

Assuming that no embankment is built above the natural ground surface and the climate warming rate R_0 is 0, equation (4) is used as the upper boundary condition to calculate for 50 years until the ground temperature distribution is stable. The calculated result is taken as the initial temperature field under the natural ground surface, and the initial temperature inside the embankment is assumed to be 10°C.

In the first few years after the construction, the internal temperature field of embankment is significantly affected by the construction. Therefore, the starting time of this simulation is determined to be July 2006, when the embankment construction had been completed for 4 years and the internal temperature was basically stable.

3.4. Model Validation. With the above settings, the model is used to simulate the change process of the ground temperature distribution at section K1068 + 750 in the next 50 years. In order to validate the accuracy of the model, ground temperatures of the section on the sunny and shady sides in July 2012 and January 2013 when the surface ground temperature was the highest and the lowest were selected and compared, as shown in Figure 8. The complex environmental factors and simplification of boundary conditions make the simulated ground temperature and measured value have errors in the active layer, which is most significant on the sunny side in July 2012 (Figure 8(a)). As shown in Figures 8(a)–8(d), the simulated values of the ground temperature in the permafrost layer on both sides of the

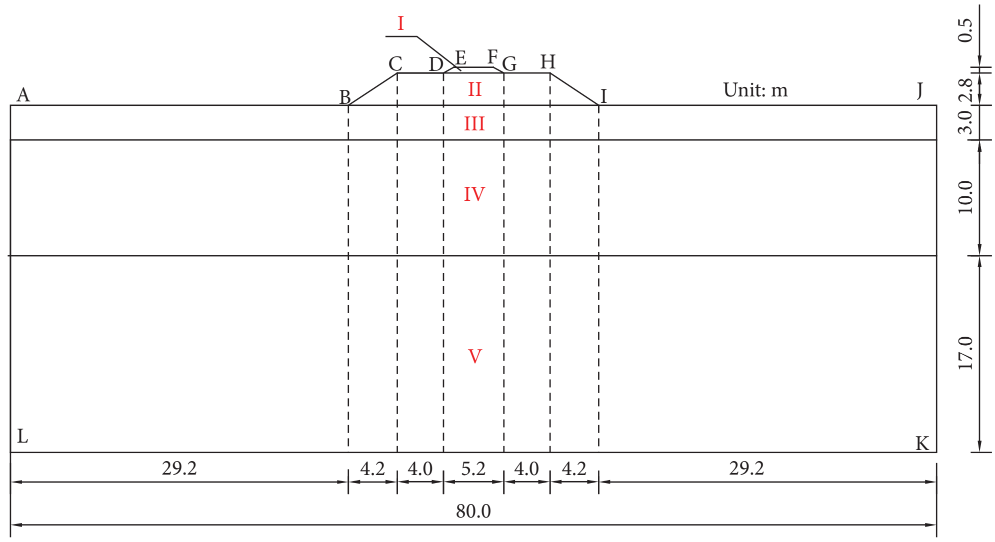

Figure 7: Physical model profile of section K1068 + 750. I: ballast; II: embankment fill; III: sandy soil; IV: gravel soil; V: strongly weathered stone.

Table 1: Thermal parameters of different materials in the model.

Properties	ρ (kg·m^{-3})	C_f (J·m^{-3}·°C^{-1})	C_u (J·m^{-3}·°C^{-1})	λ_f (W·m^{-1}·°C^{-1})	λ_u (W·m^{-1}·°C^{-1})	L (J·m^{-3})
Ballast	2100	1.006×10^6	1.006×10^6	0.346	0.346	0
Embankment fill	1980	3.781×10^6	4.415×10^6	1.98	1.91	2.04×10^7
Sandy soil	1900	2.329×10^6	2.561×10^6	2.61	1.92	2.26×10^7
Gravel soil	1400	1.434×10^6	1.756×10^6	1.63	0.93	2.30×10^7
Strongly weathered stone	1700	3.138×10^6	3.568×10^6	1.82	1.47	3.81×10^7

Note. ρ is the density of the material; L is the latent heat per unit volume.

Table 2: Temperature parameters of upper boundary condition.

Variables	T_0 (°C)	A (°C)
Natural ground surface	−0.5	10
Sunny slope surface	1	12
Shady slope surface	−1.2	13
Top surface of embankment	0.38	14.5

embankment agree with the measured values, which indicates that the model can be used to simulate the changes of the permafrost under section K1068 + 750.

3.5. Numerical Results. Figure 9 shows the ground temperature distribution of embankment at different times calculated by the model. Based on the analysis of the ground temperature distribution under the embankment in 2022, which is 20 years after the embankment construction, it is found that the ground temperature under the embankment is significantly higher than that at the same depth of undisturbed site (Figure 9(a)). For example, there is an unfrozen zone surrounded by 0°C isotherm under the embankment, while the undisturbed site soil at the same depth is frozen. In addition, the depth of the −0.4°C and −0.5°C isotherms under the embankment in the figure is greater than that of the undisturbed sites on both sides, which also indicates that the ground temperature under the embankment is higher. It can also be found in Figure 9(a) that the ground temperature on the sunny side of the embankment is higher than that on the shady side. An obvious feature is that the unfrozen zone surrounded by the 0°C isotherm under the embankment mentioned above is closer to the sunny slope. And the −0.4°C and −0.5°C isotherms are also deeper on the sunny side.

Comparing Figures 9(a)–9(f) (corresponding to the 20th, 25th, 30th, 35th, 40th, and 50th year after the embankment construction, respectively) showed that the ground temperature under both the undisturbed site and the embankment increased year by year. The 0°C isotherm of the undisturbed site declined from 5.47 m in 2022 to 10.50 m in 2052, with a decrease range of 5.03 m (the depth is calculated from the top surface of the embankment). The 0°C isotherm under the center of the embankment has declined from 2.51 m in 2022 to 12.95 m in 2052, with a decreasing range of 10.44 m. Similarly, the isotherms of −0.2°C, −0.4°C, and −0.5°C decrease greatly. The change of the above isotherms

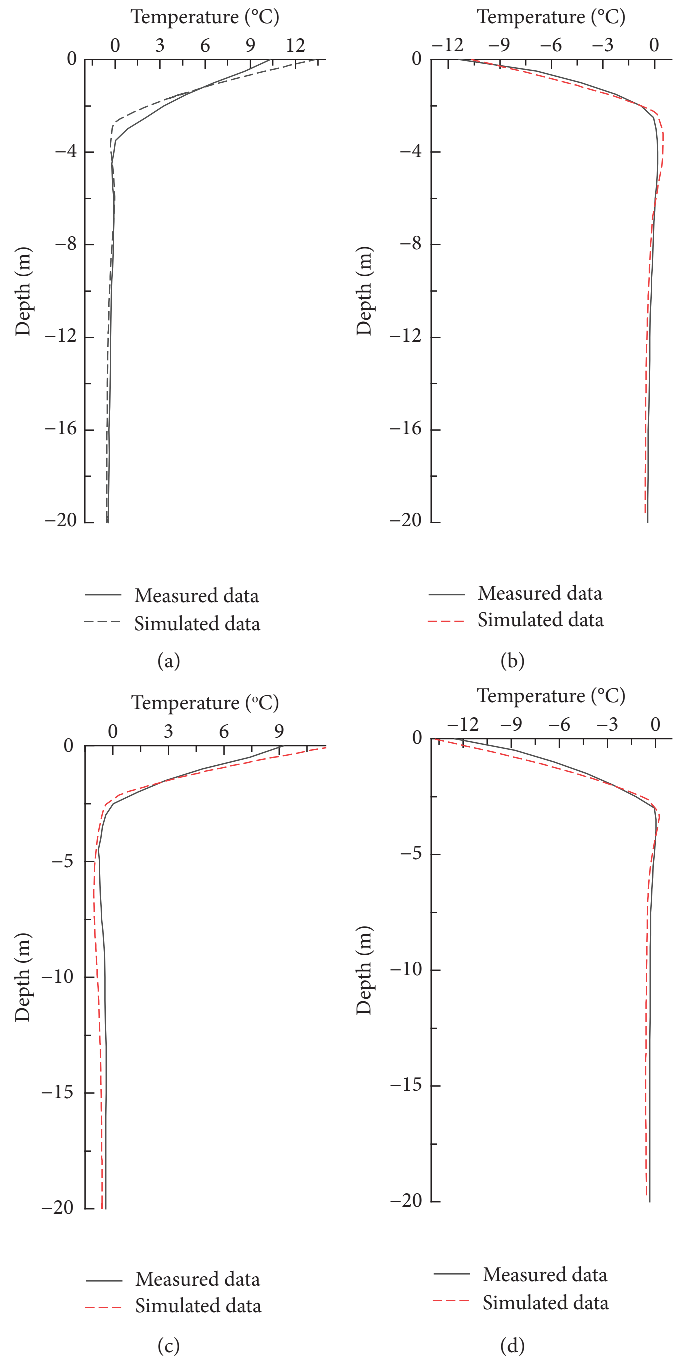

Figure 8: Simulated and measured temperature values at different depths on the sunny and shady slope. (a) Sunny shoulder Jul. 2012. (b) Sunny shoulder Jan. 2013. (c) Shady shoulder Jul. 2012. (d) Shady shoulder Jan. 2013.

in Figure 9 also indicates that the increase of ground temperature under the embankment is greater than that of the undisturbed site from 2022 to 2052.

To explore the process of permafrost warming under the embankment and the difference of ground temperature between the sunny and shady sides in more details, the simulated changes of ground temperature at different depths were analysed from 2020 to 2050, as shown in Figure 10. The temperature profile on October 15 was selected for analysis because it reached the annual maximum melting and the permafrost under the embankment had the worst thermal stability. On the sunny side of the embankment, the PT declined from 6.52 m in 2020 to 12.61 m in 2050, with a decline range of 6.09 m (Figure 10(a)). The permafrost beneath the embankment continued warming from 2020 to 2050. And the same as the monitoring results of ground temperature from 2006 to 2019, the warming range decreases with the increase of depth. The ground temperature near the original permafrost table (at 7 m depth) increased by 1.41°C. At the depth of 15 m, the ground temperature

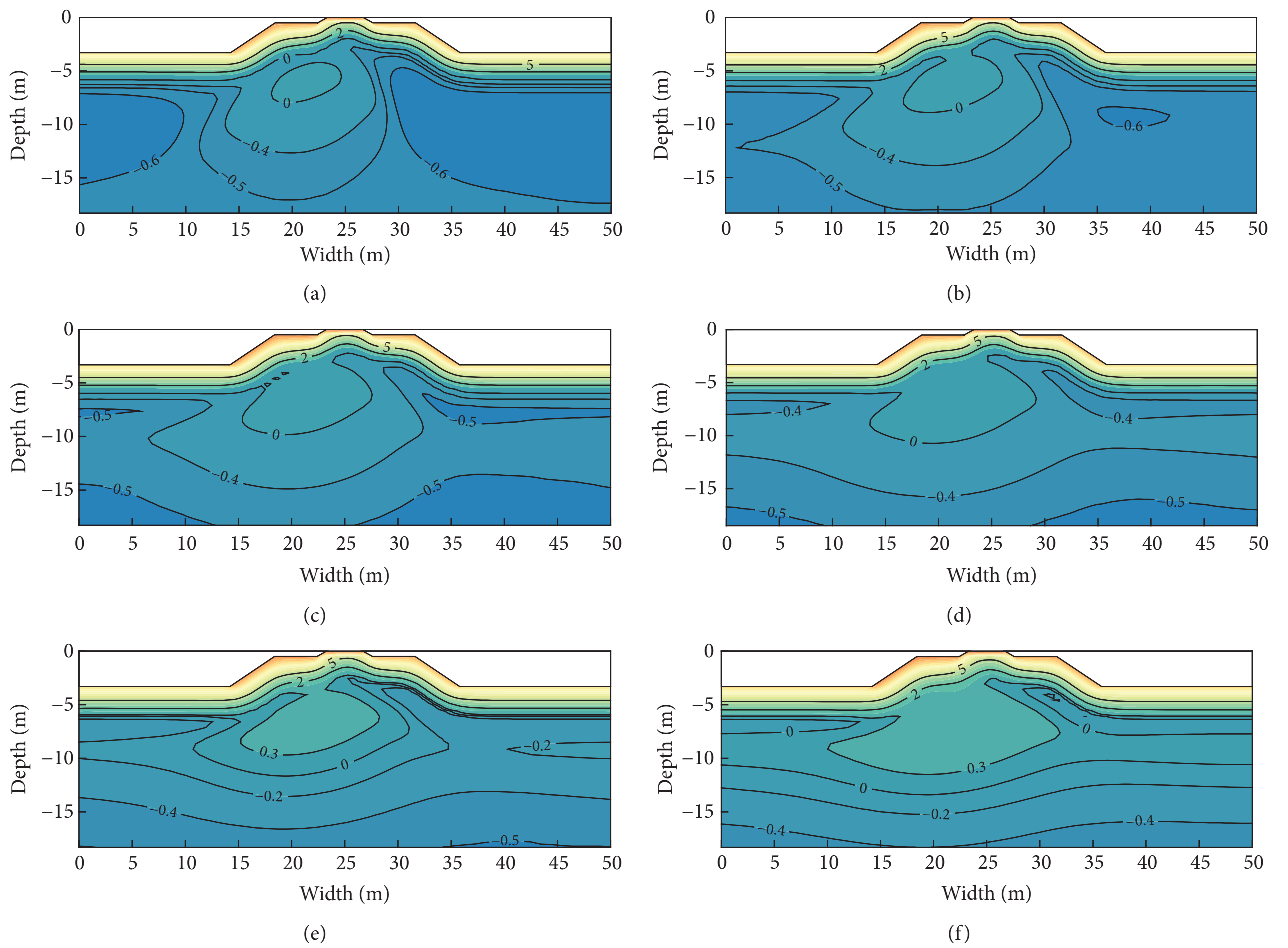

Figure 9: Simulated ground temperature distribution of embankment (unit: °C). (a) 2022/7/1. (b) 2027/7/1. (c) 2032/7/1. (d) 2042/7/1. (e) 2037/7/1. (f) 2052/7/1.

increased by 0.24°C from 2020 to 2050. The analysis of ground temperature change on the shady side of embankment shows that the PT declined from 4.05 m in 2020 to 10.24 m in 2050, with a decline range of 6.19 m (Figure 10(b)). The permafrost on the shady side is also warming and the range of warming decreases with increasing depth. At a depth of 7 m, the ground temperature increased by 0.82°C, which was significantly less than that at the sunny side. At a depth of 15 m, the ground temperature on the shady side increased by 0.21°C, which is smaller than that on the sunny side. Changes in permafrost thickness (corresponding to changes in the PT) and temperature both indicate that permafrost degradation is faster on the sunny side.

It is worth noting that there is an obvious difference between the simulated depth of the PT 6.52 m in 2020 and the measured depth of the PT 9.18 m in 2019. The reason for this phenomenon is that the PT is significantly affected by the active layer above it, which fluctuates greatly in temperature. However, as has been verified above, this phenomenon mainly occurs in the shallow layer, and the results obtained by the simulation are generally reliable.

4. Discussion

Both human activities and environmental changes can affect the thermal state of permafrost and cause permafrost degradation. The degradation of permafrost in the undisturbed site is mainly caused by the continuous warming of the climate, while the degradation of permafrost under the embankment is affected by both engineering activities and climate warming. The influence of climate warming on permafrost is mainly determined by geological conditions and surface factors such as vegetation conditions [38]. The engineering activity of embankment construction not only changes the original natural surface, but also affects the water-heat balance of soil [39–41]. Therefore, the degradation rate of permafrost under embankment is generally much faster than that of permafrost in the adjacent undisturbed site [42]. This conclusion has also been verified in

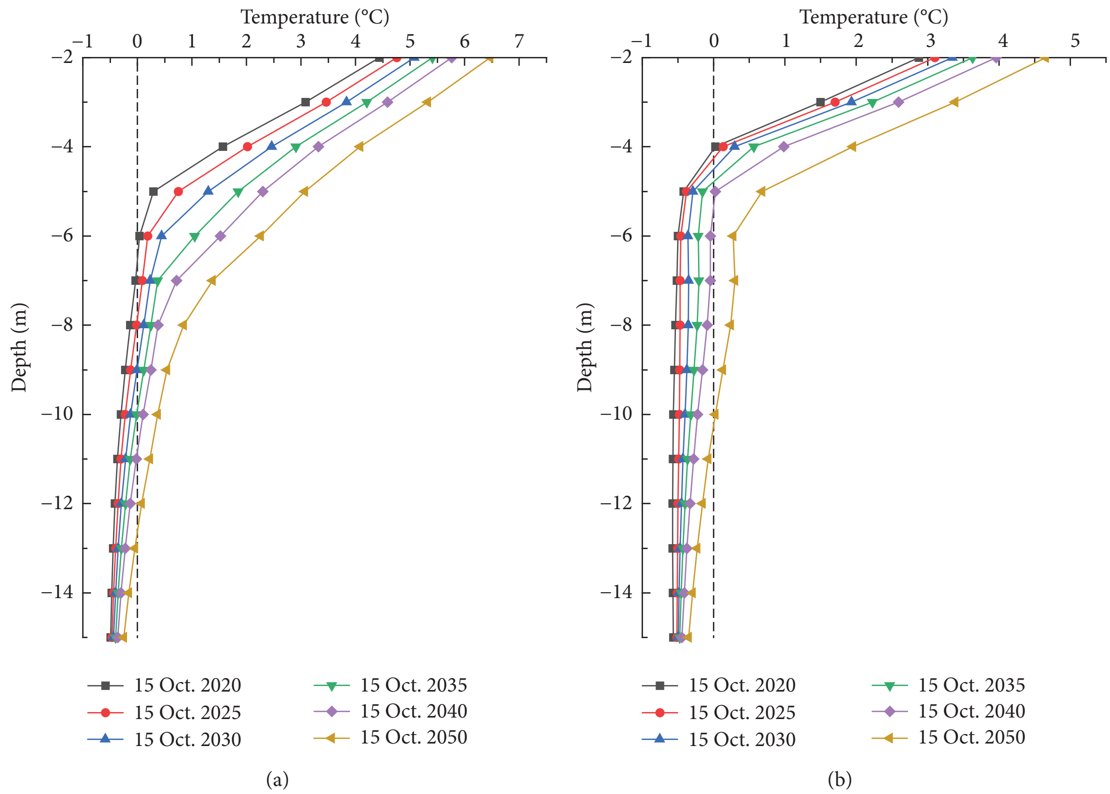

Figure 10: Simulated ground temperature profiles on Oct. 15th at the sunny shoulder (a) and the shady shoulder (b).

the simulation results of this study. For example, from 2022 to 2052, the decreasing depth of 0°C isotherm in the center of embankment is twice that of the undisturbed site, as shown in Figure 8. The monitoring and simulation results show that the permafrost degradation occurs in the undisturbed site and the embankment at section K1068 + 750 at different rates.

The difference of solar radiation on both sides of the subgrade determined by the direction of the embankment results in the uneven degradation of permafrost under permafrost [43–45]. The study shows that in the northern hemisphere, the temperature difference in the embankment with east-west orientation is the largest, and that with south-north orientation is the smallest, while K1068 + 750 is close to northeast-southwest orientation [46, 47]. Therefore, on section K1068 + 750, although the embankment is geometrically symmetric, the distribution of ground temperature on the sunny side and the shady side is different. From 2006 to 2019, the permafrost under the sunny side of the embankment has degraded significantly, characterized by the temperature increase of the permafrost above 18 m by at least 0.1°C and the PT declined by 2.46 m (Figure 4). However, the permafrost temperature changes under the shady side are more complicated. The temperature of the upper permafrost (defined the upper and lower parts with a depth of 7 m as before) is relatively stable and even the PT is rose due to less solar radiation. The lower permafrost of the shady side warmed but only slightly. The consumption of cold storage in the lower permafrost is the prerequisite for the thermal stability of the permafrost of the shady side, which means that this stability is not sustainable [48]. In the future, continued climate warming will eventually lead to the degradation of permafrost on the shady side, whether in upper or lower layers. The simulation results show that from 2020 to 2050, the depth of the PT will increase by more than 6 m under both the sunny and shady sides of the embankment, and the MAGT will increase by more than 0.2°C. For the embankment with unstable thermal regime, such as section K1068 + 750, strengthening measures should be taken in time, which can not only slow down the degradation of permafrost under the embankment but also adjust the asymmetry distribution of ground temperature on the sunny and shady sides. Studies have shown that crushed rock revetment, thermosyphons, and their composite forms, which can change the thermal convection between embankment and external environment, are the most commonly used and most effective strengthening measures along the QTR [21, 42, 49, 50]. The asymmetric setting of these measures can also help to change the uneven distribution of temperature on the sunny and shady sides of the embankment, so as to avoid the formation of longitudinal cracks. Spraying materials with high albedo or putting the awning on the sunny slope of embankment can also slow down the warming of the permafrost on the sunny side by adjusting the radiation [46, 51].

5. Conclusion

In this study, the thermal regime of section K1068 + 750 was analysed by monitoring data, and the ground temperature change process of this section under climate warming was simulated by establishing a 2D heat transfer model. Based on the results, the degradation characteristics of permafrost under the embankment were studied. Furthermore, the unevenness of ground temperature caused by the sunny-shady slope effect was discussed. The following conclusions can be drawn:

(1) Since the operation of the QTR in 2006, the permafrost under section K1068 + 750 has been degrading. The combined effects of engineering activities and climate warming make the degradation rate faster than that of undisturbed sites. This indicates that the traditional embankment cannot maintain its thermal stability in such a badly unstable warm permafrost region.

(2) The asymmetry of solar radiation makes the degradation rate of permafrost on the sunny side and the shady side of the embankment different. On the sunny side, where radiation is stronger, the permafrost has been in a process of degradation since 2006, with the PT declining and the temperature increasing. On the shady side of the embankment, the thermal regime of permafrost is relatively stable in the first few years, but the simulation results show that the permafrost will eventually degenerate. For the section with insufficient stability, strengthening measures should be taken as soon as possible to slow down the warming of permafrost and adjust the ground temperature distribution on the sunny and shady sides.

Data Availability

The data used to support the findings of this study are available from the corresponding author upon request.

Conflicts of Interest

The authors declare that they have no conflicts of interest related to the publication of this manuscript.

References

[1] G. Cheng, "A roadbed cooling approach for the construction of qinghai-tibet railway," *Cold Regions Science and Technology*, vol. 42, no. 2, pp. 169–176, 2005.

[2] Q. B. Wu, G. D. Cheng, W. Ma, F. Niu, and Z. Z. Sun, "Technical approaches on permafrost thermal stability for qinghai-tibet railway," *Geomechanics and Geoengineering*, vol. 1, no. 2, pp. 119–127, 2006.

[3] G. D. Cheng, "Construction of qinghai-tibet railway with cooled roadbed," *China Railway Science*, vol. 24, no. 3, pp. 1–4, 2003.

[4] G. D. Cheng, "Interaction between Qinghai-Tibet Railway engineering and permafrost and environmental effects," *Bulletin of the Chinese Academy of Sciences*, vol. 17, no. 7, pp. 21–25, 2002.

[5] Y. H. Mu, W. Ma, Y. Z. Liu, and Z. Z. Sun, "Monitoring investigation on thermal stability of air-convection crushed-rock embankment," *Cold Regions Science and Technology*, vol. 32, no. 2-3, pp. 160–172, 2010.

[6] Q. Wu and F. Niu, "Permafrost changes and engineering stability in qinghai-xizang plateau," *Chinese Science Bulletin*, vol. 58, no. 10, pp. 1079–1094, 2013.

[7] W. Yu, W. Liu, L. Chen, X. Yi, F. Han, and D. Hu, "Evaluation of cooling effects of crushed rock under sand-filling and climate warming scenarios on the Tibet Plateau," *Applied Thermal Engineering*, vol. 92, pp. 130–136, 2016.

[8] W. Ma, G. Feng, Q. Wu, and J. Wu, "Analyses of temperature fields under the embankment with crushed-rock structures along the qinghai-tibet railway," *Cold Regions Science and Technology*, vol. 53, no. 3, pp. 259–270, 2008.

[9] W. Ma, Y. Mu, Q. Wu, Z. Sun, and Y. Liu, "Characteristics and mechanisms of embankment deformation along the qinghai-tibet railway in permafrost regions," *Cold Regions Science and Technology*, vol. 67, no. 3, pp. 178–186, 2011.

[10] Z. Z. Sun, W. Ma, S. J. Zhang, Z. Wen, and G. L. Wu, "Embankment stability of the qinghai–tibet railway in permafrost regions," *Journal of Cold Regions Engineering*, vol. 32, no. 1, pp. 1–7, 2018.

[11] Q. Wu, Y. Sheng, Q. Yu, J. Chen, and W. Ma, "Engineering in the rugged permafrost terrain on the roof of the world under a warming climate," *Permafrost and Periglacial Processes*, vol. 31, no. 3, pp. 417–428, 2020.

[12] H. Liu, F. Niu, and H. Guan, "An engineering evaluation index of thermal asymmetry in subgrade and its optimal design in cold regions," *Cold Regions Science and Technology*, vol. 137, pp. 1–6, 2017.

[13] Y. L. Chou, Y. Sheng, Y. W. Li et al., "Sunny-shady slope effect on the thermal and deformation stability of the highway embankment in warm permafrost regions," *Cold Regions Science and Technology*, vol. 63, no. 1-2, pp. 78–86, 2010.

[14] Y. Song, L. Jin, H. Peng, and H. Liu, "Development of thermal and deformation stability of qinghai-tibet highway under sunny-shady slope effect in southern tanglha region in recent decade," *Soils and Foundations*, vol. 60, no. 2, pp. 342–355, 2020.

[15] Y. Mu, W. Ma, Q. Wu, Z. Sun, Y. Liu, and G. Qu, "Thermal regime of conventional embankments along the qinghai-tibet railway in permafrost regions," *Cold Regions Science and Technology*, vol. 70, pp. 123–131, 2012.

[16] Y. H. Mu, W. Ma, F. J. Niu, Y. Z. Liu, R. Fortier, and Y. C. Mao, "Long-term thermal effects of air convection embankments in permafrost zones: case study of the qinghai–tibet railway, China," *Journal of Cold Regions Engineering*, vol. 32, no. 4, pp. 1–10, 2018.

[17] Z.-z. Sun, W. Ma, S.-j. Zhang, Y.-h. Mu, H.-b. Yun, and H.-l. Wang, "Characteristics of thawed interlayer and its effect on embankment settlement along the qinghai-tibet railway in permafrost regions," *Journal of Mountain Science*, vol. 15, no. 5, pp. 1090–1100, 2018.

[18] F. Niu, M. Liu, G. Cheng, Z. Lin, J. Luo, and G. Yin, "Long-term thermal regimes of the qinghai-tibet railway embankments in plateau permafrost regions," *Science China Earth Sciences*, vol. 58, no. 9, pp. 1669–1676, 2015.

[19] J. Luo, F. Niu, M. Liu, Z. Lin, and G. Yin, "Field experimental study on long-term cooling and deformation characteristics of crushed-rock revetment embankment at the qinghai-tibet railway," *Applied Thermal Engineering*, vol. 139, pp. 256–263, 2018.

[20] Q. Wu, H. Zhao, Z. Zhang, J. Chen, and Y. Liu, "Long-term role of cooling the underlying permafrost of the crushed rock structure embankment along the qinghai-xizang railway," *Permafrost and Periglacial Processes*, vol. 31, no. 1, pp. 172–183, 2019.

[21] Y. Hou, Q. Wu, J. Dong, J. Luo, M. Zhang, and Z. Ye, "Numerical simulation of efficient cooling by coupled RR and TCPT on railway embankments in permafrost regions," *Applied Thermal Engineering*, vol. 133, pp. 351–360, 2018.

[22] M. H. Liu, F. J. Niu, J. Luo, G. A. Yin, and L. Zhang, "Performance, applicability, and optimization of a new slope cooling and protection structure for road embankment over warm permafrost," *International Journal of Heat and Mass Transfer*, vol. 162, Article ID 120388, 2020.

[23] B. W. Tai, Q. B. Wu, Z. Q. Zhang, and X. M. Xu, "Study on thermal performance of novel asymmetric crushed-rock-based embankment on the qinghai-tibet railway in permafrost region," *International Journal of Thermal Sciences*, vol. 152, Article ID 106333, 2020.

[24] H. L. Wu, J. Liu, and X. Zhang, "Feasibility study on use of cellular concrete for air convection embankment on permafrost foundations in fairbanks, alaska," *Transportation Geotechnics*, vol. 22, Article ID 100317, 2020.

[25] S. Y. Li, Y. M. Lai, M. Y. Zhang, and Y. H. Dong, "Study on long-term stability of qinghai–tibet railway embankment," *Cold Regions Science and Technology*, vol. 57, no. 2-3, pp. 139–147, 2009.

[26] L. Chen, W. Yu, X. Yi, D. Hu, and W. Liu, "Numerical simulation of heat transfer of the crushed-rock interlayer embankment of qinghai-tibet railway affected by aeolian sand clogging and climate change," *Cold Regions Science and Technology*, vol. 155, pp. 1–10, 2018.

[27] C. X. Tang, Z. Y. Zhu, F. Luo, Z. H. He, Z. Y. Zou, and X. H. Guo, "Deformation behaviour and influence mechanism of thaw consolidation of embankments on the qinghai-tibet railway in permafrost regions," *Transportation Geotechnics*, vol. 28, Article ID 100513, 2021.

[28] X. Hou, J. Chen, H. Jin, P. Rui, J. Zhao, and Q. Mei, "Thermal characteristics of cast-in-place pile foundations in warm permafrost at beiluhe on interior qinghai-tibet plateau: field observations and numerical simulations," *Soils and Foundations*, vol. 60, no. 1, pp. 90–102, 2020.

[29] G. S. Taylor and J. N. Luthin, "A model for coupled heat and moisture transfer during soil freezing," *Canadian Geotechnical Journal*, vol. 15, no. 4, pp. 548–555, 1978.

[30] W. D. An, *Interaction Among Temperature, Moisture and Stress Fields in Frozen Soil*, Lanzhou University Press, Lanzhou, China, 1990.

[31] Y. Lai, W. Pei, and W. Yu, "Calculation theories and analysis methods of thermodynamic stability of embankment engineering in cold regions," *Chinese Science Bulletin*, vol. 59, no. 3, pp. 261–272, 2014.

[32] M. Zhang, X. Zhang, S. Li et al., "Evaluating the cooling performance of crushed-rock interlayer embankments with unperforated and perforated ventilation ducts in permafrost regions," *Energy*, vol. 93, pp. 874–881, 2015.

[33] X. Z. Xu, J. C. Wang, and L. X. Zhang, *Physics of Frozen Soil*, Science Press, Beijing, China, 2001.

[34] Y. M. Lai, M. Y. Zhang, and S. Y. Li, *Theory and Application of Cold Regions Engineering*, Science Press, Beijing, China, 2009.

[35] D. H. Qin, *The Comprehensive Evaluating Report on the Environment Evolvement in West China*, Science Press, Beijing, China, 2002.

[36] L. N. Zhu, "Study of the adherent layer on different types of ground in permafrost regions on the qinghai-xizang plateau," *Journal of Glaciology and Geocryology*, vol. 10, no. 1, pp. 35–39, 1988.

[37] Y. Lai, L. X. Zhang, S. J. Zhang, and L. Mi, "Cooling effect of ripped-stone embankments on qing-tibet railway under climatic warming," *Chinese Science Bulletin*, vol. 48, no. 6, pp. 598–604, 2003.

[38] C. J. Tong and Q. B. Wu, "The effect of climate warming on the qinghai-tibet highway, China," *Cold Regions Science and Technology*, vol. 24, no. 1, pp. 101–106, 1996.

[39] Q. B. Wu, B. Shi, and H. Y. Fang, "Engineering geological characteristics and processes of permafrost along the qinghai–xizang (tibet) highway," *Engineering Geology*, vol. 68, no. 3-4, pp. 387–396, 2003.

[40] H.-j. Jin, Q.-h. Yu, S.-l. Wang, and L.-z. Lü, "Changes in permafrost environments along the qinghai-tibet engineering corridor induced by anthropogenic activities and climate warming," *Cold Regions Science and Technology*, vol. 53, no. 3, pp. 317–333, 2008.

[41] W. Ma, Y. H. Mu, J. M. Zhang, W. B. Yu, Z. W. Zhou, and T. Chen, "Lateral thermal influences of roadway and railway embankments in permafrost zones along the qinghai-tibet engineering corridor," *Transportation Geotechnics*, vol. 21, Article ID 100285, 2019.

[42] Q.-H. Mei, J. Chen, J.-C. Wang et al., "Strengthening effect of crushed rock revetment and thermosyphons in a traditional embankment in permafrost regions under warming climate," *Advances in Climate Change Research*, vol. 12, no. 1, pp. 66–75, 2021.

[43] M. Zhang, Y. Lai, Z. Gao, and W. Yu, "Influence of boundary conditions on the cooling effect of crushed-rock embankment in permafrost regions of qinghai-tibetan plateau," *Cold Regions Science and Technology*, vol. 44, no. 3, pp. 225–239, 2006.

[44] Z. Kun, D. Li, N. Fujun, and M. Yanhu, "Cooling effects study on ventilated embankments under the influence of the temperature differences between the sunny slopes and the shady slopes," *Cold Regions Science and Technology*, vol. 65, no. 2, pp. 226–233, 2011.

[45] M. Zhang, W. Pei, S. Li, J. Lu, and L. Jin, "Experimental and numerical analyses of the thermo-mechanical stability of an embankment with shady and sunny slopes in a permafrost region," *Applied Thermal Engineering*, vol. 127, pp. 1478–1487, 2017.

[46] J. Chenji, Z. Y. Huzeyong, S. Doushun, and Z. Y. Qianzeyu, "Yin-yang slope problem along qinghai-tibetan lines and its radiation mechanism," *Cold Regions Science and Technology*, vol. 44, no. 3, pp. 217–224, 2006.

[47] B. Tai, J. Liu, Z. Yue, J. Liu, Y. Tian, and T. Wang, "Effect of sunny-shady slopes and strike on thermal regime of subgrade along a high-speed railway in cold regions, China," *Engineering Geology*, vol. 232, pp. 182–191, 2018.

[48] J. Liu, B. Tai, and J. Fang, "Ground temperature and deformation analysis for an expressway embankment in warm

permafrost regions of the tibet plateau," *Permafrost and Periglacial Processes*, vol. 30, no. 3, pp. 208–221, 2019.

[49] W. Ma, Z. Wen, Y. Sheng, Q. Wu, D. Wang, and W. Feng, "Remedying embankment thaw settlement in a warm permafrost region with thermosyphons and crushed rock revetment," *Canadian Geotechnical Journal*, vol. 49, no. 9, pp. 1005–1014, 2012.

[50] Y. D. Hou, Q. B. Wu, Y. Z. Liu, Z. Q. Zhang, and S. R. Gao, "The thermal effect of strengthening measures in an insulated embankment in a permafrost region," *Cold Regions Science and Technology*, vol. 116, pp. 49–55, 2015.

[51] W. J. Feng, W. Ma, L. X. Zhang, and Z. J. Wu, "Application of awning to roadway engineering in permafrost regions," *Chinese Journal of Geotechnical Engineering*, vol. 25, no. 5, pp. 567–570, 2003.

Hindawi
Advances in Materials Science and Engineering
Volume 2021, Article ID 5539916, 14 pages
https://doi.org/10.1155/2021/5539916

Research Article

Study on the Freeze-Thaw Problems in the Winter Construction of the Lianghekou Earth-Core Rockfill Dam and the Countermeasures for Prevention

Qihao Yu,[1] **Xiu-Ling Ren**,[1,2] **Pan Yue**,[3] **Gui-Ke Zhang**,[3] **Jun-Feng Wang**,[1] **Yan-Hu Mu**,[1] **and En-Long Liu**[1,4]

[1]*State Key Laboratory of Frozen Soil Engineering, Northwest Institute of Eco-Environment and Resources, Chinese Academy of Sciences, Lanzhou 730000, Gansu, China*
[2]*University of Chinese Academy of Sciences, Beijing 100049, China*
[3]*Yalong River Hydropower Development Company, Ltd., Chengdu 610065, Sichuan, China*
[4]*State Key Laboratory of Hydraulics and Mountain River Engineering, College of Water Resources and Hydropower, Sichuan University, Chengdu 610065, Sichuan, China*

Correspondence should be addressed to Qihao Yu; yuqh@lzb.ac.cn

Received 2 March 2021; Revised 12 April 2021; Accepted 30 June 2021; Published 14 July 2021

Academic Editor: Shengwen Tang

Winter construction in seasonally frozen soil areas is inevitable. The variation of ambient temperature causes the freeze-thaw of the filling soils and its impact is significant, and whether the countermeasures can be effectively established and adopted is particularly important for the management and control of the construction quality of the project. This paper conducts systematic research based on the winter construction process of the dam core wall of the Lianghekou Hydropower Station, which is the third highest earth-core rockfill dam in the world under construction. The results show that for the construction site in the seasonally frozen soil area, there is a development process of the short-term frozen soils for the filling soils under the environment with low temperature in winter. The soil underwent a high-frequency freeze-thaw process wherein it was frozen at night and completely thawed during the day. During the freezing process, a large number of thin-layered segregated ice developed inside the soil to form a thin-layered or integral cryostructure, which will have an adverse effect on the engineering properties and the quality of the filling soils. And, the field tests demonstrate that the filling compaction degree of the frozen soils is difficult to meet the designed requirements. In order to effectively cope with the adverse effect of the freeze-thaw on the construction quality during the construction process, based on the analysis of the freeze-thaw characteristics of soils and its influence, and the energy exchange process of soils on-site, the principles and methods for establishing the freeze prevention system during the winter construction process are established, and a comprehensive monitoring system suitable for on-site is established in this paper. This research will provide an important reference for the scientific management and efficiency improvement of the winter construction process of the dams in cold regions.

1. Introduction

The freeze-thaw process and freezing duration of soils are closely related to air temperature in the frozen soil regions [1–3]. Studies have found that air temperature, ground temperature, and moisture content of soils are the main factors that affect the initial freeze-thaw time of the active layer [4] and the speed of the freeze-thaw process of soils [5]. In the process of engineering construction, the freeze-thaw process of soils and the frost heave and thawing sedimentation have seriously affected the stability and safe operation of the engineering structures [6, 7]. The freezing process of soils is often accompanied by shrinkage and expansion, water absorption and dehydration, and compaction processes, leading to the complex stress conditions and shear failure of soils [8]. They have a significant impact on the microscopic structure of soils, will change the permeability, strength, and mechanical properties of soils [9–15], and will affect the filling quality, permeability, and stability of the project. In order to avoid the adverse impact of the freeze-thaw process of soils on the project, different measures have been taken for freeze-thaw prevent and control. For example, controlling the temperature during the pouring process, using different thermal insulation materials for heat storage, or active heating [16], or adopting thin paving and dry grinding (the thickness of the loose paving soils is about 60 cm) for the freeze prevention and control [17]. For example, during the construction of the Xiaolangdi Dam and the Shuiniujia Hydropower Station Dam in the low-altitude regions, in order to cope with the adverse effects of the winter construction, the main measures were to control the temperature and moisture content of soils, fill soils by district, and quickly pave, quickly compact, and quickly monitor the soils [18, 19]. At the same time, during different construction periods, sealing treatment was done by flat rolling surface calendaring and covering the thermal insulation materials, and two layers of gravelly soil were used as the thermal insulation layer during the period that the construction stopped [19].

However, there are few researches regarding the freeze-thaw of soils and the freeze prevention and control problem during the filling process of the high earth-core rockfill dams in the high-cold and high-altitude seasonally frozen soil areas. Therefore, with the development of water conservancy and hydropower resources and the vigorous development of the project in high-altitude areas in western China, it is important to study the variation of freeze-thaw and engineering characteristics of soils during the freezing period, and to develop effective freeze prevention and control measures. And, this research will provide the theoretical basis and technical support for solving the problem of engineering frozen soil, improving the construction efficiency of the project in winter, and ensuring the filling quality of the project.

2. Engineering Background

The Lianghekou Hydropower Station is located on the main stream of the Yalong River in Yajiang County, Ganzi Tibetan Autonomous Prefecture, Sichuan Province, China. It is the "Leading" reservoir in the middle and lower reaches of the Yalong River, and is a controlling reservoir power station project of the cascade power stations in the middle and lower reaches of the Yalong River. It belongs to the gravelly earth-core rockfill dam with a maximum height of 295 m, and is the second highest earth-core rockfill dam under construction in China and the third highest in the world. This region belongs to a typical high-cold and high-altitude region with the development of flakes and islands permafrost and seasonally frozen soil, and the seasonally freeze-thaw effect is strong [20–22]. The average elevation of the dam site is close to 3000 m, the winter of this region is from late November to the early March of the following year with short sunshine duration, and the climate is cold and dry. The annual average air temperature in the dam site is about 10.9°C, and the extreme minimum air temperature can reach up to −15.9°C. Since the filling of the dam core wall in November 2016, there are short-term and high-frequency freeze-thaw cycles in winter. The soil basically freezes at night and thaws during most period of the daytime, which seriously affects the filling speed and quality of the soils in the dam core wall. The interior of the dam core wall is filled with gravelly soil, and the contact region on both sides between the gravelly soil and the concrete cover is contact clay (the horizontal width is 4 m). Gravelly soil is a mixture of silty clay and gravel with a certain particle size in the ratio of 6 : 4, the mass moisture content is about 8.1%, and the corresponding dry density is about 2.2 g/cm^3. The filling mass moisture content and dry density of contact clay are about 16.8% and 1.81 g/cm^3, respectively.

During the construction of the dam core wall in the winter of 2016–2018 (November to March of the following year), the meteorological conditions, the freeze-thaw process of gravelly soil and contact clay were monitored in detail on-site. At the same time, the relationship between the stacking process of soils and ground temperature of soils, the influence of each work flow and time nodes in the construction process on the freeze-thaw process of soils, and the freeze prevention and control measures and their effectiveness were investigated in detail.

3. Changing Characteristics and Impacts of the Freeze-Thaw of Soils

During the filling process of the dam in winter, the freeze-thaw mainly affects the construction links of the dam core wall. In the environment with negative temperature, the analysis of the variation of the freeze-thaw of soils is helpful to understand the freeze-thaw characteristics of soils, and the analysis of the cryostructure characteristics generated inside the soils is beneficial to understand the reason of the variation of the engineering properties of soils under the effects of freeze-thaw.

3.1. Observational System. In order to monitor the data of the meteorological conditions, the ground temperature of gravelly soil and contact clay in the dam core wall and other different sites in the dam, the observational systems of the meteorological and the ground temperature of soils have been established at different sites of the dam. In order to avoid mutual interference between the engineering construction and observational process, and at the same time to obtain continuous and true observational data on-site, the meteorological observational system adopted a mobile weather observational station, that is, the weather station can move in a certain range of the center region of the dam core wall according to the construction process and the construction conditions of machines on-site, and the weather station was always in working condition. The observational contents of the weather station included the conventional observational items such as wind speed and direction, air temperature, total solar radiation, and precipitation. The ground temperature observational system was mainly arranged in the region where the contact clay and gravelly soil were stopped filling, conducted alternately and continuously at intervals of multiple days. The schematic diagram of the ground temperature observational system of gravelly soil and contact clay with and without covering the thermal insulation materials on the surface of the dam core wall is shown in Figure 1. The ground temperature probe was a thermistor temperature sensor (the accuracy is 0.01°C), and the interval of the observational depth from the ground surface to 12 cm was 3 cm; the intervals from 12 cm to 100 cm were 8 cm, 14 cm, 26 cm, and 40 cm, respectively. The temperature data were collected by the CR3000 data logger (Campbell Scientific, Inc., U.S.), and the time interval was 10 min.

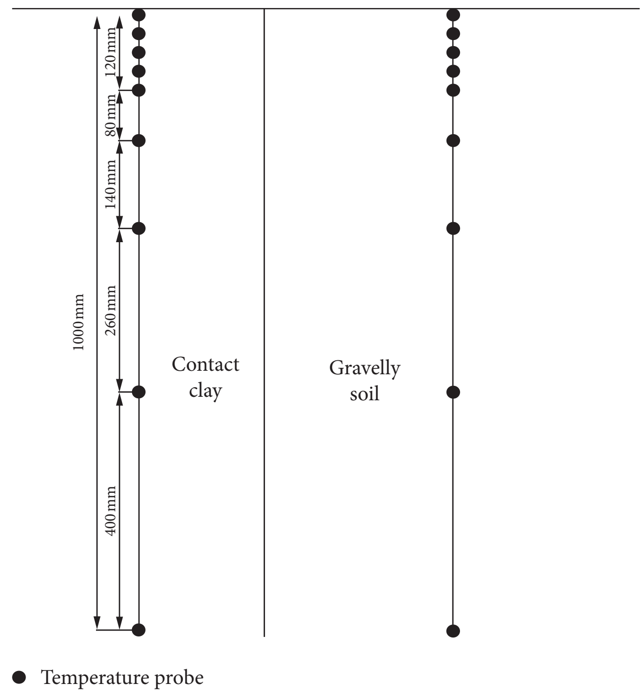

Figure 1: Schematic diagram of the ground temperature observational system.

3.2. Changing Process of Air Temperature in the Winter Construction Period. Figure 2 shows the changing process of air temperature with time in the dam core wall at an interval of 10 min from November 22, 2016, to February 28, 2017. In order to analyze the variation characteristics of air temperature within one day (24 h) in the winter observational period, the data of air temperature in the dam core wall from 20:00 on January 15th to 20:00 on January 16th, 2017, is selected for analysis. The daily changing process curve of air temperature on the coldest day of the winter is shown in Figure 3, and it typically represents the daily variation characteristics of air temperature in winter. It can be found from Figure 3 that air temperature is negative at night, reaching a certain value of negative temperature and continuing for a period, while the temperature is positive during the rest of the period. In addition, it can be seen from Figure 2 that air temperature is negative on most of the nights, so the soils will basically freeze on most of the nights.

Table 1 shows the statistical results of air temperature and the maximum frozen depth of the compacted gravelly soil without covering the thermal insulation materials in different periods. It can be seen from the table that from early December to early February of the following year, the frequency of the occurrence of negative air temperature at night, about 88%, is the largest. Therefore, the freezing phenomenon of soils mainly occurs during this period. However, from late November to early December and mid-to-late February of the following year, both the frequency of the occurrence of negative air temperature and the freezing of soils are relatively low. At the same time, the statistics of the maximum frozen depth of the compacted gravelly soil that were observed on-site during the corresponding period with different daily minimum air temperatures is shown in Table 1. It can be seen from Table 1 that during the observational period, when the daily minimum air temperature is below −5°C, the maximum frozen depth of gravelly soil can reach up to about 19.7 cm.

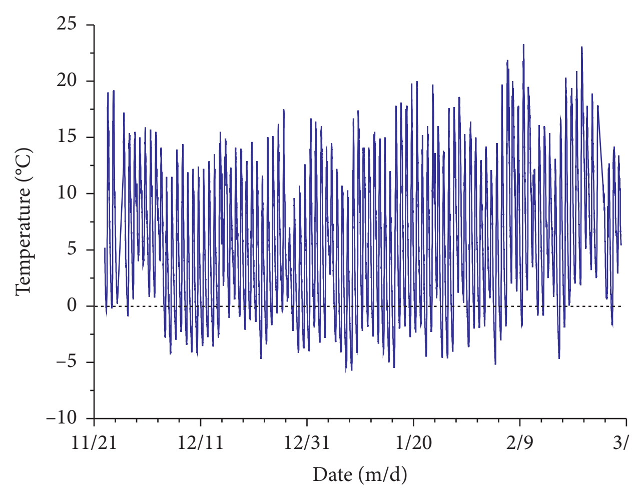

Figure 2: Variation of air temperature of the dam core wall from November 22, 2016, to February 28, 2017.

3.3. Variation of Freeze-Thaw and Its Effects on the Soils. As the variation of ambient temperature, the effects caused by the freeze-thaw of soils are mainly manifested in the formation of cryostructure inside the soils, and the variation of the engineering properties of the soils.

3.3.1. Formation of Cryostructure inside Soils and Its Influence. During the winter construction of the dam, under the effect of the negative air temperature, and during the freezing process of the filling soil from the ground surface downward, not only the ground surface was frozen but also the moisture inside the soil migrated to the freezing front, aggregated, and coagulated, resulting in the relative spatial arrangement of the solid components such as soil particles, segregated ice in the frozen soil, that is, cryostructure [23]. Under the on-site environmental conditions, the contact clay frozen at a depth of about 10–15 cm, and mainly developed the thin segregated ice with the thickness of about 1 mm, further formed a thin-layered cryostructure (Figure 4). Gravelly soil mainly formed the integral cryostructure with integral freezing and without obvious development of segregated ice inside, and it was

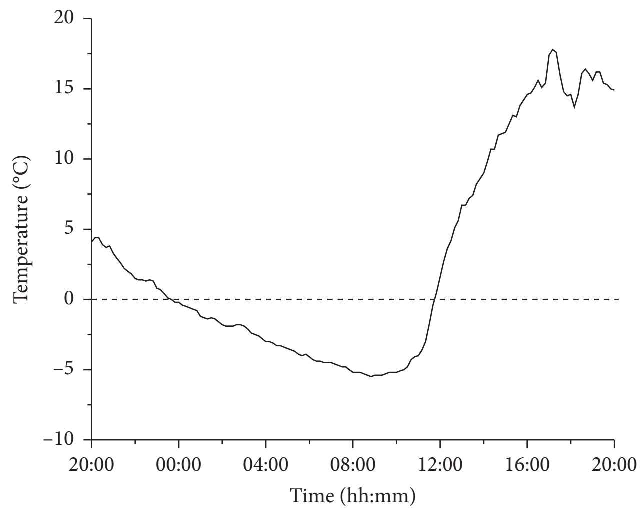

Figure 3: Variation of air temperature of the dam core wall with time from 20:00 on January 15th to 20:00 on January 16th, 2017.

Table 1: Statistical results of air temperature and the maximum frozen depth of the compacted gravelly soil without covering the thermal insulation materials.

Stage	Period	The number of days (day) Total number of days (day)	Daily minimum air temperature (°C) 0~−3	−3~−5	<−5	Frequency of the occurrence of negative air temperature (%)
Stage 1	16/11/22–16/12/3	12	3	0	0	25
Stage 2	16/12/4–17/2/6	65	30	23	4	88
Stage 3	17/2/7–17/2/18	19	4	1	0	26
The maximum frozen depth of gravelly soil (cm)			14.2	16.0	19.7	

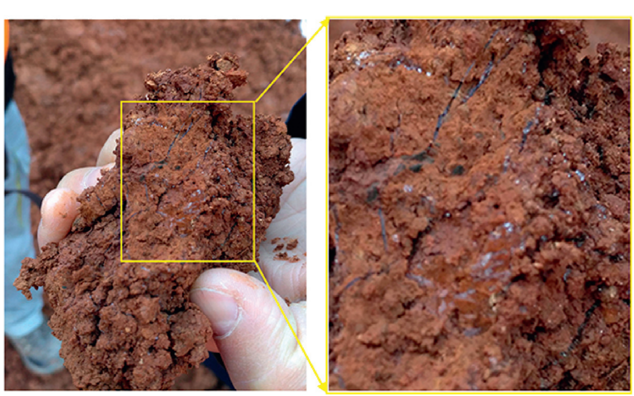

(a) (b)

Figure 4: Photograph of the thin-layered cryostructure inside contact clay on-site.

(a) (b)

Figure 5: On-site rolling and compacting test of gravelly soil during the winter construction process (a) and the frozen soil block that is difficult to compact (b).

more prominent in the compacted soils (Figure 5). As the ambient air temperature rises, the ice interlayer in the frozen soil will thaw and the moisture will dissipate. However, for the filled soils that have been compacted, firstly, for the soils affected by freeze-thaw, during the process of the moisture migration and the formation of ice interlayer, 9% volume expansion due to the water-ice phase transition will increase the volume of frozen soil, which will further lead to the decrease of the compaction degree of the compacted filling soils, thus deviating from the quality requirements of the project. Secondly, the horizontal permeability and the filling quality of the soils in the dam core wall will be affected by the unidirectional freeze-thaw cycle from the ground surface downward.

3.3.2. Impacting of Freeze-Thaw on the Engineering Properties of Soils. The basic physical properties of soils will change after freeze-thaw [24–26], which will further change the engineering properties of soils [27–30]. Under the influence of freeze-thaw, the density of the compacted soil decreases, the void ratio of soil increases, and the permeability coefficient of soil increases by about 1 to 2 orders of magnitude [31–33]. The results of laboratory mechanical tests on different types of soils show that in an environment with low temperature, the strength of soils after being frozen is higher than that of soils before being frozen, and as the temperature continues to decrease, the compressive strength of soils continues to increase [27, 34, 35]. In order to further verify the influence of frozen soil on the compaction degree of the filling soil, the field rolling and compacting test of the frozen soil was carried out in the winter of 2016 (Figure 5). The convex block rolling and compacting machine (Hunan Sany Road Machinery Co., Ltd., China) was used to perform vibration rolling and compacting 10 times according to the normal process, and then the detection of the field compaction degree index was carried out. Firstly, it was found through detecting that after the frozen soil was rolled and compacted, although the larger frozen soil blocks on the surface were significantly reduced, there were still a large number of small frozen soil blocks, and there were still some frozen soil blocks with a diameter of about 10 cm at the bottom of the compacted layer. Secondly, the detecting data (Table 2) of the compaction degree of the gravelly soil after being rolled and compacted show that under the condition that both the moisture content and dry density of the soil remain basically unchanged, the compaction degree of the specimen is far less than or far away from the compaction degree requirement of 99%, and the minimum compaction degree of one of the specimens is only 85.1%. The field rolling and compacting test in winter proves that in this case, as the soil freezes and the compressive strength increases greatly, the compaction degree of the soil is difficult to meet the actual needs on-site.

4. Basic Analysis of the Freeze Prevention and Control of Soils

It can be seen from the above analysis that the freeze-thaw will have an important impact on the engineering properties and quality of the filling soils. Therefore, the effective organization of the winter construction process of the dam and the control of key links are particularly important for the improvement of field work efficiency. The analysis of the variation and mechanism of the freeze-thaw of soils can provide a theoretical basis for the establishment and selection of various subsequent prevention and control measures of freeze-thaw.

4.1. Freeze-Thaw Process of Soils On-Site. Figure 6 shows the changing process of the ground temperature of gravelly soil on-site from 20:00 on January 15th to 20:00 on January 16th, 2017. The vertical axis is from the ground surface to the observational depth, and the horizontal axis is the observational time. The contour in the figure is the ground temperature isotherm, the zone enveloped by 0°C isotherm is the changing range and process of the freezing of soil in the depth direction with time, and the rest are the unfrozen zone. As can be seen from the figure, the freezing process of gravelly soil is mainly manifested as unidirectional freezing process that starts from the ground surface and is continuously deepening, while the thawing process is manifested as a bidirectional thawing process that mainly thaws from the ground surface downward, and secondly thaws from the bottom of the frozen layer upward. In this paper, the daily freezing duration of gravelly soil refers to the time interval between the start and end freezing time of soil. The daily thawing duration refers to the time interval between the start thawing time and the total thawed time of soil. The freezing duration is relatively long and occupies most of the duration of the freeze-thaw process of soil, while the thawing duration is relatively short. At the same time, it is found through the statistical analysis of the data that the start thawing time for the frozen soil is generally about 9:00 to 10:00, and the latest thawing time is about 12:00. The duration varies according to the frozen depth of soil and the environmental conditions.

Figure 7 shows the variation of daily thawing duration of the compacted gravelly soil without covering the thermal insulation materials on the dam core wall from December 18, 2016, to February 22, 2017. The observational data show that the frozen soil could completely thaw after the ground surface begins to thaw for about 3 h in the morning of the coldest period in winter. Therefore, it can be seen from the spatial and temporal change characteristics of soils that during the thawing process, the thawing of the ground surface does not mean that the frozen soil has completely thawed. It should be combined with the observational data of the on-site ground temperature to control the start time of construction in the dam core wall during the daytime, so as to avoid a situation wherein the soil is difficult to compact due to the existence of the frozen soil blocks inside the soil after the construction starts, which will affect the filling quality of the project.

4.2. The Effect of Freeze-Thaw on Different Types of Soils. Although some studies have shown that the freeze-thaw will affect the engineering properties of soils and change the soil structure, the arrangement, and connection of soil particles [25], resulting in a significant weakening of the shear strength of soils [36, 37], the moisture content, low temperature, and action time are the main impacting factors [38]. In these studies, the freeze-thaw test conditions mostly with different low temperatures below −5°C, ten times to a dozen number of freeze-thaw cycles, and relatively high moisture content of soil. However, it is necessary to pay attention to the significant difference between the indoor test and the actual situation on-site, or how to correctly refer to the indoor research results in the engineering practice. Firstly, the moisture content of gravelly soil is only about 8.1%, and the number of days when the daily minimum air temperature is below −5°C is very limited at the Lianghekou construction site. Secondly, when the minimum ground

Table 2: Basic indicators after being field rolled and compacted of the filled gravelly soil.

Number	Air temperature (°C)	Measured moisture content (%)	Optimum moisture content (%)	Dry density (g/cm^3)	Dry density control value (g/cm^3)	Compaction degree (%)
5Yc2-1	−1.3	10.6	9.0	1.99	2.083	94.0
5Yc2-2	−2.2	10.5	9.1	1.95	2.105	92.3
5Yc2-3	−4.9	9.5	9.1	2.04	2.095	85.1

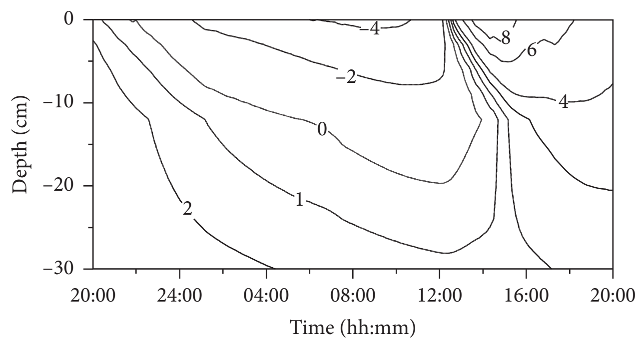

Figure 6: Changing process of ground temperature of the compacted gravelly soil without covering the thermal insulation materials on the dam core wall from 20:00 on January 15th to 20:00 on January 16th, 2017 (unit: °C).

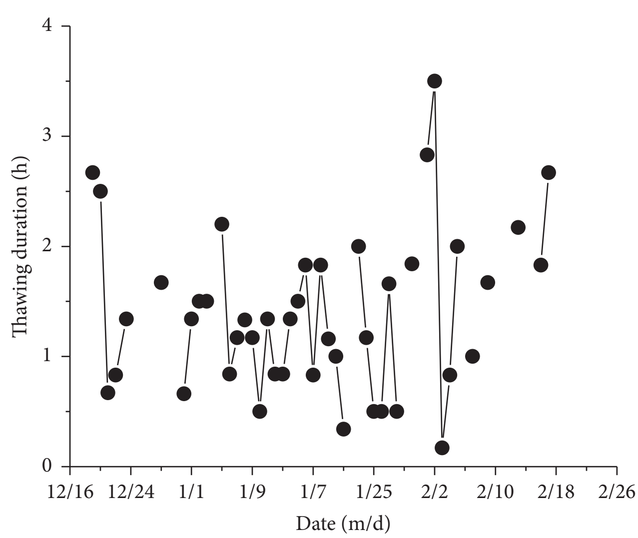

Figure 7: Variation of the daily thawing duration of the compacted gravelly soil without covering the thermal insulation materials on the dam core wall from December 18, 2016, to February 22, 2017 with time.

temperature is reached, the freezing duration of soil is relatively short. It can be seen from Figure 6 that during the 14 h freezing period of soil, the duration of the ground surface temperature that reaching the lowest temperature of − 4.5°C is only about 2 h. And in most of the period, the ground temperature is about −2°C. Thirdly, the thickness of the frozen soil layer that reaches the low temperature is relatively thin. The depth of the surface soil with the ground temperature below −4°C is only about 2 cm (Figure 6), which accounts for about 10% of the frozen depth of 19.7 cm. In order to further verify the influence of the freeze-thaw process on the engineering properties of soils, relevant on-site and indoor tests were carried out during the construction process of the Lianghekou Hydropower Station in the winter of 2017, and the test results were consistent. Figure 8 shows the stress-strain relationship curves of gravelly soil with the initial moisture content of 9.0% after different numbers of freeze-thaw cycles at the cooling temperature of −5°C and then compacted indoor. It can be seen from the figure that after gravelly soil underwent different numbers of freeze-thaw cycles and then compacted, when the number of freeze-thaw cycles is less than 5, the variation of the strain of the soil specimens is small under the same stress condition. It indicates that under the condition that the minimum air temperature is higher than −5°C and the number of freeze-thaw cycles is less than 5, the mechanical properties, permeability, and other engineering properties of gravelly soil after freeze-thaw cycles and then compacted will not affect the quality of the project. Due to space limitations, the permeability of gravelly soil is not analyzed here. Secondly, for the loose gravelly soil, due to the relatively large space between soil particles and small moisture content, the amount of moisture migration in the soil is small and the development of cryostructures is relatively limited after freezing. After the soil completely thawed, the limited residual cryostructure can be completely eliminated through the mutual dislocation and the rearrangement of soil particles during the rolling and compacting process of large machines. Therefore, during the period that the construction stops at night, it is a feasible and efficient way to cover the loose soils on the compacted soils, which is conductive to the rapid construction on-site. Reducing according to the conventional safety coefficient of the project, which indicates that as long as the frozen depth of soils does not exceed 60% of the thickness of the loose soil layer under the limited numbers of freeze-thaw cycles on-site, the method of covering the loose soil can be adopted.

However, for the compacted gravelly soil and contact clay, attention should be paid to the occurrence of the freezing of soils. Firstly, after the gravelly soil is compacted by the machine, the porosity of soil reduces greatly and the connection between the fine particles becomes closer (Figure 9), which results in good connectivity between the capillary water in the pores and the bound water in the outer layer of the particles. Under freezing conditions at night, large amount of unfrozen moisture migrates to the frozen front and it is easy to form an integral horizontal layered segregated ice, causing separation between soil layers, and its residual structure is easy to change the integral permeability. Therefore, the compacted gravelly soil should avoid the occurrence of the freezing phenomenon. Secondly, for contact clay, due to the large filling moisture content of

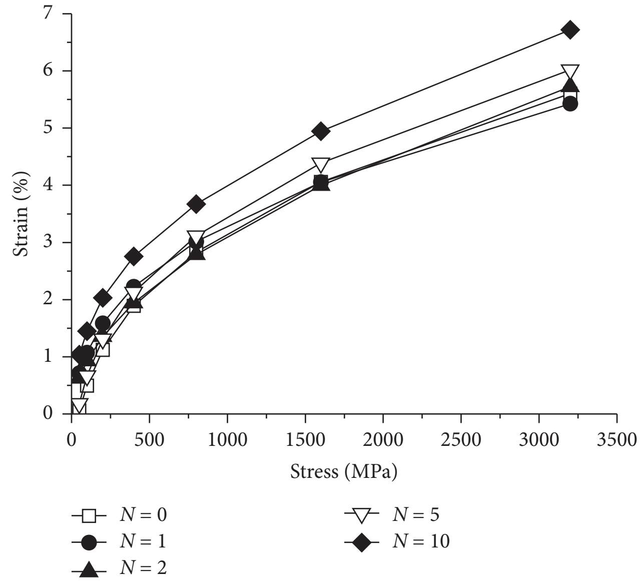

Figure 8: Stress-strain relationship curves of gravelly soil with a moisture content of 9.0% experiencing different numbers of freeze-thaw cycles at the cooling temperature of −5°C and then being compacted.

(a) (b)

Figure 9: Photograph of gravelly soil before and after being compacted. (a) Loose gravelly soil. (b) Compacted gravelly soil.

about 17%, it is easy to form a layered cryostructure under on-site freezing conditions (Figure 4), and considering the small proportion of contact clay on-site, the occurrence of the freezing phenomenon of the filled contact clay should also be avoided.

4.3. Utilization and Control of the Energy Exchange Process of Soils. Frozen soil has temperature below 0°C and contains ice, which is the result of heat exchange between the soil and the external environment. The formation of the frozen soil is firstly due to the continuous loss of heat energy inside the soil and the continuous drop in temperature. Secondly, when the water-ice phase transition process of soil around 0°C is completed and accompanied with the release of the large amounts of heat (the latent heat of water phase change is 335 kJ/kg), as well as the free water in the soil is compeletly frozen, the soil changes from the thawing state to the frozen state [7, 39, 40]. Thus, the circulation continuously drives the freezing of the underlying soil and the deepening of the frozen depth (Figure 6). At the same time, the heat capacity of the filling soil affected by factors such as temperature, compaction degree, and moisture content are the basic conditions for the inherent variation of soil, while the interface state between the ground surface and atmosphere (roughness of the soil surface, whether there is soil blocker, etc.) is the important external factor that affects the strength of their interaction. Among them, the inherent and external factors can be manually intervened and controlled during the winter construction process. For example, it is possible to increase the temperature of the incoming soil, or maintain and slow down the cooling process of the compacted soil. The surface layer is covered with thermal insulation materials, for actively controlling the temperature of the surface layer and preventing the soils from freezing through the energy supplement methods. And, by increasing the moisture content of the surface layer, extending the duration to complete the water-ice phase transition process around 0°C is a feasible theoretical basis for freeze prevention and control.

5. Establishment of the Freeze Prevention and Control System of Soils

The establishment of the freeze prevention and control system mainly includes the principles, methods, and implementation approaches of prevention and control, as well as the monitoring systems, and which should be able to play an effective role in the actual projects.

5.1. Establishment of the Prevention and Control Principles. The establishment of the prevention and control principle of dam construction in winter is the foundation of various prevention and control works, and it will also have an important impact on the construction efficiency and filling quality. Through the continuous analysis and summary of the prevention and control principles during the three winter constructions of the Lianghekou Hydropower Station, a set of principles and technical systems suitable for the winter construction of dams in the seasonally frozen soil areas in China have been explored and established.

In 2016, for the first time in the winter construction process of the dam core wall of the Lianghekou Hydropower Station, the requirements of "cannot freeze" for the filling soils per the specification was followed [41]. And, the construction principle of "the frozen soil cannot fill the dam and the filled soil in the dam cannot freeze" was established, that is, the soil mixed in the Canpeichang and the soil pulled by the construction vehicles must not contain the frozen soil, and all the filled soil in the dam core wall must not be frozen. Based on this principle, under the environment with low temperature, the soil mixed in the Canpeichang, during the transportation process by vehicles and in the dam core wall were all covered with the thermal insulation materials. And in order to ensure that the filled soil will not freeze, adjusted covering single-layer or double-layer thermal insulation materials at anytime according to the monitoring situation on-site. Under these kinds of construction conditions, for the construction area of nearly 20,000 m^2 of the dam surface, it took a lot of time for manual covering and putting away the thermal insulation materials, and the time taken for covering and putting away the thermal insulation materials was about 2 h and 3 h each day, respectively. The dam core wall was rectangular along the river in the initial stage of filling the dam core wall. In order to save the time for covering and putting away the thermal insulation materials, the dam surface was divided into two halves (upstream and downstream) along the direction perpendicular to the river according to the on-site construction requirements, and which carries out the construction alternately for a period of several days as a cycle. However, in this case, the effective construction duration was only about 9 to 10 h every day, which caused the construction progress in the winter of that year to fail to meet the requirements of the overall construction progress. More importantly, due to the impact of the energy exchange process of the filling soil, for the compacted soil the surface has been covered with the thermal insulation materials. And, as the soil has been in the process of releasing heat and the temperature of the soil has continued to decrease, the soil surface still was frozen under the environment with relatively high air temperature in mid-February, 2017.

In view of the problems that occurred during the construction process in the winter of 2016 and 2017, through the successful research on the large-scale equipment for covering and putting away the thermal insulation materials and the significant improvement of efficiency, as well as the understanding of the energy balance process of soils, the principle of "fast construction" was further added based on the above construction principles. And, by adopting the construction measures of "the left and right banks were covered with the thermal insulation materials by circulation every day, and the upstream and downstream were subdivided into flow operations," that is, the dam core wall was divided into two halves of zones near the left and right banks, and the filling was carried out in rotation and with the small filling surface flow operation every day. The operation effectively avoided the long-term placement of the compacted soils and reduced the heat loss of the soils. The on-site ground temperature observational data show that since the initial temperature of the soils is basically maintained at 6–8°C, the heat energy of the soils has been supplemented in time during the circulation construction process every day. Although the freezing index of air temperature of −1069°C·h in the winter of 2017 is greater than that of −969°C·h in 2016, and the daily minimum air temperature of −6.8°C in 2017 is 1.1°C lower than that of −5.7°C in the previous year, that is, in the case of the relatively colder environmental conditions, the frozen depth of gravelly soil becomes shallower without covering the thermal insulation materials. Among them, by comparing the observational data during the same coldest period (January 9 to 14 of the following year), it can be seen that during the same period, under the premise that the negative accumulated air temperature of 2017 is greater than that of the previous year, the frozen depth of gravelly soil during the filling process in 2017 is reduced by about 50% on average compared with that of the previous year (Figure 10).

Based on the abovementioned field and indoor tests and the summary of experience, during the construction process in the winter of 2018, further perfected and established were the new construction principles, "the frozen soil cannot fill the dam, the frozen soil cannot be rolled and compacted, the soil after rolled and compacted cannot freeze, rapid construction, timely coverage." Among them, "the frozen soil cannot be rolled and compacted" means that the loose soil can undergo a limited number of freeze-thaw processes, but the frozen loose soil must be completely thawed before

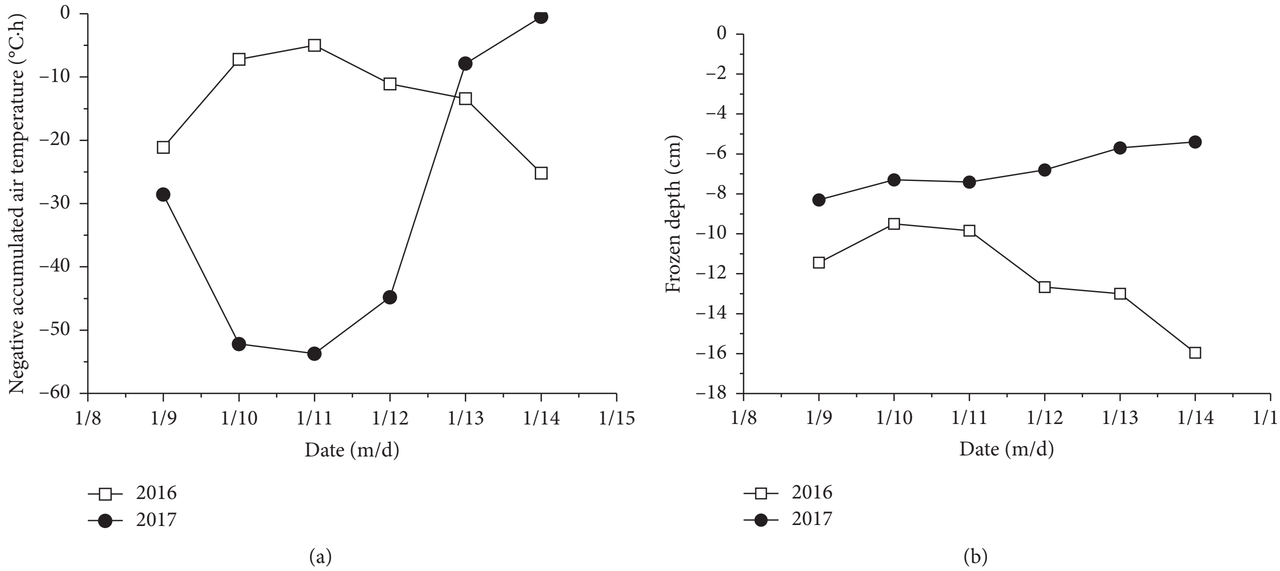

Figure 10: Variation of the negative accumulated air temperature and the frozen depth of the compacted gravelly soil without covering the thermal insulation materials with time from January 9 to 14, 2017 and from January 9 to 14, 2018. (a) Variation of the negative accumulated air temperature. (b) Frozen depth of the compacted gravelly soil without covering the thermal insulation materials.

subsequent rolling and compacting operations can be carried out. Based on the established ground temperature observational system (Figure 1), it can be determined that the internal of the loose soil is completely thawed when the internal temperature of the soil is all higher than 0°C. "The soil cannot freeze after rolled and compacted" means that the filled soil after being rolled and compacted must ensure that it will not freeze to avoid the residual and adverse effects of cryostructures. "Rapid construction" means that the soils with relatively high temperature can enter the site in time, supply the heat energy in time, and enhance the capability of frost resistance. "Timely coverage" refers to the effective combination of specific measures such as timely coverage of loose soil and the thermal insulation materials to enhance the flexibility and initiative of the on-site construction process and improve the construction efficiency. The total filling volume of gravelly soil in the dam core wall during the winter construction period is shown in Table 3. As the construction period in winter is not exactly the same every year, the data are calculated from the end of November of the current year to the middle of February of the following year for the unified comparison. It can be seen from the table that with the continuous improvement of the annual construction principles, the filling volume of gravelly soil continues to increase. Through the establishment of the construction principles, the construction quality is effectively ensured and the goal of preventing floods from flooding is successfully realized, which lay a solid foundation for the power station to shut down the gates and store water on schedule.

5.2. Selection of the Methods for Prevention and Control of the Freeze-Thaw of Soils. Based on the establishment of the above prevention and control theoretical basis and construction principles, a relatively effective prevention and control system can be formed by adopting the feasible methods to ensure the efficient and smooth construction of the dam core wall in winter.

Table 3: Total filling volume of gravelly soil of the dam core wall during the winter construction.

Year	2016	2017	2018
Total filling volume of gravelly soil (million m^3)	9.9	20.5	24.3

5.2.1. The Measure of Covering the Thermal Insulation Materials. The thermal insulation measures are mainly to reduce the heat dissipation of soil and reduce the temperature by covering the ground surface with the thermal insulation materials and changing the heat exchange conditions on the surface of soil. Figure 10 shows the changing process of the ground surface temperature of the compacted gravelly soil with and without covering the thermal insulation materials on the dam core wall in the winter of 2016. It can be seen from the observational data that the ground surface temperature of gravelly soil is basically negative every day without covering the thermal insulation materials, while it is basically positive with covering the thermal insulation materials, and the negative temperature only occurs on three days, indicating that the soil has basically not frozen. It can be seen that using the thermal insulation materials to cover the surface of the dam core wall can greatly reduce or eliminate the freezing of soils. Although it is difficult to cover and put away the thermal insulation materials on the dam core wall with an area of 10, 000 m^2 of the filling surface, the invention and application of the retractable machines has improved the construction efficiency and made this construction method feasible. And, covering the thermal insulation materials should be one of the important freeze prevention and control measures during the winter construction process.

As this kind of measure will increase the construction cost and have a certain impact on the construction schedule, attention should be paid to the following problems during the implementation process. The first problem is the selection of the types of the thermal insulation materials. It is affected by the environment with low temperature at night. After the thermal insulation material is covered, a large amount of condensed water will collect on the surface of the thermal insulation material that is in contact with the soil, which will have a greater adverse effect on the thermal insulation, the difficulty of retracting, and the durability of the thermal insulation materials. Therefore, the materials should preferably have a waterproof film on the surface. Secondly, determination of the thermal insulation properties of the thermal insulation materials. The determination of the type and thickness of the intermediate fabric of the thermal insulation material is mainly based on different air temperature conditions on-site and the ground temperature conditions, and the thermal insulation performance of the geotextile is selected through the thermal calculations. Thirdly, considering that the thermal insulation material is retracted by large machines and the tensile strength of the materials can meet the requirements. With regard to the above aspects, through the full comparison, demonstration, and use of various thermal insulation materials of cotton, geotextiles, and different fabric structures in the Lianghekou Project, the preferred thermal insulation material is the special geotextile with the waterproof film on the top and bottom, and polypropylene with the mass of 500~800 g/m^2 in the middle. Fourthly, in the implementation process of this kind of measure, through the determination of the implementation time and target of this kind of measure, the comprehensive realization of the best economic and engineering effectiveness can be achieved. Combining the experiments in the Lianghekou region, it can be found from Figures 2 and 11 that in late December, or from the end of the current year to the beginning of February of the following year, air temperature is relatively low at night and the negative temperature basically exists. The compacted gravelly soil has a higher probability of freezing and the frozen depth is deeper without covering the thermal insulation materials, so the thermal insulation material should be covered. However, from mid-November to mid-December, and in February of the following year, both the frequency of the occurrence of negative air temperature at night and the freezing of the compacted gravelly soil without covering the thermal insulation materials are relatively low, or only the ground surface freezes and frosts. Therefore, not covering the thermal insulation materials on the gravelly soil in the dam core wall during this period is an option.

In addition, due to the relatively small proportion of contact clay, and the effect of freeze-thaw on the internal structure and engineering properties of soils, the dam of Lianghekou Hydropower Station has adopted complete and double protection measures, that is, when one layer of the thermal insulation material is used to cover gravelly soil, two layers of the thermal insulation materials are used to cover contact clay. Through the observations during the construction process in winter, it was found that contact clay did not freeze with covering the thermal insulation materials.

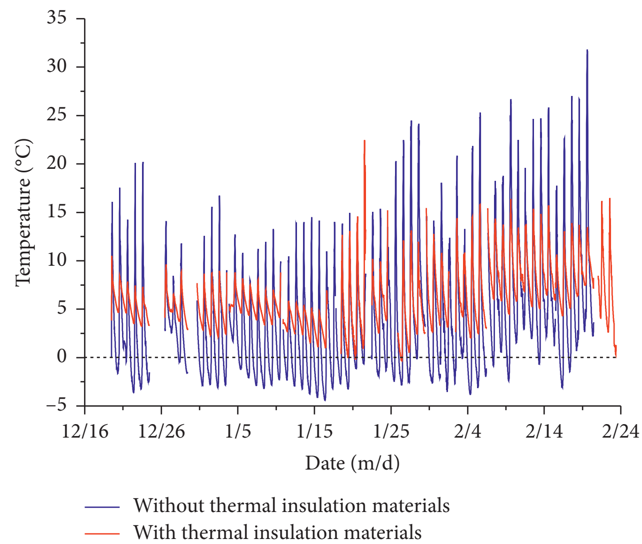

Figure 11: Variation of the ground surface temperature of the compacted gravelly soil with and without covering the thermal insulation materials on the dam core wall with time from December 18, 2016 to February 22, 2017.

5.2.2. Covering Loose Soils. According to the above field and indoor test results for the engineering properties of soils under the conditions of covering loose soils, it has been found that the engineering properties of the loose soils remain unchanged when the minimum air temperature on-site is not below −5°C and there a limited number of freeze-thaw cycles, and the engineering properties of soils still meet the construction requirements. Therefore, covering the loose soil on the compacted soil protects the lower soil layer from freezing and meets the normal construction process at the same time. Loose soil is relatively loose, the internal porosity is relatively large, and the overall thermal conductivity of soil is relatively small, which is beneficial to protect the lower compacted soil. Therefore, in the dam core wall of the Lianghekou Hydropower Station from the winter of 2017, the last process before the construction stopped was to cover the loose soil with a thickness of 30 cm on the compacted soil in the dam core wall. At the same time, this layer of soil entered the site toward the end before the construction stopped; the initial temperature of the soil was relatively high, which was beneficial for the further improvement of the frost resistance of soil. Subsequently, after a thorough inspection and confirming that the frozen soil had completely thawed on the following day, the follow-up rolling and compacting operations were carried out in time. Therefore, one of the important methods to improve the efficiency of engineering construction was to make reasonable arrangement and management of the on-site engineering procedures, rational use of the environmental conditions, and timely covering of the loose soils.

5.2.3. Process Control in Different Seasons. It can be seen from Figure 2 that the changing process of air temperature of the construction site in winter shows that air temperature in the whole winter is at a negative state at night for most of the period. However, due to the difference in its magnitude characteristics and changing process, the thermal characteristics of the filling soil will cause the freeze-thaw characteristics (frozen depth, internal structure, etc.) of soils to change. Therefore, dividing different stages according to the changing process of environmental air temperature is conductive to the scientific control of the on-site construction links and the improvement of production efficiency.

Firstly, it can be seen from the abovementioned changing process and value characteristics of air temperature that, during the period of about 4 months in winter, the daily minimum air temperature is relatively high from mid-November to the end of the current year and February of the following year, the daily minimum air temperature in January of the following year is relatively the lowest, and the probability of freezing and the frozen depth of soils also change accordingly. Therefore, using the end of December of the current year and the beginning of February of the following year as the time nodes to divide the three phases of the winter construction period, and adopting different construction techniques in different periods will achieve better construction efficiency and economic benefits. In addition, statistics on the meteorological data of the dam core wall of the Lianghekou Hydropower Station in the winter of 2016–2018 found that the division nodes of the three periods will change in different years; these two time nodes have the characteristics of dynamically moving with the change of regional climate, that is, with the changing process of the long-term air temperature of 10–15 days in this region, the two time nodes will move forward or backward to different degrees. This phenomenon is very conductive to the control and decision-making of the on-site construction process.

Secondly, because the environment and the internal conditions of soils are different in different stages, different measures should be adopted in the construction process of the project. In the first stage, both the minimum air temperature and ground temperature at night are relatively high, and the soil has high heat storage and anti-freezing ability, which should not be frozen. It can adopt the construction methods of mainly covering the loose soil, and at the same time covering the thermal insulation materials under the extreme air temperature conditions. In the second stage, since the environment is the coldest in the entire winter, in order to weaken the freezing effect of loose soil and completely avoid the freezing of the compacted soil, the thermal insulation materials can be covered in time after paving the loose soils. In the third stage, although the ambient temperature is basically similar to that of the first stage, after the soil has undergone the heat release process in winter, the ground temperature of the lower filled soil is the lowest in the whole winter, and it is easier to cause the soil to freeze by the cooling of the external environment. For example, in mid-February, 2017, the air temperature at the Lianghekou Hydropower Station rose significantly, but the ground surface was only partially frozen at night, which was then eradicated. Therefore, in this stage, it can comprehensively adopt the freeze prevention and control measures of the above two stages based on the on-site observational results.

5.2.4. Process Control of Time. This aspect is mainly the management and control of different time nodes in the construction process during the daily changing process. In terms of the construction process, based on the abovementioned analysis of the freeze-thaw characteristics of the filling soil, the rapid construction of the filling process of the dam surface can be timely covered by the filling soil during the daily circulation process. It can supply the thermal energy of the filling soil in time and slow down the cooling of the ground temperature of the lower soils, and maintain the ground temperature always at a high state, thereby improving the anti-freezing ability of the filling soils. The control of the process nodes mainly lies in the control of the stop time of the construction at night and the start time of construction the next day, and it is relatively difficult to control the stop time of the construction at night. Due to the later, the stop time of the construction at night, the lower the ground temperature, the heat release intensity of the soil will be stronger and the decreasing amplitude of the thermal energy accumulated in the soil will be larger, which will lead to a significant increase in the freezing probability of the soil. Therefore, the end time of construction at night, the completion paving time of the loose soil, or the late or early completion time of covering the thermal insulation materials will have completely different prevention and control effects. Figure 12 shows the variation of ground surface temperature of the loose gravelly soil with covering the thermal insulation materials at different times at night under different air temperature conditions on December 9 and 14, 2018. The observational data show that due to the different times of covering the thermal insulation materials, the covering times in Figures 12(a) and 12(b) are 0:20 and 23:10, respectively, and the difference between the time of covering the thermal insulation materials before and after is about 1.2 h. Under the colder environmental conditions, the daily minimum air temperature is higher than that of the day with higher air temperature, and the duration of negative temperature is longer (Figure 12(b)). However, due to the timely coverage of the thermal insulation materials and the timely protection of the thermal energy, the ground surface temperature of soils always keeps at a positive temperature, and the soil does not freeze at night (Figure 12(b)). Under the environment with low temperature, the soil with covering the thermal insulation materials still freezes due to the long-time heat dissipation of soils (Figure 12(a)).

5.3. Establishment of the Monitoring System for the Freeze-Thaw State of Soils. In the winter construction process, the establishment of the on-site comprehensive monitoring system is the prerequisite and guarantee for the scientific management and control of the construction process and the assurance of project quality. Based on the analysis of the

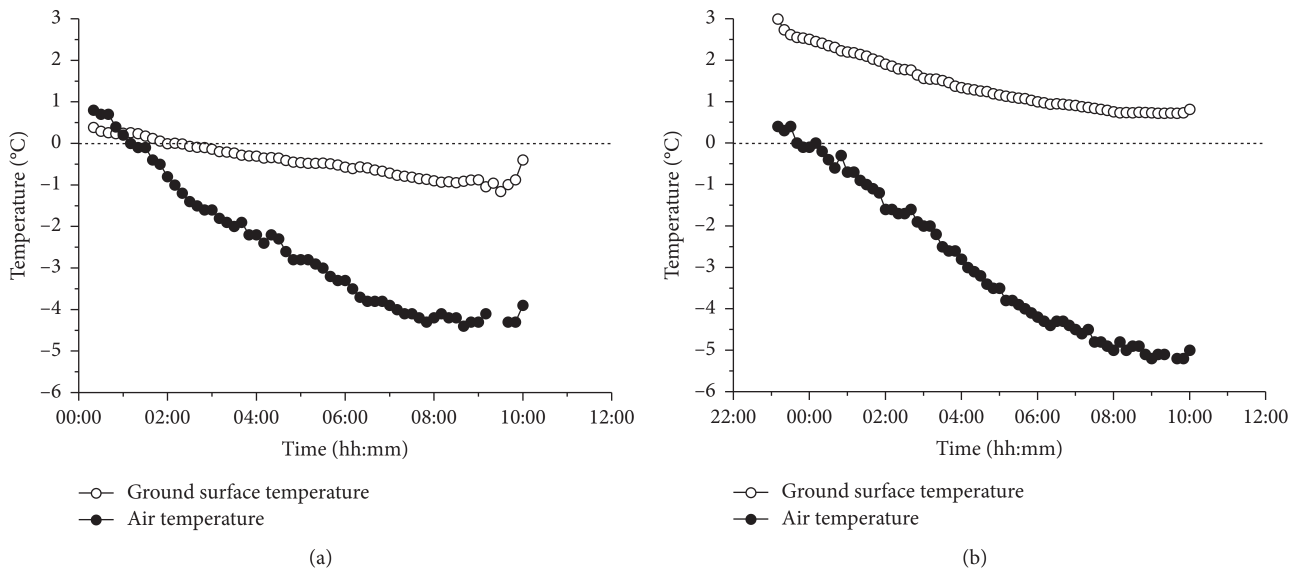

Figure 12: Variation of air temperature and ground surface temperature of the loose gravelly soil with covering the thermal insulation materials with time. (a) December 9, 2018. (b) December 14, 2018.

monitoring data of the monitoring system, it is possible to timely analyze and evaluate the region and range of the freeze-thaw process of soils, as well as the possible effects and impacts. Therefore, the on-site freeze-thaw monitoring system should be one of the important parts of the prevention and control system of winter construction. The monitoring system should be established in terms of the monitoring principles, methods, and contents, as well as the identification and evaluation systems.

(1) In terms of the monitoring principles: the monitoring system should carry out different levels and aspects of monitoring for different sites such as the dam core wall, Canpeichang, and Beiliaocang according to the actual situation on-site. Taking the dam core wall as an example, it should be established in all dimensions from different dimensions such as time and space. In terms of time, the entire winter (from mid-November to early March of the following year in Lianghekou) construction process should be monitored. During the construction process on the current day, continuous monitoring should be possible, and in particular, the continuous changing process of the monitoring content at night should be ensured. In terms of spatial distribution, it should be able to range from the ground surface temperature of the construction surface of the dam core wall to the ground surface temperature of the typical temperature characteristic unit. For example, in different regions of the Lianghekou construction site with different sunshine, the filling and compacting processes are different. And the ground temperature conditions at different depths of the typical temperature characteristic units. As a result, a three-dimensional monitoring system with different levels, interrelated and temperature as the core, is established.

(2) In terms of methods and contents: through the comprehensive application of the technical methods such as the long-distance and near-distance infrared detection, temperature probe monitoring, instruments and artificial recognition of freeze-thaw, meteorological monitoring, the meteorological conditions (wind speed, air temperature, solar radiation, precipitation, etc.), ground surface temperature, ground temperature at different depths of soil, and the freeze-thaw condition of the ground surface can be observed, monitored, and identified. As a result, a multielements comprehensive observational method has been formed, which include the meteorological conditions and ground temperature, automatic and manual, qualitative, and quantitative observations.

(3) Evaluation and prediction: through the establishment of the whole dam surface and three-dimensional observational database, as well as combined with the analysis of the characteristics and variations of the freeze-thaw, it is possible to carry out the evaluation of the freezing region, status, and the engineering impact during the construction process. At the same time, it can also carry out the predictive analysis based on this, and provide references and suggestions for the field construction decisions.

6. Conclusions

In view of the winter construction process of the dam core wall of the Lianghekou Hydropower Station under construction in the seasonally frozen soil area, according to the on-site meteorological conditions and the ground temperature observational data in the winter of 2016–2018, the freeze-thaw process of the main filling soils (gravelly soil and contact clay) and the effect of freeze-thaw on the engineering properties of soils were studied. Then, a comprehensive freeze prevention and control system for the soils was established. The following main conclusions were drawn:

(1) During the winter construction period of the Lianghekou Hydropower Station, which is located in the seasonally frozen soil area, the construction site of the dam core wall has the environmental conditions for the development of the short-term frozen soil. The soil will undergo a freeze-thaw process that freezes on most of the nights and thaws for the major part of the day. There will be a large number of thin or integral cryostructures formed inside the soil after freeze-thaw, which will affect the physical and mechanical properties, permeability, and other engineering properties of soil, and directly affect the filling quality of soil on-site.

(2) Based on the analysis of the measured data, it is found that the freezing characteristics and frequency of soils will change under different environments and construction conditions. Adjusting the construction schedule and coverage frequency, changing the initial temperature of the incoming soil, maintaining and slowing down the cooling process of soil after filling, changing the heat exchange process of soil by covering the loose soil and the thermal insulation materials on the surface of the compacted soil, and effectively controlling the development and existence of cryostructure will have important effects on the on-site freeze prevention and control of engineering quality.

(3) Through the research on the freeze-thaw process of the filling soil, the freeze-thaw effect of the loose soil, and the energy balance process of soils, the freeze prevention and control principles, as well as methods suitable for the winter construction process of the dam core wall have been established. Through the comparative analysis of the changing process of air and ground temperature, in different periods, different methods of covering loose soil and timely covering the thermal insulation materials are proposed for different types of soils, which play an important role in ensuring the filling quality of soils, shortening the construction duration, and reducing the engineering cost.

(4) This article mainly carried out relevant analysis and research on the winter construction process in Lianghekou Hydropower Station. The project is located in the typical seasonally frozen soil area in China, the construction will continue throughout the whole winter, and the construction of the dam core wall with tens of thousands of square meters area, high-quality construction requirements. Therefore, making the research results of this article have good typicality and representativeness and have a good reference for the similar projects in this type of regions.

Data Availability

The data used to support the findings of this study have not been made available because the experimental data involved in the paper are all obtained based on the authors' designed experiments and need to be kept confidential. The data are still being used for further research.

Conflicts of Interest

The authors declare that they have no conflicts of interest.

Acknowledgments

The work was supported by the Second Tibetan Plateau Scientific Expedition and Research (STEP) Program (Grant no. 2019QZKK0905), National Natural Science Funds of China (Grant no. 42071095), and the Science and Technology Project of Yalong River Hydropower Development Company (Grant no. YLLHK-LHA-2019006).

References

[1] T. Zhang, R. L. Armstrong, and J. Smith, "Investigation of the near-surface soil freeze-thaw cycle in the contiguous United States: algorithm development and validation," *Journal of Geophysical Research*, vol. 108, no. D22, pp. 1–14, 2003.

[2] K. Wang, T. Zhang, and X. Zhong, "Changes in the timing and duration of the near-surface soil freeze/thaw status from 1956 to 2006 across China," *The Cryosphere*, vol. 9, no. 3, pp. 1321–1331, 2015.

[3] L. Zhao, C. L. Ping, D. Yang, G. Cheng, Y. Ding, and S. Liu, "Changes of climate and seasonally frozen ground over the past 30 years in Qinghai-Xizang (Tibetan) Plateau, China," *Global and Planetary Change*, vol. 43, no. 1-2, pp. 19–31, 2004.

[4] G. Y. Liu, C. W. Xie, and S. H. Yang, "Spatial and temporal variation characteristics on the onset dates of freezing and thawing of active layer and its influence factors in permafrost regions along the Qinghai-Tibet Highway," *Journal of Glaciology and Geocryology*, vol. 40, no. 6, pp. 1067–1078, 2018, in Chinese.

[5] M. X. Yang, C. D. Yao, and X. H. Gou, "Freeze-thaw process of soil along the Qinghai-Tibet Highway and water-heat distribution characteristics," *Progress in Nature Science*, vol. 10, no. 5, pp. 443–450, 2000, in Chinese.

[6] Y. W. Zhou, D. X. Guo, G. D. Cheng et al., *Frozen Soil in China*, Science Press, Beijing, China, 2000, in Chinese.

[7] Z. W. Wu and Y. Z. Liu, *Frozen Ground and Engineering Construction*, Ocean Press, North Melbourne, Australia, 2005, in Chinese.

[8] X. Z. Xu, J. C. Wang, and L. X. Zhang, *Frozen Soil Physics*, Science Press, Beijing, China, 2010, in Chinese.

[9] N. K. Tovey, "Quantitative analysis of electron micrographs of soil microstructure," in *Proceeding of the International Symposium on Soil Structure*, pp. 50–58, Moscow, Russia, August 1973.

[10] M. Ghazavi and M. Roustaie, "The influence of freeze-thaw cycles on the unconfined compressive strength of fiber-reinforced clay," *Cold Regions Science and Technology*, vol. 61, no. 2-3, pp. 125–131, 2010.

[11] M. Christ and Y. C. Kim, "Experimental study on the physical-mechanical properties of frozen silt," *KSCE Journal of Civil Engineering*, vol. 13, no. 5, pp. 317–324, 2009.

[12] M. D. Shen, Z. W. Zhou, and S. J. Zhang, "Effect of stress path on mechanical behaviours of frozen subgrade soil," *Road Materials and Pavement Design*, .

[13] Z. W. Zhou, W. Ma, S. J. Zhang, Y. H. Mu, and G. Y. Li, "Experimental investigation of the path-dependent strength and deformation behaviours of frozen loess," *Engineering Geology*, vol. 265, Article ID 105449.

[14] L. Wang, F. X. Guo, Y. Q. Lin, H. Yang, and S. W. Tang, "Comparison between the effects of phosphorous slag and fly ash on the C-S-H structure, long-term hydration heat and volume deformation of cement-based materials," *Construction and Building Materials*, vol. 250, Article ID 118807, 2020.

[15] L. Wang, T. S. He, Y. X. Zhou et al., "The influence of fiber type and length on the cracking resistance, durability and pore structure of face slab concrete," *Construction and Building Materials*, vol. 2822021, Article ID 122706.

[16] Z. T. Wang, "Problems in winter construction of laxiwa hydropower station," *Water Conservancy Science and Technology and Economy*, vol. 20, no. 8, pp. 109–113, 2014, in Chinese.

[17] J. B. Wang, Z. P. Wang, and F. J. Zhang, "Study on winter filling construction technologies of sand and gravelly material in Aertashi dam," *Water Power*, vol. 44, no. 2, pp. 80–83, 2018, in Chinese.

[18] B. Wang, Q. F. Wang, and J. Zhou, "Construction of impervious soil in Xiaolangdi dam," *Northwest Hydropower*, vol. 4, pp. 36–39, 1999, in Chinese.

[19] P. L. Que, "Research on winter construction of crushed stone soil core wall of Shuiniujia Hydropower Station Dam," *Water conservancy and Hydropower Construction*, vol. 4, pp. 116–119, 2013, in Chinese.

[20] L. N. Zhu, Z. W. Wu, Y. Z. Liu, X. M. Guo, and D. Q. Li, "Effects of permafrost degradation on environment in the east of Qinghai-Xizang (Tibet) Plateau," *Marine Geology & Quaternary Geology*, vol. 15, no. 3, pp. 129–136, 1995, in Chinese.

[21] L. N. Zhu, Z. W. Wu, E. M. Zang, B. W. Pan, Y. Z. Liu, and G. X. Tao, "Difference of permafrost degeneration in the east of the Tibetan Plateau," *Journal of Glaciology and Geocryology*, vol. 18, no. 2, pp. 104–110, 1996, in Chinese.

[22] S. L. Wang, X. R. Luo, and P. F. Guo, "The distributive characteristics of frozen ground in the east of Qinghai-Xizang Plateau," *Journal of Glaciology and Geocryology*, vol. 13, no. 2, pp. 131–140, 1991, in Chinese.

[23] G. Q. Qiu, J. R. Liu, and H. X. Liu, *Frozen Soil Physics*, Gansu Science and Technology Press, Lanzhou, China, 1994, in Chinese.

[24] P. Viklander, "Permeability and volume changes in till due to cyclic freeze/thaw," *Canadian Geotechnical Journal*, vol. 35, no. 3, pp. 471–477, 1998.

[25] J. C. Edwin and J. G. Anthony, "Effect of freezing and thawing on the permeability and structure of soils," *Engineering Geology*, vol. 13, no. 1-4, pp. 73–92, 1979.

[26] K. D. Eigenbrod, "Effects of cyclic freezing and thawing on volume changes and permeabilities of soft fine-gained soils," *Canadian Geotechnical Journal*, vol. 33, no. 4, pp. 529–537, 1996.

[27] X. X. Chang, W. Ma, and D. Y. Wang, "Study on the strength of frozen clay at high confining pressure," *Journal of Glaciology and Geocryology*, vol. 29, no. 4, pp. 636–639, 2007, in Chinese.

[28] M. Huo, S. J. Wang, J. Z. Zhang, and L. Jin, "Experimental study on influences of water content and temperature on mechanical properties of ice-rich frozen soil," *Journal of Hydraulic Engineering*, vol. 41, no. 10, pp. 1165–1172, 2010, in Chinese.

[29] X. Zhu, Z. Y. Cai, Y. H. Huang, C. Zhang, and W. L. Guo, "Research on mechanical properties of expansive soils under cyclic action of coupling wetting-drying and freeze-thaw and density," *Journal of Hydraulic Engineering*, vol. 51, no. 3, pp. 286–294, 2020, in Chinese.

[30] S. Tang, Y. Wang, Z. C. Geng, and X. F. Xu, "Structure, fractality, mechanics and durability of calcium silicate hydrates," *Fractal and Fractional*, vol. 5, no. 2, Article ID 5020047, 2021.

[31] H. Y. Wang, S. R. Tang, Y. H. Xing, and X. K. Zhang, "Hydraulic conductivity of compacted wide grading gravel soils under freeze-thaw cycling," *Journal of Engineering Geology*, vol. 23, no. 3, pp. 498–504, 2015, in Chinese.

[32] T. F. Zimmie and C. LaPlante, "The effect of freeze-thaw cycles on the permeability of a fine-grained soil," in *Proceedings of 22nd Mid-Atlantic Industrial Waste Conference*, pp. 580–593, Drexel University, Phailadelphia, PenSylvania, June 1990.

[33] J. Xu, Z. Q. Wang, J. W. Ren, and J. Yuan, "Experimental research on permeability of undisturbed loess during the freeze-thaw process," *Journal of Hydraulic Engineering*, vol. 47, no. 9, pp. 1208–1217, 2016, in Chinese.

[34] X. Huang, D. Q. Li, F. Ming, H. Bing, and W. W. Peng, "Experimental study of the compressive and tensile strengths of artificial frozen soil," *Journal of Glaciology and Geocryology*, vol. 38, no. 5, pp. 1346–1352, 2016, in Chinese.

[35] H. P. Li, C. N. Lin, J. B. Zhang, and Y. L. Zhu, "Uniaxial compressive strength of saturated frozen clay at constant strain rate," *Chinese Journal of Geotechnical Engineering*, vol. 26, no. 1, pp. 105–109, 2004, in Chinese.

[36] T. F. Hu, J. K. Liu, Q. Z. Wang, and J. H. Fang, "Experimental study on undrained strength characteristics of silty clay after freeze-thaw cycling," *Journal of Central South University*, vol. 49, no. 6, pp. 1481–1490, 2018, in Chinese.

[37] S. Yin, L. Li, and Y. D. Bian, "Experimental study on shear performance of compaction silt under frozen-thaw cycle," *Highway Engineering*, vol. 44, no. 5, pp. 42–46, 2019, in Chinese.

[38] Z. Zhang, W. Ma, and J. L. Qi, "Structure evolution and mechanism of engineering properties change of soils under effect of freeze-thaw cycle," *Journal of Jilin University (Earth Science Edition)*, vol. 43, no. 6, pp. 1904–1914, 2013, in Chinese.

[39] H. Bing and W. Ma, "Experimental study on freezing point of saline soil," *Journal of Glaciology and Geocryology*, vol. 33, no. 5, pp. 1106–1113, 2011, in Chinese.

[40] H. Bing and W. Ma, "Laboratory investigation of the freezing point of saline soil," *Cold Regions Science and Technology*, vol. 67, no. 1-2, pp. 79–88, 2011.

[41] National Economic and Trade Commission of the People's Republic of China, *DL/T 5129-2013 Construction Specification of Roller Compacted Earth-Rock Dam*, China Electric Press, Beijing, China, 2013, in Chinese.

Hindawi
Advances in Materials Science and Engineering
Volume 2021, Article ID 6166489, 9 pages
https://doi.org/10.1155/2021/6166489

Research Article

Modeling of Moisture Content of Subgrade Materials in High-Speed Railway Using a Deep Learning Method

LiLei Chen,[1] Jing Chen ,[1] Chao Wang,[1] Yanhua Dai,[1,2] Rongyan Guo,[1] and Qian Huang[1,2]

[1]*College of Civil Engineering, Shaoxing University, Shaoxing 312000, China*
[2]*Key Laboratory of Rock Mechanics and Geohazards of Zhejiang Province, Shaoxing 312000, China*

Correspondence should be addressed to Jing Chen; jingchen.sxu@gmail.com

Received 6 May 2021; Revised 15 June 2021; Accepted 20 June 2021; Published 9 July 2021

Academic Editor: Yanhu Mu

Moisture content of subgrade materials is an essential factor affecting frost heave deformation of high-speed railway subgrade in a seasonally frozen region. Modeling and predicting moisture transport play an important role in analyzing the subgrade thermal and hydraulic conditions in cold regions. In this study, a long short-term memory (LSTM) model was proposed based on subgrade material moisture in two sections during one winter and spring cycle from 2015 to 2016. The reliability of the model was verified by comparing the monitoring data with the model results. The results demonstrate that the LSTM model can be effectively used to forecast the dynamic characteristics of the moisture of subgrade materials. The data of simulated moisture content of subgrade materials have a root mean square error ranging from 0.17 to 0.47 in the training phase and from 0.20 to 10.5 in the testing phase. The proposed model provides a novel method for long-term moisture prediction in subgrade materials of high-speed railways in cold regions.

1. Introduction

Seasonally frozen ground is mainly distributed in high-latitude areas such as northeast China, north China, and northwest China, accounting for 53.5% of China's total land area [1, 2]. Subgrade materials in cold regions undergo several freeze-thaw cycles every year, leading to subgrade degradation [3–5]. The frost heave problem of high-speed railway foundations in seasonally frozen regions has garnered significant attention and research interest from experts and scholars. Through field monitoring and laboratory tests, it was found that soil properties, temperature, and moisture content were the main factors affecting the frost heave of the subgrade [6–13]. Zhang et al. [14] performed indoor frost heaving tests under different moisture contents for five types of coarse-grained soils and 13 types of fine-grained soils. The results demonstrated that moisture content was the most important factor causing frost heaving [15].

The variation in the moisture content of subgrade materials is affected by climate, thermal properties of soil particles, loading conditions, and soil texture [16–19]. Several experiments and numerical models have focused on one or two controlling factors that may affect moisture transport. However, they are time-consuming and sometimes cannot predict the long-term dynamics of moisture content, for instance, Khoury et al. [20] found that a change in the subgrade moisture content affected the performance of pavement materials. Naji et al. [21] used a mathematical model to predict the relationship between soil elastic modulus and moisture content. They used the model to predict the change in pavement bearing capacity caused by seasonal changes in moisture content. Through on-site monitoring, Lin et al. [22] found that moisture content change was related to the nature of subgrade filling. However, few studies have simulated and predicted the moisture variation in high-speed railway subgrades in cold regions.

Deep learning methods based on artificial neural networks can quickly extract effective data features from massive monitoring data and analyze the nonlinear change relationship of monitoring data, which can thereafter be used to effectively predict the change in subgrade moisture content; therefore, artificial neural network has been widely used in the overall evaluation of subgrade engineering [23]. The long and short-term network is a special recursive neural network that can solve complex problems and learn fast [24]. For instance, Chen et al. [25] used this model to predict the dynamic swelling deformation of a high-speed railway subgrade.

The embankment of the Lanzhou–Xinjiang high-speed railway, located in northwest China, has been operating since December 2014. The mean annual air temperature is approximately 4.8°C at the Minle weather station near the monitoring site. The highest and lowest temperatures were 35.0 and −31.5°C, respectively. The annual mean rainfall was recorded as 381.2 mm, whereas the annual mean evaporation was 1623.0 mm in 2015. The start and end dates of snowfall were September 30, 2015, and May 19, 2016, respectively. The recorded maximum natural snow depth was 220 mm, whereas the recorded maximum natural frozen depth was 184 cm from 2015 to 2016 [22].

In this study, the long short-term memory (LSTM) model was established to simulate long-term moisture changes in subgrade materials. We examined the applicability of the LSTM model to the prediction of time-series data of the moisture of subgrade materials in high-speed railways and compared field monitoring data and model outputs.

2. Methods

The subgrade of the Lanzhou–Xinjiang high-speed railway consists of four main layers: a 0.4 m height concrete layer, 0.5 m height nonfrost susceptible crushed rock layer, 1.8 m height low-frost susceptible crushed rock layer, and an underlying soil layer. In this study, two monitoring sections of subgrade, K2020 + 024 and K2028 + 746, were selected, and their moisture contents were measured using a gravimetric method with six soil moisture sensors [22] (Figure 1). The data were recorded at 4 h intervals from August 2015 to April 2016. The measuring method and working principle of the soil moisture sensors were the same as those of Mittelbach et al. [26]. The moisture sensor was a QSY8909A moisture sensor produced by Sichuan Qishiyuan Science and Technology Co., Ltd. Its measuring range was 0–100%, length was 6 cm, diameter was 3 mm, probe material was stainless steel, and temperature range was −25–80°C [27].

In the K 2020 + 024 and K 2028 + 746 sections in the concrete layer, the moisture content of 0.2 m soil started to fluctuate slightly. Subsequently, it began to decline rapidly and tended to be constant in December 2015. It began to fluctuate again in late March 2016. The moisture content of 0.5 m soil began to fluctuate and rise, reached a peak in February 2016, and thereafter began to fluctuate and descend. In nonfrost susceptible A/B fillings, and the variation trend of moisture content at 1.0 m was approximately the same as that at 0.5 m.

As shown in Figure 2, the soil moisture content is affected by temperature, rainfall, and other factors. Its monitoring data have some noise and exhibit prominent nonlinear characteristics; therefore, it is difficult to predict them.

In this study, there are missing values in the data due to the communication failure of detection equipment and other factors. For missing data, detection data between adjacent time points were used for interpolation processing. To accelerate the convergence rate of the model, the data were normalized according to the characteristics of the test data and requirements of the LSTM model. The normalization calculation formula is as follows:

$$x_i = \frac{x_i - \min x_i}{\max x_i - \min x_i}, \quad (1)$$

where x_i denotes the moisture content monitoring data, whereas $\min x_i$ and $\max x_i$ represent the minimum and maximum values of x_i, respectively [23].

The LSTM model [23] is a neural network model proposed by Hochreiter in the 1990s; its model structure is as shown in Figure 3. It contains a particular unit, namely, the memory block in the recursive hidden layer. The memory block includes a cell state and three gated mechanisms (input, forget, and output gates) for controlling the flow of information. The sigmoid function implements a gating mechanism. After the data flows in, they first enter the forget gate. After part of the redundant information is discarded to obtain the critical feature data, the data enter the input gate to control the data update. Finally, they pass through the output gate as output. The mathematical expression for this process is as follows.

First, the forget gate f_t calculates the cell state that needs to be retained at the previous moment through the activation function as follows [23]:

$$i_f = \sigma\left(W_f \cdot [h_{t-1}, x_t] + b_f\right), \quad (2)$$

where W_f and b_f denote the weight matrix and bias of the forget gate, respectively, σ denotes the sigmoid function, and h_{t-1} represents the output at moment $t-1$ [23].

Second, the input gate i_t retains information regarding the current input x_t to be updated to the current cell state C_t as follows [23]:

$$i_t = \sigma\left(W_i \cdot [h_{t-1}, x_t] + b_i\right). \quad (3)$$

Thereafter, the output gate o_t controls the information that comes out as follows [23]:

$$o_t = \sigma\left(W_o \cdot [h_{t-1}, x_t] + b_o\right). \quad (4)$$

Based on the previous input and output information, the following formula can be used to calculate the nonlinear output [23]:

$$\widetilde{C}_t = \tanh\left(W_c \cdot [h_{t-1}, x_t] + b_c\right). \quad (5)$$

Finally, the new cell state can be expressed as follows [23]:

$$\begin{aligned} C_t &= f_t * C_{t-1} + i_t * \widetilde{C}_t, \\ h_t &= o_t * \tanh(C_t). \end{aligned} \quad (6)$$

Figure 1: Fieldwork of the automatic monitoring system of moisture content of subgrade materials of high-speed railway in cold regions.

By controlling the input gate, the influence of redundant information can be avoided, and information of the previous time is retained in the network owing to the forgetting gate. This model addresses long-term dependence and gradient disappearance problems encountered by traditional recurrent neural networks in prediction tasks, and it is now widely used in time-series forecasting [25, 28, 29].

In this study, root mean square error (RMSE) and R-score (R^2) were used to evaluate the performance of the model. The smaller the RMSE value calculated, the closer the R^2 value is to 1 and the higher the accuracy and reliability of the model prediction. The specific formula is as follows:

$$\mathrm{RMSE} = \sqrt{\frac{1}{n}\sum_{i=1}^{n}\left(y_i - \hat{y}_i\right)^2},$$
$$R^2 = 1 - \frac{\sum_{i=1}^{n}\left(y_i - \hat{y}_i\right)^2}{\sum_{i=1}^{n}\left(y_i - \overline{y}_i\right)^2}, \tag{7}$$

where n denotes the number of predicted samples, whereas y_i, $\overline{y_i}$, and $\hat{y}_i$ denote the measured values, mean of the measured values, and predicted value, respectively.

3. Results and Discussion

The training of the LSTM model requires the monitoring data to be preprocessed. In this study, according to the commonly used split ratio, the holdout method was used to split the dataset, with the training set accounting for 80% and validation set accounting for 20%. The monitoring data of August 1, 2015, solstice on February 11, 2016, were used as the training set, whereas the detection data of February 12, 2016, solstice on March 31, 2016, were used as the validation set. The training set was used to train the weight of the model, whereas the validation set was used to evaluate the model performance. Because the selection of hyperparameters has a significant impact on the performance of the model [30], it is necessary to set the hyperparameters of the model before the training begins. In this study, the number of cells in the LSTM model was considered as the critical hyperparameter, and the candidate operations of the hyperparameter was [5, 10, 20, 30, 40, 50]. To accurately evaluate the performance of the model on the specified parameter performance and avoid the instability of the performance of a single training session, the average error of five repeated training sessions was used as the evaluation indicator. The error statistics of the hyperparameter search training are as shown in Figure 4. It is observed from the figure that when the number of units is 10, the model has a minor error and higher computational efficiency. After several experiments, the number of units in the model was determined to be 10, the epoch was set to 200, and learning rate was 0.001. The model was implemented using TensorFlow framework. In this study, the gradient descent algorithm was applied to update the weight of the model. The adaptive moment (Adam) estimation was selected as the optimization algorithm for the training process of the model. In comparison with other optimization algorithms, the Adam algorithm is more efficient in terms of calculation and it has a better effect in practical applications [31].

The calculated results of R^2 and RMSE indices on the training and validation sets of the trained model are summarized in Table 1. From the table, the prediction effect of the LSTM model is the best when the depth of the LSTM model in R^2 of section K2028 reaches 0.94. In the training set of moisture content at all depths, R^2 was greater than 0.95, indicating that the model fitted the training data well. However, there was a gap between R^2 in the test and training sets, indicating that the model had an overfitting phenomenon. The RMSE error of the model is small for each moisture content dataset, thereby proving that the LSTM model is suitable for the prediction of soil moisture content and it has a specific application potential.

To more intuitively compare the prediction effect of the model on different moisture contents, a comparison between the predicted value of the model and the measured value on the two sections, K2020 + 024 and K2028 + 746, is as shown in Figures 5 and 6. It is observed from Figure 4 and Table 1 that the prediction accuracy of the model decreases with an increase in depth possibly because the change in soil moisture content is a gradual accumulation process, and the change in the soil moisture content in a period of shallow depth is easier to learn from the historical trend. With the increase in the predicted time steps, the deviation of soil moisture content at a depth of 1.0 m in the two sections increases, and the model's prediction ability is weak.

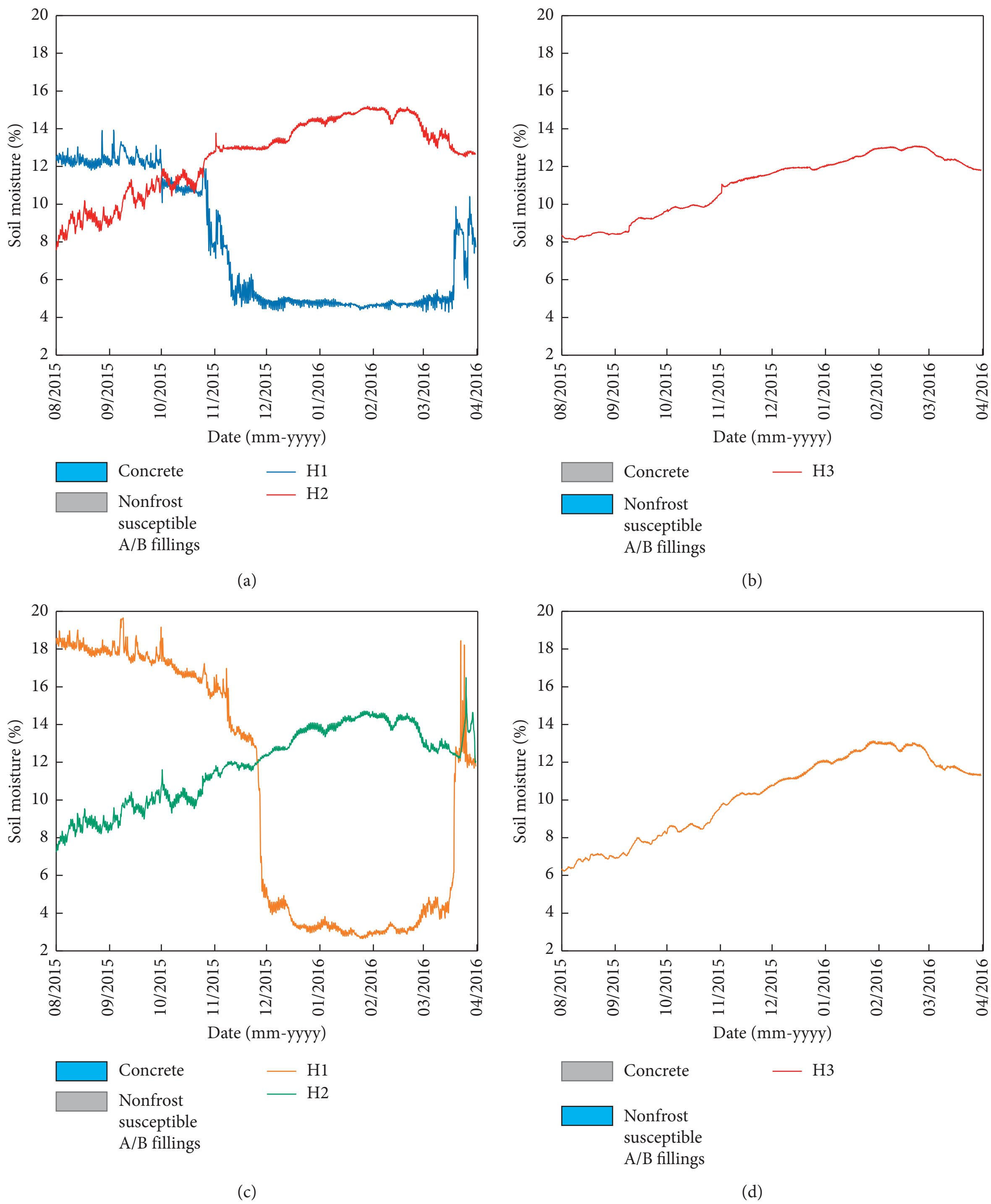

Figure 2: Variations in moisture content were measured at three depths in two sections from August 2015 to March 2016. *Note.* H1 to H3 represents depth of 0.2, 0.5, and 1.0 m, respectively. (a-b) K 2020 + 024 section. (c-d) K 2028 + 746 section.

In this study, we use an LSTM model to predict the moisture content of subgrade materials in high-speed railways based on one-year field monitoring data. The model achieved great performance for predicting moisture content of subgrade materials above 0.5 m in the two sections. However, we found that the prediction accuracy of the moisture content of subgrade materials below 0.5 m was slightly lower than those of others. This phenomenon may be attributed to the sample size and model parameters [32]. In addition, our model does not consider the detailed influential factors of soil moisture and soil particle structure, which may affect the model outputs.

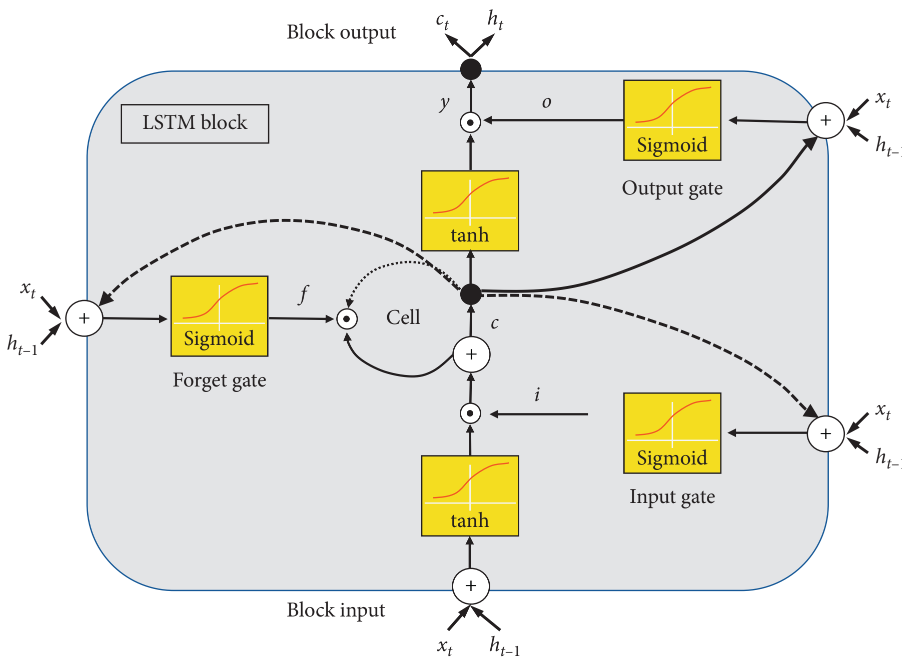

FIGURE 3: LSTM model structure.

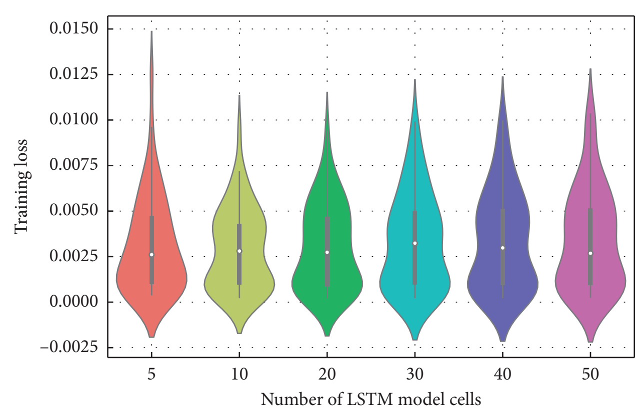

FIGURE 4: Training loss LSTM model with different number of units.

TABLE 1: Performance evaluation index of the model.

Section	R^2		RMSE	
	Train set	Test set	Train set	Test set
K2020 + 024 H1	0.99	0.90	0.36	0.51
K2020 + 024 H2	0.98	0.92	0.31	0.24
K2020 + 024 H3	0.95	0.87	0.17	0.21
K2028 + 746 H1	0.99	0.93	0.47	1.05
K2028 + 746 H2	0.99	0.94	0.23	0.20
K2028 + 746 H3	0.98	0.89	0.28	0.20

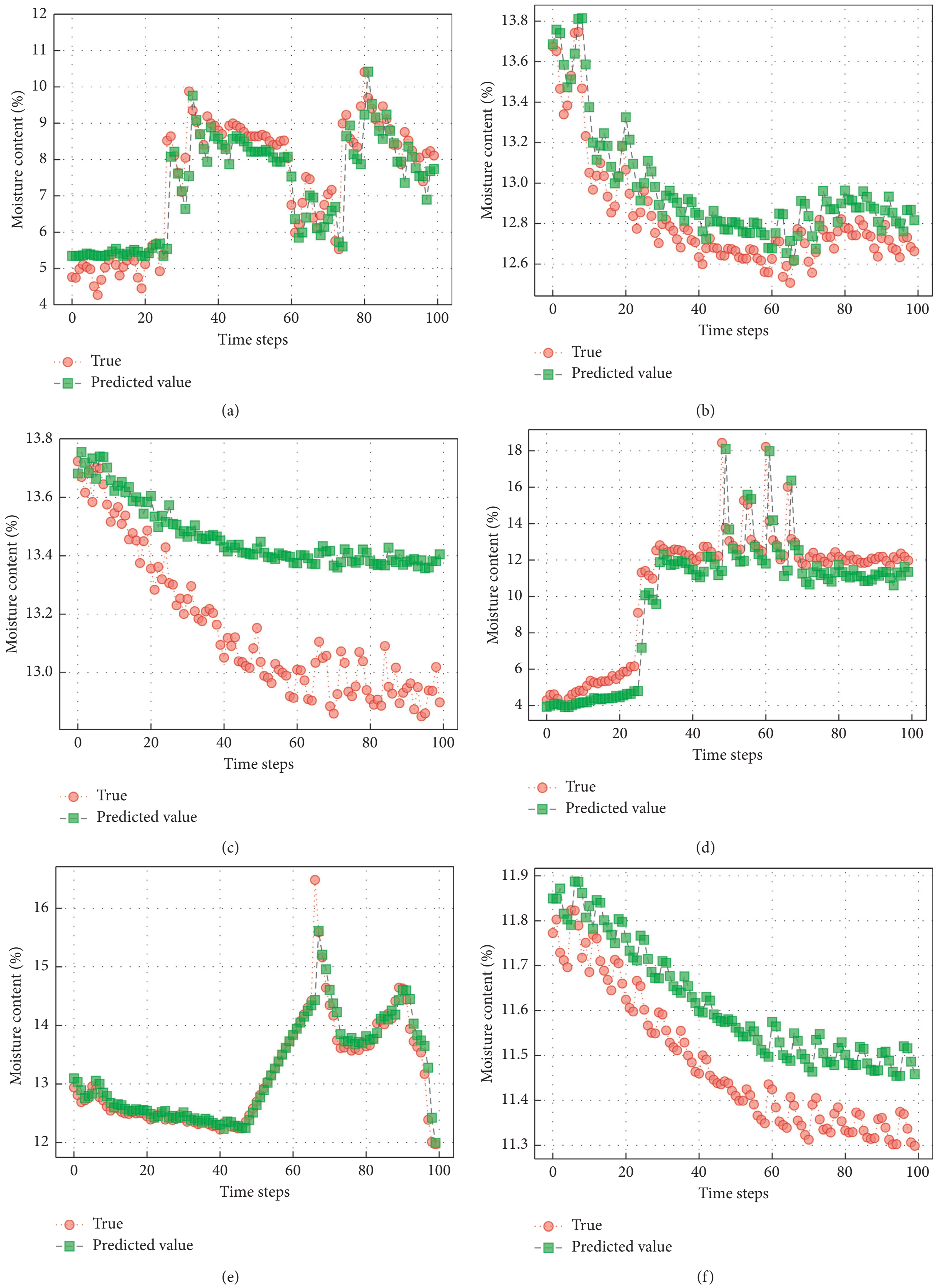

Figure 5: Predicting results of two subgrade sections in the three depths. (a–c) K 2020 + 024 section. (d–f) K 2028 + 746 section.

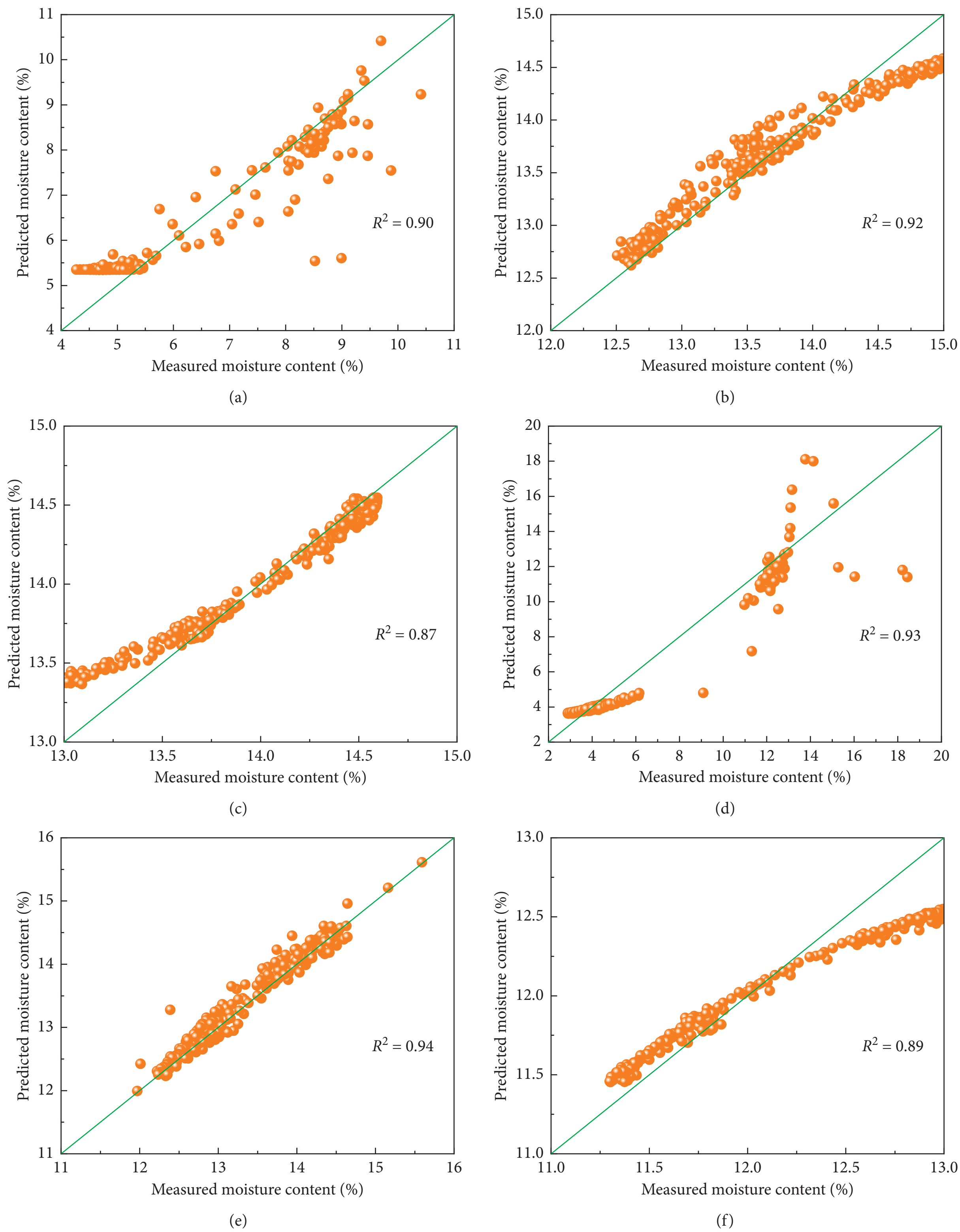

FIGURE 6: Comparison of the predicted values of the soil moisture with measured values (a–c) K 2020 + 024 section. (d–f) K 2028 + 746 section.

4. Conclusions

Based on soil moisture measurement data at different depths of two sections of the Lan–Xin high-speed railway and combined with the LSTM deep neural network model, this study explored the application of this model in the short-term prediction of temporal series changes in soil moisture content. The specific conclusions are as follows:

(1) Aiming at obtaining a nonlinear law for soil moisture monitoring data, the number of model units was determined using the hyperparameter search method

(2) The LSTM neural network model has a strong generalization ability in the short-term prediction of soil moisture content, and it can be used for soil moisture content prediction tasks

(3) For a significant number of soil moisture prediction tasks at different depths, the LSTM model has higher prediction accuracy in the shallower depth; it has the best prediction effect for the depth of 0.5 m in a specific time period

In conclusion, the strategy discussed in this study, based on field monitoring data and a deep neural network model, can effectively extract the dynamic characteristics of soil moisture content monitoring. It can effectively predict the soil moisture content in a specific period of time, thereby providing a practical reference for the safety of train operation.

Data Availability

The figures and tables data used to support the findings of this study are included within the article.

Conflicts of Interest

The authors declare that they have no conflicts of interest.

Acknowledgments

This work was financially supported by the Strategic Priority Research Program of the Chinese Academy of Sciences (Grant no. XDA19070504), National Natural Science Foundation of China (Grant no. 41801043), and Open Fund of State Key Laboratory of Frozen Soil Engineering (Grant no. SKLFSE201712). The authors thank Prof. Fu Jun Niu, Prof. Zhan Ju Lin, and Dr An Yuan Li for their while support field data.

References

[1] X. Xu, J. Wang, and L. Zhang, *Physics of Frozen Soil*, Science Press, Beijing, China, 2nd edition, 2010.

[2] T. Zhang, R. G. Barry, K. Knowles, J. A. Heginbottom, and J. Brown, "Statistics and characteristics of permafrost and ground-ice distribution in the northern hemisphere1," *Polar Geography*, vol. 23, no. 2, pp. 132–154, 1999.

[3] B. Tai, Z. Yue, T. Sun, S. Qi, L. Li, and Z. Yang, "Novel anti-frost subgrade bed structures a high speed railways in deep seasonally frozen ground regions: experimental and numerical studies," *Construction and Building Materials*, vol. 269, Article ID 121266, 2021.

[4] Y. Yu and A. Deng, "Mechanism and prevention of highway distress in seasonal frost area," in *Geotechnical Engineering for Disaster Mitigation and Rehabilitation,* Springer, Berlin, Germany, 2008.

[5] S. Zhang, D. Sheng, G. Zhao, F. Niu, and Z. He, "Analysis of frost heave mechanisms in a high-speed railway embankment," *Canadian Geotechnical Journal*, vol. 53, no. 3, pp. 520–529, 2016.

[6] L. Z. Wu, Q. Xu, and R. Q. Huang, "Analysis of freezing-thawing test process of unsaturated clay," *Rock and Soil Mechanics*, vol. 32, no. 4, pp. 1025–1028, 2011.

[7] S. Li, D. Nie, and J. Wu, "Experimental study on the frost heave and water change of a certain kind of silty clay," *Resource environment and engineering*, vol. 24, no. 5, pp. 615–618, 2010.

[8] P. Li, X. Xu, and F. Chen, "Research status and progress of frozen margin and frost heave model," *Journal of Glaciology and Geocryology*, vol. 22, no. 1, pp. 90–95, 2000.

[9] F. Padilla, J.-P. Villeneuve, and J. Stein, "Simulation and analysis of frost heaving in subsoils and granular fills of roads," *Cold Regions Science and Technology*, vol. 25, no. 2, pp. 89–99, 1997.

[10] T. S. Vinson, F. Ahmad, and R. Rieke, "Factors important to the development of frost heave susceptibility criteria for coarse-grained soils," Transportation Research Board, Washington, DC, USA, 1986, pp. 124–131, Transportation Research Board N1089.

[11] D. Sheng, S. Zhang, and H. E. Zuoyue, "Assessing frost susceptibility of soils," *Chinese Journal of Rock Mechanics and Engineering*, vol. 33, no. 2, pp. 594–605, 2014.

[12] Z. Huixin, W. Zhiqin, and L. Zhaoyu, "Experimental study on frost heave of silty clay in seasonally frost soil regions," *Procedia Engineering*, vol. 28, pp. 282–286, 2012.

[13] H. Liu, F. Niu, Y. Niu, Z. Lin, J. Lu, and J. Luo, "Experimental and numerical investigation on temperature characteristics of high-speed railway's embankment in seasonal frozen regions," *Cold Regions Science and Technology*, vol. 81, pp. 55–64, 2012.

[14] Y. C. Zhang, X. Li, X. F. Zhang, and D. Q. Zhang, "Research on frost heave susceptibility and classification of coarse grained soil of highway subgrade in seasonally frozen ground region," *Yan Tu Gong Cheng Xue Bao*, vol. 29, no. 10, pp. 1522–1526, 2007.

[15] Q. Wang, J. Liu, X. Zhu, J. Liu, and Z. Liu, "The experiment study of frost heave characteristics and gray correlation analysis of graded crushed rock," *Cold Regions Science and Technology*, vol. 126, pp. 44–50, 2016.

[16] N. N. Khoury and M. M. Zaman, "Correlation between resilient modulus, moisture variation, and soil suction for subgrade soils," *Transportation Research Record: Journal of the Transportation Research Board*, vol. 1874, no. 1, pp. 99–107, 2004.

[17] M. Chikira, "Eastward-propagating intraseasonal oscillation represented by chikira-sugiyama cumulus parameterization. part II: understanding moisture variation under weak temperature gradient balance," *Journal of the Atmospheric Sciences*, vol. 71, no. 2, pp. 615–639, 2014.

[18] B. B. Teltayev and E. A. Suppes, "Temperature in pavement and subgrade and its effect on moisture," *Case studies in thermal engineering*, vol. 13, Article ID 100363, 2019.

[19] R. A. Tarefder and M. Ahmad, "Evaluation of pore structure and its influence on permeability and moisture damage in

asphalt concrete," *International Journal of Pavement Engineering*, vol. 18, no. 3, pp. 274–283, 2017.
[20] N. Khoury, R. Brooks, M. M. Zaman, and C. N. Khoury, "Variations of resilient modulus of subgrade soils with postcompaction moisture contents," *Transportation Research Record: Journal of the Transportation Research Board*, vol. 2101, no. 1, pp. 72–81, 2009.
[21] K. Naji, "Resilient modulus-moisture content relationships for pavement engineering applications," *International Journal of Pavement Engineering*, vol. 19, no. 7, pp. 651–660, 2018.
[22] Z. Lin, F. Niu, X. Li et al., "Characteristics and controlling factors of frost heave in high-speed railway subgrade, northwest China," *Cold Regions Science and Technology*, vol. 153, pp. 33–44, 2018.
[23] S. Hochreiter and J. Schmidhuber, "Long short-term memory," *Neural Computation*, vol. 9, no. 8, pp. 1735–1780, 1997.
[24] A. Sagheer and M. Kotb, "Time series forecasting of petroleum production using deep LSTM recurrent networks," *Neurocomputing*, vol. 323, pp. 203–213, 2019.
[25] J. Chen, A. Li, C. Bao et al., "A deep learning forecasting method for frost heave deformation of high-speed railway subgrade," *Cold Regions Science and Technology*, vol. 185, Article ID 103265, 2021.
[26] H. Mittelbach, I. Lehner, and S. I. Seneviratne, "Comparison of four soil moisture sensor types under field conditions in Switzerland," *Journal of Hydrology*, vol. 430-431, pp. 39–49, 2012.
[27] J. Guo, J. Chen, and Y. Hu, "Time series prediction for deformation of the metro foundation pit based on wavelet intelligence model," *Chinese Rock and Soil Mechanics*, vol. 41, no. 1, pp. 299–304, 2020.
[28] Y. Tian and L. Pan, "Predicting short-term traffic flow by long short-term memory recurrent neural network," in *Proceedings of the 2015 IEEE International Conference on Smart city/SocialCom/SustainCom (SmartCity)*, pp. 153–158, IEEE, Chengdu, China, December 2015.
[29] D. M. Nelson, A. C. Pereira, and R. A. De Oliveira, "Stock market's price movement prediction with LSTM neural networks," in *Proceedings of the 2017 International Joint Conference on Neural Networks (IJCNN)*, pp. 1419–1426, IEEE, Anchorage, AK, USA, May 2017.
[30] W. Tian, Z. Liao, and J. Zhang, "An optimization of artificial neural network model for predicting chlorophyll dynamics," *Ecological Modelling*, vol. 364, pp. 42–52, 2017.
[31] D. P. Kingma and J. Ba, "Adam: a method for stochastic optimization," 2014, https://arxiv.org/abs/1412.6980.
[32] F. Zhang, S. Wu, J. Liu et al., "Predicting soil moisture content over partially vegetation covered surfaces from hyperspectral data with deep learning," *Soil Science Society of America Journal*, 2020.

Hindawi
Advances in Materials Science and Engineering
Volume 2021, Article ID 4921365, 14 pages
https://doi.org/10.1155/2021/4921365

Research Article

Study on the Freeze-Thaw Process of the Lining Structures of a Tunnel on Qinghai-Tibet Plateau with the Consideration of Lining Frost Damage

Hong Yu[1,2] **Kun Zhang**[3] **Xiaoming Zhu**[4] **Zhizhuo Tian**[3] **and Qinglong Zhang**[3]

[1]*Gansu Province Highway Traffic Construction Group Co., Ltd., Lanzhou 730030, China*
[2]*State Key Laboratory of Frozen Soil Engineering, Northwest Institute of Eco-Environment and Resources, Chinese Academy of Sciences, Lanzhou 730000, China*
[3]*Gansu Provincial Transportation Research Institute Group Co., Ltd., Lanzhou 730000, China*
[4]*Gansu Province Transport Planning Survey & Designing Institute Co., Ltd., Lanzhou 730030, China*

Correspondence should be addressed to Kun Zhang; zhangkun2020@163.com

Received 6 May 2021; Accepted 24 June 2021; Published 8 July 2021

Academic Editor: Hao Zheng

In seasonally frozen ground, there are many frost problems in highway road tunnel after its excavation due to the heat exchange between the cold air and lining structure inside the tunnel. To mitigate these frost-related damages, thermal insulation layer is widely used at entrance and exit sections of the tunnel. In this study, a coupled mathematical model of heat, moisture, and stress was built for tunnels in seasonally permafrost regions. Then, based on the field-observed air temperature inside a roadway tunnel at Altun Mountain on the Qinghai-Tibet Plateau (QTP), seasonal freeze-thaw process of the surrounding rocks (SR) and lining structures were numerically investigated with the consideration of insulation methods: without insulation (WTIL) and laying the insulation layer on the inner surface of the second lining structure (STIL). Combined with the principle of Miner damage accumulation, the stress regimes of the lining structures of tunnel were investigated in WTIL and STIL. The results show that there was a significantly thermal disturbance of the SR after the tunnel excavation. In the 5th year of the operation period, the maximum seasonal freeze depth (MSFD) of the SR can reach 1.6 m at the vault of the arch and that at the inverted arch was only 1.0 m due to the pavement inside the tunnel. Then, both the absolute maximum value of the maximum principal stress (MAPS) and minimum principal stress (MIPS) in cold season were bigger than those in warm season comparing the value of the stress filed of the lining structure. In the same way, both the MAPS and MIPS of the lining structure in WTIL are bigger than those in STIL in numerical simulation. The positions of the maximum tensile stress of the primary lining structure in STIL and WTIL were inverted arch. For the lining structures, the greater tensile stress was generally harmful. Thus, the inverted arch of the tunnel should be laid on the insulation layer.

1. Introduction

Frozen ground is defined as soil or rock including ice with a temperature at or below 0°C, which can be divided into permafrost and seasonal permafrost [1]. In China, permafrost regions and seasonally frozen regions account for about 20% and 55% of the total land area, which are mainly distributed in the western, northeastern China, and Qinghai-Tibet Plateau [1–6]. In recent years, more and more engineered infrastructures were built in seasonally frozen regions of China. Highway tunnels, as one of the common engineered structures, are commonly affected by the frost damage [7, 8]. After the excavation, the temperature, stress, and even water fields of SR change due to the heat exchange between the lining structure and the air inside the tunnel [8–11]. As we known, the physical and mechanical properties of frozen soils (rocks) are connected closely to their temperature conditions and moisture contents. Hence, with the changes in temperature and moisture fields, the mechanical properties of frozen soils will also change significantly. For the tunnels in seasonally frozen regions, there are frost deformations and moisture migrations in the SR due to the heat exchange with the cold air in winter, leading to deformation, cracking, and destruction of the lining structure [9–11]. The problems related to freezing of the lining structures and SR generally seriously affect the safe operation and the traffic of the tunnel. Engineering practices indicated that the frost damage to the tunnels in seasonally frozen regions was serious and common [12]. Thus, it is necessary to study the frost damage mechanisms and prevention methods to the tunnels in seasonal frozen regions.

To mitigate frost related damage, thermal insulation is widely used at entrance and exit section of the tunnels. Moreover, the study methods of the frost damage problems including filed test measurement, evaluation method, and numerical simulation are widely used to gain the factors thermal insulation design needed. Since 1963, Johansen et al. [13] carried out long-term observations of air-temperature beside a tunnel near the Alaska and gained the distribution of air temperature beside the tunnel. Through the field test measurement of a tunnel in cold environment, Okada and Matsumoto [14] studied the day variation of air temperature and the maximum frozen depth inside the tunnel. Nie [15] observed the air temperature inside and outside a seasonal frost tunnel in Daxing'anling Mountain, Northeast of China. The results showed that the part length of variation rate of air temperature inside the tunnel occupied 1/2 of the whole length of the tunnel. Lai et al. [16] studied the difference of the air temperature inside Daban Mountain tunnel, a road tunnel in Qinghai province, under the conditions of thermal insulation gate set in the entrance and exit of the tunnel. The results showed that the thermal insulation effect of installation of the thermal insulation door was better than that of installation of the snow shelter. Based on the results of field test measurement, the temperature, stress, and moisture fields of the SR and lining structures could be investigated according to the conservation law of mass and energy. In 1973, the Harlan model proposed by Harlan was widely used in the permafrost engineering, which could describe the coupling effect of the moisture migration and temperature flux [17]. Based on the Clapeyron equation and Kelvin equation, Shingo [18] studied the force power of the liquid water migration. Taylor and Luthin [19] proposed a coupling model with the consideration of moisture and temperature in freezing process of the soils according to the Harlan model. Shoop and Bigl [20] used the simulation methods of the coupling model of moisture and temperature to investigate the results of a large-scale freeze-thaw test. Hansson et al. [21] proposed a coupling model of moisture and temperature based on the Richards equation and the model validity was demonstrated combined the comparison of the simulated and freezing test results. Based on the above theories and observed data, many scholars studied insulation methods and the freeze-thaw process of lining and SR. Using heat transfer theory and percolation theory, Lai et al. [22] proposed the coupling model with the consideration of the temperature, moisture, and stress of the lining and SR inside the tunnel. Combined the Galiaojin method, the calculation formula of this model could be gained, which was widely used in related studies of seasonal frozen tunnels. Zhang et al. [23] studied the freeze-thaw process of SR inside a seasonal frozen tunnel under the conditions of different construction seasons, different initial temperatures, and different insulation materials using finite element methods. With the consideration of the wind filed inside the tunnel, Tan et al. [24] investigated the temperature filed of SR inside the tunnel, Galongla tunnel on the QTP, under the conditions of different wind speeds and temperatures. Zhou et al. [25] established a mathematical optimization model with the consideration of the factors including insulation parameters, tunnel depth, and economic costs. Ma et al. [26] analyzed the insulation effect of different insulation thicknesses and laying positions and established the relationship between the insulation effect and the thicknesses. Combining Plath's equation and Fourier integral transform, Liu et al. [27] studied the temperature filed of a tunnel in cold environment under the conditions of different convective heat transfer coefficients, different insulation thicknesses, and different initial temperatures.

In this paper, the Altun Mountain highway tunnel was taken as the research object. In order to observe the air temperatures inside the tunnel, corresponding measurement sensors and a weather station were installed inside and outside the tunnel. According to the design of Altun Mountain highway tunnel, geological survey report, and monitoring meteorological data, a coupling model considering the damage of tunnel lining structure was established. With the model, the distribution of temperature field of surrounding rock body under different insulation laying methods was systematically studied by using numerical method. Under the different methods, the temperature field of SR and the stress field of lining were compared and analyzed with the equivalent indoor experimental freeze-thaw damage model. It is hoped that the filed observations and numerical simulations in this study would provide references for thermal insulation design of tunnels built in seasonally frozen regions.

2. Mathematical Model and Governing Equations

2.1. Liquid Water Flows. Based on the law of mass conservation, the equivalent volume of water content θ without the consideration of water vapor and salt migration in freeze-thaw soils can be written as [5, 21, 28]

$$\frac{\partial \theta}{\partial t} = \frac{\partial \theta_u}{\partial t} + \frac{\rho_i}{\rho_w}\frac{\partial \theta_i}{\partial t} = \nabla\left(q_{lh} + q_{lT}\right), \qquad (1)$$

where θ, θ_u, and θ_i are the equivalent volume of water, unfrozen water, and ice content, respectively ($m^3 \cdot m^{-3}$); ρ_i and ρ_w are the density of ice and water ($kg \cdot m^{-3}$); t is the time; and q_{lh} and q_{lT} are the liquid water flux density related to pressure head gradient and temperature gradient, respectively ($m \cdot s^{-1}$).

Based on thecHarlan model, there is a similar law of liquid water migration in frozen and unfrozen unsaturated soil, which can be described by Richard equation [1, 17]. In a previous study, the regulation law of liquid water migration in freeze-thaw soils can be assumed to Darcy's law [5, 29]. The flux density of liquid water under the potential gradient in freeze-thaw soil can be written as [5, 17, 21, 28, 29]

$$q_{lh} = -K_{lh}\nabla(h + y), \tag{2}$$

where y is the vertical coordinate (m); h is the pressure head of liquid water in freeze-thaw soils (m); and K_{lh} is the water conductivity coefficient of liquid water under potential gradient in freeze-thaw soils ($\mathrm{m{\cdot}s^{-1}}$). The liquid water flux density q_{lT} related to temperature gradient can be written as

$$q_{lT} = -K_{lT}\nabla(T), \tag{3}$$

where K_{lT} is the water conductivity coefficient related to temperature gradient ($\mathrm{m^2{\cdot}K^{-1}{\cdot}s^{-1}}$), which can be written as

$$\begin{aligned} K_{lT} &= K_{lh}\left(hG_{wT}\frac{1}{\gamma_0}\frac{\mathrm{d}\gamma}{\mathrm{d}T}\right), \\ \gamma &= 75.6 - 0.1425T - 2.38\times10^{-4}T^2, \end{aligned} \tag{4}$$

where G_{wT} is gain factor, which can evaluate the temperature effect due to the surface tension of solid granule; γ is surface tension of the solid granule; and γ_0 is the surface tension of the solid granule at 25°C (approximately 71.89 $\mathrm{g{\cdot}s^{-2}}$). Then, the mass conservation equation of liquid water in freeze-thaw soil can be written as [5, 30]

$$\frac{\partial\theta}{\partial t} = \nabla\cdot\left[K_{lh}\nabla(h + y) + K_{lT}\nabla(T)\right]. \tag{5}$$

Soil-water characteristic curve (SWCC) can describe the connection between liquid water and energy in freeze-thaw soil. Based on a previous study, the relationship among matric, volume water content, and saturation in freeze-thaw soils also can be described by SWCC [29]. In this study, the hydraulic properties of unsaturated freeze-thaw soil based on van Genuchten model and Mualem model can be written as [30, 31]

$$\begin{aligned} h &= \frac{-\left(S_e^{(1/-m)} - 1\right)^{(1/n)}}{\alpha}, \\ S_e &= \frac{\theta_l - \theta_r}{\theta_s - \theta_r} = \begin{cases} \dfrac{1}{\left[1 + |\alpha h|^n\right]^m}, & h < 0, \\ 1, & h \geq 0, \end{cases} \\ K &= \begin{cases} K_s S_e^i\left[1 - \left(1 - S_e^{(1/m)}\right)^m\right]^2, & h < 0, \\ K_s, & h \geq 0, \end{cases} \end{aligned} \tag{6}$$

where S_e is effective saturation of soils; K_s is saturation water conductivity coefficient ($\mathrm{m{\cdot}s^{-1}}$); θ_l, θ_s, and θ_r are liquid water, saturated liquid water, and residual water content, respectively ($\mathrm{m^3{\cdot}m^{-3}}$); α is the derivative of the soil intake value ($\mathrm{m^{-1}}$); and n and l are experience parameters and $m = 1 - 1/n$ [31].

2.2. Heat Transfer. With the considerations of the convection, phase change of ice-water and liquid water migration, heat transfer during the transient flow in freeze-thaw soils can be written as [1, 3–5, 17, 21, 28, 29]

$$C\frac{\partial T}{\partial t} = \frac{\partial}{\partial x}\left(\lambda\frac{\partial T}{\partial x}\right) + \frac{\partial}{\partial y}\left(\lambda\frac{\partial T}{\partial y}\right) + L\rho_i\frac{\partial\theta_i}{\partial t} + C_w\nabla\left[\left(K_{lh}\nabla(h + y) + K_{lT}\nabla T\right)T\right], \tag{7}$$

where C is volume heat capacity; λ is thermal conductivity; and L is the latent heat of freezing of liquid water (approximately $3.34\times10^5\ \mathrm{J{\cdot}kg^{-1}}$).

In freeze-thaw soils, a part of liquid water can exist even at a very low temperature, which is unfrozen water. In previous studies, the empirical expression as follows is used to describe the variation of maximum unfrozen water content $\theta_{u\max}$ under low temperatures in freeze-thaw soils [1, 3–5, 28, 29]:

$$\theta_{u\max} = a(T - 273.15)^{-b}, \tag{8}$$

where a and b are experimental parameters. Then, based on the law of conservation of mass, the volume liquid water content θ_l can be written as [5, 28, 29]

$$\theta_l = \begin{cases} \theta, & \text{others}, \\ \theta_{u\max}, & T < T_f \text{ and } \theta > \theta_{u\max}, \end{cases} \tag{9}$$

where T_f is the freezing point of the soil, which is assumed to be 0°C in this study. Based on a previous study, the freezing point of soil should be a temperature value where ice starts to grow [32].

2.3. Mechanism Equation. Based on the theory of linear momentum balance, the equation of linear momentum in the lining structures and SR can be written as [8]

$$\sigma_{ij,j} + \rho f_i = \rho\frac{\mathrm{d}V_i}{\mathrm{d}t}, \tag{10}$$

where σ_{ij} is the component of stress tensor; ρ is the density; and f_i is the component of volume force. Only with the consideration of the gravity in volume force, f_i can be written as

$$f_i = g_i = (0, 0, g)^T, \tag{11}$$

where g is the acceleration of gravity (approximately 9.8 $\mathrm{m/s^2}$).

Combining equation (10) with equation (11), the equation of static equilibrium in the lining structure and SR can be described as

$$\sigma_{ij,j} + \rho f_i = 0. \tag{12}$$

Based on the previous studies and theories related to the linear thermal stress, the elastic deformation displacement and stress produced by external force can be superposed with those produced by the temperature action algebraically. Hence, combined the theory of elastic mechanics, the stress in the lining structure and SR can be written as

$$\varepsilon = \varepsilon_{ij}^{e} + \varepsilon_{ij}^{T} + \varepsilon_{ij}^{i}, \tag{13}$$

where ε is the stress in the lining structure and SR; ε_{ij}^{e} is the increment of elastic stress; ε_{ij}^{T} is the increment of heat stress produced by the temperature action; and ε_{ij}^{i} is the increment of stress produced by the frost expansion due to ice-water phase change and liquid water migration, which can be described as [6]

$$\varepsilon_{ij}^{i} = 0.09(\theta - \theta_w) + (\theta - n). \tag{14}$$

The elastic constitutive equation in lining structure and SR can be written as

$$\sigma_{ij} = C_{ijkl}^{e}\left(\varepsilon_{kl} - \varepsilon_{kl}^{T} - \varepsilon_{ij}^{i}\right) = C_{ijkl}^{e}\left[\varepsilon_{kl} - \beta_s(T_s - T_{s0})\delta_{kl} - \varepsilon_{ij}^{i}\right], \tag{15}$$

where T_s and T_{s0} are the temperatures of the lining structure and SR and reference temperature (approximately 20°C), respectively; β_s is coefficients of linear thermal expansion of the lining structure and SR; and C_{ijkl}^{e} is the elasticity matrix. Combining equation (12) with equation (15), it can be gained as follows:

$$\left[C_{ijkl}^{e}\varepsilon_{kl}\gamma(T_s - T_{s0})\delta_{ij} - \varepsilon_{ij}^{i}\right]_{,j} + \rho f_i = 0. \tag{16}$$

It is assumed that the deformation of the lining structure and SR are all small deformations. Hence, based on the elastic mechanics, the geometric equation of lining structure and SR can be written as

$$\mathrm{d}\varepsilon_{ij} = \frac{1}{2}\left(\frac{\partial \mathrm{d}u_i}{\partial x_j} + \frac{\partial \mathrm{d}u_j}{\partial x_i}\right), \tag{17}$$

where ε_{ij} is the component of stress tensor and u_i is the component of the deformation. Combined with equation (16), the mechanism equation of lining structure and SR can be written as

$$\left[\frac{1}{2}C_{ijkl}^{e}\left(\frac{\partial \mathrm{d}u_i}{\partial x_j} + \frac{\partial \mathrm{d}u_j}{\partial x_i}\right) - \gamma_s(T_s - T_{s0})\delta_{ij} - \varepsilon_{ij}^{i}\right]_{,j} + \rho f_i = 0. \tag{18}$$

According to previous and related studies, the equivalent elastic modulus E and equivalent poison's ratio v of the SR in freezing and thawing processes can be written as [33]

$$E = \frac{\left[c_s E_s(1 - 2v_i) + c_i E_i(1 - 2v_s)\right]\left[c_s E_s(1 + v_i) + c_i E_i(1 + v_s)\right]}{c_s E_s(1 - 2v_i)(1 + v_i) + c_i E_i(1 - 2v_s)(1 + v_s)},$$

$$v = \frac{c_s E_s v_s(1 - 2v_i)(1 + v_i) + c_i E_i v_i(1 - 2v_s)(1 + v_s)}{c_s E_s(1 - 2v_i)(1 + v_i) + c_i E_i(1 - 2v_s)(1 + v_s)}, \tag{19}$$

where c_s and c_i are the volume contents of the solid granule and ice, respectively.

3. A Tunnel Built on the Qinghai-Tibet Plateau

3.1. Study Area and Tunnel. In this study, a highway tunnel on the QTP was used to study the freeze-thaw process of the lining structure of tunnels in seasonal frost regions. The study area is located at southeast edge of the QTP, with an elevation above 3000 m. According to Lenghu weather station closet to this site, the mean annual air temperature is about 3.6°C, and the maximum and minimum air temperatures are 26.9 and −21.7°C in past 10 years, respectively (Figure 1). Meanwhile, this engineering site is in an alpine and semi-arid climate zone, with a little annual precipitation.

3.2. Air Temperature Observation along the Tunnel. The tunnel on the QTP has a length of 7,527 m and faces potential frost damage according to the air temperature data monitored by Lenghu weather station. In previous studies, the section closest to the entrance of the tunnel generally suffers worst frost damage. To gain the variation of air temperature at that entrance (D1) of the tunnel (Figure 2), an air temperature sensor was placed at 5 m from the entrance. The sensor used in this monitoring test was manufactured and calibrated by TASCO (Japan), with a calibrated range from −30 to 60°C and a resolution smaller than 1.0°C. The date acquisition of air temperature was set as 4 hours.

4. Numerical Simulations

4.1. Computational Model. Based on previous studies and related works, the boundary error in numerical simulations would be less than 10% when the computational domain is 3–5 times of the equivalent diameter of the tunnel [5, 34]. Then, the computational model was constructed based on the actual section D1 of the tunnel in this study (Figure 3). The insulation methods were considered in this study: without insulation (WTIL) and laying the insulation layer on the inner surface of the second lining structure (STIL).

According to the geological survey conducted, the SR at D1 section of tunnel can be simplified as one kind material. The thermal and hydraulic parameters of the SR and lining structure are listed in Table 1, which were gained based on the borehole drilling, related laboratory tests, and previous studies [1, 17, 21, 28, 29].

For the lining structures of tunnel in seasonal frost regions, the effect of freeze-thaw circle is one of main factors affecting the mechanical properties of lining structures. At present, although massive rapid freeze-thaw test data of concrete have been accumulated, it was still considerably

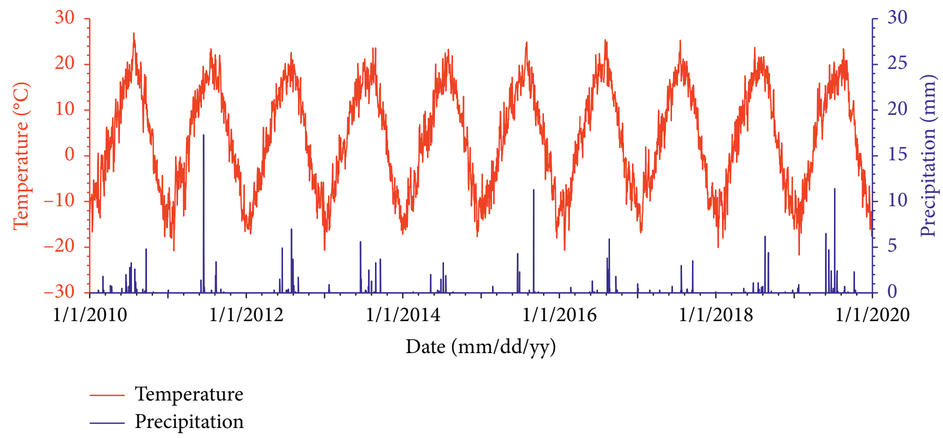

Figure 1: Observation of air temperature and precipitation in the study area monitored by Lenghu weather station.

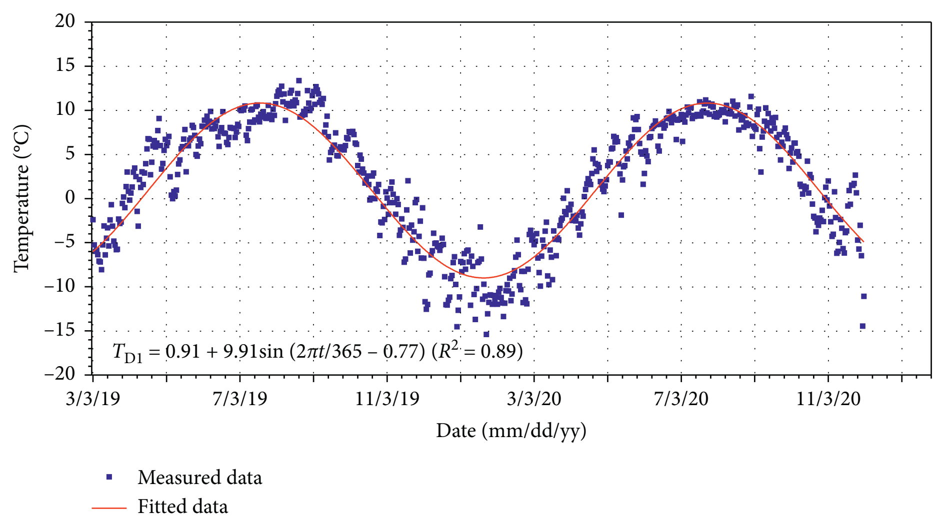

Figure 2: Observation of air temperature at D1 inside the tunnel monitored with a temperature sensor.

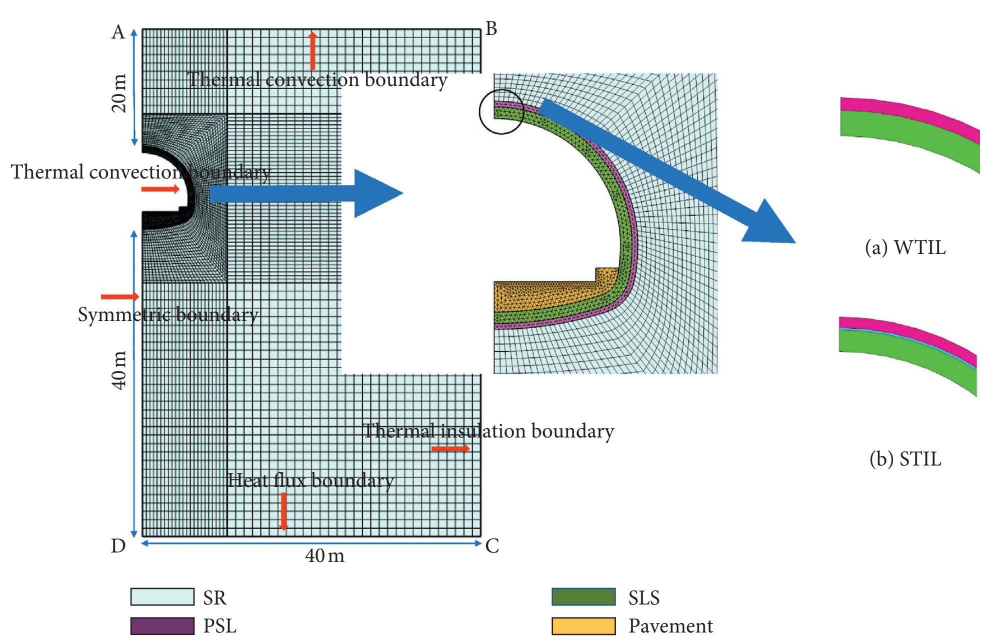

Figure 3: Numerical model of the Altun mountain tunnel.

Table 1: Thermal and hydraulic parameters of lining structures, insulation layer, and SR in the simulation.

Parameters	λ_u W/(m·°C)	λ_f W/(m·°C)	C_u J/(kg·°C)	C_f J/(kg·°C)	a	b	α (m^{-1})	θ_r	θ_s	K_s (m·s^{-1})	ρ (kg·m^{-3})	L_s (J·m^{-3})
PLS	2	2	2.30×10^6	2.30×10^6	—	—	—	—	—	—	2500	—
SLS	2	2	2.30×10^6	2.30×10^6	—	—	—	—	—	—	2500	—
TIL	0.037	0.037	9.40×10^5	9.40×10^5	—	—	—	—	—	—	188	—
SR	1.47	1.82	2.09×10^6	1.84×10^6	9.3	0.52	2.3	0.02	0.25	1.2×10^{-8}	1700	3.77×10^7

difficult to apply in practical prediction of concrete durability and freeze-thaw damage due to the great differences of freeze-thaw between in actual and lab environments. In previous studies and related works, based on the principle of Miner damage accumulation, Liu and Tang established a calculation expression of equivalent lab freeze-thaw cycles of concrete by comparing and analyzing the difference and relation between the actual and lab environments [35]. Then, the expression of equivalent freeze-thaw cycles N_{eq} in lab tests of concrete can be written as

$$N_{eq} = \left(\sum_i \frac{N_i}{N_{Fi}}\right) N_F = \left(\sum_i \frac{N_i}{\kappa_i^{-\xi} N_F}\right) N_F = \sum_i \kappa_i^{\xi} N_i, \quad i = 1, 2, \ldots, \tag{20}$$

where N_{eq} is the equivalent freeze-thaw cycles in lab tests of concrete; N_1 is the number of freeze-thaw cycles in actual environment of concrete; N_{F1} is the fatigue life under different freeze-thaw cycles in actual environment of concrete; κ_i is the proportional coefficient between hydrostatic pressures in lab and actual environments; and ξ is a material parameter related to concrete (approximately 0.946), which is a constant under the assumption that the properties of concrete materials do not change with the freeze-thaw environment [36]. Based on previous studies and related works, κ_i can be written as

$$\kappa_i \approx \frac{\dot{T}_i}{\dot{T}} \approx \frac{T_i/t}{T/t_2}, \tag{21}$$

where ΔT_i is the difference between daily maximum air temperature and minimum temperature in actual environment; t_1 is the time interval between daily maximum air temperature and minimum temperature in actual environment; ΔT is the difference between maximum air temperature and minimum temperature in lab environment; and t_2 is the time interval between daily maximum air temperature and minimum temperature in lab environment. In previous studies, $\Delta T/t_2$ is approximately 12.5°C/h [37]. Based on the measured air temperature data in this study, κ_i can be calculated using equation (21), as shown in Table 2. Meanwhile, the equivalent freeze-thaw cycles in lab tests of concrete (EFTC) of this tunnel is 0.92 $1/y$ in actual environment with WTIL.

But for STIL, the EFTC of the lining structure would be smaller with the effect of insulation layer. Due to the limited of actual site operation, there was no temperature sensor laying in the lining structure of the tunnel. Then, based on the measured air temperature, the EFTC with STIL can be gained using numerical simulation in this study.

According to the construction instructions of the tunnel, a 5 cm thick insulation material was laid with STIL. In numerical simulation, the thermal conductivity and specific heat capacity of insulation layer were set as 0.025 W/(m·°C) and 5000 kg·°C, respectively. Based on measured air temperature, the maximum air temperature at D1 section was 17.3°C and the minimum was −17.5°C. Using equation (21), k_i was 2.9 under most unfavorable situation. In numerical simulation, the inner surface of TIL with STIL was set as convection heat transfer boundary and the air temperature can be written as

$$T_{air} = \begin{cases} \dfrac{34.8t}{12} - 17.3, & 0 \le t \le 12\,\text{h}, \\[2ex] -\dfrac{34.8\,(t-12)}{12} + 17.5, & 12\,\text{h} \le t \le 24\,\text{h}. \end{cases} \tag{22}$$

Based on the simulation results, it could be found that the temperature of the inner surface of the TIL is basically the same as the air temperature after the whole freeze-thaw cycle, while the change of inner surface of the second lining structure is much smaller than that of inner surface of TIL (Figure 4). Meanwhile, the EFTC of the second lining structure (SLS) under STIL was 0.17 $1/y$ using equation (21).

Based on previous studies and related works, the relationship between the dynamic elastic modulus and time of concrete can be written as [38]

$$\begin{aligned} E_{n1} &= -7.07 + 3.54e^{(n/59.89)} + 3.54e^{(n/73.20)}\left(R^2 = 0.99\right), \\ E_{n2} &= -5.16 + 2.58e^{(n/84.38)} + 2.58e^{(n/103.13)}\left(R^2 = 0.97\right), \end{aligned} \tag{23}$$

where E_{n1} and E_{n2} are the dynamic elastic modulus of primary lining structure (PLS) and second lining structure (SLS), respectively, and n is the number of freeze-thaw cycles in lab environment. In this study, the physical parameters in numerical simulation are listed in Table 3.

4.2. Boundary Conditions. The thermal boundary conditions of the tunnel in the numerical simulation were determined as follows. The upper boundary AB and the inner wall of the tunnel were set as heat convection boundary. According to the geothermal gradient beneath the tunnel, the heat flux at CD was 0.03 W/m^2. The lateral boundary BC was thermal insulation boundary and AD was the symmetry boundary. The water boundary conditions were determined as follows. The boundaries AB, BC, and CD were set as waterproof boundaries without the consideration of rainfall on the water content of SR. The boundary AD was also set as symmetry boundary. The stress boundary conditions were determined as follows. The displacement of boundary BC in lateral

Table 2: The calculation value of κ_i at D1 section of the tunnel using equation (21).

Date	Minimum air temperature (°C)	Maximum air temperature (°C)	Time interval (h)	k_i
2019/11/21	−0.47	1.90	12	0.02
2019/11/22	−0.12	2.50	8	0.03
2019/11/25	−2.55	1.00	12	0.02
2019/11/27	−1.05	2.00	8	0.03
2019/11/28	−6.77	1.20	16	0.04
2020/3/7	−2.67	0.80	8	0.03
2020/3/18	−3.07	1.30	8	0.04
2020/3/19	−2.45	0.60	8	0.03
2020/3/20	−2.23	0.80	8	0.03
2020/3/22	−1.47	1.70	8	0.03
2020/3/23	−1.80	0.90	8	0.03
2020/3/25	−1.08	2.00	8	0.03
2020/3/26	−1.28	0.30	8	0.02
2020/3/27	−0.65	1.80	8	0.02
2020/3/29	−1.98	0.50	8	0.02
2020/3/30	−2.35	0.50	8	0.03
2020/4/1	−1.90	1.80	12	0.02
2020/4/2	−3.33	1.20	8	0.05
2020/4/4	−2.87	0.40	8	0.03
2020/4/5	−1.53	2.20	12	0.02
2020/4/6	−2.00	0.80	8	0.03
2020/5/7	−1.87	0.30	8	0.02
2020/10/10	−0.63	3.30	16	0.02
2020/10/11	−2.02	1.00	20	0.01
2020/10/14	−2.67	2.10	20	0.02
2020/10/15	−3.03	0.50	16	0.02
2020/10/16	−2.20	1.40	16	0.02
2020/10/17	−2.43	0.10	8	0.03
2020/10/18	−1.33	2.20	16	0.02
2020/10/22	−0.15	4.00	16	0.02
2020/10/24	−0.83	4.10	16	0.02
2020/10/25	−2.63	0.20	16	0.01
2020/10/29	−2.15	3.20	16	0.03
2020/11/2	−2.37	0.40	16	0.01
2020/11/8	−0.83	0.60	8	0.01
2020/11/10	−0.65	2.30	12	0.02
2020/11/16	−4.72	2.90	16	0.04

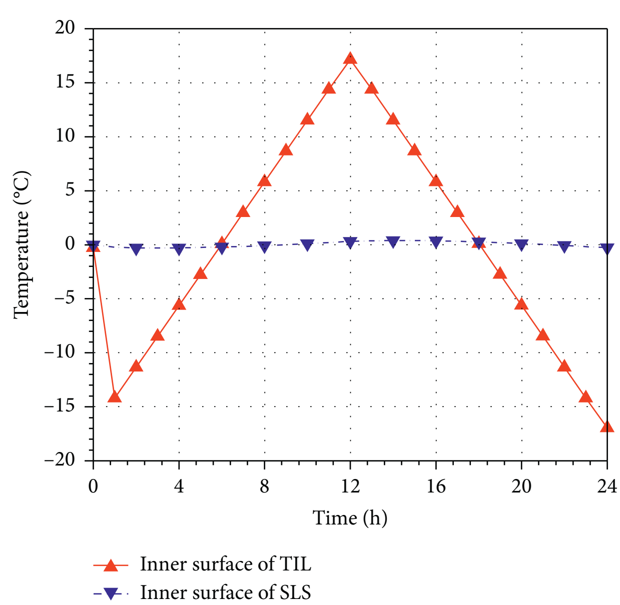

Figure 4: The variation of temperatures at inner surfaces of TIL and SLS.

Table 3: The physical parameters of lining structure and SR in numerical simulation.

	Density (kg/m^3)	Elastic modulus (MPa)	Poisson's ratio	Thermal expansion coefficient (1/°C)
SR	1800	900	0.3	5×10^{-5}
PSL	2500	2800	0.2	6×10^{-5}
SLS	2500	3000	0.2	6×10^{-5}
TIL	188	0.2	0.2	5×10^{-5}

direction was set as 0 m. The displacement of boundary CD in vertical direction was also 0 m. The boundary AD was set as symmetry boundary.

With the mathematical model including liquid water flows, heat transfer, and mechanism equation mentioned above, the frost problem could be solved by the commercial software of COMSOL Multiphysics. The spatial and temporal discretization of mathematical model and governing equations were carried out through using finite method [5]. This simulation was conducted over a time period of 50 years before the tunnel excavation to gain the initial field conditions. After the excavation, the boundary conditions were set as the ones described above.

5. Results and Analysis

5.1. Long-Term Thermal and Stress Regimes at D1 of the Tunnel. For the most tunnels in permafrost regions on the QTP, the MSFD generally occurs in mid-April. In the following analysis, the timepoint was chosen to investigate the long-term thermal regimes of the SR and stress regimes of the lining structures.

Figure 5 shows the thermal regimes at D1 in WTIL on April 15 in 5 years of the operation period of the tunnel. It can be seen that, due to the heat exchange between the air changing with the time and the lining structures, the SR close to the lining structures had a lower temperature on April 15 in 5 years of the operation period, while with the distance from the lining structures increasing, the temperature of the SR gradually rose. In the 5$^{\text{th}}$ year of the operation period, the MSFD of the SR was 1.6 m, approximately. Then, due to the geometrical shape of the tunnel, the thermal regimes of different position of the tunnel were considerably different. For example, the MSFD of the SR at the inverted arch was obviously smaller than that of the vault, while the MSFD of the SR at the foot of arch was situated between the two.

Figure 6 shows the stress regimes of the primary lining structure at D1 in WTIL on April 15 in 5 years of the operation period of the tunnel. It can be seen that both the MAPS and MIPS of the primary lining structure in cold season are bigger than those in warm season. For example, the absolute maximum value of MAPS in cold season was −3.6 MPa, while that in warm season was −2.3 MPa. Moreover, the absolute maximum value of MIPS in cold season was −1.4 MPa, while that in warm season was −1.0 MPa. The tensile stress of the primary lining structure was 0.7 MPa in cold season and 0.2 MPa in warm season. It reflected that in cold season, due to the heat exchange between the cold air and the SR, the liquid water in the SR was transferred to the solid ice leading the frost heave force loading on the primary lining structure, while in warm

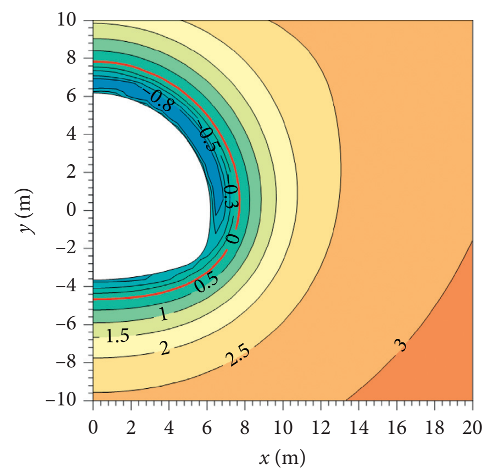

Figure 5: Thermal regimes at D1 in WTIL on April 15 in 5 years of the operation period of the tunnel.

season, there was no frost heave force surrounding the primary lining structure. Moreover, the material of the primary lining structure belonged to be the material which cannot resist too much tensile stress. Then, it was considerably essential to decrease the tensile stress related to the frost heave force on the primary lining structure.

Figure 7 shows the stress regimes of the second lining structure at D1 in WTIL on April 15 in 5 years of the operation period of the tunnel. It can be seen that the size relationship of the MAPS and MIPS of the second lining structure was generally the same as that of the primary lining structure. For example, the absolute maximum value of the MAPS of the second lining structure in cold season was −5.4 MPa, which was 0.9 MPa bigger than that in warm season. The absolute maximum value of the MIPS of the second lining structure in cold season was −2.8 MPa, which was also 1.7 MPa bigger than that in warm season. Moreover, the tensile stress in cold season was 0.8 MPa, while that in warm season was only 0.46 MPa.

The above results showed that in cold season both the absolute values of MAPS and MIPS of the primary and second lining structure were bigger than those in warm season. Moreover, both the values of tensile stress of the primary and second lining structure were bigger than those in warm season. For the lining structures of the tunnel, which cannot resist too much tensile stress, it was considerably essential to decrease the tensile stress related to the frost heave force on lining structures.

5.2. Impacts of Insulation Laying Methods on Thermal Regimes at D1 of the Tunnel in Cold Seasons. Figure 8 shows thermal regimes of SR at D1 in WTIL and STIL on April 15 in 5 years

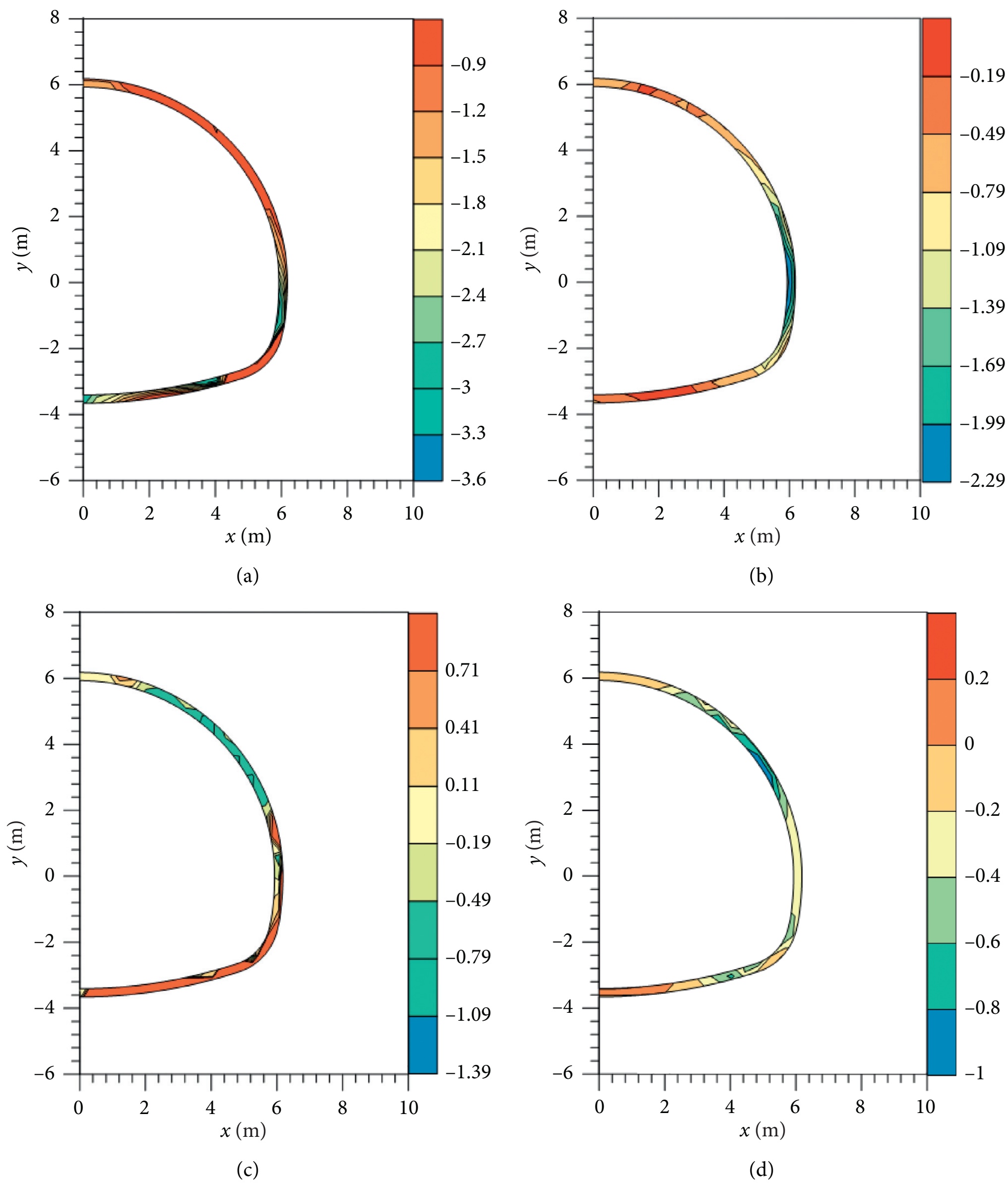

Figure 6: Stress regimes of the primary lining structure at D1 in WTIL on April 15 in 5 years of the operation period of the tunnel. (a) MAPS in cold season. (b) MAPS in warm season. (c) MIPS in cold season. (d) MIPS in warm season.

of the operation period of the tunnel. The MSFD calculated from the outer surface of the primary lining in WTIL was 1.6 m at vault of the tunnel and it was only 1.0 m at the inverted arch, while in STIL, the MSFD at vault of the tunnel was 0.1 m and it at the inverted arch was 1.0 m. The value of the MSFD can reflect the thermal effect of the heat exchange between the air inside the tunnel and the lining structure. Then, the values of MSFD at vault and inverted arch in WTIL were generally bigger than those in STIL. Moreover, although there was insulation layer laid on the surface of the lining structure, the values of MSFD at inverted arch were basically the same both in WTIL and in STIL due to the design of insulation layer. In STIL, only the lining structure above the foot of the arch was laid on the insulation layer due to the difficulties of laying below the pavement inside the tunnel.

5.3. Impacts of Insulation Laying Methods on Stress Regimes at D1 of the Tunnel in Cold Seasons. Figure 9 shows MAPS in STIL, MAPS in WTIL, MIPS in STIL, and MIPS in WTIL of the primary lining structure at D1 on April 15 in 5 years of the operation period of the tunnel. It can be seen that both the MAPS and MIPS of the primary lining structure in WTIL are bigger than those in STIL. For example, the absolute maximum value of MAPS in STIL was −3.6 MPa, while that in WTIL was −5.8 MPa. Moreover, the absolute maximum value of MIPS in STIL was only −1.4 MPa, while that in

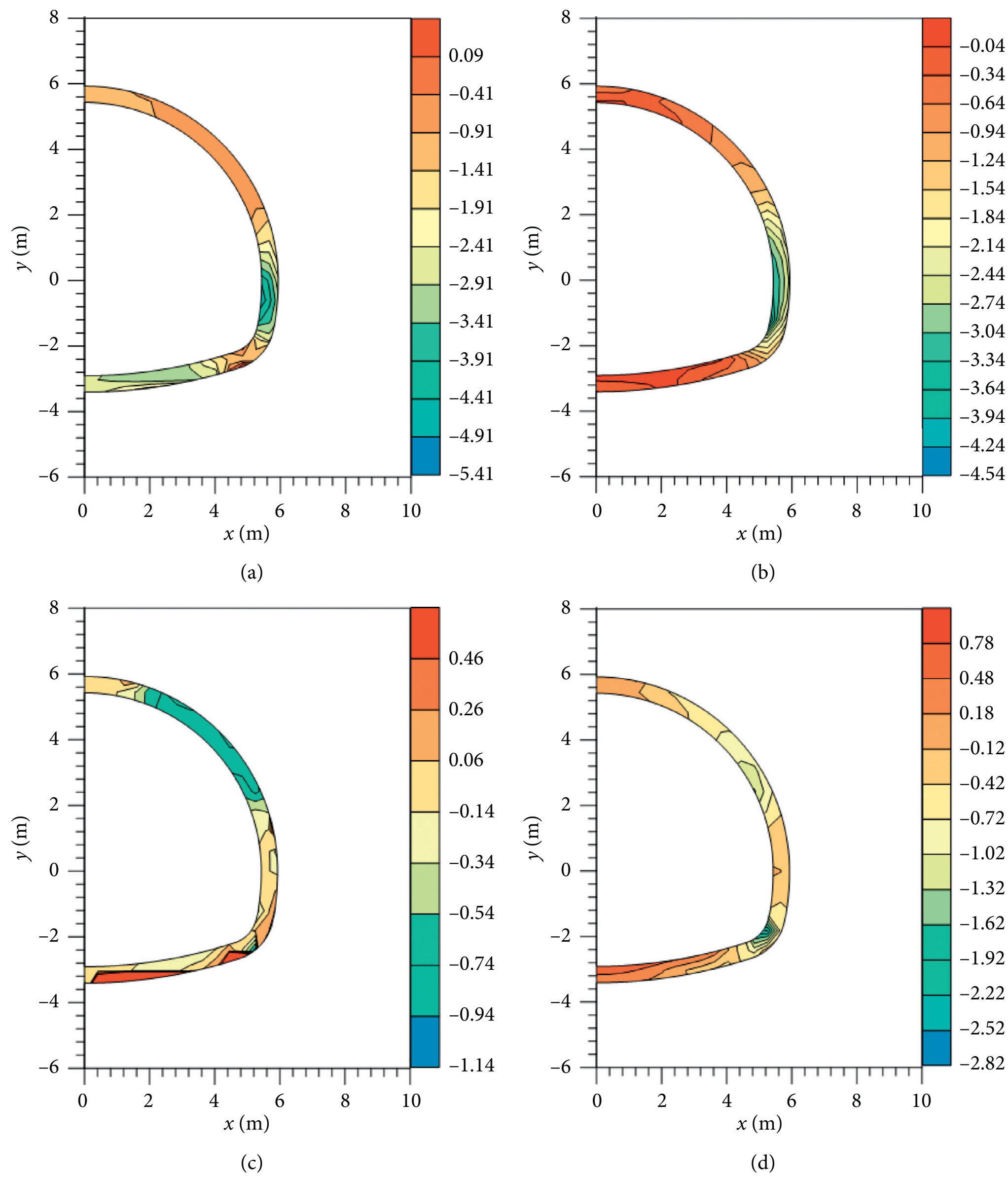

FIGURE 7: Stress regimes of the second lining structure at D1 in WTIL on April 15 in 5 years of the operation period of the tunnel. (a) MAPS in cold season. (b) MAPS in warm season. (c) MIPS in cold season. (d) MIPS in warm season.

WTIL was −3.0 MPa. The tensile stress of the primary lining structure was 0.7 MPa in STIL and 0.2 MPa in WTIL. It reflected that in STIL, due to the existence of the insulation layer, the thermal effect of heat exchange between the cold air and the lining structure decreased. Then, with this thermal effect, the liquid water in the SR was transferred to the solid ice leading the frost heave force loading on the primary lining structure. This meant that, in STIL, the values of the MAPS and MIPS were all smaller than those in WITL due to the existence of the insulation layer. Moreover, both the positions of the maximum absolute value of MAPS in STIL and WTIL were at the hance of the arch. The positions of the maximum tensile stress of the primary lining structure in STIL and WTIL were at the hance and inverted arch.

Figure 10 shows MAPS in STIL, MAPS in WTIL, MIPS in STIL, and MIPS in WTIL of the second lining structure at D1 on April 15 in 5 years of the operation period of the tunnel. It can be seen that both the MAPS and MIPS of the second lining structure in WTIL were bigger than those in STIL. For example, the absolute maximum value of MAPS in STIL was −5.4 MPa, while that in WTIL was −11.0 MPa. Moreover, the absolute maximum value of MIPS in STIL was only −1.1 MPa, while that in WTIL was −4.7 MPa. The tensile stress of the primary lining structure was 0.5 MPa in STIL and 2.3 MPa in WTIL. It reflected that in STIL, due to the existence of the insulation layer, the thermal effect of heat exchange between the cold air and the lining structure decreased. Then, with this thermal effect, the

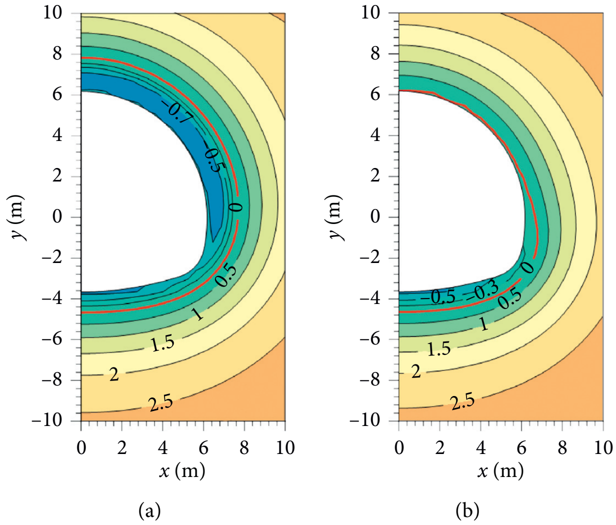

Figure 8: Thermal regimes of SR at D1 in (a) WTIL and (b) STIL on April 15 in 5 years of the operation period of the tunnel.

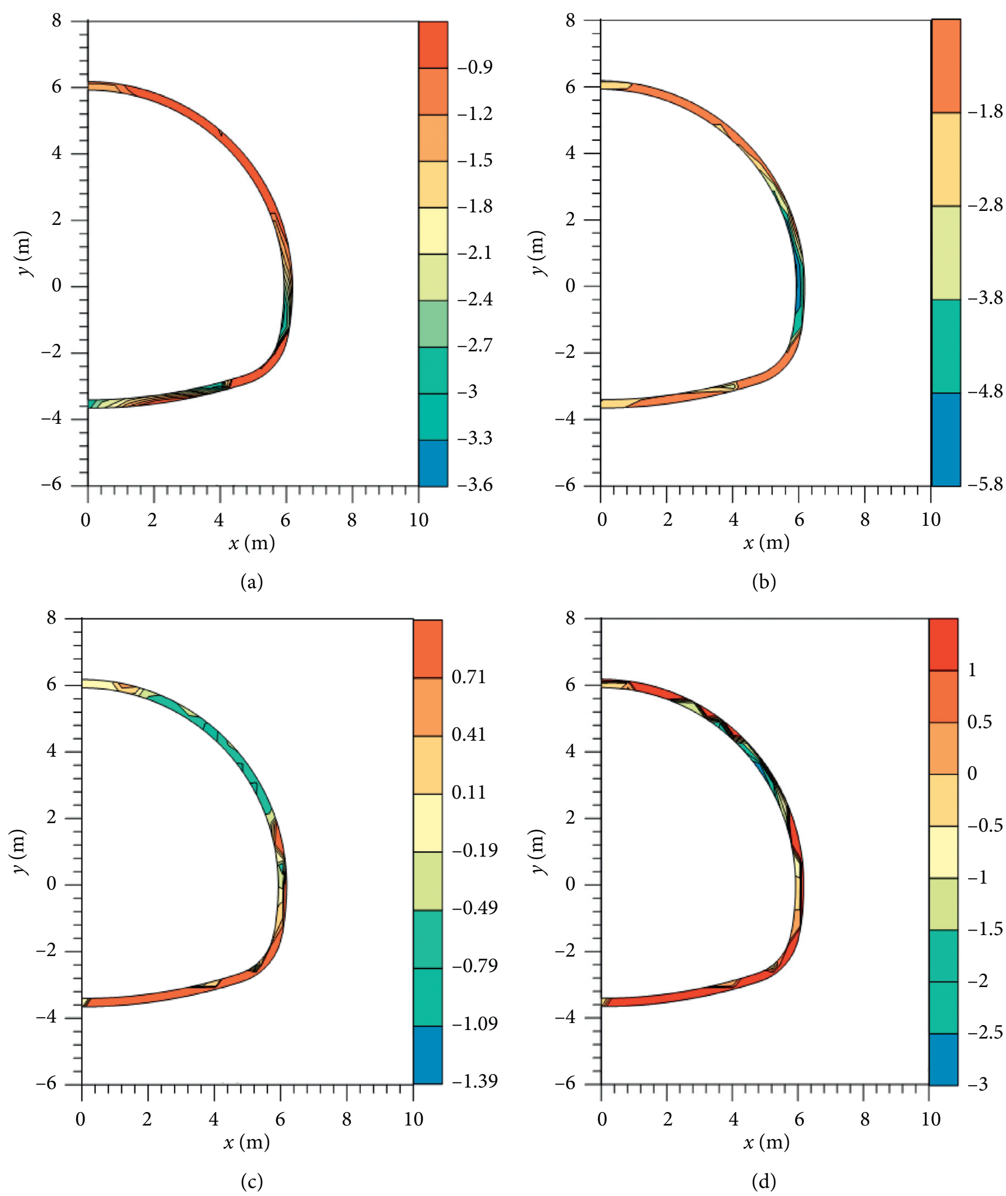

Figure 9: Stress regimes of the primary lining structure at D1 on April 15 in 5 years of the operation period of the tunnel. (a) MAPS in STIL. (b) MAPS in WTIL. (c) MIPS in STIL. (d) MIPS in WTIL.

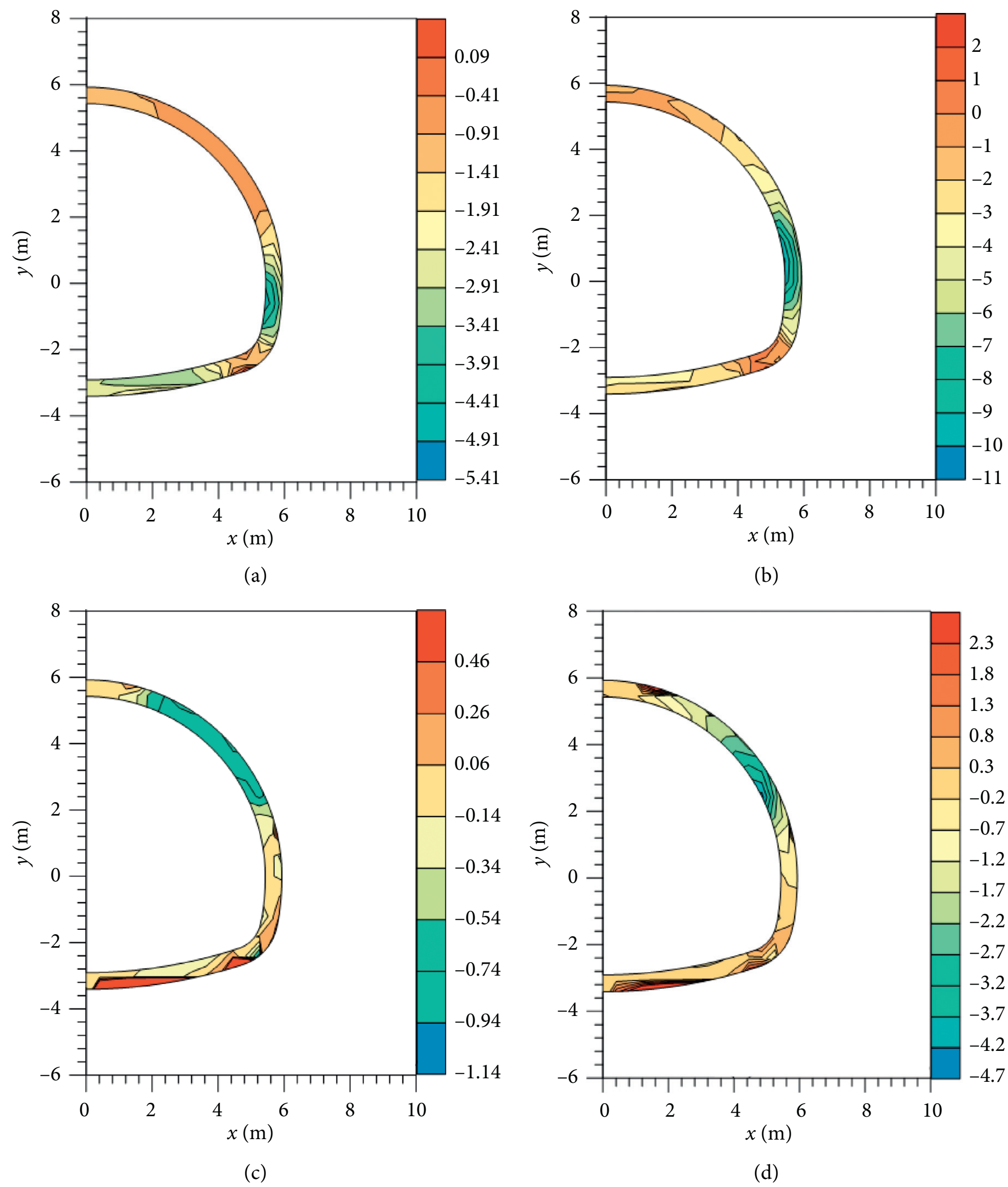

Figure 10: Stress regimes of the second lining structure at D1 on April 15 in 5 years of the operation period of the tunnel. (a) MAPS in STIL. (b) MAPS in WTIL. (c) MIPS in STIL. (d) MIPS in WTIL.

liquid water in the SR was transferred to the solid ice leading to the frost heave force loading on the primary lining structure. This meant in STIL the values of the MAPS and MIPS were all smaller than those in WITL due to the existence of the insulation layer. Moreover, both the positions of the maximum absolute value of MAPS in STIL and WTIL were at the hance of the arch. The positions of the maximum tensile stress of the primary lining structure in STIL and WTIL were at the inverted arch. For the lining structures, the greater tensile stress was generally harmful. Thus, the inverted arch of the tunnel should be laid on the insulation layer.

6. Conclusions

In seasonal permafrost regions, there are many frost problems of the tunnel due to the heat exchange between the air and lining structure after excavation. In this paper, a coupled mathematical model of heat, moisture transfer, and stress was constructed to investigate the long-term thermal and stress regimes of lining structures and SR of Altun highway tunnel on the QTP. Using numerical simulations, thermal and stress regimes of the tunnel in cold seasons were analyzed during a 5-year period, as well as the impact of the insulation layer methods. The conclusions were obtained as follows:

(1) In seasonally permafrost regions, there was a significant thermal disturbance of the SR after the tunnel excavation. In the 5^{th} year of the operation period, the MSFD of the SR can reach 1.6 m at the vault of the arch. Moreover, the MSFD at the inverted arch was only 1.0 m due to the pavement inside the tunnel, while the MSFD of the SR of the foot of arch was situated between the two, which reflects that the thermal regimes of different positions of the tunnel were considerably different due to the geometrical shape of the tunnel.

(2) Both the absolute maximum value of MAPS and MIPS in cold season were bigger than those in warm season. In the 5^{th} year of the operation period, the absolute maximum value of MAPS in cold season was −3.6 MPa, while that in warm season was −2.3 MPa. Moreover, the absolute maximum value of MIPS in cold season was −1.4 MPa, while that in warm season was −1.0 MPa. The tensile stress of the primary lining structure was 0.7 MPa in cold season and 0.2 MPa in warm season. And the law of stress regimes of primary lining structure was the same as those of the second lining structure. It reflected that in cold season, due to the heat exchange between the cold air and the SR, the liquid water in the SR was transferred to the solid ice leading to the frost heave force loading on the lining structure, while in warm season, there was no frost heave force surrounding the lining structure.

(3) Both the MAPS and MIPS of the lining structure in WTIL are bigger than those in STIL.

The absolute maximum value of MAPS of the primary lining in STIL was −3.6 MPa, while that in WTIL was −5.8 MPa. Moreover, the absolute maximum value of MIPS of primary lining in STIL was only −1.4 MPa, while that in WTIL was −3.0 MPa. The tensile stress of the primary lining structure was 0.7 MPa in STIL and 0.2 MPa in WTIL. And the law of stress regimes of primary lining structure was the same as those of the second lining structure. It reflected that in STIL, due to the existence of the insulation layer, the thermal effect of heat exchange between the cold air and the lining structure decreased, while the position of maximum value of MAPS and MIPS differs in STIL and WTIL. The positions of the maximum tensile stress of the primary lining structure in STIL and WTIL were at the hance and inverted arch, while the positions of the maximum tensile stress of the primary lining structure in STIL and WTIL were at the inverted arch. For the lining structures, the greater tensile stress was generally harmful. Thus, the inverted arch and the hance of the tunnel should be laid on the insulation layer.

Data Availability

The data used to support the findings of this study are available from the corresponding author upon request.

Conflicts of Interest

The authors declare that there are no conflicts of interest related to this manuscript.

Acknowledgments

This study was supported by a research program funded by the Department of Transportation of Gansu Province (No. 2017-008).

References

[1] X. Z. Xu, J. C. Wang, and L. X. Zhang, *Physics of Frozen Soil*, Science Press, Beijing, China, 2010.

[2] D. H. Qin, *Cryosphere Science*, Meteorological Press, Beijing, China, 2014.

[3] H. Yu, K. Zhang, X. M. Zhu, Z. Z. Tian, Y. H. Mu, and G. Q. Bi, "Numerical study on thermal insulation of a roadway tunnel at southeast edge of the Qinghai-Tibet plateau," *Earth and Environment Science*, vol. 719, Article ID 032068, 2021.

[4] K. Zhang, X. M. Zhu, H. Yu, Z. Z. Tian, Y. H. Mu, and G. Q. Bi, "Comparison thermal insulation effects of different thermal insulation materials for a roadway tunnel at southeast edge of the Qinghai-Tibet plateau," *Earth and Environment Science*, vol. 719, Article ID 032084, 2021.

[5] H. Yu, H. W. Han, W. Ma, Z. K. Ding, and L. Chen, "Long-term thermal regimes of subgrade under a drainage channel in high-altitudinal permafrost environment," *Advance in Materials Science and Engineering*, vol. 2021, Article ID 6613114, 12 pages, 2021.

[6] Y. M. Lai, M. Y. Zhang, and S. Y. Li, *Theory and Application of Cold Regions Engineering*, Science Press, Beijing, China, 2009.

[7] X. D. Bai, "Numerical calculation model of water-thermal-force coupling in tunnel section of cold area," Ph.D. Dissertation, Lanzhou Jiaotong University, Lanzhou, China, 2019.

[8] X. J. Tan, "Study on the mechanism of frost heave of tunnel in cold region with high altitude and related insulation technology," Ph.D. Dissertation, Institute of Rock and Soil Mechanics, Chinese Academy, Wuhan, China, 2010.

[9] H. Q. Xie, C. He, and Y. L. Li, "Study on insulating layer thickness by phase-change temperature field of highway tunnel in cold region," *Chinese Journal of Rock Mechanics and Engineering*, vol. 26, no. 2, pp. 4397–4440, 2007.

[10] Y. W. Zhou, D. X. Guo, and G. Q. Qiu, *Geocryology in China*, Science Press, Beijing, China, 2000.

[11] S.-b. Xie, Q. Jian-jun, L. Yuan-ming, Z. Zhi-wei, and X. Xiang-tian, "Effects of freeze-thaw cycles on soil mechanical and physical properties in the Qinghai-Tibet plateau," *Journal of Mountain Science*, vol. 12, no. 4, pp. 999–1009, 2015.

[12] G. Deng, "Investigation of frost protection design for tunnels in high altitude cold regions," Ph.D. Dissertation, Southwest Jiaotong University, Chendu, China, 2012.

[13] N. I. Johansen, S. L. Huang, and N. B. Aughenbaugh, "Alaska's CRREL permafrost tunnel," *Tunnelling and Underground Space Technology*, vol. 3, no. 1, pp. 19–24, 1988.

[14] K. Okada and Y. Matsumoto, "Actual state of frost penetration depth in railway tunnel and its analysis against periodic change of atmospheric temperature," *Doboku Gakkai Ronbunshu*, vol. 1990, no. 424, pp. 179–186, 1990.

[15] F. M. Nie, "Dynamic state of air temperature in railway tunnels in cold regions," *Journal of Glaciology and Geocryology*, vol. 10, no. 4, pp. 450–453, 1988.

[16] Y. M. Lai, Z. W. Wu, S. J. Zhang, W. B. Yu, and Y. S. Deng, "In-situ observed study for effect of heat preservation in cold regions tunnels," *Journal of the China Railway Society*, vol. 25, no. 1, pp. 81–86, 2003.

[17] R. L. Harlan, "Analysis of coupled heat-fluid transport in partially frozen soil," *Water Resources Research*, vol. 9, no. 5, pp. 1314–1323, 1973.

[18] I. Shingo, "Driving force for water migration in frozen clayey soil," *Soil Science & Plant Nutrition*, vol. 26, no. 2, pp. 215–227, 1980.

[19] G. S. Taylor and J. N. Luthin, "A model for coupled heat and moisture transfer during soil freezing," *Canadian Geotechnical Journal*, vol. 15, no. 4, pp. 548–555, 1978.

[20] S. A. Shoop and S. R. Bigl, "Moisture migration during freeze and thaw of unsaturated soils modeling and large scale experiments," *Cold Regions Science and Technology*, vol. 25, no. 1, pp. 33–45, 1997.

[21] K. Hansson, J. Simunek, M. Mizoguchi, and M. T. van Genuchten, "Water flow and heat transport in frozen soil: numerical solution and freeze-thaw applications," *Vadose Zone Journal*, vol. 3, pp. 693–704, 2004.

[22] Y. M. Lai, Z. W. Wu, Y. L. Zhu, C. X. He, and L. N. Zhu, "Nonlinear analysis for the coupled problem of temperature and seepage fields in cold regions tunnels," *Science in China, Series D*, vol. 29, no. 1, pp. 89–96, 1999.

[23] X. F. Zhang, Y. M. Lai, W. B. Yu, and S. J. Zhang, "Non-linear analysis for the freezing-thawing situation of the rock surrounding the tunnel in cold regions under the conditions of different construction seasons, initial temperatures and insulations," *Tunnelling and Underground Space Technology*, vol. 17, no. 3, pp. 315–325, 2002.

[24] X. J. Tan, W. Z. Chen, D. S. Yang et al., "Study on the influence of airflow on the temperature of the surrounding rock in a cold region tunnel and its application to insulation layer design," *Applied Thermal Engineering*, vol. 67, no. 1-2, pp. 320–334, 2014.

[25] Y. F. Zhou, X. F. Zhang, and J. H. Deng, "A mathematical optimization model of insulation layer's parameters in seasonally frozen tunnel engineering," *Cold Regions Science and Technology*, vol. 101, pp. 73–80, 2014.

[26] Q. G. Ma, X. X. Luo, Y. M. Lai, F. J. Niu, and J. Q. Hao, "Numerical investigation on thermal insulation layer of a tunnel in seasonally frozen regions," *Applied Thermal Engineering*, vol. 138, pp. 280–291, 2018.

[27] W. W. Liu, Q. Feng, C. Wang, C. K. Lu, Z. Z. Xu, and W. T. Li, "Analytical solution for three-dimensional radial heat transfer in a cold-region tunnel," *Cold Regions Science and Technology*, vol. 164, Article ID 102787, 2019.

[28] J. M. Zhang, "Study on roadbed stability in permafrost regions on Qinghai-Tibetan plateau and classification of permafrost in highway engineering," Ph.D. Dissertation, University of Chinese Academy of Sciences, Lanzhou, China, 2004.

[29] M. L. Zhang, Z. Wen, K. Xue, L. Z. Chen, and D. S. Li, "A coupled model for liquid water, water vapor and heat transport of saturated-unsaturated soil in cold regions: model formulation and verification," *Environmental Earth Sciences*, vol. 75, no. 8, pp. 1–19, 2016.

[30] M. T. van Genuchten, "A closed-form equation for predicting the hydraulic conductivity of unsaturated soils," *Soil Science Society of America Journal*, vol. 44, no. 5, pp. 892–898, 1980.

[31] Y. Mualem, "A new model for predicting the hydraulic conductivity of unsaturated porous media," *Water Resources Research*, vol. 12, no. 3, pp. 513–522, 1976.

[32] H. P. Hu, S. X. Yang, and Z. D. Lei, "A numerical simulation for heat and moisture transfer during soil freezing," *Journal of Hydraulic Engineering*, vol. 7, pp. 1–8, 1992.

[33] Z. W. Zhu, J. G. Ning, and W. Ma, "Study on a constitutive model of frozen soil based on damage and moisture-thermal-mechanism numerical simulation," *Scientia Sinica*, vol. 40, no. 6, pp. 758–772, 2010.

[34] Y. X. Xia and Y. D. Wang, *Mechanical Calculation of Tunnel Structure*, People's Communications Press, Beijing, China, 2001.

[35] X. L. Liu and G. P. Tang, "Research on prediction method of concrete freeze-thaw durability under field environments," *Chinese Journal of Rock Mechanics and Engineering*, vol. 26, no. 12, pp. 2412–2419, 2007.

[36] H. Cao, W. Z. Tan, and X. L. Liu, "Loss of mechanical properties of concrete under freeze-thaw cycles," in *Proceedings of the 5th National Structural Engineering Academic Conference*, Chicago, IL, USA, 1996.

[37] H. Cai, "Prediction model of frost resistance durability of concrete," Ph.D. Dissertation, Tsinghua University, Beijing, China, 1998.

[38] R. X. He, H. J. Jin, S. P. Zhao, and Y. S. Deng, "Review of status and progress of the study in thermal conductivity of frozen soil," *Journal of Glaciology and Geocryology*, vol. 40, no. 1, pp. 116–126, 2018.

Hindawi
Advances in Materials Science and Engineering
Volume 2021, Article ID 5999874, 11 pages
https://doi.org/10.1155/2021/5999874

Research Article

Fuzzy Random Characterization of Pore Structure in Frozen Sandstone: Applying Improved Niche Genetic Algorithm

Yao Ya-feng ,[1,2,3] Lin Jian ,[3] Ge Jian,[4] Peng Shi-long,[3] Yin Jian-chao,[3] and Ouyang Li-na[3]

[1]*School of Architectural Engineering, Nantong Vocational University, Nantong 226001, China*
[2]*Anhui University of Science and Technology, Post-Doctoral Research Station for Safety Science and Engineering, Huainan 232001, China*
[3]*Anhui Key Laboratory of Building Structure and Underground Engineering, Anhui Jianzhu University, Hefei 210037, China*
[4]*School NZIHT, Western Institute of Technology at Taranaki, New Plymouth 4032, New Zealand*

Correspondence should be addressed to Lin Jian; 281198837@qq.com

Received 5 May 2021; Accepted 16 June 2021; Published 29 June 2021

Academic Editor: Xiao Dong Zhao

Nuclear magnetic resonance (NMR) technology provides an innovative method employed in detecting the porous structures in frozen rock and soil masses. On the basis of NMR relaxation theory, fuzzy random characteristics of the NMR T_2 spectrum and pore structure are deeply analyzed in accordance with the complex and uncertain distribution characteristics of the underground rock and soil structure. By studying the fuzzy random characteristics of the NMR T_2 spectrum, the fuzzy random conversion coefficient and conversion method of the T_2 spectrum and pore size distribution are generated. Based on the niche principle, the traditional genetic algorithm is updated by the fuzzy random method, and the improved niche genetic algorithm is proposed. Then, the fuzzy random inversion of the conversion coefficient is undertaken by using the improved algorithm. It in turn makes the conversion curve of the T_2 spectrum and pore size distribution align with the mercury injection test curve in diverse pore apertures. Compared with the previous least square fitting method, it provides a more accurate approach in characterizing complicated pore structures in frozen rock and soil masses. In addition, the improved niche genetic algorithm effectively overcomes the shortcomings of the traditional genetic algorithm, such as low effectiveness, slow convergence, and weak controllability, which provides an effective way for parameter inversion in the section of frozen geotechnical engineering. Finally, based on the T_2 spectrum test of frozen sandstone, the fuzzy random characterization of frozen sandstone pore distribution is carried out by using this transformation method. The results illustrate that the conversion coefficient obtained through the improved algorithm indirectly considers the different surface relaxation rates of different pore sizes and effectively reduces the diffusion coupling effects, and the pore characteristics achieved are more applicable in engineering practices than previous methods.

1. Introduction

As a key objective in frozen geotechnical engineering, frozen rock and soil masses are random, porous, and heterogeneous, characterised by noticeable composition complexity, structural diversity, and extreme anisotropy. Therefore, accurately obtaining the microscopic structures for frozen rock and soil under different conditions is of great significance when studying its physical and mechanical properties. Nowadays, there are a multitude of experimental approaches in detecting the pore structure of rock and soil. Amongst them, low-field nuclear magnetic resonance testing is a nondamaging and repeatable technology, known for its high effectiveness and reliability. This technology has become one of the important methods applied in detecting porous structure characteristics for frozen rock and soil masses [1].

The low-field nuclear magnetic resonance testing is based on the mechanism of nuclear magnetic resonance theory, and the NMR relaxation spectrum is acquired by measuring and inversing the relaxation signal. This technology establishes the conversion relationship between the relaxation time and pore size measurement and obtains the pore distribution rule [2]. Therefore, the accurate acquisition of the pore distribution law not only relies on nuclear magnetic resonance testing technology but also requires an accurate conversion method of relaxation time and pore size measurement.

In view of this problem, previous scholars had carried out a lot of research that generally fell among four types of methods: the first type was based on nuclear magnetic resonance test theory. Assuming the linear relationship between T_2 spectrum and pore distributions, the NMR T_2 spectrum detected was converted to the NMR capillary force curve and then fitted to determine the best conversion coefficient through the mercury intrusion test [3]. The second was underlaid on the principle of similarity. According to the NMR T_2 spectrum, power functions were used to construct the NMR capillary force curve. Combined with test data from mercury injection or gas adsorption, the conversion coefficient was finally achieved by data inversion [4]. The third method was to modify the NMR T_2 spectrum by eliminating the effects of boundary pores and then obtain the corresponding conversion coefficients through integration of first and second methods [5]. The fourth one was to compute the pseudocapillary pressure curve using the two-dimensional equilateral scale conversion coefficient and obtain the longitudinal conversions between the NMR T_2 spectrum and pore distribution curve [6].

Due to lacking of computational models, former researchers, to a certain extent, chose neglecting the Brownian motion of the fluid molecules, which behaves in a highly degree of randomness, and specific physical and chemical environments where the fluid flows through when interpreting NMR relaxation signals [7]. Meanwhile, pore structures measured by methods such as mercury injection and gas adsorption were majorly restricted by the flow of working fluids and the relevant injecting pressures. Therefore, it also possessed a strong fuzziness [8]. It can be seen that existing testing and converting technologies are disputable in characterizing the complex structures of the rock and soil masses, and their anisotropic distribution characteristics, because of ignoring the natural phenomena of randomness and fuzziness, ultimately lead to misleading results in pore structure observation.

Hence, this study set forth to expound fuzzy and random properties existed in NMR T_2 spectrum interpretation and pore structure observation. Based on fuzzy random theory, an improved niche genetic algorithm was proposed to enhance the intelligence of the existing computational model and furthermore applied in the domain of NMR T_2 spectrum detecting optimization.

2. Theoretical Basis

2.1. Test Conditions and Basic Hypotheses

(1) The hydrogen nuclear resonance signal of the tested rock and soil can only be generated by the working fluid

(2) The saturated pores of each aperture only produce a corresponding T_2 value, and perturbation and interference from echo train signal are ignored

(3) The voids remain in only two states: fully saturated and fully unsaturated

2.2. The Relationship between NMR Transverse Relaxation Characteristics and Pore Structure. The low-field NMR T_2 spectrum test of the rock and soil mass is tested by CPMG (Carr–Purcell–Meiboom–Gill) pulse sequence. The direct result is a series of spin echo trains generated by a specific pulse sequence. The amplitude of the echo train represents the total magnetization signal under this relaxation time. The initial amplitude of the echo train is directly proportional to the number of hydrogen nuclei in the fluid under test. The amplitude of the spin echo train can be fitted with the sum of a set of exponential decay curves. The decay constant of each exponential curve is the T_2 distribution.

Within a single pore, mathematically, the corresponding relationship between T_2 distribution and pore size has proved, and the equation is

$$\frac{1}{T_2} = \frac{1}{T_{2B}} + \frac{1}{T_{2S}} + \frac{1}{T_{2\,D}} = \frac{1}{T_{2B}} + \frac{1}{T_{2S}} + \frac{(\gamma G T_E)^2 D}{12}, \quad (1)$$

$$\frac{1}{T_2} \approx \frac{1}{T_{2S}} = \frac{Sh}{V}\frac{n_m}{T_{2M}} = \rho_2 \left(\frac{S}{V}\right)_{\text{pore}} = \rho_2 \frac{F_s}{r}, \quad (2)$$

where T_{2B} is the volume relaxation time, determined by the inherent properties of the fluid, T_{2S} is the surface relaxation time, $T_{2\,D}$ is the diffusion relaxation time, γ is the hydrogen nuclear gyromagnetic ratio, G is the effective magnetic field gradient, T_E is the CPMG pulse sequence echo interval, D is the effective diffusion coefficient, S is the surface area of the pore, h is the thickness of the fluid layer that can relax, V is the volume of the pore, n_m is the proportion of paramagnetic ions, T_{2M} is the relaxation time of coupling between paramagnetic ions and protons, ρ_2 is the surface lateral relaxation strength, F_s is the geometric factor of pore shape, and r is the capillary radius.

It can be seen from the above equation that the pore geometry is different; the ratio of the pore surface area to the volume and the lateral surface relaxation rate are also different. Therefore, the amplitude of the T_2 spectrum represents signals of different strengths at this relaxation time, that is, indirectly indicates the number of specific pore shapes, as shown in Figure 1.

The T_2 spectrum obtained by the nuclear magnetic resonance test can be considered as the statistical result of the pore distribution law of the tested rock and soil. However, a large number of experimental studies have shown that the geometry and distribution of pores in the tested rock and soil have fuzzy randomness. Consequently, the conversion parameters between the T_2 spectrum and the aperture must be fuzzy and random. If the traditional conversion equation is directly used to convert the T_2 spectrum and the aperture of the rock and soil mass, a certain degree of distortion will inevitably occur.

2.3. Fuzzy Random Characteristics of Rock and Soil Pores. Under normal circumstances, in order to achieve the conversion of T_2 spectrum and pore size, high-pressure mercury

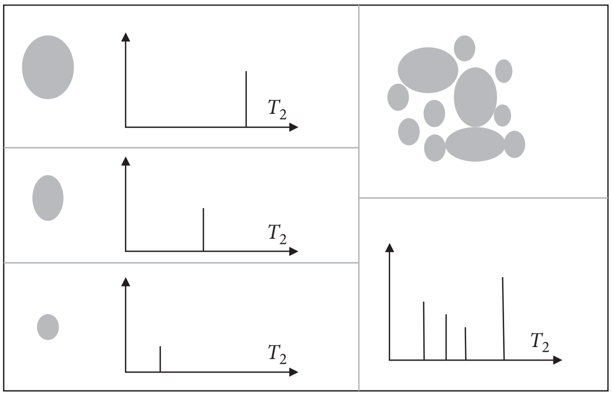

Figure 1: Pore characteristics and relaxation characteristics (according to the data in Figure 1 in [9], it was redrawn with the new algorithm in the manuscript).

intrusion, gas adsorption, and micro-CT tests are used to determine the content of the known pore size and perform conversion calculations based on this [10–12].

Taking the mercury injection test as an example, the relationship between capillary pressure and capillary diameter can be expressed as

$$P_c = \frac{2\sigma\cos\theta}{r}, \tag{3}$$

where P_c is the capillary pressure, σ is the fluid interfacial tension, and θ is the wetting contact angle.

According to equations (2) and (3), we can get

$$\frac{2\sigma\cos\theta}{P_c} \approx F_s \times \rho_2 \times T_2. \tag{4}$$

After the above equation is properly adjusted, the following can be obtained:

$$P_c = C_1 \times \frac{1}{T_2}, \tag{5}$$

where C_1 is the conversion coefficient between T_2 spectrum and capillary pressure, which can be expressed as the following equation:

$$C_1 = \frac{2\sigma\cos\theta}{\rho_2 \times F_s}. \tag{6}$$

It can be seen that there is a one-to-one correspondence between the mercury intrusion P_c test and the free pore signal in the NMR T_2 spectrum, that is, each of the mercury intrusion P_c tests corresponds to a C_1 value. Therefore, when the mercury intrusion test is used to convert the nuclear magnetic resonance T_2 spectrum from a certain rock and soil mass, the conversion coefficient C_1 should not be a fixed constant as stated in previous research literature. It is influenced by many factors in practical engineering, so it should be a fuzzy random value. The current conversion coefficient method is to use the least square method to fit the T_2 spectrum and the mercury intrusion aperture cumulative curve, so as to obtain the best single-value conversion coefficient. Obviously, this method ignores the fuzzy random characteristics of pore distribution and pore geometry in the rock and soil mass.

According to equations (2) and (6), it can be derived that T_2, r, and C_1 have the following relationship:

$$T_2 = \frac{C_1}{P_c} = \frac{C_1 r}{2\sigma\cos\theta} = Cr, \tag{7}$$

where C is the conversion coefficient between the T_2 spectrum and aperture, which can be expressed as

$$C = \frac{C_1}{2\sigma\cos\theta}. \tag{8}$$

It can be seen from the above expression that when using the mercury intrusion capillary pressure curve and nuclear magnetic resonance T_2 spectrum for aperture conversion, the conversion relationship between T_2 and r can be obtained by inversion of the capillary pressure curve by combining equations (6) and (7).

When analyzing the pore characteristics of rock and soil, we often divide the aperture type into small, medium, and large pores with regard to their diameters. The pore diameters obtained by mercury intrusion testing are connected mesopores and macropores. When performing pore size conversion, we need to distinguish mesopores and macropores that are connected in the NMR T_2 spectrum. However, the classification of pore size is a relatively fuzzy concept, and different classification standards immediately lead to different results. The results of the mercury intrusion test depend on its internal pore connectivity characteristics and pore wall structures, which also encompass a certain degree of randomness.

In summary, in the domain of engineering, due to the uncertainty of the pore distribution and pore geometry in the rock and soil mass, the conversion coefficient obtained by the traditional algorithm alone cannot accurately express the pore characteristics of the rock and soil mass. Therefore, the fuzzy random transformation of equation (7) can be adapted as

$$T_2 = \widetilde{C}r, \tag{9}$$

where $\widetilde{C}$ is the fuzzy random conversion coefficient.

According to equation (9), a fuzzy random intelligent algorithm should be introduced to optimize the conversion coefficient C so as to more effectively analyze the pore characteristics of the rock and soil mass.

3. Improved Niche Genetic Algorithm

3.1. Traditional Genetic Algorithm. The genetic algorithm originated from the imitation of biological heredity and evolution in nature. In the 1960s, Professor Holland of Michigan University in the United States proposed that when researching and designing artificial adaptive systems, he can learn from the mechanism of biological genetics and use the group method to perform adaptive search to achieve the purpose of optimizing actual engineering [13–15]. He randomly generates a set of initial solutions within the scope of the solution space and calculates the fitness of each individual in the population. If the termination condition is not satisfied, the program is coded, and then, the genetic operator is used to select, cross, and mutate the population to form a new population. The fitness of the population is calculated by decoding until the optimization criterion is satisfied, and the global optimal solution is finally obtained.

The characteristic of the algorithm is that the coding method uses a fixed-length binary symbol string to represent the individuals in the population, and three basic genetic operators are used in the iterative operation, namely, the selection operator, the crossover operator, and the mutation operator. However, when dealing with practical complex problems, the traditional genetic algorithm exposes some disadvantages, such as poor stability, large amount of computation, and difficulty in controlling nonlinear constraints. Especially, in the process of engineering fuzzy random problems, it appears powerless.

3.2. Niche Improvement of Genetic Algorithm. The genetic algorithm adjusts the degree of similarity between individuals through the sharing function. Since the similarity has fuzzy randomness [16, 17], the fitness of the traditional genetic algorithm can be improved by fuzzy randomness based on the niche principle.

Niche originated from the concept of biology, which represents the special living environment of species under a few conditions. Therefore, the niche principle can be described as follows: classify individuals of a certain generation according to attributes and divide their respective categories. Rank individuals in the corresponding category according to fitness; then, select the top few in each category to form a new population. Under the condition that the niche criterion is not met, we adopt the methods of selection, crossover, and mutation to form a new individual and continue to cycle until the criterion is met. The niche principle can avoid the local optimum, while ensuring convergence efficiency by fuzzy random searching solution space through the genetic algorithm, which provides an effective tool for parameter optimization of the uncertain problem function [18].

The improved genetic algorithm is obtained by using the fuzzy random niche principle [19–21]. The concept is as follows:

(1) Initialize the value of the genetic algebraic counter $t \longleftarrow 1$: categorize according to attributes, and randomly select M gene elements, which are arranged and combined as the individuals of the initial population $Z(t)$, and then, the genetic fitness of each element $F_i\,(i = 1, 2, 3, \ldots, M)$ is calculated by the equation:

$$F_i = \sum_{k=1}^{m} \omega_k (\widetilde{\omega} - f_k), \tag{10}$$

$$\omega_k = \frac{a_k}{\sum_{l=1}^{M} a_l}, \tag{11}$$

where a_k is a random number and $\widetilde{\omega}$ is a fuzzy number between 0 and 1.

(2) Arrange in the descending order according to the fitness of the individual: the higher fitness is more likely to be inherited, and the previous individual with the greater fitness N is retained $(N < M)$.

(3) Random selection operator: according to the selection probability Z_{is}, the initial population $Z(t)$ is selected proportionally. The method is roulette random sampling to obtain the individual $Z'(t)$ after the selection operation:

$$Z_{is} = \frac{F_i}{\sum_{i=1}^{M} F_i}, \quad i = 1, 2, \ldots, M, \tag{12}$$

where M is the group size and F_i is the fitness of the individual, which can be obtained by the equation:

$$F_i = \frac{\#N_i \cdot \sum_{i=1}^{M} F_i}{M}, \tag{13}$$

where N_i represents the expected survival number in the next generation group, M represents the group size, and $\#N_i$ is the integer part of N_i.

(4) Fuzzy crossover operator: the crossover operation is performed on the selected individual $Z'(t)$ according to the crossover probability Z_C. The method is single-point fuzzy crossover, and then, the individual $Z'(t)$ after crossover is obtained:

$$Z_c(i) = Z_c \sqrt{\left(1 - \frac{1}{M}\right)}, \tag{14}$$

where $Z_c(i)$ represents the fuzzy crossover probability of the individual i and Z_c is the regular crossover probability.

(5) Fuzzy mutation operator: the variation operation of the probability Z_m is carried out on the crossover individual. The method is Gaussian fuzzy mutation, and the individual $Z'''(t)$ after mutation is obtained:

$$Z_m(i) = 1 - \frac{2}{\exp(1 - (i/M)) + 1}, \tag{15}$$

where $Z_m(i)$ represents the fuzzy mutation probability of the individual $i$the new individual gene value after Gaussian fuzzy mutation is

$$G = \mu + \sigma\left(\sum_{i=1}^{M} \widetilde{r}_i - \frac{M}{2}\right), \tag{16}$$

where μ and σ are, respectively, the mean value and standard deviation of Gaussian fuzzy variation, which are obtained by equations (17) and (18), and $\widetilde{r}_i$ are fuzzy numbers between 0 and 1:

$$\mu = \frac{U_{\min}^k + U_{\max}^k}{2}, \tag{17}$$

$$\sigma = \frac{U_{\max}^k - U_{\min}^k}{6}, \tag{18}$$

where $U_{\max}^k$ and $U_{\min}^k$ are the maximum and minimum of the gene at the mutation point.

(6) Fuzzy genetic evolution based on the niche principle: M individuals obtained after Gaussian mutation are merged with N individuals retained with greater fitness to generate a new generation of population. The Hamming distance between any two individuals in the new population is calculated according to the equation:

$$\left\| X_i - Y_j \right\| = \sqrt{\sum_{k=1}^{M} \left(x_{ik} - x_{jk} \right)^2}, \tag{19}$$

where $i = 1, 2, \ldots, M + N - 1$ and $j = i + 1, \ldots, M + N$.

When $\|X_i - Y_j\| < L$ (L is the niche distance), its fitness is calculated according to equation (10). The values of $F(X_i)$ and $F(Y_i)$ are compared, and niche punishment for individuals with small fitness is through the following equation:

$$F'(X) = \begin{cases} F(X), & X \text{ satisfies the constraint condition}, \\ F(X) - Z(X), & \text{otherwise}, \end{cases} \tag{20}$$

where $F(X)$ is the original adaptation function of the individual at the time of initialization, $F'(X)$ is the new adaptive function of the individual after the correction of the niche penalty function, and $Z(X)$ is the niche fuzzy penalty function, which is obtained by the fuzzy coefficient method or Lagrange method.

(7) The individuals of the new generation of population are recalculated according to equation (20) to obtain the new fitness, and the individual values are arranged in the descending order. As in step (2), the individual with the greater value of new fitness ($N < M$) is re-retained.

(8) Set the termination condition of the genetic algorithm: if the threshold value does not meet the conditions, the first M individuals are selected as a new round of continuous evolution according to step (7). Until the criteria are met, output the best individual and exit the loop.

According to the above idea, a flowchart about the improved niche genetic algorithm is created, as shown in Figure 2.

4. Fuzzy Random Inversion of Conversion Coefficient between T_2 Spectrum and Pore Size Distribution

4.1. Fuzzy Random Inversion of Conversion Coefficient. In order to verify the effect of the improved algorithm, the NMR test data of sandstone samples in [9] is taken as an example to analyze. The fuzzy random inversion of the conversion coefficients for different pore sizes is undertaken by using the improved niche genetic algorithm to analyze the fuzzy random characteristics of sandstone pore sizes which are more in line with the actual engineering conditions. According to the improved niche genetic algorithm, MATLAB is used for programming. Initialize $t = 1$, $M = 150$, $N = 80$, $Z_c = 0.75$, $Z_{is} = 0.80$, and $Z_m = 0.1$; the distance parameter between niches is 0.65, the coding adopts real number coding, and the length is 13 bits; the fuzzy random parameter C is the population individual, the penalty coefficient is set to 10^{-20}, and the termination algebra is 1000.

Based on the NMR test data and after loop iterations according to the improved niche genetic algorithm, the global optimal solution is the fuzzy random inversion value of the conversion coefficient. Taking into account the fuzzy random characteristics of the pore size distribution, the classification method of [1, 22–25] is used to distinguish the pore type, that is, the transverse relaxation time T_2 is less than 5.8 ms for small apertures, 5.8~33 ms for medium apertures, and greater than 33 ms for large apertures, respectively. The results of comparing the transformation coefficient inversion with the least square method and the niche genetic method under different aperture conditions are shown in Table 1.

As shown in Table 1, the conversion coefficient $\widetilde{C}$ inverted by the improved niche genetic algorithm effectively reflects the fuzzy random characteristics of the pore distribution, pore shape, and pore size of the underground rock and soil with interval values, which is more reasonable than the fixed conversion coefficient fitted by the traditional least square method.

Considering that the conversion coefficients after fuzzy random inversion in Table 1 are fuzzy interval values, in order not to lose generality, equation (21) can express the fuzzy random state of different apertures:

$$\widetilde{b} = \bigcup_{\alpha \in (0,1]} \alpha [0.6 + (\alpha - 1)0.1, 0.6 + (1 - \alpha)0.1], \tag{21}$$

where $\widetilde{b}$ is the aperture fuzzy random state function and α is the constraint level ($\alpha = 0.75$). According to the fuzzy interval algorithm, the fuzzy random conversion coefficient $\widetilde{C}$ can be calculated.

Taking the sandstone GG5-1 sample in [9] as an example, according to the conversion coefficient of T_2 spectrum and pore radius obtained, the least square method and improved niche genetic algorithm are used to convert the T_2 spectrum, respectively. The result comparison for conversion curves and mercury injection testing curve is shown in Figure 3.

By comparing the curves, it is found that the improved niche genetic algorithm can effectively invert the conversion coefficients. This new algorithm makes the T_2 spectrum conversion curve better match the mercury intrusion test in the case of small aperture, medium aperture, and large aperture. Compared with the previous least squares fitting method, the curve can more accurately reflect the actual characteristics of the pore structure of rock and soil.

4.2. Algorithm Efficiency Comparison. The RedHat 9.0 system is configured on the LINUX host, and the least square method, traditional genetic algorithm, and improved niche

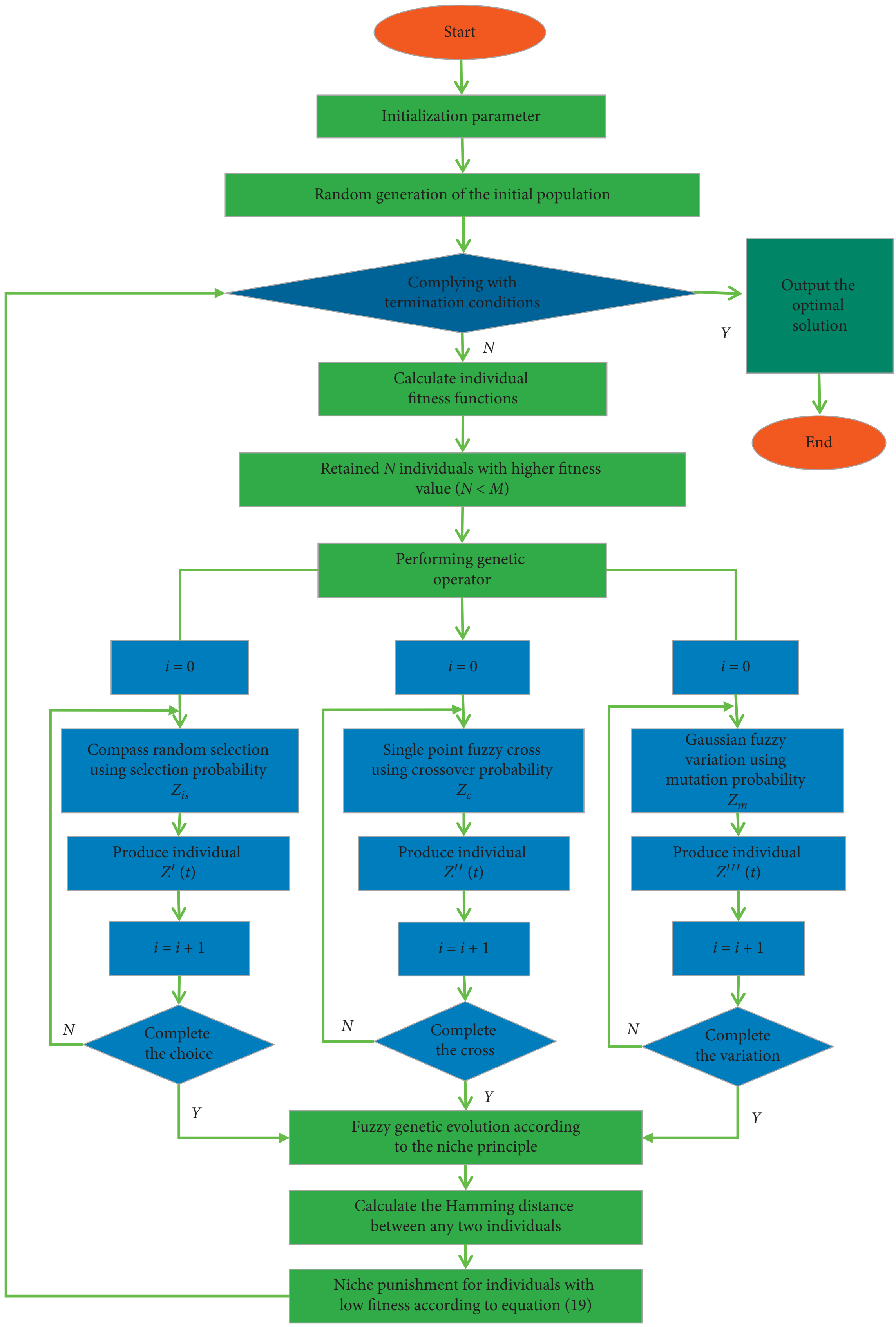

Figure 2: Flowchart of the improved niche genetic algorithm.

Table 1: Comparison of conversion coefficient inversion results.

Aperture type	Least squares method	Improved niche genetic algorithm	
		C_{min}	C_{max}
Small aperture	31.95	24.37	40.62
Medium aperture	45.34	36.52	58.71
Large aperture	62.07	48.19	76.35

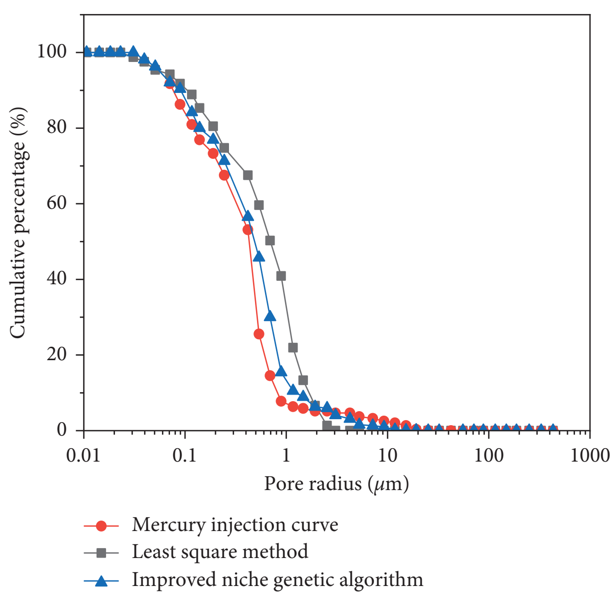

Figure 3: Comparison of T_2 spectrum conversion curves (according to the data in Figure 1 in [9], it was redrawn with the new algorithm in the manuscript).

genetic algorithm are used to simulate the inversion process of the conversion coefficient. The comparison effect of the inversion efficiency of various algorithms is shown in Figure 4.

As can be seen from the algorithm comparison figure, with the increase of the problem scale, the improved niche genetic algorithm has the characteristics of smaller error, higher efficiency, and obvious robustness compared with other algorithms.

5. Fuzzy Random Analysis of Pore Structure of Frozen Sandstone

5.1. T_2 Spectrum Test during Freezing. Applying the fuzzy random analysis method in this paper and taking the coarse sandstone of Jurassic Anding Formation as the object, the low-field NMR test system (MesoMR23-060V-I, Niumai Company, Suzhou, China) is used to conduct the T_2 spectrum test in the freezing process [26, 27]. Select a sample of quartz sandstone, which has a saturated water content of 8.02% and a dry density of 2.13 g/cm^3, see Figure 5.

In the early stage, through the results of the T_2 spectrum measured every hour under the same temperature condition, it is known that the T_2 signal can be stabilized after a single temperature point is maintained for 1.5 to 2.3 hours.

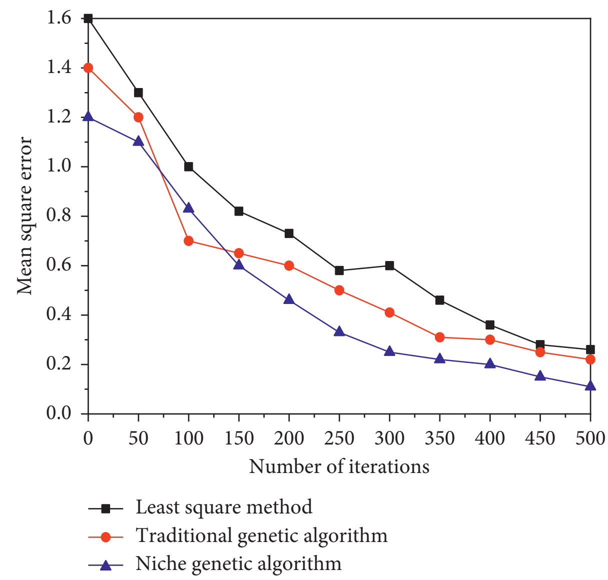

Figure 4: Contrast of algorithm efficiency.

Therefore, in order to ensure that the sample temperature reaches a stable state at each temperature point, each temperature point should be maintained for 3 hours. The cooling path adopted is shown in Figure 6. During the freezing process, the T_2 spectrum test procedure is as follows: (1) make sandstone into a cylindrical sample with a diameter of 25 mm and a height of 60 mm. (2) Pressurize and saturate the sample in a vacuum saturation device for 24 hours, and set the pressure to 0.1 MPa. (3) After the saturation, the CPMG sequence is used to sequentially perform the T_2 spectrum test on the saturated sample during the cooling process.

The T_2 spectra at different temperature points obtained from the test are shown in Figure 7.

5.2. Fuzzy Random Conversion and Analysis of T_2 Spectrum. According to the fuzzy random interval values of the T_2 spectrum and aperture conversion coefficient retrieved by the improved niche genetic algorithm in Table 1 and combined with the fuzzy random distribution of different apertures, as shown in equation (21), the fuzzy random conversion coefficient is obtained by using the fuzzy interval operation. Thus, the T_2 spectra of frozen sandstone are converted to interpret pore distribution curves, as shown in Figure 8.

Comparing the aperture distribution and the T_2 spectrum, it can be found that, with the decrease of temperature in the T_2 spectrum, the pores distributed in the small pore size range have shifted to the direction of short relaxation time. In many references, it is believed that it is caused by the influence of diffusion coupling [28, 29]. However, the result of Figure 8 shows that this phenomenon does not exist in the aperture distribution after fuzzy random conversion. The reason is that the improved niche genetic algorithm is used to carry out fuzzy random inversion of pore parameters in this paper, and the conversion coefficient obtained indirectly takes into account the different surface relaxation rates of

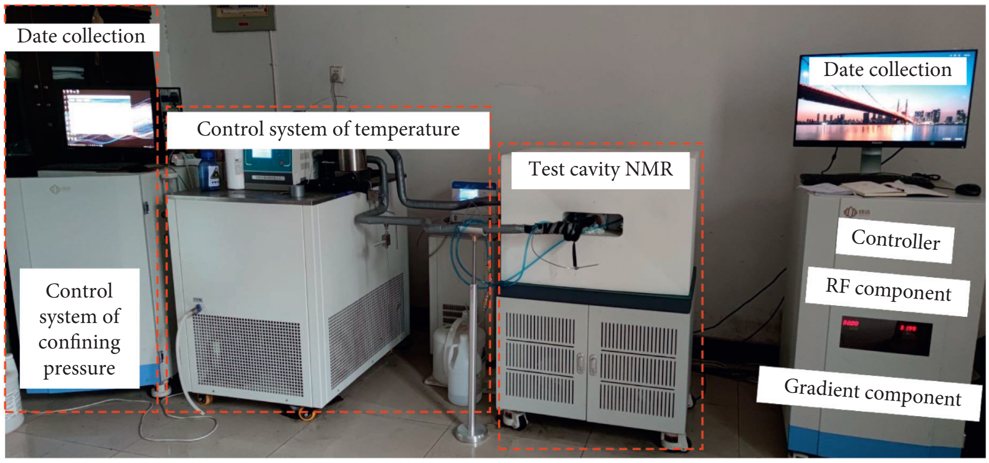

FIGURE 5: Low-field nuclear magnetic resonance test system (model MesoMR23-060V-I).

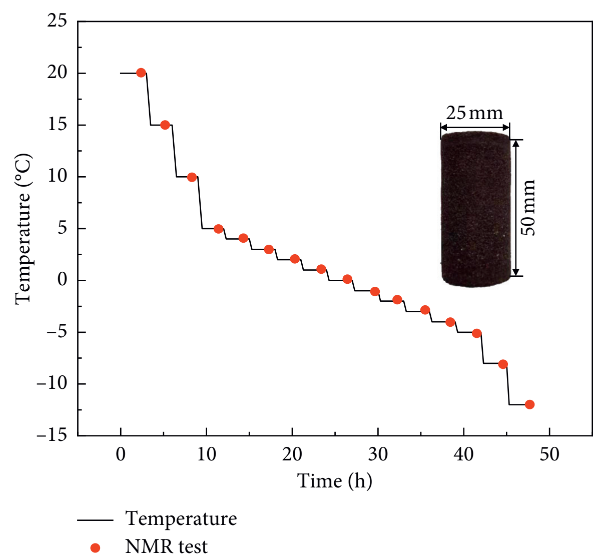

FIGURE 6: Schematic diagram showing freezing process and associated testing times.

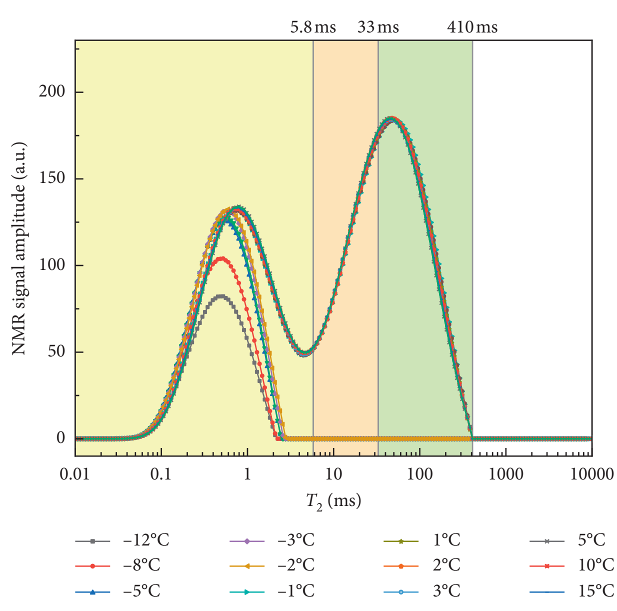

FIGURE 7: T_2 spectra during freezing.

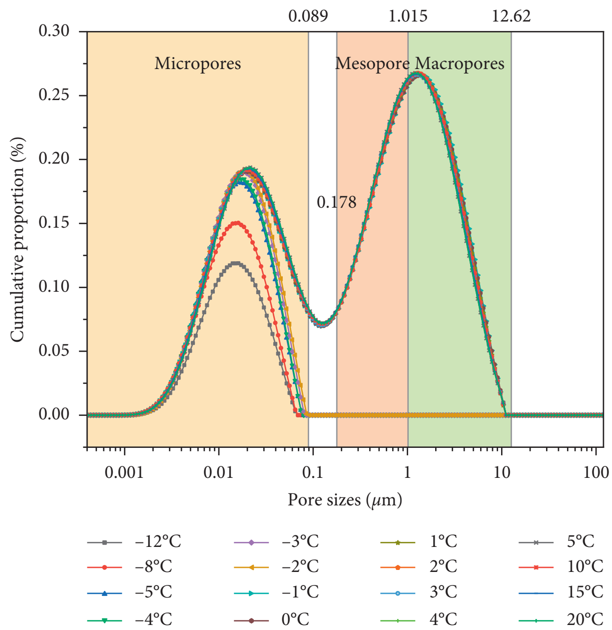

Figure 8: Pore size distribution during freezing.

Table 2: T_2 value and pore size of different pores.

Aperture type	T_2 (ms)	Inversion results under different conditions (μm)	
		Only small aperture	All aperture ranges exist
Small aperture	0.1~5.8	<0.089	<0.178
Medium aperture	5.8~33	—	0.178~1.015
Large aperture	33~410	—	1.015~12.62

different pore sizes, thus effectively reducing the characterization of the diffusion coupling phenomenon.

From the inverted pore size distribution diagram, it can be seen that when the freezing temperature decreases from positive temperature to −2°C, the frozen pores are only distributed in the range of large aperture and medium aperture. However, according to T_2 spectra, some pores distributed in the range of small aperture are frozen. The classification range of the pore size obtained by the inversion of the improved niche genetic algorithm is shown in Table 2. As shown in the table, the upper limit of the small aperture of this rock is 0.089 μm and the upper limit of the medium aperture is 1.015 μm.

It is found that the pore size is inversely proportional to the degree of water confinement. Therefore, the larger the pore size in the freezing process, the higher the freezing temperature is required. In other words, the pore size range of the multipeak distribution should be greatly different after the sudden drop in water content. In conclusion, for the frozen rock in this experiment, the pore structure characterization obtained according to the fuzzy random method is more consistent with the actual engineering situation.

6. Conclusion

In this paper, the fuzzy random characteristics of the NMR T_2 spectrum and pore structure are deeply analyzed in accordance with the complex and uncertain distribution characteristics of the underground frozen rock and soil structures. By studying the fuzzy random characteristics of the NMR T_2 spectrum, the fuzzy random conversion method of T_2 spectrum and pore size distribution is generated, and the following conclusions can be drawn:

(1) The traditional genetic algorithm is updated by the fuzzy random method in terms of the niche principle, and the improved niche genetic algorithm is proposed. The improved algorithm effectively overcomes the shortcomings of the traditional genetic algorithm, such as low effectiveness, slow convergence, and weak controllability, which provides an effective way for parameter inversion in the section of frozen geotechnical engineering.

(2) The fuzzy random inversion of the conversion coefficient is carried out by using the improved niche genetic algorithm. It in turn makes the conversion curve of T_2 spectrum and pore size distribution align with the mercury injection test curve in diverse pore apertures. Compared with thre previous least square fitting method, it provides a more accurate approach in characterizing complicated pore structures in frozen rock and soil masses.

(3) Based on the T_2 spectrum test of frozen sandstone, the fuzzy random transformation method is used to

characterize the frozen sandstone pore distribution. The results show that the conversion coefficient obtained by the improved niche genetic algorithm indirectly considers the different surface relaxation rates of different pore sizes and effectively reduces the diffusion coupling phenomenon, and the pore characteristics obtained are more consistent with the engineering practice than the previous methods.

Data Availability

The data used to support the findings of this study are included within the article.

Conflicts of Interest

The authors declare that they have no conflicts of interest.

Acknowledgments

The authors express their sincere appreciation to Chief Engineers Xing-Zhong Yi and Xia Zhou and to Dr. Yan Zhu and Hua Shen for their enthusiastic support in providing related information. This work was supported by the National Natural Science Foundation of China (Grant no. 51874005), Jiangsu Construction System Science and Technology Plan Project of China (Grant no. 2017ZD062), Natural Science Foundation in Anhui Province of China (Grant no. 2008085ME165), Nantong Municipal Science and Technology Program of China (Grant no. MS12018054), and "Qinglan Project" for Training of University Teachers in Jiangsu Province of China.

References

[1] A.-f. Li, X.-x. Ren, G.-j. Wang, Y. Z. Wang, and K. G. Wang, "Characterization of pore structure of low permeability reservoirs using a nuclear magnetic resonance method," *Journal of University of Petroleum (Edition of Natural Science)*, vol. 39, no. 6, pp. 92–98, 2015.

[2] Y.-D. He, Z.-Q. Mao, and X.-J. Ren, "An improved method of using NMR T_2 distribution to evaluate pore size distribution," *Chinese Journal of Geophysics*, vol. 48, no. 2, pp. 373–378, 2005.

[3] X.-x. Kong, D.-s. Xiao, S. Jiang, S. Lu, B. Sun, and J. Wang, "Application of the combination of high-pressure mercury injection and nuclear magnetic resonance to the classification and evaluation of tight sandstone reservoirs: a case study of the Linxing block in the Ordos basin," *Natural Gas Industry*, vol. 40, no. 3, pp. 38–47, 2020.

[4] Y. Yun, C.-j. Wang, F.-s. Zhang et al., "Characterization of micro-pore throats in the shale gas reservoirs of Zhaotong national shale gas demonstration area," *Natural Gas Industry*, vol. 41, no. 1, pp. 78–85, 2021.

[5] T.-d. Liu, T.-p. Zhao, G.-r. Li, and Y. J. Shi, "An improved method to evaluate pore size distribution of tight sandstone reservoir using NMR," *Well Logging Technology*, vol. 36, no. 2, pp. 119–123, 2012.

[6] J.-l. Su, J.-m. Sun, T. Wang, and S. W. Zhang, "An improved method of evaluating reservoir pore structure with nuclear magnetic log data," *Journal of Jilin University (Earth Science Edition)*, vol. 41, no. 1, pp. 380–386, 2011.

[7] G. R. Coates, L. Z. Xiao, and M. G. Prammer, *NMR Logging Principles and Applications*, vol. 8, Petroleum Industry Press, Beijing, China, 2007.

[8] Q. Dai, Q. Luo, C. Zhang et al., "Pore structure characteristics of tight-oil sandstone reservoir based on a new parameter measured by NMR experiment: a case study of seventh member in Yanchang pormation, Ordos basin," *Acta Petrolei Sinica*, vol. 37, no. 7, pp. 887–897, 2016.

[9] T. Fang, L. Zhang, N. Liu et al., "Quantitative characterization of pore structure of tight gas sandstone reservoirs by NMR T_2 spectrum technology: a case study of carboniferous-permian tight sandstone reservoir in Linqing depression," *Acta Petrolei Sinica*, vol. 38, no. 8, pp. 902–915, 2017.

[10] S. Karimi, *Pore-Scale assessment of Middle Bakken Reservoir Using Centrifuge, Mercury Injection, Nitrogen Adsorption, NMR, and Resistivity Instruments*, Colorado School of Mines, Golden, CO, USA, 2017.

[11] M. M. Labani, R. Rezaee, A. Saeedi et al., "Evaluation of pore size spectrum of gas shale reservoirs using low pressure nitrogen adsorption, gas expansion and Mercury porosimetry: a case study from the Perth and Canning basins, western Australia," *Journal of Petroleum Science and Engineering*, vol. 112, pp. 7–16, 2013.

[12] W. V. Loebenstein and V. R. Deitz, "Surface-area determination by adsorption of nitrogen from nitrogen-helium mixtures," *Journal of Research of the National Bureau of Standards*, vol. 46, no. 1, pp. 51–55, 1951.

[13] S. Li, Y. Liu, and D. Wang, "Structural vibration parameter identification method based on genetic algorithm," *Journal of China University of Mining & Technology*, vol. 30, no. 5, pp. 256–259, 2001.

[14] W. Gao and Y. Zheng, "Backanalysis in geotechnical engineering based on fast-convergent genetic algorithm," *Chinese Journal of Geotechnical Engineering*, vol. 23, no. 1, pp. 120–122, 2001.

[15] Z.-y. Zhao, L. Wang, B.-h. Wang et al., "Strategy research on improved genetic algorithm," *Computer Application*, vol. 26, no. S2, pp. 189–191, 2006.

[16] L. M. San José-Revuelta, "A new adaptive genetic algorithm for fixed channel assignment," *Information Sciences*, vol. 177, no. 13, pp. 2655–2678, 2007.

[17] X. Yin, Y. Zhong, Q. Guo et al., "Improved GA-based identification method of power function model for rock joints," *Coal Geology & Exploration*, vol. 44, no. 1, pp. 85–89, 2016.

[18] P. F. Konatantinos and A. T. Theodore, "Adaptive design optimization of wireless sensor networks using genetic algorithms," *Computer Networks*, vol. 51, pp. 1031–1051, 2007.

[19] J. Liu and Y. Wang, "Improved genetic algorithm in back analysis for seepage parameters of fissured rock masses," *Rock and Soil Mechanics*, vol. 24, no. 2, pp. 237–241, 2003.

[20] Y. Xiang and H. Su, "Inverse analysis for mechanical parameters based on genetic algorithm," *Journal of Yangtze River Scientific Research Institute*, vol. 20, no. 6, pp. 55–58, 2003.

[21] D. Mao, J. Zou, J. Li et al., "Application of projection pursuit method based on genetic algorithm to vulnerability assessment of flood disasters," *Journal of Glaciology and Geocryology*, vol. 32, no. 2, pp. 389–396, 2010.

[22] H. Tian and C. Wei, "A NMR-based testing and analysis of adsorbed water content," *Scientia Sinica Technologica*, vol. 44, no. 3, pp. 295–305, 2014.

[23] G. Martinez and L. Davis, "Petrophysical measurements on shales using NMR," in *Proceedings of the 2000 SPE/AAPG*

Western Regional Meeting, Society of Petroleum Engineers, Long Beach, CA, USA, 2000.

[24] H. Zhou, F. Gao, X. Zhou et al., "The translation research of different types sandstone of Yungang grottoes in NMR T_2-mercury capillary pressure," *Progress in Geophysics*, vol. 28, no. 5, pp. 2759–2766, 2013.

[25] V. Yakov and L. S. Win, "A practical approach to obtain primary drainage capillary pressure curves from NMR core and log data," *Petrophysics*, vol. 42, no. 4, pp. 334–343, 2001.

[26] Y. Yao and D. Liu, "Comparison of low-field NMR and mercury intrusion porosimetry in characterizing pore size distributions of coals," *Fuel*, vol. 95, pp. 152–158, 2012.

[27] C. H. Lyu, Z. F. Ning, Q. Wang, and M. Chen, "Application of NMR T_2 to pore size distribution and movable fluid distribution in tight sandstones," *Energy & Fuels*, vol. 32, no. 2, pp. 1395–1405, 2018.

[28] S. L. Codd, S. J. Vogt, J. A. Hornemann et al., "NMR relaxation measurements of biofouling in model and geological porous media," *Organic Geochemistry*, vol. 42, no. 8, pp. 965–971, 2011.

[29] Z. Tian, "NMR diffusional coupling of multiple-scale porous rock and its detection," *Chinese Journal of Geophysics*, vol. 64, no. 3, pp. 1119–11130, 2021.

Hindawi
Advances in Materials Science and Engineering
Volume 2021, Article ID 1411185, 10 pages
https://doi.org/10.1155/2021/1411185

Research Article

Performance Evaluation of Waste Crumb Rubber/Silica Fume Composite Modified Pervious Concrete in Seasonal Frozen Regions

Guobao Luo ,[1,2] Pin Zhao ,[2] Yangpeng Zhang,[3,4] and Zhengzhuan Xie[3,4]

[1]*State Key Laboratory of Mechanical Behavior and System Safety of Traffic Engineering Structures, Shijiazhuang Tiedao University, Shijiazhuang 050043, China*
[2]*Key Laboratory of Roads and Railway Engineering Safety Control (Shijiazhuang Tiedao University), Ministry of Education, Shijiazhuang 050043, China*
[3]*Guangxi Transportation Science & Technology Group Co. Ltd., Nanning 5300007, China*
[4]*Guangxi Key Lab of Road Structure and Materials, Nanning 5300007, China*

Correspondence should be addressed to Pin Zhao; zhaopin1115@126.com

Received 22 April 2021; Revised 7 June 2021; Accepted 16 June 2021; Published 24 June 2021

Academic Editor: Xiao Dong Zhao

The waste crumb rubber (WCR) and silica fume (SF), as industrial waste and byproduct, are widely used as additives in road construction materials, which can not only realize waste utilization and protect the environment but also reduce the consumption of building material resources. At present, most of the research has focused on the properties of concrete modified only by WCR or SF; there are few studies concentrated on composite modified concrete by the two, especially the study on pervious concrete (PC). This article aims to study the mechanical strength, deformability, and freeze-thaw (F-T) resistance of waste crumb rubber/silica fume composite modified pervious concrete (RSFPC). The RSFPC and control specimens were manufactured in the lab. The experiments of compressive strength, flexural strength, flexural failure strain, flexural elastic modulus, and F-T cycles were conducted. In addition, the properties of RSFPC were compared with WCR and SF single modification PC. The results indicate that the composite modification of WCR and SF can give full play to the advantages of the two materials so that the strength property and elastic modulus of PC will not be decreased and the F-T resistance and deformability can be greatly improved. Compared to a single modification group by WCR or SF, RSFPC has a more balanced and comprehensive performance, which will greatly expand the application of PC.

1. Introduction

In the process of urbanization, the unprecedented levels of urbanization not only brings great convenience to people's life but also causes many social and environmental problems [1–3]. Due to the excessive consumption of natural resources and the increase of carbon emissions, global climate change is becoming more and more obvious. Extreme severe weather conditions such as high temperature and flood frequently occur [4–6]. At the same time, the urban surface is covered by a dense concrete structure, which blocks the flow of water and gas between underground and ground, causing many urban problems, such as urban waterlogging, groundwater recession, noise pollution, and urban heat island phenomenon [7–10]. With the increasing prominence of urban problems and people's awareness of environmental protection, it has become the focus of people's attention to construct green and sustainable development of city-people-environment. Thus, China has proposed the concept of sponge city in 2012 [11]. In 2015, the first batch of sponge city construction pilot city was determined, and 16 cities were shortlisted. Meanwhile, state finance provided 10 billion CNY as support.

The most important component of sponge city construction is urban pervious pavement; it is a kind of pavement structure with connected pores that can realize the functions of being permeable and breathable. It can well solve the urban problems brought by impervious pavement, and it is an ecological and environmental protection pavement structure [12, 13]. Compared with the traditional impervious pavement structure, the pervious pavement has several advantages: (1) raising the groundwater level and replenish groundwater resources, (2) reducing urban surface runoff and alleviate urban waterlogging, (3) reducing urban noise pollution and improving urban living environment, and (4) alleviating urban heat island phenomenon and improving the urban ecological environment. At present, PC is widely used in parks, sidewalks, light vehicle roads, and squares [14–16]. Generally speaking, the permeability and compressive strength of PC can meet the engineering requirements [17–20]. However, when PC is used as road surface or base layer, it will often be subjected to the repeated vehicle loads, which requires that PC not only has sufficient strength but also has certain deformability to resist fatigue [21]. Moreover, the porous structure of PC makes the adverse effect of F-T more serious than that of ordinary concrete. So, the F-T resistance of PC is also very important [22, 23]. Therefore, good deformability and F-T resistance for PC in seasonal frozen regions are as important as permeability and strength property.

WCR has been widely used in road engineering for its high toughness and antiaging properties. The application of WCR in ordinary concrete shows that WCR can effectively improve the deformation property, F-T resistance, toughness, vibration, and noise reduction performance of concrete, but it has a negative impact on its strength [24–28]. SF, as a byproduct of the smelting industry with abundant silica, is an excellent cement-based modified material and has a broad application prospect in cement concrete [29, 30]. The research has already verified that the addition of SF can significantly improve the strength and F-T resistance of concrete [31, 32].

Although mature and extensive research has been conducted on the application of WCR or SF in ordinary concrete, their application in PC is rarely reported, especially the modification with two kinds of materials simultaneously. The researches on rubberized PC showed that the addition of WCR significantly decreased the mechanical properties and abrasion resistance, but it had a crucial positive effect on the ductility and vibration reduction performance of PC [33, 34]. In addition, the properties of rubberized PC were pertinent to the particle size of WCR. The adverse effect of fine rubber on mechanical properties was less than that of coarse rubber. At the same time, the positive influence of fine rubber on deformability was better than that of coarse rubber [35, 36]. Therefore, the WCR with relatively small particles is the preference in modifying pervious concrete, which is different from ordinary concrete. In terms of SF, it had been verified that the SF-reinforced PC had great advantages in mechanical strength and durability, but the deformability was not improved [37–39]. The compressive strength of PC, with 10% SF replacement, had been greatly improved by more than 80% [38]; this great increase in compressive strength was worthy of further study to verify. The properties of PC modified or reinforced with WCR or SF, on the whole, need to be studied extensively and in-depth.

Based on the current research progress, a large number of studies on WCR or SF single modification concrete have been conducted by domestic and foreign scholars, and considerable research findings were achieved. It can be seen that, due to the high elasticity of WCR, the addition of it can significantly improve the deformability of concrete under load, thus improving concrete toughness. At the same time, the addition of WCR will weaken the bonding between concrete components, resulting in the reduction of concrete strength. The rich silica content of SF leads to a further chemical reaction between SF and cement hydration products to produce a stronger gel, which improves the strength and durability of concrete. PC, as pavement material in practical engineering, requires not only sufficient strength to bear the action of load but also good deformability to bear the action of repeated load. In addition, the frost resistance of PC is the most important index of durability when it is used in seasonal frozen regions. Therefore, the development of PC with good deformability, superior frost resistance, and high strength is an important basis for the application. Considering the advantages of WCR or SF, in order to give full play to the characteristics of both materials, combined with previous research performed by our group [30, 35], this article conducted the laboratory investigation on the mechanical property and F-T resistance of RSFPC. The research outline is shown in Figure 1.

2. Experimental Materials and Methods

2.1. Raw Materials. The ordinary Portland cement of 42.5 and SF were used as cementitious materials for RSFPC. The coarse aggregate with 4.75–9.5 mm and WCR with a particle size of 40 mesh, obtained from a local factory, were selected in the article. The technical properties of all the above materials can be found in [30, 35]. Besides, a superplasticizer was applied and its properties are listed in Table 1. The experiment water is tap water.

2.2. Mix Design. With equal volume replacement of cement, the effect of different SF contents on the properties of PC has been studied by our group [30]. The research indicated that 12% SF presented better modification effectiveness, so in this study, the SF incorporation level was selected as 12%. In addition, the effect of particle size of WCR on the properties of PC indicated that the fine WCR showed better improvement than that of the coarse WCR [35], so the fine WCR was selected and the incorporation level of WCR for RSFPC was set as 4%, 6%, and 8% of cementitious material quality. The volumetric method was adopted to design RSFPC in accordance with the Chinese national standard [40]. The water-to-binder ratio was 0.3, and the designed porosity was 15%. The content of the superplasticizer was 0.8%. The mix design is shown in Table 2.

2.3. Specimen Preparation and Test Methods. The preparation method, the production, and curing condition of RSFPC specimens have been reported in detail in [21]. The

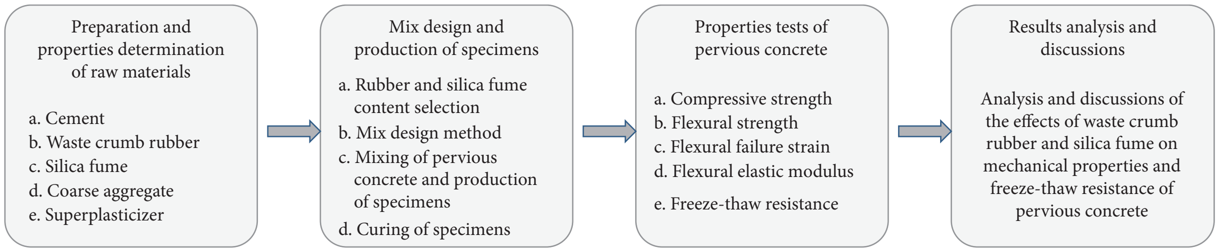

Figure 1: The research outline of the article.

Table 1: Technical index of superplasticizer.

Uniformity parameters		Properties parameters	
Morphology	Liquid	Water-reducing rate (%)	25
pH	7.0–8.0	Air content (%)	1.5
Density (kg/m^3)	0.98–1.02	Difference between initial setting times (min)	+35
Effective content (%)	20–25	Difference between final setting times (min)	+50
Chloride ion content (%)	0.01	7 d compressive strength ratio (%)	163
Alkali content (%)	0.02	28 d compressive strength ratio (%)	159

Table 2: Mix design of RSFPC (in kg/m^3).

Mix ID	WCR content (%)	SF content (%)	Coarse aggregate	Cement	Water	PAS 1	WCR	SF
WCR4 + SF12	4	12	1503	413.0	140.8	3.75	18.8	56.3
WCR6 + SF12	6	12	1503	413.0	140.8	3.75	28.2	56.3
WCR8 + SF12	8	12	1503	413.0	140.8	3.75	37.5	56.3

[1]Polycarboxylic acid superplasticizer.

sizes of the specimens are as follows: cube specimen with $100 \times 100 \times 100$ mm for compressive strength and F-T cycles tests; prism specimen with $100 \times 100 \times 400$ mm for flexural experiments. All experiments were conducted according to GB/T 50081-2002 and 50082-2009 [41, 42]. The test method for rapid freeze-thaw was adopted. The freezing time was about 2.5 hours and the thawing time was about 1.5 hours. The lowest and highest temperatures in the center of the specimen were −18°C and 5°C, respectively. As shown in Figure 2, a three-point bending test is adopted for the flexural experiment. In order to accurately determine the flexural failure strain and flexural elastic modulus of RSFPC, the midspan displacement of the three-point bending specimen under load was recorded by a micrometer gauge placed on the bottom of the specimen. The flexural failure strain and flexural elastic modulus can be calculated by

$$\varepsilon = \frac{6h\Delta}{L^2}, \quad (1)$$

$$E = \frac{L^3 \left(F_{0.5} - F_0\right)}{4Bh^3 \left(\Delta_{0.5} - \Delta_0\right)}, \quad (2)$$

where ε is the flexural failure strain; Δ is the deflection corresponding to flexural failure load (mm); E is the flexural elastic modulus (GPa); $F_{0.5}$ is the load that equals 50% flexural failure load (kN); F_0 is the initial load of the specimen and its value can be taken as the actual load of the specimen nearest to 2 kN (kN); and $\Delta_{0.5}$ and Δ_0 are the displacements of the specimen corresponding to $F_{0.5}$ and F_0 (mm).

3. Experiments Results and Analysis

3.1. Experiments Results. All the property indexes of RSFPC are expressed as the average value of three specimens; the experiments results are listed in Tables 3–7.

3.2. Properties Analysis of RSFPC. In order to analyze the compound modification effectiveness of WCR and SF, the control group (without WCR and SF), WCR group (WCR modification group), and SF group (SF modification group) are introduced as comparative groups. The data of the control group, WCR group, and SF group are obtained from the previous research conducted by our team.

3.2.1. Compressive Strength. Figure 3 shows the compressive strength of RSFPC and comparative groups. It indicates that the compressive strength of RSFPC decreases with the increase of WCR contents, which means the addition of WCR has an adverse impact on the compressive strength of PC. The result is consistent with that of the WCR single modification PC reported in [35]. This is because the WCR on the interfacial transition zone weakens the cementation between cement and coarse aggregate and thus decreases the bond force. Compared with WCR groups, due to the

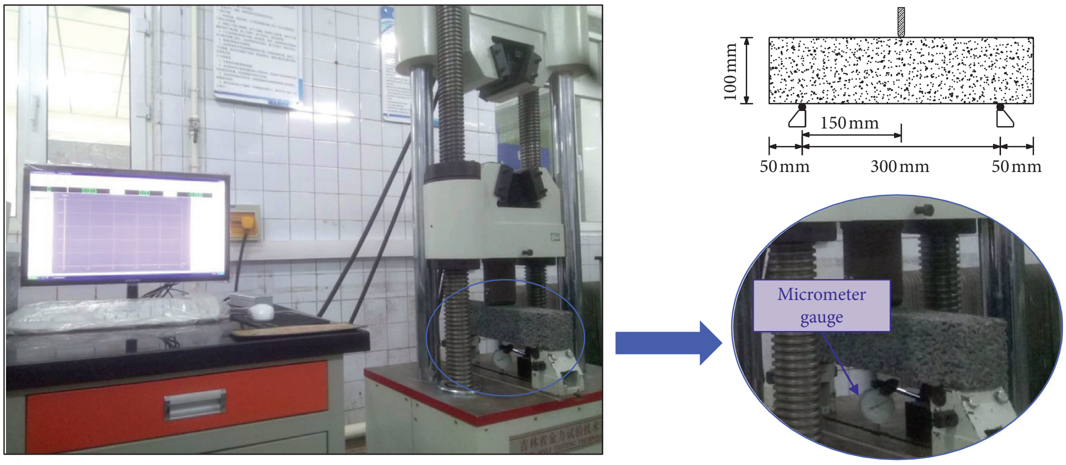

Figure 2: Three-point bending test.

Table 3: Compressive strength of RSFPC.

Mix ID	Compressive strength (MPa)				
	1	2	3	Mean	St. dev.
WCR4 + SF12	23.9	22.8	24.4	23.7	0.67
WCR6 + SF12	22.4	22.9	23.7	23.0	0.54
WCR8 + SF12	20.5	20.1	19.1	19.9	0.59

Table 4: Flexural strength of RSFPC.

Mix ID	Flexural strength (MPa)				
	1	2	3	Mean	St. dev.
WCR4 + SF12	4.78	4.59	4.66	4.68	0.08
WCR6 + SF12	4.52	4.61	4.64	4.59	0.05
WCR8 + SF12	4.11	4.05	3.95	4.04	0.07

Table 5: Flexural failure strain of RSFPC.

Mix ID	Flexural failure strain ($\mu\varepsilon$)				
	1	2	3	Mean	St. dev.
WCR4 + SF12	1546	1482	1511	1513	26
WCR6 + SF12	2194	2098	2174	2155	41
WCR8 + SF12	2401	2381	2375	2386	11

Table 6: Flexural failure strain of RSFPC.

Mix ID	Flexural elastic modulus (GPa)							
	Number	$F_{0.5}$	F_0	$\Delta_{0.5}$	Δ_0	E	Mean	St. dev.
WCR4 + SF12	1	5.311	1.992	0.152	0.143	24.9	24.0	0.68
	2	5.102	2.002	0.148	0.139	23.3		
	3	5.179	1.997	0.152	0.143	23.9		
WCR6 + SF12	1	5.021	1.995	0.152	0.142	20.4	20.9	0.36
	2	5.119	1.999	0.151	0.141	21.1		
	3	5.156	2.003	0.154	0.144	21.3		
WCR8 + SF12	1	4.566	1.989	0.159	0.147	14.5	14.4	0.26
	2	4.502	2.001	0.163	0.151	14.1		
	3	4.389	1.997	0.159	0.148	14.7		

Table 7: Compressive strength loss rate after F-T cycles of RSFPC.

Mix ID	Compressive strength loss rate (%)			
	25 F-T cycles	50 F-T cycles	75 F-T cycles	100 F-T cycles
WCR4 + SF12	2.1	5.1	12.7	19.4
WCR6 + SF12	1.3	5.2	10.9	18.3
WCR8 + SF12	1.0	5.0	10.1	15.6

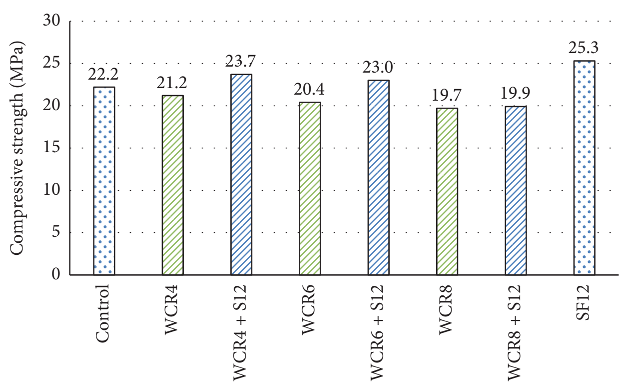

Figure 3: The compressive strength of RSFPC.

reinforcement of SF, RSFPC has higher compressive strength under the same WCR content. The addition of SF improves the strength of the cementitious material of the PC, thus making up for the adverse effect of WCR on the strength of the cementitious material. Although the compressive strengths of all groups are lower than that of the SF group, the compressive strengths of WCR4 + SF12 and WCR6 + SF12 groups are more than 23 MPa, even higher than the control group. It indicates that the compound modification of WCR and SF for PC can meet certain compressive strength requirements. For unloaded and light pavement, such compressive strength is up to standard.

3.2.2. Flexural Strength. Figure 4 summarizes the flexural strength of RSFPC. It can be found that the flexural strengths of all RSFPC groups are higher than 4 MPa and fully meet the standard requirement of 3.0 MPa in CJJ/T135-2009. The WCR4 + SF12 and WCR6 + SF12 have similar flexural strength compared with the control group. Like compressive strength, the flexural strengths of all RSFPC groups are greater than those of the WCR groups under the same WCR contents. Compared with the SF group, with the variation of WCR content from 4% to 8%, the RSFPC's flexural strength decreases 10%, 11%, and 22%, respectively. The influence mechanism of WCR and SF on the flexural strength of PC is the same as that of compressive strength. Although WCR is unfavorable to the flexural strength, this adverse effect can be reduced by the incorporation of SF, and the flexural strength of RSFPC can reach the expected level.

3.2.3. Flexural Failure Strain. WCR is a kind of elastic material; the purpose of using WCR modification is to improve the deformability of PC. Figure 5 describes the flexural failure strain of RSFPC. It is obvious that the flexural failure strains of the WCR group and RSFPC are significantly higher than those of the control group and SF group. Due to the high elasticity, the addition of rubber makes the deformation of the PC better under the action of vehicle load, reducing the rigidity and improving the toughness of the PC. With the same amount of WCR, the flexural failure strain of the WCR group and RSFPC group are basically the same, which indicates that the WCR is the fundamental factor that creates the improvement of the flexural failure strain. Compared with the control group, the flexural failure strain of RSFPC is enhanced by 12%, 59%, and 76%, respectively. It means that the deformability of PC has been greatly improved, and when used as the road surface or base, PC has better fatigue properties under repeated loads.

3.2.4. Flexural Elastic Modulus. Figure 6 shows the flexural elastic modulus of RSFPC. The flexural elastic modulus of RSFPC decreases with the increasing WCR contents and it reveals that the addition of WCR makes the flexural elastic modulus aggravated. Based on the effects of WCR on the flexural strength and flexural failure strain above, on the one hand, the WCR reduces the flexural strength of PC and improves its flexural failure strain, on the other hand, thus reducing its flexural elastic modulus. RSFPC has higher flexural elastic modulus than that of the WCR group at the same WCR content because the flexural failure strain of the WCR group and RSFPC is basically the same at the same level of WCR content. However, due to the incorporation of SF, the flexural strength of RSFPC increases, resulting in a higher flexural elastic modulus. Compared with the control group, the WCR4 + SF12 group has a flexural elastic modulus of 24 GPa with a 5.3% increase, although there is a 15% decrease compared with the SF group. The flexural elastic modulus is closely related to the flexural strength and flexural failure strain, so the modification materials and its contents of RSFPC should be considered comprehensively based on its property indexes in practical application.

3.2.5. F-T Resistance. The F-T resistance is another vital index for RSFPC in seasonal frozen regions. The compressive strength loss rates of the control group, WCR group, RSFPC group, and SF group after different F-T cycles are presented in Figure 7. It is obvious that compared with the control group, the compressive strength loss rates of the WCR group, RSFPC group, and SF group under different F-T cycles are lower, which indicates that WCR modification, SF modification, and WCR and SF compound modification are all beneficial to F-T resistance of PC. The improvement of F-T resistance of PC by WCR is mainly attributed to the increase of PC deformation during the frost

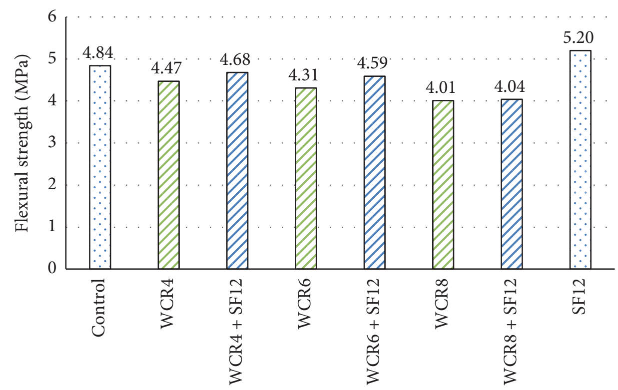

Figure 4: The flexural strength of RSFPC.

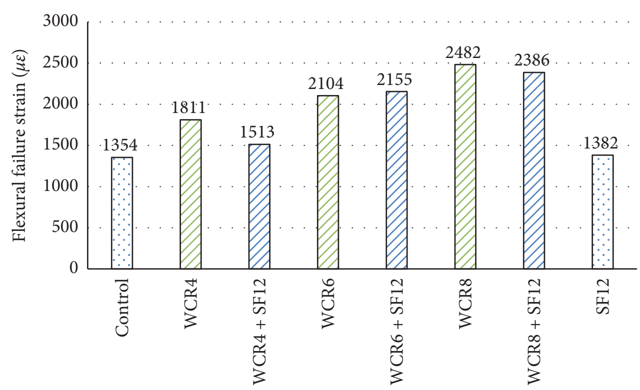

Figure 5: The flexural failure strain of RSFPC.

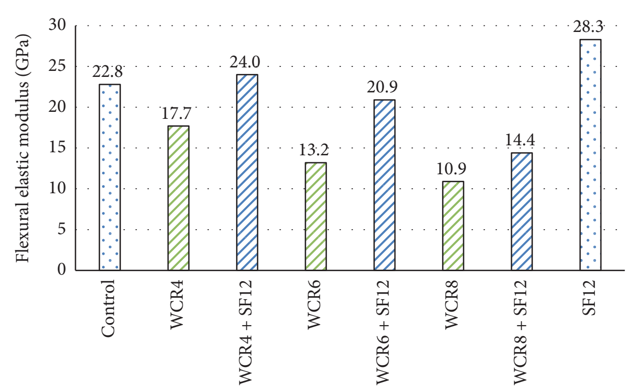

Figure 6: The flexural elastic modulus of RSFPC.

heaven. Moreover, the improvement of F-T resistance of PC by SF is because SF improves the strength of cementitious material and reduces the effectiveness of F-T damage. RSFPC group has lower compressive strength loss rates than that of WCR group with the same WCR content, which indicates that WCR and SF compound modification is better than the WCR single modification. However, compared with SF single modification, the compressive strength loss rate of WCR and SF composite modification is higher, indicating that the WCR and SF composite modification had poor F-T resistance. Although both SF and WCR can improve the F-T performance of PC, the WCR and SF composite modification is not the superposition of their single modification effect.

4. Discussion

For the road material, mechanical properties and durability are extremely important. It should not only have enough strength to bear the vehicle load but also have large deformability to resist the action of repeated load. For road materials in seasonal frozen regions, it should also have

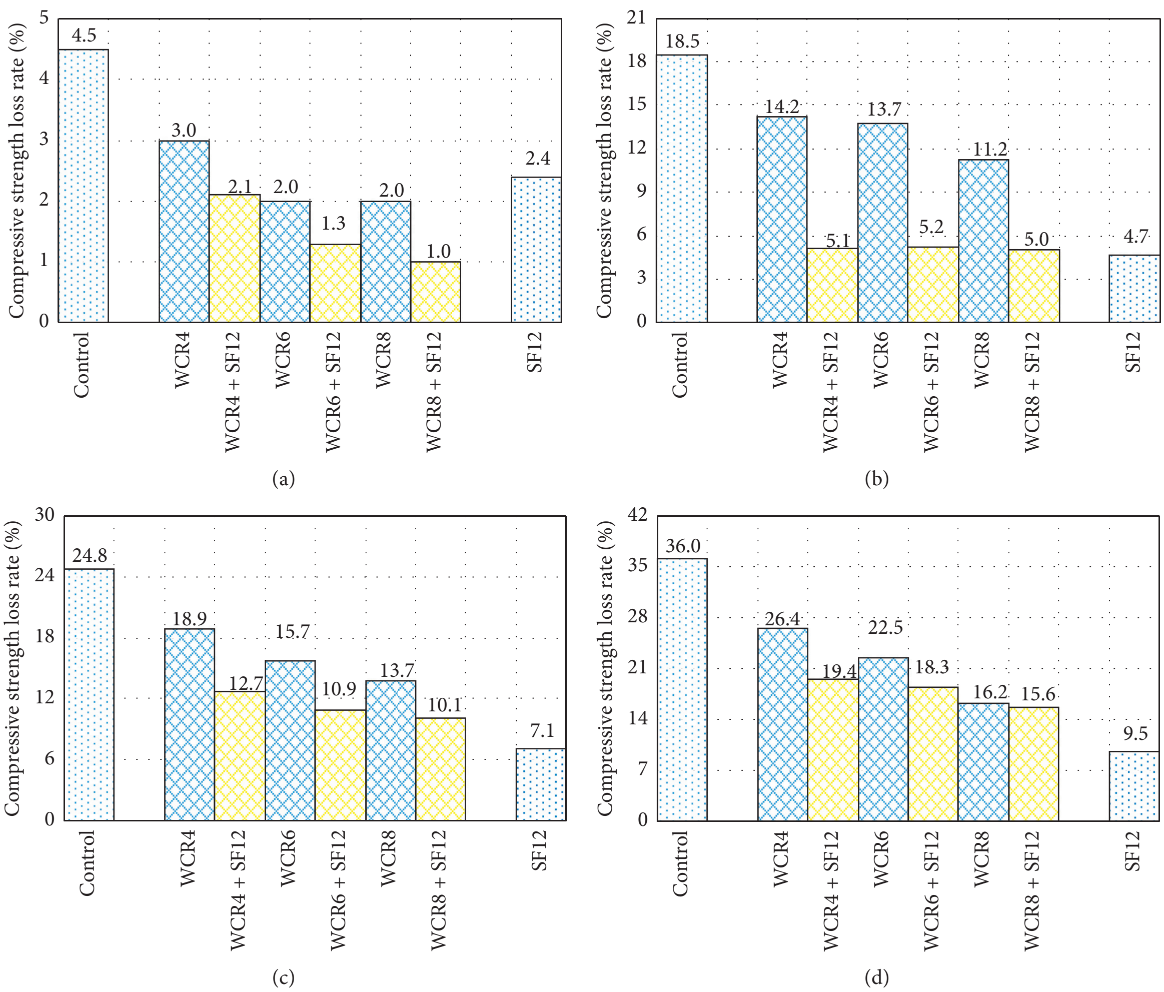

Figure 7: The compressive strength loss rate of RSFPC after different F-T cycles. (a) 25 F-T cycles; (b) 50 F-T cycles; (c) 75 F-T cycles; (d) 100 F-T cycles.

certain F-T durability; it requires that the material has comprehensive properties rather than being superior in one area and inferior in others. Due to the requirement of permeability, the porosity of PC is usually large. However, high porosity will cause a reduction in mechanical properties, such as compressive strength, flexural strength, and elastic modulus. In addition, too large porosity is very unfavorable to F-T resistance, which will accelerate the damage of PC. Meanwhile, under the action of repeated load, PC is prone to fatigue damage and failure, and its deformability is an important index that affects its service life. Therefore, PC applied in practical engineering must have a certain strength, deformability, and F-T resistance.

In Section 3, the mechanical properties and F-T resistance are discussed in detail; all kinds of property indexes for RSFPC and other PC are presented in Figure 8 with a radar map. It can comprehensively compare the differences between various property indexes of different types of PC and select PC with superior comprehensive performance. Except for the compressive strength loss rate under F-T cycles, "the larger, the better" is another property index for PC. Figure 8 shows that RSFPC with 6% WCR content has the best comprehensive performance, followed by RSFPC with 4% WCR content. These two groups have better strength, greater deformability, and higher F-T resistance. The strength and F-T resistance of SF group are better, but the deformability is poor. The control group has poor F-T resistance and deformability, while WCR groups express lower strength and elastic modulus. Therefore, it is necessary to select the

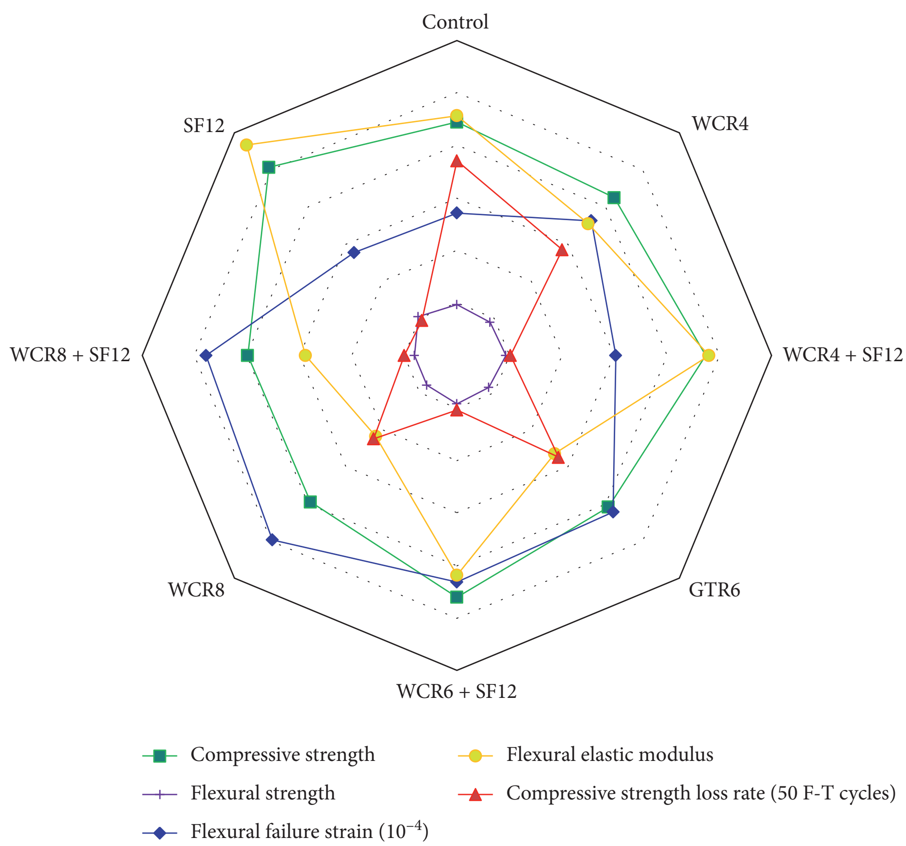

Figure 8: The radar map of properties for RSFPC.

modification type of PC reasonably according to the characteristics of practical projects and the requirements of material properties. RSFPC is recommended for the light load road in seasonal frozen regions.

5. Conclusions

In this article, the compressive strength, flexural strength, flexural failure strain, flexural elastic modulus, and F-T resistance of RSFPC were investigated. The composite modification effects of WCR and SF were analyzed.

(1) The flexural failure strain of PC indicates that WCR is the determining factor in improving the flexural deformability of PC.

(2) WCR has adverse effects on the strength and elastic modulus of PC, but these adverse effects can be improved by the addition of SF. Compared with the control group, the WCR and SF composite modification can not only guarantee the strength characteristics of PC but also enhance the F-T resistance to some extent and, at the same time, significantly improve deformability of PC.

(3) Although both SF and WCR are advantageous to the F-T resistance of PC, the improvement effect of WCR and SF composite modification is not the superposition of both, which is mainly because of their different effects on the mechanical properties of PC.

(4) Considering the mechanical properties, deformability, and F-T resistance of PC, the systematic comparison of different modification PC shows that RSFPC has a more balanced and comprehensive performance and is suggested to be the first choice in engineering application.

Data Availability

The data used to support the findings of this study are included within the article.

Conflicts of Interest

The authors declare that they have no conflicts of interest.

Authors' Contributions

G. B. Luo contributed to conceptualization, formal analysis, and investigation. P. Zhao was responsible for the methodology and writing, reviewing, and editing of the manuscript. Y. P. Zhang wrote and prepared the original draft. Z. Z. Xie was responsible for funding acquisition and formal analysis.

Acknowledgments

This research was supported by the Guangxi Key Science and Technology Project (Grant no. AB17292032). The authors would like to express their appreciation to the Road and Bridge Laboratory of Jilin University for support during the experiment.

References

[1] J. Y. Zhao, L. Yu, and Y. D. Xu, "Exploring difference in land surface temperature between the city centres and urban expansion areas of china's major cities," *International Journal of Remote Sensing*, vol. 41, pp. 8963–8983, 2020.

[2] L. J. Lin, T. Gao, M. Luo et al., "Contribution of urbanization to the changes in extreme climate events in urban agglomerations across china," *The Science of the Total Environment*, vol. 744, Article ID 140264, 2020.

[3] S. Adams, E. Boateng, and A. O. Acheampong, "Transport energy consumption and environmental quality: does urbanization matter?" *The Science of the Total Environment*, vol. 744, Article ID 140617, 2020.

[4] A. J. Echendu, "The impact of flooding on Nigeria's sustainable development goals (SDGs)," *Ecosystem Health and Sustainability*, vol. 6, 2020.

[5] H. D. Lv, L. Yang, J. S. Zhou et al., "Water resource synergy management in response to climate change in China: from the perspective of urban metabolism," *Resources, Conservation and Recycling*, vol. 163, Article ID 105095, 2020.

[6] P. Roy, S. C. Pal, R. Chakrabortty, I. Chowdhuri, S. Malik, and B. Das, "Threats of climate and land use change on future flood susceptibility," *Journal of Cleaner Production*, vol. 272, Article ID 122757, 2020.

[7] M. Santamouris and G. Y. Yun, "Recent development and research priorities on cool and super cool materials to mitigate urban heat island," *Renewable Energy*, vol. 161, pp. 792–807, 2020.

[8] E. Forero-Ortiz, E. Martinez-Gomariz, M. C. Porcuna, L. Locatelli, and B. Russo, "Flood risk assessment in an underground railway system under the impact of climate change: a case study of the Barcelona metro," *Sustainability*, vol. 12, p. 5291, 2020.

[9] M. T. Sohail, Y. Mahfooz, K. Azam, Y. Yen, G. F. Liao, and S. Fahad, "Impacts of urbanization and land cover dynamics on underground water in Islamabad, Pakistan," *Desalination and Water Treatment*, vol. 159, pp. 402–411, 2019.

[10] K.-Y. Park and M.-H. Lee, "Ulnerability analysis of urban district on the urban flood damage: a case study," *Desalination and Water Treatment*, vol. 119, pp. 27–35, 2018.

[11] Y. C. Ma, Y. Jiang, and S. Swallow, "China's sponge city development for urban water resilience and sustainability: a policy discussion," *The Science of the Total Environment*, vol. 729, Article ID 139078, 2020.

[12] J. W. Liu, H. Li, Y. Wang, and H. J. Zhang, "Integrated life cycle assessment of permeable pavement: model development and case study," *Transport Research Part D—Transport and Environment*.vol. 85, Article ID 102381, 2020.

[13] M. Brugin, M. Marchioni, G. Becciu, F. Giustozzi, E. Toraldo, and V. C. Andres-Valeri, "Clogging potential evaluation of porous mixture surfaces used in permeable pavement systems," *European Journal Environmental Civil Engineering*, vol. 24, pp. 620–630, 2020.

[14] H. El-Hassan, P. Kianmehr, and S. Zouaoui, "Properties of pervious concrete incorporating recycled concrete aggregates and slag," *Construction and Building Materials*, vol. 212, pp. 164–175, 2020.

[15] M. Saaly, M. M. Hedayat, and A. Golroo, "Performance of pervious concrete pavement under various raining conditions," *Road Materials and Pavement Design*, vol. 20, pp. 1653–1663, 2019.

[16] M. Seslija, N. Radovic, D. Jovanov, D. Kukaras, A. Starcev-Curcin, and I. Jokanovic, "Possibilities of pervious concrete application in road construction," *Tehnički Vjesnik*, vol. 25, pp. 1202–1212, 2018.

[17] S. Kant Sahdeo, G. D. Ransinchung R.N., K. L. Rahul, and S. Debbarma, "Effect of mix proportion on the structural and functional properties of pervious concrete paving mixtures," *Construction and Building Materials*, vol. 255, Article ID 119260, 2020.

[18] H. B. Liu, G. B. Luo, H. B. Wei, and H. Yu, "Strength, permeability, and freeze thaw durability of pervious concrete with different aggregate sizes, porosities, and water-binder ratios," *Applied Sciences*, vol. 8, p. 1217, 2018.

[19] L. Moretti, P. Di Mascio, and C. Fusco, "Porous concrete for pedestrian pavements," *Water*, vol. 11, p. 2105, 2019.

[20] F. Yu, D. Q. Sun, J. Wang, and M. J. Hu, "Influence of aggregate size on compressive strength of pervious concrete," *Construction and Building Materials*, vol. 209, pp. 463–475, 2019.

[21] H. B. Liu, G. B. Luo, P. L. Zhou, H. B. Wei, W. J. Li, and D. Yu, "Flexural-fatigue properties of sustainable pervious concrete pavement material containing ground tire rubber and silica fume," *Sustainability*, vol. 11, p. 4467, 2019.

[22] M. S. M. Lund, J. T. Kevern, V. R. Schaefer, and K. K. Hansen, "Mix design for improved strength and freeze thaw durability of pervious concrete fill in Pearl-chain bridges," *Materials and Structures*, vol. 50, no. 1, p. 42, 2017.

[23] M. Vancura, K. MacDonald, and L. Khazanovich, "Microscopic analysis of paste and aggregate distresses in pervious concrete in a wet, hard freeze climate," *Cement and Concrete Composites*, vol. 33, no. 10, pp. 1080–1085, 2011.

[24] O. Youssf, J. E. Mills, T. Benn et al., "Development of crumb rubber concrete for practical application in the residential construction sector-design and processing," *Construction and Building Materials*, vol. 260, Article ID 119813, 2020.

[25] J. Mo, L. Zeng, Y. Liu et al., "Mechanical properties and damping capacity of polypropylene fiber reinforced concrete modified by rubber powder," *Construction and Building Materials*, vol. 242, Article ID 118111, 2020.

[26] A. S. Eisa, M. T. Elshazli, and M. T. Nawar, "Experimental investigation on the effect of using crumb rubber and steel fibers on the structural behavior of reinforced concrete beams," *Construction and Building Materials*, vol. 252, Article ID 119078, 2020.

[27] Y. Li, S. Zhang, R. J. Wang, and F. N. Dang, "Potential use of waste tire rubber as aggregate in cement concrete: a comprehensive review," *Construction and Building Materials*, vol. 225, pp. 1183–1201, 2019.

[28] W. Gardziejczyk, A. Plewa, and R. Pakholak, "Effect of addition of rubber granulate and type of modified binder on the viscoelastic properties of stone mastic asphalt reducing tire/road noise (SMA LA)," *Materials*, vol. 13, p. 3446, 2020.

[29] Y. S. Wang, Z. H. Xu, J. B. Wang, Z. H. Zhou, P. Du, and X. Cheng, "Synergistic effect of nano-silica and silica fume on hydration properties of cement-based materials," *Journal of Thermal Analysis and Calorimetry*, vol. 140, pp. 2225–2235, 2019.

[30] H. B. Liu, G. B. Luo, L. H. Wang, W. S. Wang, W. J. Li, and Y. F. Gong, "Laboratory evaluation of eco-friendly pervious concrete pavement material containing silica fume," *Applied Sciences*, vol. 9, p. 73, 2019.

[31] R. Shirdam, M. Amini, and N. Bakhshi, "Investigating the effects of copper slag and silica fume on durability, strength, and workability of concrete," *International Journal of Environmental Research*, vol. 13, pp. 909–924, 2019.
[32] M. H. Mizan, T. Ueda, and K. Matsumoto, "Enhancement of the concrete-PCM interfacial bonding strength using silica fume," *Construction and Building Materials*, vol. 259, Article ID 119774, 2020.
[33] S. Mondal and K. P. Biligiri, "Crumb rubber and silica fume inclusions in pervious concrete pavement systems: evaluation of hydrological, functional, and structural properties," *Journal of Testing and Evaluation*, vol. 46, pp. 892–905, 2018.
[34] M. Gesoglu, E. Guneyisi, G. Khoshnaw, and S. Ipek, "Investigating properties of pervious concretes containing waste tire rubbers," *Construction and Building Materials*, vol. 63, pp. 206–213, 2014.
[35] H. B. Liu, G. B. Luo, Y. F. Gong, and H. B. Wei, "Mechanical properties, permeability, and freeze thaw resistance of pervious concrete modified by waste crumb rubbers," *Applied Sciences*, vol. 8, p. 1843, 2018.
[36] A. A. Aliabdo, A. M. Abd Elmoaty, and A. M. Fawzy, "Experimental investigation on permeability indices and strength of modified pervious concrete with recycled concrete aggregate," *Construction and Building Materials*, vol. 193, pp. 105–127, 2018.
[37] D. A. Mann, "The effects of utilizing silica fume in portland cement pervious concrete," University of Missouri-Kansas City, Kansas, Misssouri, USA, Master of Science, 2014.
[38] P. T. A. Zerdi, M. A. Samee, H. Ali, and T. Zerdi, "Study of silica fume incorporation in pervious concrete," *International Journal of Science and Research*, vol. 5, pp. 532-533, 2016.
[39] G. Adil, J. T. Kevern, and D. Mann, "Influence of silica fume on mechanical and durability of pervious concrete," *Construction and Building Materials*, vol. 247, Article ID 118453, 2020.
[40] Ministry of Housing and Urban-Rural Construction of the People's Republic of China, *Technical Specification for Pervious Cement Concrete Pavement*, Ministry of Housing and Urban-Rural Construction of the People's Republic of China, Beijing, China, 2009, in Chinese.
[41] Ministry of Housing and Urban-Rural Construction of the People's Republic of China, *Standard for Test Method of Mechanical Properties on Ordinary Concrete*, Ministry of Housing and Urban-Rural Construction of the People's Republic of China, Beijing, China, 2002, in Chinese.
[42] Ministry of Housing and Urban-Rural Construction of the People's Republic of China, *Standard for Test Methods of Long-Term Performance and Durability of Ordinary Concrete*, Ministry of Housing and Urban-Rural Construction of the People's Republic of China, Beijing, China, 2009, in Chinese.

Hindawi
Advances in Materials Science and Engineering
Volume 2021, Article ID 5403567, 14 pages
https://doi.org/10.1155/2021/5403567

Research Article

Study on the Effect of Unilateral Sand Deposition on the Spatial Distribution and Temporal Evolution Pattern of Temperature beneath the Embankment

Ling Chen ,[1,2] Hong Yu ,[1,3] Xiaolin Li ,[4] and Zekun Ding [1,2]

[1]*State Key Laboratory of Frozen Soils Engineering, Northwest Institute of Eco-Environment and Resources, Chinese Academy of Sciences, Lanzhou Gansu 730000, China*
[2]*University of Chinese Academy of Sciences, Beijing 100049, China*
[3]*School of Civil Engineering, Lanzhou University of Technology., Lanzhou Gansu 730050, China*
[4]*College of Civil Engineering and Architecture, Jiaxing University, Jiaxing 314001, China*

Correspondence should be addressed to Ling Chen; chenling@lzb.ac.cn

Received 6 May 2021; Accepted 12 June 2021; Published 21 June 2021

Academic Editor: Hao Zheng

In the context of climate warming and the frequent wind-sand hazards in the Qinghai-Tibet Engineering Corridor (QTEC), the construction of the embankment will affect the thermal regime of permafrost underground. The influence of embankment construction on the variation of the permafrost table beneath it is different, especially for the regime with different mean annual ground temperatures (MAGTs). In this study, the effects of the unilateral sand particles deposition on the spatial distribution and temporal evolution pattern of temperature beneath the embankment are investigated through the numerical simulations, in which the heat transfer is considered. The model is validated by the field observed data of soil temperatures around an experimental zone built at the sand hazard area in Honglianghe, the interior of Qinghai-Tibet Plateau (QTP). The simulated results indicate that the temperature field beneath the embankment is asymmetrically distributed under the condition of unilateral sand particles deposition. This asymmetry gradually weakened with the increase of operation time and the gradual adjustment of the permafrost temperature field. By comparing the permafrost table beneath the natural surface, the sand deposition center, and the middle of the embankment center, it could be found that the unilateral sand particles deposition has less effect on the degradation of the permafrost table in the center of the embankment. However, for the center of the sand deposition, the change of the permafrost table is larger with the increase of time and the corresponding rate of permafrost table degradation is higher than that without sand particles deposition, especially for the high-temperature permafrost. In addition, with different sand thickness and width conditions, the effect of "narrow-thick" form sand particles deposition on the temperature field beneath embankment is greater than that of "wide-thin" form sand deposition. Hence, in order to reduce its impact on the long-term thermal condition beneath the embankment, it is necessary to clean the thicker deposition sand particles at the toe of the embankment.

1. Introduction

The Qinghai-Tibet Engineering Corridor (QTEC) is the most important link between the Tibet Autonomous Region and inner China, the width of which is several kilometers at wider sections but only hundreds of meters at narrow section [1]. Within the corridor, there are several major linear infrastructures including the Qinghai-Tibet Highway, Qinghai-Tibet Railway, Qinghai-Tibet Power Transmission Line, and Golmud to Lhasa Oil Pipeline and some optical communication cables. In recent years, human activities and increasing air temperature have caused significant grassland degradation and desertification in the QTEC [2–5]. Following the impacts, particularly the construction of the highway and the railway embankments, the energy of near-surface wind flow within the corridor has been disturbed, as well as the original relatively stable sand movement [6]. Hence, the wind-sand hazards were very serious around the highway and railway embankments, particularly in some river valleys and basins that the highway and railway traverse (Figure 1).

In the permafrost, the construction of the embankment will disturb the heat balance of the original surface. The strong heat absorption of asphalt pavement will lead to more rapid permafrost degradation beneath the highway [7–9]. In addition, the change of the thermal-mechanical properties of permafrost will cause embankment and pavement damage, including longitudinal cracks and uneven settlement [10–12]. Hence, in order to reduce the impact of the human activities, a lot of effective engineering structural measures have been considered and used in the construction of highway and railway embankment including the crushed-rock and duct-ventilated embankments. Due to the excellence of the crushed-rock and duct-ventilated embankments, they have been widely used to ensure the thermal stability of highways and railways in permafrost regions of the QTEC [13–19]. However, in the context of climate warming and the expanding scope of human activities, the wind-sand hazards around the embankment in the QTEC have become more and more serious in the last few years [20–23]. The sand particles deposition around the embankment will not only change the surface boundary but also affect the cooling effect of the construction of crushed-rock or duct-ventilated embankments [24–26]. Research studies have shown that with the increasing thickness of sand in the rock layer, the critical temperature difference between the sand-free layer increases, and the Ra number decreases, and the natural convection intensity weakens gradually [27–30]. However, in these research studies, several assumptions about the sand deposition around the embankment are proposed. The distribution of sand particles deposition is generally assumed to be the same at the two slopes of the embankment. The prevailing wind direction within the corridor is west and northwest, and the corridor is from northeast to southwest [1]. Then, the two slopes of embankments of both the railway and highway are generally windward and leeward slopes, respectively. Thus, there should be a considerable difference in the sand deposition on the two slopes. However, the difference was not considered within these previous research studies, which will undermine the accuracy of evaluation on thermal impacts of sand particles deposition on the embankments installed with air-cooled structures.

In this study, a two-dimensional numerical model of the heat transfer for highway embankment is established. In the numerical model, three different mean annual ground temperatures (MAGTs) of the permafrost, in which the embankment is located, are considered, as well as the unilateral sand particles deposition at the toe of the embankment. Field observed data of soil temperatures around an experimental zone are used to validate the numerical model. Through numerical simulations, the effects of unilateral sand deposition on the spatial distribution and temporal evolution pattern of temperature beneath the embankment are investigated. The results of this study could provide informative references for highways constructed in permafrost zones, in which the wind-sand hazards frequently occur around the embankment.

2. Methods

2.1. Governing Equations. According to the experiment, in freeze-thaw soil layers, the ratio of heat conduction is far larger than that of the heat convention [31]. In this article, by ignoring the heat convection, the heat transfer progress considering the heat conduction and phase change in freeze-thaw soil layers can be described as follows [32–34]:

$$C_e^* \frac{\partial T}{\partial t} = \frac{\partial}{\partial x}\left(\lambda_e^* \frac{\partial T}{\partial x}\right) + \frac{\partial}{\partial y}\left(\lambda_e^* \frac{\partial T}{\partial y}\right), \quad (1)$$

where C_e^* is the equivalent volume heat capacity and λ_e^* is the equivalent thermal conductivity. According to the method of sensible heat capacity, the equivalent volume heat capacity C_e^* and the equivalent thermal conductivity λ_e^* in freeze-thaw soils can be written as follows [32–34]:

$$C_e^* = \begin{cases} C_f, & T < (T_m - \Delta T), \\ \dfrac{L}{2\Delta T} + \dfrac{C_u + C_f}{2}, & (T_m - \Delta T) \le T \le (T_m + \Delta T), \\ C_u, & T > (T_m + \Delta T^*), \end{cases}$$
$$\lambda_e^* = \begin{cases} \lambda_f, & T < (T_m - \Delta T), \\ \lambda_f + \dfrac{\lambda_u - \lambda_f}{2\Delta T}\left[T - (T_m - \Delta T)\right], & (T_m - \Delta T) \le T \le (T_m + \Delta T), \\ \lambda_u, & T > (T_m + \Delta T), \end{cases} \quad (2)$$

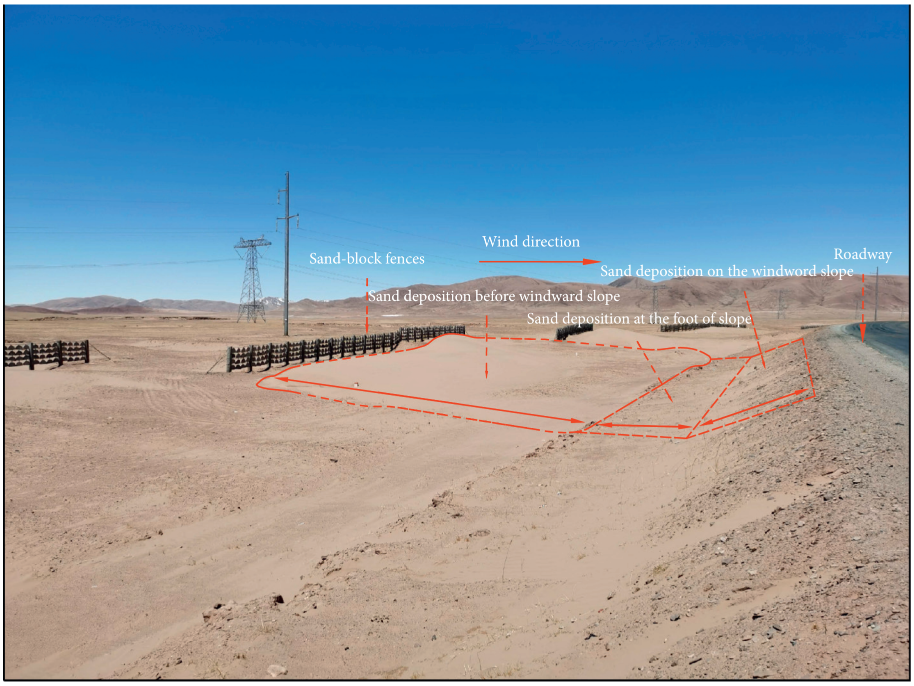

(a)

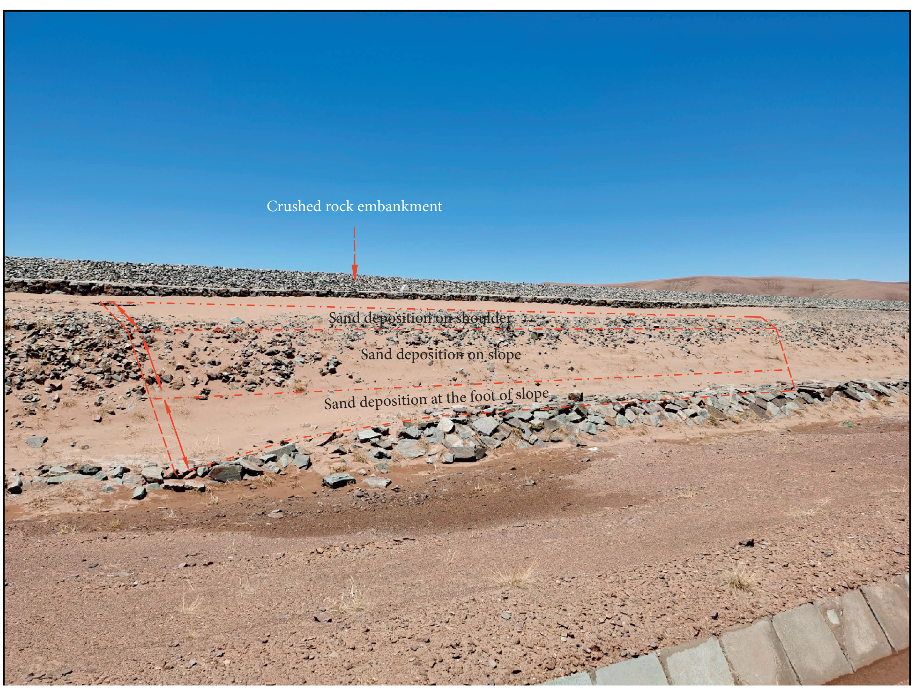

(b)

FIGURE 1: Wind-blown sand deposition around the embankments of the Qinghai-Tibet Roadway (a) and Qinghai-Tibet Railway (b).

where $T_m \pm T$ is the temperature range of phase change; C_u and λ_u are the volume heat capacity and thermal conductivity of unfrozen soil; C_f and λ_f are the volume heat capacity and thermal conductivity of frozen soil; L is the latent heat of phase change per unit volume.

2.2. Physical Model. A physical model of a highway without sand particles deposition near the toe of the embankment (NSE) is shown in Figure 2(a), and a highway with sand particles deposition near the toe of the embankment (SE) in Figure 2(b). In the model, part I is embankment fill, part II

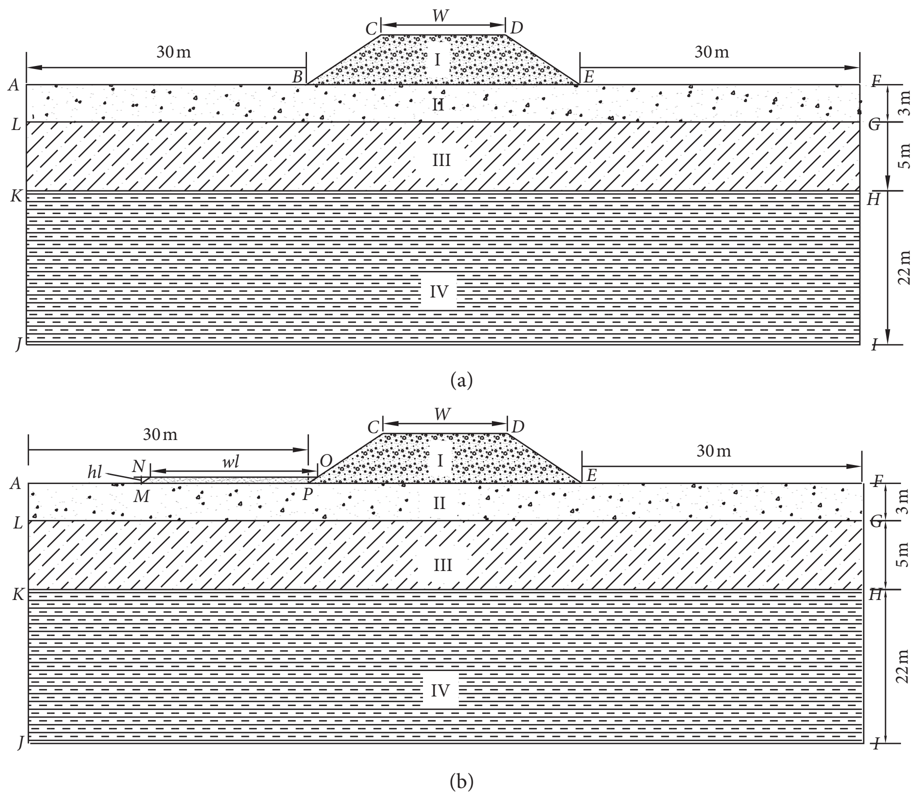

FIGURE 2: Schematic diagrams of expressway embankment: (a) no sand embankment; (b) unilateral sand embankment.

(0~3 m) is gravel and clayey layer, part III (3~8 m) is silty clay, and part IV(8~30 m) is weathered mudstone. The height of the embankment is 4 m and the width of its paving is 10 m. The gradient of the slope is 1 : 1.5. The widths of the sand deposition are determined as 7.1, 10, and 16.7 m. The thicknesses of sand particles deposition are determined as 0.3, 0.5, and 0.7 m. The computational domain is extended by 30 m wide from the outside slop toe of the embankment in the horizontal direction and 30 m height beneath the natural surface in the vertical direction. The thermal parameters of soil layers are given in Table 1 [33].

2.3. Boundary. According to the IPCC report, the air temperature in Qinghai-Tibetan Plateau (QTP) will be warmed up by 2.6°C in the future 50 years because of climate change [35]. Based on the adhered layer theory [12, 36], the thermal boundary conditions of the computational domain are expressed as follows:

The temperature at natural surfaces of the NSE model (AB and EF) and the SE model (AM and EF) is as follows:

$$T_n = T_a + 2.5 + 12.5\sin\left(\frac{2\pi}{8760}t_h + \frac{\pi}{2}\right) + \frac{2.6}{8760 \times 50}t_h. \quad (3)$$

The temperature at the side slopes of the NSE model (BC and DE) and the SE model (OC and DE) is as follows:

$$T_s = T_a + 4.5 + 13.5\sin\left(\frac{2\pi}{8760}t_h + \frac{\pi}{2}\right) + \frac{2.6}{8760 \times 50}t_h. \quad (4)$$

The temperature at the asphalt pavement surface of the NSE model and SE model (CD) is as follows:

$$T_p = T_a + 6.5 + 13.9\sin\left(\frac{2\pi}{8760}t_h + \frac{\pi}{2}\right) + \frac{2.6}{8760 \times 50}t_h. \quad (5)$$

The temperature at the sand particles deposition surface of the SE model (NO and NM) is as follows:

$$T_{sp} = T_a + 4.3 + 14.0\sin\left(\frac{2\pi}{8760}t_h + \frac{\pi}{2}\right) + \frac{2.6}{8760 \times 50}t_h, \quad (6)$$

where t_h is the time; T_a is the mean annual air temperature at which the embankment is located, being determined as −3.0, −3.5, and −4.0°C, respectively. The geothermal heat flux of 0.03 W/m^2 is applied to the bottom boundary (IJ) in both models. The lateral boundaries (ALKI and FGHI) are assumed to be adiabatic. With the governing equations and boundary conditions above, the problem is solved numerically using the commercial software of Fluent 14.0.

The temperature boundary of the natural ground surface without consideration of climate warming is used to calculate the initial temperature fields beneath the embankment (parts II, III, and IV). The obtained stable temperature fields on July 15 are taken as the initial temperature condition of these parts, as shown in Figure 3.

2.4. Model Validation. To validate the reliability of the computational model and parameters, numerically simulated results of soil temperature beneath the sand particles

Table 1: Thermal parameters of soil layers.

Physical variable	ρ_s (kg·m^{-3})	λ_f W/(m·°C)	C_f J/(m^3·°C)	λ_u W/(m·°C)	C_u J/(m^3·°C)	L J/m^3
Embankment fill	2060	1.98	1.913×10^6	1.92	2.22×10^6	2.04×10^7
Gravel and clayey	1800	1.82	9.06×10^5	1.60	1.17×10^6	7.73×10^7
Weathered mudstone	1800	1.82	1.846×10^6	1.47	2.09×10^6	3.77×10^7
Silty clay	1600	1.35	1.879×10^6	1.13	2.35×10^6	6.03×10^7
Sand	2650	0.258	1.610×10^6	0.258	1.61×10^6	0

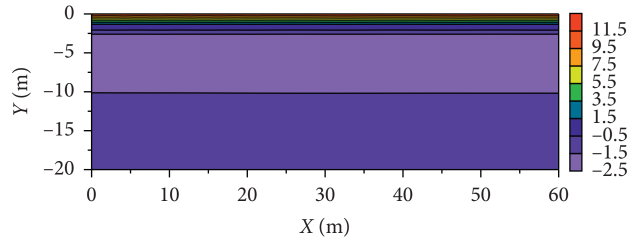

Figure 3: Initial temperature condition of parts II, III, and IV (unit: °C).

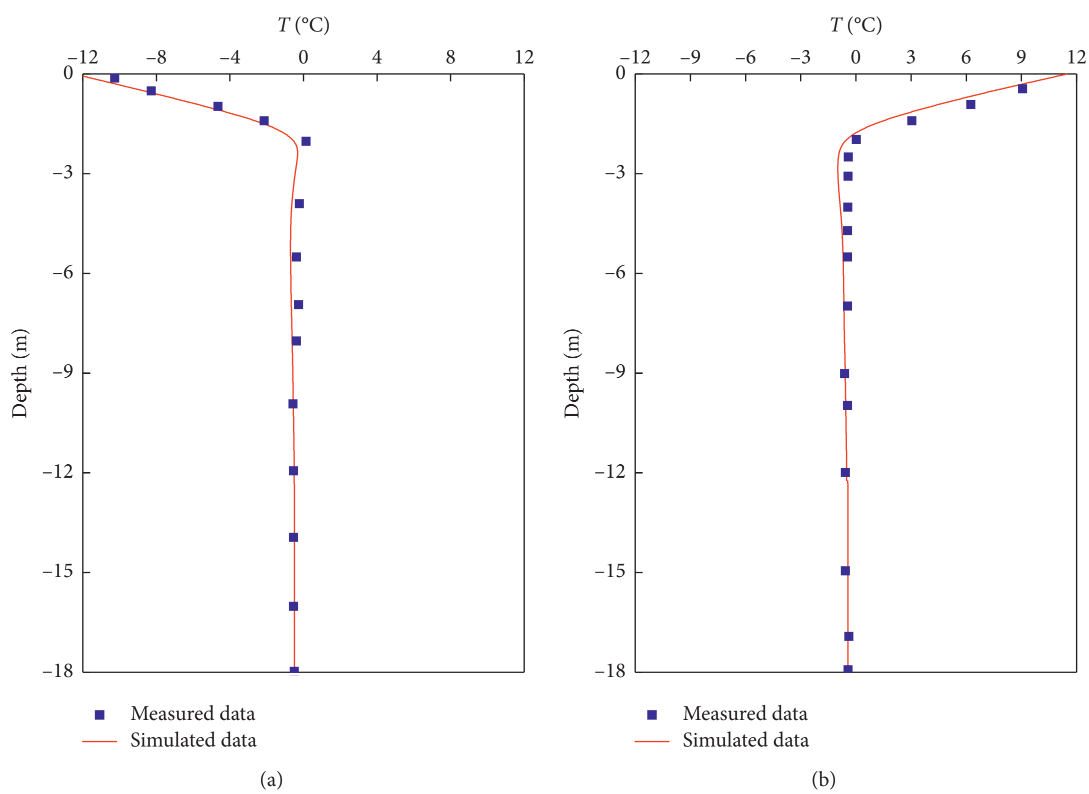

Figure 4: Field measured and numerically simulated ground temperatures vs. depth at 40 cm sandy surface on (a) April 15 and (b) July 15.

deposition surface are compared with the field measured data on April 15 and July 15 [37], as shown in Figure 4. It could be seen that the agreement between field measured data and numerically simulated results is good. However, there are some slight discrepancies between the simulated results and field measured data, especially on July 15. The simulated results of soil temperature are lower than those of the measured data within the active layer. The discrepancies may be attributed to the simplifications of boundary and soil strata in the computational model. Overall, the comparison shows that the computational model and the parameters can be used for simulating the spatial distribution and temporal evolution pattern of temperature beneath the embankment in permafrost zones.

3. Results and Analysis

3.1. Variation of Temperature beneath the Embankment without Sand Deposition. For the NSE, without consideration of the sunny-shady slope effect, Figure 5 shows soil temperature distribution beneath the NSE, in which the embankment is located with different MAGTs, in October 15 in the 5th, 20th, and 50th year after the embankment construction. The soil temperature distribution is given from the centerline of the embankment to 20 m away from the slop toe (Parts 1–3 in Figure 2(a)).

In the 5th year after the embankment construction (Figure 5(a)), the distribution pattern of the ground temperature field under the NSE in different MAGT permafrost zones is basically the same. The permafrost table beneath the centerline of the embankment (CE) is higher than that beneath the natural surface (NS). As for the permafrost zone with different MAGTs of −0.5, −1.0, and −1.5°C, the increase of the permafrost table is 0.3, 1.6, and 2.0 m, respectively. In addition, due to the increase in the thermal area of the asphalt pavement of the embankment and the structure, the internal heat absorption of the embankment will increase sharply. The trend of the geothermal line changes in different permafrost zones. In the permafrost zone with the MAGT of −0.5°C, it can be seen that the depth of the geothermal line of −0.4°C beneath the NS is the same as that beneath the CE. In contrast, in the permafrost zone with two MAGTs of −1.0 and −1.5°C, the depth of the geothermal line of −0.4°C beneath the NS is lower than that beneath CE (Figure 5(a)). It reveals that the thermal disturbance to different MAGT permafrost zones is different in the early stage of embankment construction.

With the operational time increasing, the permafrost table and the permafrost warming beneath the NS and the embankment decline, especially for the CE. The internal heat absorption of the embankment will lead to a significant downward trend of the geothermal line beneath the CE. In the 20th year after construction of the embankment, the permafrost table beneath the NS in the permafrost zone with the MAGT of −0.5, −1.0, and −1.5°C is 2.7, 2.2, and 2.0 m, respectively. Meanwhile, the permafrost table beneath the CE in the permafrost zone with the MAGT of −0.5, −1.0, and −1.5°C is 3.8, 2.6, and 1.2 m, respectively (Figure 2(b)). In the 50th year after the construction of the embankment, due to the "heat gathering" effect of the asphalt pavement and the structure of the embankment, the permafrost table beneath the CE in permafrost zones with three different MAGTs is lower than that beneath the NS. The difference in the permafrost table is 5.5, 2.1, and 1.7 m, respectively (Figure 5(c)).

Hence, considering the warming of the permafrost beneath NS and the CE in the context of climate warming and human engineering activities, the change rate of the permafrost can be used to evaluate the degradation of the permafrost. The variation of the permafrost table beneath the CE and the NS is listed in Table 2. As for the three different MAGT permafrost zones, it can be seen that the higher the MAGT is, the greater the rate of degradation of the permafrost beneath the CE and NS will be. In addition, with the operation of the embankment, the degradation of permafrost beneath the CE is higher than that of beneath the NS, which shows the thermal influence of the embankment.

3.2. Variation of Temperature beneath the Embankment with Unilateral Sand Deposition. As an obstacle structure, the construction of the embankment will change the progress of the initial flow field, including the wind flow and wind-sand flow. The redistribution of the wind-sand flow around the embankment will influence the capacity of the flow field, resulting in the sand particles deposition around the embankment. In this part, considering the influence of the ambient wind speeds, the difference of sand particles deposition around the embankment is significant, which may affect the temperature beneath the embankment. Hence, the influence of the unilateral sand particles deposition (USPD) at the toe of the embankment with the height of 4 m is investigated in this part. The width and thickness of the sand layer are 10 m and 0.5 m, respectively. The variations of the temperature beneath the embankment over the simulation period of 50 years for three initial MAGTs of −0.5, −1.0, and −1.5°C are shown in Figures 6–8.

In the 5th year after the sand particles deposition at the toe of the embankment, the USPD will induce the asymmetrical distribution of the temperature beneath the embankment. As for three different MAGTs, the lower the MAGT of the permafrost zone is, the more significant the asymmetry along the depth direction will be. From Figure 6, it can be seen that due to the USPD at the toe of the embankment, the maximum depth of zero annual amplitude of ground temperature is offset from the CE. The offsets are 5, 7.5, and 13.0 m for three different MAGTs, respectively (Figure 6). Otherwise, the permafrost table beneath the centerline of the sand particles deposition (CSD) has moved 1.0, 1.3, and 1.4 m above the NS for three different MAGTs, respectively. It reveals that the sand particles deposition can delay the degradation of the permafrost in the early stage of the sand particles deposition.

With sand particles deposition time increasing at the toe of the embankment, the influence of the USPD for the temperature beneath the embankment is different in the three different MAGT permafrost zones. In the 20th year after the sand particles deposition at the toe of the embankment, in the permafrost zone with the MAGTs of −0.5°C, the temperature field beneath the embankment is symmetrically distributed with the maximum depth of zero annual amplitude of ground temperature locating at the CE. The influence of the USPD on the temperature beneath the embankment gradually weakens. In contrast, for the permafrost zones of the MAGT of −1.0 and −1.5°C, the asymmetrical distribution of the temperature beneath the embankment is still significant. The offsets of the centerline are 3.0 and 5.0 m for two different MAGTs, respectively (Figure 7). With the sand particles deposition for 20 years, the permafrost table beneath the CSD has moved 0.4, 1.1, and 1.3 m upward above the NS for three different MAGTs of −0.5, −1.0, and −1.5°C, respectively. It reveals that with the

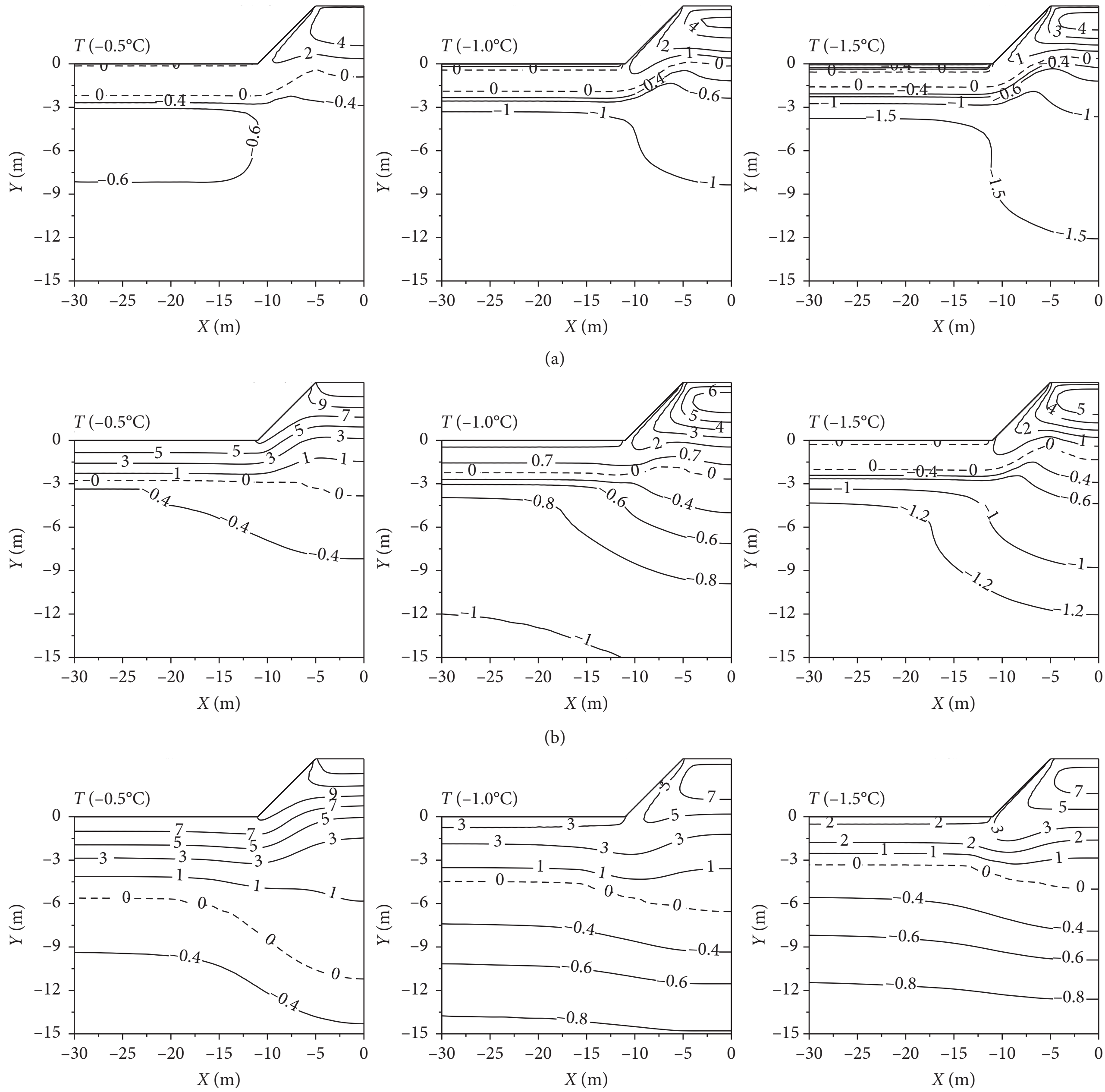

Figure 5: Distribution of the temperature field beneath the NSE under the annual ground temperature of −0.5°C, −1.0°C, and 1.5°C in October of the 5th, 20th, and 50th years (unit: °C).

Table 2: The change rate of the permafrost table beneath the NS and CE under different mean annual ground temperatures (unit: m/a).

Time	Temperature					
	−0.5°C		−1.0°C		−1.5°C	
	NS	EC	NS	EC	NS	EC
5 a∼20 a	0.04	0.20	0.03	0.16	0.02	0.01
20 a∼50 a	0.11	0.23	0.07	0.13	0.05	0.13

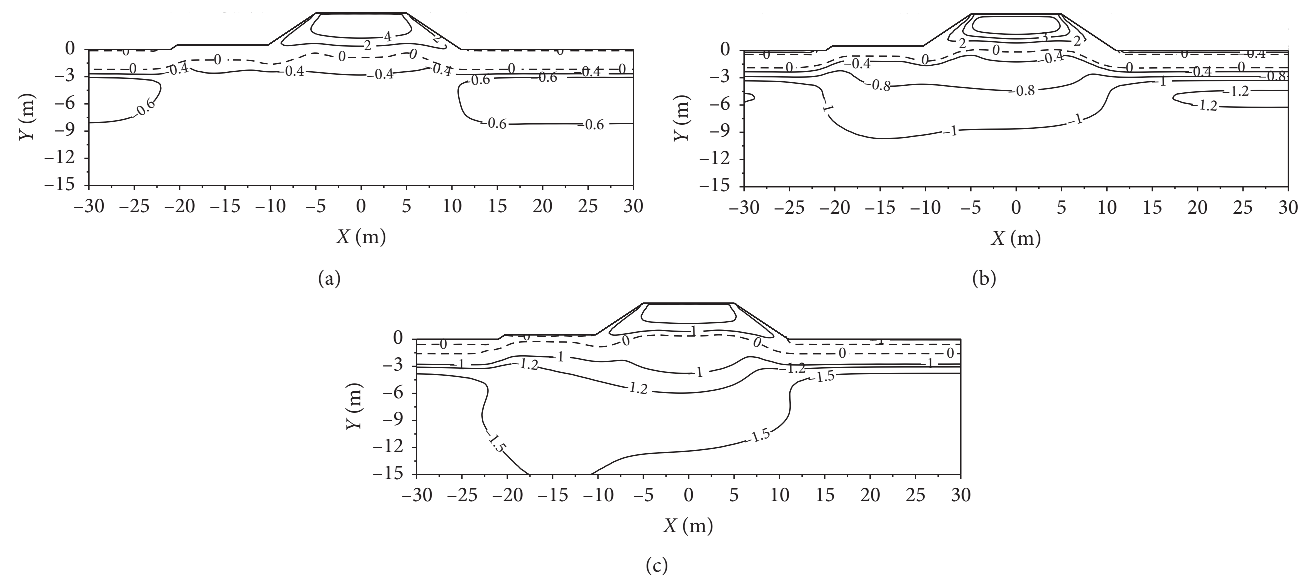

Figure 6: Distribution of the temperature field beneath the SE in October of the 5th year under the different mean annual ground temperatures: (a) −0.5°C, (b) −1.0°C, and (c) −1.5°C (unit: °C).

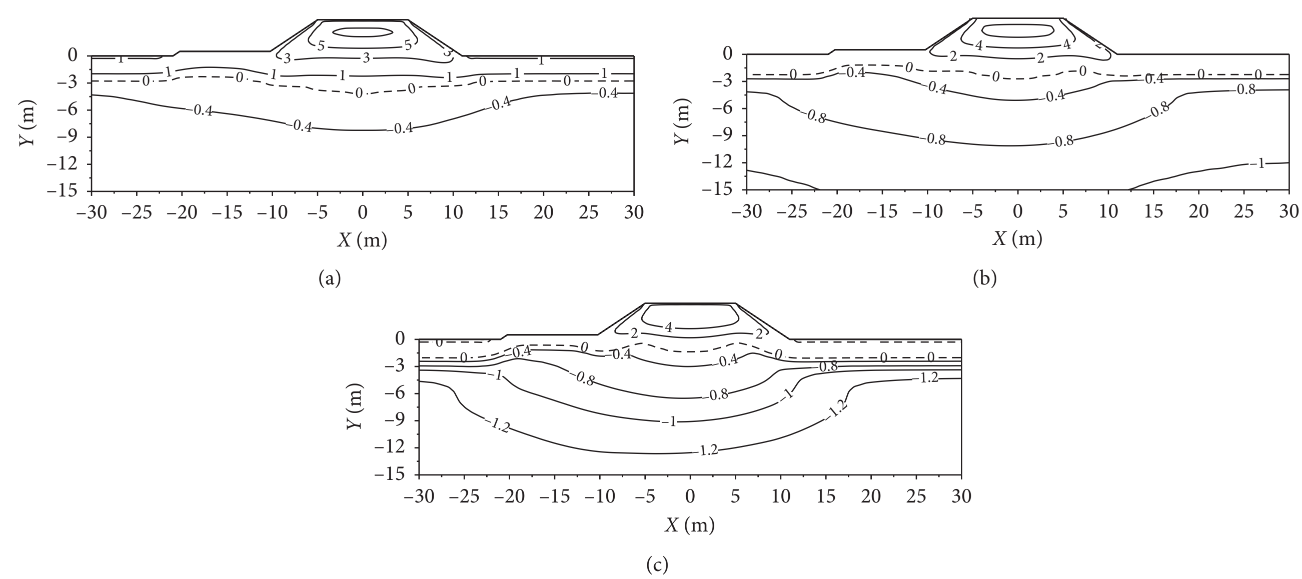

Figure 7: Distribution of the temperature field beneath the SE in October of the 20th year under the different mean annual ground temperatures: (a) −0.5°C, (b) −1.0°C, and (c) −1.5°C (unit: °C).

time of USPD increasing, the sensitivity of the permafrost to sand particles deposition gradually weakens and the protective effect of sand particles deposition on permafrost gradually disappears (Figure 8). In addition, in the 50th year after the sand particles deposition at the toe of the embankment, the influence of the USPD at the toe of the embankment could be ignored for three different MAGT permafrost zones. The distribution of the temperature beneath the embankment is symmetrical. However, with the sand particles deposition lasting for 50 years, the permafrost table beneath the CSD is lower than that beneath the NS in the permafrost zone with MAGT of −0.5°C. Meanwhile, the permafrost table beneath the centerline of the sand particles deposition is basically the same as the NS for the two MAGTs of −1.0 and −1.5°C, respectively (Figure 9). Thus, by comparing the variation of the permafrost beneath the sand particles deposition and the NS in three different MAGTs, it could be found that with the time of sand particles at the toe of the embankment increasing, the asymmetrical distribution of the temperature beneath the embankment is gradually weakening. What is more, the influence of the sand particles deposition can mitigate the degradation of the permafrost beneath it, especially for the permafrost zone with the MAGRs of −1.0 and −1.5°C. Within 50 years of the

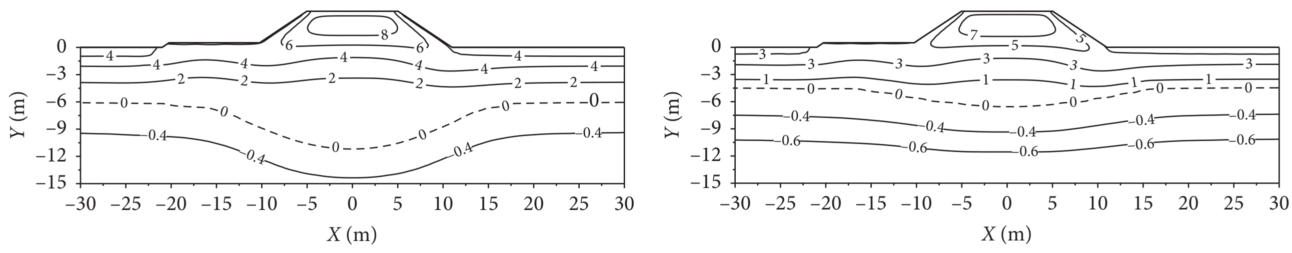

(a)

(b)

(c)

Figure 8: Distribution of the temperature field beneath the SE in October of the 50th year under the different mean annual ground temperatures: (a) −0.5°C, (b) −1.0°C, and (c) −1.5°C (unit: °C).

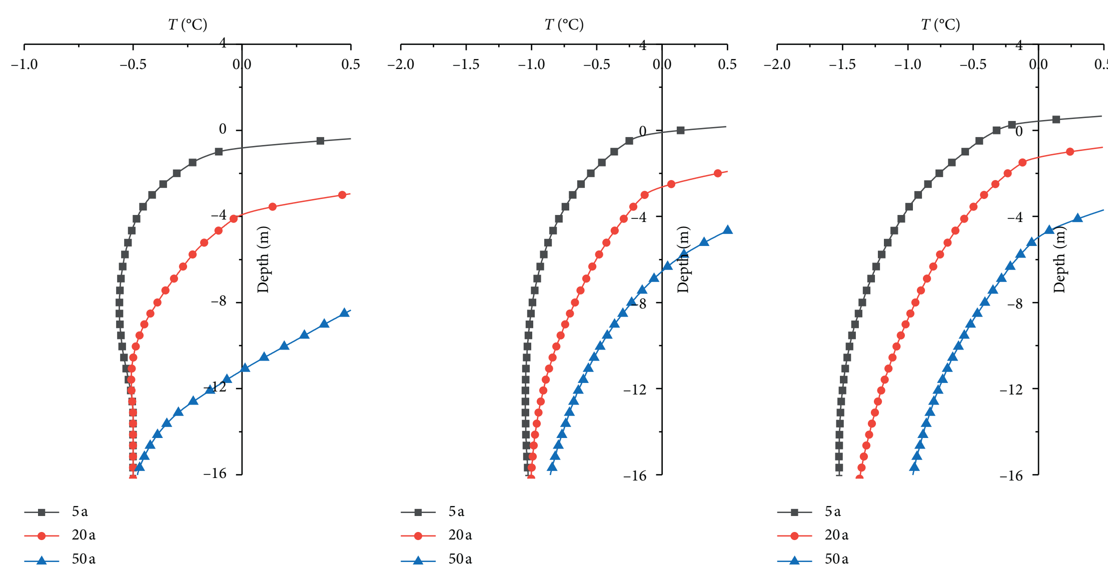

(a)

(b)

(c)

Figure 9: Variation in soil temperature beneath the CE in October of the 5th, 20th, and 50th years under different mean annual ground temperatures: (a) −0.5°C, (b) −1.0°C, and (c) −1.5°C.

sand particles deposition, the permafrost table beneath the CSD is higher than that beneath the NS (Table 3).

3.3. Effect of Unilateral Sand Particles Deposition on Temperature at Different Locations around the Embankment. The variations of the temperature beneath the CE and the toe of the embankment (TES), at which the sand particles are deposited, are shown in Figures 9 and 10. It could be seen that with the increase of time, the variations of the temperature beneath different surface boundaries in three different MAGT permafrost zones vary significantly. In Figures 9 and 10, it can be seen that 50 years after the sand particles deposition at the toe of the embankment, the maximum depth of zero annual amplitude of ground temperature beneath the CE and TES is about 16 and 14 m, respectively. Compared with the embankment without sand particles deposition at the toe, the sand particles deposition has little influence on the value of the maximum depth of zero annual amplitude of ground temperature.

Additionally, Tables 4 and 5 show the variation of the permafrost table beneath the CE and CES (the center of the embankment without sand particles deposition), TES and the toe without sand particles deposition (TE) in October of

Table 3: Variation of the permafrost table under different boundaries (unit: m).

Temperature	NS			CSD		
	5 a	20 a	50 a	5 a	20 a	50 a
−1.0°C	2.0	2.2	4.4	1.0	1.6	4.5
−1.5°C	1.6	2.0	3.2	0.6	1.0	3.4

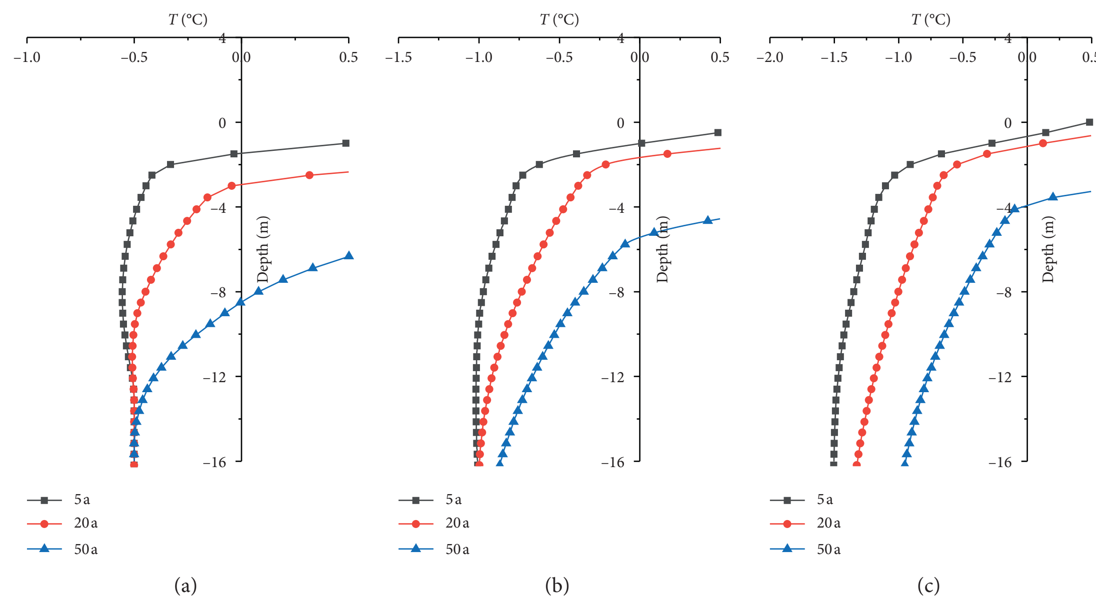

Figure 10: Variation in soil temperature beneath the TE in October of the 5th, 20th, and 50th years under different mean annual ground temperatures: (a) −0.5°C, (b) −1.0°C, and (c) −1.5°C.

Table 4: Variation of the table permafrost beneath the CE and CES under different mean annual ground temperatures (unit: m).

Temperature	CE			CES		
	5 a	20 a	50 a	5 a	20 a	50 a
−0.5°C	−0.88	−3.98	−11.18	−0.79	−4.15	−11.25
−1.0°C	−0.10	−2.60	−6.52	−0.11	−2.73	−6.60
−1.5°C	+0.45	−1.27	−4.99	+0.41	−1.27	−4.95

Table 5: Variation of the table permafrost beneath the TE and TES under different mean annual ground temperatures (unit: m).

Temperature	TE			TES		
	5 a	20 a	50 a	5 a	20 a	50 a
−0.5°C	−2.19	−3.28	−8.32	−1.52	−2.99	−8.53
−1.0°C	−1.84	−2.40	−5.57	−1.04	−1.72	−5.50
−1.5°C	−1.55	−2.01	−3.84	−0.64	−1.20	−3.99

the 5th, 20th, and 50th years with three different MAGTs. Comparing the permafrost table beneath the CE and CES with different MAGTs and times, it can be found that the USPD at the toe of the embankment has little influence on the variation of the permafrost table beneath the CE (Table 4). However, as for the toe of the embankment (Table 5), 5 years after the sand particles deposition, the permafrost table beneath the toe of TES in three different MAGTs is 1.52, 1.04, and 0.64 m, the value of which is 0.67, 0.80, and 0.91 m higher than that beneath the TE, respectively. With the sand particles deposition increasing to 20 years, the permafrost table beneath the TES is 0.29, 0.68, and 0.81 m higher than that beneath the TE, respectively. Moreover, after 50 years of the sand particles deposition, the value of the increase is −0.21, 0.00, and −0.15 m, respectively. Hence, from the result of the comparison between the permafrost table beneath the TES and TE, it could be found that as for the three different MAGTs permafrost zones, the USPD at the toe of the embankment has a significant influence on the permafrost table beneath the toe of embankment. From the 5th year of sand particles deposition to 20th year, the sand particles deposition could improve the permafrost table beneath the toe of the embankment, especially for the permafrost zone with the MAGT of −1.5°C. However, with the time of sand particles deposition increasing, the influence of the sand particles deposition may induce the temperature of permafrost to increase and accelerate the degradation of the permafrost. Hence, as for the permafrost zone with different MAGTs, the adoption of sand

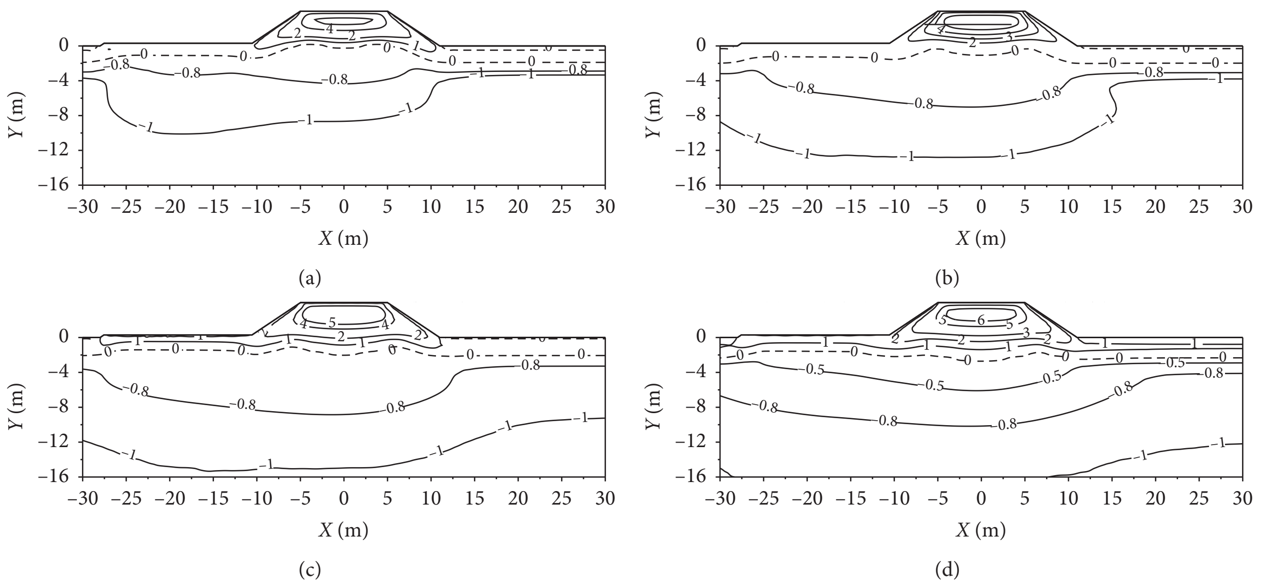

Figure 11: Distribution of the temperature field beneath the SE with the sand deposition thickness of 0.3 m in cold season of 5 a, 10 a, 15 a, and 20 a (unit: °C).

control measures is beneficial to protect the permafrost by considering the time of sand particles deposition around the embankment.

3.4. Effect of Different Forms of Sand Particles Deposition on the Temperature of Permafrost. Based on the study in the previous section, it can be concluded that within 20 years of the sand particles deposition, the sand particles deposition has a significant protective effect on the permafrost beneath it. Hence, in order to study the thermal effects of different forms of sand particles deposition (thick and thin of the sand layer) on the permafrost, under the condition of the MAGT −1.0°C, the thermal effects of sand particles deposition on the permafrost ground temperature with different thin and thick of the sand layer are given in Figures 11 and 12.

In Figure 11, with the thickness of the sand layer being 0.3 m, the isotherms beneath the toe of the embankment with sand particles deposition vary significantly, inducing the asymmetrical distribution of the geothermal field beneath the embankment. The depths of −1.0°C isotherm beneath the NS are compared, which are 5 m away from the two toes of the embankment. The depth of the −1.0°C isotherm beneath the toe without sand particles deposition has moved 6.5, 4.0, 3.3, and 1.7 m upward compared with the toe with 0.3 m thick sand layer after the sand particles deposition of 5, 10, 15, and 20 years, respectively. In addition, in Figure 12, with the thickness of sand layer being 0.7 m, it can be found that the distribution of the ground temperature field is basically the same as that of the 0.3 m condition. As for the −1.0°C isotherm, the depth of it beneath the toe without sand particles deposition has moved 4.8, 2.8, 1.4, and 1.3 m upward compared with the toe with 0.7 m thick sand layer after the sand particles deposition of 5, 10, 15, and 20 years, respectively. This means that with the time of the sand particles deposition increasing, the "wide and thin" type of sand particles deposition has a greater influence on the depth of the lower ground temperature field than that of the "narrow and thick" type of sand particles deposition.

To investigate permafrost warming beneath different thin and thick sand layers in the context of climate warming, the variations of the permafrost table beneath the CE, TE, TES, and CSD are shown in Tables 6 and 7 within 20 years of the sand particles deposition. It could be found that the two different sand particles deposition forms have less effect on the variation of permafrost table beneath CE and TE. However, there is a significant effect on the permafrost table beneath the CSD and TES. In Table 6, with the thickness of the sand layer being 0.3 m, the degradation rate of the permafrost beneath the CSD, TES, and TE is 0.03, 0.05, and 0.04 $m \cdot a^{-1}$, respectively. Additionally, in Table 7, with the thickness of the sand layer being 0.7 m, the degradation rate of the permafrost beneath the CSD, TES, and TE is 0.03, 0.04, and 0.04 $m \cdot a^{-1}$, respectively. This means that, within 20 years of sand particles deposition, no matter which form of the sand layer is, the deposition of the sand particles could weaken the degradation rate of the permafrost. However, as for the TES, the more the thickness of the sand layer, the smaller the degradation rate of permafrost.

As for the embankment in the permafrost zone, the main disease is thaw collapse, which is closely related to the variation of the permafrost table. After 5 years of the two forms of sand particles deposition ("wide and thin" and "narrow and thick"), the difference of the permafrost table, the location of which is beneath the two toes of the embankment, between the two toes of the embankment is 0.49 and 0.88 m, respectively (Tables 6 and 7). However, the

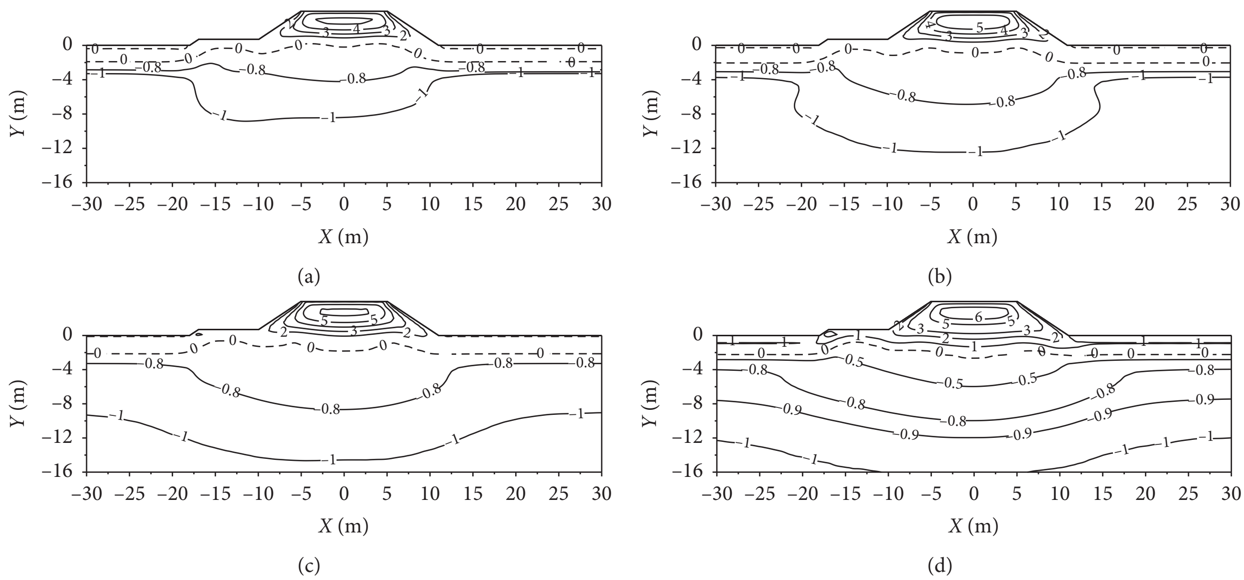

Figure 12: Distribution of the temperature field beneath the SE with the sand deposition thickness of 0.7 m in cold season of 5 a, 10 a, 15 a, and 20 a (unit: °C).

Table 6: Variation of the permafrost table beneath the SE with the sand thickness of 0.3 m in October 15th of 5th, 10th, 15th, and 20th years (unit: m).

Temperature	CE	TE	TES	CSD
5 a	−0.23	−1.89	−1.40	−1.08
10 a	−1.05	−1.99	−1.53	−1.27
15 a	−2.00	−2.13	−1.93	−1.46
20 a	−2.69	−2.45	−2.23	−1.55

Table 7: Variation of the permafrost table beneath the SE with the sand thickness of 0.7 m in October 15th of 5th, 10th, 15th, and 20th years (unit: m).

Temperature	CE	TE	TES	CSD
5 a	−0.19	−1.88	−1.00	−0.31
10 a	−0.88	−2.01	−1.12	−0.46
15 a	−1.83	−2.16	−1.29	−0.61
20 a	−2.61	−2.48	−1.64	−0.78

degradation rate of the permafrost table with the sand layer thickness of 0.3 m is greater than that with the sand layer thickness of 0.7 m. With the sand particles deposition time increasing and the context of the climate warming, the difference of permafrost table between two toes of the embankment will induce uneven settlement significantly, especially for the embankment with the "narrow and thick" sand particles deposition at the toe of the embankment. Hence, in order to reduce its impact on the long-term thermal condition beneath the embankment, it was necessary to clean the thicker deposition sand particles at the toe of the embankment.

4. Conclusion

In permafrost areas, the engineering activities will have a considerable influence on the project and the underlying permafrost. As an engineering structure, the constructions of the road project will produce certain disturbance to the original relatively stable wind-sand flow along the route, leading to the redistribution of the flow field around the embankment and the emergence of sand particles deposition. The deposition and coverage of sand particles around the embankment can change the thermal conditions of the permafrost embankment. In this article, a mathematical model of heat transfer for freeze-thaw soil is constructed to investigate the long-term thermal effects of sand particles deposition at the toe of the embankment in the permafrost with different MAGTs. Based on the above numerical analyses and comparisons, the following conclusions can be drawn:

(1) The thermal disturbance of the construction of the embankment in the permafrost zone with different MAGTs varies significantly. With time increasing, the degradation rate of the permafrost largely differs in different parts around the embankment. After 50 years of the construction of the embankment, the permafrost table beneath the CE in the permafrost zones with three different MAGTs is 11.5, 6.5, and 5.0 m. In contrast, the value of which beneath the NS is 6.0, 6.5, and 5.0 m. Therefore, the construction of the highway embankment will increase the heat absorption within the embankment and accelerates permafrost degradation.

(2) The influence of the USPD will induce the distribution of the temperature beneath the embankment asymmetry significantly, especially for the embankment in the permafrost with different MAGTs. The lower the MAGT of the permafrost, the more significant the asymmetry of the temperature distribution. With the time of sand particles deposition increasing, the asymmetry of ground temperature field in three different MAGTs weakens gradually. Moreover, The influence of the sand particles deposition can mitigate the degradation of the permafrost beneath it, especially for the permafrost zone with the MAGRs of −1.0 and −1.5°C. Within 50 years of the sand particles deposition, the permafrost table beneath the CSD is higher than that beneath the NS.

(3) From the variation of the temperature distribution at different parts of the embankment, the influence of the USPD on the permafrost table beneath the CE could be ignored. In contrast, for the TES, with the time of sand particles deposition increasing, the degradation rate of permafrost table at the TES is greater than that at the TE, especially for permafrost with the MAGT −0.5°C. After 50 years of the sand particles deposition at the toe of the embankment, the permafrost table has moved 0.21 m upward beneath the TE compared with that beneath the TES.

(4) With different sand thickness and width conditions, the effect of "narrow and thick" form sand particles deposition on the temperature field beneath embankment was greater than that of "wide and thin" form sand deposition. Hence, in order to reduce its impact on the long-term thermal condition beneath the embankment, it was necessary to clean the thicker deposition sand particles at the toe of the embankment.

Data Availability

The data used to support the findings of this study are available from the corresponding author upon request.

Conflicts of Interest

The authors declare that they have no conflicts of interest related to this manuscript.

Acknowledgments

This research was supported by the Natural Science Foundation of China (41630636 and 41772325) and the Research Project of the State Key Laboratory of Frozen Soils Engineering (SKLFSE-ZY-17).

References

[1] M. Wei, F. J. Niu, and Y. H. Mu, "Basic research on the major permafrost projects in the Qinghai-Tibet plateau," *Advance Earth Science*, vol. 11, no. 27, pp. 1185–1191, 2012.

[2] G. D. Cheng and T. H. Wu, "Responses of permafrost to climate change and their environmental significance, Qinghai-Tibet Plateau," *Journal of Geophysical Research*, vol. 112, 2007.

[3] J. W. Harden, C. D. Koven, C. L. Ping et al., "Field information links permafrost carbon to physical vulnerabilities of thawing," *Geophysical Research Letters*, vol. 39, 2012.

[4] M. Sivakumar, "Interactions between climate and desertification," *Agricultural and Forest Meteorology*, vol. 142, no. 2, pp. 143–155, 2007.

[5] Q. B. Wu, W. B. Yu, and H. J. Jin, "No protection of permafrost due to desertification on the Qinghai–Tibet Plateau," *Scientific Reports*, vol. 7, no. 1, 2017.

[6] S. Xie, J. Qu, and Y. Pang, "Dynamic wind differences in the formation of sand hazards at high- and low-altitude railway sections," *Journal of Wind Engineering and Industrial Aerodynamics*, vol. 169, pp. 39–46, 2017.

[7] Q. H. Yu, W. Gu, J. Qian, J. M. Zhang, and X. C. Qian, "Problem analysis of high-grade highway construction in permafrost regions," *Highways*, vol. 11, pp. 74–80, 2010.

[8] Q. H. Yu, K. Fan, J. Qian, L. Guo, and Y. H. You, "Key issues of highway construction in permafrost regions in China," *Science China Press: Technological Science*, vol. 44, no. 4, pp. 425–432, 2014.

[9] W. Ma, Y. H. Mu, S. B. Xie, Y. C. Mao, and D. Chen, "Thermal-mechanical influences and environmental effects of expressway construction on the Qinghai-Tibet permafrost engineering corridor," *Advances in Earth Science*, vol. 32, no. 5, pp. 459–464, 2017.

[10] Z. Zhou, W. Ma, S. Zhang, H. Du, Y. Mu, and G. Li, "Multiaxial creep of frozen loess," *Mechanics of Materials*, vol. 95, pp. 172–191, 2016.

[11] Z. Zhou, W. Ma, S. Zhang, Y. Mu, and G. Li, "Effect of freeze-thaw cycles in mechanical behaviors of frozen loess," *Cold Regions Science and Technology*, vol. 146, pp. 9–18, 2018.

[12] W. Pei, L. Jin, M. Zhang, S. Li, and Y. Lai, "Study of the time-dependent thermal behavior of the multilayer asphalt concrete pavement in permafrost regions," *Construction and Building Materials*, vol. 193, pp. 162–172, 2018.

[13] G. Cheng, "A roadbed cooling approach for the construction of Qinghai-Tibet Railway," *Cold Regions Science and Technology*, vol. 42, no. 2, pp. 169–176, 2005.

[14] G. Doré, F. Niu, and H. Brooks, "Adaptation methods for transportation infrastructure built on degrading permafrost," *Permafrost and Periglacial Processes*, vol. 27, no. 4, pp. 352–364, 2016.

[15] D. J. Goering and P. Kumar, "Winter-time convection in open-graded embankments," *Cold Regions Science and Technology*, vol. 24, no. 1, pp. 57–74, 1996.

[16] S. A. Harris and D. E. Pedersen, "Thermal regimes beneath coarse blocky materials," *Permafrost and Periglacial Processes*, vol. 9, no. 2, pp. 107–120, 1998.

[17] Y. Lai, W. Pei, and W. Yu, "Calculation theories and analysis methods of thermodynamic stability of embankment engineering in cold regions," *Chinese Science Bulletin*, vol. 59, no. 3, pp. 261–272, 2014.

[18] W. Ma, G. D. Cheng, and Q. B. Wu, "Construction on permafrost foundations: lessons learned from the Qinghai–Tibet railroad," *Cold Regions Science and Technology*, vol. 59, no. 1, pp. 3–11, 2009.

[19] Q. B. Wu, Y. Z. Liu, J. M. Zhang, and C. J. Tong, "A review of recent frozen soil engineering in permafrost regions along Qinghai-Tibet highway, China," *Permafrost and Periglacial Processes*, vol. 13, no. 3, pp. 199–205, 2002.

[20] H. J. Jin, Q. H. Yu, and S. L. Wang, "Changes in permafrost environments along the Qinghai–Tibet engineering corridor induced by anthropogenic activities and climate warming," *Cold Regions Science and Technology*, vol. 53, no. 3, pp. 317–333, 2008.

[21] M. X. Yang, S. L. Wang, T. D. Yao, X. H. Gou, A. X. Lu, and X. J. Guo, "Desertification and its relationship with permafrost degradation in Qinghai-Xizang (Tibet) plateau," *Cold Regions Science and Technology*, vol. 39, no. 01, pp. 47–53, 2004.

[22] S. B. Xie, J. J. Qu, B. Liu, and X. T. Xu, "Advance in research on the sand hazards and its control along the Qinghai-Tibet railway," *Journal of Desert Research*, vol. 34, no. 01, pp. 42–48, 2014.

[23] S. L. Wang, L. Zhao, and S. X. Li, "Interaction between permafrost and desertification on the Qinghai-Tibet plateau," *Journal of Desert Research*, vol. 1, pp. 33–39, 2002.

[24] J. Malenfant-Lepage, G. Doré, D. Fortier, and P. Murchison, "Thermal performance of the permafrost protection techniques at Beaver Creek experimental road site, Yukon, Canada," in *Proceedings of the 10th International Conference on Permafrost*, Salekhard, Russia, June-2012.

[25] S. B. Xie, J. J. Qu, Y. M. Lai, X. T. Xu, and Y. J. Pang, "Key evidence of the role of desertification in protecting the underlying permafrost in the Qinghai–Tibet Plateau," *Scientific Reports*, vol. 5, 2015.

[26] K. C. Zhang, J. J. Qu, K. T. Liao, Q. H. Niu, and Q. J. Han, "Damage by wind-blown sand and its control along Qinghai-Tibet Railway in China," *Aeolian Research*, vol. 1, no. 3, pp. 143–146, 2010.

[27] L. Chen, W. B. Yu, C. S. Yang, X. Yi, and W. B. Liu, "Conductivity of aeolian sand on the Tibet Plateau based on microstructure," *Journal of Glaciology and Geocryology*, vol. 36, no. 5, pp. 1220–1226, 2014.

[28] W. Yu, W. Liu, L. Chen, X. Yi, F. Han, and D. Hu, "Evaluation of cooling effects of crushed rock under sand-filling and climate warming scenarios on the Tibet Plateau," *Applied Thermal Engineering*, vol. 92, pp. 130–136, 2016.

[29] L. Chen, W. B. Yu, F. L. Han, W. B. Liu, and X. Yi, "Impacts of aeolian sand on cooling effect of crushed-rock embankment of Qinghai-Tibet Railway," *Journal of Glaciology and Geocryology*, vol. 37, no. 1, pp. 147–155, 2015.

[30] L. Chen, W. Yu, X. Yi, D. Hu, and W. Liu, "Numerical simulation of heat transfer of the crushed-rock interlayer embankment of Qinghai-Tibet Railway affected by aeolian sand clogging and climate change," *Cold Regions Science and Technology*, vol. 155, pp. 1–10, 2018.

[31] W. D. An, Z. W. Wu, and W. Ma, *Interaction Among Temperature, Moisture and Stress fields in Frozen Soil*, Lanzhou University Press, Lanzhou, China, 1990.

[32] Y. Lai, Q. Wang, F. Niu, and K. Zhang, "Three-dimensional nonlinear analysis for temperature characteristic of ventilated embankment in permafrost regions," *Cold Regions Science and Technology*, vol. 38, no. 2-3, pp. 165–184, 2004.

[33] J. M. Zhang, J. Z. Zhang, and Y. Z. Liu, "Study on the reasonable embankment height of Qinghai-Tibet railway in permafrost regions," *China Railway Science*, vol. 27, no. 5, pp. 28–34, 2006.

[34] M. Zhang, X. Zhang, S. Li, D. Wu, W. Pei, and Y. Lai, "Evaluating the cooling performance of crushed-rock interlayer embankments with unperforated and perforated ventilation ducts in permafrost regions," *Energy*, vol. 93, pp. 874–881, 2015.

[35] D. H. Qin, *The Comprehensive Evaluating Report on the Environment Evolvement in West China*, Science Press, Beijing, China, 2002.

[36] L. N. Zhu, "Study of the adherent layer on different types of ground in permafrost regions on the Qinghai-Xizang Plateau," *Journal of Glaciology and Geocryology*, vol. 10, no. 1, pp. 8–14, 1988.

[37] L. Y. Wang, Q. B. Wu, and G. L. Jiang, "Numerical simulation of the effect of aeolian sand accumulation on permafrost," *Journal of Glaciology and Geocryology*, vol. 40, no. 4, pp. 738–747, 2018.

Hindawi
Advances in Materials Science and Engineering
Volume 2021, Article ID 3290831, 12 pages
https://doi.org/10.1155/2021/3290831

Research Article

Analysis of Influence Factors of Pore Water Pressure Change in Frozen Soil

Kun Zhang[1] **and Lianhai Zhang**[2]

[1]*Gansu Transportation Research Institute Group Co.,Ltd., Lanzhou 730000, China*
[2]*State Key Laboratory of Frozen Soil Engineering, Chinese Academy of Sciences, Lanzhou 730000, China*

Correspondence should be addressed to Lianhai Zhang; zhanglh@lzb.ac.cn

Received 22 April 2021; Accepted 9 June 2021; Published 19 June 2021

Academic Editor: Hao Zheng

In this article, changes of pore water pressures (PWP) in silty clay subjected to freezing and thawing were measured under an open-system condition. A total of five soil samples were tested, with water contents of 10.70%, 18.28%, 23.98%, 31.00%, and 37.65%, respectively. Each experienced a first-step freezing stage, a thawing stage, and a second-step freezing stage. The results showed that changes in PWP depended on the water content, soil type, salinity, ice content, air, pressure, temperature, and others. The PWP minimum with initial water content has a "w-shaped double-valley" characteristic, which described two PWP minima existing in two optimum water contents as initial water content increased. An influence-factor analysis of PWP was proposed and gave a reasonable interpretation on the "w-shaped double-valley" characteristic of PWP. In addition, the tensiometer method to measure PWP in frozen soil was further discussed with regard to its advantages and disadvantages.

1. Introduction

Construction and operation in cold regions may encounter many environmental and engineering problems, such as permafrost degradation, frost heaving, icing, thaw settlement, thermokarst, and infrastructure failure. With the development of our country's economy and implementation of Western development strategy, increasing projects are built in cold regions, including railway, highway, power transmission line, and petroleum pipeline. Therefore, increasing research work begins to focus on the deformation process of frozen soil involving construction of these projects. Frost heave and thaw settlement are two uppermost hazards generally causing significant damages during engineering construction and operation, and accurate prediction of the deformation process is an important issue that needs to be urgently solved.

Water migration and ice segregation as two essential issues of the frost heave and thaw settlement problem have always been of interest to researchers [1, 2]. When soils are subjected to freezing, soil water freezes in situ with volume increasing of 9%, or freezes in ice segregation way with volume increasing of 109%. During ice segregation, water migration occurs. Numerous investigations have focused on the mechanisms of water migration and ice segregation, and many theories and models have been proposed and studied, including primary heaving theory [3–5], second heaving theory [6–8], and segregation potential theory [9, 10]. Moreover, PWP measurement in freezing soil has been an essential and key research work for further exploring the mechanisms of water migration and ice segregation [11].

However, most of investigations on PWP were empirical speculations or model calculations without direct experiment data support. The measurement method of PWP has been a challenge; only little work was focused on this research, including hygrometer method [12], axis-translation technique [13–15], Pf-meter method [16], and tensiometer method [17–21]. Recently, increasing attention began to focus on the tensiometer method. Zhang et al. [22] gave a further improvement to this method based on previous investigations on the measurement of PWP during soil freezing. Using the novel PWP gauge, the PWP of sandy soil was measured in laboratory [22]. Based on the testing results, a change mode of PWP was suggested, and then the frozen fringe process is analyzed, including the consolidation of unfrozen zone, ice segregation, water migration, the applicability of the generalized Clausius–Clapeyron equation (GCCE), and phase transition [23]. In addition, soil type is a key influence factor for the frost heave and thaw settlement deformation, and water migration and ice segregation are more likely to occur in the frost-susceptible soils. Therefore, compared to sandy soil, silty clay as a frost-susceptible soil is more helpful to reveal the behaviors of water migration and ice segregation.

Herein, we performed a series of PWP measurements on silty clay subjected to freezing and thawing, and then a detailed analysis on influence factors of the PWP is presented, which will favor a further understanding of phase change processing of soil water during soil freezing and thawing.

2. Materials and Methods

2.1. Sample Preparation. Silty clay as a typical type of soil along the Qinghai-Tibet railway was tested, and the grain size distribution and Atterberg limit of this soil are shown in Table 1. The soil samples were prepared and tested at the State Key Laboratory of Frozen Soil Engineering in Lanzhou, China. The soil was thoroughly mixed with certain water content and then hammered by a plane hammer into a cylindrical Perspex cell. Therefore, each soil sample had a diameter of 101 mm. A total of five soil samples were prepared and measured during the experiments. The water content of samples CN1, CN2, CN3, CN4, and CN5, respectively, were 10.70%, 18.28%, 23.98%, 31.00%, and 37.65%. Other specific soil sample parameters, such as the initial water content and height, are shown in Table 2.

2.2. Testing Program and Condition. The cylindrical Perspex cell packed with the tested soil sample was put into the box of the freeze-thaw cycling test machine. All of the temperature probes and porous ceramic cups of PWP gauges were inserted into the soil sample through the small holes in the wall of the cell. Figure 1 is the detailed probe arrangements on the cylindrical Perspex cell. The detailed sketch of freeze-thaw cycling test machine and the design of PWP probe refer to the article written by Zhang et al.[22]. Each sample experienced a process that included three stages: a first-step freezing stage (abbreviated as fre1), a thawing stage (thw), and a second-step freezing stage (fre2). Every step-freezing stage (fre1 or fre2) was also divided into three steps (abbreviated as I, II, and III) according to different top plate temperatures. In every step of the freezing stage (fre1 or fre2), the testing time is approximately 48 hours. In the thawing stage, soil sample thawed under room temperature with a time of approximately 24 hours. All temperature conditions of the samples tested are listed in Table 2. During testing, PWP, temperature, and water volume absorbed into soil sample were measured and recorded. After every test ended, the water content distribution of each sample was also obtained using gravimetric method.

3. Results

3.1. Water Migration Volume. Figure 2 is the variations of water volume absorbed into silty clay samples CN1, CN2, CN3, and CN4. As shown in Figure 2, the water volumes absorbed into samples have the characteristics as follows:

(1) During soil freezing, the water volumes absorbed into samples CN1, CN2, CN3, and CN4 linearly increased over time. This implied that increasing water was absorbed into samples during freezing.

(2) Samples with different water contents differed greatly in water volumes absorbed into the samples, and the water volumes absorbed into samples decreased as the initial water content increased. For example, as shown in Figure 2, after the same testing time (312 hours), the water volumes absorbed into samples CN1, CN2, CN3, and CN4 are approximately 471.87, 309.60, 379.52, and 238.98 cm^3, respectively. The average migration rates of water absorbed into samples are approximately 0.027, 0.018, 0.022, and 0.014 cm^3/M.

(3) As the initial water content increased, sample in the early stage of freezing experienced a state transition from water absorption to drainage. For example, in the early stage of freezing (fre1.I), water was absorbed into sample CN1 but squeezed out of samples CN2, CN3, and CN4. This state difference exactly explained why sample with lower initial water content had a larger water volume absorbed into it.

(4) In the thawing stage, except little water absorbed into the samples in the early stage of thawing, no water was absorbed into samples.

Figure 3 is the water content distributions of samples CN1, CN2, CN3, and CN5 at the end of each testing. As shown in Figure 3, we found the following:

(1) Water content of the bottom part of sample (the unfrozen zone) was smaller than that of the upper part of sample (the frozen zone), which implied that there exists water migration from the unfrozen zone to frozen zone.

(2) Water contents at the bottom part of all samples (the unfrozen zone) were smaller than the initial contents, which implied that there existed certain consolidation in the unfrozen zone.

3.2. Displacement of Soil Sample. Figure 4 is the variations of displacement of samples CN1, CN2, and CN4 during freezing and thawing. As shown in Figure 4, samples CN1, CN2, and CN4 differed greatly in displacement during freezing and thawing and presented some characteristics as follows:

(1) During soil freezing, there existed heaving of sample; the heaving displacement decreased as the water content increased; for each sample, the heaving displacement in the second freezing stage (fre2) was

Table 1: Grain size distribution and Atterberg limits of soils tested.

Soil type	Liquid limit	Plastic limit	Particle size (mm)						
			<0.075	0.075–0.1	0.1–0.25	0.25–0.5	0.5–1.0	1.0–2.0	>2.0
Silty clay (%)	25.5	11.9	19.83	51.90	17.0	7.43	2.90	0.47	0.0

Table 2: Temperature conditions of soil samples tested.

Samples	Initial water content (%)	Height (mm)	Temperature (°C)				
			Fre1		thw	Fre2	
			Top plate (I/II/III)	Bottom plate (I/II/III)		Top plate (I/II/III)	Bottom plate (I/II/III)
CN1	10.70	112.3	−5/−8/−11	1.5		−3/−5/−11	1.5
CN2	18.28	107.0	−11/−14/−17	1.0		−5/−9/−12	3.0
CN3	23.98	121.0	−3/−7/−14	3.0	*R*	−3/−7/−14	3.0
CN4	31.00	121.0	−3/−7/−11	3.0		−3/−7/−11	3.0
CN5	37.65	125.0	−5/−10/−15	1.0		−5/−10/−15	1.0

∗R denotes room temperature.

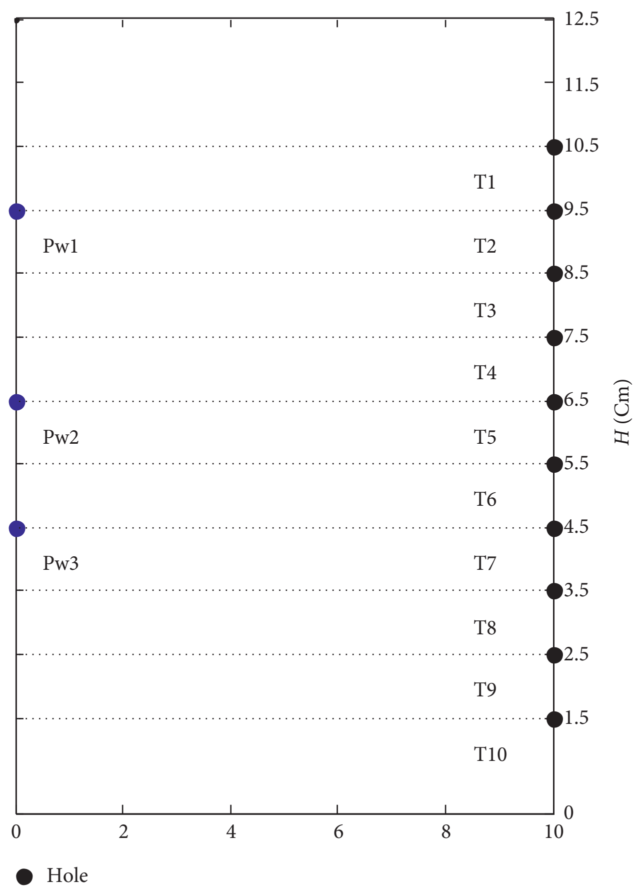

Figure 1: Probe arrangement on the cylindrical perspex cell. Pw1, Pw2, and Pw3 for pore water pressure probes; T1–T10 for temperature probes.

larger than that in the first freezing stage (fre1). For example, in the first freezing stage (fre1), the heaving of samples CN1, CN2, and CN4 is approximately 4.38, 1.80, and 1.79 mm, respectively; in the second freezing stage (fre2), the heaving of samples CN1, CN2, and CN4 is approximately 5.79, 2.20, and 3.92 mm, respectively. During soil freezing, the measured displacement, actually, is a sum of deformations of the frozen zone and the unfrozen zone. The deformation of the frozen zone was induced by a frost heave process, which generally induced the surface lifting. However, the deformation of the unfrozen zone might be induced by two different processes according to water content. When water content was large, the unfrozen zone mainly experienced a consolidation process, which generally induced the surface collapse. Conversely, when water content was low, the unfrozen zone mainly experienced an expanding process because some water was absorbed into this zone from the reservoir bottle, which generally induced the surface lifting. Therefore, the surface lifting decreased as the water content increased. However, the heaving displacements in the second freezing stage (fre2) were larger than those in the first freezing stage (fre1), which may be attributed to the fact that the displacements induced by consolidation in the second freezing stage (fre2) are smaller, compared to those in the first freezing stage (fre1).

(2) During soil thawing, there existed settlement in all of samples; the settlement increased as the water content increased. For example, the thawing of samples CN1, CN2, and CN4 is approximately 0.55, 1.65, and 9.49 mm, respectively. This thawing settlement is mainly ascribed to the consolidation and frost heaving during freezing which are both increase with water contents increase. Therefore, the settlement increased as the water content increased during thawing.

3.3. PWPs during Soil Freezing and Thawing. Figures 5–9 are the variations of PWP of samples CN1, CN2, CN3, CN4, and CN5 during the freezing and thawing. As shown in

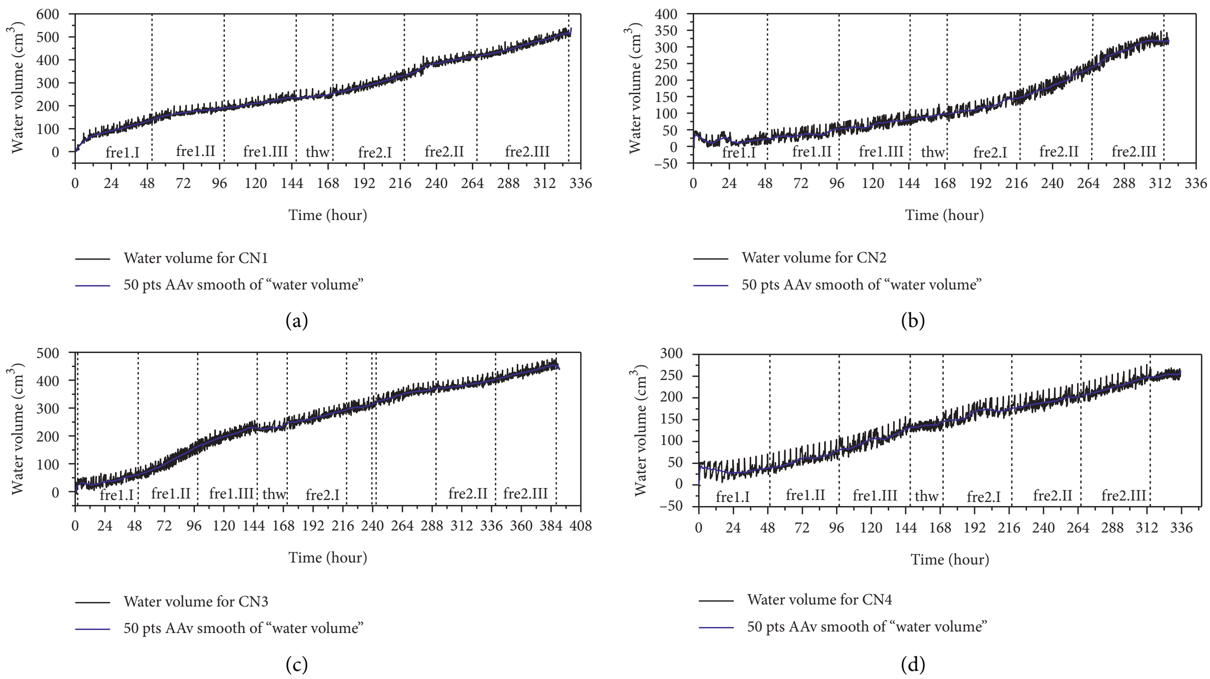

Figure 2: Variations of water volume absorbed into silty clay samples CN1, CN2, CN3, and CN4.

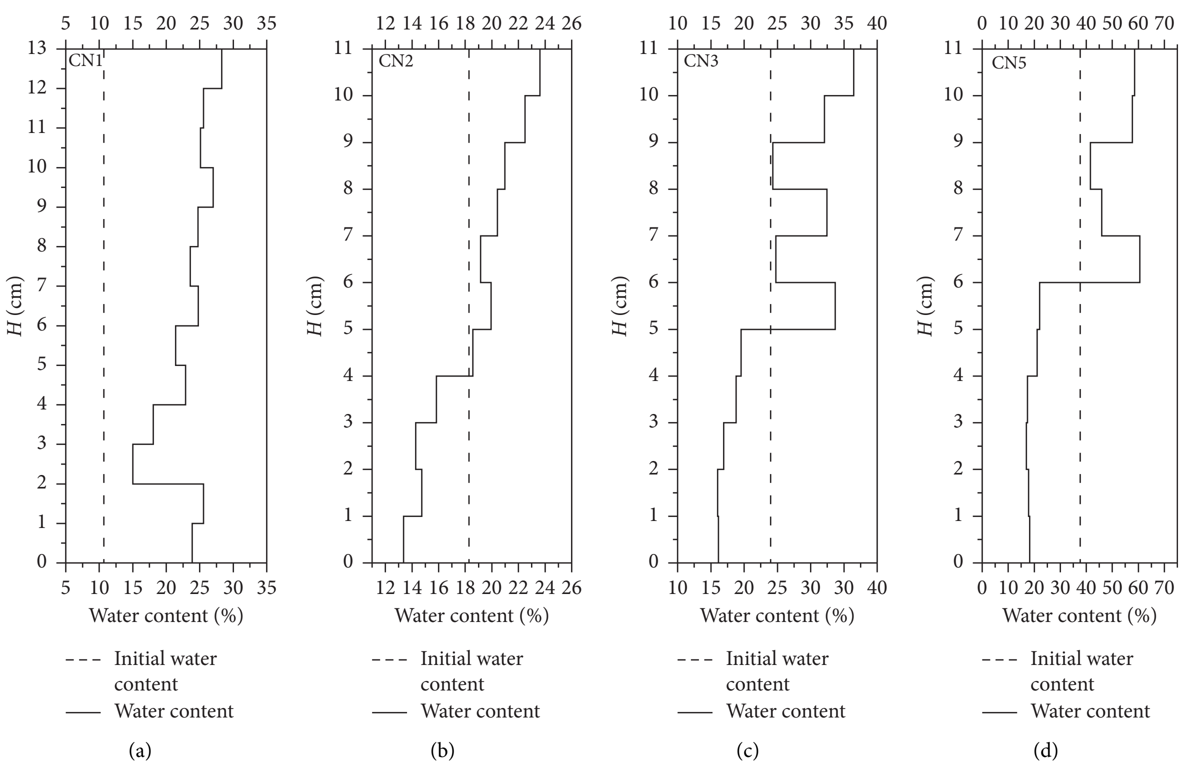

Figure 3: Water content distributions of samples CN1, CN2, CN3, and CN5 at the end of tests.

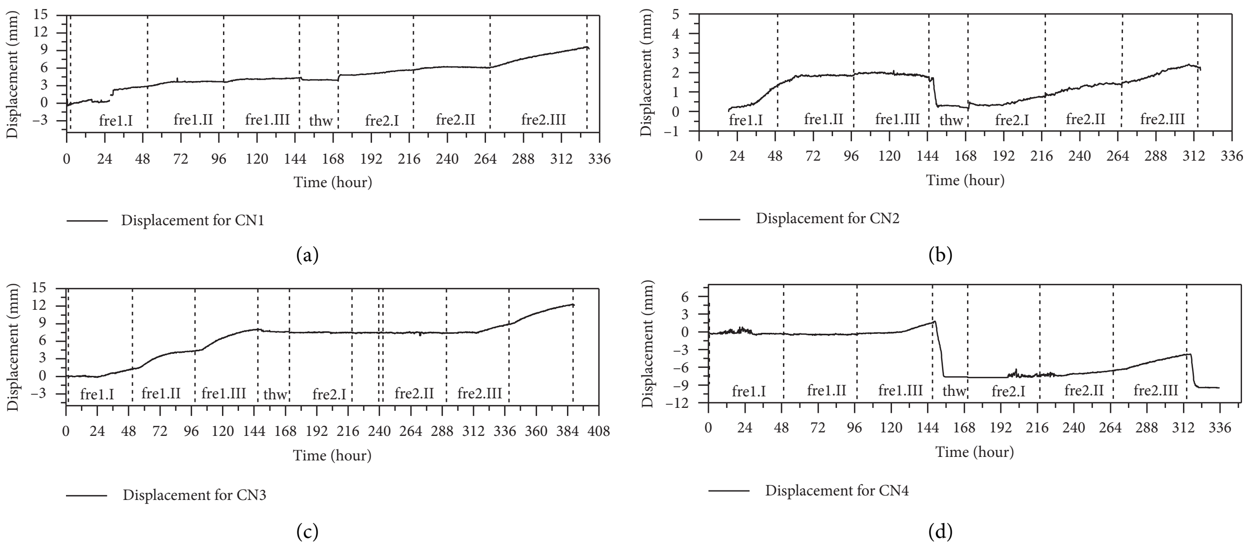

Figure 4: Variations in displacement of samples CN1, CN2, CN3, and CN4 during freezing and thawing.

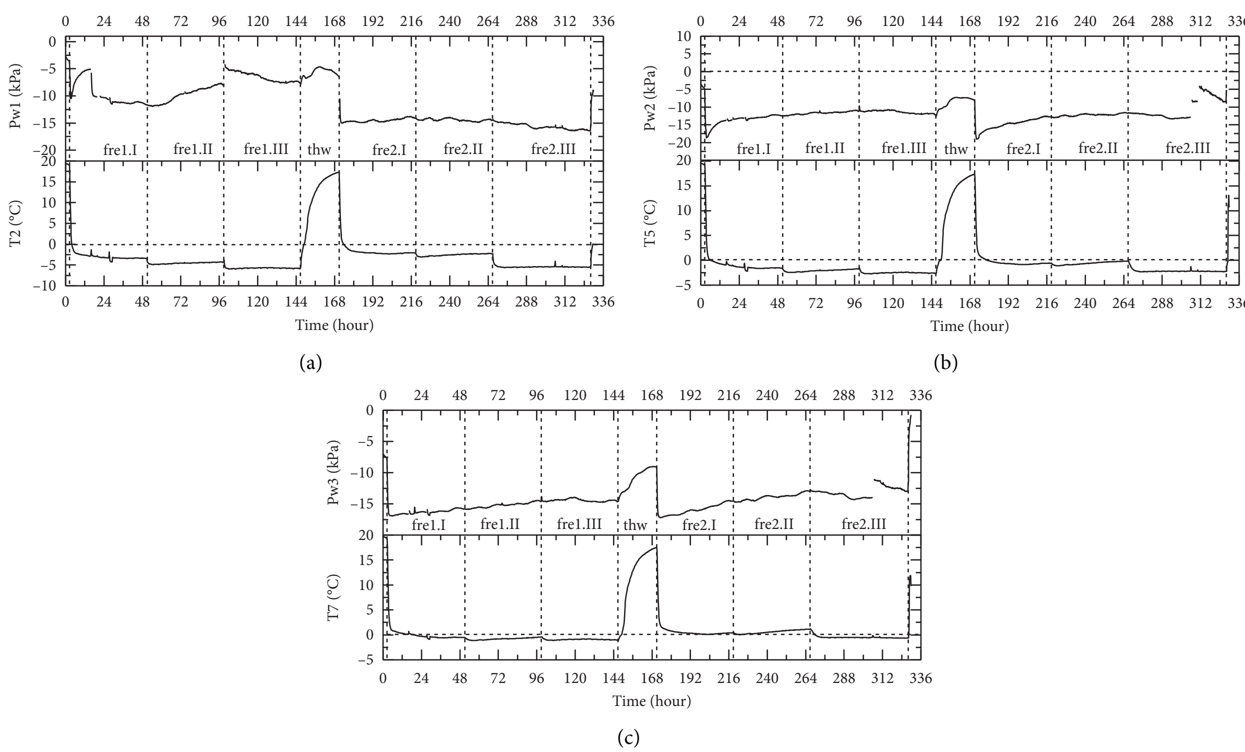

Figure 5: (a) Variation in the pore water pressure Pw1 and temperature T2 during the freezing and thawing of sample CN1. (b) Variation in the pore water pressure Pw2 and temperature T5 during the freezing and thawing of sample CN1. (c) Variation in the pore water pressure Pw3 and temperature T7 during the freezing and thawing of sample CN1.

Figure 5–9, we found some characteristics in the PWP as follows:

(1) During soil freezing, PWP decreased as temperature decreased. However, PWP in sample with low water content was less sensitive to the temperature change.

(2) During soil thawing, PWP increased as temperature increased.

(3) During soil freezing, the drop of PWP increased as the soil depth increased.

(4) The minimum of PWP with initial water content had a "w-shaped double-valley" characteristic, which described that two minima of PWP exist in two different water contents as initial content increased. Table 3 is the minima of PWP during every freezing

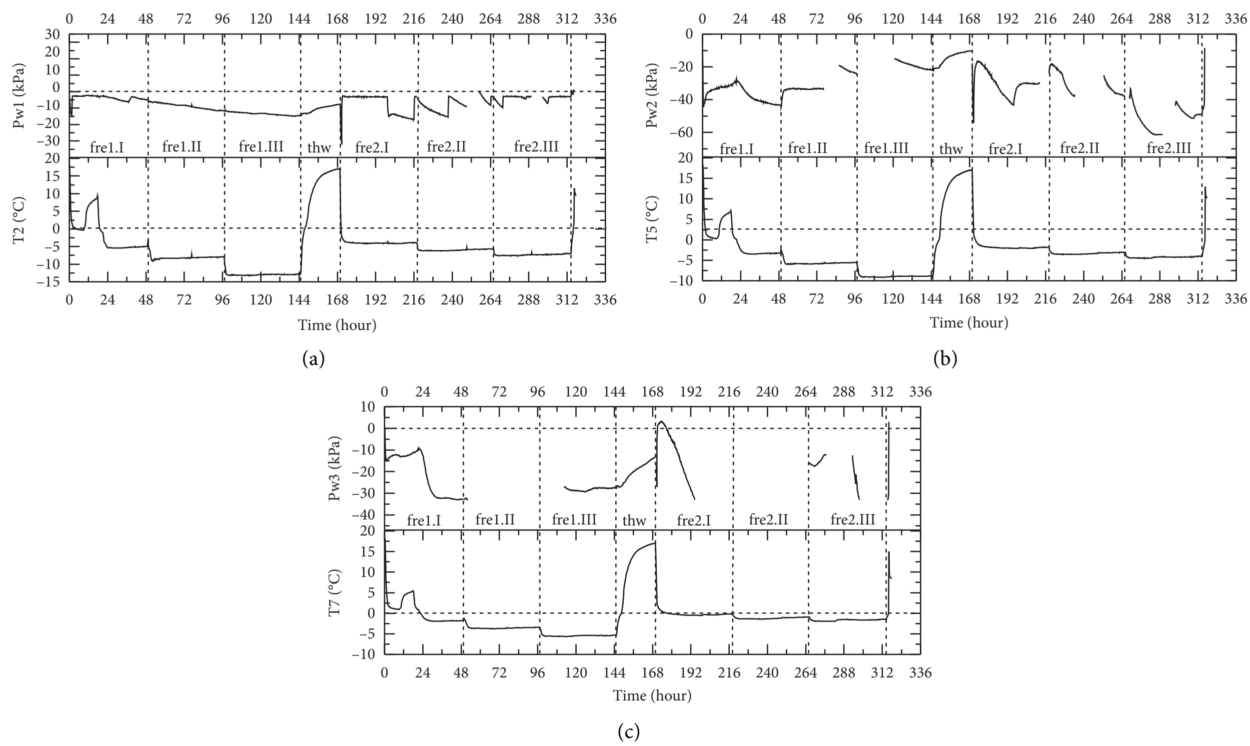

Figure 6: (a) Variation in the pore water pressure Pw1 and temperature T2 during the freezing and thawing of sample CN2. (b) Variation in the pore water pressure Pw2 and temperature T5 during the freezing and thawing of sample CN2. (c) Variation in the pore water pressure Pw3 and temperature T7 during the freezing and thawing of sample CN2.

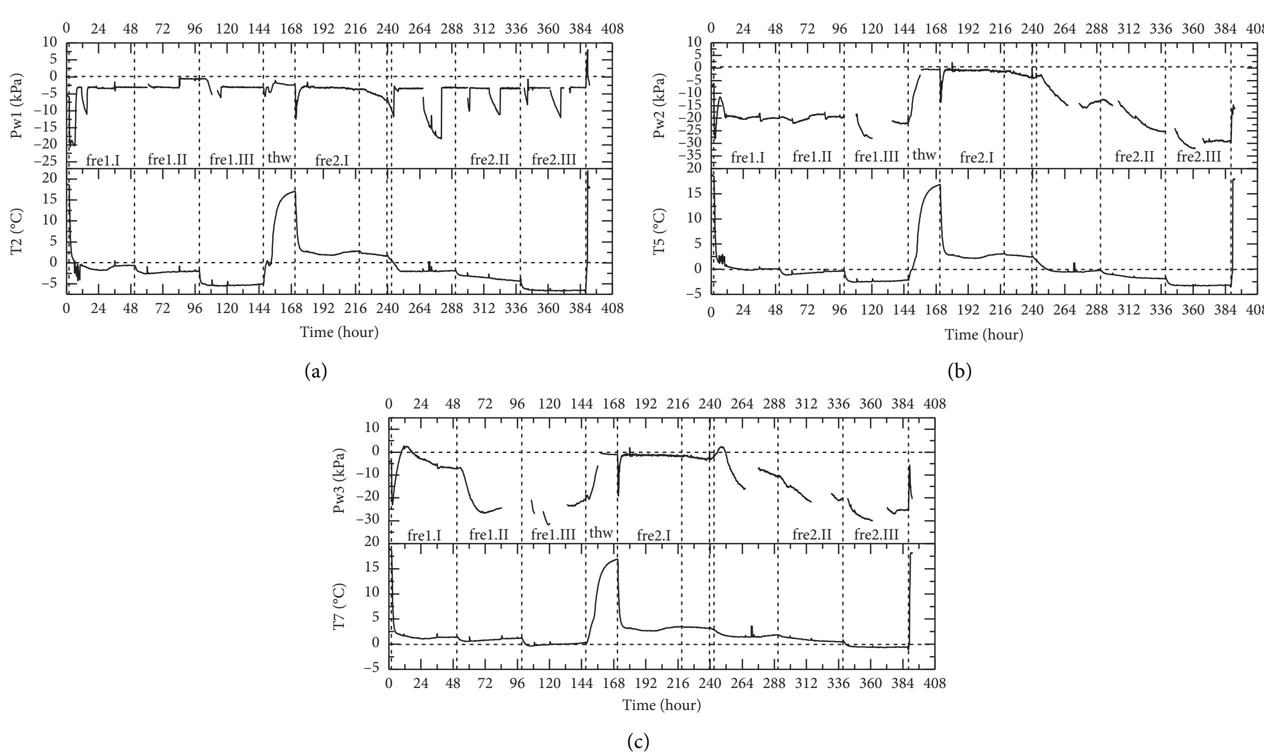

Figure 7: (a) Variation in the pore water pressure Pw1 and temperature T2 during the freezing and thawing of sample CN3. (b) Variation in the pore water pressure Pw2 and temperature T5 during the freezing and thawing of sample CN3. (c) Variation in the pore water pressure Pw3 and temperature T7 during the freezing and thawing of sample CN3.

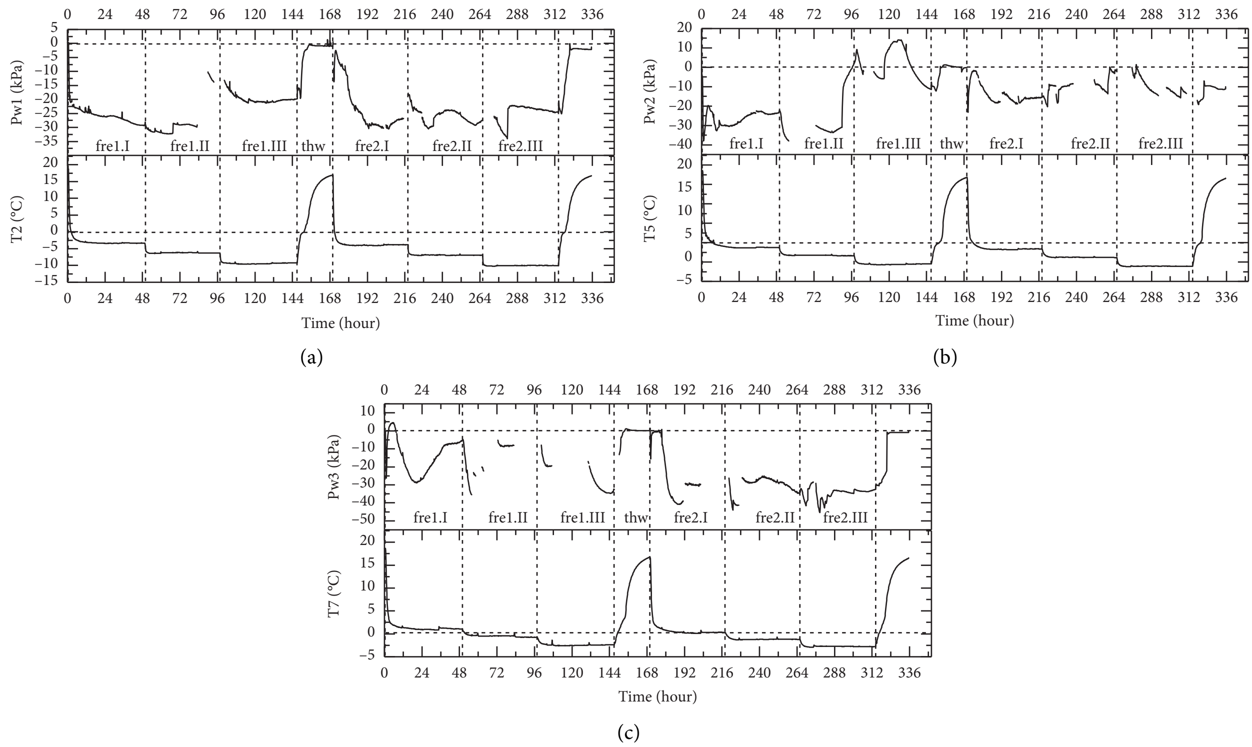

Figure 8: (a) Variation in the pore water pressure Pw1 and temperature T2 during the freezing and thawing of sample CN4. (b) Variation in the pore water pressure Pw2 and temperature T5 during the freezing and thawing of sample CN4. (c) Variation in the pore water pressure Pw3 and temperature T7 during the freezing and thawing of sample CN4.

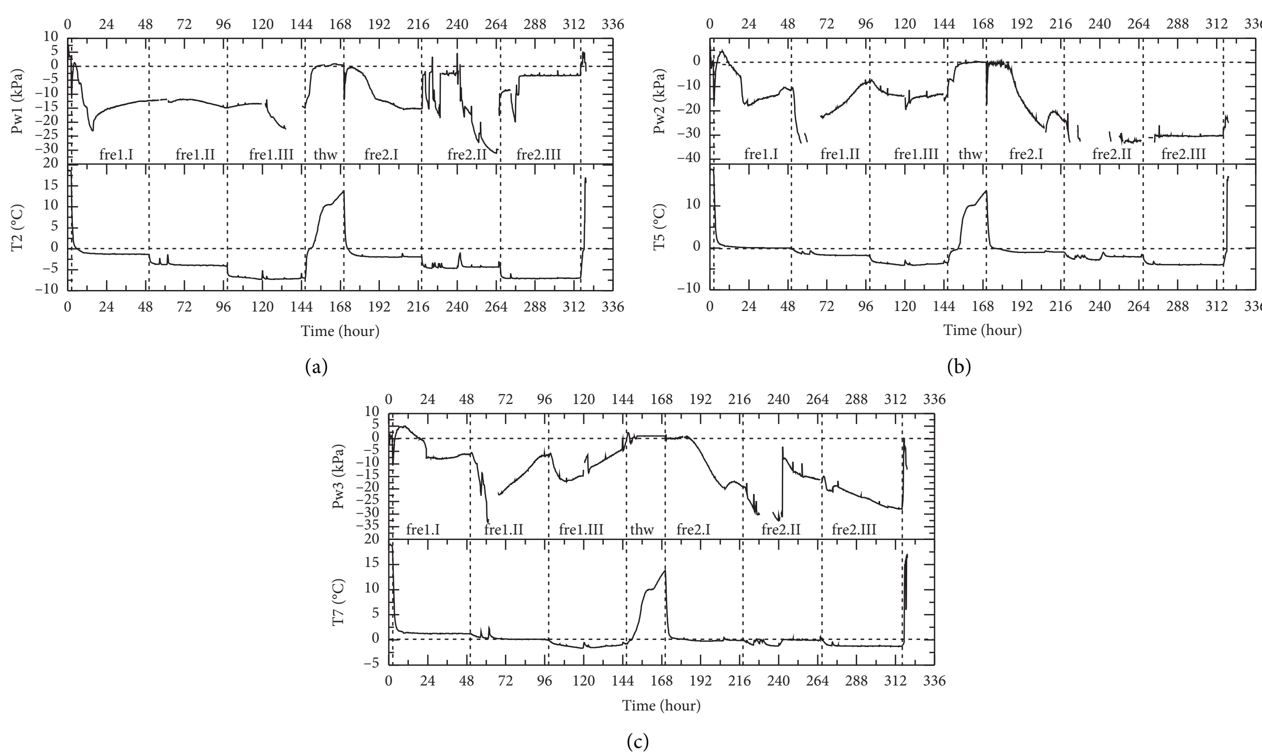

Figure 9: (a) Variation in the pore water pressure Pw1 and temperature T2 during the freezing and thawing of sample CN5. (b) Variation in the pore water pressure Pw2 and temperature T5 during the freezing and thawing of sample CN5. (c) Variation in the pore water pressure Pw1 and temperature T7 during the freezing and thawing of sample CN5.

Table 3: The minima of pore water pressure during every freezing stage (fre1 and fre2) during tests.

Samples	Initial water content %	Fre1			Fre2		
		Minimum of PWP (kPa)					
		Pw1	Pw2	Pw3	Pw1	Pw2	Pw3
CN1	10.70	−12.49	−18.689	−16.93	−16.42	−19.07	−17.21
CN2	18.28	−14.89	−44.75	−32.99	−17.22	−61.46	−33.02
CN3	23.98	−20.5	−27.99	−31.72	−18.22	−32.00	−29.33
CN4	31.00	−32.31	−37.93	−35.43	−34.02	−19.29	−45.46
CN5	37.65	−23.12	−33.18	−33.14	−31.16	−33.23	−32.52

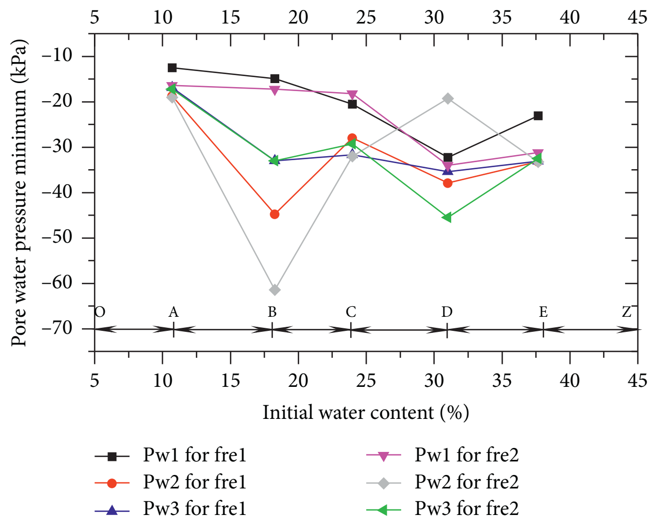

Figure 10: Minima of PWP with different initial water contents. *OA*, *AB*, *BC*, *CD*, *DE*, and *DZ* correspond to different water content ranges, respectively.

stage (fre1 and fre2) of testing. Figure 10 is the minima of PWP with different initial water contents, which was plotted based on Table 3. For example, as shown in Figure 10, the initial water content of *A*, *B*, *C*, *D*, and *E* corresponded to the water contents of being 10.70%, 18.28%, 23.98%, 31.00%, and 37.65%, respectively. The PWP change tendencies differed greatly in the different water content ranges, decreasing in the range of *AB* and *CD*, increasing in the range of *BC* and *DE*. This implied that soil water has different free energy states in different ranges of water content. For the sake of analysis, water content is divided into six ranges, including *OA*, *AB*, *BC*, *CD*, *DE*, and *DZ*.

4. Influence Factor of PWP

Change of PWP upon freezing is affected by temperature, pressure, soil type, air, ice content, water content, water supply condition, salinity, supercooling, and others [23, 24]. Based on PWP measurements of silty clay, we gave a detailed discussion on some key influencing factors of PWP.

4.1. Influence of Temperature on PWP. If the PWP variations over time were related to temperature changes over time in the same depth of the soil sample, a temperature dependence of the PWP could be established. As shown in Figure 11, the PWP with temperature generally experienced a change mode including three phases. In the first phase, the PWP generally had a slight increasing as the temperature decreased. In the second phase, the PWP had a fast drop as the temperature decreased. In the third phase, the PWP slightly increased as the temperature decreased. Using the PWP Pw2 of sample CN5 in the fre1.I step as an example (Figure 11), at first, the PWP had a slight increase of approximately 5 kPa and then decreased to a minimum −20.0 kPa as the temperature decreased; finally, it increased slightly as the temperature decreased.

When the soils experienced a further second or third freezing step, the soils still experienced a similar change mode as described in the first freezing step above when the temperature had a sudden drop. The PWP decreased to an extreme point and then increased slightly with decreasing temperature. Using the PWP Pw2 of sample CN5 in the fre1.II step as an example (Figure 11), at first, the PWP remained approximately −11.5 kPa, then decreased to a minimum −32.8 kPa as the temperature decreased, and finally increased slightly as the temperature decreased.

However, we must realize that the PWP change with temperature is actually a combined effect of all influence factors, not depending only on temperature. Based on phase equilibrium, the PWP change is generally described by GCCE as follows:

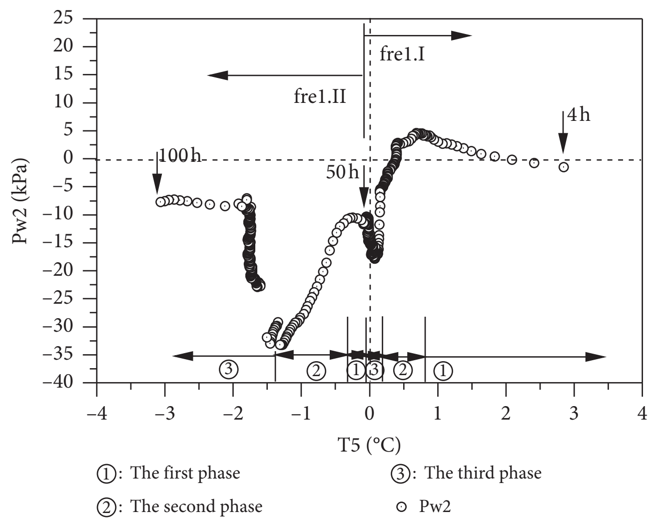

FIGURE 11: The PWP Pw2 of sample CN5 with temperature during two freezing steps (fre1.I and fre1.II).

$$\frac{u_w}{\rho_w} - \frac{u_i}{\rho_i} = L\frac{T - T_f}{T_f}; \quad T_s \le T \le T_f, \tag{1}$$

where L is the latent heat of fusion; T_f is the freezing point of water; T is the temperature of the ice and water; ρ_w and ρ_i are the densities of water and ice, respectively; u_w and u_i is the gauge pressure of water and ice; and T_s is the ice segregation temperature. The PWP change depends only on the temperature, irrespective of ice pressure. However, soil freezing may be more inclined to be a nonequilibrium (irreversible) thermodynamic process [23], and thus the PWP change should have some time effect, which needs further research.

4.2. Influence of Ice Pressure on PWP. In a range of high water content (DE), irrespective of ice-water phase transition, ice skeleton begins to form and bear the vast majority of load as the water content increases, ice pressure increases based on effective stress principle, and thus the PWP increases. In addition, as the water content increases, the strength of ice skeleton increases, and part of unfrozen water is confined in the occluded space by ice. When there occurs the ice-water phase change in soils, a larger ice pressure occurs because of a larger density of water than ice. The PWP increases as ice pressure increases, based on the GCCE (1).

Based on the effects above, we suggested that the PWP induced by ice pressure increases as water content increases in the range of high water content (DE), especially when the unfrozen water is confined in the occluded space by ice. For example, as shown in Figure 9(b), during the freezing stage (fre1.III) of sample CN4, although the temperature $T5$ is subzero, the maximum of PWP Pw2 reached 15 kPa. The high PWP may be ascribed to the fact that the PWP probe is confined in an occluded space by ice. Therefore, the PWP has a fast increase because of ice-water phase change.

4.3. Influence of Soil Type on PWP. Compared to the results of sandy soil that are referred to by Zhang et al. [22], silty clay differs greatly from sandy soil in the change characteristic of PWP as follows:

(1) The PWP drop of silty clay is larger than that of sandy soil during the freezing, which may be ascribed to the differences in particle size composition, pore size, surface energy, permeability, specific surface area, etc.

(2) In the early stage of freezing, silty clay has a slight increase in PWP, while sandy soil remains constant. The difference implied that soil water of silty clay is more susceptible to pressure, compared to sandy soil. The differences in the PWP may result from a combination of two factors. First, the PWP in the sandy soil sample has a faster dissipation rate than the PWP in the silty clay sample because of the higher permeability of sandy soil. Second, silty clay may have a more significant increase in frost heaving stress than the sandy soil during freezing.

(3) In silty clay, the PWP at a position can be affected by the PWP at its adjacent position, while in sandy soil, the PWP at a position is not affected by the PWP at its adjacent position. This may be ascribed to two factors: one is that the permeability of sandy soil is larger than silty clay; the other is that more unfrozen water content of silty clay than sandy soil favors building a connected path for water migration.

(4) The PWP of sandy soil has a different change mode between the first- (fre1) and the second- (fre2) step freezing (i.e., before and after the freeze-thaw process). This implies that the physical and mechanical properties of sandy soil experience a significant change after freeze-thaw cycles. However，the PWP of silty clay has not a different change mode between the first- (fre1) and the second- (fre2) step freezing. This may be because the number of freeze-thaw cycles is so small (one freeze-thaw cycle) to induce a significant change in the physical and mechanical properties of silty clay.

In addition, ice material also can bear load and absorb water as soil does, and thus ice can be regarded as a special type of soil, in some sense.

4.4. Influence of Air on PWP. In unsaturated soil, the total soil suction is composed of matric and osmotic suctions, which can be presented as follows:

$$\psi = (u_a - u_w) + \pi, \tag{2}$$

where ψ is the total soil suction; $(u_a - u_w)$ is the matric suction; u_a is the pore air pressure; and π is the osmotic suction. The osmotic suction depends on the solute concentration. The item on the osmotic suction is ignored because no or little salinity exists in the soil tested, and thus the total soil suction is presented as follows:

$$\psi = (u_a - u_w). \tag{3}$$

In addition, in terms of the partial vapor pressure of soil water, the total soil suction can be presented as follows (Richards, 1965):

$$\psi = \frac{RT}{v_{w0}\omega_v} \ln\left(\frac{\overline{u}_v}{\overline{u}_{v0}}\right), \tag{4}$$

where R is the molar gas constant; T is the absolute temperature; v_{w0} is the specific volume of water; ω_v is the molecular mass of water vapor; $\overline{u}_v$ is the partial pressure of pore water vapor; and $\overline{u}_{v0}$ is the saturation pressure of water vapor over a flat surface of pure water at the same temperature. Based on equations (3) and (4), we can present the PWP as follows:

$$u_w = u_a - \frac{RT}{v_{w0}\omega_v} \ln\left(\frac{\overline{u}_v}{\overline{u}_{v0}}\right). \tag{5}$$

When the water content of sample is low, the axis-translation technique is generally used to measure the soil-water characteristic curve; a high air pressure is generally applied. The air pressure has a further sharp increase as water content further decreases, and thus, the first item on the right side of equation (5) is larger, while the total soil suction has a logarithmic relationship with the partial pressure of pore water vapor, based on equation (4). Therefore, when the water content is low, the second item of equation (5) is also relatively larger. Based on a combined effect of the first and second items, in a range of low water content (OA), the PWP change is little as water content change.

4.5. Influence of Water Content on PWP. The PWP change depends on water content. During soil freezing, PWPs in samples with low water content were less sensitive to the temperature change, while PWPs in samples with larger water content were sensitive to the temperature change. When water content of soil sample is low, the phase transitions between ice, water, and vapor are nearly stopped. Therefore, the change of PWP with temperature is less sensitive. However, when water content of soil sample is larger, the phase transition between ice and water is very significant. Therefore, the PWP change with temperature is sensitive.

5. Analysis on Influence Factor of PWP

The "w-shaped double-valley" characteristic in PWP is actually a response of soil water energy state to varied factors, which is a combined effect from temperature, pressure, salinity, matric potential, ice content, air, etc. We can describe this relationship as followss:

$$\Delta P_{wf} = \Delta P_{wT} + \Delta P_{wp} + \Delta P_{wc} + \Delta P_{ws} + \Delta P_{wi} + \Delta P_{wG}, \tag{6}$$

where ΔP_{wf} is the total PWP change; ΔP_{wT} is the PWP change induced by the temperature gradient when the soil sample is saturated; ΔP_{wP} is the PWP change that is influenced by the internal stress changes of the soil (which involves the changes of external load and frost heaving stress or ice pressure); ΔP_{wc} is the PWP change induced by the solute concentration; ΔP_{ws} is the PWP change induced by the soil matrix, i.e., matric potential; ΔP_{wi} is the PWP change induced by the ice matrix; and ΔP_{wG} is the PWP change induced by air.

Figure 12 is the influence-factor decoupling analysis on PWP with initial water content, which is described based on equation (6). Refer to Section 4.1, ΔP_{wT} mainly depends on the temperature in the temperature ranges of phase transition and thus nearly remains constant with water content increasing. ΔP_{wc} remains zero or a slight depression because no or little salinity exists in the soil tested. In the range of low water content, as initial water content increases, the matric suction decreases and thus ΔP_{ws} increases. As initial water content increases, ice content and its specific surface area increase, and ice skeleton forms. The matric suction of ice skeleton increases and thus ΔP_{wi} decreases. When initial water content is low, almost all of pores remain connect and are full of air, and thus PWP is mainly affected by air pressure. Therefore, ΔP_{wG} decreases as air content decreases. When initial water content is high, almost all of pores remain connect and are full of ice, and the unfrozen water is generally confined in a closed space. Therefore, ΔP_{wP} increases because of volume increasing induced by ice-water phase change as water content increases in the ranges of high water content.

Based on influence-factor analysis method, we can present a reasonable interpretation to the "w-shaped double-valley" characteristic of PWP. The PWP valley V1 is ascribed to a combined effect of ΔP_{wG} and ΔP_{ws}. Both of them intersect at point A. When the initial water content is smaller than point A, the drop rate of ΔP_{wG} is larger than the increase rate of ΔP_{ws}; when the initial water content is larger than point A, the drop rate of ΔP_{wG} is smaller than the increase rate of ΔP_{ws}. Therefore, there exists a minimum of PWP in point A. Similarly, the PWP valley V2 is ascribed to the combined effects of ΔP_{wi} and ΔP_{wP}. Both of them intersect at point B. When the initial water content is smaller than point B, the drop rate of ΔP_{wi} is larger than the increase rate of ΔP_{wP}; when

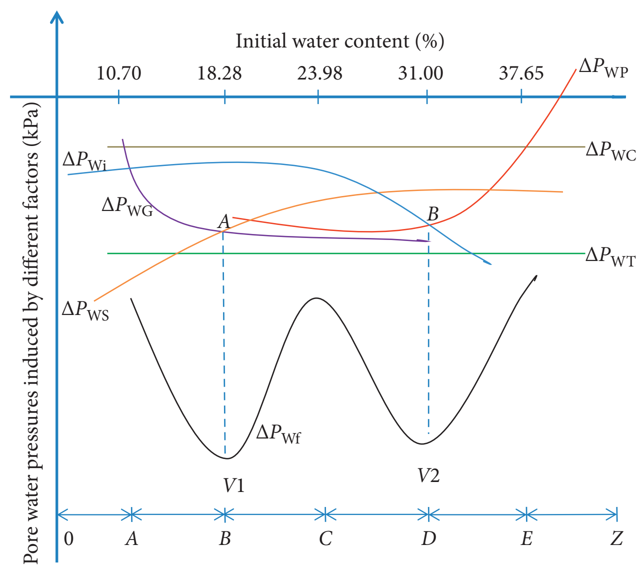

FIGURE 12: Influence-factor analysis of PWP with initial water content. *OA*, *AB*, *BC*, *CD*, *DE*, and *DZ* correspond to different water content ranges, respectively.

the initial water content is larger than point A, the drop rate of ΔP_{wi} is smaller than the increase rate of ΔP_{wP}. Therefore, there exists a minimum of PWP at point B.

The different PWP is commonly referred to as the free energy state of soil water, which refers to the content and energy of free water, capillary water, weakly bound water, strongly bound water, and interfaces between ice, water, and air. In addition, the soil water state is closely related to the pore morphology, mineral composition, and grain size composition. These issues all need a further detailed research.

6. Discussion on the Tensiometer Method for PWP Measurement in Frozen Soil

Using tensiometer method, we found that PWP had a drop during soil freezing and increased during soil thawing. Therefore, a reasonable change tendency in PWP can be measured using this method, which indicated that the method is valid. However, there still exist some limitations in the method, which is mainly embodied in the following four disadvantages:

(1) Cavitation occurs in the inner liquid of probe lead to measurement failure. For example, as shown in Figures 5–9, the discontinuity of data is mainly ascribed to the measurement failure induced by cavitation occurring in the inner liquid of probe. This problem is always a challenge for design of this kind of probe. To avoid cavitation occurring and obtain consistent and valid data, the probe must be reasonably saturated before testing.

(2) The porous ceramic cup is relatively smaller in strength, easy to fracture when subjected to high stress. Therefore, the probe is not suitable to apply under high stress condition. During soil freezing, a high frost heaving stress occurs in the soil because of frost heave. A high stress also can occur in the soil under heavy external load. The high stress frequently makes the probe fracture and failure.

(3) The PWP has generally a broad change range (from −100 kPa to several megapascals) during soil freezing under heavy load. Therefore, the positive measuring range is much larger than the negative measuring range, and the significant difference between positive and negative measuring range will impose restrictions on the accuracy of probe.

(4) It is always questioned whether or not the PWP of frozen soil with low water content can be measured. The method is based on a thermodynamic equilibrium between liquid in the sensor and unfrozen water film in the soil. However, the unfrozen water is relatively less and has a poor fluidity in the frozen soil with low water content. This low water content will cut off the connection of water film and further destroy the thermodynamic equilibrium required by the probe.

In conclusion, a more detailed investigation on the method will be performed to measure the PWP of soils subjected to negative temperature and high stress.

7. Conclusions

The following conclusions can be obtained from the PWP measurement of silty clay subjected to freezing and thawing:

During soil freezing, as temperature decreases, PWP first has a slight increase, then decreases to a minimum, and finally has a slight increase. During soil thawing, PWP increases as temperature increases.

The PWP minimum has a "w-shaped double-valley" characteristic as initial water content increases.

The PWP changes depend on multifactors. An influence-factor analysis of PWP was proposed and gave a reasonable interpretation on the "w-shaped double-valley" characteristic of PWP.

The method to measure PWP used in this article is valid for the PWP measurement during soil freezing and thawing. However, there still exist some limitations for further research.

Data Availability

The data are available from the corresponding author upon request.

Conflicts of Interest

The authors declare that they have no conflicts of interest regarding the publication of this paper.

Acknowledgments

The authors would like to thank the Natural Science Foundation of China (no. 41501072) and Department of Transportation of Gansu Province (no. 2017-008) for their financial support.

References

[1] S. Taber, "Frost heaving," *The Journal of Geology*, vol. 37, no. 5, pp. 428–461, 1929.
[2] S. Taber, "The mechanics of frost heaving," *The Journal of Geology*, vol. 38, no. 4, pp. 303–317, 1930.
[3] D. H. Everett, "The thermodynamics of frost damage to porous solids," *Transactions of the Faraday Society*, vol. 57, pp. 1541–1551, 1961.
[4] D. H. Everett and J. M. Haines, "Capillary properties of some model pore systems with special reference to frost damage," *Rilem Bulletin*, vol. 27, pp. 31–36, 1965.
[5] L. H. Gold, "A possible force mechanism associated with the freezing of liquids in porous materials," *Highway Research Board Bulletin*, vol. 168, pp. 65–72, 1957.
[6] R. D. Miller, "Frost heaving in non-colloidal soils," in *Proceedings of the 3rd international Conference on Permafrost*, pp. 708–713, Alberta, Canada, July 1978.
[7] K. O'neill, "The physics of mathematical frost heave models: a review," *Cold Regions Science and Technology*, vol. 6, no. 3, pp. 275–291, 1983.
[8] K. O'Neil and R. D. Miller, "Exploration of a rigid ice model of frost heave," *Water Resources Research*, vol. 21, no. 3, pp. 281–296, 1985.
[9] J.-M. Konrad and N. R. Morgenstern, "A mechanistic theory of ice lens formation in fine-grained soils," *Canadian Geotechnical Journal*, vol. 17, no. 4, pp. 473–486, 1980.
[10] J.-M. Konrad and N. R. Morgenstern, "The segregation potential of a freezing soil," *Canadian Geotechnical Journal*, vol. 18, no. 4, pp. 482–491, 1981.
[11] L. Zhang, W. Ma, C. Yang, and S. Dong, "A review and prospect of the thermodynamics of soil subjected to freezing and thawing," *Journal of Glaciology and Geocryology*, vol. 35, no. 6, pp. 1505–1518, 2013.
[12] K. Watanabe, M. Takeuchi, Y. Osada, and K. Ibata, "Micro-chilled-mirror hygrometer for measuring water potential in relatively dry and partially frozen soils," *Soil Science Society of America Journal*, vol. 76, no. 6, 2012.
[13] E. J. Chamberlain, "Overconsolidation effects of ground freezing," *Engineering Geology*, vol. 18, no. 1–4, pp. 97–110, 1981.
[14] J.-M. Konrad, "Pore water pressure at an ice lens: its measurement and interpretation," *Cold Regions Science and Technology*, vol. 16, no. 1, pp. 63–74, 1989.
[15] J. T. C. Seto and J.-M. Konrad, "Pore pressure measurements during freezing of an overconsolidated clayey silt," *Cold Regions Science and Technology*, vol. 22, no. 4, pp. 319–338, 1994.
[16] Z. Wen, T. Zhang, Y. Sheng et al., "Managing ice-rich permafrost exposed during cutting excavation along Qinghai–tibetan railway: experiences and implementation," *Engineering Geology*, vol. 122, no. 3, pp. 316–327, 2011.
[17] K. D. Eigenbrod, S. Knutsson, and D. C. Sheng, "Pore-water pressures in freezing and thawing fine-grained soils," *Journal of Cold Regions Engineering*, vol. 10, no. 2, pp. 77–92, 1996.
[18] C. Harris and M. C. Davies, "Pressures recorded during laboratory freezing and thawing of a natural silt-rich soil," in *Proceedings of the 7th International Conference on Permafrost Conference*, pp. 23–27, Yellowknife, Canada, June 1998.
[19] R. W. McGaw, R. L. Berg, and J. W. Ingersoll, "An investigation of transient processes in an advancing zone of freezing," in *Proceedings of the Permafrost: 4th International Conference*, pp. 821–825, Washington, DC, USA, July 1983.
[20] Y. Miyata and S. Akagawa, "An experimental study on static soild-liquid phase equilibrium in the pores of a porous medium," *Heat Transfer—Japanese Research*, vol. 26, no. .2, pp. 69–83, 1997.
[21] Y. Miyata and S. Akagawa, "An experimental study on dynamic soild-liquid phase equilibrium in the pores of a porous medium," *JSME International Journal Series B*, vol. 41, no. 3, pp. 590–600, 1998.
[22] L. Zhang, W. Ma, C. Yang, and C. Yuan, "Investigation of the pore water pressures of coarse-grained sandy soil during open-system step-freezing and thawing tests," *Engineering Geology*, vol. 181, pp. 233–248, 2014.
[23] W. Ma, L. Zhang, and C. Yang, "Discussion of the applicability of the generalized Clausius-Clapeyron equation and the frozen fringe process," *Earth-Science Reviews*, vol. 142, pp. 47–59, 2015.
[24] L. Zhang, W. Ma, C. Yang, Z. Wen, Z. Wen, and S. Dongau, "An investigation of pore water pressure and consolidation phenomenon in the unfrozen zone during soil freezing," *Cold Regions Science and Technology*, vol. 130, pp. 21–32, 2016.

Hindawi
Advances in Materials Science and Engineering
Volume 2021, Article ID 3763181, 22 pages
https://doi.org/10.1155/2021/3763181

Research Article

Dynamic Parameters and Hysteresis Loop Characteristics of Frozen Silt Clay under Different Cyclic Stress Paths

Furong Liu ,[1,2] Zhiwei Zhou,[1] Wei Ma ,[1,2] Shujuan Zhang,[1] and Zhizhong Sun[1]

[1]*State Key Laboratory of Frozen Soil Engineering, Northwest Institute of Eco-Environment and Resources, Chinese Academy of Sciences, Lanzhou 730000, China*
[2]*University of Chinese Academy of Sciences, Beijing 10004, China*

Correspondence should be addressed to Wei Ma; mawei@lzb.ac.cn

Received 16 April 2021; Accepted 28 May 2021; Published 8 June 2021

Academic Editor: Hao Zheng

In cold regions, the long-term stability of engineering facilities is unavoidably influenced by the negative temperature, freeze-thaw process, dry-wet process, and dynamic loading conditions induced by earthquakes and traffic loads. In order to investigate the effects of different cyclic stress paths on the evolution of dynamic mechanical properties of frozen silt clay, a series of cyclic triaxial tests with variation confining pressure (VCP) or constant confining pressure (CCP) were performed. Triaxial low-temperature apparatus (MTS-810) was taken advantage of to simulating various cyclic stress paths by changing cyclic loading conditions of axial stress and confining pressure. In this paper, the evolution features of the axial resilient modulus, damping ratios, and the shape of hysteresis loops with an increase in the number of load cycles under different dynamic stress paths are comprehensively studied. The results show that the loading angle of cyclic stress path and the phase difference between cyclic axial stress and confining pressure are the main factors that remarkably affect the development characteristics of the resilient modulus and damping ratio. With increasing of the loading angle and phase difference, the resilient modulus increases, but damping ratio increases with increasing of loading angle and with decreasing of phase difference. With the continuous increase in the number of loading cycles, the samples of frozen soil show compacting and hardening characteristics. With an increase in the number of load cycles, the shape of hysteresis loop becoming narrows, the resilient modulus decreases at the initial stage and then gradually increases, and the damping ratio stably decreases. According to contrastively analyzing the evolution of dynamic parameters and the shape features of hysteresis loops under various cyclic stress paths, it can be clearly discovered that the evolution of sample microstructure and the development of dynamic characteristics of frozen samples have obvious dependence on the cyclic stress path. Therefore, the effects of variable confining pressure (VCP) on dynamic behaviors of frozen soils are nonnegligible in practical cold region engineering.

1. Introduction

With the continuous expansion of human living space, more and more engineering facilities (such as railways, highways, cannels, and pipelines) have been built in cold regions [1–4]. Meanwhile, the serviceability of these infrastructures is inevitably affected by the environmental change and geological hazard such as global-warming-related deformation, frozen-thaw, dry-wet process, and dynamic loading (e.g., earthquakes, traffic loads, or ocean wave storms) [5–9]. Especially dynamic load that is induced by earthquake, such as the 8.1-magnitude Kunlun Mountains earthquake in November 2001, caused serious cracks on some sections of the Qinghai-Tibet highway and the Qinghai-Tibet railway [10], seriously threatening the safety of the infrastructures. Long-term dynamic load may lead to vertical deformation exceeding the acceptable limit, and the infrastructures may lose serviceability [11]. Therefore, many investigations on the dynamic properties of frozen soil have been conducted [11–15]. But, those works mainly focus on dynamic properties of the frozen soil under constant confining pressure (CCP) condition. For seismic load, the S-wave and P-wave acting on the subgrade will be in random combination with different amplitudes, frequencies, and loading orders, while the CCP condition can only simulate a specific combination of normal stress and shear stress. Also, for the case of vehicle load acting on the surface structure, the lateral stress will also change passively with the change of the axial load, instead of remaining constant due to the Poisson effect of geotechnical materials. Therefore, it is very limited to simulate complex in situ dynamic stress field by axial vibration loading under CCP condition. Cai et al. [16] compared the one-way cyclic triaxial behaviors of saturated clay under several stress paths with VCP and CCP. The study found that VCP tests were more appropriate than CCP tests in the simulation of traffic loading conditions because the VCP stress paths can provide the coupling effects of the variable deviatoric stress and variable confining pressure. The study by Gu et al. [17] indicated that vibration sources applied a repeated loading on the subsurface soil layers may lead to complex stress field, in which all the stress states of the soil elements may generally vary in long-term workings. However, the case of VCP is more suitable for simulating the actual stress field [18, 19]. But, similar research methods are never used in the laboratory test for frozen soils. Due to the existence of the ice, the mechanical properties of frozen soil are more complex than those of unfrozen soils [20–26]. In order to further develop the understanding for the dynamic mechanical properties of frozen silt clay under complex stress field, the triaxial low-temperature apparatus (MTS-810) was used to simulate various cyclic stress paths. To some extent, the evolution law of resilience modulus with the number of load cycles increase under a special dynamic stress path can partly reflect the development characteristics of mechanical properties of the frozen soil samples. Therefore, the law can further reflect the stress path dependence of mechanical property evolution under dynamic stress path. The damping ratio is an important index to represent the soil's ability of absorbing vibration energy. The hysteresis curve reflects the characteristics of elastic-plastic deformation, stiffness, and energy dissipation of soils under dynamic load. The hysteresis curve is the basis of determining and analyzing nonlinear dynamic response [27]. Meanwhile, the microscopic damage characteristics of rock and soil materials can be analyzed by the development of the macroscopic shape of the hysteretic curve. Therefore, this paper emphatically studied the evolution law of the dynamic parameters and the shape of hysteresis loop with increasing number of load cycles under different cyclic stress paths. According to the work in [11, 28], the dynamic modulus and damping ratio of the frozen soil are influenced by the many factors, such as the dynamic stress (strain) amplitude, temperature, and moisture content. Ling et al. [29] studied the relationship between the dynamic elastic modulus ratio and normalized shear strain under varies different conditions through loading step by step. But, for multistage loading, the mechanical properties of the frozen soil are inevitably influenced by the previous stress history. Zhang et al. [30] carried out a series research about dynamic resilient modulus and damping ratio with axial strain development, and the evolution law of mechanical properties of frozen soil samples during increasing of axial strain was revealed. But, few investigation works were focused on the evolution of dynamic parameters and the hysteresis shape of frozen soils with increasing number of loading cyclic under different dynamic stress paths.

In this paper, dynamic tests with three types of cycle stress paths were simulated to present the evolution characteristics of resilient modulus, damping ratios, and shape of hysteresis loops of frozen samples with increasing loading cyclic under different cycle stress paths. Moreover, the main influencing factors of mechanical properties for frozen soil are deeply analyzed.

2. Experimental Program

2.1. Test Apparatus, Test Materials, and Sample Preparation. Dynamic tests with variable confining pressure (VCP) or constant confining pressure (CCP) were conducted by the low-temperature triaxial apparatus (MTS-810) at the temperature of −6°C. The apparatus can control the amplitudes, frequency, and waveform of the axial stress and confining pressure, and the initial phase difference between the axial loading and confining pressure can be set up independently. The hydraulic oil was used in the confining pressure system. The outer wall of the chamber is wrapped around pipes that allow the cooling liquid to flow. So, the hydraulic oil not only provides pressure medium but also ensures if the required negative temperature environment is stable. The main parameters about the test systems are described as follows: the maximum axial load and confining pressure are 100 kN and 20 MPa, respectively, the range of the axial frequency is 0–50 Hz, the maximum displacement is 85 mm, and the range of temperature is room temperature of −30°C. The experimental data are automatically collected by the computer system.

In this study, the test material is silty clay collected from the site along the Qinghai-Tibetan Railway, China. The basic physical parameters are given in Table 1. The grain size distribution of the soil is shown in Figure 1.

Before the test, soils are placed under the sun for 3-4 days and then pulverized and sieved through a 2.0 mm screen to generate the prepared sample. Afterwards, appropriate amount of soil and deionized water were utilized to prepare the spare soil with a water content of 20.5%, which was placed in a sealed bag for more than 24 h. After that, appropriate amount of spare soil was taken to prepare samples with a height of 125.0 mm (the error is ±0.5 mm) and a diameter of 62.0 mm. The quality of the spare soil determines the dry density level of the sample (1.64 g/cm^3). Then, the specimens were put into a copper mold, with permeable stone on top and bottom, and fixed with an iron frame. Then, the samples with the mold were placed in a jar with an air extractor (shown in Figure 2(a)) and were held for 4 h under pressure 600 kPa. Then, the deionized water was injected into the jar through the pressure, and the samples were soaked for at least 24 h. Subsequently, the samples were taken out from the jar and were placed in a refrigerator with a temperature of −30°C for more than 24 h. Then, all the samples were carefully trimmed with a height of 125.0 mm and diameter of 61.8 mm on a lathe in a cold room under the temperature of −6°C, and then, each sample was sealed with

Table 1: Basic parameters of silty clay.

Liquid limit (%)	Plasticity limit (%)	Liquid plastic limit index (%)	Dry density (g/cm^3)
32.55	21.15	11.4	1.64

a piece of rubber membrane as well as two resinous end caps as shown in Figure 2(b). Prior to the start of the experiment, all samples were placed in a thermostat at −6°C. The sample contrast before and after the experiment is shown in Figure 2(c).

2.2. The Dynamic Stress Path. In this paper, three types of cyclic stress path are adopted in this investigation: (1) three directions of cycle stress path are selected on the stress plane of normal stress and shear stress ($\sigma_d - \tau_d$ plane) to perform three groups of experiments under approximate equal stress path length, as shown in Figure 3(a); (2) as shown in Figure 3(b), the nonlinear cyclic stress path on the $\sigma_d - \tau_d$ plane is obtained by changing the phase difference between principal stress σ_{1d} and σ_{3d}; and (3) cyclic stress paths with roughly equal deviatoric stress amplitude are simulated on the plane of mean principal stress and deviatoric stress ($p_d - q_d$ plane) to observe the influence of mean principal stress on the dynamic characteristics of frozen soil samples, described in Figure 3(c). To distinctly express the characteristics of different cyclic stress paths, the parameters' amplitude ratio η^{ampl} and the half-length value of cyclic stress path A and loading angle for cyclic stress paths α on the stress plane of $\sigma_d - \tau_d$ and amplitude ratio ζ^{ampl} and half-length of the cyclic stress path B on the stress plane of $p_d - q_d$, as well as the principal stress σ_{1d} and σ_{3d} vibration equations, were introduced in [31]. Also, the loading angle for the cyclic stress path on the stress plane of $p_d - q_d$ is expressed as follows:

$$\beta = \mathrm{arct}g\zeta^{\mathrm{ampl}}. \tag{1}$$

The condition of all the test samples are summarized in Tables 2 and 3.

3. Test Results and Discussion

3.1. Dynamic Resilient Modulus. In order to accurately describe the evolution characteristics of resilient modulus of frozen silty clay with an increase in the number of load cycles under different cyclic stress paths, the calculation method is adopted as in Figure 4. When the deviator stress is partly unloading Δq, it will produce the corresponding axial strain rebound $\Delta\varepsilon_r$. Therefore, we define the axial resilient modulus E_r as follows:

$$E_r = \frac{\Delta q}{\Delta \varepsilon_r}. \tag{2}$$

Based on the measured values, the relationship between the standard logarithm of cycle number lg$N$ and resilient modulus E_r under all stress paths is a fitted quadratic. The fitting parameters a, b, and c and R^2 are shown in Table 4, and the expression is given by the following equation:

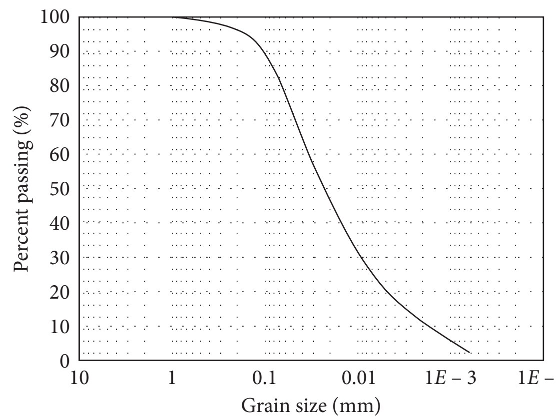

Figure 1: The grain size distribution of silty clay.

$$E_r = a + b \cdot \lg N + c \cdot (\lg N)^2. \tag{3}$$

The relationship between the number of load cycles N and resilient modulus E_r with different half-length of cycle stress paths value A in the same direction and different loading directions with approximately equal half-length are shown in Figure 5. The solid lines represent the optimal fitting of the experimental data. It could be seen that the resilient modulus E_r decreases rapidly with the increase of cyclic loading before the initial vibration stage. After that, the resilient modulus retains a slightly upward trend. With an increase in the half-length of the cyclic stress path on the same cyclic loading direction, the initial stage resilient modulus decreases. Also, the difference of resilient modulus is obvious in this stage. Subsequently, it is clear that, with an increase in the number of cyclic loading, the resilient modulus level at the same loading direction is getting closer and closer. This phenomenon precisely illustrates that, with the continuous dynamic loading, the samples are strengthening. For the same cycle stress loading direction, although the stress path length is different, the samples were induced the same anisotropic behavior structure to adapt the stress field. Obviously, with an increase in the loading angle α of cycle stress path, the resilient modulus E_r increases. Compared to the half-length of the cyclic stress path, the loading angle of the cyclic stress path has a more obvious influence on the resilient modulus, which indicates that the loading angle of the cyclic stress path is the main factor affecting the resilience characteristics of frozen soil.

As shown in Figure 6, the development tendency of E_r is obtained under the different phase difference φ of principal stress σ_{1d} and σ_{3d}. The whole variation trends are identical with the former cases; E_r decreases in the initial some hundred cycles and then enters a stable increase stage. The comparison results illustrate that E_r increases as the phase difference increases under the same number of load cycles. According to analyzing those nonlinear stress paths in a

(a) (b)

(c)

Figure 2: (a) The apparatus used for the air extractor; (b) the prepared samples before the testing; and (c) sample contrast before and after the test.

normal-shear stress plane, the path loci for $\varphi = 45^{\circ}$ and $\varphi = 270^{\circ}$or $\varphi = 90^{\circ}$ and $\varphi = 225^{\circ}$ are similar but rotate in opposite directions. Obviously, when the dynamic stress path rotates in an anticlockwise direction, E_r is larger than that in the clockwise condition. For nonlinear cyclic stress paths, the loading orders of normal and shear stress are different from those for the linear condition of synchronous and asynchronous loading. As is shown in Figure 3(b), for

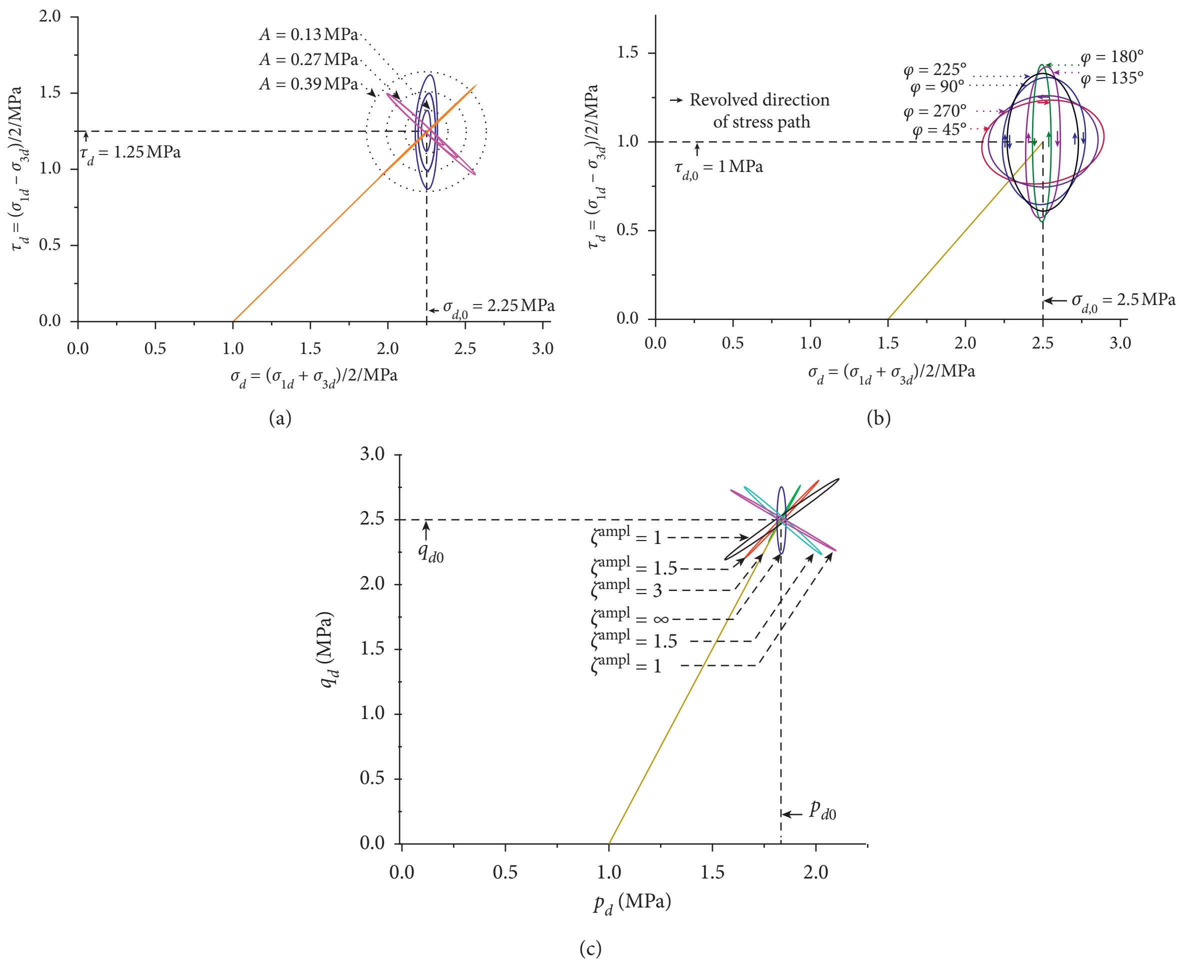

Figure 3: Three types dynamic stress path: (a) the same length under different inclination angles; (b) the different phase difference of principal stress; and (c) the same deviatoric stress amplitude with different inclination angles.

Table 2: Details of the test conditions.

Sample no.	σ_{1d}^{ampl} (MPa)	σ_{3d}^{ampl} (MPa)	η^{ampl}	A (MPa)	φ (°)
1-1-1	0.141	0.140	0	0.141	0
1-1-2	0.290	0.248	0	0.269	0
1-1-3	0.431	0.352	0	0.391	0
1-2-1	0.195	0	1	0.138	0
1-2-2	0.387	0	1	0.273	0
1-2-3	0.568	0	1	0.402	0
1-3-1	0.133	−0.139	∞	0.136	180
1-3-2	0.272	−0.239	∞	0.265	180
1-3-3	0.394	−0.383	∞	0.389	180
1-4-1	0	0.184	−1	0.130	0
1-4-2	0	0.380	−1	0.269	0
1-4-3	0	0.546	−1	0.386	0
2-1	0.455	0.431	0		0
2-2	0.473	0.428			45
2-3	0.464	0.422			90
2-4	0.463	0.429			135
2-5	0.444	0.442	∞		180
2-6	0.443	0.456			225
2-7	0.466	0.429			270

TABLE 3: Details of the test conditions.

Sample no.	σ_{1d}^{ampl}/(MPa)	σ_{3d}^{ampl}/(MPa)	ζ^{ampl}	B (MPa)	φ (°)
3-1	0.11	0.366	−1	0.38	0
3-2	0	0.273	−1.5	0.328	0
3-3	0.176	0.086	∞	0.262	180
3-4	0.255	0	3	0.269	0
3-5	0.369	0.085	1.5	0.336	0
3-6	0.461	0.178	1	0.393	0

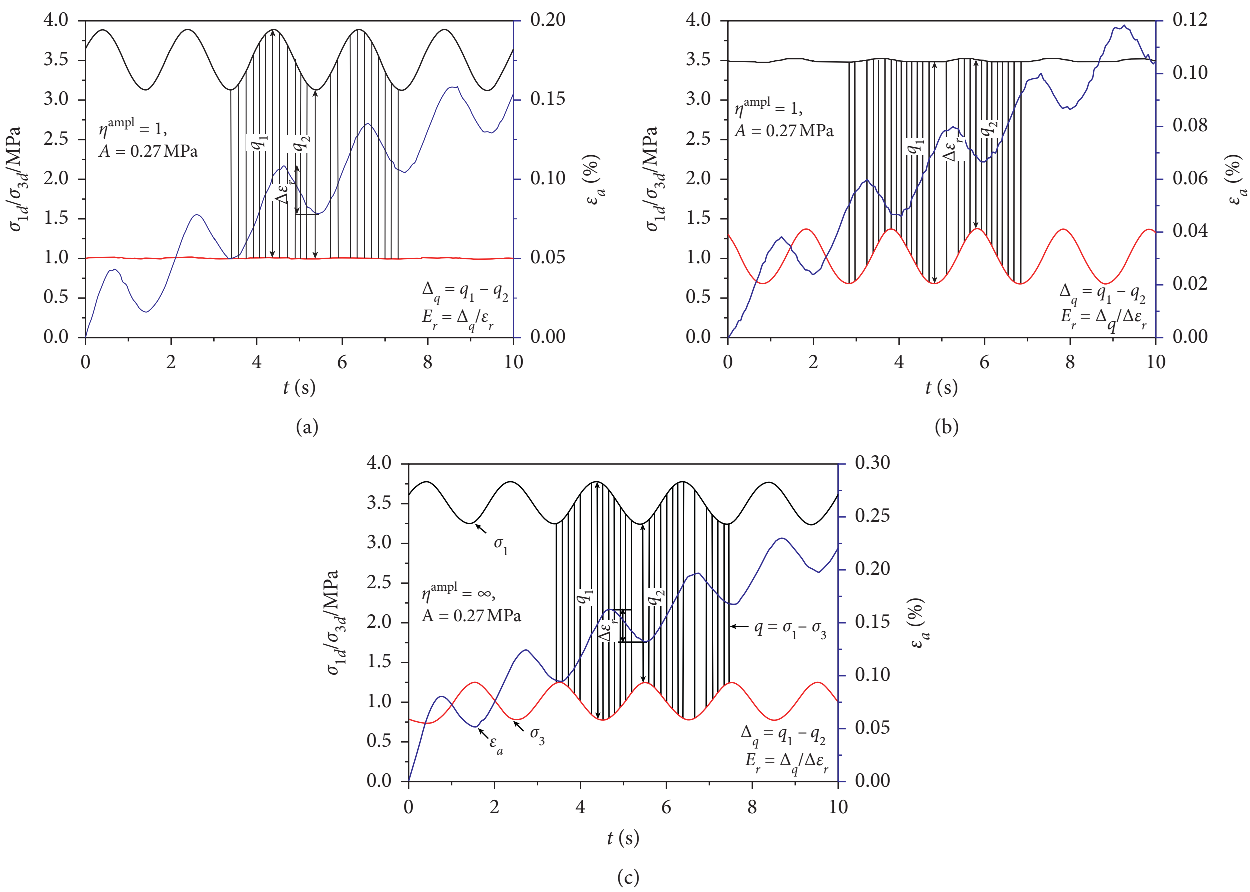

FIGURE 4: The resilience modulus calculation methods under different dynamic stress paths.

the clockwise stress path rotation, when the shear stress is loading from the minimum value to the maximum value, the normal stress is unloading from the middle value to the minimum and then loading to the middle value. When the shear stress is unloading from the maximum value to the minimum value, the normal stress is loading from the middle value to the maximum value and then unloading to the middle value. For the anticlockwise condition, the loading order of normal stress is completely opposite to that in the former case in the process of shear stress loading or unloading. Therefore, in the process of shear stress unloading, the normal stress level during cyclic stress path clockwise rotation is higher than that during counterclockwise rotation. Also, the normal stress first increased and then decreases when the clockwise condition, but first decreases and then increases for the case of counterclockwise condition in the shear stress unloading process. This means that, in the process of shear stress unloading, along the clockwise stress path, the produced rebound elastic strain is larger than that in the anticlockwise condition.

In order to understand how the amplitude of the mean principal stress p^{ampl} affected the dynamic proprieties of frozen silty clay, a new series of tests are conducted under the approximately equal amplitude of deviatoric stress q^{ampl}. The comparison results of permanent strain accumulation with loading cyclic number are shown in Figure 7 for further confirming the effects of amplitude ratio ζ^{ampl} on the accumulation deformation behaviors. The absolute value of ζ^{ampl} decreases, namely, the length of dynamic stress path increases and the axial strain is faster accumulating under

Table 4: Fitting parameters and R^2 of resilient modulus under various dynamic stress paths.

Testing condition			a	b	c	R^2
$\eta^{ampl} = 1$	$A = 0.13$		3.477	−0.77	0.122	0.86
$\eta^{ampl} = 1$	$A = 0.27$		2.651	−0.34	0.065	0.737
$\eta^{ampl} = 1$	$A = 0.39$		2.445	−0.372	0.0822	0.931
$\eta^{ampl} = \infty$	$A = 0.13$		5.007	−1.298	0.242	0.826
$\eta^{ampl} = \infty$	$A = 0.27$	I	3.632	−0.749	0.174	0.956
$\eta^{ampl} = \infty$	$A = 0.39$		3.171	−0.722	0.178	0.958
$\eta^{ampl} = -1$	$A = 0.13$		8.258	−2.737	0.486	0.897
$\eta^{ampl} = -1$	$A = 0.27$		5.322	−0.889	0.203	0.825
$\eta^{ampl} = -1$	$A = 0.39$		4.884	−1.368	0.362	0.958
		$\varphi = 45^\circ$	1.904	−0.14	0.06	0.983
		$\varphi = 90^\circ$	2.203	−0.251	0.074	0.935
II		$\varphi = 135^\circ$	2.401	−0.386	0.11	0.953
		$\varphi = 180^\circ$	2.499	−0.416	0.12	0.938
		$\varphi = 225^\circ$	2.94	−0.477	0.118	0.897
		$\varphi = 270^\circ$	3.32	−0.393	0.087	0.912
$\zeta^{ampl} = 1$			2.125	−0.26	0.03	0.939
$\zeta^{ampl} = 1.5$			2.165	−0.324	0.051	0.651
$\zeta^{ampl} = 3$	III		2.932	−0.51	0.09	0.752
$\zeta^{ampl} = \infty$			3.774	−0.669	0.128	0.793
$\zeta^{ampl} = -1.5$			6.502	−1.39	0.281	0.776
$\zeta^{ampl} = -1$			9.072	−3.163	0.72	0.818

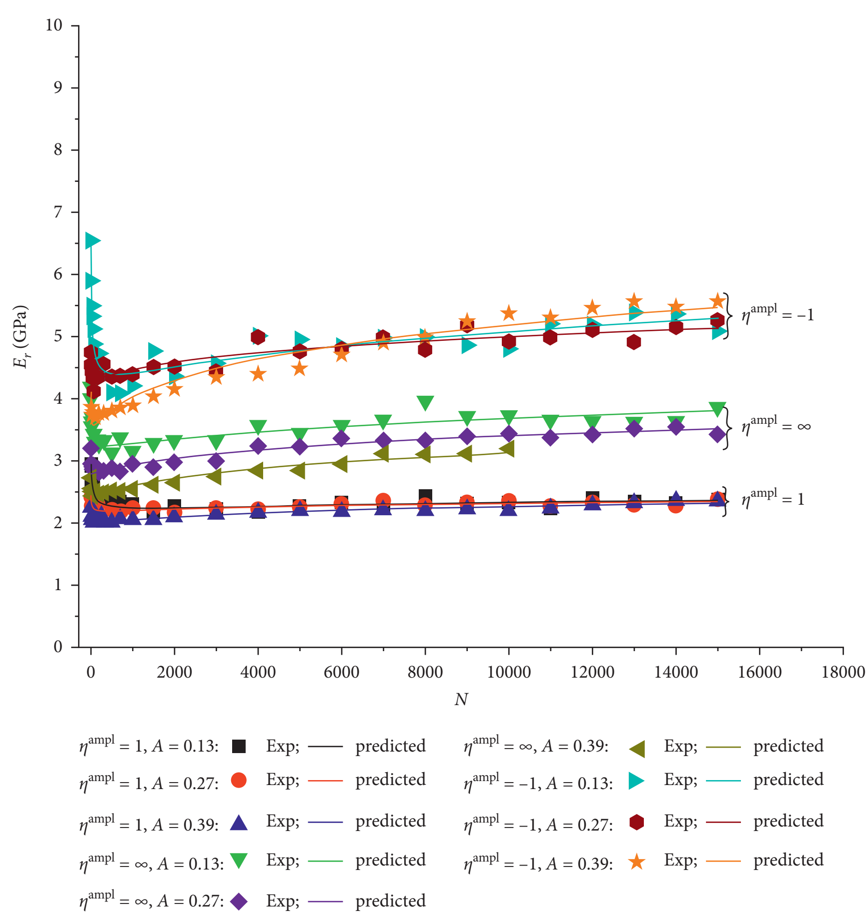

Figure 5: The relationship between resilient modulus and the number of loading cycles under different loading angles and length of dynamic stress paths.

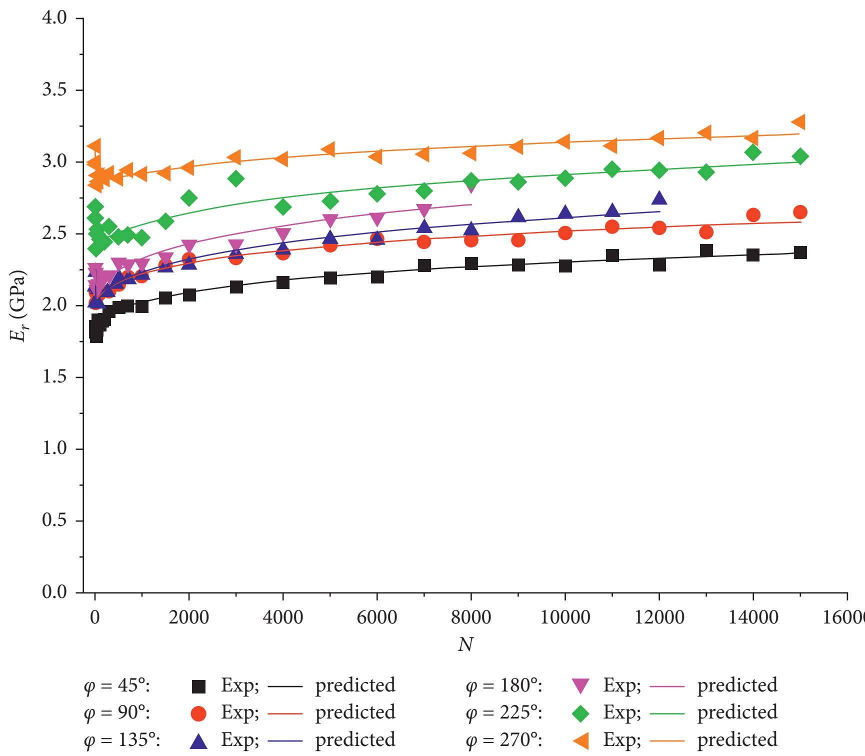

FIGURE 6: Relationship between resilient modulus and the number of load cycles with a different phase difference of principal stress.

approximately equal amplitude of deviatoric stress. Through the result, it is discovered that the increase in amplitude of mean principal stress can obviously accelerate the permanent axial strain accumulation, but the loading order of deviatoric stress and mean principal stress is not obvious for the strain accumulation of this frozen soil.

The relationship between resilient modulus E_r and lg$N$ is plotted in Figure 8. Obviously, as the cyclic stress loading angle increases, the resilient modulus increases. It is remarkable fact that the elastic deformation characteristic has an obvious dependence on the cycle stress path, and the loading sequence between deviatoric stress and mean principal stress is markedly affected by resilient modulus. Comparing to the influence of mean principal stress amplitude on resilient modulus, the loading sequence are more important for the evolution law of the resilient modulus. The primary reason lies in the fact that both the mean principal stress and deviatoric stress have the property of producing elastic strain. For the condition of synchronous loading and unloading, the elastic strain is produced by deviatoric stress and mean principal stress storing and releasing simultaneously, but for case of asynchronous loading and unloading, the released elastic strain because of the unloading of deviatoric stress is partially offset by the elastic strain which is produced by the mean principal stress loading process.

3.2. Damping Ratio. The damping ratios λ_d of materials are an important parameter to measure the capacity of the soil to absorb the vibration energy during each cyclic loading process. For unfrozen soil, the mechanisms of material damping are contributed to friction between soil particles, strain rate effect, and nonlinear soil behavior [32]. From dynamic theory for soils mechanics, the hysteretic damping ratio of unfrozen soil is calculated as described in Figure 9, and its formulation is expressed as follows:

$$\lambda_d = \frac{1}{4\pi}\frac{W_D}{W_S}, \tag{4}$$

where W_D stands for the area of hysteresis loop and W_S represents the area of shadow triangle. For frozen soil, damping primarily reflected the viscosity properties of ice and particles that was generally estimated by the damping ratio [8]. The calculation method damping ratio for frozen soil is shown in Figure 10, and the formulation is given by

$$\lambda_d = \frac{1}{\pi}\frac{W_E}{W_\Delta}, \tag{5}$$

where W_E stands for the area of the hysteresis loop ABDA and W_Δ stands for the area of the shadow triangle ΔCEF. The damping ratio reflected the absorption ratio of energy during a single vibration. All the relationships between the standard logarithm of the number of load cycle lg$N$ and the damping ratios were fitted by the following equation:

$$\lambda_d = a + b \cdot \lg N + c \cdot (\lg N)^2 + d \cdot (\lg N)^3. \tag{6}$$

The fitting parameters a, b, c, and d and R-square are given in Table 5.

Typical test results for the evolution law of damping ratio λ_d and lg$N$ under different dynamic stress paths with

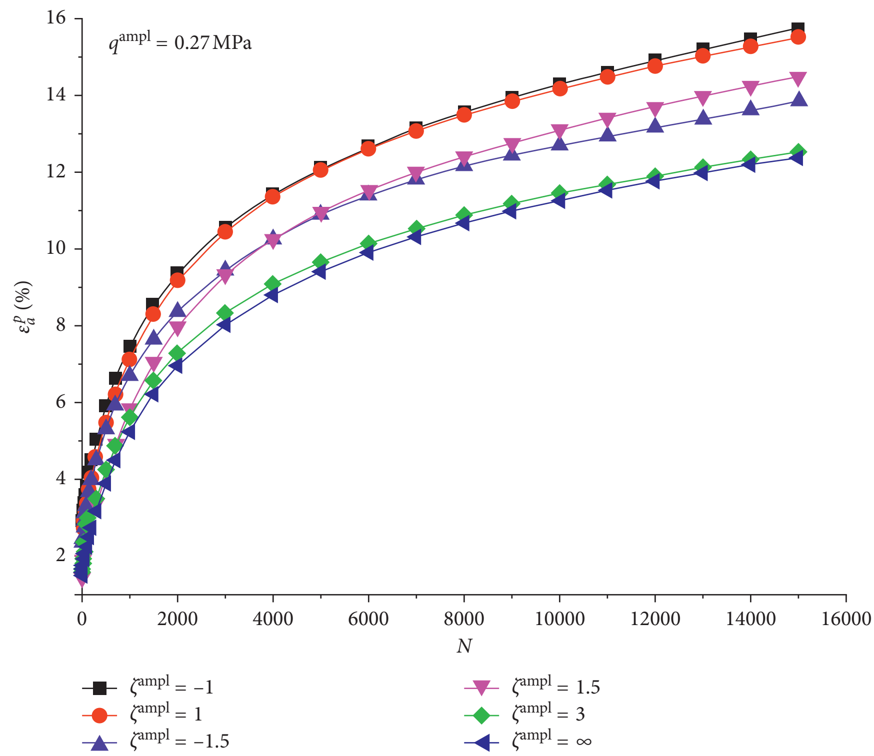

Figure 7: Axial accumulation strain with increasing loading cycle under different amplitude ratios.

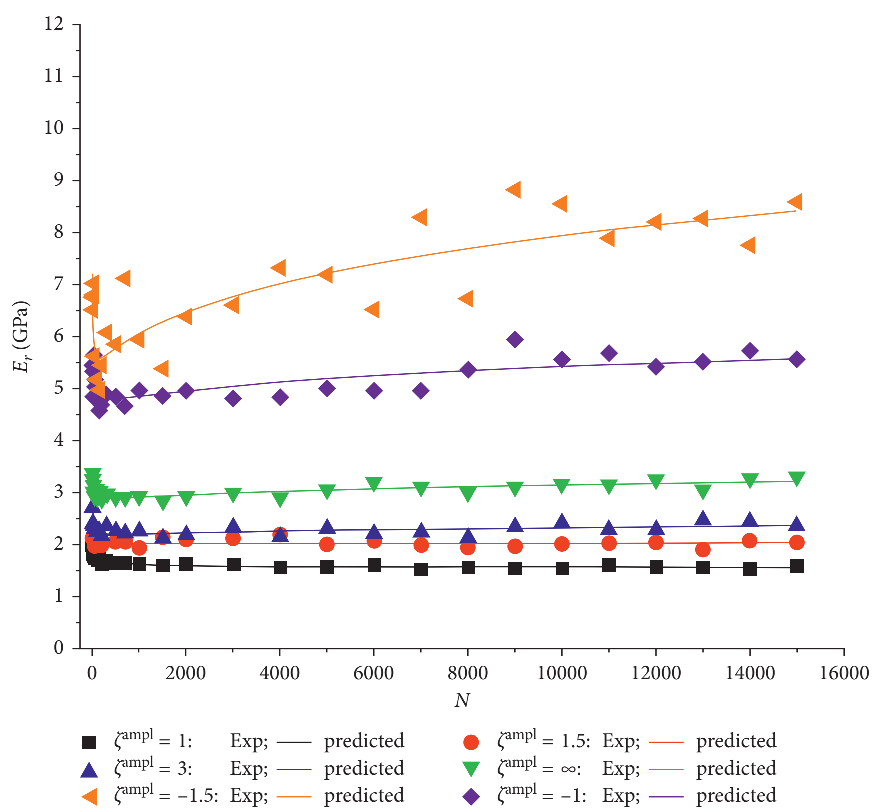

Figure 8: Relationship between resilient modulus and the number of load cycles under different ζ^{ampl} values.

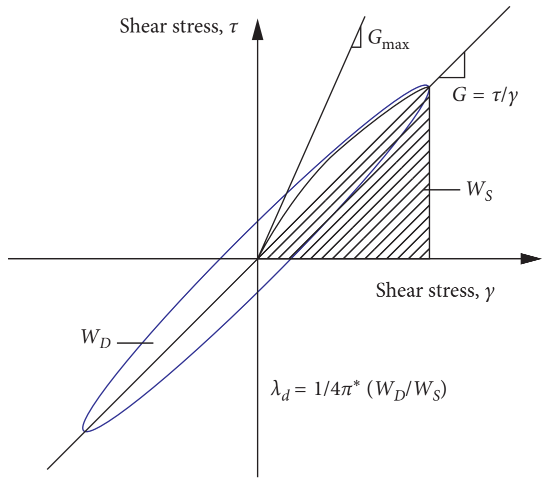

Figure 9: Hysteresis loop for one cycle of loading showing the calculation method of damping ratio in theory.

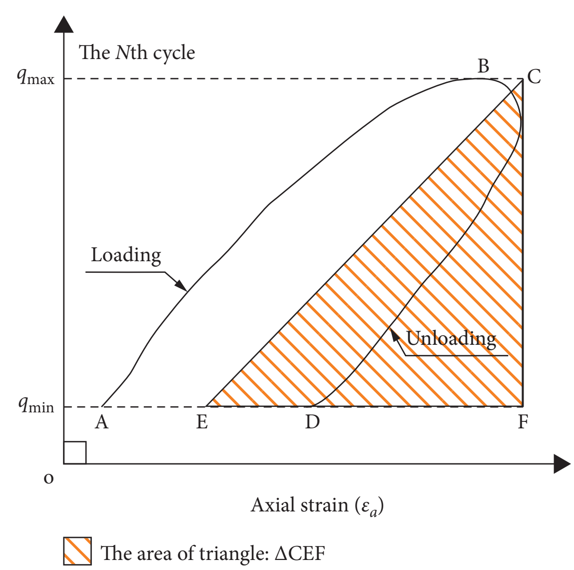

Figure 10: The calculation method of damping ratio for frozen soil.

approximately equal half-length of cycle stress path or for different half-lengths with the same cycle load direction are shown in Figure 11. In the figure, the solid lines represent the optimal fitting of the experimental data. It can be discovered that the length of the cycle stress path and cyclic stress loading angle are the key elements which influence the shape of the curve, and when the cyclic stress loading angle increases and the length of cyclic stress path decreases, the damping ratio increases. Comparing with the length of dynamic stress paths, the loading angle of cyclic stress is the most important factor for affecting the damping ratio, and when the cyclic stress loading angle $\alpha > 90^{\circ}$, the dynamic damping ratio is obviously large than that when $\alpha < 90^{\circ}$. The curves of damping ratio get closer with equal amount increases in the length of the dynamic stress path under the same cyclic loading direction. With an increase in the number of load cycles, the damping ratio decreases and gets closer and closer under the same cyclic stress path direction. The results illustrated that the similar microstructures are induced by the loading in the same cyclic load direction.

The relationship between λ_d and lg$N$ with different phase differences of principal stress is shown in Figure 12. It is clearly seen that the damping ratio increases with a decrease of the phase difference of principle stress under the same cycle load numbers. As is shown in Figure 3(b), with increasing phase difference of principle stress, the rotation direction of the nonlinear cycle stress path is clockwise when $\varphi < 180^{\circ}$ and then the path direction turns counterclockwise when $\varphi > 180^{\circ}$. When $\varphi = 45^{\circ}$and $\varphi = 270^{\circ}$ or $\varphi = 90^{\circ}$and $\varphi = 225^{\circ}$, the stress path loci are similar but rotate in opposite directions, so the damping ratio has a great difference. Therefore, the loading order of normal and shear stress distinctly affects the damping ratio. The vibration energy absorption rate of frozen soil is clearly affected by the coupled effect of normal and shear stress.

Figure 13 describes the relationship between λ_d and lg$N$ under approximately equal amplitude of deviator stress. With an increase in the number of load cycles, the damping ratio decreases. The result indicates that the effect of the amplitude ratio on the damping ratio is not obvious when $\zeta^{ampl} > 0$. But, when $\zeta^{ampl} < 0$, the damping ratio is markedly lager than that in the former condition, and with an increase in cyclic loading, the angle value increases. According to the contrast the loading methods, it is found that, for synchronous loading of the mean principal stress and deviatoric stress ($\zeta^{ampl} > 0$), the loading energy produced by the two loads is stored and released simultaneously. Similar as previously described about resilient modulus lager when $\zeta^{ampl} < 0$, the axial deformation is mainly plastic deformation during the deviatoric stress loading process, and the recoverable elastic deformation is very limited to the deviatoric stress in the unloading process. Therefore, the comprehensive effect shows that the loading energy is mainly absorbed by the samples in the process of deviatoric stress loading and unloading process. From the findings, it can be concluded that the different vibration combination of deviatoric stress and mean principal stress is obviously affected the energy absorption rate, and this point is always ignored by investigators.

3.3. Hysteresis Loop. This paper defined the hysteretic curve as the deviatoric stress-axial strain relationship under one cyclic loading. In this part, the hysteresis loops of each cyclic loading stress path when $N = 10$–11, 100–101, 1000–1001, and 10000–10001 are given in Figures 14–16. It can be seen that the area of hysteresis loops gets narrower and denser and the bottom opening gets smaller as the cycle number increases. It is evident that, for a single cycle, the ability of frozen soil to absorb vibration energy increases, the microstructure damage of the sample and unrecoverable strain decrease, and the samples are strengthened, and the deformation is the main elastic deformation with the increase of the number of load cycles. The testing result indicates that the shape of hysteresis loop varies greatly under different stress paths.

Table 5: Fitting parameters and R^2 of damping ratio under various dynamic stress paths.

Testing condition			a	b	c	d	R^2
$\eta^{\mathrm{ampl}} = 1$	$A = 0.13$		0.517	−0.104	−0.033	0.0076	0.995
$\eta^{\mathrm{ampl}} = 1$	$A = 0.27$		0.608	−0.342	0.073	−0.0055	0.998
$\eta^{\mathrm{ampl}} = 1$	$A = 0.39$		0.644	−0.409	0.105	−0.0099	0.997
$\eta^{\mathrm{ampl}} = \infty$	$A = 0.13$		0.678	−0.195	0.012	0.0059	0.994
$\eta^{\mathrm{ampl}} = \infty$	$A = 0.27$	I	0.741	−0.419	0.099	−0.0092	0.998
$\eta^{\mathrm{ampl}} = \infty$	$A = 0.39$		0.716	−0.430	0.110	−0.0106	0.996
$\eta^{\mathrm{ampl}} = -1$	$A = 0.13$		0.916	−0.161	−0.033	0.0076	0.989
$\eta^{\mathrm{ampl}} = -1$	$A = 0.27$		0.961	−0.438	0.102	−0.0098	0.989
$\eta^{\mathrm{ampl}} = -1$	$A = 0.39$		0.836	−0.327	0.067	−0.0059	0.996
		$\varphi = 45^\circ$	0.643	−0.352	0.111	−0.0106	0.971
		$\varphi = 90^\circ$	0.737	−0.493	0.159	−0.0167	0.982
II		$\varphi = 135^\circ$	0.743	−0.588	0.204	−0.0235	0.981
		$\varphi = 180^\circ$	0.778	−0.645	0.222	−0.0258	0.992
		$\varphi = 225^\circ$	0.639	−0.607	0.216	−0.0258	0.985
		$\varphi = 270^\circ$	0.207	−0.250	0.069	−0.0062	0.918
$\zeta^{\mathrm{ampl}} = 1$			0.475	−0.193	0.026	0	0.993
$\zeta^{\mathrm{ampl}} = 1.5$			0.525	−0.252	0.046	−0.003	0.988
$\zeta^{\mathrm{ampl}} = 3$			0.527	−0.227	0.034	−0.0017	0.995
$\zeta^{\mathrm{ampl}} = \infty$	III		0.534	−0.223	0.034	−0.002	0.993
$\zeta^{\mathrm{ampl}} = -1.5$			0.734	−0.109	0.043	0.0093	0.967
$\zeta^{\mathrm{ampl}} = -1$			0.949	−0.108	0.027	0.0044	0.987

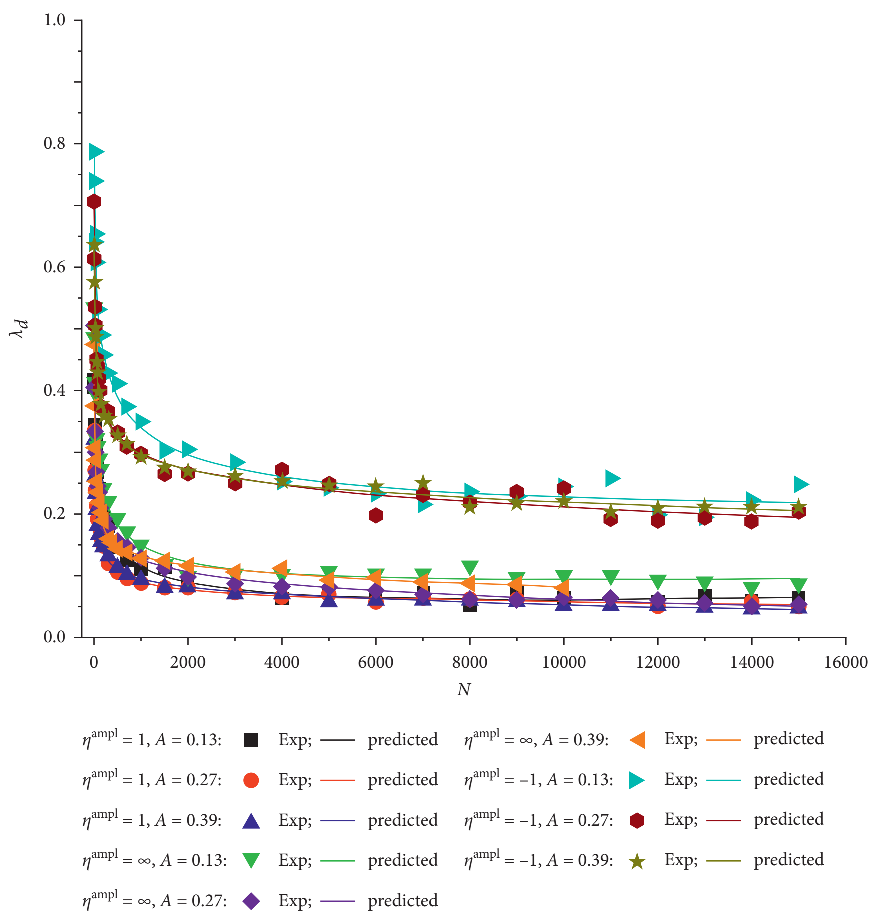

Figure 11: The damping ratios with an increase in the number of load cycles under different dynamic stress paths.

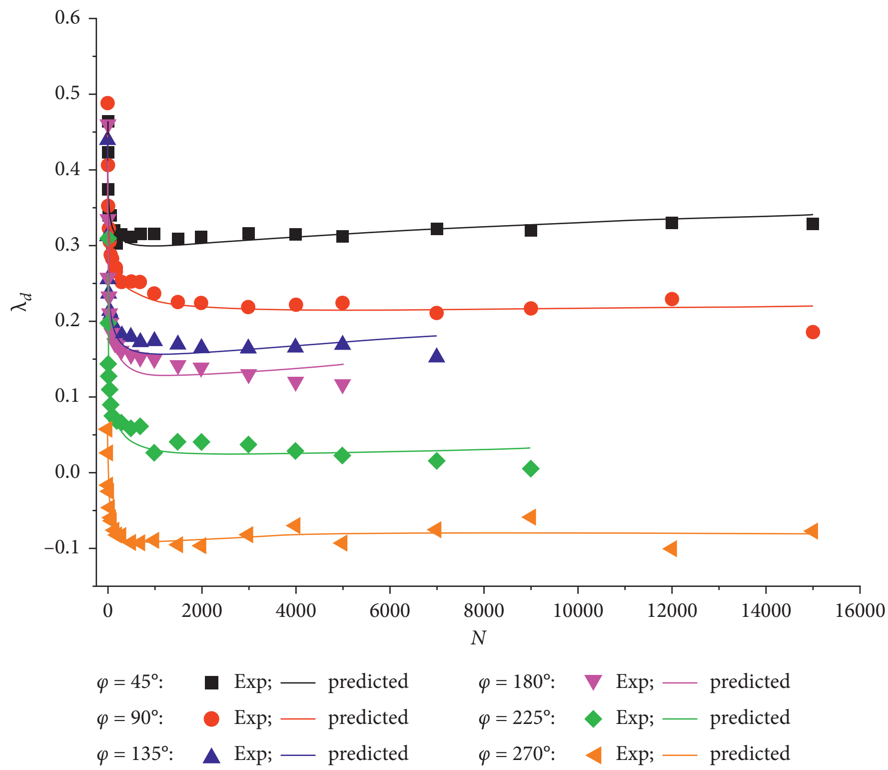

FIGURE 12: The relationship between damping ratios and number of load cycles with different phase differences.

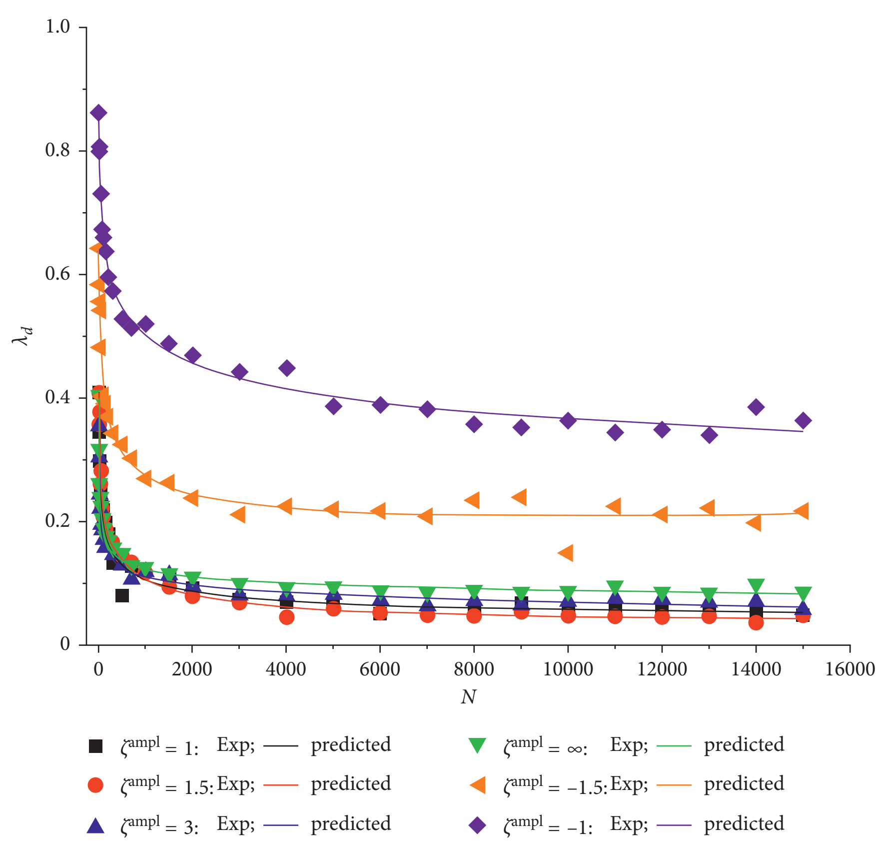

FIGURE 13: The damping ratios development with an increase in the number of loading cycles under the condition of different dynamic stress paths with the similar deviatoric stress amplitude.

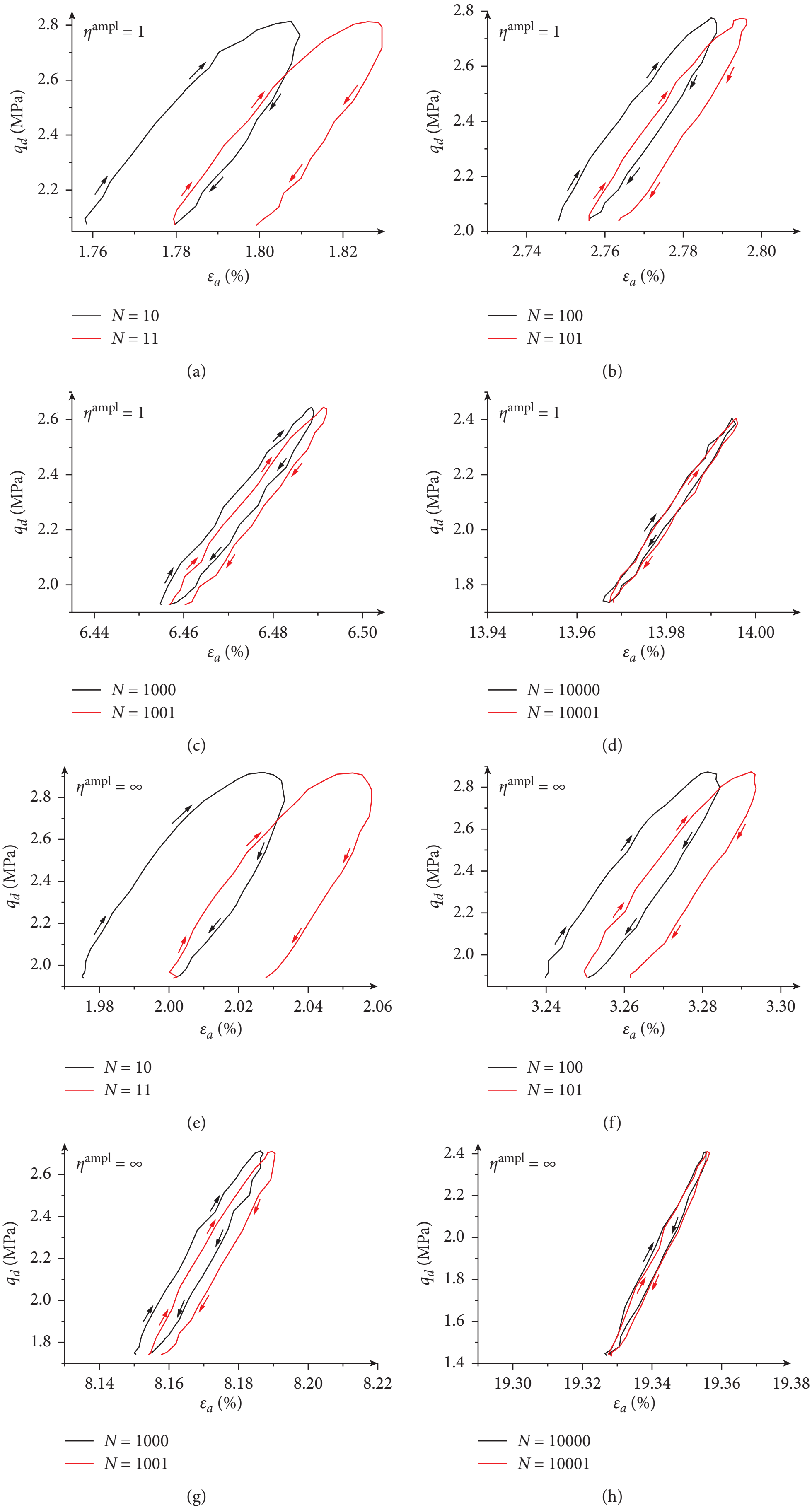

Figure 14: Continued.

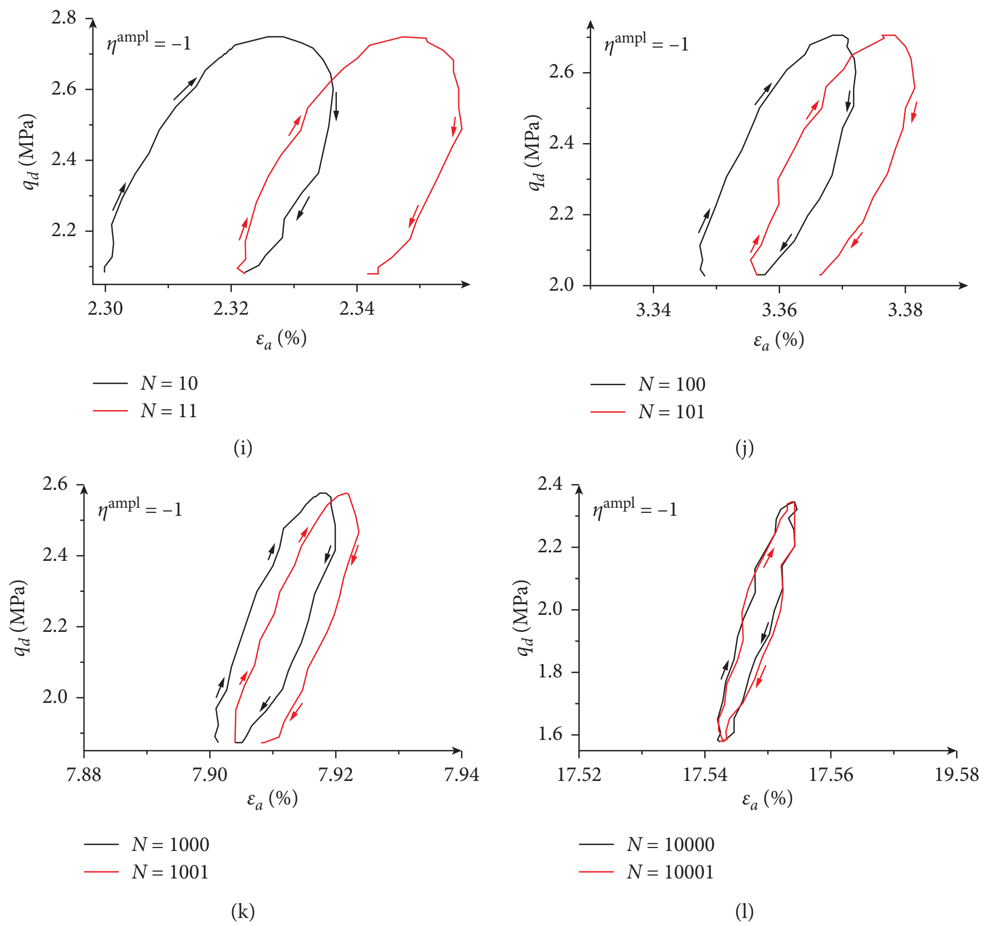

Figure 14: The hysteresis loops of different dynamic stress paths with the same half-length value of dynamic stress paths.

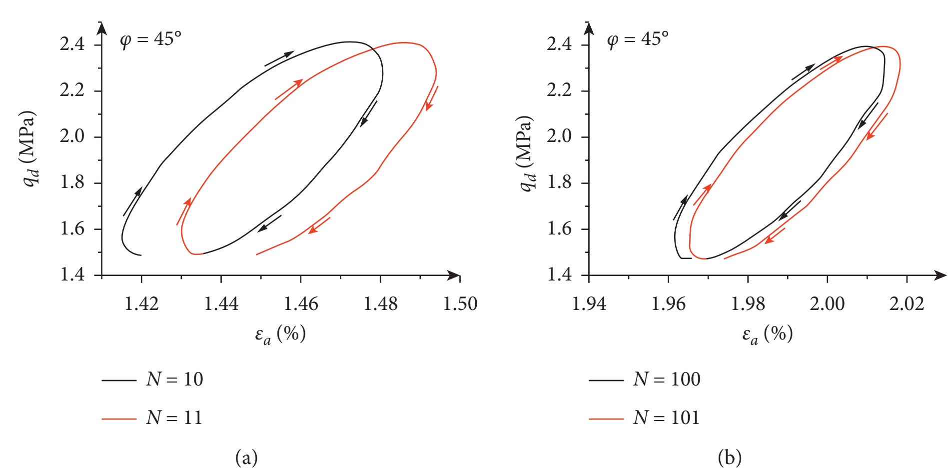

Figure 15: Continued.

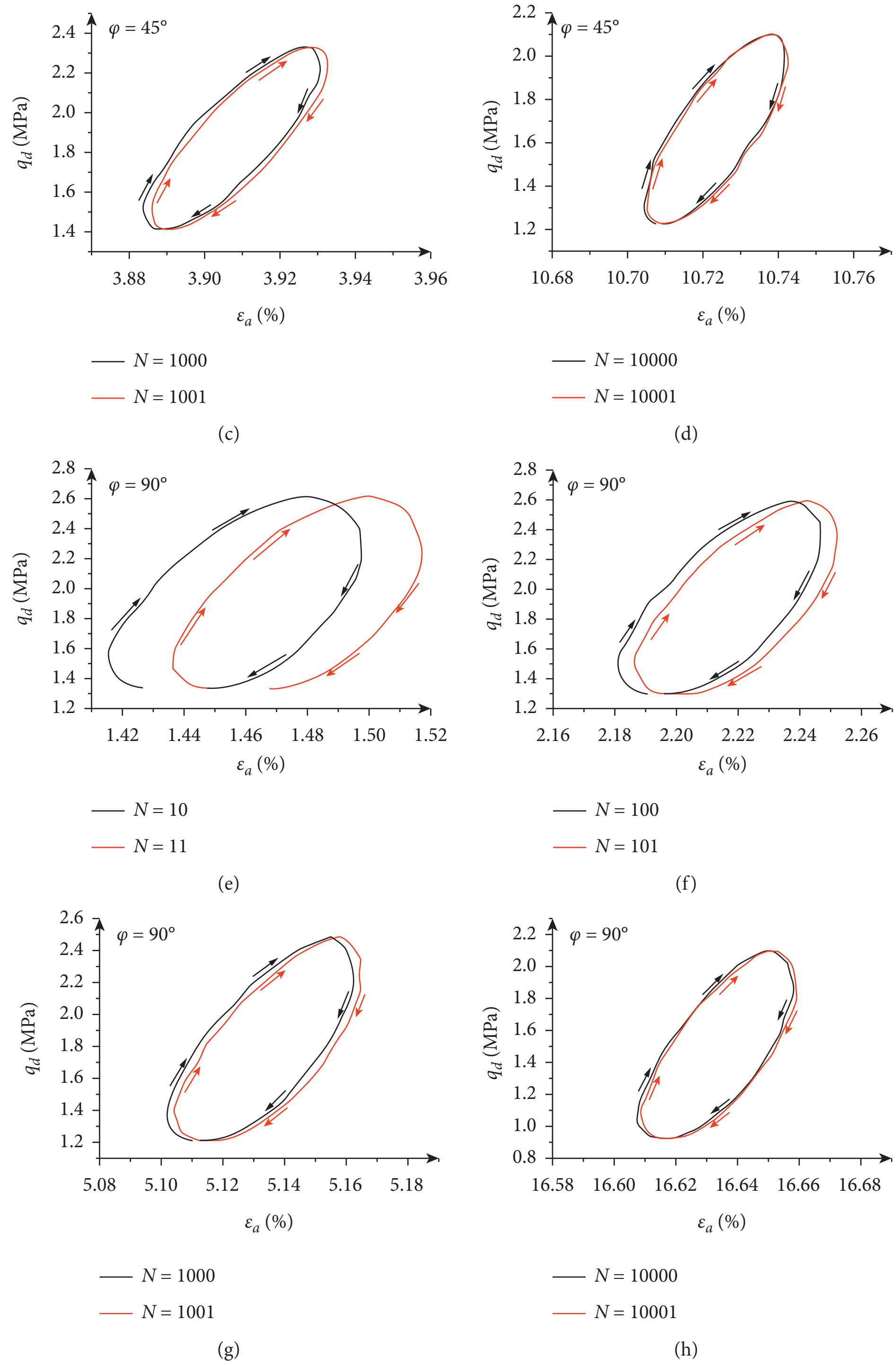

Figure 15: Continued.

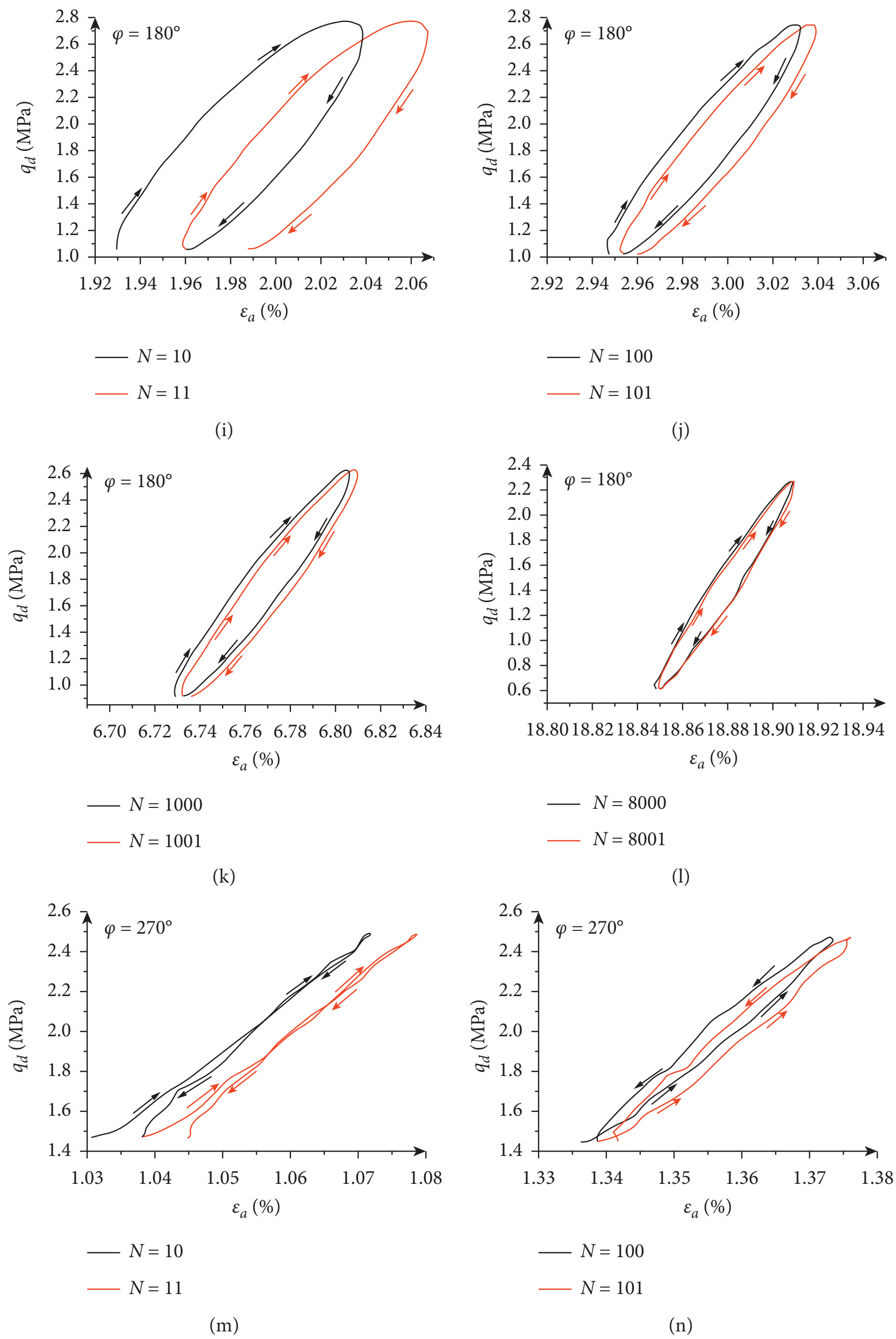

Figure 15: Continued.

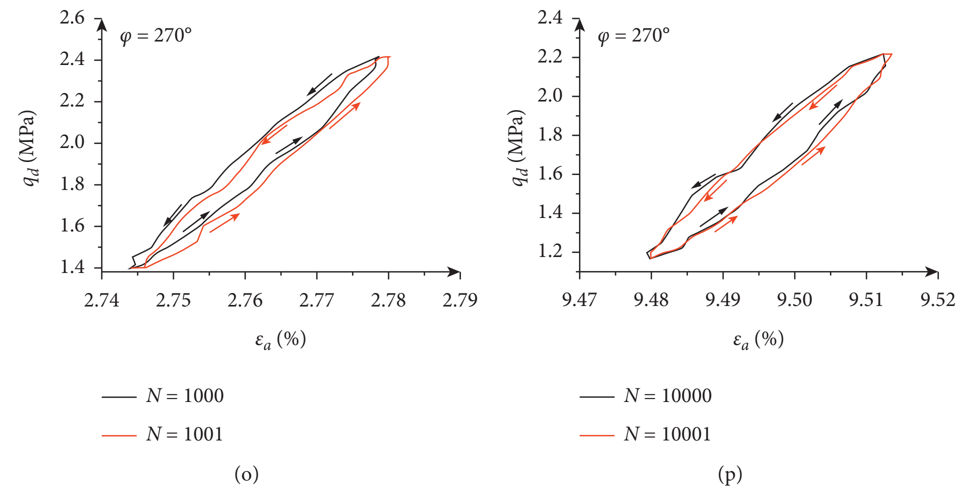

Figure 15: The hysteresis loops of different principal stress phase differences.

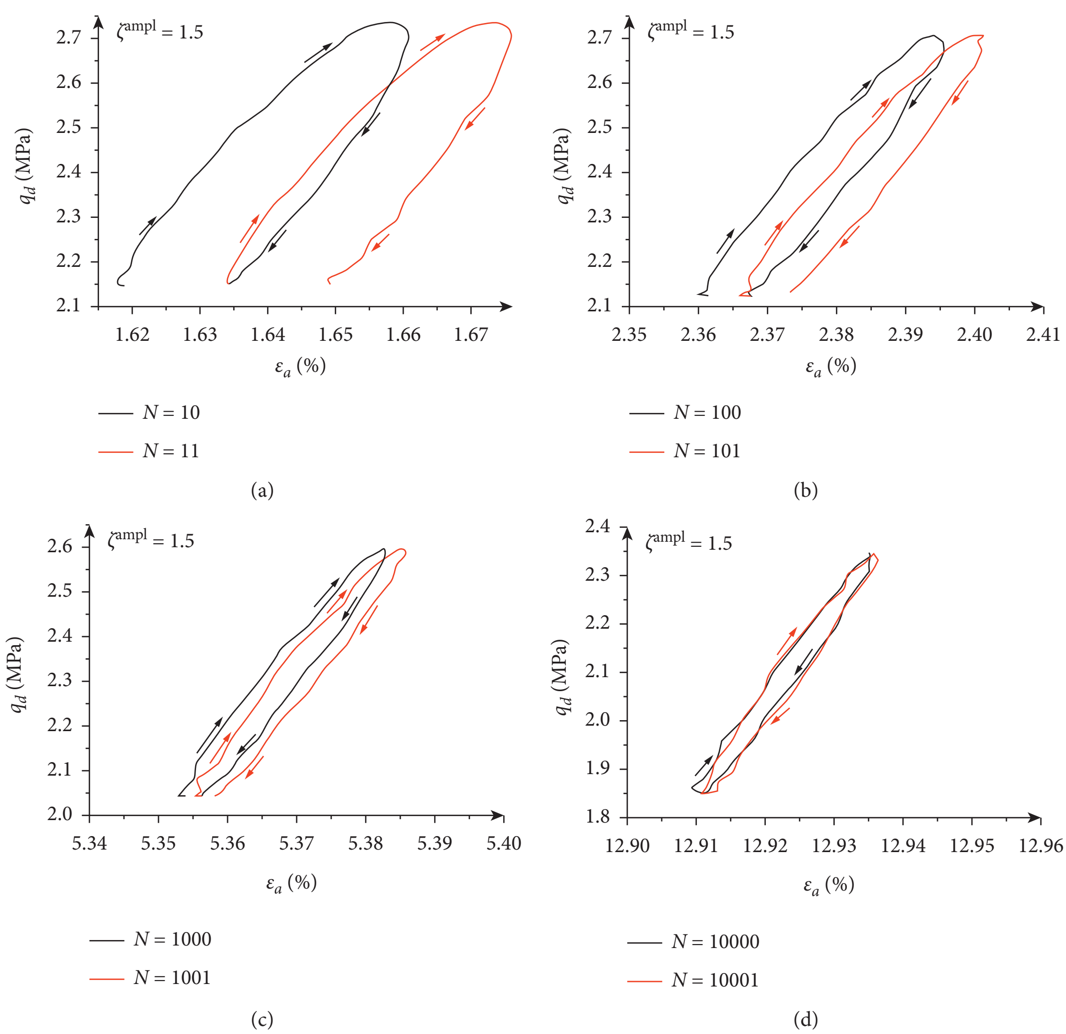

Figure 16: Continued.

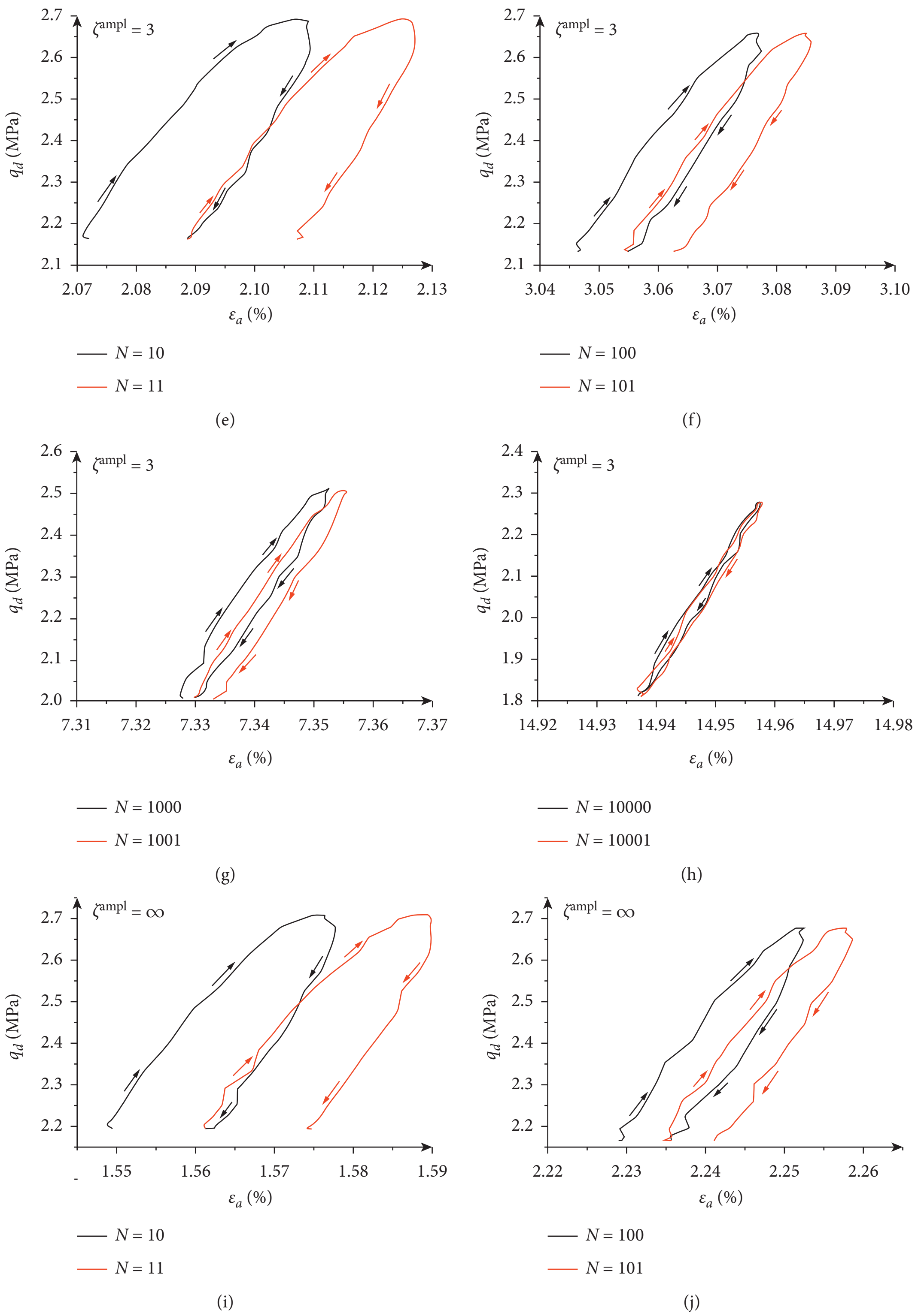

Figure 16: Continued.

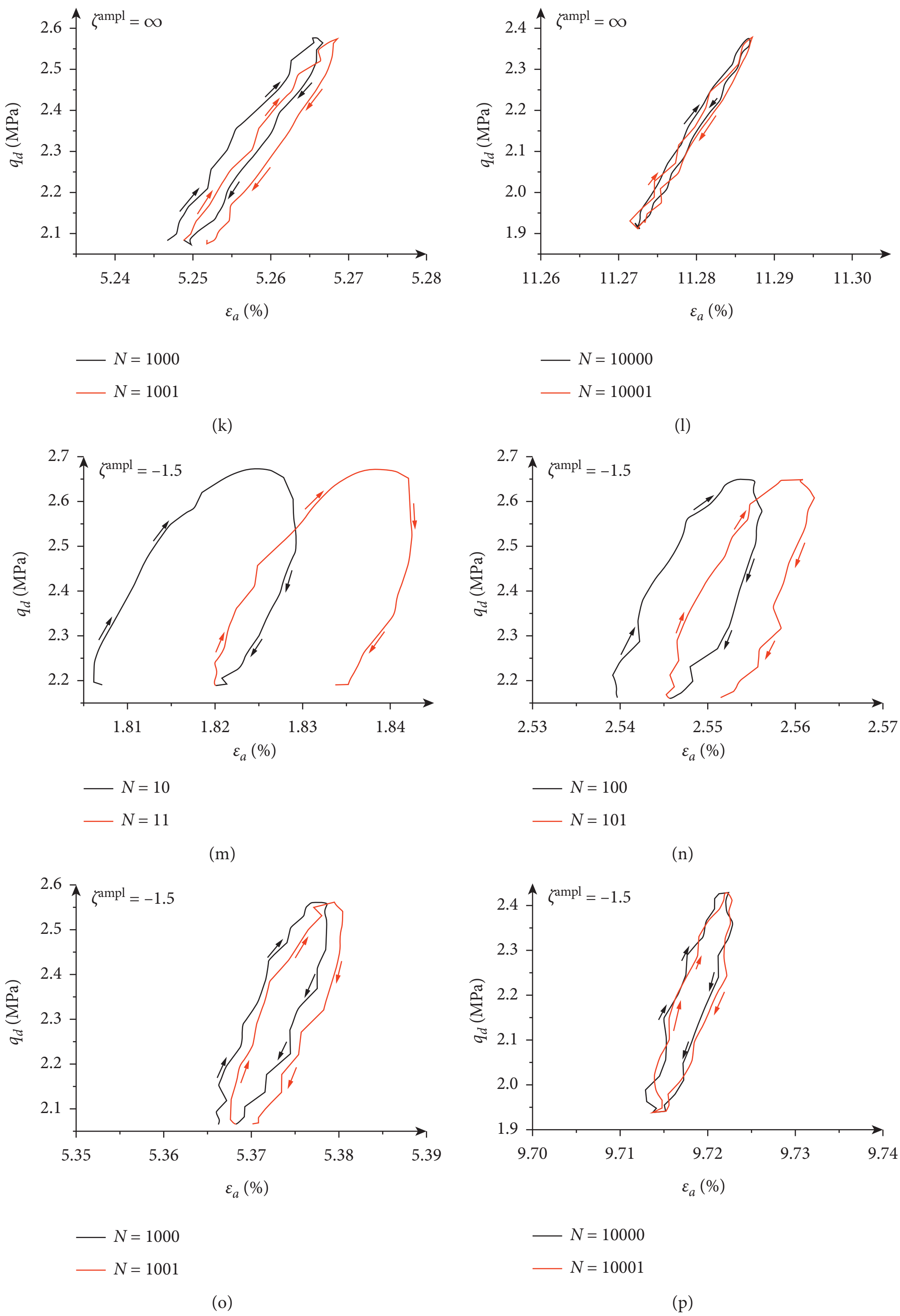

Figure 16: The hysteresis loops with different amplitude ratios under the same amplitude of deviatoric stress.

The sharp of hysteresis loops of different cycle stress paths under the same half-length ($A = 0.27$ MPa) is shown in Figure 14. It is obvious that the sharps of hysteresis loops with $\eta^{\text{ampl}} = 1$ and $\eta^{\text{ampl}} = -1$ are obviously different. The cycle stress path of different amplitude ratios η^{ampl} with the same length of cyclic loading paths is shown in Figure 3(a). The major difference between cyclic stress paths lies in the different combinations of normal and shear stress amplitude and order of the two loading and unloading. Shear and normal stress loading or unloading take place simultaneously when the amplitude ratio $\eta^{\text{ampl}} = 1$, but when $\eta^{\text{ampl}} = -1$, the two stresses' vibrations are asynchronous. Comparing with the two kinds of hysteresis loop, it is found that the hysteresis loop is fatter when $\eta^{\text{ampl}} = -1$ than when $\eta^{\text{ampl}} = 1$. The curve of hysteresis loops bulge outward in the process of loading and unloading for the condition of $\eta^{\text{ampl}} = -1$. This means that, with shear stress loading and normal stress unloading, the axial strain is increasing faster and faster. Then, with the shear stress unloading and normal stress loading, the corresponding axial strain changes to rebound. Compared with the case $\eta^{\text{ampl}} = 1$, the slope of the hysteresis curves is relatively stable. Therefore, it may be concluded that shear stress loading and normal stress unloading process is more likely to cause microstructure damage, and the loading of normal stress in the shear stress unloading process can partly heal the damage.

It is shown in Figure 15 that the sharp of hysteresis loops which is caused by nonlinear cycle stress paths are significantly different with the linear condition. For different phase differences of principle stress, the sharps of hysteresis loops have a distinct difference, especially when the rotation direction of the dynamic stress path is opposite (such as $\varphi = 45^\circ$ and $\varphi = 270^\circ$). With an increase in the phase difference, the area of hysteresis loop decreases under the same number of loading cycles. When $\varphi = 270^\circ$, the deviatoric stress loading curve is below the unloading curve that leads to the calculated damping ratio being negative. Also, the negative increases with an increase in the number of loading cycles. Therefore, the normal stress obviously affected the shape of hysteresis loops and the state absorption or release of vibration energy. It is clear that the shape of the hysteresis loop obviously depends on the cyclic loading stress path and affected by the normal and shear stress coupling effect.

As is shown in Figure 16, which reflected the shape of hysteresis loops with different cyclic loading stress paths and cycle numbers under approximately equal deviatoric stress amplitude, the difference of the hysteresis loop is not obvious when $\zeta^{\text{ampl}} > 0$. With an increase in the number of load cycles, the hysteresis loop becomes narrow and maintains a steady slope. This result illustrated that the major deformation of the sample in the last stage is elastic deformation. Similar with the former results, the shape of hysteresis loops is greatly different when $\zeta^{\text{ampl}} < 0$. It is obviously fatter than the case of $\zeta^{\text{ampl}} > 0$. So, it is illustrated that ability of energy dissipation is stronger during the asynchronous loading of deviatoric stress and mean principal stress than during synchronous loading.

In summary, the loading order of normal stress and shear stress or mean principal stress and deviatoric stress is a significant factor that affected the dynamic resilient modulus, damping ratio, and the hysteresis shape of frozen samples. The result clearly reflected that the initial isotropy microstructures of remold frozen soil samples induced different anisotropy structures by different cyclic loading stress paths. Therefore, the evolution of frozen soil microstructure with an increase in the number of load cycles has an obvious cyclic loading stress path dependence.

4. Conclusions

In this paper, a series of cycle triaxial tests under variable confining pressure or constant confining pressure were conducted on frozen silt clay at the temperature of -6°C and frequency of 0.5 Hz to simulate various near-linear or nonlinear dynamic stress paths. The evolution of dynamic parameters and characteristics of the hysteresis loop with an increase in the number of cyclic loading under different dynamic stress paths are investigated. The main findings are summarized as follows:

(1) With the continuous dynamic loading, the parameters resilient modulus E_r and damping ratio λ_d rapidly decrease in the initial loading stage first and then go into the stability development stage. The shape of hysteresis loops is getting narrower and denser. As the cyclic loading angle of the stress path increases, the resilient modulus E_r and damping ratio λ_d increase. Compared to the length of the dynamic stress path, the inclination angle of the cyclic stress path is the main factor to affect the resilient modulus E_r and damping ratio λ_d.

(2) The curves of $E_r - N$ and $\lambda_d - N$ under the same cyclic stress path loading direction with different half-lengths of the cycle stress path are getting closer and closer. This result indicates that the same cyclic loading direction can induce the frozen samples to produce a similar anisotropy microstructure.

(3) When the slope of the near-linear cycle stress path is opposite, or the rotation direction of the nonlinear cycle stress path is opposite, the dynamic parameters and the shape of the hysteresis loop are significantly different. This result reflects that the evolution of the dynamic characteristic of frozen soil is influenced by the coupling effect of normal and shear stress or deviatoric and mean principle stress. The mechanical property development of frozen soil has an obvious cyclic loading stress path dependence.

Data Availability

The data used in this study are provided in this manuscript.

Additional Points

1. A series of dynamic triaxial tests were conducted on frozen silt clay by using different cyclic stress paths2. Effect of cyclic stress paths on dynamic parameters and hysteresis loop characteristics of frozen silt clay were investigated in detail3.

The influence of dynamic amplitude, cyclic stress path direction, phase difference, and rotation direction on dynamic parameters and hysteresis loop characteristics were systematically analyzed4. The evolution law of elastic-plastic deformation caused by normal and shear stress coupling is studied experimentally

Conflicts of Interest

The authors declare that they have no conflicts of interest.

Acknowledgments

This research was supported by the National Natural Science Foundation of China (grant no. 41571064) and the National Key Research and Development Program of China (no. 2017YFC0405101).

References

[1] W. Ma, J. Qi, and Q. Wu, “Analysis of the deformation of embankments on the qinghai-tibet railway,” *Journal of Geotechnical and Geoenvironmental Engineering*, vol. 134, no. 11, pp. 1645–1654, 2008.

[2] H.-j. Jin, Q.-h. Yu, S.-l. Wang, and L.-z. Lü, “Changes in permafrost environments along the Qinghai-Tibet engineering corridor induced by anthropogenic activities and climate warming,” *Cold Regions Science and Technology*, vol. 53, no. 3, pp. 317–333, 2008.

[3] Q. Wu and F. Niu, “Permafrost changes and engineering stability in Qinghai-Xizang plateau,” *Chinese Science Bulletin*, vol. 58, no. 10, pp. 1079–1094, 2012.

[4] D. Luo, L. Liu, H. Jin, X. Wang, and F. Chen, “Characteristics of ground surface temperature at chalaping in the source area of the yellow river, northeastern Tibetan plateau,” *Agricultural and Forest Meteorology*, vol. 281, Article ID 107819, 2020.

[5] Y. W. Zhou, D. X. Guo, G. Q. Qui, and G. D. Cheng, *China Frozen Soil*, Science Press, Beijing, China, 2000.

[6] S. P. Zhao, Y. L. Zhu, P. He, and D. Y. Wang, “Testing study on dynamic mechanics parameters of frozen soil,” *Chinese Journal Rock Mechanics Engineering*, vol. 22, no. z2, pp. 2677–2681, 2003.

[7] J. R. Xu, Z. X. Zhao, and Y. Ishikawa, “Extensional stress field in the central and southern Qinghai-Tibetan plateau and the dynamic mechanism of geothermic anomaly in Yangbajain area,” *Chinese Journal Geotechnical Engineering*, vol. 20, no. 5, pp. 77–81, 2005.

[8] S. Wang, J. Qi, and Z. Y. Yin, “A review of the dynamic behavior of frozen soils,” *Geotechnical Engineering Journals SEAGS and AGSSEA*, vol. 46, no. 3, pp. 37–44, 2015.

[9] Z. Zhou, W. Ma, S. Zhang, C. Cai, Y. Mu, and G. Li, “Damage evolution and recrystallization enhancement of frozen loess,” *International Journal of Damage Mechanics*, vol. 27, no. 8, pp. 1131–1155, 2018.

[10] E. D. Guo, D. S. Wang, M. Lu, and G. B. Shao, “Damage to lifeline during ms 8.1earthquake near Qinghai-Xinjiang border,” *Earthquake Engineering and Engineering Vibration*, vol. 22, no. 3, pp. 77–81, 2002.

[11] Q.-L. Li, X.-Z. Ling, L.-N. Wang, F. Zhang, J.-H. Wang, and P.-J. Xu, “Accumulative strain of clays in cold region under long-term low-level repeated cyclic loading: experimental evidence and accumulation model,” *Cold Regions Science and Technology*, vol. 94, pp. 45–52, 2013.

[12] M. O. Al-Hunaidi, P. A. Chen, J. H. Rainer, and M. Tremblay, “Shear moduli and damping in frozen and unfrozen clay by resonant column tests,” *Canadian Geotechnical Journal*, vol. 33, no. 3, pp. 510–514, 1996.

[13] L. X. Wang, Q. L. Hu, X. Z. Ling, D. S. Cai, and X. Y. Xu, “Experimental study on dynamic shear modulus of remolded frozen silty clay for Qinghai-Xizang railway,” *Earthquake Engineering and Engineering Vibibration*, vol. 27, no. 2, pp. 177–180, 2007.

[14] S. J. Zhang, Y. M. Lai, S. Y. Li, and X. X. Chang, “Dynamic strength of frozen soils,” *Chinese Journal Geotechecnical Engineering*, vol. 30, no. 4, pp. 595–599, 2008.

[15] X. Ling, Q. Li, L. Wang, F. Zhang, L. An, and P. Xu, “Stiffness and damping ratio evolution of frozen clays under long-term low-level repeated cyclic loading: evidence and evolution model,” *Cold Regions Science and Technology*, vol. 86, pp. 45–54, 2013.

[16] Y. Cai, C. Gu, J. Wang et al., “One-way cyclic triaxial behavior of saturated clay: comparison between constant and variable confining pressure,” *Journal of Geotechnical and Geoenvironmental Engineering*, vol. 139, no. 5, pp. 797–809, 2013.

[17] C. Gu, J. Wang, Y. Cai, Z. Yang, and Y. Gao, “Undrained cyclic triaxial behavior of saturated clays under variable confining pressure,” *Soil Dynamics and Earthquake Engineering*, vol. 40, pp. 118–128, 2012.

[18] L. Sun, C. Gu, and P. Wang, “Effects of cyclic confining pressure on the deformation characteristics of natural soft clay,” *Soil Dynamics and Earthquake Engineering*, vol. 78, pp. 99–109, 2015.

[19] J. Wang, Z. Zhou, X. Hu, L. Guo, and Y. Cai, “Effects of principal stress rotation and cyclic confining pressure on behavior of soft clay with different frequencies,” *Soil Dynamics and Earthquake Engineering*, vol. 118, pp. 75–85, 2019.

[20] W. Ma and D. Y. Wang, *Mechanics of Frozen Soil*, Science Press, Beijing, China, 2014.

[21] S. Zhang, Y. Lai, Z. Sun, and Z. Gao, “Volumetric strain and strength behavior of frozen soils under confinement,” *Cold Regions Science and Technology*, vol. 47, no. 3, pp. 263–270, 2007.

[22] F. A. Tezera, C. S. David, U. A. Lukas, and W. B. Kevin, “Tensile strength and stress-strain behavior of Devon silt under frozen fringe conditions,” *Cold Region Science and Technology*, vol. 68, pp. 85–90, 2011.

[23] Z. Zhou, W. Ma, S. Zhang, Y. Mu, S. Zhao, and G. Li, “Yield surface evolution for columnar ice,” *Results in Physics*, vol. 6, pp. 851–859, 2016.

[24] C. Cai, W. Ma, Z. Zhou et al., “Laboratory investigation on strengthening behavior of frozen China standard sand,” *Acta Geotechnica*, vol. 14, no. 1, pp. 179–192, 2018.

[25] Z. Zhou, W. Ma, S. Zhang, Y. Mu, and G. Li, “Experimental investigation of the path-dependent strength and deformation behaviours of frozen loess,” *Engineering Geology*, vol. 265, Article ID 105449, 2020.

[26] M. Shen, Z. Zhou, and S. Zhang, “Effect of stress path on mechanical behaviours of frozen subgrade soil,” *Road Materials and Pavement Design*, pp. 1–30, 2020.

[27] F. Luo, S. P. Zhao, W. Ma, D. G. Jiao, and X. B. Kong, “Quantitative research on morphological characteristics of hysteretic curves of Qinghai-Hai-Tibet frozen clay,” *Chinese Journal Rock Mechcanics and Engineering*, vol. 32, no. 1, pp. 208–215, 2013, in Chinese.

[28] X. Yu, H. Liu, R. Sun, and X. M. Yuan, “Improved Hardin-Drnevich model for the dynamic modulus and damping ratio

of frozen soil," *Cold Regions Science and Technology*, vol. 153, pp. 64–77, 2018.

[29] X.-Z. Ling, Z.-Y. Zhu, F. Zhang et al., "Dynamic elastic modulus for frozen soil from the embankment on Beiluhe Basin along the Qinghai-Tibet Railway," *Cold Regions Science and Technology*, vol. 57, no. 1, pp. 7–12, 2009.

[30] D. Zhang, Q. Li, E. Liu, X. Liu, G. Zhang, and B. Song, "Dynamic properties of frozen silty soils with different coarse-grained contents subjected to cyclic triaxial loading," *Cold Regions Science and Technology*, vol. 157, pp. 64–85, 2019.

[31] F. Liu, Z. Zhou, S. Zhang, W. Ma, and Z. Sun, "Experimental investigation of accumulation deformation properties of frozen silt clay under different cyclic stress-paths," *Cold Regions Science and Technology*, vol. 163, pp. 108–118, 2019.

[32] J. Zhang, R. D. Andrus, and C. H. Juang, "Normalized shear modulus and material damping ratio relationships," *Journal of Geotechnical and Geoenvironmental Engineering*, vol. 131, no. 4, pp. 453–464, 2005.

Hindawi
Advances in Materials Science and Engineering
Volume 2021, Article ID 5519035, 14 pages
https://doi.org/10.1155/2021/5519035

Research Article

Longitudinal Deformation Model and Parameter Analysis of Canal Lining under Nonuniform Frost Heave

Pengfei He [1] **Jianhua Dong** [2,3] **Xin Ren**,[2,3] **and Xiaolei Wu** [2,3]

[1] *School of Science, Lanzhou University of Technology, Lanzhou 730050, China*
[2] *School of Civil Engineering, Lanzhou University of Technology, Lanzhou 730050, China*
[3] *Key Laboratory of Disaster Prevention and Mitigation in Civil Engineering of Gansu Province, Lanzhou University of Technology, Lanzhou 730050, China*

Correspondence should be addressed to Jianhua Dong; djhua512@163.com

Received 5 January 2021; Revised 19 February 2021; Accepted 5 May 2021; Published 20 May 2021

Academic Editor: Ying-hao Huang

Due to the unique hydrothermal environments, the frost heave failure of the concrete lining of water conveyance canals in cold regions is still frequent. The deformation of lining after frost heaving and the stress distribution calculated by the mechanical model can be the reference for the lining design. However, previous research mainly focused on the mechanical model of the cross-section while having little attention for the longitudinal nonuniform frost heave damage. In this study, a mechanical model of the bottom lining under the nonuniform frost heave deformation is built based on the Euler–Bernoulli beam and the Pasternak foundation model, and the analytical solution of the model is obtained. The internal stress of the lining is analyzed during the changes of subgrade coefficient, shear rigidity, transition section length, and frost heave amount inside the model. Also, the calculation process is proved to be correct. The result shows that dangerous cross-sections are at the start and the end of the transition sections. The maximum normal stress and the tangential stress increase when the subgrade coefficient and the frost heave amount increase and the shear modulus and transition section length decrease. The frost heave amount in the frozen ground subgrade increases constantly, while the temperature decreases, but at the same time, the shear rigidity of the subgrade increases with it. The former increases the stress of lining, and the latter decreases it. Therefore, during the frost heaving process, the internal force of lining is coupled with these two elements. By analyzing a water conveyance canal lining under the nonuniform frost heave in the Xinjiang Tarim irrigation district, the maximum normal stress of the dangerous lining cross-section is greater than its tensile strength when the transition section length smaller than 7 m at the frost heave amount is 0.031 m.

1. Introduction

The area where the surface temperature is continuously lower than 0°C throughout the year or the coldest season is called the frozen ground, and about 50% of the land area on the earth belongs to the frozen ground [1]. In the process of soil freezing, the volume of pore water after freezing will increase by 9% to cause frost heave. Simultaneously, the water in the unfrozen soil migrates to the freezing edge due to the temperature gradient and form segregated ice, which will also cause frost heave [2]. Therefore, engineering structures in the cold regions often suffer from the effects of frost heave damage.

In China, about 52% of the land is in the frozen ground, such as the Xinjiang Uygur Autonomous Region. It is in the arid area of the middle-temperature zone and cold and arid in winter, and a large scale of the area is covered with seasonally frozen soil [3]. The days when the maximum temperature is below 0°C can be up to 130 days, and the temperature difference between day and night is great. Due to scarce precipitation and extremely uneven distribution of the water resources, many reservoirs and long-distance conveyance canals have been built to meet factory and mine production, urban life, and farmland irrigation. More than 90% of farmland irrigation water depends on the supply of conveyance canals [4, 5]. Therefore, the secure operation of these reservoirs and long-distance conveyance canals is critical to the production and life of the people in these regions.

To reduce leakage, the water conveyance canals are usually paved with concrete lining on the slope and bottom of the canals, which significantly improves the water utilization efficiency of the canal system [6, 7]. However, in the years of the operation process, due to repeated freezing and thawing, hydraulic scouring, and other external loads effects, it is inevitable that the lining and joints will rupture and cause leakage. Leakage during the water delivery period can cause loss of foundation soil, the collapse of canal slopes, and instability of lining. During the water outage period in winter, the water content of the base soil is generally higher due to the previous leakage, and the subzero temperature conditions and the higher fine-grained soil content in the base soil of the canal make the canal foundation have sufficient conditions for frost heave to occur. Also, the temperature in the seasonally frozen soil area drops slowly, the freezing rate is relatively low, and the water has sufficient time to migrate to the soil near the lining, which causes a significant frost heave effect [8]. The frost heave of the canal foundation soil in some areas can reach 15 cm [9]. Due to the mutual restraint between the slope lining and the floor lining and the upper berm, the frost heave deformation cannot be released, the resulting frost heave force causes the lining to break in extreme cases, further aggravating the leakage of the canal during the water delivery period. This repeated process leads the water conveyance canal to be in a vicious circulation of “frost heave, lining damage, leakage, and more severe frost heave.”

Many water conservancy projects were built in 1950s and 1960s and were limited by the low construction technology level and conditions at that time; most of the canal foundations used local soil materials containing a large number of fine particles during the construction process and then laying concrete lining slabs in the reservoir and large canal in order to prevent leakage. At the same time, small branch canals were rarely lined. Due to insufficient understanding of the frost heaving problem at that time and the long-term hydraulic erosion and repeated freeze-thaw effects in the later operation process, these projects are still frequently having damage issues, one of which is the frost heaving failure on the lining plate of the concrete lining canal. For example, Xiao et al. [10] found a serious frost heaving issue in the water conveyance canals lining in the Tarim irrigation district in Xinjiang, especially rigid lining canals. Qin et al. [4] found that the concrete slabs of reservoirs in Xinjiang were prone to cracks near the water level in winter under the effect of frost heave force and ice pressure. Sun et al. [11] found that there were also serious issues of freezing damage to lining panels in reservoirs and water conveyance canals in Heilongjiang Province. Tian’s et al. research [12] shows that the primary cause of the horizontal damage on the concrete lining of the drainage canal of the Qinghai-Tibet Railway subgrade is the horizontal frost heave force, and the main cause of the longitudinal damage is the uneven frost heave displacement. In some other cold region’s water conservancy projects, there are also lining damage caused by the frost heave effect [13–15].

To avoid the abovementioned problems, engineers used soil replacement, laying thermal insulation, and other measures to reduce frost heave damage effectively [7, 16]. However, many early built canals could not be rebuilt, and the problem of frost damage still occurs frequently. Therefore, many scholars have conducted numerous theoretical calculations and experimental studies on the frost heave failure mechanism of the concrete lining in frozen soil areas, which provide scientific references for the repair and treatment of canals with severe frost damage. Li et al. [17] and Li et al. [18] conducted a numerical simulation of the frost heave failure mechanism of the lining canals. However, there were many influencing factors to be considered in the simulation process, and the calculation process was complicated and cumbersome, which was very inconvenient in the application of engineering practice. Therefore, it is still necessary to analyze the force characteristics and failure mechanism of the lining under frost heave effects through simple and convenient theoretical calculation methods. Wang [19] investigated the lining damage of the canals in the cold regions and found that frost heave deformation was the main cause of the lining fracture. By a mechanical model, the lining slab was simplified into a simply supported beam. The force analysis of the concrete lining with different cross-section shapes under the simultaneous actions of frost heaving force, and freezing force was carried out using the material mechanics method. The calculation results were consistent with the field test. The failure position of the lining slope and the maximum stress cross-section were at 1/3 from the bottom of the canal, and the maximum normal stress of the bottom lining was in the middle position. Since then, many scholars have used this model to analyze the force and deformation characteristics of the lining under frost heave in different conditions [20, 21]. However, the above method did not consider the deformation coordinative of the lining and the base soil deformation during frost heave. To overcome this defect, researchers calculated the force characteristics of the lining under frost heave effects based on the Winkler elastic foundation beam theory and constructed a judgment criterion for lining frost heave failure. The calculation results were consistent with the on-site monitoring data [10, 22].

However, the abovementioned models are based on the deformation characteristics of the cross-section of the canals and studying the failure characteristics of the lining cross-sections. Due to differences in the geological conditions of the water conveyance canals subgrade in the longitudinal direction of the canal line, there will inevitably be uneven frost heave deformation along the longitudinal direction, and lining damage will also be caused under extreme conditions. There are few reports on the model and analysis of the longitudinal deformation and force characteristics of the lining under frost heave effects. This study takes the longitudinal deformation of the water conveyance canal lining in the cold region under the action of nonuniform frost heave as the research object, based on the Pasternak model to establish the mechanical model of the bottom lining and calculates the key parameters in the model. Combined with a typical engineering case, the longitudinal deformation and stress characteristics of the bottom lining are calculated and analyzed.

2. Model and Methods

Due to the differences in geology and construction conditions and the effects of long-term leakage and freeze-thaw cycles, the amount of frost heave at different locations in the longitudinal direction of the lining will be different, leading to the bending deformation of the lining. Because the slope lining is laid inclined vertically, the bending stiffness is relatively larger in the vertical direction, and it is not prone to cause damage in the longitudinal direction. The bottom lining is laid horizontally, and the bending stiffness is small in the vertical direction. Under the effect of nonuniform frost heave deformation, the cross-sectional stress is prone to be too large and leading to damage. Therefore, a mechanical model is established for the bottom lining. Figure 1 is a schematic diagram of the nonuniform frost heave deformation of the bottom lining. The x-direction is the longitudinal direction of the canal (canal line direction), and the y-direction is the vertical direction. Assuming that the AO section is the no-frost heave section, the BC section is a frost heave section, and its maximum frost heave deformation amount is Δ; the OB section is a frost heave transition section with a length of l. The coordinate system is established as shown in Figure 1; then, the deformation of the entire lining in the y-direction can be expressed by formula (1).

$$y_0 = \begin{cases} 0, & x < 0, \\ \dfrac{\Delta}{l} x, & l > x > 0, \\ \Delta, & x > l. \end{cases} \quad (1)$$

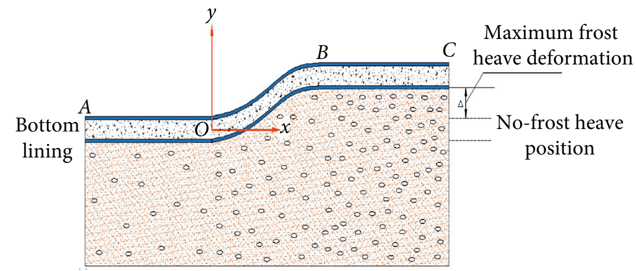

Figure 1: Schematic diagram of nonuniform frost heave deformation of bottom lining.

2.1. Basic Assumptions and Conventions. Due to the complex physical-mechanical properties of frozen soil and various external factors, the stress and strain of frozen soil are showing obvious characteristics of nonlinear, irreversible, and time-varying [22–24]. It must be a tedious work to solve the interaction between frozen soil and structure by considering all the influencing factors. To obtain meaningful data for practical engineering problems, combining the existing research and engineering practice experience, the following assumptions and agreements are made [10, 19, 22].

(1) Only consider the vertical deformation of the bottom lining caused by nonuniform frost heave in the longitudinal direction, ignore the influence of the axial force of the bottom lining, and the friction resistance between the bottom lining and the foundation soil on the longitudinal deformation, and simplify the mechanical analysis model as a plane strain problem.

(2) During the frost heave, the deformation of the lining and the foundation soil is in a coordinated and balanced state, and the process of failure of the lining is considered a quasistatic process. The stress analysis only considers the limit state at the maximum frost heave amount.

(3) The canal foundation is regarded as the elastic foundation obeying the Pasternak model, and the lining is regarded as the Euler–Bernoulli beam. The final deformation of the bottom lining is the deformation amount under restrictions such as slope lining, lining's weight, and so on.

(4) The deformation of the foundation soil only considers the range of frost penetration

2.2. Frozen Soil-Lining Interaction Model. The elastic foundation beam model can better reflect the interaction between the structure and soil. The Winkler model assumes that the surface displacement at each point of the soil medium is proportional to the stress acting at that point [25]. However, the mechanical activation behavior of the soil in the model is completely discontinuous, and the soil is completely irrelevant to the stresses or displacements of other points, even the nearest ones on the interface of the foundation, which is contrary to the actual mechanical activation behavior of the soil. To overcome the abovementioned defects, the two-parameter model introduces mutual mechanical action between the spring elements of the Winkler model to eliminate its discontinuous behavior [26]. Among many two-parameter models, the soil behavior model proposed by Pasternak assumes that there is a shearing interaction between the spring elements, and this shearing interaction is achieved by connecting the spring elements to a layer of vertical elements which can only produce lateral shearing deformation but not compressible [27]. During the freezing process of the soil mass, the elastic modulus and shear strength increase with the decrease of temperature [28]. Moreover, during the deformation of the superstructure, the foundation must bear a certain amount of shearing force. Therefore, the Pasternak model corresponds with the actual engineering situation of the mechanical properties of the frozen soil than the Winkler model.

Consider the bottom lining as an Euler–Bernoulli infinite long beam, which adopts the Pasternak model to the frozen ground, and the differential equation of displacement under plane strain conditions is [26, 27]

$$EIy^{(4)} - Gby^{(2)} + kby = q_0, \quad (2)$$

where b is the effective width, G is the shear stiffness of the elastic layer, k is the foundation coefficient, E is the elastic modulus of the beam, I is the moment of inertia of the beam, and q_0 is the normal load acting on the beam. According to assumption (6), the normal load acting on the lining is balanced with part of the foundation counterforce. Only the deformation of the lining caused by frost heave is considered. Therefore, equation (2) can be transformed into a homogeneous type for the solution.

Let $\beta = \sqrt[4]{kb/4EI}$, $\gamma = \sqrt{k/G}$, and $\rho = (\beta/\gamma)^2 = G/\sqrt{kEI/b}$. Then, the homogeneous differential equation corresponding to equation (2) becomes

$$y^{(4)} - 4\beta^2\rho y^{(2)} + 4\beta^4 y = 0. \tag{3}$$

2.3. Model Solution. The solutions of equation (3) can be divided into three cases, which are $\rho > 1$, $\rho = 1$, and $\rho < 1$. The condition of $\rho < 1$ satisfies most projects, which is also proved in the following parameter analysis and calculation of engineering examples [26]. Considering the boundary condition (1), the solution of the differential equation (3) can be expressed [28–30]. In the AO section, the frost heave deformation is 0, and the solution of equation (3) is

$$\begin{aligned} y_1 &= \left(A_1 e^{-\varphi_1 x} + A_2 e^{\varphi_1 x}\right)\cos \varphi_2 x \\ &\quad + \left(A_3 e^{-\varphi_1 x} + A_4 e^{\varphi_1 x}\right)\sin \varphi_2 x. \end{aligned} \tag{4a}$$

In the BC section, the frost heave deformation is Δ, and the solution of equation (3) is

$$\begin{aligned} y_3 &= \left(A_1 e^{-\varphi_1 x} + A_2 e^{\varphi_1 x}\right)\cos \varphi_2 x \\ &\quad + \left(A_3 e^{-\varphi_1 x} + A_4 e^{\varphi_1 x}\right)\sin \varphi_2 x + \Delta. \end{aligned} \tag{4b}$$

The OB section is the transition section, the frost heave amount is $(\Delta/l)x$, and the solution of equation (3) is

$$\begin{aligned} y_2 &= \left(A_5 e^{-\varphi_1 x} + A_6 e^{\varphi_1 x}\right)\cos \varphi_2 x \\ &\quad + \left(A_7 e^{-\varphi_1 x} + A_8 e^{\varphi_1 x}\right)\sin \varphi_2 x + \frac{\Delta}{l}x. \end{aligned} \tag{4c}$$

The above three equations (4a)–(4c) should meet the following boundary conditions:

When $x \longrightarrow \infty$, then $y_3 = \Delta$

When $x \longrightarrow -\infty$, then $y_1 = 0$

Substituting the boundary conditions into equations (4a)–(4c), the following equation can be obtained.

$$y_1 = A_2 e^{\varphi_1 x}\cos \varphi_2 x + A_4 e^{\varphi_1 x}\sin \varphi_2 x, \tag{5a}$$

$$y_3 = A_1 e^{-\varphi_1 x}\cos \varphi_2 x + A_3 e^{-\varphi_1 x}\sin \varphi_2 x + \Delta, \tag{5b}$$

$$\begin{aligned} y_2 &= \left(A_5 e^{-\varphi_1 x} + A_6 e^{\varphi_1 x}\right)\cos \varphi_2 x \\ &\quad + \left(A_7 e^{-\varphi_1 x} + A_8 e^{\varphi_1 x}\right)\sin \varphi_2 x + \frac{\Delta}{l}x. \end{aligned} \tag{5c}$$

There are still eight unknown coefficients in equations (5a)–(5c). Thus, the continuity conditions of the points O and B should also be satisfied.

When $x = 0$, $y_1 = y_2$, $y_1' = y_2'$, $y_1'' = y_2''$, $y_1''' = y_2'''$

When $x = l$, $y_2 = y_3$, $y_2' = y_3'$, $y_2'' = y_3''$, $y_2''' = y_3'''$

After substituting the above 8 continuity conditions into equations (5a)–(5c), simultaneously, the equations to obtain the equation coefficients $A_1 \sim A_8$ are as follows:

$$A_1 = \frac{\left[\Delta e^{\varphi_1 l}\left(3\varphi_1^2\varphi_2 e^{-\varphi_1 l} - \varphi_2^3 e^{-\varphi_1 l} + \varphi_1^3 \sin \varphi_2 l + \varphi_2^3 \cos \varphi_2 l - 3\varphi_1^2\varphi_2 \cos \varphi_2 l - 3\varphi_1\varphi_2^2 \sin \varphi_2 l\right)\right]}{\left[4l\varphi_1\varphi_2\left(\varphi_1^2 + \varphi_2^2\right)\right]}, \tag{6a}$$

$$A_2 = \frac{\left[\Delta e^{-\varphi_1 l}\left(3\varphi_1^2\varphi_2 e^{\varphi_1 l} - \varphi_2^3 e^{\varphi_1 l} - \varphi_1^3 \sin \varphi_2 l + \varphi_2^3 \cos \varphi_2 l - 3\varphi_1^2\varphi_2 \cos \varphi_2 l + 3\varphi_1\varphi_2^2 \sin \varphi_2 l\right)\right]}{\left[4l\varphi_1\varphi_2\left(\varphi_1^2 + \varphi_2^2\right)\right]}, \tag{6b}$$

$$A_3 = \frac{\left[\Delta e^{\varphi_1 l}\left(-3\varphi_1\varphi_2^2 e^{-\varphi_1 l} + \varphi_1^3 e^{-\varphi_1 l} - \varphi_1^3 \cos \varphi_2 l + \varphi_2^3 \sin \varphi_2 l + 3\varphi_1\varphi_2^2 \cos \varphi_2 l - 3\varphi_1^2\varphi_2 \sin \varphi_2 l\right)\right]}{\left[4l\varphi_1\varphi_2\left(\varphi_1^2 + \varphi_2^2\right)\right]}, \tag{6c}$$

$$A_4 = \frac{\left[\Delta e^{-\varphi_1 l}\left(3\varphi_1\varphi_2^2 e^{\varphi_1 l} - \varphi_1^3 e^{\varphi_1 l} + \varphi_1^3 \cos \varphi_2 l + \varphi_2^3 \sin \varphi_2 l - 3\varphi_1\varphi_2^2 \cos \varphi_2 l - 3\varphi_1^2\varphi_2 \sin \varphi_2 l\right)\right]}{\left[4l\varphi_1\varphi_2\left(\varphi_1^2 + \varphi_2^2\right)\right]}, \tag{6d}$$

$$A_5 = \frac{\left[\Delta\left(3\varphi_1^2 - \varphi_2^2\right)\right]}{\left[4l\varphi_1\left(\varphi_1^2 + \varphi_2^2\right)\right]}, \tag{6e}$$

$$A_6 = \frac{\left[\Delta e^{-\varphi_1 l}\left(-\varphi_1^3 \sin \varphi_2 l + \varphi_2^3 \cos \varphi_2 l + 3\varphi_1\varphi_2^2 \sin \varphi_2 l - 3\varphi_1^2\varphi_2 \cos \varphi_2 l\right)\right]}{\left[4l\varphi_1\varphi_2\left(\varphi_1^2 + \varphi_2^2\right)\right]}, \tag{6f}$$

$$A_7 = \frac{\left[\Delta\left(\varphi_1^2 - 3\varphi_2^2\right)\right]}{\left[4l\varphi_2\left(\varphi_1^2 + \varphi_2^2\right)\right]}, \tag{6g}$$

$$A_8 = \frac{\left[\Delta e^{-\varphi_1 l}\left(\varphi_1^3 \cos \varphi_2 l + \varphi_2^3 \sin \varphi_2 l - 3\varphi_1\varphi_2^2 \cos \varphi_2 l - 3\varphi_1^2\varphi_2 \sin \varphi_2 l\right)\right]}{\left[4l\varphi_1\varphi_2\left(\varphi_1^2 + \varphi_2^2\right)\right]}. \tag{6h}$$

After obtaining the solution of the differential equation (3) of the bottom lining, the rotation angle (θ), bending moment (M), and shearing force (Q) of the lining can be calculated.

$$\theta = y', \tag{7}$$

$$M = -EIy'', \tag{8}$$

$$Q = Q_c + Q_s = -EIy''' + Gby'. \tag{9}$$

In equation (9), the first term of shear force is the shearing force of the lining slab, and the second one is the shearing force of the elastic foundation.

2.4. Model Parameters

2.4.1. Foundation Coefficient k. Generally, the foundation coefficients can be obtained through experiments or calculating the mechanical parameters of the foundation soil [25]. However, the interaction between the frozen soil ground and the lining is that the displacement of the surface of the foundation occurs with the frost heave. However, due to the external constraints, part of the frost heave displacement is restricted, resulting in frost heave force on the structures. Therefore, the relationship between frost heave force and frost heave displacement can be regarded as the relationship between the pressure on the foundation surface and the displacement at that point. Xiao et al. [10] calculated the lateral deformation of the canal lining and obtained the foundation coefficient considering the interaction process between the lining and the foundation during the frost heave deformation process which can be expressed as

$$k = \frac{E_f}{H_f}, \tag{10}$$

where E_f is the elastic modulus of frozen soil, and H_f is the depth of frozen penetration.

This is the same as the foundation coefficient calculation method of Kanie et al. [28] in calculating the nonuniform frost heave of oil pipelines in the frozen soil layer.

In the usual melted soil foundation, Tanahashi [26] simplified Vesic's formula and recommended to calculate the foundation coefficient under the condition of one-dimensional plane strain by the following formula:

$$k' = \frac{(1-\mu)E_f}{(1+\mu)(1-2\mu)H}. \tag{11}$$

When taking the Poisson ratio $\mu = 0.2, 0.25, 0.3$, and 0.35, the ratio k'/k calculated by equations (10) and (11) is shown in Figure 2. H is the depth of an elastic layer. It can be seen that the ratio of the foundation coefficient obtained by the two calculation methods approaches one as the Poisson ratio decreases. The Poisson ratio of the frozen soil decreases as the temperature decreases [23], indicating that the frozen soil coefficient calculation method obtained in this study is in accordance with the engineering reality.

2.4.2. Foundation Shear Stiffness G. There are many methods to determine the shear stiffness (G) of the foundation, but the results are different. For example, Tanahashi [26], Song et al. [31], and Li [32] used the following formula to calculate the shear stiffness of the foundation:

$$G = \frac{E_f t}{6(1+\mu)}, \tag{12}$$

where t is the thickness of the shear layer.

It can be seen that with the difference in the thickness of the shear layer, the variation range of the foundation shear stiffness is very large. In actual engineering, the thickness of the shear layer is related to various factors such as soil physical properties, beam properties and dimensions, external load characteristics, and so on. Therefore, a constant foundation shear stiffness is unable to be selected [33]. To facilitate calculation and analysis, Ma et al. [34] determined simply the relationship between the foundation stiffness coefficient and the foundation coefficient by the following formula:

$$R = \frac{G}{k}. \tag{13}$$

When R is 0, the model degenerates into a Winkler elastic foundation beam model.

3. Parameters Analysis

It can be seen from equations (2) and (3) that the internal force of the lining is affected by the foundation coefficient k, the shear modulus G (R), the transition length l, and the frost heave displacement Δ. This section will analyze and discuss

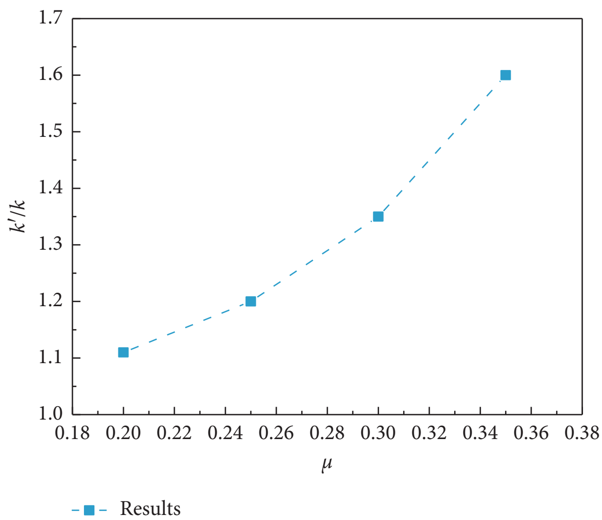

Figure 2: Values of $k\prime/k$ for different Poisson ratios.

the internal force of the lining under the effects of the abovementioned parameters.

3.1. Effects of Foundation Coefficient k. It can be seen from formula (10) that when considering the interaction between frost heave deformation and frost heave force of the bottom lining, the foundation coefficient is related to the elastic modulus and the depth of frozen penetration. In the following parameter analysis, the typical frozen depth in Xinjiang, China, can be selected as 2 m [35]. The elastic modulus of the frozen soil layer is closely related to the physical properties, moisture content, and temperature of the soil mass [23]. Because the coarse-grained soil is frost heaving insensitive soil, the main cause of frost heaving deformation is silty clay. According to the data of Wang et al. [36] and the water transferring project from the Irtysh River to Urumqi, the selected foundation coefficients are 2.5×103, 13.8×103, 33×103, 45×103, and $58\times 103\,\mathrm{kN{\cdot}m^{-3}}$ for analysis. Other relevant parameters are $EI = Ebh3{\cdot}12^{-1} = 58666\,\mathrm{kN{\cdot}m^2}$, $b = 4\,\mathrm{m}$, $h = 0.2\,\mathrm{m}$, $E = 2.2\times 106\,\mathrm{kPa}$, $R = 1$, $l = 10\,\mathrm{m}$, and $\Delta = 0.02\,\mathrm{m}$. The maximum normal stress on the cross-section is calculated by $\sigma_{\max} = My_{\max}/I$, and the maximum shear stress on the cross-section of the lining slab is calculated by $\tau_{\max} = 3Q_s/2A$. The calculation results are shown in Figures 3–5.

Figure 3 shows the distribution of lining deflection and rotation angle along the longitudinal direction for different foundation coefficients. It can be seen from Figure 3(a) that the deflection of the lining completely coincides when foundation coefficients are different. At the beginning ($x = 0$) and endpoint ($x = 10$) of the transition section, the deflection did not suddenly become 0 but smoothly transitioned to 0. The deflection in the frost heave section is 0.02 m consistent with the set boundary conditions. It can be seen from Figure 3(b) that the foundation coefficient has a certain effect on the rotation angle of the beam. With the increase of the foundation coefficient, the changing trend of the rotation angle is more intense. At the midpoint of the transitional section ($x = 5$), the rotation angle is 0. At the same time, Figure 3 shows that the deflection and rotation angle of the lining are in line with the actual engineering experience, and the calculation method and process in the previous section are verified to be correct.

Figure 4 shows the distribution laws of the maximum normal stress and the maximum shear stress of the lining slab along the longitudinal direction at different foundation coefficients. From the figure, the dangerous points where the maximum stress is located is at the beginning and the endpoint of the transition. With different foundation coefficients, the maximum normal stress and maximum shear stress at the attachment of the dangerous points change intensely, and the change at other positions is relatively slow.

Figure 5 shows the variation law of the maximum normal stress and maximum shear stress of the dangerous section of the bottom lining with the changing foundation coefficient. It can be seen that as the foundation coefficient increases, the maximum normal stress and the maximum shear stress increase nonlinearly, and the growth rate gradually decreases, satisfying the power function relationship.

3.2. Effects of Shear Stiffness G. The change in shear stiffness reflects the interaction between the spring elements of the soil mass. At the same time, it can reflect the continuity of foundation deformation to a certain extent [25]. According to formula (13), the change in shear stiffness can be expressed by the coefficient R. In this section, $R = 1$, 0.8, 0.5, 0.01, and 0 are used for analysis. When R is 0, the model degenerates into the Winkler model. Other parameters are $k = 33000\,\mathrm{kN{\cdot}m^{-3}}$, $l = 10\,\mathrm{m}$, and $\Delta = 0.02\,\mathrm{m}$. Figure 6 shows the distribution situation of deflection and rotation angle of the bottom lining at different values of R. It can be seen that as the R decreases, the maximum normal stress and shear stress at the beginning and endpoint of the transition section increase because the load on the shear layer decreases lead to the lining bears more load.

Figure 7 shows the variation law of maximum normal stress and shear stress of dangerous section of bottom lining with different R values. It can be seen that as the R value increases, the two stresses significantly decrease, the maximum normal stress decreases by 24.4%, and the maximum shear stress decreases by 37.2%, indicating that the shear resistance of frozen soil ground has a significant impact on the stress distribution characteristics of the lining. The frost heave amount increases continuously while the temperature decreases, while the shear stiffness of the foundation will also increase with it. The former increases the lining stress, while the latter reduces the lining stress, so the internal force of the lining changes couple mutually with them during the frost heave process.

3.3. Effects of Different Transition Length l. Due to the differences in geological conditions including water, heat, and load during construction and operation, the frost heave characteristics of the canal foundation soil at different positions in the longitudinal direction are different, causing the

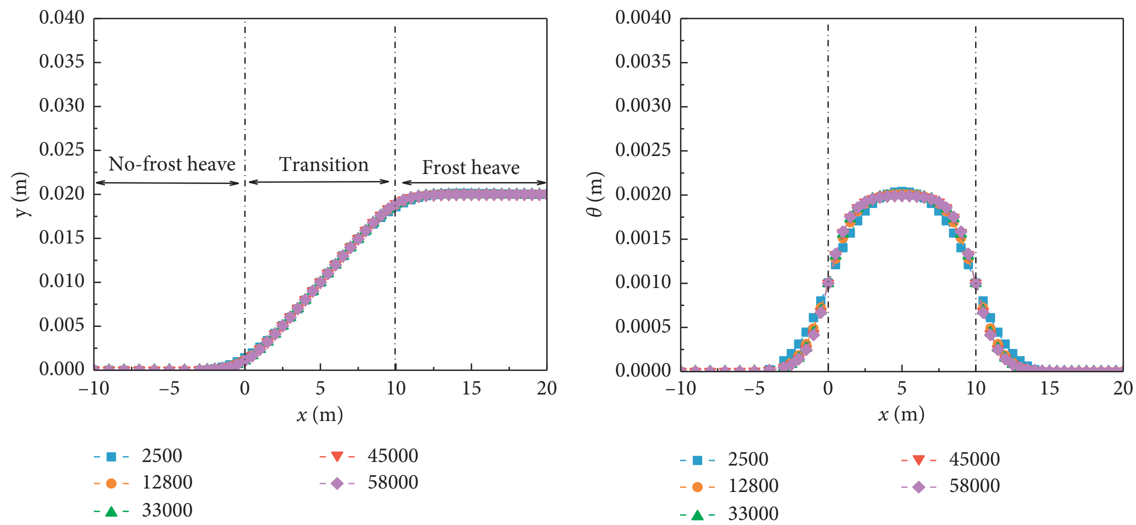

(a) (b)

Figure 3: Effects of different foundation coefficients on the distribution of lining deflection (a) and rotation angle (b).

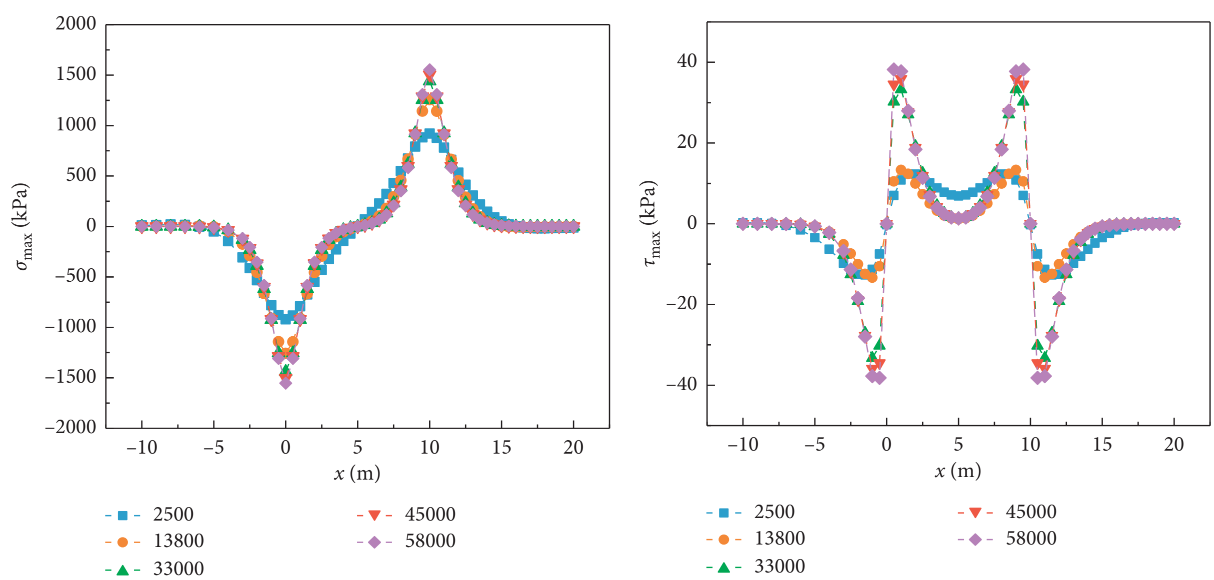

(a) (b)

Figure 4: Distribution law of maximum normal stress (a) and maximum shear stress (b) of bottom lining under different foundation coefficients.

transition section length to change. In this section, the transition section length is 5, 10, 15, and 20 m for analysis. Other parameters are $k = 33000\,\text{kN·m}^{-3}$, $R = 1$, and $\Delta = 0.02$ m.

Figure 8 shows the distribution law of the maximum normal stress and the maximum shear stress of the bottom lining cross-section at different transition lengths. It can be seen that as the transition section length increases, the maximum normal stress and shear stress of the dangerous section decrease, which is in line with the actual engineering situation.

Figure 9 shows the effect of different transition section lengths on the maximum normal stress and shear stress of the dangerous section. It can be seen that as the transition section length increases, the maximum stress and shear stress decrease significantly and change nonlinearly.

3.4. Effects of Different Frost Heave Amount Δ. The canals in the cold regions will inevitably face the frost heaving issues. Different soil properties, temperature, and moisture conditions cause different frost heave amounts. It is pointed out

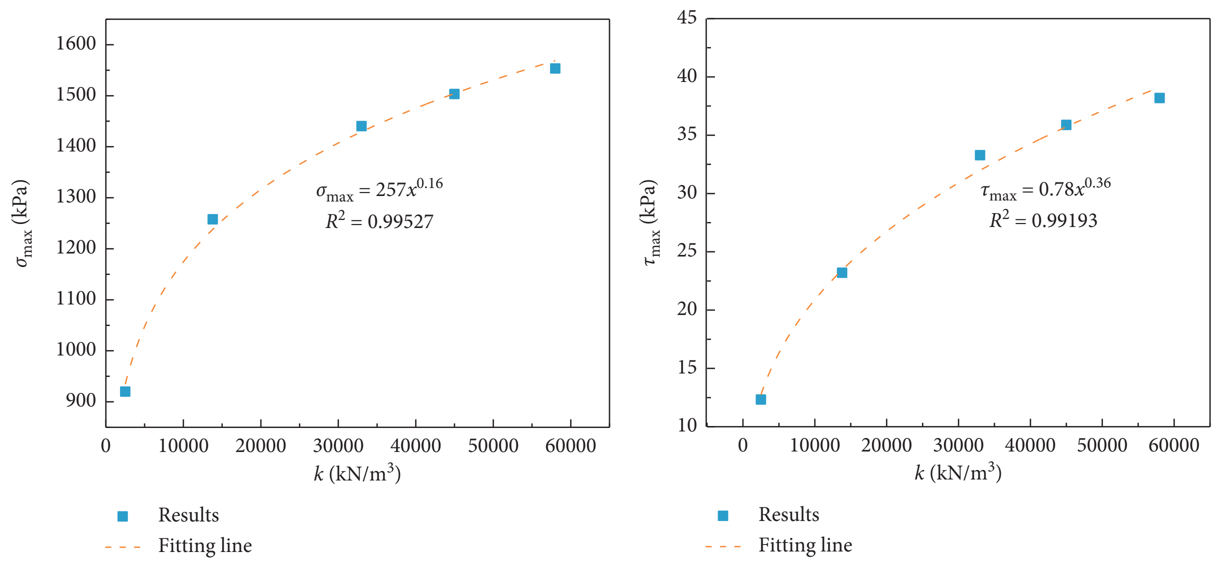

(a) (b)

Figure 5: Variation law of maximum normal stress (a) and maximum shear stress (b) of the dangerous section with the changing foundation coefficients.

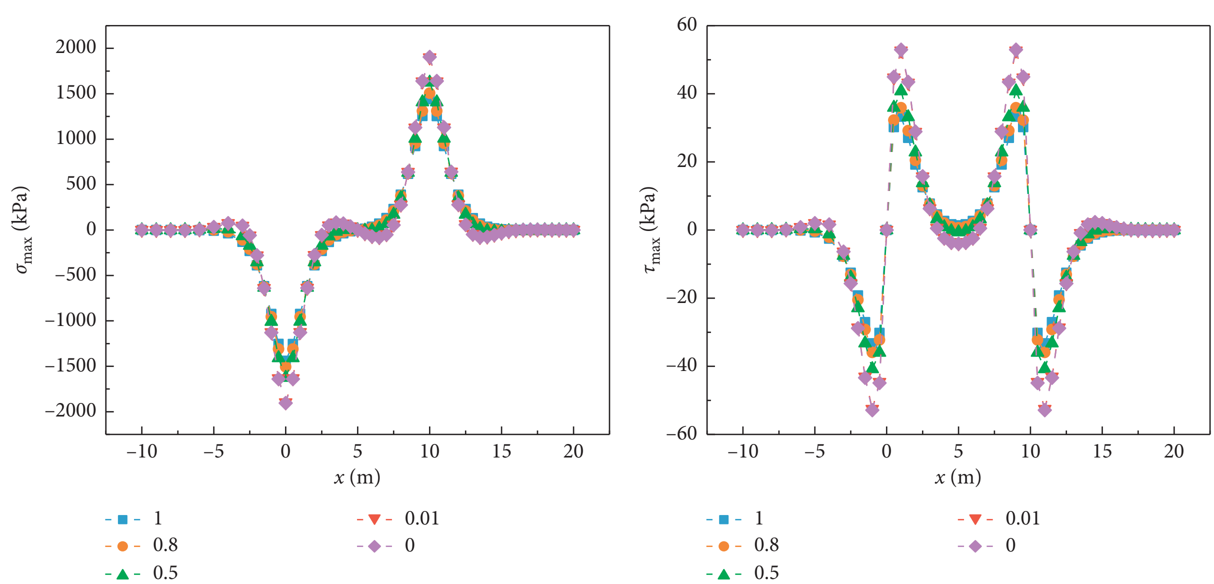

(a) (b)

Figure 6: Distribution situation of maximum normal stress (a) and maximum shear stress (b) of bottom lining at different R values.

in the standard designing specification for antifrost heaving of the canal project that the concrete lining can be allowed to generate a certain amount of frost heave displacement during the canal construction, and the purpose of reducing frost heave force and costs has achieved [37]. However, in the actual construction and operation process, due to the inevitable leakage and possible external water supply, the frost heave of the foundation soil of the canal may exceed the allowed design value, causing damage to the lining. In this section, 0.01, 0.02, 0.04, 0.06, and 0.08 m of frost heave amounts are selected for analysis. Other parameters are $k = 33000\,\mathrm{kN{\cdot}m^{-3}}$, $R = 1$, and $l = 20$ m.

Figure 10 shows the maximum normal stress and shear stress of the lining cross-section under different frost heave amounts. It can be seen that the frost heave amount has a significant effect on the stress of the dangerous section.

Figure 11 shows the effect of different frost heave amounts on the maximum normal stress and shear stress of the dangerous section. It can be seen that the maximum normal stress and shear stress increase linearly with the

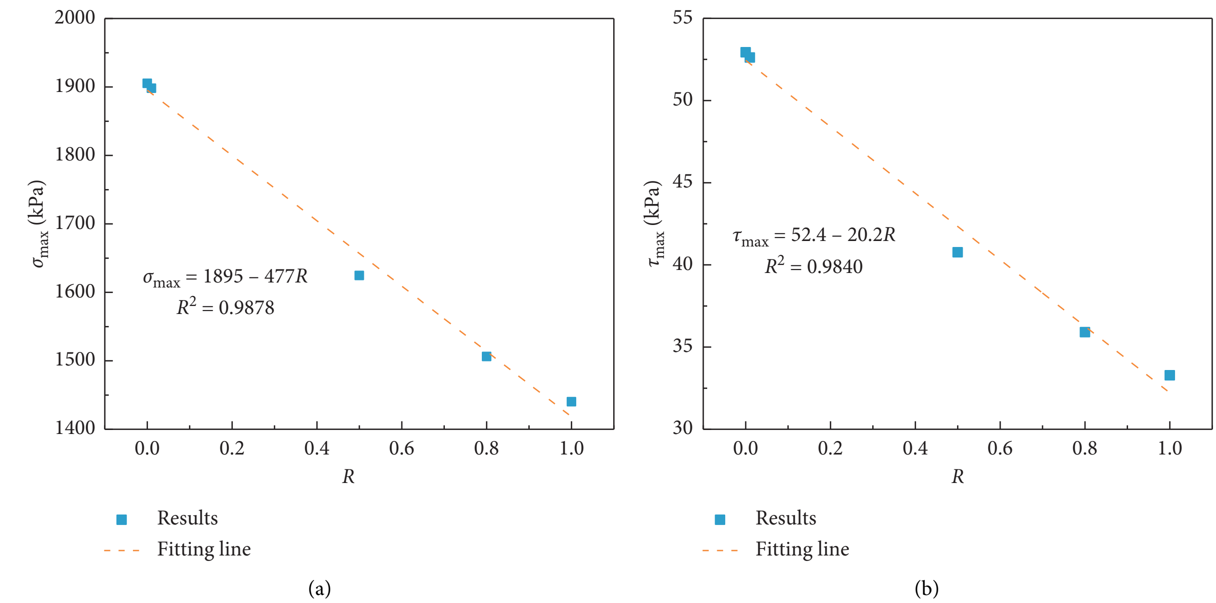

Figure 7: Effects of different R values on the maximum normal stress (a) and maximum shear stress (b) of the dangerous section.

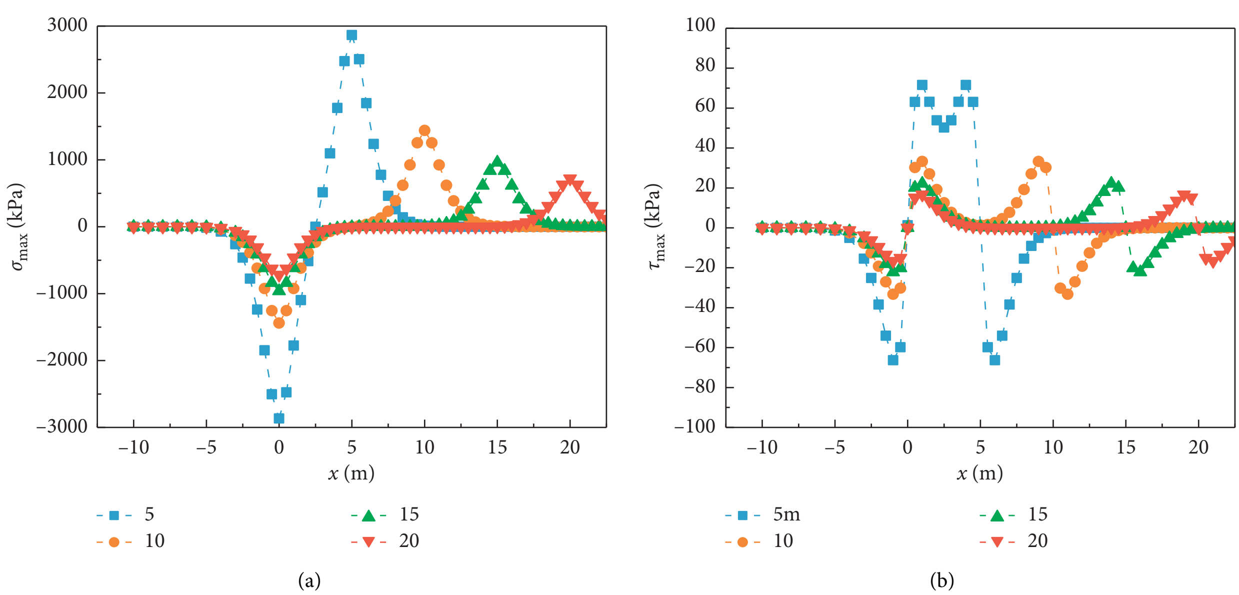

Figure 8: Distribution law of maximum normal stress (a) and maximum shear stress (b) of the cross-section at different transition section lengths.

increase of frost heave amount. When the frost heave amount is 0, the maximum stress is also 0.

4. Engineering Case

In the Tarim irrigation district of Xinjiang, more than 2355 km of canals have been constructed. Due to the abundant surface water and relatively shallow embedment depth, the canal lining has severe frost heave failure [10]. The typical cast-in-place canal lining is concrete lining (C15), with a slab thickness of 0.08 m and a bottom width of 2 m. The minimum temperature of the frozen soil layer on the slope and the canal's bottom in winter is −14.7°C and −9.4°C, respectively. The elastic modulus of the frozen soil layer takes the value of the minimum temperature in winter, which is safe, and the frozen depth of the canal is about 1 m. According to site observations, the maximum frost heave displacement at the bottom canal is 0.022 m. However, as the groundwater level changes, the maximum frost heave displacement may increase. According to estimates, when the

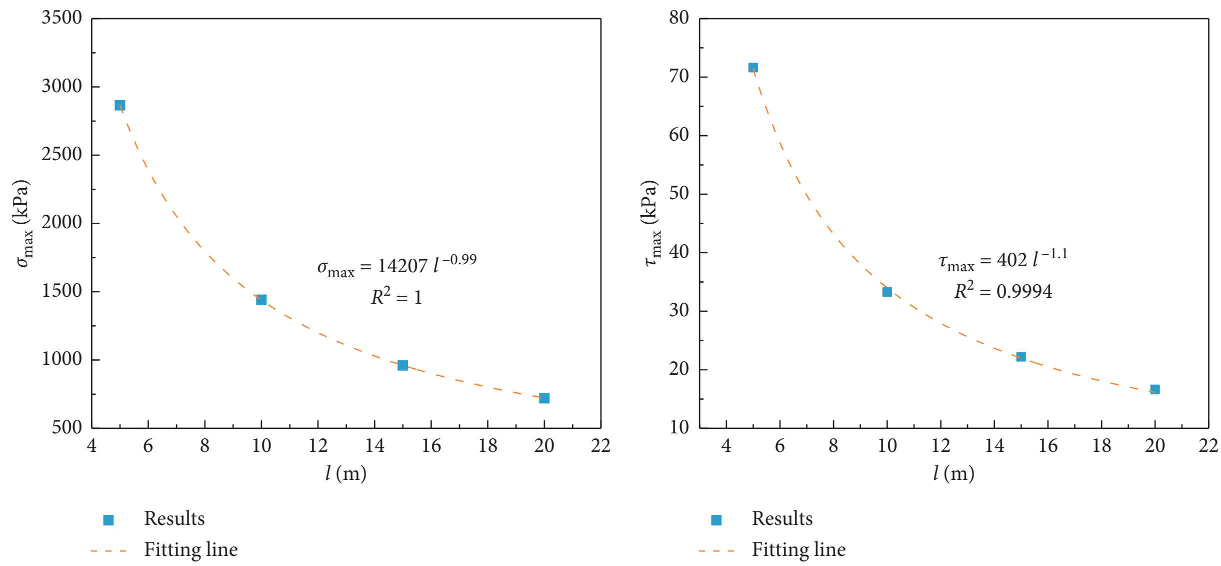

(a) (b)

Figure 9: Effects of different transition lengths on the maximum normal stress (a) and maximum shear stress (b) of the dangerous section.

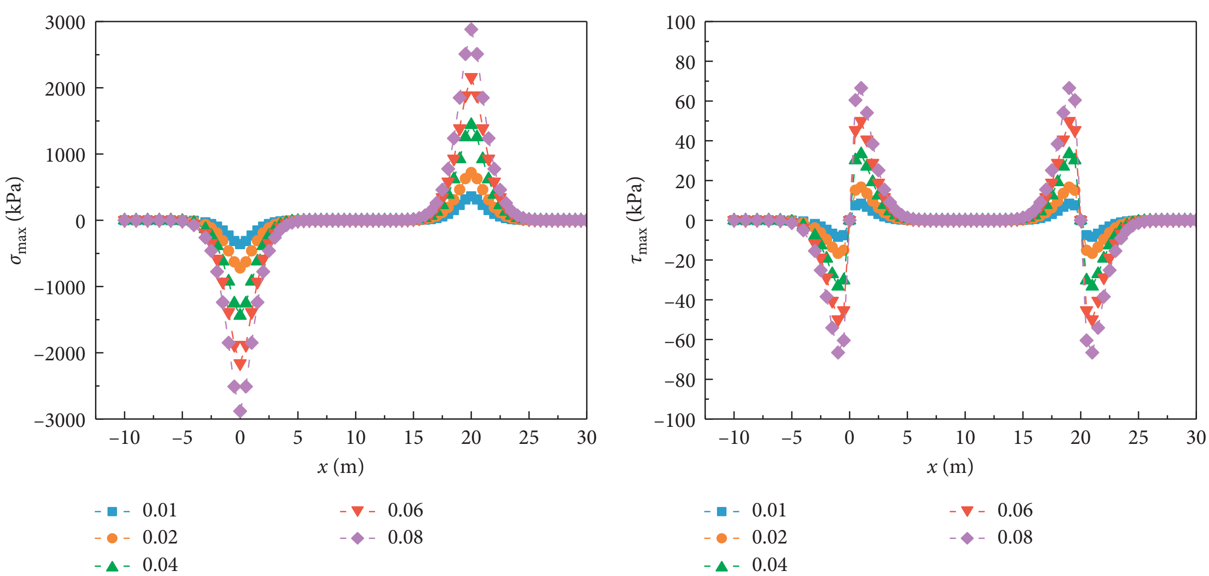

(a) (b)

Figure 10: Distribution law of maximum normal stress and maximum shear stress of the lining cross-section under different frost heave amounts.

groundwater level is 3.0, 3.5, 4.0, 4.5, and 5.0 m, the maximum frost heave amounts are 0.031, 0.022, 0.015, 0.01, and 0.005 m, respectively [10].

Xiao et al. [10, 38] monitored and calculated the horizontal deformation of the lining, but the longitudinal deformation caused by nonuniform frost heave has not been studied. Therefore, the longitudinal deformation is analyzed according to the calculation method in this study. The selected parameters are $E = 2.2 \times 104$ MPa, $E_f = 2.35$ MPa, $k = 2.35$ MPa·m^{-1}, $R = 1$, $G = 2.35$ MPa·m, $EI = 1.877$ MPa, and $l = 10$ m.

Figure 12 shows the effect of different frost heave amounts on the maximum normal stress and shear stress of the dangerous section of the lining. It can be seen that with the increase of frost heave amounts, the maximum normal stress and shear stress of the dangerous section increase linearly, and the growth speed at the transition section of 5 m is greater than that at the transition section of 10 m. The maximum tensile stress of C15 concrete lining is 1.27×103 kPa [39], and the designing tensile stress is 0.91×103 kPa. Therefore, when the transition section is 5 m and the frost heave amount reach 0.022 m, the lining is about

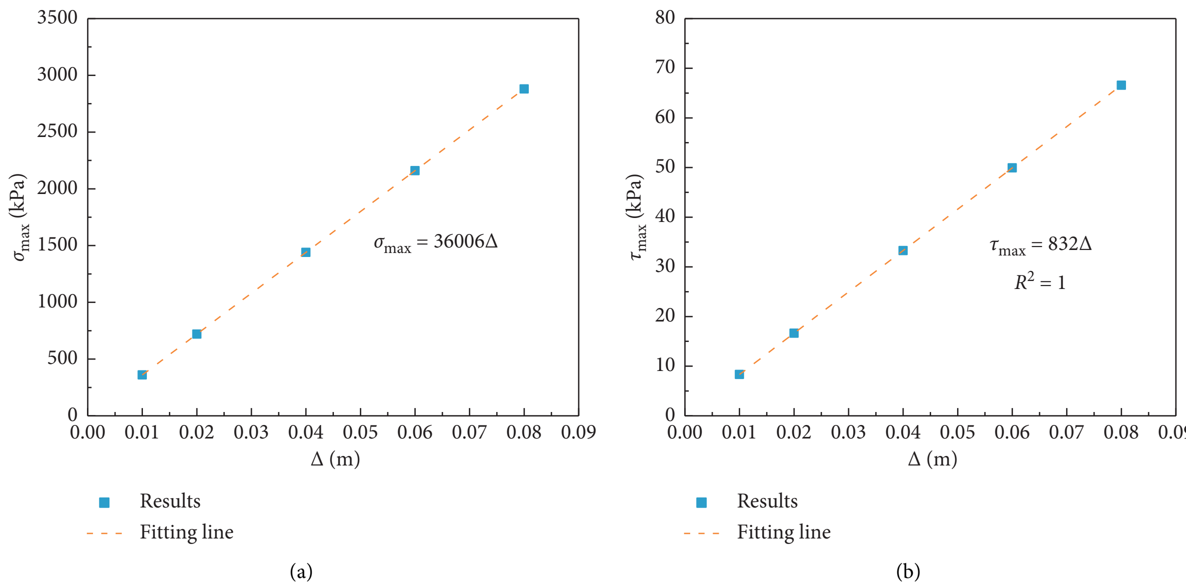

Figure 11: Effects of different frost heave amounts on maximum normal stress (a) and maximum shear stress (b).

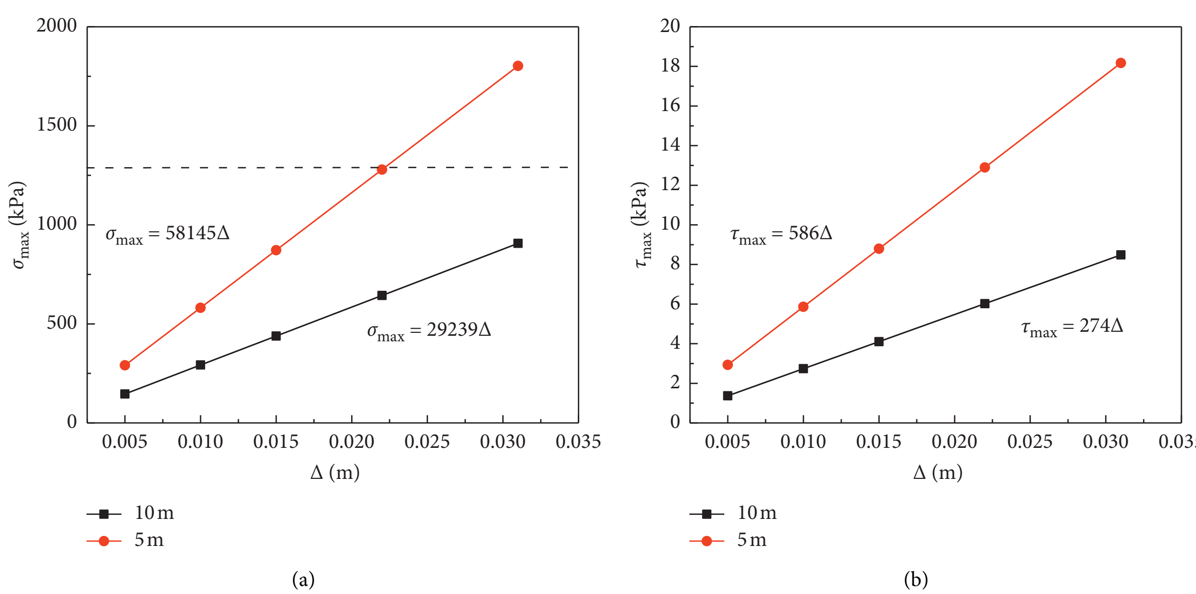

Figure 12: Effects of different frost heave amounts on the maximum normal stress (a) and maximum shear stress (b) of the dangerous section.

to at the limit state, which is close to the maximum allowable frost heave amount for designing specification. When the transition section is 10 m and the frost heave amount reach 0.043 m, the lining is at the limit state, which is greater than the maximum allowable frost heave amount for designing specification. The maximum shear stress of the cross-section is far less than the ultimate shear strength and is in a safe state.

Figure 13 shows the effect of different transition lengths on the maximum normal stress and shear stress of the dangerous section when the frost heave amount $\Delta = 0.031$ m. It can be seen that as the transition section length increases, the maximum normal stress and shear stress decrease significantly. When the transition section length is 7 m, the maximum normal stress is lower than the ultimate tensile stress of the lining. When the transition section length is

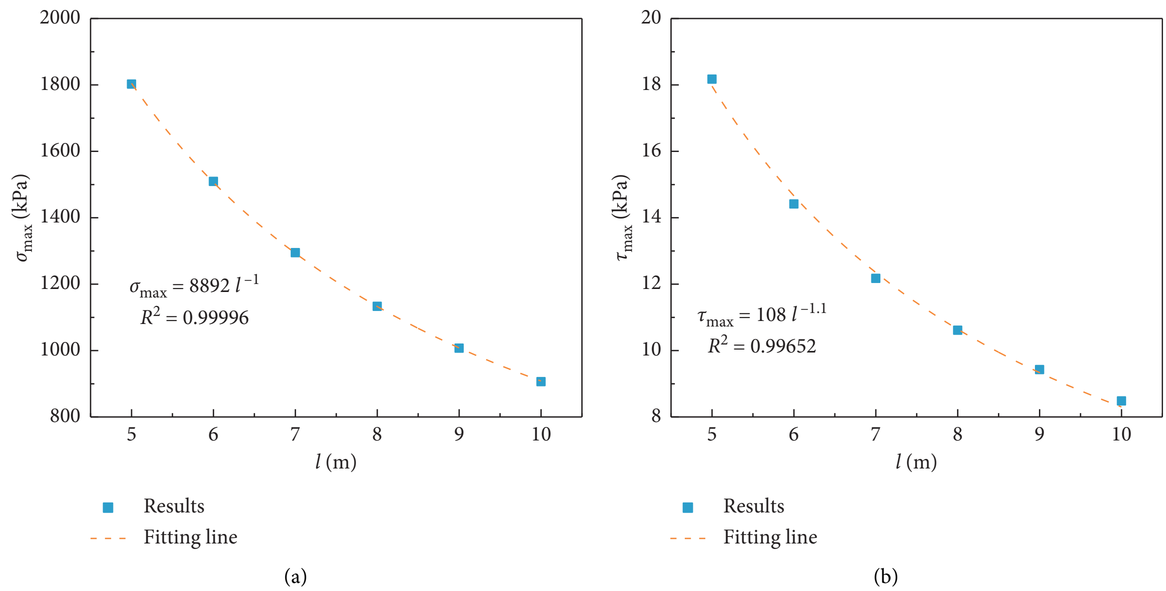

Figure 13: Effects of different transition lengths on the maximum normal stress (a) and maximum shear stress (b) of the dangerous section when the frost heave amount $\Delta = 0.031$ m.

9.8 m, the maximum normal stress is lower than the designing tensile stress of the lining. Therefore, it is recommended to design expansion joints with a longitudinal separation of at least 7 m in the canal design process to relieve the internal stress of the lining.

5. Conclusion

To analyze the longitudinal mechanical characteristics of the canal lining in the cold regions under nonuniform frost heave, based on the Pasternak elastic foundation beam model, the longitudinal deformation model of the bottom lining is established. The changing law of the maximum tensile stress and shear stress in the lining are analyzed when the key parameters k, G, L, and Δ change in the model. Finally, in conjunction with engineering example, the effects of frost heave amounts and transition section lengths on the safety of a typical canal lining in the Tarim irrigation area in Xinjiang are analyzed. The following conclusions are obtained:

(1) Due to the low bending rigidity of the concrete lining, the bottom lining along the longitudinal direction is simplified. The longitudinal lining is regarded as a beam, and the force acting on the lining is simplified. The Pasternak elastic foundation beam model of the bottom lining under the action of longitudinal nonuniform frost heave is established, and the analytical solution of the model is given.

(2) Calculate the influence of factors such as foundation coefficient, foundation shear modulus, transition section length, and frost heave amount on the internal force of the lining. The dangerous section of the lining is at the beginning and endpoint of the transition section. The maximum normal stress and shear stress of the dangerous section increase as the foundation coefficient and frost heave amount increase and the shear modulus and transition section length decrease.

(3) The frost heave amount continuously increases while the temperature of frozen soil foundation decreases, but the shear stiffness of the foundation will also increase with it. The former increases the lining stress, while the latter reduces it, so during the frost heave process, the internal force of lining changes are coupled with them.

(4) Through the analysis of the longitudinal deformation of the lining of a water delivery canal under nonuniform frost heave action in the Tarim irrigation district of Xinjiang, when the local maximum frost heave amount is 0.031 m and the transition section length is less than 7 m, the maximum normal stress of the dangerous lining section is greater than its maximum tensile strength. Thus, it is recommended to set expansion joints with a separation of at least 7 m on the floor lining of this section of the channel.

Because it is relatively difficult to monitor the longitudinal frost heave deformation of the lining, the calculation results in this study cannot be verified by experimental data at present. However, the comparison with the actual engineering phenomenon shows that the analytical solution is correct. In the follow-up work, on-site monitoring of longitudinal deformation and indoor model tests will be carried out to further study the model.

Data Availability

The data used to support the findings of this study are included within the article.

Conflicts of Interest

The authors declare that they have no conflicts of interest.

Acknowledgments

This work was supported by the National Natural Science Foundation of China (42001058 and 51778275) and Longyuan Young Innovative and Entrepreneurial Talents (2020RCXM120).

References

[1] Y. Zhou, D. Guo, G. Qiu, G. Chen, and S. Shu, *Geocryology in China*, Science Press, Beijing, China, 2000.
[2] O. B. Andersland and B. Landanyi, *Frozen Ground Engineering*, John Wiley & Sons, Inc. and ASCE American Society of Civil Engineering, Hoboken, NJ, USA, 2nd edition, 2004.
[3] S. Zhang, Z. Pu, J. Li et al., "Response of the maximum depth of seasonal freezing to the cumulated negative temperature on Xingjiang," *Journal of Glaciology and Geocryology*, vol. 35, no. 6, pp. 1419–1427, 2013.
[4] Z. Qin, Y. Lai, Y. Tian, and F. Yu, "Frost-heaving mechanical model for concrete face slabs of earthen dams in cold regions," *Cold Regions Science and Technology*, vol. 161, pp. 91–98, 2019.
[5] Z. Cai, H. Chen, Y. Huang, and C. Zhang, "Failure mechanism of canal slopes of expansive soils considering action of wetting-drying cycles," *Chinese Journal of Geotechnical Engineering*, vol. 41, no. 11, pp. 1977–1982, 2018.
[6] A. Zia and M. Ali, "Behavior of fiber reinforced concrete for controlling the rate of cracking in canal-lining," *Construction and Building Materials*, vol. 155, pp. 726–739, 2017.
[7] P. He and W. Ma, "Study of canals in cold regions of China: achievements and prospects," *Journal of Glaciology and Geocryology*, vol. 42, no. 1, pp. 182–194, 2020.
[8] Q. Miao, F. Niu, Z. Lin, J. Luo, and M. Liu, "Comparing frost heave characteristics in cut and embankment sections along a high-speed railway in seasonally frozen ground of Northeast China," *Cold Regions Science and Technology*, vol. 170, Article ID 102921, 2020.
[9] R. Zhang and Z. Wang, "The progress of the research on the prevention and cure of the irrigation channel frozen injury in the seasonal frozen soil," *Agricultural Research in Arid Areas*, vol. 25, no. 3, pp. 236–240, 2007.
[10] M. Xiao, Z. Wang, Q. Liu, Y. Wang, J. Ge, and X. Wang, "Elastic foundation beam model of frost heave damage of trapezoidal canal considering interaction between frozen soil and lining structure," *Shuli Xuebao*, vol. 48, no. 10, pp. 1229–1239, 2017.
[11] J. Sun, G. Li, Q. Zhang, and H. Zhang, "Stability analysis of earth-rock dam slope on the action of ice cover," *Journal of Heilongjiang Hydrology Engineering College*, vol. 1, pp. 26–28, 1998.
[12] Y. Tian, Z. Yang, B. Tai, Y. Li, and Y. Sheng, "Damage and mitigation of railway embankment drainage trench in warm permafrost: a case study," *Engineering Geology*, vol. 261, Article ID 105276, 2019.
[13] K. Hirayama, *Thrust on Hydraulic Structures Due to the Thermal Expansion of Ice Cover*, Vol. 9, Technology Rep Iwate University, Morioka, Japan, 1976.
[14] X. Liu, P. Liu, and H. Li, "Application of fracture mechanics to analyze frost breakage of reservoir revetments in cold regions," *Journal of Glaciology Geocryology*, vol. 32, no. 3, pp. 543–548, 2010.
[15] R. Sadzevicius, V. Damulevicius, and R. Skominas, "The technical state of earth dams in Lithuania," *Journal of Environment Engineering Landsec Management*, vol. 21, no. 3, pp. 180–188, 2013.
[16] P. An, Y. Xing, and A. Zhang, "Thickness calculation and numerical simulation of insulation board for canal using partial insulation method," *Transaction of the CSAE*, vol. 29, no. 17, pp. 54–62, 2013.
[17] S. Li, M. Zhang, Y. Tian, W. Pei, and H. Zhong, "Experimental and numerical investigations on frost damage mechanism of a canal in cold regions," *Cold Regions Science and Technology*, vol. 116, pp. 1–11, 2015.
[18] S. Li, Y. Lai, M. Zhang, W. Pei, C. Zhang, and F. Yu, "Centrifuge and numerical modeling of the frost heave mechanism of a cold-region canal," *Acta Geotechnica*, vol. 14, no. 4, pp. 1113–1128, 2019.
[19] Z. Wang, "Establishment and application of mechanics models of frost heaving damage of concrete lining trapezoidal open canal," *Transaction of the CSAE*, vol. 3, pp. 24–29, 2004.
[20] H. Jiang, Z. Wang, Y. Wang, Q. Liu, and J. Ge, "Study on anti-frost heave mechanism and application of reasonable joint for large size trapezoidal canal with arc-bottom," *Transaction of the CSAE*, vol. 50, no. 8, pp. 947–959, 2019.
[21] J. Ge, Z. Wang, Y. Niu et al., "Elastic foundation beam unified model for ice and frost damage concrete canal of water delivery under ice cover," *Transaction of the CSAE*, vol. 36, no. 1, pp. 90–98, 2020.
[22] Z. Li, X. Yao, L. Yang, H. Shao, and Z. Wang, "Frost heave mechanical model of concrete lining trapezoidal canal based on elastic foundation beam theory," *Transaction of the CSAE*, vol. 35, no. 15, pp. 110–117, 2019.
[23] Z. Zhou, W. Ma, S. Zhang, Y. Mu, and G. Li, "Effect of freeze-thaw cycles in mechanical behaviors of frozen loess," *Cold Regions Science and Technology*, vol. 146, pp. 9–18, 2018.
[24] Z. Zhou, W. Ma, S. Zhang, Y. Mu, and G. Li, "Experimental investigation of the path-dependent strength and deformation behaviors of frozen loess," *Engineering Geology*, vol. 265, Article ID 105449, 2020.
[25] A. Selvadurai, *Elastic Analysis of Soil-Foundation Interaction*, Elsevier Scientific, Amsterdam, Netherlands, 1979.
[26] H. Tanahashi, "Formulas for an infinitely long Bernoulli-euler beam on the pasternak model," *Soils and Foundations*, vol. 44, no. 5, pp. 109–118, 2004.
[27] Z. Feng and R. Cook, "Beam elements on two-parameter elastic foundations," *Journal of Engineering Mechanics*, vol. 109, no. 6, pp. 1390–1402, 1983.
[28] S. Kanie, S. Akagawa, K. Kim, and T. Mikami, "Estimation method of frost heaving for chilled gas pipeline buried in frost susceptible soil," *International Conference on Cold Regions Engineering*, pp. 1–12, 2006.
[29] I. Coskun, H. Engin, and A. Ozmutlu, "Response of a finite beam on a tensionless Pasternak foundation under symmetric and asymmetric loading," *Structural Engineering and Mechanics*, vol. 30, no. 1, pp. 21–36, 2008.
[30] L. Huang, Y. Sheng, X. Hu, S. Wang, X. Huang, and B. He, "Stress analysis of pipelines subjected to frost heave based on the theory of elastic foundation beam," *Journal of Glaciology and Geocryology*, vol. 40, no. 1, pp. 70–78, 2018.
[31] G. Song, X. Bian, and J. Jiang, "Deformation behaviors and bearing capacity of geosynthetics-reinforced pavement," *Journal of Shanghai Jiaotong University*, vol. 45, no. 5, pp. 653–658, 2011.

[32] F. Li, "Research on superposition method of interaction between soil frost heave and beams on foundation," *Rock and Soil Mechanics*, vol. 30, no. 1, pp. 79–85, 2009.

[33] Y. Liang, Y. Li, and M. Huang, "Simplified method for laterally loaded piles based on Pasternak double-parameter spring model for foundations," *Chinese Journal of Geotechnical Engineering*, vol. 35, pp. 300–304, z1, 2013.

[34] X. Ma, J. W. Butterworth, and G. C. Clifton, "Static analysis of an infinite beam resting on a tensionless Pasternak foundation," *European Journal of Mechanics—A/Solids*, vol. 28, no. 4, pp. 697–703, 2009.

[35] X. Xu, *Physics of Frozen Soil*, Science Press, Beijing, China, 2010.

[36] S. Wang, J. Qi, F. Yu, and X. Yao, "A novel method for estimating settlement of embankments in cold regions," *Cold Regions Science and Technology*, vol. 88, pp. 50–58, 2013.

[37] SL23-2006, *Design Code for Anti-frost-heave of Canal and its Structure*, China Water & Power Press, Beijing, China, 2005.

[38] M. Xiao, *Studies on Channel Damage Mechanism and Tis Prevention Measures in Tarim Irrigation*, Tarim University, Xinjiang, China, 2011.

[39] GB 50010-2010, *Code For Design of Concrete Structures*, China Architecture & Building Press, Beijing, China, 2015.

Hindawi
Advances in Materials Science and Engineering
Volume 2021, Article ID 9949468, 9 pages
https://doi.org/10.1155/2021/9949468

Research Article

Experimental Study of Rainfall Infiltration in an Analog Fracture-matrix System

Zhen Zhong,[1,2] **Huicai Gao**,[1] **and Yunjin Hu**[1,2]

[1]*College of Civil Engineering, Shaoxing University, Shaoxing 312000, China*
[2]*Center of Rock Mechanics and Geohazards, Shaoxing University, Shaoxing 312000, China*

Correspondence should be addressed to Yunjin Hu; huyunjin@zju.edu.cn

Received 4 March 2021; Accepted 30 April 2021; Published 15 May 2021

Academic Editor: Hao Zheng

In this study, an experimental apparatus was developed to investigate unsaturated infiltration in an analog fracture-matrix system. Fracture and adjacent matrix is simulated by sands with various particle sizes. Four rainfall infiltration experiments were performed on the analog fracture-matrix system at a constant rainfall rate of 100 mm/h. The process of rainfall infiltration is measured by a combination method of tensiometers and quick moisture apparatus. The measured results reveal that fracture-matrix interactions certainly exert influences on the hydraulic behaviour of unsaturated fractured matrix, and the fluid flow mainly infiltrates along the nonuniform paths within the matrix. Moreover, it is observed that the influences are greater when using a coarser sand to mimic the fracture. Specifically, the wetting phase in the matrix moves faster than that in the fracture; the fracture, therefore, acts as a vertical capillary barrier, but there exists lateral water exchange from the matrix to the fracture. Overall, this study has demonstrated the importance of fracture/matrix interactions, which should be considered when dealing with unsaturated flow through permeable matrices.

1. Introduction

Unsaturated zone is widely distributed in geoformation, and the fluid flow in unsaturated zone is different from that in the saturated zone. Exploration of unsaturated fluid flow in fractured rocks is of special interest to several fields, including the disposal of nuclear waste [1–3] and subsurface contaminant remediation [4–8].

The experiment plays a fundamental role in understanding flow processes in unsaturated fractured rocks, and it usually starts with the research on fluid flow through a single fracture, which has attracted substantial attentions since Lomize firstly introduced a conceptual model of using parallel glass plates to fabric open fractures [9]. Henceforth, a bunch of experiments have been carried out with remarkable progresses achieved [5, 10–15]. Nicholl and Glass developed an optical visualization technique to explore the wetting phase flow through two-phase structures (water and gas) in an analog rough-walled fracture [16]. The experimental scenario was analogous to single-phase flow through fractures, where the gas phase was invariant under steady-state conditions. The measured relative permeability was proportional to saturation (wetting phase) by third order. Brown et al. studied fluid flow paths within a fracture plane fabricated by assembling two transparent epoxy fracture surfaces together [17]. The measured fluid velocities were found to range over several orders of magnitude, and the maximum velocity was five times larger than the average velocity, indicating that channeling flow in fractured media could cause the fast breakthrough of contaminants. Su et al. performed flow visualization experiments on a fracture replica to study the liquid distribution and behaviour of seepages [18]. It was observed that infiltrating water advanced in unsaturated fractures along highly localized, nonuniform flow paths. Sun et al. developed an experimental device to explore rainfall infiltration in an artificial fracture [19]. The obtained relationships of saturation to capillary pressure and saturation to unsaturated hydraulic conductivity were both found to be nonlinear. Hu et al. developed an experimental apparatus for the determination of the unsaturated hydraulic properties of an analogous fracture [20]. They reported that there exists hysteresis between drainage and imbibition processes. Qian et al. conducted laboratory experiments to investigate fluid flow through a single fracture with various surface roughnesses and apertures [15]. An empirical exponential function was found to fit well the relationship between the mean velocity and the hydraulic gradient, and the fitting parameter for the exponential function was around 0.5 when hydraulic gradients ranged from 0.003 to 0.02.

The aforementioned experiments usually neglect fracture/matrix interactions, but both field and laboratory tests have addressed the significant influence of fracture/matrix interactions on unsaturated seepage through fractured media [21–23]. Salve et al. performed liquid-release tests in highly fractured welded tuffs at Yucca Mountain. They revealed that both fracture flows and faults-matrix interactions play critical roles in the wetting-phase movement within unsaturated fractured rocks [22]. Salve et al. carried out field tests by releasing water directly into nonwelded tuffs at Yucca Mountain [23]. The field tests suggested when the matrix and fault were dry, water injected into the fault was mostly absorbed by the adjacent matrix. Moreover, although the fault started to dry immediately after one infiltration event, the surrounding matrix would retain moisture for a few months. Roels et al. further performed moisture uptake experiments in a rough fracture fabricated by two halves of a fractured brick [24]. They observed that the wetting front in the fracture with aperture of 0.01 mm fell behind the wetting front in the matrix. Sakaki conducted wetting experiments of a rock matrix adjacent to a single vertical fracture to understand some of the fundamental mechanisms controlling fracture-matrix interactions [25]. Results showed that the wetting front within the matrix was approximately parallel to the fracture and propagated mainly in the horizontal direction, indicating that water absorption was predominantly one-dimensional orthogonal to the vertical fracture. Rangel-German et al. developed a two-dimensional micromodel to simulate moisture uptake from fracture to surrounding matrix [26]. The experimental results showed that the water uptake rate was depended critically on the water infiltration rate through fractures. Huang et al. designed an experimental apparatus to investigate the transport of vertical flow in unsaturated fractured sandstone [13]. It was observed that the fracture enlengthened the time for the wetting phase to break through the matrix, arising the accumulation of water in the matrix around the inlet end of the fracture, which tended to enhance the local flow in the matrix.

Even though substantial efforts have been made to uncover the hydraulic behaviours of unsaturated flow through the single fracture-matrix system [7, 27–30], there is still a lack of laboratory experiments for the determination of unsaturated hydraulic properties, including suction and saturation, under fracture/matrix interactions. Here, we followed the methods of Zhong et al. [31] to present an experimental apparatus for assessing unsaturated fluid flow through an analog fracture-matrix system. Sands with different particle-size ranges are used as an analog to simulate the fracture and matrix, respectively. The apparatus is capable of taking fracture/matrix interactions into considerations; then, rainfall infiltration tests, aiming at exploring the impact of fracture/matrix interactions on the hydraulic behaviours of the unsaturated matrix and fracture, are conducted.

2. Materials and Methods

It is usually difficult to install time domain reflectometry (TDR) probes in rock mass to measure unsaturated hydraulic properties, and accuracy of the measurement is sensitive to the contact between the probe and the rock. Here, an experimental model is designed to use sand with different particle sizes to mimic the fracture and the matrix, respectively. This is feasible with respect to the facts that unsaturated seepage within the fracture and sand are both under joint actions of capillary and gravity forces [32]. Table 1 summarizes physical properties of sand, which was sieved into three grain size fractions: 0.315~0.63, 0.63~1.25, and 1.25~2.50 mm, and it was classified into medium sand (MS), coarse sand (CS), and very coarse sand (VS) according to particle size ranges.

As illustrated in Figure 1, the experimental system consists of a water supply tank, a sand tank, two stainless-steel holders, and measuring devices. Figure 2 shows the detail drawing of the water supply tank and the sand tank. The water supply tank, with a length $\times$ width $\times$ height of $0.62\,\mathrm{m} \times 0.62\,\mathrm{m} \times 0.20\,\mathrm{m}$, stands on the high stainless steel holder, and it has twenty-five needles (an inside diameter of 0.5 mm) uniformly distributed at its bottom to generate rainfall for the sand tank, which is situated at the low stainless steel holder right below the water supply tank. The water supply tank has a spillway at its front wall to obtain stable overflow. The sand tank (0.42 m in length, 0.42 m in width, and 0.6 m in height) is made of transparent plexiglass to make direct observation of the fluid flow processes possible. The sand tank has two layers along its height, noted as the upper and lower layers. Both layers are partitioned into 3 zones, named zone F, M1, and M2, respectively, by the glass sheet (see Figures 1 and 2). Zone M1 and zone M2 of the upper layer are packed with a finer sand of height 0.35 m to mimic "matrix." Consequently, a vertical gap (30 mm in thick) is created in the middle, and a coarser sand is used to fill the gap (Zone F) to form "fracture" [33]. The aperture of fracture is approximately estimated by multiplying the gap thickness by coarse sand's porosity [34]. The lower layer is used to collect the water drained from the sample. During the experiments, the capillary pressure of the fractured matrix is measured by nine tensiometers (TEN, TOP Instrument Co., Ltd.) distributed at various depths within the fracture and matrix, while the saturation is monitored by quick moisture apparatus (TZS-1K, TDR, TOP Instrument Co., Ltd.) through the observation holes drilled at the backside of the sank tank.

Four experiments, indicated as experiments A, B, C, and D, respectively, were carried out under an invariant rainfall rate of 100 mm/hr. The top boundary of the sample could be considered as a boundary of constant flux boundary conditions (100 mm/hr) under unsaturated flow, while four sidewalls are subjected to zero-flow boundaries. Experimental scenarios based on different combinations of sand

Table 1: Physical properties of sand with various ranges of particle size.

Sand classification	Particle size ranges (mm)	Bulk density (g/cm^3)	Porosity	Saturated conductivity (cm/s)
Medium sand (MS)	0.315~0.63	1.99	0.25	$2.1e-3$
Coarse sand (CS)	0.63~1.25	1.72	0.35	$3.5e-3$
Very coarse sand (VS)	1.25~2.50	1.59	0.40	$5.2e-3$

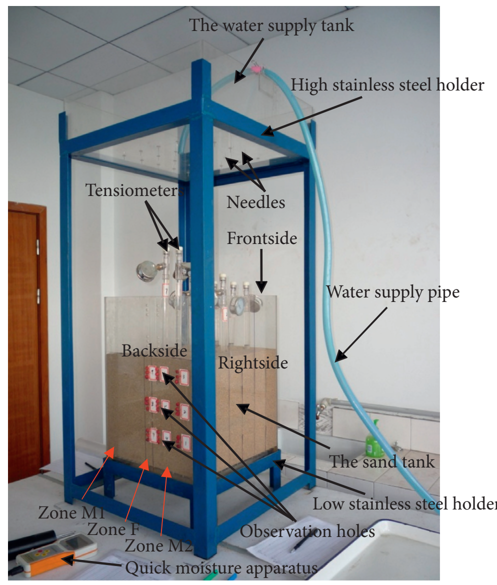

Figure 1: Illustration of the experimental setup.

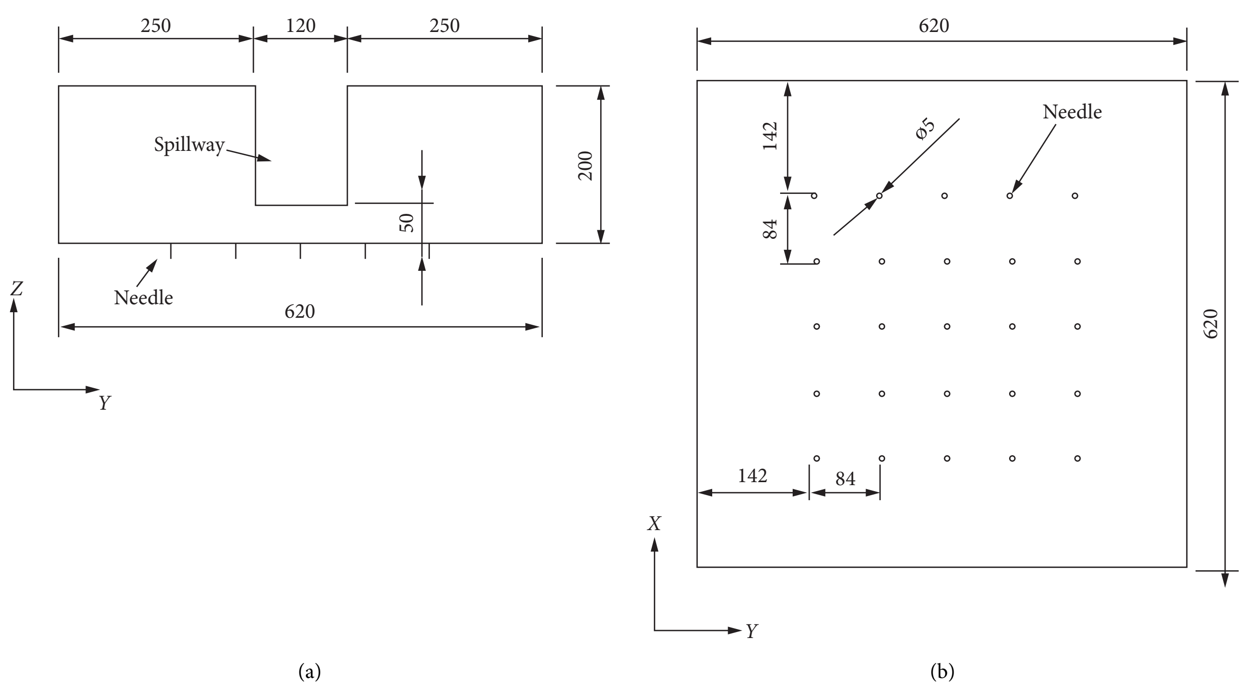

Figure 2: Continued.

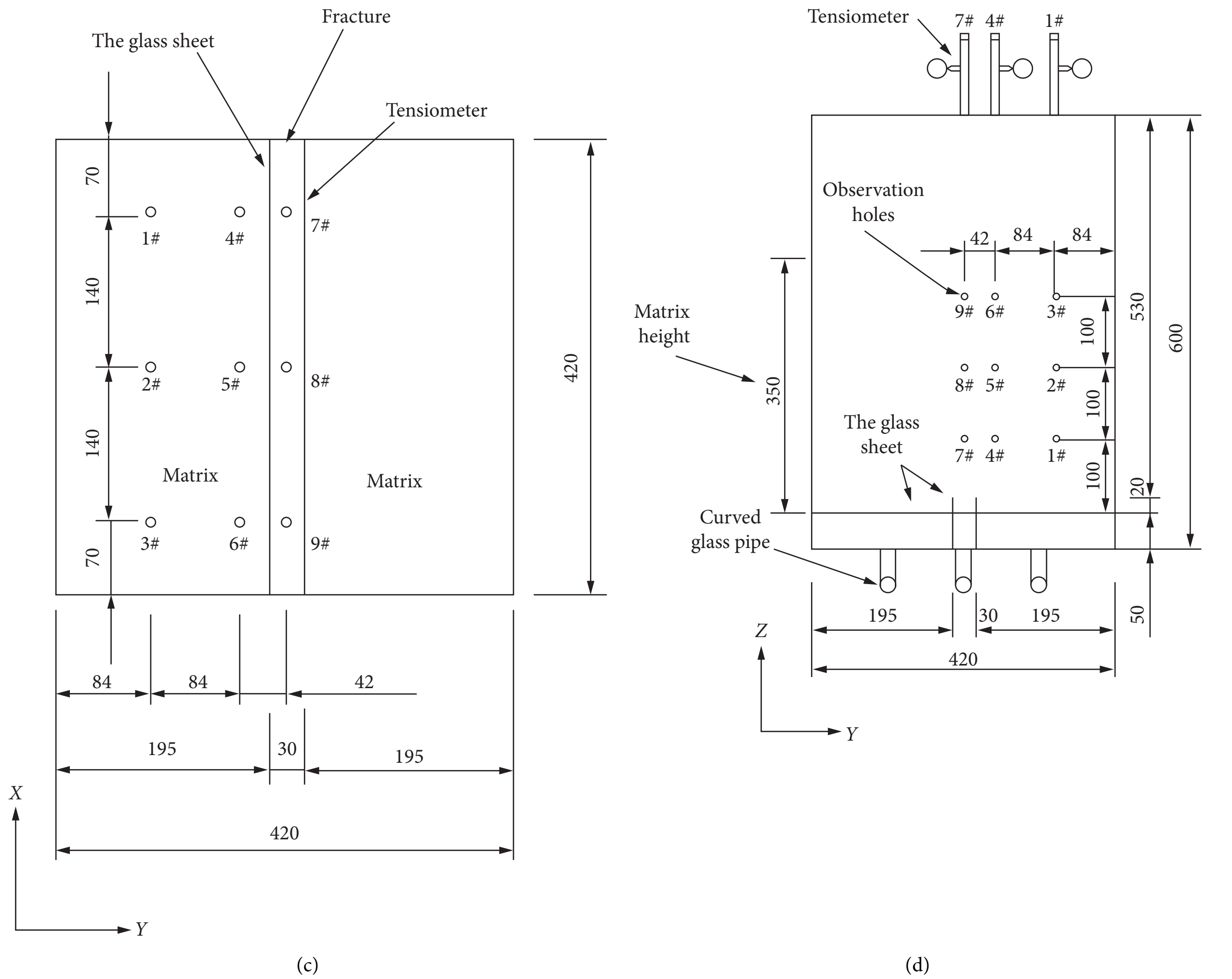

Figure 2: Annotated sketches of the experimental apparatus: (a) sectional view and (b) top view of the water supply tank; (c) top view and (d) sectional view of the sand tank, unit (mm).

are displayed in Table 2. The initial suction and saturation are recorded using the tensiometer and quick moisture apparatus located at various depths, respectively. Water is delivered continuously to the water supply tank via a water supply pipe during the experiment, and the constant rainfall is obtained when water level keeps constant. The real-time capillary pressure and water saturation at different positions are consistently monitored during the rainfall infiltration within the fractured matrix. Effluent from the coarse- and fine-grained sand were collected separately and measured.

3. Results and Discussion

Experiment A, B, and C, using MS with particle sizes in the range of 0.315~0.63 to represent the matrix, are performed to assess the influence of fracture flow on the hydraulic behaviour of the matrix. Figure 3 shows matrix suction-time curves for tensiometers located at 1#, 4#, 2#, and 5#, and it is obvious that fracture aperture has significant impacts on hydraulic properties of matrix, since it takes fewer time for matrix to get full saturated (suction drop to zero) as fracture aperture becomes larger. This might be caused by the joint effects of capillary barrier of fracture and fracture/matrix interactions. Specifically, it is easier for the rainfall to penetrate the matrix with smaller pores compared to the fracture with larger pores; besides, the rainfall falling on the fracture tend to accumulate around the upper boundary of the fracture induced by the capillary effect, and accumulated water is absorbed by the matrix through both sides of the fracture-matrix interface. Consequently, infiltrated rainfall mainly travel through the fractured matrix along the vertical paths within the matrix, while fracture acts as a barrier, where accumulated water will flow to the matrix. The amount of water, flowing from fracture to surrounding matrix, increases with an increase in fracture aperture, and small portion of the water, driven by the hydraulic gradient between fracture and matrix, will return to the fracture (see inset A in Figure 4(a)).

Matrix suction is plotted against saturation in Figure 5. The evolution of matrix suction experiences two periods as water advancing the matrix and fracture. It decreases gradually at first before drops dramatically to zero.

Table 2: Experimental conditions showing different combinations of sand selected to mimic "Fracture" and "Matrix."

Experiments	Sand used to mimic "fracture"	Fracture aperture/mm (gap thickness × sand porosity)	Sand used to mimic "matrix"
A	MS	7.5	MS
B	CS	10.5	MS
C	VS	12.0	MS
D	CS	10.5	CS

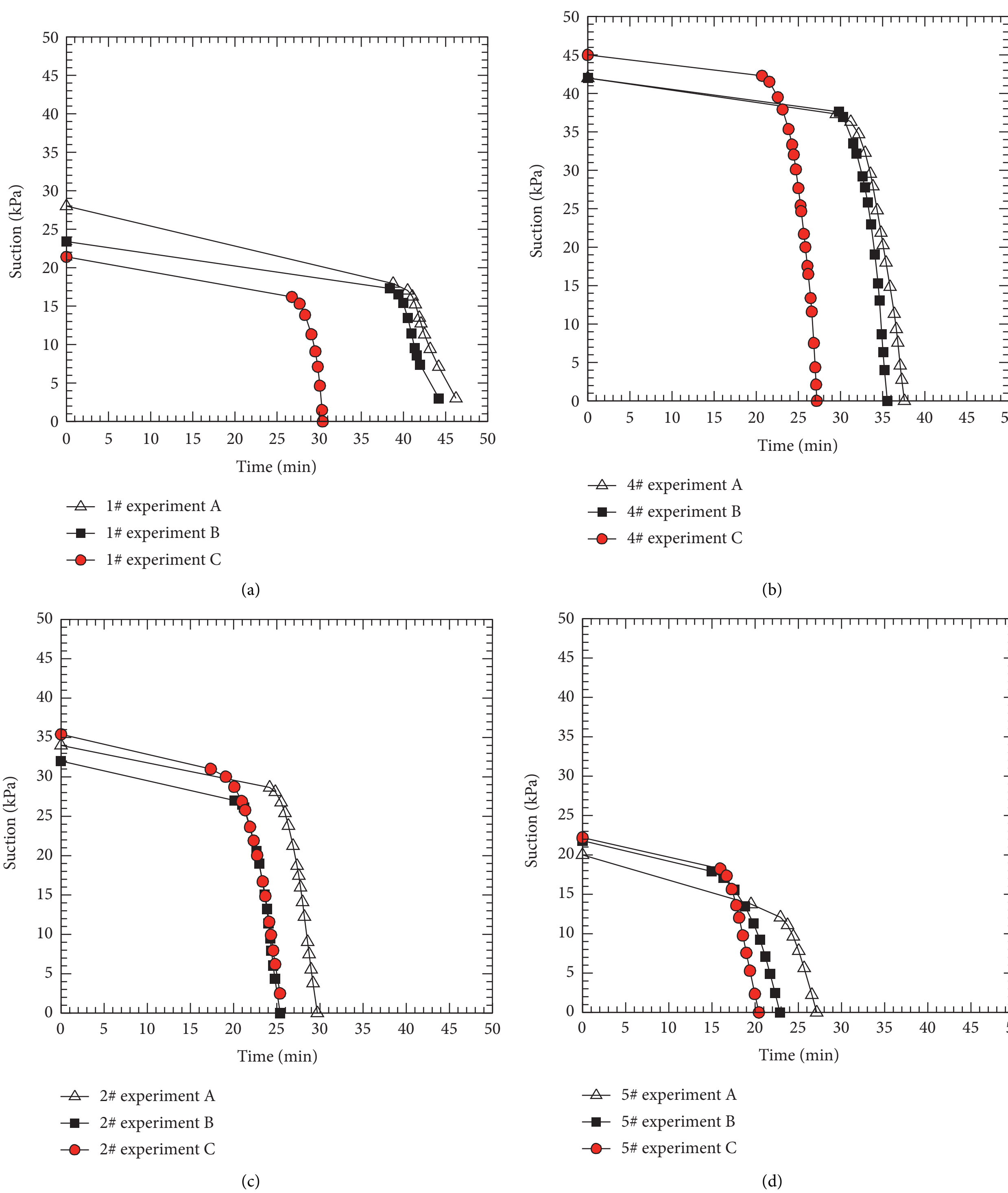

Figure 3: Evolution of matrix suction measured with tensiometers located at various depths of: (a) 1# (250 mm depth); (b) 4# (250 mm depth); (c) 2# (150 mm depth); (d) 5# (150 mm depth).

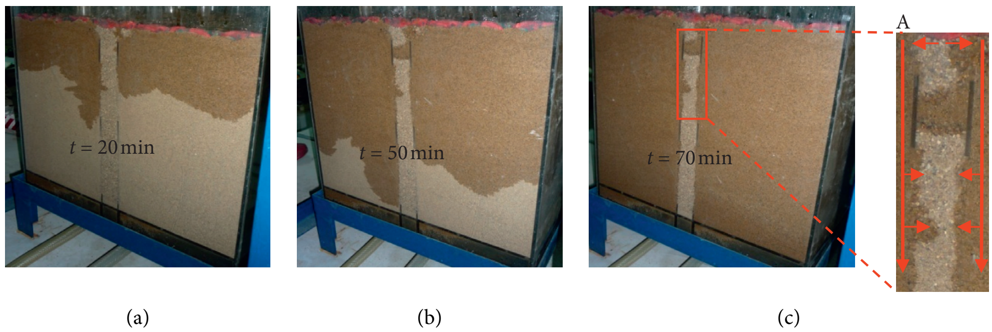

FIGURE 4: Vertical infiltration of water into an analog fracture-matrix system. A is the flow direction of the partial enlargement of main plot at 70 min.

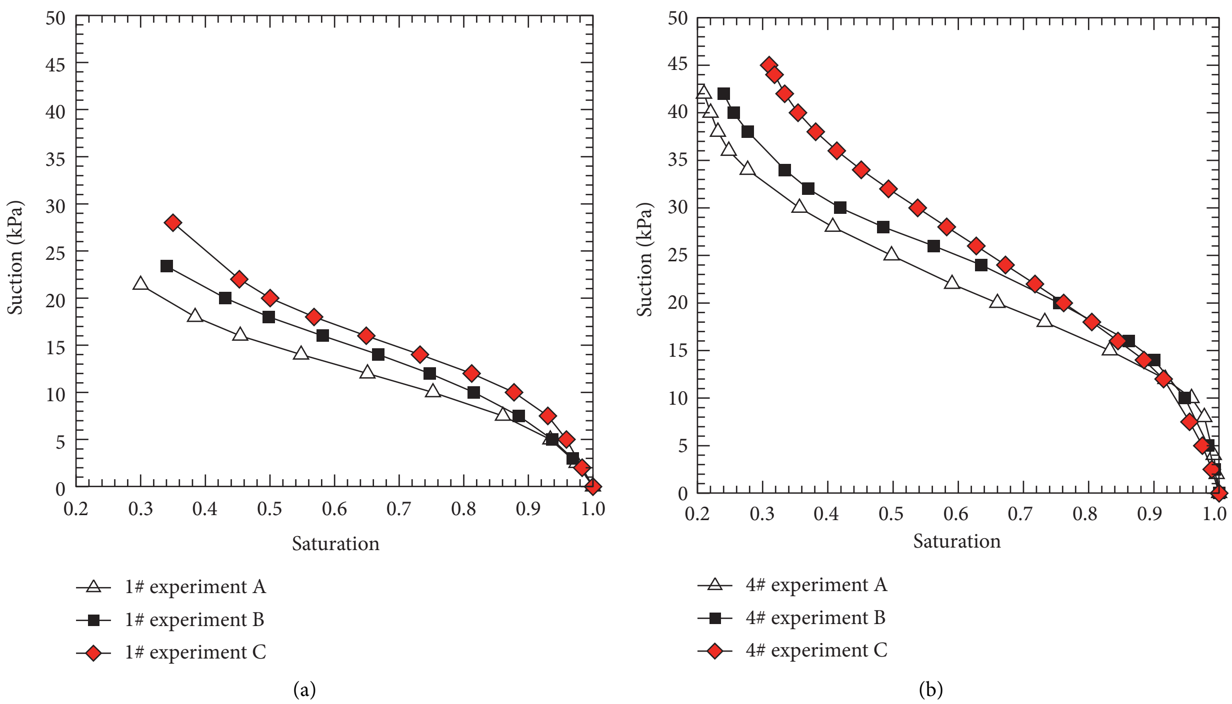

FIGURE 5: Continued.

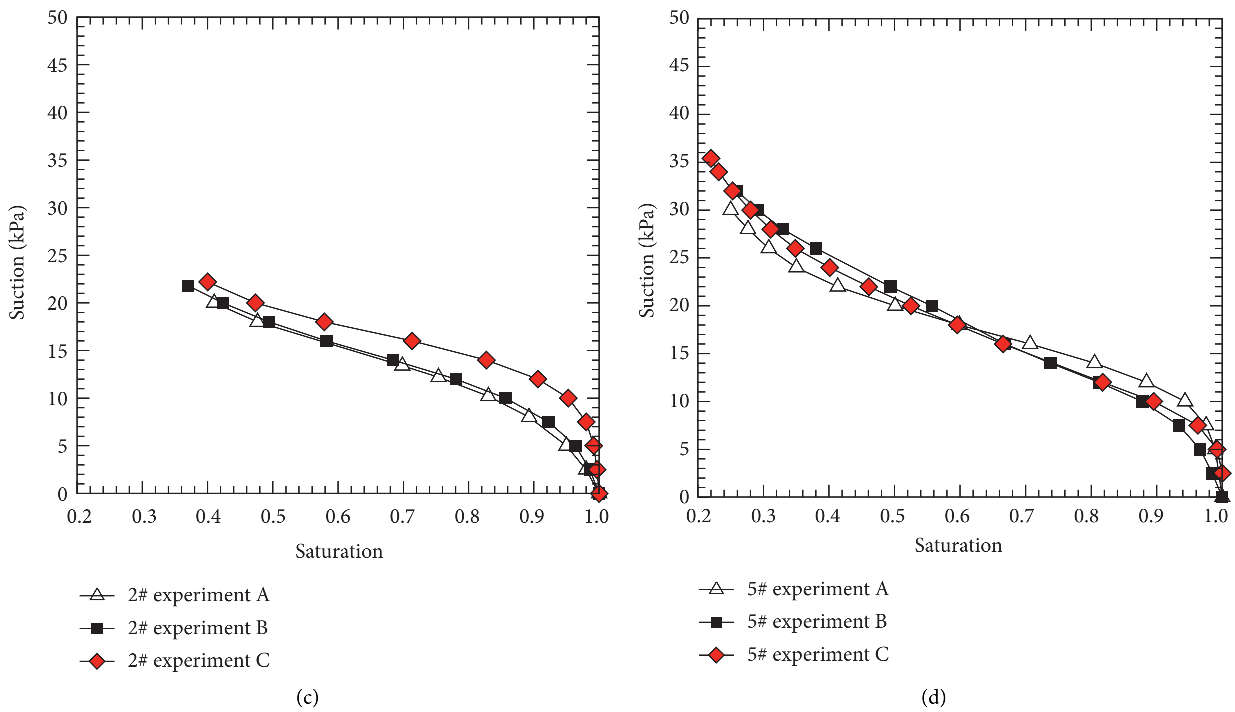

FIGURE 5: Relationships between matrix suction and saturation tensiometers located at different depths of (a) 1# (250 mm depth), (b) 4# (250 mm depth), (c) 2# (150 mm depth), and (d) 5# (150 mm depth).

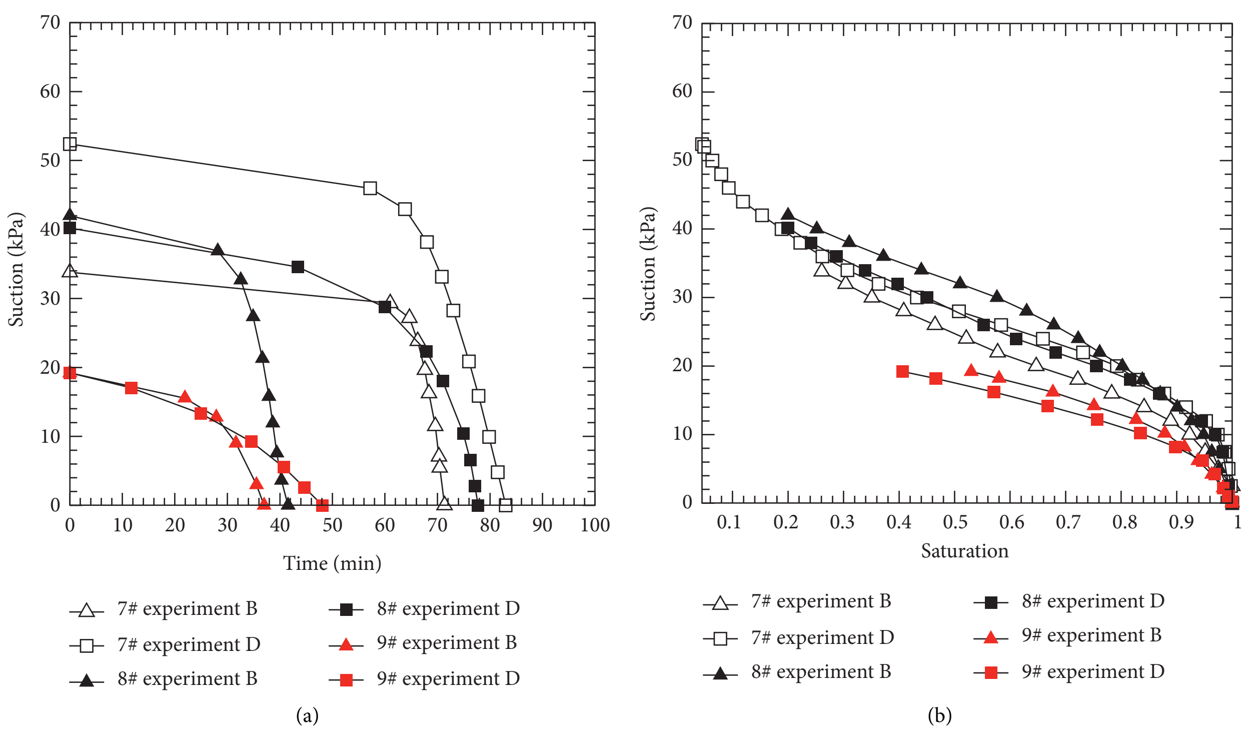

FIGURE 6: Plot of the experimental results for tensiometers in the fracture: (a) suction versus time; (b) suction versus saturation.

The results of experiment B and D with CS to simulate fracture are compared in Figure 6. Figure 6(a) describes evolution of capillary pressure (suction) in fracture. At the beginning of rainfall, both fracture and matrix are dry with low saturation, so infiltrated rainfall tend to occupy the matrix with smaller pores, leaving fracture with larger pores remain in dry. This can result in a hydraulic connection between fracture and adjacent matrix, fracture start to absorb water from matrix because of hydraulic gradient between them. The matrix provides an extra source of water for the fracture under this circumstance, and it would be easier for water to move from a finer matrix to the fracture. The finer the matrix, the quicker the suction in fracture drops to zero. Since both the fracture and matrix are actually porous media (sand), the fracture's suction-saturation curves, as indicated in Figure 6(b), are similar to those of the matrix.

The wetting front evolution of the experiment C is displayed in Figure 4. It is observed that infiltrated water mainly travels through unsaturated fracture-matrix system along nonuniform, localized preferential flow paths. Inset A in Figure 4 is a close-up view of rainfall infiltration at 70 min, and it can also be concluded that flow primarily migrates downwards via the matrix in the direction parallel to the fracture, and the wetting phase within the matrix moves quicker than that in the fracture, even though some portion of water is driven back to fracture because of the hydraulic gradient between fracture and matrix. Those observations are similar with that observed in [24].

4. Conclusions

This paper presents a new experimental apparatus to study unsaturated flow in fractured rock. Sands with various ranges of particle sizes are chosen as analogous materials to mimic fracture and matrix, respectively. Then, rainfall experiments were performed on an analog fracture-matrix system to evaluate unsaturated infiltration processes in both "fracture" and adjacent "matrix." It is observed that unsaturated flow primarily migrate downwards via the matrix along nonuniform, localized preferential flow paths, which is quite different from the results from saturated flow, where the fracture is usually considered as a major conduit. Moreover, the preferential flow in the matrix will be enhanced since the fracture acts as a capillary barrier, and this enhancement is greater by using a coarser sand to simulate the fracture. Besides, there also exists hydraulic connection between the fracture and adjacent matrix, and fluid flow tends to transport from the fracture to the matrix due to hydraulic gradient between them, bringing in additional water supply for the fracture along the direction transversal to it. In general, it is suggested that hydraulic connection between fracture and surrounding matrix should not be ignored in unsaturated flow, especially when the matrix is permeable.

Data Availability

The data that support the findings of this study are available from the corresponding author upon reasonable request.

Conflicts of Interest

The authors declare that they have no conflicts of interest.

Acknowledgments

The authors thank Junjun Zhang from Zhejiang University for the technical assistance in the designing of the experimental system. This research was financially supported by National Natural Science Foundation of China (Grant nos. 51509154, 41977256, and 41907167), Natural Science Foundation of Zhejiang Province (Grant no. LGJ20E090001), and International Scientific and Technological Cooperation Projects of Shaoxing University (Grant no. 2019LGGH1008).

References

[1] G. P. Lu, H. H. Liu, and R. Salve, "Long term infiltration and tracer transport in fractured rocks: field observations and model analyses," *Journal of Hydrology*, vol. 396, no. 1-2, pp. 33–48, 2011.

[2] H.-H. Liu, "Non-Darcian flow in low-permeability media: key issues related to geological disposal of high-level nuclear waste in shale formations," *Hydrogeology Journal*, vol. 22, no. 7, pp. 1525–1534, 2014.

[3] I. Faoro, D. Elsworth, and T. Candela, "Evolution of the transport properties of fractures subject to thermally and mechanically activated mineral alteration and redistribution," *Geofluids*, vol. 16, no. 3, pp. 396–407, 2016.

[4] N. Natarajan and G. S. Kumar, "Solute transport in a coupled fracture-matrix system with sinusoidal fracture geometry," *International Journal of Engineering Science and Technology*, vol. 2, no. 6, pp. 1886–1992, 2010.

[5] C.-L. Cheng, E. Perfect, B. Donnelly et al., "Rapid imbibition of water in fractures within unsaturated sedimentary rock," *Advances in Water Resources*, vol. 77, pp. 82–89, 2015.

[6] B. R. Jones, J. L. Van Rooy, and M. A. Dippenaar, "On the differing role of contact obstacles on variably saturated flow in vertical and horizontal fractures," in *IAEG/AEG Annual Meeting Proceedings*, A. Shakoor and K. Cato, Eds., Springer, San Francisco, CA, USA, 2018.

[7] Z. Yang, S. Xue, X. Zheng, and Y. F. Chen, "Partitioning dynamics of gravity-driven unsaturated flow through simple T-shaped fracture intersections," *Water Resources Research*, vol. 55, no. 8, pp. 7130–7142, 2019.

[8] J. Qian, Z. Chen, H. Zhan, and H. Guan, "Experimental study of the effect of roughness and Reynolds number on fluid flow in rough-walled single fractures: a check of local cubic law," *Hydrological Processes*, vol. 25, no. 4, pp. 614–622, 2011.

[9] G. M. Lomize, *Flow in Fractured Rocks*, Gosemergoizdat, Moscow, Russia, 1951.

[10] R. J. Glass, M. J. Nicholl, S. E. Pringle, and T. R. Wood, "Unsaturated flow through a fracture-matrix network: dynamic preferential pathways in mesoscale laboratory experiments," *Water Resources Research*, vol. 38, no. 12, pp. 17–21, 2002.

[11] T. R. Wood, R. J. Glass, T. R. Mcjunkin et al., "Unsaturated flow through a small fracture-matrix network: Part 1. experimental observations," *Vadose Zone Journal*, vol. 3, no. 1, pp. 90–100, 2004.

[12] J. Z. Qian, Z. Chen, H. B. Zhan, and S. H. Luo, "Solute transport in a filled single fracture under non-Darcian flow," *International Journal of Rock Mechanics and Mining Sciences*, vol. 48, no. 1, pp. 132–140, 2011.

[13] Z. Yong, Z. F. Zhou, Z. B. Yu, and M. J. Nicholl, "Effect of a vertical fracture on horizontal unsaturated seepage flow," *Journal of Hydrodynamics*, vol. 23, no. 1, pp. 127–134, 2011.
[14] T. Noffz, M. Dentz, and J. Kordilla, "Analogue fracture experiments and analytical modeling of unsaturated percolation dynamics in fracture cascades," *Vadose Zone Journal*, vol. 18, no. 1, pp. 1–9, 2019.
[15] J. Qian, H. Zhan, W. Zhao, and F. Sun, "Experimental study of turbulent unconfined groundwater flow in a single fracture," *Journal of Hydrology*, vol. 311, no. 1–4, pp. 134–142, 2005.
[16] M. J. Nicholl and R. J. Glass, "Wetting phase permeability in a partially saturated horizontal fracture," in *Proceedings of the 5th International Conference on High Level Radioactive Waste Management*, vol. 2, pp. 2007–2019, Las Vegas, NV, USA, May 1994.
[17] S. Brown, A. Caprihan, and R. Hardy, "Experimental observation of fluid flow channels in a single fracture," *Journal of Geophysical Research: Solid Earth*, vol. 103, no. B3, pp. 5125–5132, 1998.
[18] G. W. Su, J. T. Geller, K. Pruess, and F. Wen, "Experimental studies of water seepage and intermittent flow in unsaturated, rough-walled fractures," *Water Resources Research*, vol. 35, no. 4, pp. 1019–1037, 1999.
[19] Y. Sun, E. Z. Wang, and X. H. Chen, "Experiment studies for unsaturated flow in a single fracture under rainfall," *Journal of Tsinghua University (Science and Technology)*, vol. 39, no. 11, pp. 14–17, 1999, in Chinese.
[20] Y. J. Hu, B. Y. Su, and G. H. Mao, "An experimental approach for determining unsaturated hydraulic properties of rock fractures," *Nordic Hydrology*, vol. 35, no. 3, pp. 251–260, 2004.
[21] E. R. Rangel-German and A. R. Kovscek, *Matrix-fracture Interaction in Single Matrix Blocks*, Stanford University Petroleum Research Institute Twenty-Third Annual Report, Stanford, CA, USA, 2000.
[22] R. Salve, J. S. Y. Wang, and C. Doughty, "Liquid-release tests in unsaturated fractured welded tuffs: I. Field investigations," *Journal of Hydrology*, vol. 256, no. 1-2, pp. 60–79, 2002.
[23] R. Salve, C. M. Oldenburg, and J. S. Y. Wang, "Fault-matrix interactions in nonwelded tuff of the paintbrush group at Yucca mountain," *Journal of Contaminant Hydrology*, vol. 62-63, pp. 269–286, 2003.
[24] S. Roels, K. Vandersteen, and J. Carmeliet, "Measuring and simulating moisture uptake in a fractured porous medium," *Advances in Water Resources*, vol. 26, no. 3, pp. 237–246, 2003.
[25] T. Sakaki, *The role of fracture-matrix interaction in drying of unsaturated fractured rock experiments and modeling*, Ph.D. thesis, University of Colorado, Denver, CO, USA, 2004.
[26] E. R. Rangel-German and A. R. Kovscek, "A micromodel investigation of two-phase matrix-fracture transfer mechanisms," *Water Resources Research*, vol. 42, no. 3, p. W03401, 2006.
[27] F. Ren, G. Ma, Y. Wang, T. Li, and H. Zhu, "Unified pipe network method for simulation of water flow in fractured porous rock," *Journal of Hydrology*, vol. 547, pp. 80–96, 2017.
[28] J. R. Nimmo, K. M. Creasey, K. S. Perkins, and B. B. Mirus, "Preferential flow, diffuse flow, and perching in an interbedded fractured-rock unsaturated zone," *Hydrogeology Journal*, vol. 25, no. 2, pp. 421–444, 2017.
[29] B. Xiao, X. Zhang, W. Wang et al., "A fractal model for water flow through unsaturated porous rocks," *Fractals*, vol. 26, no. 2, Article ID 1840015, 2018.
[30] X. Li and D. Li, "A numerical procedure for unsaturated seepage analysis in rock mass containing fracture networks and drainage holes," *Journal of Hydrology*, vol. 574, pp. 23–34, 2019.
[31] Z. Zhong, Y. J. Hu, X. H. Zhang, and G. L. Chen, "Laboratory study of unsaturated flow in a single fracture-matrix system: a conceptual model," *Applied Mechanics and Materials*, vol. 212-213, pp. 377–382, 2012.
[32] J. E. Houseworth, "An analytical model for solute transport in unsaturated flow through a single fracture and porous rock matrix," *Water Resources Research*, vol. 42, no. 1, Article ID W01416, 2006.
[33] R. C. Starr, R. W. Gillham, and E. A. Sudicky, "Experimental investigation of solute transport in stratified porous media, 1. The nonreactive case," *Water Resources Research*, vol. 21, no. 7, pp. 1035–1041, 1985.
[34] Y.-S. Wu, M. Ye, and E. A. Sudicky, "Fracture-flow-enhanced matrix diffusion in solute transport through fractured porous media," *Transport in Porous Media*, vol. 81, no. 1, pp. 21–34, 2010.

Hindawi
Advances in Materials Science and Engineering
Volume 2021, Article ID 9924869, 13 pages
https://doi.org/10.1155/2021/9924869

Research Article

The Effect of Freeze-Thaw Damage on Corrosion in Reinforced Concrete

Xiao-Chun Lu[1], **Bin Guan**[1], **Bo-Fu Chen**[1], **Xin Zhang**[2], **and Bo-bo Xiong**[1]

[1]*College of Hydraulic and Environmental Engineering, Three Gorges University, Yichang, China*
[2]*China Yangtze Power Co., Ltd., Beijing, China*

Correspondence should be addressed to Bin Guan; 201908150021023@ctgu.edu.cn and Bo-Fu Chen; chenbofu@ctgu.edu.cn

Received 22 March 2021; Revised 3 May 2021; Accepted 4 May 2021; Published 15 May 2021

Academic Editor: Yanhu Mu

The existing studies of the corrosion of reinforced concrete have mainly focused on the interface area and chemical ion erosion, ignoring the specific service environment of the reinforced concrete. In this study, the effect of freeze-thaw damage was investigated via corrosion experiments under different freeze-thaw cycle conditions. Steel reinforcement corrosion mass, ultimate pull-out force, corrosion rate, and bond slippage were chosen as characteristic parameters in the experiments, and scanning electron microscopy (SEM) analysis was used to explain the mechanism of action of freeze-thaw damage on corrosion. The results showed that, under identical corrosion conditions, the mass of steel reinforcement corrosion and corrosion rate increased by 39.6% and 39.7% when comparing 200 freeze-thaw cycles to 0 cycles, respectively. The ultimate pull-out force and bond slippage after 200 freeze-thaw cycles decreased by 73% and 31%, respectively, compared with 0 freeze-thaw cycles. In addition, SEM analysis indicated that microstructure damage caused by freeze-thaw cycles accelerated the corrosion reaction and decreased cementitious properties, leading to decreasing ultimate pull-out force and bond slippage. The effect of freeze-thaw cycles and steel reinforcement corrosion on the macro mechanical properties of concrete is not a simple superposition.

1. Introduction

Steel reinforcement corrosion (SRC) is one of the main causes of reinforced concrete damage, which is widely concerned in civil engineering [1, 2]. SRC refers to the intrusion of external acid substances and reaction with $Ca(OH)_2$ under the action of water and air, which results in the destruction of the steel passivation film and the damage of reinforced concrete [3, 4]. Compared with other reinforced concrete structures, hydraulic concrete is more easily damaged because of its long-term contact with reservoir water [5, 6], occurring in concrete-face slabs of rockfill dams, diversion tunnels, and spillways [7]. In addition, the real service environment of hydraulic concrete is more complex, which is not only affected by SRC, but also freeze-thaw damage, chemical erosion, dry-wet damage, and other functions that accelerate the degradation of the hydraulic concrete [8, 9]. Especially in cold regions, hydraulic concrete is highly susceptible to freeze-thaw cycles due to seasonal variations of temperature and nearly 100% of reinforced concrete structure in northeast China suffers from local or large-area freeze-thaw damage [10, 11]. Freeze-thaw damage and SRC of reinforced concrete are common phenomena in cold regions.

Hydraulic concrete structures in contact with acidic water are susceptible to the chemical erosion due to the porousness of concrete [12]. The chloride and sulfate ions can transfer into pores and react with steel reinforcement passivation film, leading to damage and corrosion of reinforced concrete [13, 14]. According to Powers' classical hydrostatic pressure theory [15], freeze-thaw cycles lead to changes in the pore structure and ion transport properties of concrete at the micro level, producing microcracks that may accelerate ion transport and steel reinforcement corrosion rate. In general, the SRC caused by freeze-thaw damage will lead to the decrease of mechanical strength and the acceleration of corrosion rate in concrete structure [16, 17]. Thus, the corrosion damage of reinforced concrete in cold regions is more complicated.

In recent years, many studies focused on the effects of freeze-thaw damage and corrosion on the properties of reinforced concrete, including combined and alternate actions [18]. Ma et al. found that frost damage aggravates the rate and degree of rebar corrosion under freeze-thaw environments [19]. Wang et al. [20] studied the coupled effects of freeze-thaw cycling and chloride ions corrosion for steel reinforcement in concrete and found the serious spalling occurred with increasing freeze-thaw cycles. Berrocal et al. [21] investigated the corrosion of steel bars embedded in fibres reinforced concrete under chloride attack and found the fibres can suppress crack width in concrete. Zhang et al. [22] found the initial damage degree will accelerate the degradation rate of strength in reinforced concrete by investigating the influence of the degree of damage on the degradation of concrete under freeze-thaw cycles. For the corrosion characteristic parameters of reinforced concrete subjected to freeze-thaw cycles, Ji et al. [23] carried out experiments on the bonding properties of reinforced concrete under 50 freeze-thaw cycles by means of central pull-out tests and found the effect of freeze-thaw damage on bond strength turns larger with the increase of the diameter of the test steel bar. He et al. [24] conducted beam bond failure tests to study the effect of freeze-thaw cycles and corrosion on bonding and slip performance of concrete and discussed the relationship between crack width and chloride ion erosion. Liu et al. [25] investigated the bond behavior between the RAC and the deformed steel bars after the freeze-thaw cycles and found the bond strength gradually decreased as the freeze-thaw cycles. Zhang et al. [26] studied the bonding performance of concrete and its reinforcements under freeze-thaw cycles and chloride ion corrosion. Besides, the effect of freeze-thaw damage on SRC depends on the evolution of microscopic properties in reinforced concrete. Sicat et al. [27] investigated the real-time deformational behavior of the interfacial transition zone (ITZ) in concrete during freeze-thaw cycles and found the ITZ exhibited higher deformation than the matrix and aggregate due to its higher porosity and weaker strength. Yao et al. [28] studied the microcrack evolution process of concrete subjected to freeze-thaw cycles and multisalt solution attack. Luo et al. [29] investigated the effect of cyclic freeze-thaw on the shear strength of new-old concrete interfaces.

All of the above research mainly focuses on bond properties (bond strength and bond slippage) of concrete and its steel reinforcement under different freeze-thaw cycles. However, the assessment index cannot fully reflect the effect of freeze-thaw damage on the steel reinforcement corrosion and the corrosion mass, corrosion ratio, and rate should be considered. Besides, the number of freeze-thaw cycles may not be enough to explain the effect of higher degree of freeze-thaw damage on SRC in reinforced concrete. The selected sample points in the microscopic experiment are limited, and the relationship between macroscopic properties and microstructure is not clear enough. In general, it is necessary to further study the effect of freeze-thaw cycles on SRC from a micro level. Understanding the failure mechanism of reinforced concrete under freeze-thaw cycles is also valuable for predicting concrete durability and changing the corrosion resistance of reinforced concrete in cold regions.

In this paper, the effect of freeze-thaw cycles on corrosion in reinforced concrete was investigated via steel reinforcement corrosion experiments. First, reinforced concrete samples were made and exposed to different freeze-thaw cycles. The index changes of the quality of steel reinforcement, interfacial bond slippage, and ultimate pull-out force were investigated by the central pull-out test. In addition, the mechanism of steel reinforcement corrosion and material properties were analyzed via scanning electron microscopy (SEM) of the concrete around the central point of the steel reinforcement. The experimental results are of great theoretical value and practical significance for durability evaluation and structural improvement of concrete structures during service life.

2. Materials and Experimental Procedure

To determine the influence of freeze-thaw cycles on the corrosion of reinforced concrete, a series of orthogonal experiments were designed with different freeze-thaw cycles and corrosion times. First, the specimens were exposed to different freeze-thaw cycles: D_0 (no freeze-thaw cycle), D_1 (50 freeze-thaw cycles), D_2 (100 freeze-thaw cycles), D_3 (150 freeze-thaw cycles), and D_4 (200 freeze-thaw cycles). Then, different electrochemical-accelerated steel-reinforcement corrosion processes were performed on the specimens: X_0 (no corrosion), X_1 (5.85 d), X_2 (15.6 d), and X_3 (23.4 d), with the corrosion times from X_0 to X_4 corresponding to 0%, 3%, 8%, and 12% of the theoretical corrosion ratio, respectively.

2.1. Materials and Specimen Preparation. Granite gravel (size ranges of 5–20 mm, 20–40 mm), river sand (fineness modulus of 2.4–2.7), PO42.5-type Portland cement, and Class-I fly ash were used to make the specimens. Additives were included, including a highly efficient naphthalene water-reducing agent and an air-entraining agent, with the mixture proportion of the concrete shown in Table 1. Test specimens consisted of HRB335 screw-thread steel with a diameter of 20 mm and a length of 400 mm embedded into the center of concrete, with the length, width, and depth of the concrete being 100 mm, 100 mm, and 200 mm, respectively. In addition, unbonded segments on both ends of the specimens were obtained using PVC pipe, and the annular space between the steel reinforcement and the PVC tube was filled with polyurethane foam to avoid concrete flowing into it during the casting procedure. Before casting the specimen, the unbonded segments of steel reinforcement were brushed with epoxy resin for anticorrosion purposes. The specimens were removed from their molds after 72 h and stored for 90 d at 25°C and 98% relative humidity. The Chinese standards for steel ("Steel for the Reinforcement of Concrete-Part 2: Hot Rolled Ribbed Bars") and design code for concrete-face rockfill dams [30, 31] were referred to for specimen preparation. A detailed size of the specimen is shown in Figure 1.

Table 1: Mix proportions concrete (kg/m^3).

Water–cement ration	Wsp (%)	Water	Cement	Fly ash	Sand	Aggregate	Water-reducing agent	Air-entraining agent
0.4	0.3	11.7	279.2	85	553.2	1290.8	1	0.02

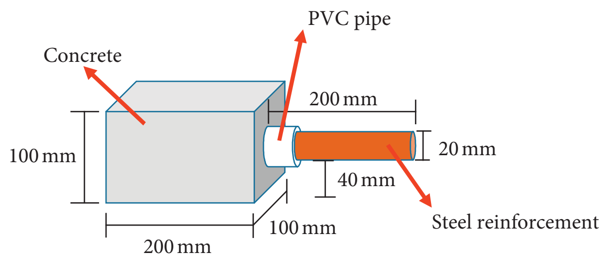

Figure 1: Details of stereoscopic specimen.

2.2. Experimental Procedure. The experimental procedure included the freeze-thaw cycle process, accelerated corrosion process, and measuring details. The macroscopic parameters of measurement included the mass of corrosion, corrosion rate, pull-out force, and bond slippage. The microscopic parameters of measurement included scanning electron microscopy (SEM) and porosity, which was obtained by the water absorption method [32]. The general testing procedure is shown in Figure 2.

2.2.1. Freeze-Thaw Cycles Process. The specimens were immersed in water for 4 d before the freeze-thaw tests were carried out, which aimed to make the concrete in a water-saturated state. The freeze-thaw cycle tests were performed with a freeze-thaw machine (type TR-TSDRSL) according to Chinese code GB/T 50082-2009 [33]. In each freeze-thaw cycle, the temperature of the control specimen decreased from 8°C ± 2°C to −17°C ± 2°C and then increased back to 8°C ± 2°C within 4 h. During the test, specimens were taken out for inspection after 50 freeze-thaw cycles. After reaching a predefined number of freeze-thaws ($n = 0$, 50, 100, 150, and 200), the specimens were removed from the machine. At the same time, key parameters such as the ultimate pull-out force and bond slippage were measured for comparison after the accelerated corrosion experiment. Finally, the steel reinforcement corrosion tests, central pull-out tests, and SEM tests were carried out.

2.2.2. Accelerated Corrosion Process. Accelerated corrosion tests were carried out similarly to the freeze-thaw cycle tests. The specimens were dried in a ventilated oven at a temperature of 50° C until they reached constant weight for calculating the extent of the steel reinforcement corrosion. In general, electrochemical-accelerated-corrosion speeds up the chloride ions corrosion process and ensures accuracy for the test results [34]. To eliminate the influence of humidity on concrete resistance and chloride ions transporting rates, this test adopted the full immersion method [35]. The specimens were kept in an aqueous salt solution containing 5% NaCl to start the accelerated steel reinforcement corrosion test. The anode of a direct current (DC) regulated power supply was connected to the steel, while the cathode was connected to a copper sheet immersed in NaCl solution in parallel mode. Through the electrolysis reaction, the anode electron loss led the steel surface to generate Fe^{2+}, which reacted with water in the solution to generate rust. The 50 mA was applied to accelerate the corrosion process; the total corrosion time was 5.85 d (3% theoretical corrosion ratio), 15.6 d (8% theoretical corrosion ratio), and 23.4 d (12% theoretical corrosion ratio), respectively.

2.2.3. Measuring Details. To investigate the effect of freeze-thaw and corrosion on bond behavior, the bond strength and load characteristic parameters were measured by central pull-out experiments based on the Chinese Code of Standard for test methods of concrete structures GB/T 50152-2012 [36]. The pull-out test used a WAW-Y1000 C microcomputer-controlled electrohydraulic servo universal testing machine and the loading rate was 0.2 kN/S to 500 kN/S. The failure mode of all the specimens was attributed to splitting failure. The experiment was loaded from 0 kN until the reinforced concrete specimen was destroyed and a displacement sensor was set on the loading end of the central pull-out specimens to measure the bond slippage (mm) of the loading end.

The corroded steel reinforcements were taken out when the pull-out test was completed and were then cleaned with 5% HCl solution and neutralized with $Ca(OH)_2$ solution. The specimens were flushed with clean water and placed into a drying device at 20°C for 4 h. The mass of the steel reinforcements was weighed by electronic scales with an accuracy of 0.01 g. The steel reinforcement corrosion ratio was calculated with

$$W_n = \frac{G_0 - G_n}{G_0} \times 100\%, \tag{1}$$

where G_0 is the mass of the steel reinforcement before the freeze-thaw test (g), n is the number of freeze-thaw cycles, G_n is the mass of the steel reinforcement after n cycles of freeze-thaw (g), and W_n is the actual corrosion ratio of the steel reinforcement (%).

The macroscopic mechanical properties of reinforced concrete, such as the ultimate pull-out force and bond slippage, were determined from internal microstructure characteristics. The purpose of the SEM tests was to reveal the effect of freeze-thaw cycles on the microstructure of reinforced concrete from a micro level and then to reveal the mechanism of freeze-thaw cycles on steel reinforcement corrosion. Thus, to obtain the microstructure evolution of concrete (after varied freeze-thaw cycles) throughout the corrosion process, several measuring points were chosen; from the surface to the interior, the points were defined as the central point, the internal point, and the edge point. In addition, the sample's central point was taken from the

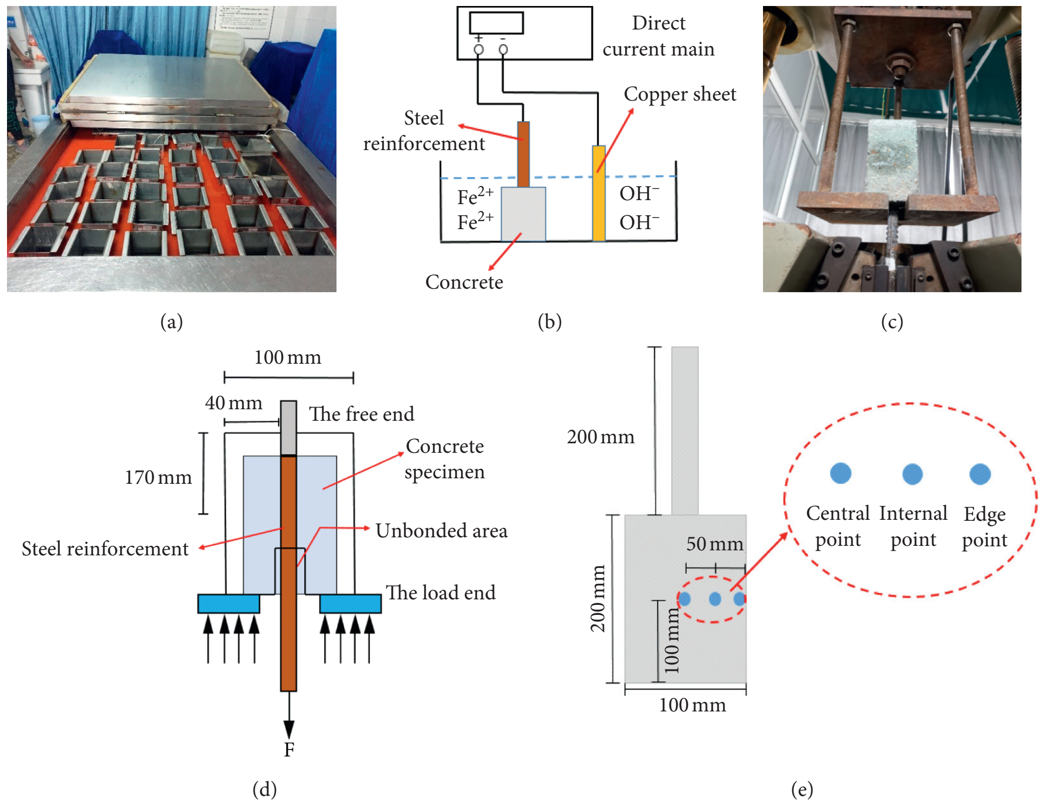

Figure 2: Flow diagram of the experiment. (a) Freeze-thaw test. (b) Accelerated steel corrosion test. (c) Pull-out test loading process. (d) Schematic diagram of the steel reinforcement pull-out test. (e) Samples and points for porosity measurement (mm).

center of the bonding segment between the steel reinforcement and the concrete. The samples (about 1 mm thick, 3 mm long, and 3 mm wide) were cut from the cross section of the specimen by a diamond saw. A JEOLO JSM 7500F SEM was used to observe the microstructure with an optimal resolution of 1 nm (15 kv). In addition, the samples were treated with high-pressure gold spray before testing for high-quality imaging.

3. Experimental Results

3.1. Surface Change. The corrosion state and surface corrosion cracks can arguably reflect the effect of freeze-thaw cycles on steel reinforcement corrosion. The surface change of a reinforced concrete specimen is shown in Figure 3, and the differences of surface change under different freeze-thaw cycles are obvious. Naturally, more corrosion products were produced by the increasing number of freeze-thaw cycles.

The surface of specimens not subjected to freeze-thaw changed only slightly after 5.85 d (3% theoretical corrosion ratio), and the edge of the specimens peeled off after 15.6 d (8% theoretical corrosion ratio). The surface color of the specimens subjected to 100 freeze-thaw cycles deepened, and large areas of the steel reinforcement in the bond section of the specimen began to rust after 5.85 d (3% theoretical corrosion ratio). It is difficult to generate expansion cracks before lower freeze-thaw cycles because the entrained air bubbles can reduce the expansion stress of freezing water. Notably, the specimen suffered from corrosion cracking after 23.4 d (12% theoretical corrosion ratio). For the specimen subjected to 200 freeze-thaw cycles, the mortar on its surface completely fell off, and the concrete at the edge was severely peeled after 15.6 d (8% theoretical corrosion ratio). Corrosion cracks with larger widths can be seen on the surface of specimens after 23.4 d (12% theoretical corrosion ratio). With increased corrosion time, the surface damage of the specimens was very serious, and a large number of $Fe(OH)_3$ had accumulated. In general, corrosion time had a significant impact on the damage process of the specimens. After the same number of freeze-thaw cycles, higher initial corrosion times led to more serious degradation; the reason for this is that micro cracks in the concrete caused by freeze-thaw cycles increased the corrosion expansive pressure and accelerated steel reinforcement corrosion, which produced even more micro cracks. Therefore, with increasing numbers of freeze-thaw cycles, it became easier for internal corrosion products to transfer into the exterior.

3.2. Corrosion Behavior

3.2.1. Mass of Corrosion. The mean corrosion extent of the specimens after varied freeze-thaw cycles is shown in Figure 4. The mass of corrosion in steel reinforcement continuously increased with increased corrosion times. After 23.4 corrosion times (12% theoretical corrosion ratio), the

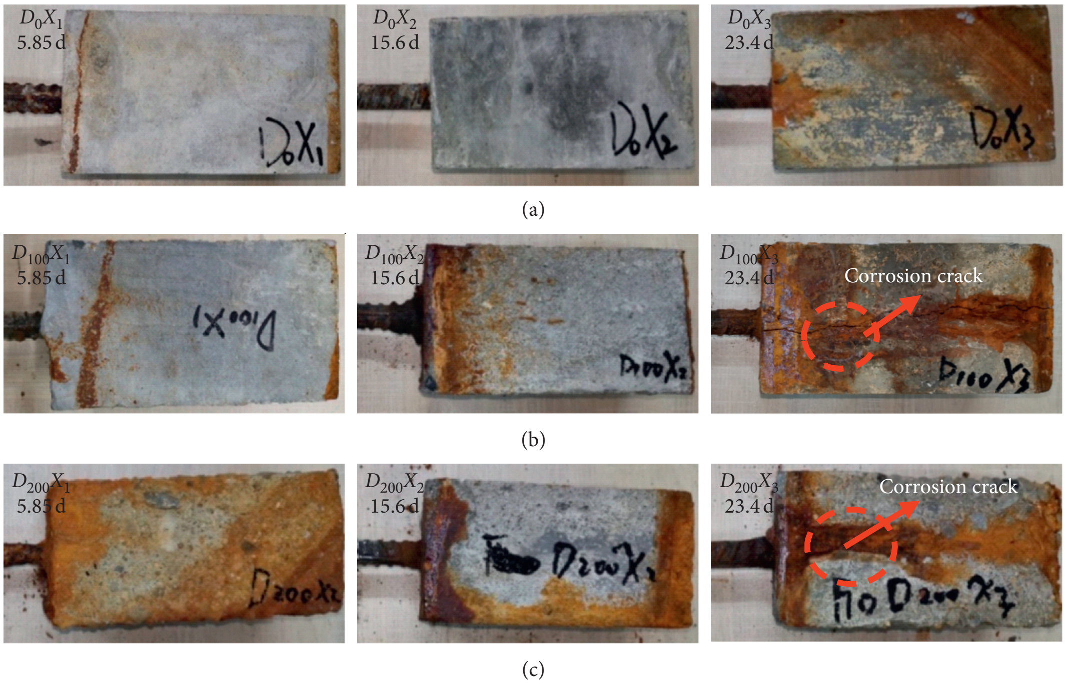

FIGURE 3: Surface changes of specimens under different freeze-thaw cycles. (a) 0 cycles of freeze-thaw. (b) 100 cycles of freeze-thaw. (c) 200 cycles of freeze-thaw.

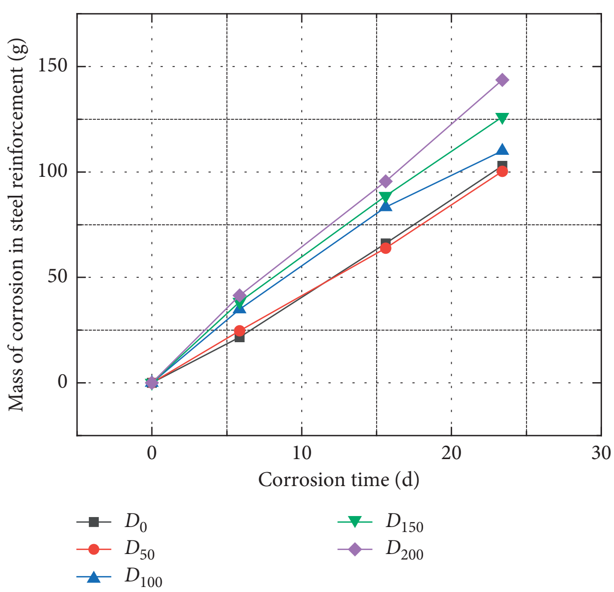

FIGURE 4: The mass change of steel reinforcement after varied corrosion times.

final corrosion mass of the specimens corresponding to 0, 50, 100, 150, and 200 freeze-thaw cycles was 102.9 g, 100.352 g, 110.054 g, 126.126 g, and 143.688 g, respectively. The significant difference in corrosion mass of the steel reinforcement after 0 freeze-thaw cycles (102.9 g) and 200 freeze-thaw cycles (143.688 g) is attributed to micro cracks in the concrete caused by freeze-thaw cycles increasing the transport properties of water and ions, which accelerates the corrosion reaction. Therefore, the more freeze-thaw cycles, the easier it is for external water molecules and chloride ions to transfer into the interior of the specimen.

3.2.2. Corrosion Rate. Figure 5 shows the relationship between the actual corrosion ratio and the number of freeze-thaw cycles. The theoretical corrosion ratios of steel reinforcement, X_0, X_1, X_2, and X_3, are compared with the actual corrosion ratios of steel reinforcement, Y_0, Y_1, Y_2, and Y_3. It could be observed the actual corrosion ratio was lower than the theoretical corrosion ratio before 100 freeze-thaw cycles due to differences in both chloride consumption and specimen casting in the experiment. It is clear that the deviation of the actual and theoretical corrosion ratios was not large. After 100 freeze-thaw cycles, the difference between the actual corrosion ratio and theoretical corrosion ratio increases. The higher the corrosion ratio, the steeper the curve becomes, corresponding to a faster corrosion ratio of the specimen. The deviation of the corrosion ratio of X_3 and Y_3 for 200 freeze-thaw cycles was 0.0266, which is significantly higher than the deviation of X_3 and Y_3 (0.0087) after 150 freeze-thaw cycles. This is due to the permeability coefficient of the chloride ions and the specific resistance both decreasing with increased numbers of freeze-thaw cycles, resulting in generating a large amount of $Fe(OH)_3$. Thus, the actual corrosion ratio exceeded the theoretical corrosion ratio.

Figure 6 shows the relationship between actual corrosion rate and corrosion time. The corrosion rate of the specimens increased with the number of freeze-thaw cycles before the 5.85 d mark (3% theoretical corrosion ratio). However, the increased rate varied with different numbers of freeze-thaw cycles, and the corrosion rate of the steel was significantly accelerated after 50 cycles. The corrosion rate was

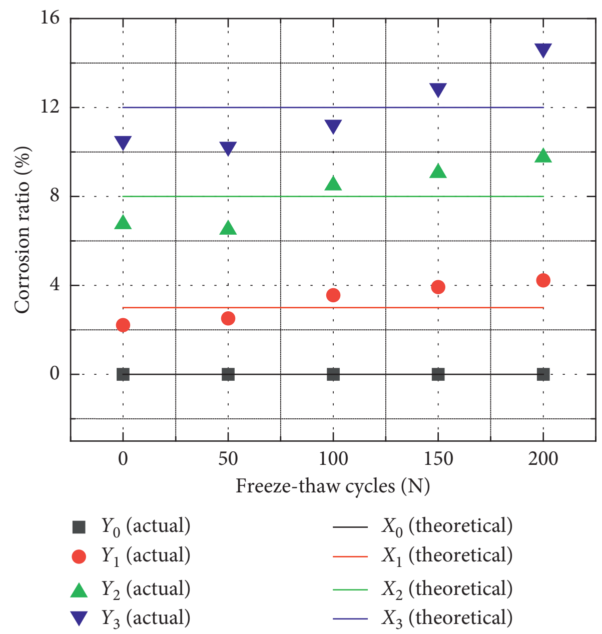

FIGURE 5: The difference between the actual corrosion ratio and theoretical corrosion ratio.

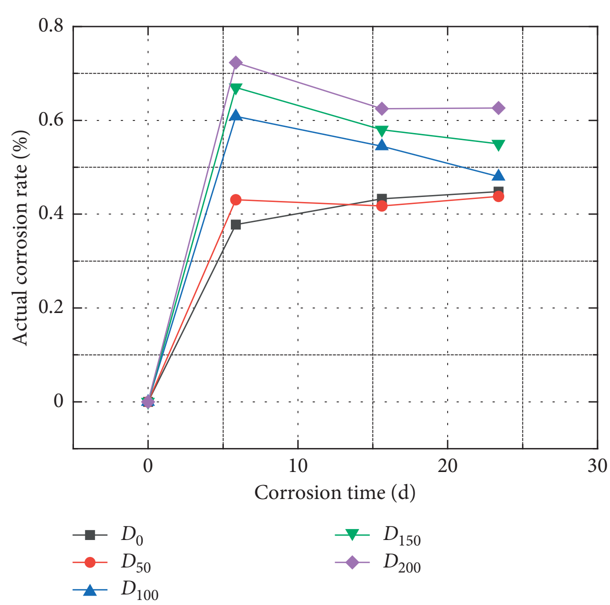

FIGURE 6: The change of corrosion rate in different corrosion times.

particularly similar within the initial corrosion time. The corrosion rate of the specimens decreases after 5.85 d (3% theoretical corrosion ratio) because of the accumulation of corrosion products. When the corrosion time reaches the 23.4 d (12% theoretical corrosion ratio), the corrosion rate at 200 cycles increased by 0.6%, a 0.2% increase compared to 100 cycles (0.4%). This indicated that the generated corrosion products decreased the transport property of chloride ions, resulting in a slower corrosion ratio. The combined action of the two effects led to the freeze-thaw cycles having a significant effect on steel reinforcement corrosion.

3.3. Bond Behavior

3.3.1. Ultimate Pull-Out Force. The ultimate pull-out force at various corrosion times is illustrated in Figure 7. The pull-out force decreased rapidly with increasing numbers of corrosion times, especially within the initial corrosion time (5 d), where the pull-out force was still high since the corrosion products ($Fe(OH)_3$) improved the roughness of the specimen and enhanced the frictional resistance at the reinforced concrete interface. However, the effect of freeze-thaw on the pull-out force became obvious when the corrosion time reached 23.4 d (12% theoretical corrosion ratio), where the pull-out force for 0 and 200 freeze-thaw cycles decreased by 36.2% and 75.5%, respectively. By comparison, the decrease in ultimate pull-out force for 200 freeze-thaw cycles was higher than that in 0 freeze-thaw cycles. It was obvious that the freeze-thaw cycles had a significant impact on the pull-out force of reinforced concrete. The phenomenon can be explained as follows: freeze-thaw damage decreased the strength of concrete while increasing the corrosion ratio, which led to an acceleration of the corrosion process. Thus, the influence of freeze-thaw damage and corrosion on the pull-out force of reinforced concrete was not a simple superposition problem.

3.3.2. Bond Slippage. Figure 8 shows the relationship between the bond slippage and corrosion time. It can be observed that the bond slippage of all specimens decreased with increasing corrosion time, yet it remained constant after 15.6 days (8% theoretical corrosion ratio). During corrosion, increasing freeze-thaw cycles lowered the bond slippage. For specimens with freeze-thaw cycles of 0, 50, 100, 150, and 200 cycles, the bond slippage after corrosion (15.6 d) decreased by 16.42, 8.515, 4.9, 5.414, and 4.859 mm, respectively. The bond slippage decreased by 42.5% after 200 freeze-thaw cycles compared with specimens with 0 freeze-thaw cycles. From 0 cycles to 50 cycles, the bond slippage decreased by 9 mm for uncorroded specimens. However, the bond slippage of uncorroded specimens after 100 freeze-thaw cycles decreased by 2.05 mm compared with those subjected to 50 freeze-thaw cycles, decreased by 2 mm after 150 cycles compared with 100 cycles, and decreased by 1.38 mm after 200 cycles compared with 150 cycles. According to the results discussed in Section 3.2.1, this phenomenon was due to freeze-thaw damage accelerating corrosion and producing more corrosion products, which increased the corrosion expansive pressure and made damage more serious. Thus, the effect of freeze-thaw cycles on the bond slippage had already occurred prior to corrosion because the freeze-thaw cycles changed the mechanical properties of the concrete.

3.4. Porosity Analysis. The influence mechanism of freeze-thaw cycles on steel reinforcement corrosion was further explained by analyzing the change of porosity and the relationship between porosity and freeze-thaw cycles under different corrosion ratios.

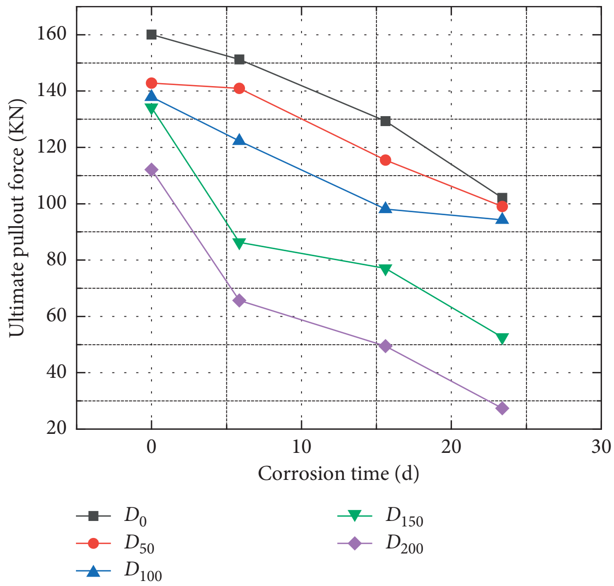

FIGURE 7: The change of ultimate pull-out force of steel reinforcements.

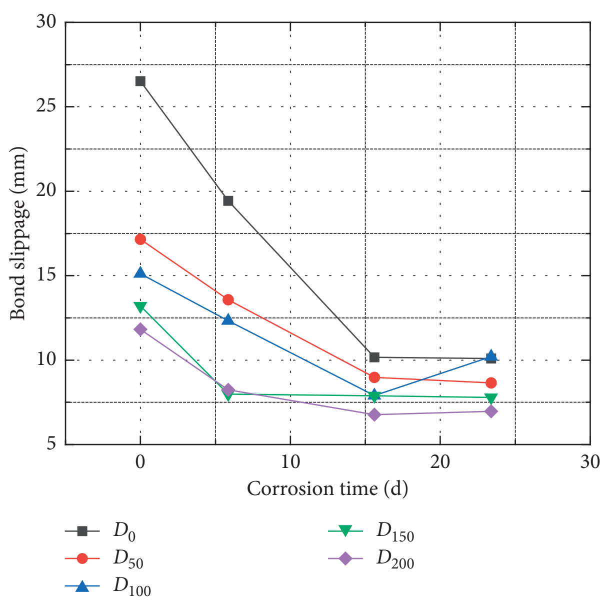

FIGURE 8: The change of bond slippage.

Figure 9 shows that porosity increased with increased numbers of freeze-thaw cycles. It can be observed that the slope of the curve in the ascending section of the edge point is larger than that of the internal point, and the ascending section of the central point is less sloped than the internal point. This showed that the freeze-thaw cycles had a significant influence on porosity from the surface to the center of the specimen. After 200 cycles, the concrete spalling deepened, and the overall structural performance was damaged. This was because the increased porosity of the edge point caused by freeze-thaw accelerated the corrosion ratio, which affected the bonding properties of the reinforced concrete.

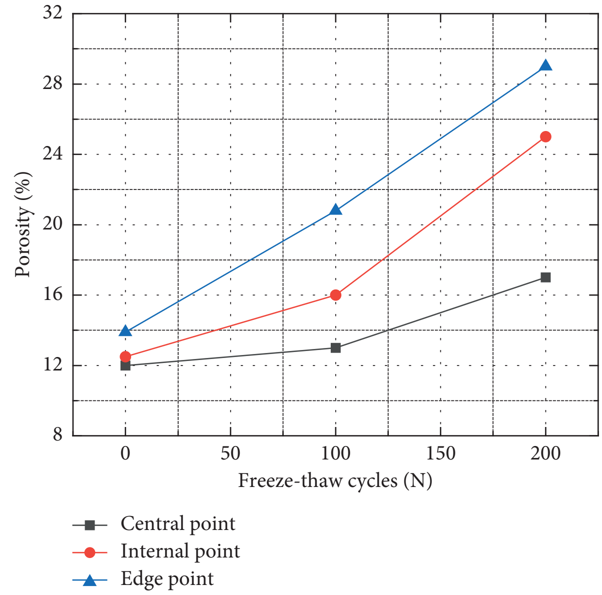

FIGURE 9: The effect of freeze-thaw cycles on the porosity of uncorroded specimens.

Figure 10 shows that the porosity of the 12% theoretical corrosion ratio group increased by 20% compared with the uncorroded group after the same number of freeze-thaw cycles. The porosity of the central point was especially greater than other positions in the initial freeze-thaw cycle. This was because the corrosion products caused damage in the central concrete but did not extend any further. The porosity of the internal point and edge point increased significantly with increasing numbers of cycles. After 100 cycles, the porosity of the edge point was greater than the central point, since the freeze-thaw cycles caused an increase in both porosity and cracks; the corrosion products developed from the center to the surface of the specimens. Both the freeze-thaw damage and corrosion made the cracks more serious, wherein the bond behavior of the reinforced concrete was almost lost. In summary, the change of porosity was related to the strength of concrete and affected the pull-out force. Additionally, the increased porosity caused by freeze-thaw also affected the transport properties of chloride ions, which accelerated the corrosion reaction.

3.5. SEM Analysis. According to the above macroscopic testing results, the freeze-thaw cycles had a significant impact on steel reinforcement corrosion. In order to further explore the effect of freeze-thaw cycles on corrosion from a microscopic perspective, the testing groups with the greatest difference among all specimens (0 cycles and 200 cycles) were selected, and SEM images before and after corrosion were compared.

3.5.1. Uncorroded Group. The pore structure of uncorroded specimens with two levels of freeze-thaw cycles is clearly observed in Figure 11 (2000x magnification). In Figure 11(a), the internal hydration of the concrete was

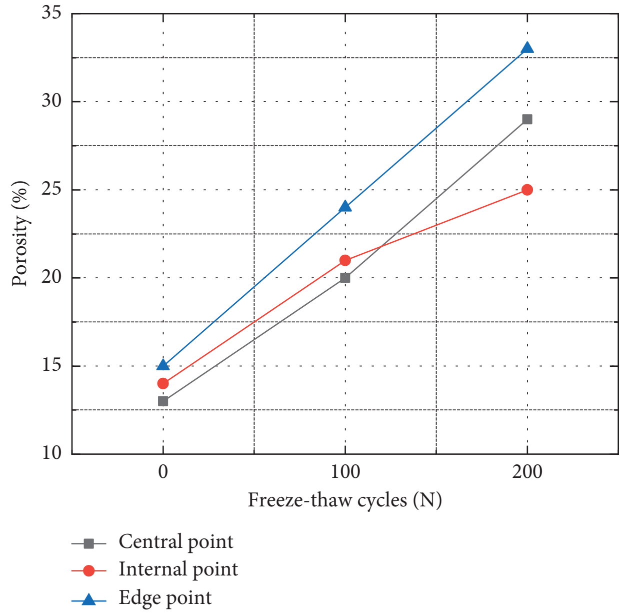

FIGURE 10: The effect of freeze-thaw cycles on the porosity of 12% theoretical corrosion ratio specimens.

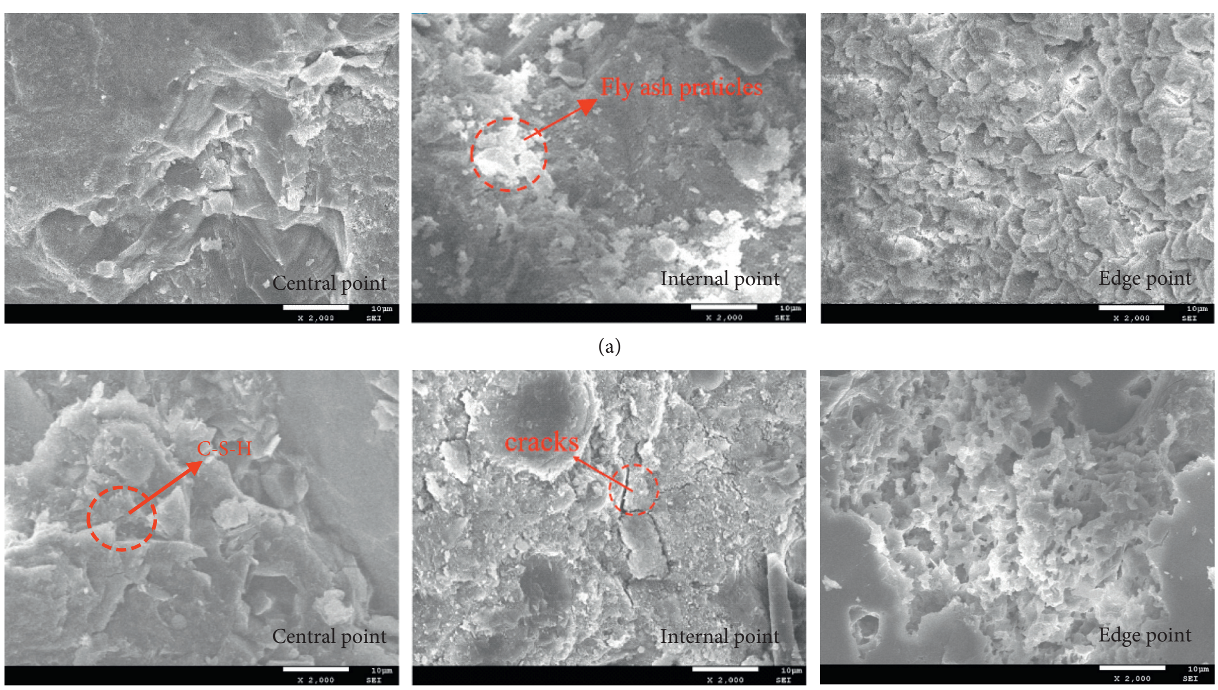

(a)

(b)

FIGURE 11: Electron microscope scanning of the uncorroded group. (a) 0 cycles of freeze-thaw without corrosion group. (b) 200 cycles of freeze-thaw without corrosion group.

complete, and the smooth and dense C-S-H structure occurred in all three positions. The overall structures in the concrete were very dense and the pores were small, and some fly ash particles could also be observed on the central point. Because fly ash was in cement paste, cement hydration was also involved in the hydration reaction, generating some calcium silicate hydrate gel.

Figure 11(b) shows the internal microstructure of uncorroded specimens after 200 freeze-thaw cycles. Compared with specimens without any cycles, the sample structure of the edge points became loose. Meanwhile, the internal and central positions were also damaged to varying levels. Some small cracks continued to expand and connect to form large cracks after 200 cycles, which had a serious impact on the material's structure.

After 200 freeze-thaw cycles, the edge point damage was greater than that of the internal point, and the damage of the internal point was greater than the central point. The path of freeze-thaw damage was from the surface to the interior. The pull-out force (Figure 7) and bond slippage (Figure 8) after 200 cycles were lower than those with 0 cycles. This was because the specimens exposed to freeze-thaw developed larger internal porosity and a looser structure, which led to a decrease in pull-out force and bond slippage.

3.5.2. Corroded Group. The pore structure of corroded specimens (23.4 d) exposed to two levels of freeze-thaw cycles is shown in Figure 12. Figure 12(a) shows that the surface of the edge point was smooth, dense, and without cracks. However, the internal point and central point changed significantly. The pores were relatively small and uniformly distributed in the internal point, but the number of pores and cracks increased in the central point. This was because the higher corrosion ratio caused a large amount of generated $Fe(OH)_3$, which damaged the specimen structure by expansive force. As shown in Figure 3, the corrosion products invaded the interior of the concrete after the steel reinforcement passivation film was destroyed, which resulted in the surface of steel reinforcement in the whole bonding section being enwrapped with $Fe(OH)_3$.

Figure 12(b) shows a large number of dense cotton balls (globular) inside the concrete, signifying the formation of corrosion products. A large number of corrosion cracks occurred upon the internal point of the specimens. The steel reinforcement corrosion developed from the center to the surface, while the freeze-thaw damage developed from the surface to the center. Thus, the internal zones of the specimens were the most seriously damaged portions. After 200 freeze-thaw cycles, a greater amount of corrosion products was present in corroded specimens compared with uncorroded specimens. This was because the pores inside the concrete samples increased gradually with increased freeze-thaw cycles. The structure also became loose, which resulted in the acceleration of chloride ions transport and then the acceleration of steel reinforcement corrosion. A large number of corrosion products were accumulated in the cracks caused by freeze-thaw damage, which resulted in the expansion of cracks and the spalling of the concrete layer. In summary, the deterioration process of concrete involves an increasing number of macro pores and expansion of micro cracks under the action of freeze-thaw cycles and steel reinforcement corrosion. In general, the deterioration process of concrete is the process of increasing the number of macro pores, decreasing the number of micro pores, and gradual expansion of micro cracks.

4. Discussion

The degradation mechanism of concrete with fitting analyses of micro and macro indices under different freeze-thaw conditions are herein discussed. The relationships between the porosity and corrosion ratio and the porosity and bond strength were obtained, further verifying the effect of freeze-thaw cycles on the corrosion of the reinforced concrete.

4.1. The Relationship between Corrosion Ratio and Porosity. In order to get reliable test results, samples were analyzed after 23.4 days (12% theoretical corrosion ratio) to determine the relationship between the porosity of the concrete edge points and the actual corrosion ratio under different freeze-thaw cycles, with the results shown in Figure 13.

Figure 13 shows a nonlinear correlation between porosity and corrosion ratio with different numbers of freeze-thaw cycles. The correlation was greater than 0.9, providing a coefficient to approximately evaluate the corrosion behavior of reinforced concrete under different freeze-thaw conditions. The actual corrosion ratio increased with porosity because the width and quantity of cracks increased with more freeze-thaw cycles. At the micro level, the freeze-thaw damage changed the number of connecting holes in concrete and ion transport performance, which accelerating the steel corrosion rate in reinforced concrete. In fact, the change of porosity had a significant effect on the actual corrosion ratio with the increases of corrosion times. Thus, for the reinforced concrete with initial damage, the longer the corrosion time, the greater the deviation of the theoretical corrosion ratio under the same porosity.

4.2. The Relationship between Bond Strength and Porosity. From the microstructure analysis, the increase of porosity led to increased ion transport, which accelerated the chemical corrosion of the reinforced concrete. In order to study the effect of freeze-thaw cycles on the bond behavior of reinforced concrete, 23.4 d samples (12% theoretical corrosion ratio) were chosen to analyze the relationship between the porosity of the concrete edge points and the bond strength under different freeze-thaw cycles. These results are shown in Figures 14 and 15.

Figure 14 shows a quadratic function correlation between the porosity and the pull-out force with different freeze-thaw cycles. In addition, when the porosity was less than 20%, the ultimate pull-out force changed only slightly. However, when the porosity was greater than 20%, the ultimate pull-out force decreased rapidly. When analyzing the pull-out tests (Figure 7), the pull-out form of steel reinforcement changed from a splitting failure to a pulling failure with increasing numbers of freeze-thaw cycles. After repeated freeze-thaw cycles, the micro cracks in the interior and numerous capillary pores increased. The path of chloride ions and sulfate ion flow was formed by those cracks.

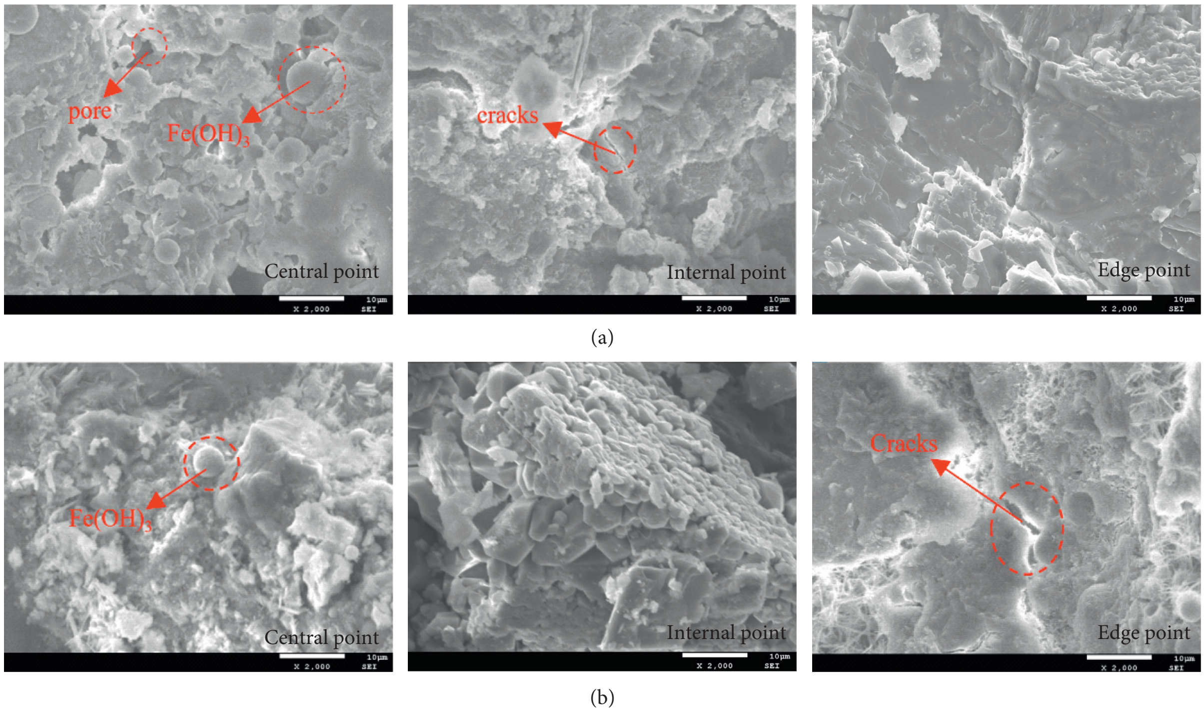

FIGURE 12: Electron microscope scans of 12% theoretical corrosion ratio. (a) 0 cycles of freeze-thaw with 12% corrosion group. (b) 200 cycles of freeze-thaw with 12% corrosion group.

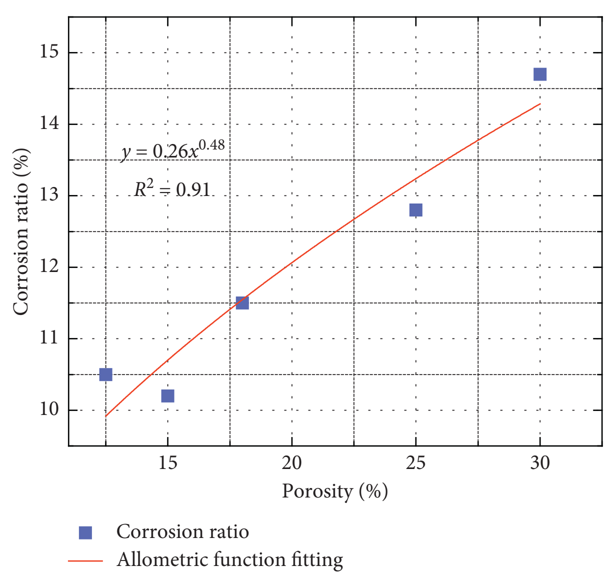

FIGURE 13: The relation between porosity and corrosion ratio.

Thus, the strength of concrete will gradually reduce and the concrete will damage due to corrosion expansive pressure caused by steel reinforcement corrosion destroying the layer of concrete. The porosity especially increased with increasing numbers of freeze-thaw cycles.

Figure 15 shows that porosity is negatively correlated with bond slippage, wherein the bond slippage decreased by 6.9 mm after increasing porosity from 0.13 to 0.28. This is because the higher number of freeze-thaw cycles and greater steel reinforcement corrosion increased the deterioration rate of bond behavior in the reinforced concrete. Due to the rapid development of macro cracks caused by the heterogeneous porosity distribution from surface to center, the surface peeling was much more serious after more freeze-thaw cycles. Freeze-thaw damage changed the porosity and ion transport properties, which led to the decrement of the bond slippage and destruction of concrete. In general, when the number of freeze-thaw cycles was small, the effect of

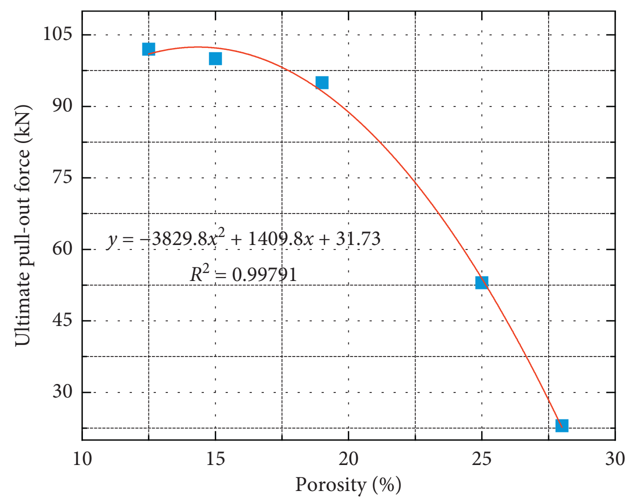

Figure 14: The relationship between porosity and ultimate pull-out force.

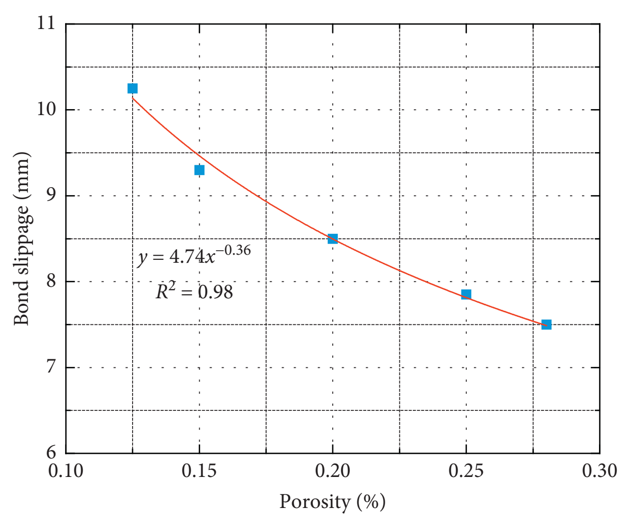

Figure 15: The relationship between porosity and bond slippage.

freeze-thaw and corrosion on the bond properties of reinforced concrete depended on the combined action of freeze-thaw cycles and corrosion. In contrast, when the number of freeze-thaw cycles reached 200 cycles, the effect of freeze-thaw and corrosion on the bond properties of reinforced concrete mainly depended on the action of freeze-thaw cycles.

5. Conclusion

The effect of freeze-thaw damage on steel reinforcement corrosion was investigated by accelerated corrosion experiments under different freeze-thaw cycles, and the evolutions of macro parameters and microstructure were obtained. The results of this study are summarized in the following concluding remarks.

(1) The surface state of specimens showed obvious change after 100 freeze-thaw cycles, and expansive cracks with large widths could be seen after 23.4 d of corrosion (12% theoretical ratio). Also, the corrosion mass and corrosion rate of steel reinforcement increased by 39.6% and 39.7% when comparing 200 freeze-thaw cycles to 0 cycles, respectively.

(2) The ultimate pull-out force and bond slippage decreased with increasing numbers of freeze-thaw cycles. However, the rate decrease varied with different corrosion times. When the corrosion time reached 23.4 d (12% theoretical corrosion ratio), the

pull-out force of 200 freeze-thaw cycles decreased by 73% compared with 0 freeze-thaw cycles. The bond slippage decrease after 200 freeze-thaw cycles was 31% of the 0-cycle value.

(3) The relationship between macroscopic mechanical properties and microscopic porosity structure indicated that the effect of freeze-thaw on steel reinforcement corrosion manifested in two aspects: first, freeze-thaw damage increased porosity, which led to a decrease in concrete strength; second, freeze-thaw damage accelerated the steel reinforcement corrosion rate, decreasing the bonding properties of the concrete.

(4) The difference between the theoretical corrosion ratio and actual corrosion ratio increased with increased numbers of freeze-thaw cycles, and the influence of freeze-thaw and corrosion on the bond properties of concrete gradually led to degradation of the concrete strength, which was dominated by freeze-thaw cycles.

Data Availability

The raw/processed data required to reproduce these findings cannot be shared at this time as the data also form part of an ongoing study.

Conflicts of Interest

The authors declare that they have no conflicts of interest.

Acknowledgments

This work was financially supported by the Educational Commission of Hubei Province of China (no. Q20201203), National Natural Science Foundation of China (no. 52009068), and National Natural Science Foundation of China (no. 51879145).

References

[1] C. A. Apostolopoulos and V. G. Papadakis, "Consequences of steel corrosion on the ductility properties of reinforcement bar," *Construction and Building Materials*, vol. 22, no. 12, pp. 2316–2324, 2008.

[2] F. P. Glasser and K. K. Sagoe-Crentsil, "Steel in concrete: Part II Electron microscopy analysis," *Magazine of Concrete Research*, vol. 41, no. 149, pp. 213–220, 1989.

[3] W. Zhou, G. Ma, and C. Hu, "Long-term deformation control theory of high concrete face rockfill dam and application," in *Proceedings of the Asia-Pacific Power and Energy Engineering Conference*, Wuhan, China, March 2011.

[4] J. A. González, S. Feliú, P. Rodríguez, E. Ramírez, C. Alonso, and C. Andrade, "Some questions on the corrosion of steel in concrete-Part I: when, how and how much steel corrodes," *Materials and Structures*, vol. 29, no. 1, pp. 40–46, 1996.

[5] A. C. Houlsby, "Discussion of "Progress in Rockfill Dams" by J. Barry cooke (October, 1984)," *Journal of Geotechnical Engineering*, vol. 112, no. 2, pp. 226-227, 1986.

[6] A. Neville, "Chloride attack of reinforced concrete: an overview," *Materials and Structures*, vol. 28, no. 2, pp. 63–70, 1995.

[7] S. Yoon, K. Wang, W. J. Weiss, and S. P. Shah, "Interaction between loading, corrosion, and serviceability of reinforced concrete," *ACI Structural Journal*, vol. 97, pp. 637–644, 2000.

[8] T. Zhang, X. Lyu, H. Liu, L. Zhang, J. Wang, and S. Gao, "Axial performance degradation of squared CFST stubs in severe cold and acid rain area," *Construction and Building Materials*, vol. 262, 2020.

[9] H. Ma and F. Chi, "Technical progress on researches for the safety of high concrete-faced rockfill dams," *Engineering*, vol. 2, no. 3, pp. 332–339, 2016.

[10] W. Zhou, S. Li, Z. Zhou, and X. Chang, "Remote sensing of deformation of a high concrete-faced rockfill dam using InSAR: a study of the Shuibuya dam, China," *Remote Sensing*, vol. 8, no. 3, p. 255, 2016.

[11] Y. Wang, Y. Cao, P. Zhang et al., "Water absorption and chloride diffusivity of concrete under the coupling effect of uniaxial compressive load and freeze-thaw cycles," *Construction and Building Materials*, vol. 209, pp. 566–576, 2019.

[12] A. F. a. Abubakar, X.-B. Zuo, S. Zou, O. O. Ayinde, and A. M. Aliyu, "Electrochemical investigation on the influence of sulfates on chloride-induced corrosion of steel bar in cement-based materials," *Journal of Sustainable Cement-Based Materials*, vol. 9, no. 2, pp. 112–126, 2020.

[13] Y. Lv, W. Zhang, F. Wu, H. Li, Y. Zhang, and G. Xu, "Influence of initial damage degree on the degradation of concrete under sulfate attack and wetting–drying cycles," *International Journal of Concrete Structures and Materials*, vol. 14, Article ID 119903, 2020.

[14] Y.-S. Yoon, J.-P. Won, S.-K. Woo, and Y.-C. Song, "Enhanced durability performance of fly ash concrete for concrete-faced rockfill dam application," *Cement and Concrete Research*, vol. 32, no. 1, pp. 23–30, 2002.

[15] T. C. Powers, "A working hypothesis for further studies of frost resistance of concrete," *Journal of the American Concrete Institute*, vol. 41, pp. 245–272, 1945.

[16] M. Pigeon, *Durability of Concrete in Cold Climates*, Taylor & Francis Group, Abingdon, UK, 2014.

[17] X. Li, "Analysis on causes and countermeasures of concrete highway bridge typical disease," *Urban Architects*, no. 18, p. 221, 2013.

[18] P. Pei, S. Zheng, Y. Zhang, and L. Dong, "Overview on the bonding of reinforced concrete under pristine, corrosive and freeze-thaw conditions," *Journal of Adhesion Science and Technology*, vol. 33, no. 7, pp. 761–789, 2019.

[19] Z. Ma, T. Zhao, J. Xiao, and T. Guan, "Evaluation of rebar corrosion in reinforced concrete under freeze-thaw environment and protection measures," *Anti-Corrosion Methods and Materials*, vol. 63, no. 2, pp. 128–136, 2016.

[20] Z. Wang, Q. Zeng, L. Wang, Y. Yao, and K. Li, "Corrosion of rebar in concrete under cyclic freeze-thaw and Chloride salt action," *Construction and Building Materials*, vol. 53, pp. 40–47, 2014.

[21] C. G. Berrocal, K. Lundgren, and I. Löfgren, "Corrosion of steel bars embedded in fibre reinforced concrete under chloride attack: state of the art," *Cement and Concrete Research*, vol. 80, pp. 69–85, 2016.

[22] W. Zhang, Y. Pi, W. Kong et al., "Influence of damage degree on the degradation of concrete under freezing-thawing cycles," *Construction and Building Materials*, vol. 260, Article ID 119903, 2020.

[23] X. Ji, Y. Song, and Y. Liu, "Effect of freeze-thaw cycles on bond strength between steel bars and concrete," *Journal of Wuhan University of Technology*, vol. 23, no. 4, pp. 584–588, 2008.

[24] H. Wang, S. He, X. Yin, and Z. Cao, "Experimental study on fatigue performance of reinforced concrete beams in corrosive environment with cyclic loads," *Structural Durability & Health Monitoring*, vol. 14, no. 2, pp. 95–108, 2020.

[25] K. Liu, J. Yan, X. Meng, and C. Zou, "Bond behavior between deformed steel bars and recycled aggregate concrete after freeze-thaw cycles," *Construction and Building Materials*, vol. 232, Article ID 117236, 2020.

[26] Y. Zhang, H. Liu, R. Tong, and J. Ren, "Effect of nano silica on freeze-thaw resistance of cement-fly ash mortars, cured in corrosive condition at different temperature," *Cement, Wapno, Beton*, vol. 24, no. 2, pp. 137–153, 2019.

[27] E. Sicat, F. Gong, T. Ueda, and D. Zhang, "Experimental investigation of the deformational behavior of the interfacial transition zone (ITZ) in concrete during freezing and thawing cycles," *Construction and Building Materials*, vol. 65, pp. 122–131, 2014.

[28] X. Yao, M. Zhang, J. Guan, L. Li, W. Bai, and Z. Liu, "Research on the corrosion damage mechanism of concrete in two freeze-thaw environments," *Advances in Civil Engineering*, vol. 2020, Article ID 8839386, 11 pages, 2020.

[29] T. Luo, C. Zhang, X. Xu, Y. Shen, H. Jia, and C. Sun, "Effects of cyclic freeze-thaw on the steel bar reinforced new-to-old concrete interface," *Molecules*, vol. 25, no. 5, p. 1251, 2020.

[30] GB 1499.2-2007, *Steel for the Reinforcement of Concrete, Part II: Hot Rolled Ribbed Bars*, General Administration of Quality Supervision, Inspection and Quarantine of the People's Republic of China, Beijing, China, 2007, in Chinese.

[31] DL/T 5016-1999, *Design Code for Concrete Face Rockfill Dams*, China Renewable Energy Engineering Institute, Beijing, China, 1999, in Chinese.

[32] T. Gonen, S. Yazicioglu, and B. Demirel, "The influence of freezing-thawing cycles on the capillary water absorption and porosity of concrete with mineral admixture," *KSCE Journal of Civil Engineering*, vol. 19, no. 3, pp. 667–671, 2015.

[33] GB/T 50082-2009, *Standard for Test Methods of Long-Term Performance and Durability of Ordinary Concrete*, Ministry of Construction of the People's Republic of China, Beijing, China, 2009, in Chinese.

[34] R. Liu, L. Jiang, J. Xu, C. Xiong, and Z. Song, "Influence of carbonation on chloride-induced reinforcement corrosion in simulated concrete pore solutions," *Construction and Building Materials*, vol. 56, pp. 16–20, 2014.

[35] Y. Cheng, Y. Zhang, Y. Jiao, and J. Yang, "Quantitative analysis of concrete property under effects of crack, freeze-thaw and carbonation," *Construction and Building Materials*, vol. 129, pp. 106–115, 2016.

[36] GB/T 50152-2012, *Standard for Test Method of Concrete Structure*, Ministry of Housing and Urban Rural Development of the People's Republic of China, Beijing, China, 2012, in Chinese.

Hindawi
Advances in Materials Science and Engineering
Volume 2021, Article ID 9988017, 15 pages
https://doi.org/10.1155/2021/9988017

Research Article

Deformation Monitoring in an Alpine Mining Area in the Tianshan Mountains Based on SBAS-InSAR Technology

Qingsong Du,[1,2,3] **Guoyu Li**,[1,2] **Yu Zhou**,[1,2,3] **Mingtang Chai**,[4] **Dun Chen**,[1,2] **Shunshun Qi**,[1,2,3] **and Gang Wu**[1,2,3]

[1]*State Key Laboratory of Frozen Soil Engineering, Northwest Institute of Eco-Environment and Resources, Chinese Academy of Sciences, Lanzhou 730000, China*
[2]*Da Xing'anling Observation and Research Station of Frozen-Ground Engineering and Environment, Northwest Institute of Eco-Environment and Resources, Chinese Academy of Sciences, Jiagedaqi 165000, China*
[3]*College of Resources and Environment, University of Chinese Academy of Sciences, Beijing 100049, China*
[4]*School of Civil and Hydraulic Engineering, Ningxia University, Yinchuan 750021, China*

Correspondence should be addressed to Guoyu Li; guoyuli@lzb.ac.cn

Received 22 March 2021; Revised 8 April 2021; Accepted 8 April 2021; Published 19 April 2021

Academic Editor: Xiao Dong Zhao

The fragile habitat of alpine mining areas can be greatly affected by surface disturbances caused by mining activities, particularly open-pit mining activities, which greatly affect the periglacial environment. SBAS-InSAR technology enables the processing of SAR images to obtain highly accurate surface deformation information. This paper applied SBAS-InSAR technology to obtain three years of surface subsidence information based on the 89-scene Sentinel-1A SLC products, covering a mining area (tailings and active areas) in the Tianshan Mountains and its surroundings from 25th December 2017 to 2nd January 2021. The data were adopted to analyze the characteristics of deformation in the study region and the mining areas, and the subsidence accumulation was compared with field GNSS observation results to verify its accuracy. The results showed that the study area settled significantly, with a maximum settlement rate of −44.80 mm/a and a maximum uplift rate of 28.04 mm/a. The maximum settlement and accumulation of the whole study area over the three-year period were −129.39 mm and 60.49 mm, respectively. The mining area had a settlement value of over 80 mm over the three years. Significantly, the settlement rates of the tailings and active areas were −35 mm/a and −40 mm/a, respectively. Debris accumulation in the eastern portion of the tailings and active areas near the mountain was serious, with accumulation rates of 25 mm/a and 20 mm/a, respectively, and both had accumulation amounts of around 70 mm. For mine tailing pile areas with river flows, the pile locations and environmental restoration should be appropriately adjusted at a later stage. For gravel pile areas, regular cleaning should be carried out, especially around the mining site and at the tunnel entrances and exits, and long-term deformation monitoring of these areas should be carried out to ensure safe operation of the mining site. The SBAS-InSAR measurements were able to yield deformations with high accuracies over a wide area and cost less human and financial resources than the GNSS measurement method. Furthermore, the measurement results were more macroscopic, with great application value for surface subsidence monitoring in alpine areas.

1. Introduction

Mining activity can cause surface deformations and negatively impacts the environment [1, 2]. If rehabilitation measures are not handled properly, they can lead to serious subsequent disasters such as mine collapse [3], slope instability [4], vegetation death over large areas [2, 5], and severe water-soil erosion [3]. These potential threats and problems are more prominent in high-altitude areas due to the fragile habitats therein [2]. The key to solving these problems is to provide theoretical support for decision-making based on a large amount of basic data such as surface deformation data. Ground settlement [6] data provide an understanding of changes in mining areas and the surrounding environment, contributing to their sustainable development. Subsidence data can also provide synchronous information on how to develop in areas containing perilous rocks, providing a basic foundation for mining safety in cold-plateau regions.

In recent years, with the development of computer technology, remote sensing (RS), and geographic information system (GIS) technology [7–9], increasingly more novel geographic analysis methods [10–12] have been used for the dynamic monitoring of surface subsidence in mining areas, among which monitoring based on interferometric synthetic aperture radar (InSAR) technology [13–15] has performed excellently. One of the advantages of InSAR over traditional time-consuming and costly monitoring methods, such as level measurements and global positioning satellite (GPS) measurements, is that it has all-day, all-weather [13, 16] observation capability. Moreover, microwaves can effectively penetrate the atmosphere and are less affected by water vapor and surface vegetation [17]. In addition, as more and more synthetic aperture radar (SAR) satellites have been launched, increasingly more materials are accessible [16, 18–21], and the data acquisition cycles have become shorter. As a result, the accuracy of these measurements has greatly improved. InSAR has the added advantage of obtaining ground deformation information over large areas at a relatively small cost. As a corollary, deformation measurements based on InSAR have becoming increasingly popular [21].

So far, InSAR technology has evolved from traditional differential interferometric synthetic aperture radar (D-InSAR) [22, 23] to multitemporal InSAR (MT-InSAR) [24] technologies, including persistent scatterer InSAR (PS-InSAR) [25–27], small baseline subsets InSAR (SBAS-InSAR) [28], and distributed scatterer InSAR (DS-InSAR) [29]. In addition, to compensate for the deficiency that D-InSAR or MT-InSAR can only acquire line-of-sight (LOS) direction deformation, the multiaperture InSAR (MAI) [30] technique has been proposed to acquire deformation information in the azimuthal direction (i.e., satellite flight direction).

These InSAR techniques have been used in a wide range of deformation monitoring applications, such as urban ground settlement [31–33], mine subsidence [34–41], earthquakes and plate movements [42–45], volcanic eruptions [46–48], infrastructure deformation [49–51], glacial drift [52–55], permafrost deformation [56–60], and landslides [61–63]. Compared to other MT-InSAR techniques, SBAS-InSAR has the advantage of being able to overcome atmospheric interference and requires a relatively small amount of data [14, 16, 21]. This method has been widely used for surface deformation monitoring with excellent results [28, 31–63].

For the above reasons, to understand the dynamic changes of subsidence in alpine mining areas, this study focuses on a mining area in the Tianshan Mountains of China as the research object, which consists of 89 scenes of Sentinel-1A level-1 single look complex (SLC) data processed via SBAS-InSAR technology to obtain the surface subsidence [35] information of the area. The subsidence information is analyzed to understand surface subsidence around the mining site and to provide recommendations for mining activities. The cumulative deformation information is also compared with data obtained from in situ global navigation satellite system (GNSS) measurements to verify the accuracy of SBAS-InSAR technology for surface deformation monitoring and subsidence measurements in alpine mining areas. From this, the extent of impact of mining activity on local environment can be understood. In addition, the obtained deformation over a large area can be used as fundamental information to provide a theoretical basic for mining policy, which is of great value to ensure environmental sustainability.

2. Regional Characteristics

The study area (Figure 1) is located in the eastern Tianshan Mountains, with geographical coordinates of 84.95–85.12°E and 43.28–43.35°N (as shown by the red box in Figure 1(a)). Its altitude ranges from 3,160 m to 4,365 m above the sea level (m.a.s.l.), with an average altitude of 3,839 m. The annual temperature has a maximum of 16°C and a minimum of −30°C [2], and it is a typical high-cold and high-altitude area. The snowline is 3,700–3,900 m.a.s.l., and the areas above the snowline are covered with glaciers, snow cover, permafrost, rock glaciers, and other periglacial geomorphology. The watershed located in the southwest of the mining area divides the rivers into two basins flowing south and north [9]. The south-flowing rivers converge with the Yili River, which is dominated by small rivers. The north-flowing rivers empty into Noor Lake, which eventually feeds into the Manas River. The maximum daily precipitation is 146 mm, the annual rainfall exceeds 1,000 mm, the evaporation is 425 mm, the maximum wind speed is 12 m/s, the average humidity is about 43%, and the wind direction is mainly north-northeast [2]. From October to April, the average temperature is below freezing, and solid precipitation such as hail and snowfall dominates this period. In contrast, from July to September, there is relatively little snowfall and warmer temperatures, making this the season appropriate for grass growth.

The mine is located along the watershed of the study area, which consists of a large open-pit iron ore mine where the extracted ore is sorted by a mobile crushing and dry sorting station [64]. The geology consists of an erosion-denudation-tectonic alpine landform and a denudation-deposition alpine-valley landform with extensive granite distribution. Two major sections, a tailings stockpile (irregular blue frame in Figure 1(c)) and an active area (irregular black frame in Figure 1(c)), are the focus of this study. The tailings stockpile includes a beneficiation region, and the active area consists of an open-pit mining area (irregular red frame in Figure 1(c)), early prospecting area, and part of the tailings waste stockpile. The rocks around the mining site are heavily weathered [64] and often have fallen rock accumulations. In addition, the rocks are subject to strong cryogenesis, gelifraction, and tectogenesis, inducing a high risk of potential geological hazards. This, coupled with the impact of the mining activities, increases the susceptibility to geological hazards, while frequent weather changes, such as high winds, snow, and hail, can easily cause

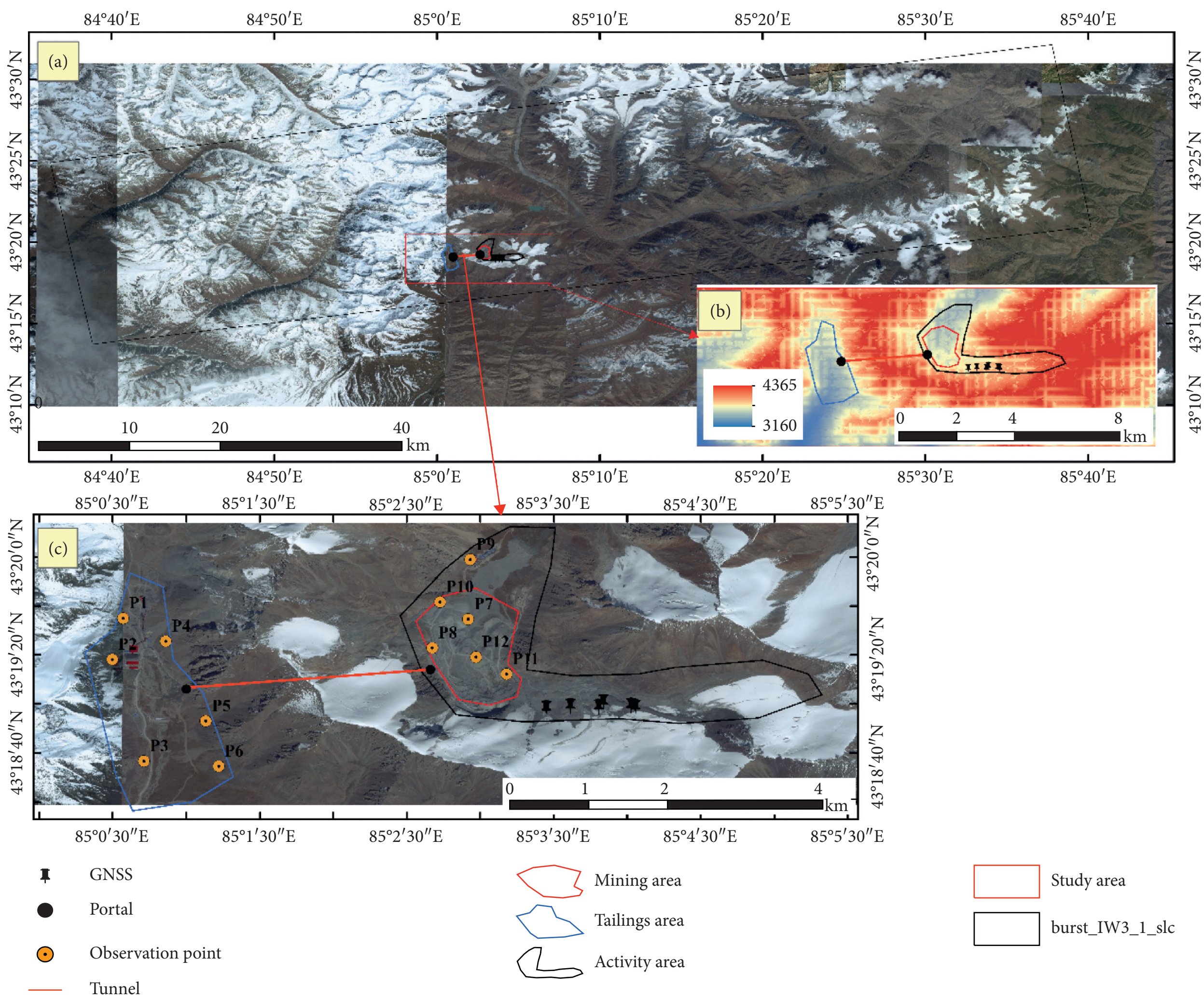

FIGURE 1: Geographical location of the study area: (a) position of the entire study area in the Sentinel-1A image; (b) DEM of the study area; (c) an enlarged view of the location of the mining area, observation points, and the GNSS points.

meteorological disasters and lead to a range of environmental and geological hazard problems.

3. Data and Methods

Sentinel-1A level-1 SLC products are available for free download from the ASF website (https://vertex.daac.asf.alaska.edu/). The time span is from 25th December 2017 to 2nd January 2020, with an average of more than two images per month, excluding cases where no data are available, for a total of 89 scene images. The precise orbital data corresponding to each scene image is available from the ESA website (https://qc.sentinel1.eo.esa.int/). There are two types of orbital data: one is the precise data created 21 days after the GNSS downlink date, and the other is the restituted product generated within 3 h of receiving the GNSS data. The precision orbital data with ephemerides have positions with accuracies better than 5 cm, and the other data have accuracies of 10 cm. The orbital data used here are the products with precise ephemerides. The digital elevation model (DEM) of the study area is the USGS EROS Archive-Digital Elevation-Shuttle Radar Topography Mission (SRTM) 1 Arc-Second Global, which has a spatial resolution of 30 m and can be obtained from the USGS EarthExplorer website (https://earthexplorer.usgs.gov/).

The GNSS static monitoring network system is located at the southwestern foot of the mountain near the mining area (Figure 1(c)), which can be used to monitor three-dimensional (3D) ground surface deformation information, and it consists of nine parts (Figure 2). The monitoring system which consists of six stations in total, one base station and five observation stations, started working on 9th October 2019. After the complex calculation between these two kinds of data, the deformation, with a temporal resolution of seconds, can be obtained. However, due to the high temperature variability in the area and the low winter temperatures, part of the stations has experienced some anomalies, and the deformation data monitored at certain times are missing. The GNSS measured deformation data used for the comparison span from 16th October 2019 to 31st May 2020 and condition with no data or abnormal data in this period have been rejected.

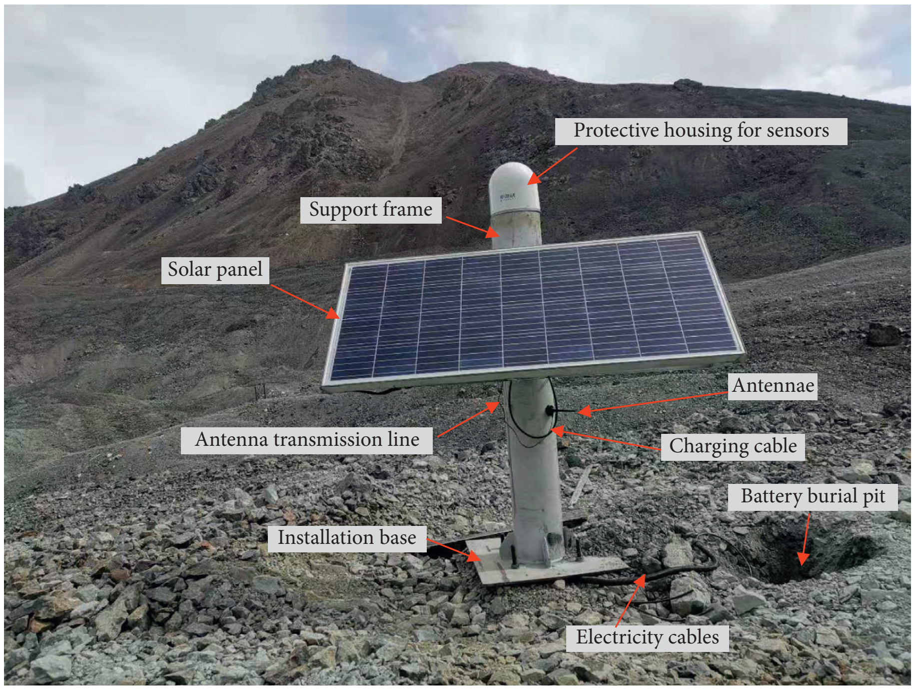

Figure 2: GNSS ground deformation monitoring instrument.

To better analyze the settlement characteristics around the mining site, six observation points were selected around each of the tailings stockpile area and the active area containing the mining activities, with six more based on topography, ground cover, and runoff distribution, for a total of 12 points, as shown in Figure 1(c). More information can be seen in Table 1.

The software used in this paper includes ArcGIS 10.6, ENVI5.3, SARscape5.2.1, OriginLab2017, and Global Mapper 14. The workflow mainly consists of data preprocessing, SBAS-InSAR processing, and data analysis, as shown in Figure 3.

3.1. Data Preprocessing. This process aims to convert the format of the data so that the different software platforms can recognize them and clip the data, thus reducing the time spent on data processing and improving the overall efficiency. Firstly, the region of interest (ROI) is mapped and converted to .shp format. Then, the DEM in .tiff format is converted to binary format using SARscape [7], and Global Mapper is applied to create isoheights of the total study area with a spacing distance of 200 m. After these two steps, the SLC data are imported and set at a resolution of 20 m × 20 m. Then, the processing images data (raster) area is sectioned with the ROI vector data (.shp). The resolution of the image depends on the pixel spacing slant range, pixel spacing azimuth, incidence angle, and multilook number, which is calculated as

$$R_{sr} = \frac{P_{sr}}{\sin(\theta)} \times N_{sr}, \tag{1}$$

$$R_a = P_a \times N_a, \tag{2}$$

where R_{sr} is the range slant resolution, R_a is the azimuth resolution, and P_{sr} and P_a are the pixel spacings of the slant range and azimuth, respectively, all in units of m. N_{sr} is the number of slant range looks and N_a is the number of azimuth looks; both are positive integers. θ is the angle of incidence in degrees.

The images used here were obtained from an ascending attitude at an angle of incidence of 39.08°, with pixel spacings of 3.73 m and 13.89 m for the slant range and azimuth, respectively. To ensure that we yielded a target deformation map with a spatial resolution of 20 m × 20 m, the multilook numbers of the slant range and the azimuth, which can be calculated by (1) and (2), were set as five and one, respectively.

Based on the SARscape software for baseline estimation and SBAS data processing, a temporal baseline threshold of 180 d and a spatial baseline threshold of 2% of the critical baseline were set for all data processing to ensure the accuracy of the results and to avoid spatiotemporal decoherence of the data as much as possible.

3.2. SBAS-InSAR Processing. A differential interferogram and coherence intensity graph are obtained by differential interference processing. The final output of this step is a flattened interferogram, where if the constant phase caused by the acquisition geometry and an input DEM are provided, the topographic phase is removed. A Goldstein adaptive filter [65] is chosen to reduce interference from noise phases while outputting the filtered product. Interferometric coherence, which is an indicator of the phase quality and the master intensity filtered image, is also generated. Then, the minimum cost flow method [66] with a coherence threshold

Table 1: Basic information of the deformation observation points.

Region	Name	Latitude N (°)	Longitude E (°)	Altitude (m)	Surface features
Tailings area	P1	43.3264	85.0095	3571.37	Tailings stockpile, close to river
	P2	43.3217	85.0083	3662.99	Close to the living area
	P3	43.3102	85.0119	3639.23	Downstream of the river
	P4	43.3238	85.0143	3562.51	Gravel slopes
	P5	43.3147	85.0189	3644.24	Gravel, close to road, portal
	P6	43.3096	85.0203	3668.44	Gravel slopes
Activity area	P7	43.3263	85.0486	3629.46	Close to road, gravel slag
	P8	43.3230	85.0446	3592.24	Close to portal, gravel slag
	P9	43.3331	85.0489	3685.94	Tailings stockpile, close to river
	P10	43.3282	85.0454	3614.84	Foot of the mountain, near road
	P11	43.3201	85.0530	3483.14	The edge of the mine
	P12	43.3220	85.0495	3611.80	Foot of the mountain, near mining

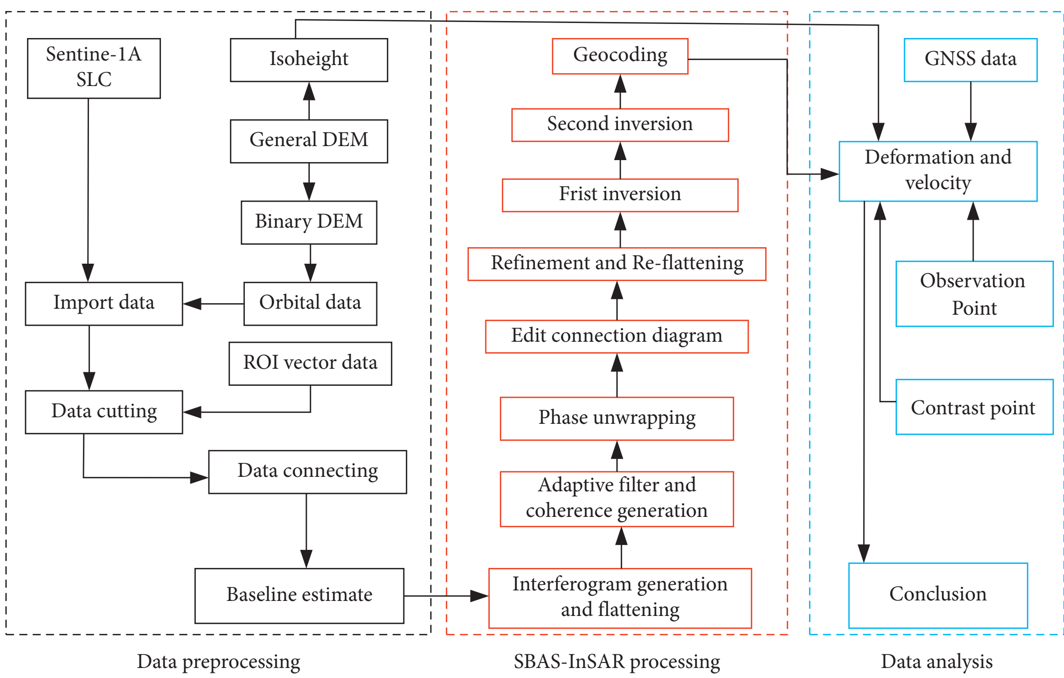

Figure 3: Data processing flow chart.

of 0.35 to unwrap the phase, which is obtained after the above processing, is employed. Finally, the interferometric image pairs are edited according to the unwrapping result, the coherence intensity graph, and the flattened interferogram to ensure that the connection diagram is correct, and image pairs are removed if the value of the coherence intensity graph is low.

After the editing process, ground control points (GCP) are selected for refinement and reflattening processing to accurately estimate the orbital parameters so that the unwrapped results are refined and the residual phase is removed. The deformation rate and residual topography are estimated by the first inversion, and the atmospheric phase error is removed by the second inversion. Multiple time series displacements are calculated and the SBAS-InSAR results are geocoded. The results consist of LOS cumulative displacements, in units of mm, and multitime series rate deformation, in units of mm/a.

3.3. Data Analysis. To visualize the displacement results and extract the features of the deformation information, we divided the results into three-year parts with a time interval of about three months in every year. We note that this choice is in keeping with the changing seasons. Then, the subsidence rate map was used to analyze the subsidence features around the mining site, select and visualize typical sites, extract their multitime subsidence information to understand the subsidence characteristics, and map the data. Finally, the subsidence information for the comparison points (CPs) was extracted and compared with the GNSS data, which were obtained from observations made during the same measurement period to verify the accuracy of the SBAS-InSAR measurements in the study area. These two kinds of data were obtained during the same observing period and from the same observing places so that the accumulated sedimentation obtained from the two methods could be compared. The accumulated sedimentation can be calculated as follows:

$$\Delta\ D = D_2 - D_1, \tag{3}$$

where ΔD is the accumulated sedimentation and D_1 and D_2 are the sedimentations of the observational starting data and end data, respectively, all units in mm.

4. Results

4.1. Baseline Estimation. The baseline information (Figures 4 and 5) of the Sentinel-1A data was obtained after calculation. The image from 21st October 2018 (yellow dots in Figures 4 and 5) was finally identified as the super master image, and the remaining images were paired with this master image for interferometric processing, which resulted in 1029 pairs of interferometric images (Figure 5). The maximum absolute normal baseline was 116.56 m, the minimum absolute baseline was 0.71 m, and the average was 50.51 m. The time baseline ranged from 12 d to 180 d. The results of processing indicated that the data were sufficient for use in the SBAS-InSAR process and they contained little decoherence.

4.2. Deformation Velocity. The deformation rate of the entire study area is shown in Figure 6. Data throughout the study area ranged from −44.80 mm/a to 28.04 mm/a, with significant subsidence at the mining area location, with rates in excess of −40 mm/a. Significant subsidence funnels exist in the northwest and southeast corners of the active area. Combined with the field investigations carried out in September 2018, a large accumulation of tailings waste was found in the northwest corner, distributing a river that flows from the mine site to Noel Lake. At the southeast foot, ground ice is developed, and a large number of turn-hole steel pipes left over from earlier prospecting are distributed, with the tops of the pipes ranging from 1 to 2 m from the present ground surface. The subsidence may be caused by the scouring and transporting actions of the river in the northwest. Besides, sinking in the southeast section of the mining area may be due to melting of this ground ice caused by early prospecting activities. In addition, there is a tendency for accumulation along the eastern part of the active area near the mountain, with an accumulation rate of greater than 20 mm/a, mainly due to rolling accumulation towards the foot of the mountain as the dangerous rock is broken by gelifraction, frost action, and physical weathering, while activities in the mine also likely increase accumulation at the foot of the mountain.

The deformation rate characteristics of the tailings pile area are similar to those of the active and mining areas, with significant subsidence in the waste piles distributed along the river in the west and uplift in the western part near the hills. Settlement is mostly pronounced in the northwest and southwest, with deformation rates exceeding −35 mm/a in the north and averaging 30 mm/a in the southwest, while in the east, at the foot of the hillside, the piles are clearly deposited at rates greater than 25 mm/a.

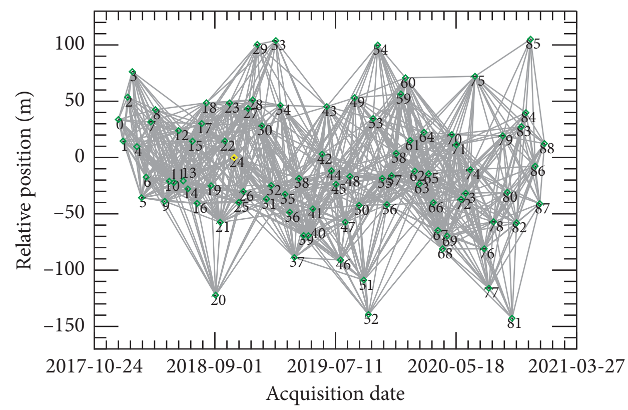

Figure 4: Spatiotemporal baseline combination of the data collection.

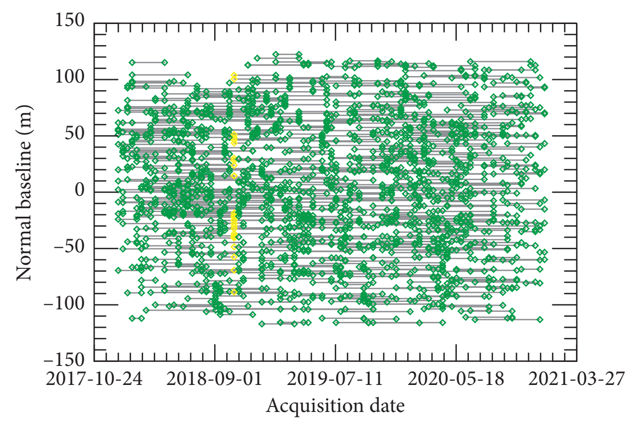

Figure 5: Interferometric image pairs of the data.

The relationship between the deformation velocity and altitude (Figure 7) shows that as the altitude rises, the velocity gets larger. Combined with Table 1 and Figures 1 and 6, we can understand that P1–P6 are located in the tailings area, which is used for mineral dressing and tailings stockpiling, while P1–P3 are located to the west of the area, and P4–P6 are near the mountain to the east of the tailings area. The deformation velocity shows that with the exception of P5, which is located in the accumulation zone, all other points are located in the settlement zone, with P1, P3, and P4 all having settlement rates in excess of 20 mm/a. P7–P12 are included in the activity area, where P8, P9, and P10 are located in the northwest of the area, P7 is in the central part near the mining working area, and P11 and P12 are in the southeast; indeed, all points except P9 are within the mining area. The deformation velocities of P7, P8, and P11 are positive and the other three are negative.

In general, the area over which the tailings were deposited has settled significantly, with an average settlement rate of over 35 mm/a and more than 40 mm/a in areas that experience river flowing. Mining activity may accelerate the surrounding perilous rock with frost fissure and frost splitting. Due to the gelifraction of glaciers and ice and the engineering blasting of the mining activity, there is large accumulation of sediment at

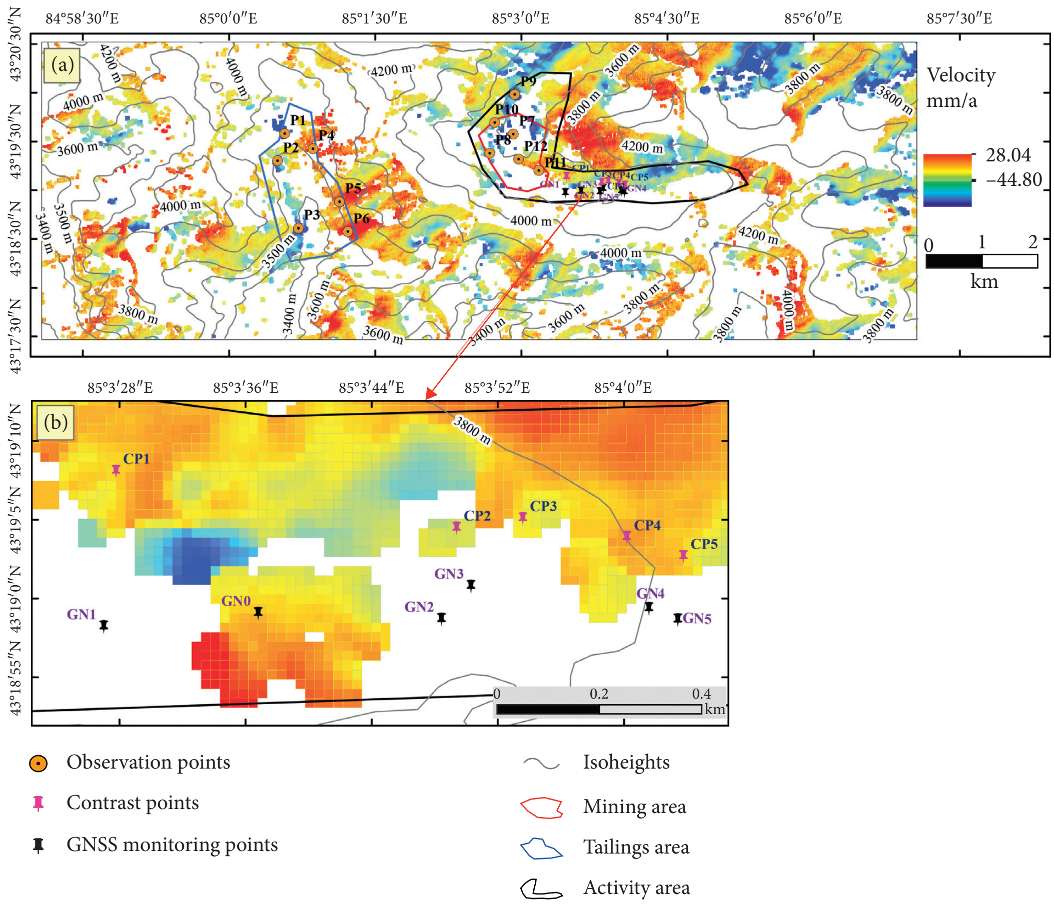

Figure 6: Deformation velocity in the study area.

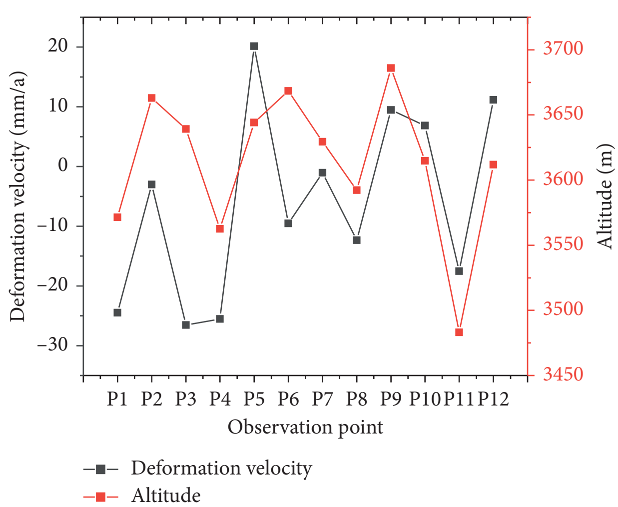

Figure 7: Relationship between the deformation velocity and altitude of the observation points.

the foot of the slope around the mining site. The settlement rate here is over 20 mm/a, which is a cause of concern. The prolonged and rapid accumulation of debris is a potential risk that could threaten the safety of mining personnel, and as the tailings area and mining area are connected by tunnels (Figure 1(c)), the safety of traffic should be a further concern.

4.3. Deformation Characteristics. Taking the LOS deformation on 25th December 2017 as a starting point, the deformation of each subsequent scene image was calculated according to (3). The 89-scene deformation results were divided into three groups at three-month intervals, with each group including a whole freeze-thaw cycle in a year, which allowed for better consistency with seasonal changes. The results are shown in Figures 8–10, corresponding to 2018, 2019, and 2020, respectively. Cold colors indicate surface deformation away from the satellite while warm colors represent displacements towards the sensors along LOS.

Comparison of the cumulative amount of minimum deformation values for these three years shows that the amount of subsidence in the study area gradually increased with date, decreasing from −12.31 mm on 31st March 2018 to −141.70 mm on 21st December 2020, with a deformation variable of up to 129.39 mm. A decrease of 79.75 mm occurred from 31st March 2018 to 27th December 2019, and a fall of 82 mm transpired from 26th March 2019 to 21st December 2020. The cumulative lift during the years 2018, 2019, and 2020 was 33.26 mm, 32.36 mm, and 37.22 mm, respectively. Meanwhile, the maximum accumulation in the study area increased by 60.49 mm from 25.93 mm on 31st March 2018 to 21st December 2020. However, unlike the changes in the minimum deposition accumulation, the maximum accumulation values fluctuated and changed rather than increasing over time.

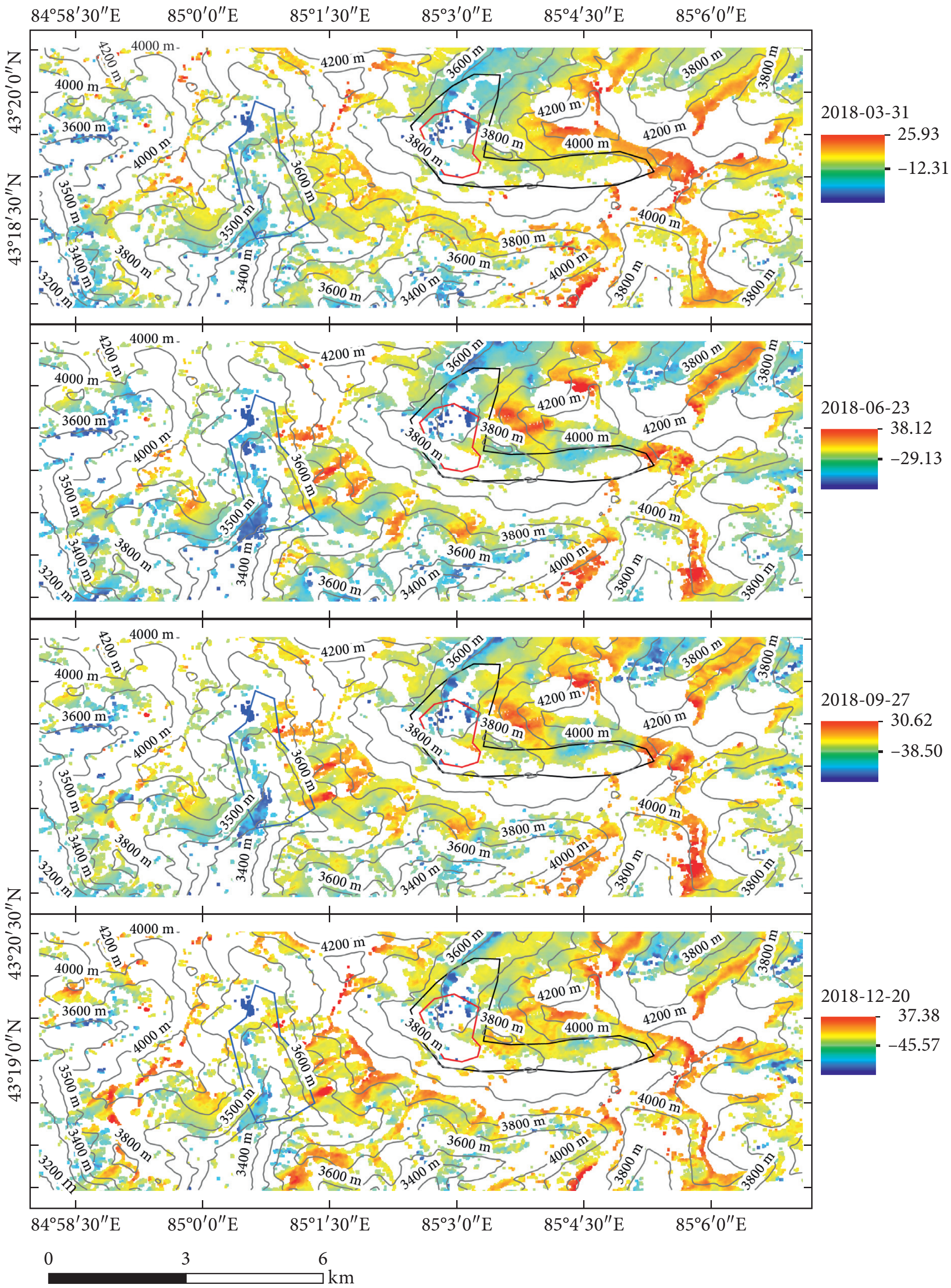

Figure 8: LOS deformation of 2018, in mm.

From Figures 7 and 11, it can be seen that there is good correspondence between the deformation piling volume and the deformation rate value. The settlement volumes at P1, P3, and P4 increased the most with time, corresponding to the largest deformation rates. The settlement volumes of points P6, P8, and P11 were the second largest, and the settlement rates accelerated after September 2019. The largest amount of accumulation occurred at P5, with an accumulation of more than 70 mm over the three years, which should be of key concern due to its proximity to the tunnel entrance. P9, P10, and P12 showed the same trend of change with uplift, but the rates of uplift were not large and fluctuated with a certain periodicity, which may be due to the regular manual cleaning and removal of the accumulation. P2 and P7 showed no obvious changes and only slight subsidence. Through the fieldwork and site investigations, it was found that P2 is in the location of the processing plant and P7 is the coal mining ladder of the mining area, both of which are relatively stable, so the deformations therein were not obvious.

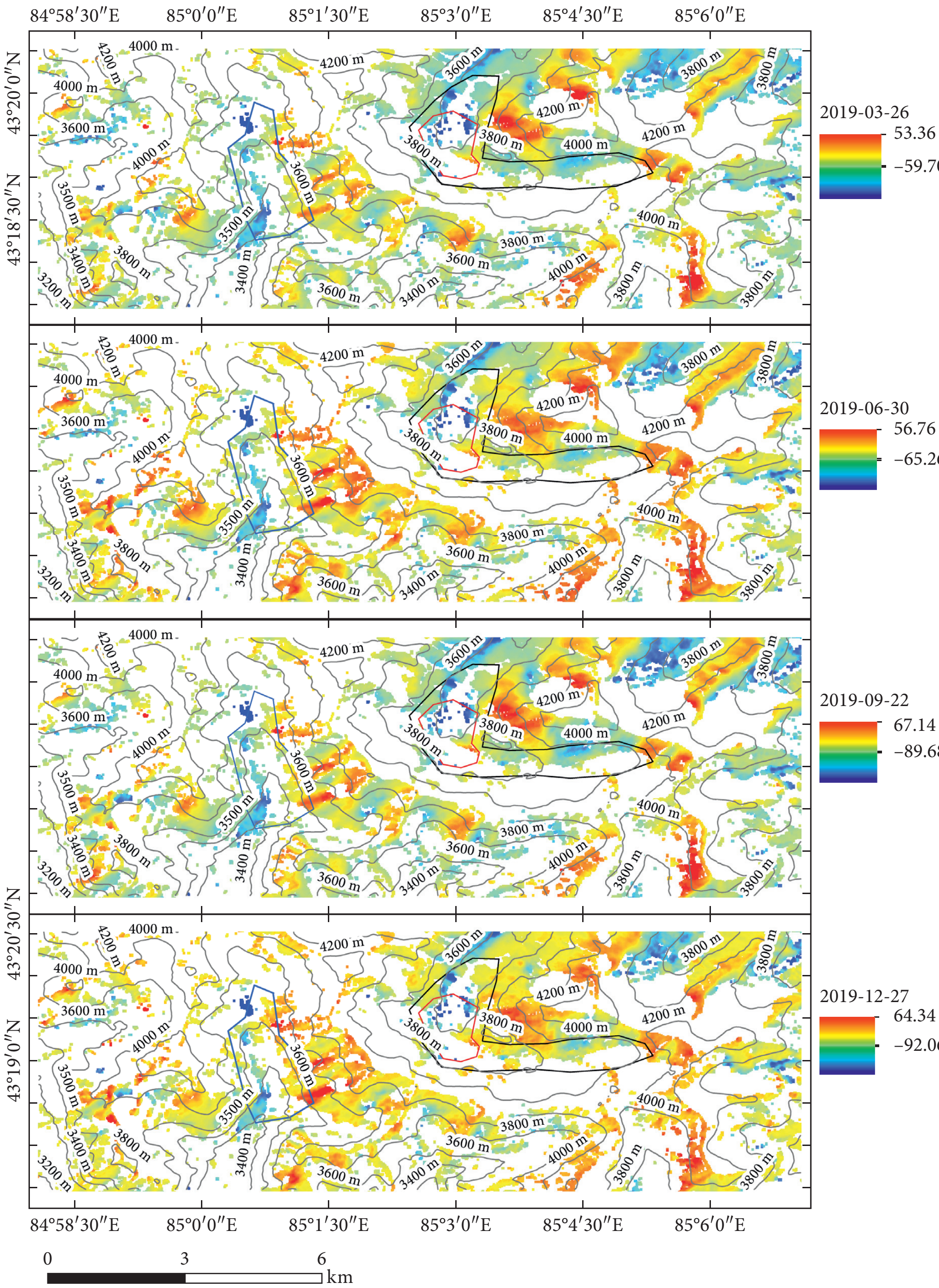

Figure 9: LOS deformation of 2019, in mm.

In summary, the tailings accumulation area and the active area mainly showed subsidence in the west along the river distribution section, while they showed uplift in the east near the foot of the mountain. The reason for this phenomenon is mainly due to the presence of a large number of tailings piles distributed along the river area, which are loose structures that are prone to collapse and can accelerate the subsidence phenomenon due to the transport and scouring effects of runoff. The area of accumulation is mainly due to the accumulation of mountain debris slides. To ensure the sustainable development and safe operation of the mine, the mine should minimize the accumulation of tailings in the river flow in the future to reduce water pollution, remove the accumulation of tailings, and carry out vegetation restoration. The piles around the mine should be cleaned regularly to ensure safe mining, and the piles at the tunnel entrance and exit locations should be monitored over a large area for a long period of time and dealt with in a timely manner.

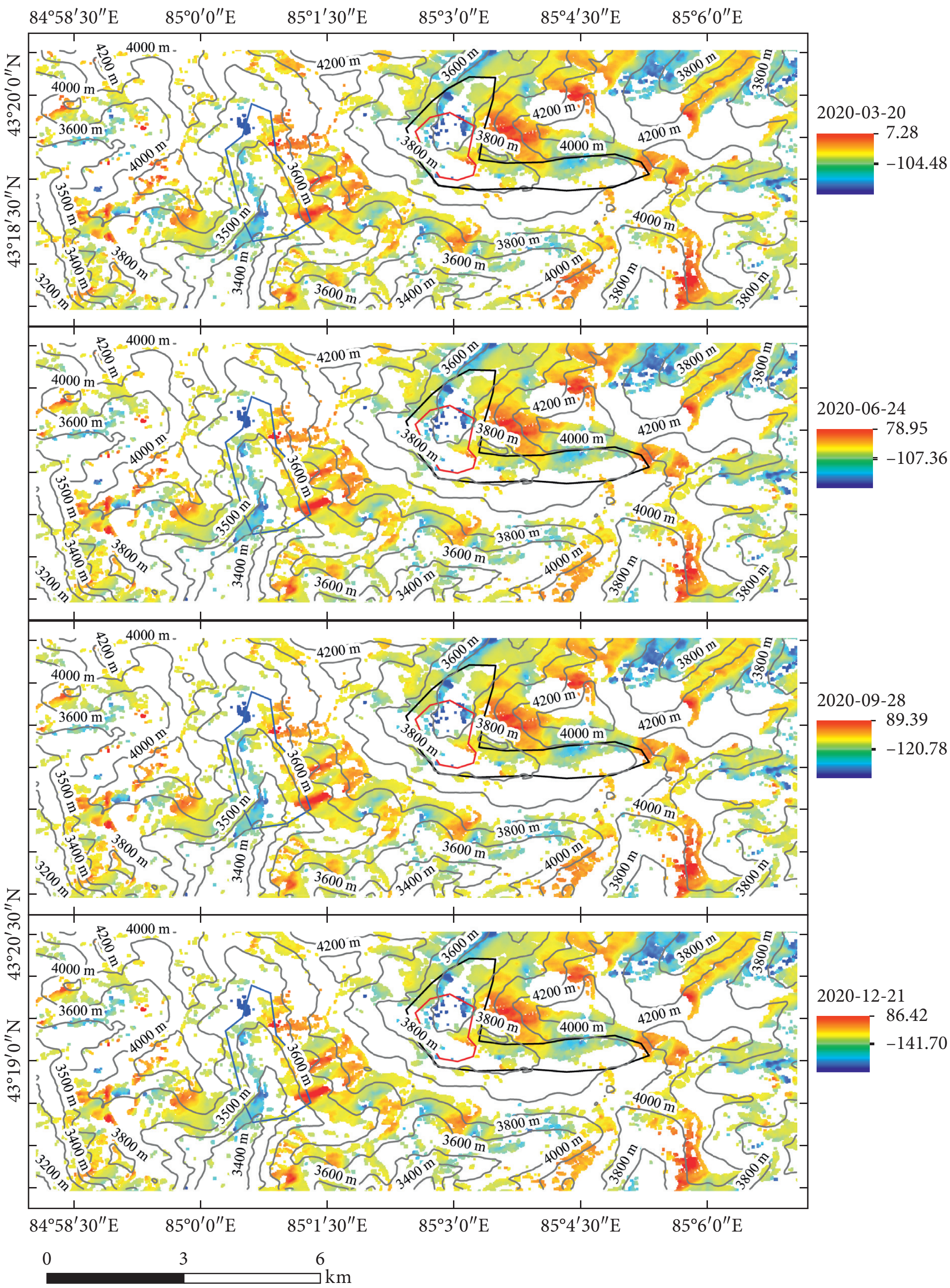

Figure 10: LOS deformation of 2020, in mm.

4.4. Deformation Precision. To verify the accuracy of the SBAS-InSAR measurement results, GNSS monitoring data and SBAS-InSAR measurements obtained from 16th October 2019 to 31st May 2020 were selected. The cumulative shape variables for the corresponding dates were calculated using (3), and the results were compared. Theoretically, the location of a GNSS observation point should be exactly the same as the location of a SBAS-InSAR measurement point; however, due to the reason of decoherence, the SBAS-InSAR monitoring results at the precise GNSS installation locations were missing, so points close to each GNSS installation location were selected as the corresponding CPs to obtain the required data for the observation period. The GNSS data were collected at an interval of 2 h, and the temporal resolution of the SBAS-InSAR monitoring results was 12 days. The results are shown in Figure 12.

As can be seen from Figure 12, the accumulations for each set of corresponding points have a high degree of agreement in the general trend, but do not match perfectly, and the GNSS observations are more prominent than the

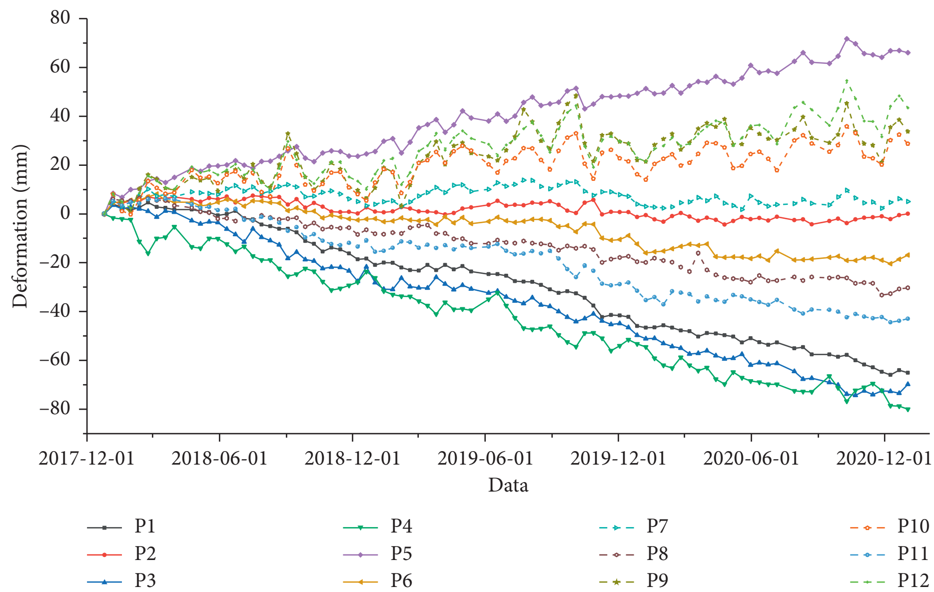

Figure 11: Deformation of the observation points.

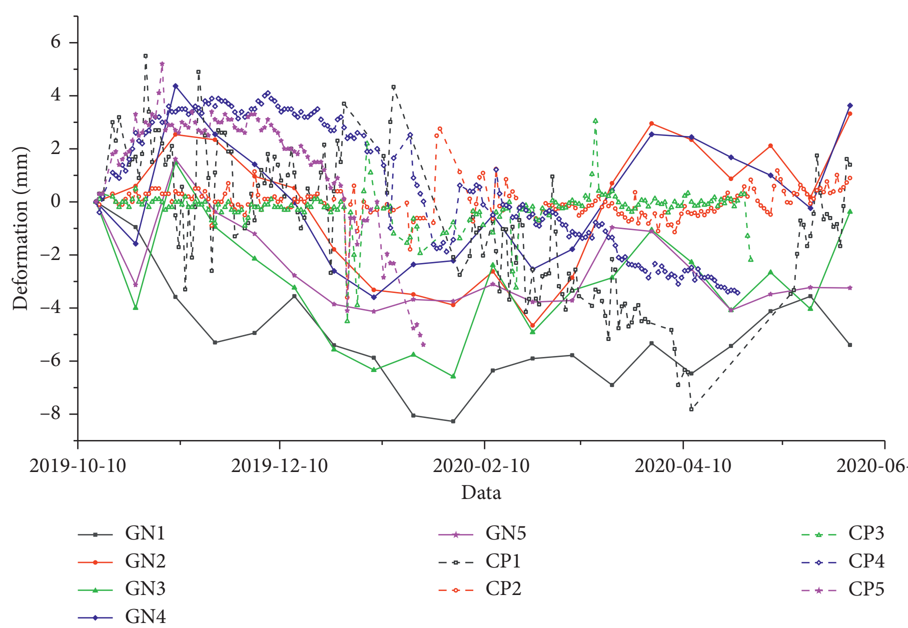

Figure 12: Comparison of the SBAS-InSAR results and the GNSS data.

SBAS-InSAR measurements in terms of variability. This phenomenon is mainly due to the inconsistent temporal resolution of the two measurements, the incomplete agreement of the observation locations, and the inconsistent orientation of the deformation values. The deformations measured by SBAS-InSAR are in the LOS direction, while the GNSS deformation measurements were selected along the x direction. Although there are many limitations that lead to some deviations in the two results, the SBAS-InSAR deformation measurements in this area have high accuracy and credibility. These results have an important reference value and can provide a theoretical basis for the restoration of mining environments and the creation of safety measures in mining areas.

In summary, the surface deformation measurement results of alpine mining areas based on SBAS-InSAR technology are highly credible and relatively accurate. Although there is a slight difference from the GNSS field observation results, the measurement results of this method lie in its wide observation range, workload, and less human and material resource requirements. GNSS measurements are highly accurate but costly, due to the large surface undulations in alpine areas and inconvenient transportation, coupled with strong frost splitting, frost stirring, congeliturbation, and frost jacking effects. Furthermore, it is difficult to keep the GNSS mounting base fixed, which can easily lead to the collapse of GNSS observation instruments, thus affecting the accuracy of the monitoring results; indeed, frequent repair and maintenance will increase the cost of GNSS observations. Therefore, SBAS-InSAR surface deformation monitoring based on Sentinel-1A has great prospects for applications in alpine and high-altitude mining areas, its monitoring results can provide a theoretical basis for environmental restoration and safety measures for construction activities in mining areas, and its accuracy is sufficient to meet general surveying and mapping requirements.

5. Discussion

Surface subsidence measurements based on SBAS-InSAR in alpine and high-altitude areas have proven to provide a wealth of information for mining sites, thus contributing to their sustainable development. However, there are some corresponding problems, such as the deformation information at the location of the mining area not being measured, the presence of a large number of blank areas throughout the study area, and the measured deformation results being in the LOS direction rather than of the vertical rise and fall of mining area deformation.

The above problems are mainly due to the decoherence of the data during differential interference. The location of the study mine is a low-lying gully, and the Sentinel-1A data used in this case are ascending, which has resulted in a significant amount of shadowing, layover, and foreshortening [16] due to the topography. In addition, there are a number of limitations inherent [14, 16] to InSAR deformation measurements, including various other phase and noise effects, as well as the correct/incorrect setting of parameters during processing. The influence of the phase manifests itself in the atmospheric phase, the noise of the system itself, and in the terrain phase [16, 21]. The influence of the parameter settings is mainly in the correct setting of the multiview numbers, the selected filtering methods, and the choice of phase unwrapping methods [66, 67]. The contributions of many scholars in recent years have led to an increasing number of parameters [17] to be set, and how to choose a set of parameters suitable for data processing in the study area requires constant trial and error and summation to obtain the optimal values. The decoherence of the data will result in the measured region being partially masked out and thus appearing as a blank in the deformation result map.

The results of deformation measurements are values in the LOS direction [14], which are limited by the InSAR measurements themselves. To obtain the real 3D deformation information of the surface, it is necessary to use simultaneous multisource data, multi-incidence angle data, etc., to obtain deformation information along more directions in the study area, so that the true 3D information of the surface can be solved with the mathematical model [4, 36, 37].

Therefore, to obtain accurate 3D surface deformation information, more data must be processed to obtain more deformation information from different aspects, in addition to combining field measurements, retrieving missing measurements by spatial interpolation, etc.

6. Conclusions

In alpine and high-altitude regions, due to the development of periglacial landforms such as ice field, ground ice, and rock glaciers, open-pit mining involves extensive surface excavation and massive accumulation of surface tailings, which can cause substantial disturbance to the ecological environment and loosen dangerous rocks around the mining site, thus posing a series of potential threats and risks. In this paper, the deformation information and annual average subsidence rate data of a mining site in Tianshan Mountain from 25th December 2017 to 2nd January 2021 were obtained by SBAS-InSAR processing of 89-scene Sentinel-1A ascending SLC data, and the measurement results were compared with field GNSS deformation measurements to verify the former's measurement accuracy. The conclusions of this study are as follows:

(1) Deformation around the mine is significant compared to the rest of the surrounding area. The maximum sedimentation rate in the study area was 44.8 mm/a, and the maximum uplift was 28.04 mm/a. The maximum sedimentation rate in the tailings area was 35 mm/a, and the maximum uplift was 25 mm/a. The active area, including the mining area, had a maximum sedimentation rate of over 40 mm/a and an accumulation rate of 20 mm/a.

(2) The overall deformation in the study area is dominated by subsidence, with the maximum subsidence amount reaching 129.39 mm during the three years. The uplift phenomenon is weaker than the subsidence phenomenon, with a maximum uplift accumulation of 60.49 mm during the three years, which is about half of the maximum subsidence. The tailings accumulation area and the active area are stacked significantly at the foot of the hill near the mountain area, which showed a three-year uplift of over 75 mm, and the tailings accumulation area distributed along the river in the west settled significantly, with a three-year settlement of over 80 mm.

(3) The deformation measurement results based on SBAS-InSAR are highly accurate and can provide a theoretical basis for environmental restoration and safety measures for construction in mining areas. Compared with GNSS measurements, the method is less costly and less labor intensive. The measurement results cover a large area, including the entire mining site and the surrounding environment, thus providing a macroscopic understanding of the impact of mining activities on the surrounding environment. The data obtained from this method have the potential for widespread use.

Data Availability

Sentinel-1A level-1 SLC products were downloaded from the ASF website (https://vertex.daac.asf.alaska.edu/); orbital data are available from the ESA website (https://qc.sentinel1.eo.esa.int/); DEM can be obtained from the USGS EarthExplorer website (https://earthexplorer.usgs.gov/); and other data are available from the corresponding author upon request.

Conflicts of Interest

The authors declare that they have no conflicts of interest.

Acknowledgments

This work was supported by the National Natural Science Foundation of China (No. U1703244), the Second Tibetan Plateau Scientific Expedition and Research Program (No. 2019QZKK0905), and the Foundation of the State Key Laboratory of Frozen Soil Engineering (No. SKLFSE-ZY-20). The authors also thank International Science Editing (http://www.internationalscienceediting.com) for editing this paper.

References

[1] F. G. Bell and L. J. Donnelly, *Mining and its Impact on the Environment*, CRC Press, Boca Raton, FL, USA, 2014.

[2] Q. S. Du, G. Y. Li, W. L. Pen, M. T. Chai, Y. Zhou, and D. Chen, "Land use changes in high cold-altitude mining area base on remote sensing technology," *Environmental Science & Technology*, vol. 43, no. 12, pp. 185–194, 2020.

[3] Z. Lin, B. Zhang, and J. Guo, "Analysis of aWater-inrush disaster caused by coal seam subsidence karst collapse column under the action of multi-field coupling in taoyuan coal mine," *Computer Modeling in Engineering & Sciences*, vol. 126, no. 1, pp. 311–330, 2021.

[4] D. P. Sainsbury, B. L. Sainsbury, and E. Sweeney, "Three-dimensional analysis of complex anisotropic slope instability at MMG's Century Mine," *Mining Technology*, vol. 125, no. 4, pp. 212–225, 2016.

[5] A. Schippers, P. G. Jozsa, W. Sand, Z. Maria Kovacs, and M. Jelea, "Microbiological pyrite oxidation in a mine tailings heap and its relevance to the death of vegetation," *Geomicrobiology Journal*, vol. 17, no. 2, pp. 151–162, 2000.

[6] S. Jiang and Y. M. Wang, "Long-term ground settlements over mined-out region induced by railway construction and operation," *Sustainability*, vol. 11, no. 3, Article ID 875, 2019.

[7] Q. S. Du and R. J. Zhao, "The production of DEM in SARscape format," *Computer Knowledge and Technology*, vol. 16, no. 7, pp. 238-239, 2020.

[8] M. T. Chai, G. Y. Li, W. Ma et al., "Assessment of freeze-thaw hazards and water features along the China-Russia crude oil pipeline in permafrost regions," *Remote Sensing*, vol. 12, no. 21, Article ID 3576, 2020.

[9] Q. S. Du, G. Y. Li, J. M. Li, and Y. Zhou, "Research on the river extraction based on the DEM data in the central west tianshan mountains," *China Rural Water and Hydropower*, vol. 10, pp. 29–33+40, 2020.

[10] J. F. Wang, Y. L. Liao, and X. Liu, *Spatial Data Analysis Tutorial*, Science Press, Beijing, China, 2nd edition, 2019.

[11] W. Lodwick, *Fuzzy Surfaces in GIS and Geographical Analysis: Theory, Analytical Methods, Algorithms, and Applications*, CRC Press, Boca Raton, FL, USA, 2008.

[12] C. Rozenblat and G. Melancon, *Methods for Multilevel Analysis and Visualisation of Geographical Networks*, Springer, Berlin, Germany, 2013.

[13] A. Ferretti, *Satellite InSAR Data: Reservoir Monitoring from Space*, EAGE Publications, Houten, Netherlands, 2014.

[14] A. Ferretti, A. Monti-Guarnieri, C. Prati, F. Rocca, and D. Massonnet, *InSAR Principles: Guidelines for SAR Interferometry Processing and Interpretation*, ESA Publications, Noordwijk, Netherlands, 2007.

[15] N. B. D Bechor and H. A. Zebker, "Measuring two-dimensional movements using a single insar pair," *Geophysical Research Letters*, vol. 33, no. 16, Article ID 26883, 2006.

[16] G. X. Liu, Q. Chen, X. J. Luo, and G. L. Cai, *Principle and Application of InSAR*, Science Press, Beijing, China, 2019.

[17] R. B. Lohman and M. Simons, "Some thoughts on the use of InSAR data to constrain models of surface deformation: noise structure and data downsampling," *Geochemistry, Geophysics, Geosystems*, vol. 6, no. 1, Article ID 841, 2005.

[18] N. Zakhvatkina, V. Smirnov, and I. Bychkova, "Satellite sar data-based sea ice classification: an overview," *Geosciences*, vol. 9, no. 4, Article ID 152, 2019.

[19] B. Han, C. B. Ding, L. H. Zhong et al., "The GF-3 SAR data processor," *Sensors*, vol. 18, no. 3, Article ID 835, 2018.

[20] J. W. Dong, S. W. Li, K. Yan, and D. J. Fu, *Remote Sensing Cloud Computing and Scientific Analysis-Application and Practice*, Science Press, Beijing, China, 2020.

[21] J. J. Zhu, Z. W. Li, and J. Hu, "Research progress and methods of InSAR for deformation monitoring," *Acta Geodaetica et Cartographic Sinica*, vol. 46, no. 10, pp. 1717–1733, 2017.

[22] H. A. Zebker and R. M. Goldstein, "Topographic mapping from interferometric synthetic aperture radar observations," *Journal of Geophysical Research*, vol. 91, no. B5, pp. 4993–4999, 1986.

[23] A. K. Gabriel, R. M. Goldstein, and H. A. Zebker, "Mapping small elevation changes over large areas: differential radar interferometry," *Journal of Geophysical Research*, vol. 94, no. B7, pp. 9183–9191, 1989.

[24] A. Khairi, M. Awaluddin, and B. Sudarsono, "Analisis deformasi seismik sesar matano menggunakan GNSS dan interferometrik SAR," *Jurnal Geodesi Undip*, vol. 9, no. 2, pp. 32–42, 2020.

[25] A. Ferretti, C. Prati, and F. Rocca, "Nonlinear subsidence rate estimation using permanent scatterers in differential SAR interferometry," *IEEE Transactions on Geoscience and Remote Sensing*, vol. 38, no. 5, pp. 2202–2212, 2000.

[26] A. Ferretti, C. Prati, and F. Rocca, "Permanent scatterers in SAR interferometry," *IEEE Transactions on Geoscience and Remote Sensing*, vol. 39, no. 1, pp. 8–20, 2001.

[27] B. Kampes, *Radar Interferometry--Persistent Scatterer Technique*, Springer, Berlin, Germany, 2014.

[28] P. Berardino, M. Costantini, G. Franceschetti, A. Iodice, L. Pietranera, and V. Rizzo, "Use of differential SAR interferometry in monitoring and modelling large slope instability at Maratea (Basilicata, Italy)," *Engineering Geology*, vol. 68, no. 1-2, pp. 31–51, 2003.

[29] Y. L. Du, S. Y. Yan, H. N. Yang, J. X. Jiang, and F. Zhao, "Investigation of deformation patterns by DS-InSAR in a coal resource-exhausted region with Spaceborne SAR imagery," *Journal of Asian Earth Sciences: X*, vol. 5, Article ID 100049, 2021.

[30] A. Pepe and F. Calò, "A review of interferometric synthetic aperture RADAR (InSAR) multi-track approaches for the

retrieval of Earth's surface displacements," *Applied Sciences*, vol. 7, no. 12, 2017.
[31] E. Chaussard, F. Amelung, H. Abidin, and S.-H. Hong, "Sinking cities in Indonesia: ALOS PALSAR detects rapid subsidence due to groundwater and gas extraction," *Remote Sensing of Environment*, vol. 128, pp. 150–161, 2013.
[32] Y. H. Zhang, H. A. Wu, Y. H. Kang, and C. G. Zhu, "Ground subsidence in the beijing-tianjin-hebei region from 1992 to 2014 revealed by multiple SAR stacks," *Remote Sensing*, vol. 8, no. 8, Article ID 80675, 2016.
[33] B. Xu, G. C. Feng, Z. W. Li, Q. J. Wang, C. C. Wang, and R. G. Xie, "Coastal subsidence monitoring associated with land reclamation using the point target based SBAS-InSAR method: a case study of shenzhen, China," *Remote Sensing*, vol. 8, no. 8, Article ID 80652, 2016.
[34] C. Carnec, D. Massonnet, and C. King, "Two examples of the use of SAR interferometry on displacement fields of small spatial extent," *Geophysical Research Letters*, vol. 23, no. 24, pp. 3579–3582, 1996.
[35] H. J. Yin, J. J. Zhu, Z. W. Li, X. L. Ding, and C. C. Wang, "Ground subsidence monitoring in mining area using DInSAR SBAS algorithm," *Acta Geodaetica et Cartographica Sinica*, vol. 40, no. 1, pp. 52–58, 2011.
[36] N. G. Alex Hay-Man, G. E. Linlin, K. Zhang et al., "Deformation mapping in three dimensions for underground mining using InSAR–Southern highland coalfield in New South Wales, Australia," *International Journal of Remote Sensing*, vol. 32, no. 22, pp. 7227–7256, 2011.
[37] W. L. Zhi, Z. F. Yang, J. Z. Jian et al., "Retrieving three-dimensional displacement fields of mining areas from a single InSAR pair," *Journal of Geodesy*, vol. 89, no. 1, pp. 17–32, 2015.
[38] H. D. Fan, D. Cheng, K. Z. Deng, B. Q. Chen, and C. G. Zhu, "Subsidence monitoring using D-InSAR and probability integral prediction modelling in deep mining areas," *Survey Review*, vol. 47, no. 345, pp. 438–445, 2015.
[39] L. Ge, H. C. Chang, and C. Rizos, "Mine subsidence monitoring using multi-source satellite SAR images," *Photogrammetric Engineering & Remote Sensing*, vol. 73, no. 3, pp. 259–226, 2005.
[40] Z. Y. Wang, J. Z. Zhang, Y. R. Yu et al., "Monitoring, analyzing, and modeling for single subsidence basin in coal mining areas based on SAR interferometry with L-band data," *Scientific Programming*, vol. 2021, Article ID 6662097, 10 pages, 2021.
[41] C. Jiang, L. Wang, X. Yu, T. Wei, S. Chi, and Q. Guo, "Prediction of 3D deformation due to large gradient mining subsidence based on InSAR and constraints of IDPIM model," *International Journal of Remote Sensing*, vol. 42, no. 1, pp. 208–239, 2021.
[42] D. Massonnet, K. Feigl, M. Rossi, and F. Adragna, "Radar interferometric mapping of deformation in the year after the Landers earthquake," *Nature*, vol. 369, no. 6477, pp. 227–230, 1994.
[43] G. Feng, S. Jónsson, and Y. Klinger, "Which fault segments ruptured in the 2008 wenchuan earthquake and which did not? New evidence from near-fault 3D surface displacements derived from SAR image offsets," *Bulletin of the Seismological Society of America*, vol. 107, no. 3, pp. 1185–1200, 2017.
[44] X. Tong, B. Smith-Konter, and D. T. Sandwell, "Is there a discrepancy between geological and geodetic slip rates along the San Andreas Fault System?," *Journal of Geophysical Research: Solid Earth*, vol. 119, no. 3, pp. 2518–2538, 2014.
[45] J. R. Elliott, R. J. Walters, and T. J. Wright, "The role of space-based observation in understanding and responding to active tectonics and earthquakes," *Nature Communications*, vol. 7, Article ID 13844, 2016.
[46] D. Massonnet, P. Briole, and A. Arnaud, "Deflation of Mount Etna monitored by spaceborne radar interferometry," *Nature*, vol. 375, no. 6532, pp. 567–570, 1995.
[47] J. Ruch, T. Wang, W. B. Xu, M. Hensch, and S. Jónsson, "Oblique rift opening revealed by reoccurring magma injection in central Iceland," *Nature Communications*, vol. 7, Article ID 12352, 2016.
[48] M. E. Pritchard and M. Simons, "An InSAR-based survey of volcanic deformation in the central Andes," *Geochemistry, Geophysics, Geosystems*, vol. 5, no. 2, Article ID Q02002, 2004.
[49] J. Eppler and B. Rabus, "Monitoring urban infrastructure with an adaptive multilooking InSAR technique," in *Proceedings of Fringes 2011*, Frascati, Italy, September 2012.
[50] M. Bakon, D. Perissin, M. Lazecky, and J. Papco, "Infrastructure non-linear deformation monitoring via satellite radar interferometry," *Procedia Technology*, vol. 16, pp. 294–300, 2014.
[51] H. Lan, L. Li, H. Liu, and Z. Yang, "Complex urban infrastructure deformation monitoring using high resolution PSI," *IEEE Journal of Selected Topics in Applied Earth Observations and Remote Sensing*, vol. 5, no. 2, pp. 643–651, 2012.
[52] T. J. Fournier, M. E. Pritchard, and S. N. Riddick, "Duration, magnitude, and frequency of subaerial volcano deformation events: new results from Latin America using InSAR and a global synthesis," *Geochemistry, Geophysics, Geosystems*, vol. 11, no. 1, Article ID Q01003, 2010.
[53] R. E. Bell, M. Studinger, C. A. Shuman, M. A. Fahnestock, and I. Joughin, "Large subglacial lakes in east Antarctica at the onset of fast-flowing ice streams," *Nature*, vol. 445, no. 7130, pp. 904–907, 2007.
[54] T. Strozzi, A. Kouraev, A. Wiesmann, U. Wegmüller, A. Sharov, and C. Werner, "Estimation of Arctic glacier motion with satellite L-band SAR data," *Remote Sensing of Environment*, vol. 112, no. 3, pp. 636–645, 2008.
[55] J. M. Zhou, Z. Li, and Q. Xin, "Deriving glacier border information based on analysis of decorrelation in SAR interferometry," *Journal of Glaciology and Geocryology*, vol. 32, no. 1, pp. 133–138, 2010.
[56] Y. E. Molan, J. W. Kim, Z. Lu, B. Wylie, and Z. L. Zhu, "Modeling wildfire-induced permafrost deformation in an alaskan boreal forest using InSAR observations," *Remote Sensing*, vol. 10, no. 3, Article ID 405, 2018.
[57] Z. J. Zhang, M. M. Wang, Z. J. Wu, and X. G. Liu, "Permafrost deformation monitoring along the qinghai-tibet plateau engineering corridor using InSAR observations with multi-sensor SAR datasets from 1997–2018," *Sensors*, vol. 19, no. 23, Article ID 5306, 2019.
[58] T. Strozzi, S. Antonnova, F. Günther et al., "Sentinel-1 SAR interferometry for surface deformation monitoring in low-land permafrost areas," *Remote Sensing*, vol. 10, no. 9, 2018.
[59] C. Xie, Z. Li, J. Xu, and X. Li, "Analysis of deformation over permafrost regions of Qinghai-Tibet plateau based on permanent scatterers," *International Journal of Remote Sensing*, vol. 31, no. 8, pp. 1995–2008, 2010.
[60] S. Wang, B. Xu, W. Shan, J. C. Shi, Z. W. Li, and G. C. Feng, "Monitoring the degradation of island permafrost using time-series InSAR technique: a case study of heihe, China," *Sensors*, vol. 19, no. 6, Article ID 1364, 2019.

[61] B. Riedel and A. Walther, "InSAR processing for the recognition of landslides," *Advances in Geosciences*, vol. 14, no. 15, pp. 189–194, 2008.
[62] T. carlà, E. Intrieri, F. Raspini et al., "Perspectives on the prediction of catastrophic slope failures from satellite InSAR," *Scientic Reports*, vol. 9, Article ID 14137, 2019.
[63] E. Kiseleva, V. Mikhailov, E. Smolyaninova et al., "PS-InSAR monitoring of landslide activity in the black sea coast of the caucasus," *Procedia Technology*, vol. 16, pp. 404–413, 2014.
[64] J. M. Li, G. Y. Li, W. L. Pen, D. Chen, Y. Zhou, and C. F. Liu, "The strength and deformation characteristics of saturated weathered granite under different temperature conditions," *Journal of Glaciology and Geocryology*, vol. 42, no. 2, pp. 523–531, 2020.
[65] I. Baran, M. P. Stewart, B. M. Kampes, Z. Perski, and P. Lilly, "A modification to the Goldstein radar interferogram filter," *IEEE Transactions on Geoscience and Remote Sensing*, vol. 41, no. 9, pp. 2114–2118, 2003.
[66] M. Costantini, "A novel phase unwrapping method based on network programming," *IEEE Transactions on Geoscience and Remote Sensing*, vol. 36, no. 3, pp. 813–821, 1998.
[67] B. Zhang, J. Li, and H. Ren, "Using phase unwrapping methods to apply D-InSAR in mining areas," *Canadian Journal of Remote Sensing*, vol. 45, no. 2, pp. 225–233, 2019.

Hindawi
Advances in Materials Science and Engineering
Volume 2021, Article ID 5575940, 12 pages
https://doi.org/10.1155/2021/5575940

Research Article

Research on the Temperature Field and Frost Heaving Law of Massive Freezing Engineering in Coastal Strata

Chaochao Zhang[1,2] **Dongwei Li**[1] **Junhao Chen**[3] **Guanren Chen**[1] **Chang Yuan**[1] **Zecheng Wang**[1] **Guosheng Ding**[4] **Xin Chen**[1] **Minghai Xia**[5] **Shengfu Wang**[1] **Bo Zhang**[1] **Ru He**[1] **and Xin Yi**[1]

[1]*School of Civil and Architecture Engineering, East China University of Technology, Nanchang 330013, China*
[2]*Nanjing Coal Mine Design & Research Institute, Nanjing 211800, China*
[3]*School of Civil Engineering, Fujian University of Technology, Fuzhou 350118, China*
[4]*Fuzhou Metro Co. Ltd., Fuzhou 350004, China*
[5]*Irrigation Management Office of Water Conservancy Project in Kuitun River Basin of Yili Kazak Autonomous Prefecture, Kuitun 833200, China*

Correspondence should be addressed to Dongwei Li; dwli2005@163.com

Received 4 February 2021; Revised 13 March 2021; Accepted 3 April 2021; Published 14 April 2021

Academic Editor: Xiao Dong Zhao

In this study, based on the background of massive freezing engineering in coastal strata, the thermal physical parameters and some freezing laws of soil were obtained through soil thermal physical tests and frozen soil frost heaving tests. When the freezing temperatures were −5°C, −10°C, −15°C, and −20°C, the frost heaving rates of the soil were 0.53%, 0.95%, 1.28%, and 1.41%, and the frost heaving forces of the soil were 0.37 MPa, 0.46 MPa, 0.59 MPa, and 0.74 MPa, respectively. In the range of test conditions, the frost heaving rate and the frost heaving force of the soil increased with the decrease of the freezing temperature, and the relationship was roughly linear with the temperature. The entire cooling process could be roughly divided into three stages: active freezing stage, attenuation cooling stage, and stability stage. The range of the frozen soil expansion did not increase linearly with the decrease of the freezing temperature, and there was a limit radius for the frozen soil expansion. A three-dimensional finite element model was established to simulate the temperature field and frost heaving of the soil under the on-site working conditions. The entire frost heaving process could be roughly divided into two stages. The calculated temperature values and the frost heaving force values were compared with the on-site measured values, and the results verified that the numerical calculation could accurately reflect the temperature field and frost heaving law of the formation.

1. Introduction

Natural frozen soil is mainly formed by the freezing of water in soil due to the low temperature of the natural environment. Artificial freezing is the use of artificial refrigeration to make the soil around the freezing pipe freeze. Then underground engineering construction is carried out under the protection of the freezing curtain. The artificial freezing method is an effective underground construction method that is widely used in mine construction and municipal engineering. Frozen soil is an extremely temperature-sensitive soil medium with rheological properties. Due to the uneven distribution of moisture, soil can produce uneven frost heaving deformation, accompanied by the generation of a frost heaving force. Frost heaving can potentially cause many engineering problems, including road cracking, foundation damage, building tilt, freezing pipe fractures, tunnel collapse, and pipeline fractures. In natural permafrost areas, frost damage control is relatively passive, such as salt injection to treat subgrade frost damage. Artificial freezing is designed artificially, and its freezing range, temperature, and time are controllable. Therefore, compared with natural frozen soil, artificial freezing can better control the influence of frost heaving and thawing settlement on the original environment and structures by controlling the freezing volume, rapid freezing, setting pressure relief holes, thawing settlement compensation grouting, and other measures.

Previous scholars have done a large amount of research on the theory of frozen soil frost heaving and the law of freezing and thawing, and they have achieved many results [1–5]. Wang et al. [6–9] studied the frost heaving characteristics and frost heaving force through frozen soil tests. Yue et al. [10] studied the variation laws of frozen soil temperature and frost heaving pressure. He et al. [11] put forward the coupling equations of water, heat, and force in the process of soil freezing. Xia et al. [12] and Wang et al. [13] analyzed the mechanical properties of frozen wall and studied the uneven frost heaving. Many achievements have been made regarding the theoretical derivation, field measurement, and numerical simulation of freezing temperature field [14–16]. Chen et al. [17–19] studied the law of the temperature field of frozen soil and its influencing factors based on a freezing project. Long et al. [20] carried out a model test and obtained the development law of the temperature. Zhang et al. [21] established a three-dimensional temperature field model and proposed a new frost heaving model. Li et al. [22] studied the optimal excavation time of soil and the variations of the saltwater temperature, soil temperature, surface performance, and tunnel deformation. Hu et al. [23–26] established a frozen soil finite element model to analyze the development law of the frozen temperature field.

In this study, based on massive freezing engineering in coastal strata, thermal physical tests and frost heaving tests were carried out to obtain the soil thermal physical parameters and the frost heaving law. Moreover, 3D numerical simulation was carried out to further explore the changes of the freezing temperature field and frost heaving law of the long connecting passage under the on-site freezing conditions. This study is expected to provide a reference for the design and construction of freezing projects.

2. Overview of Freezing Engineering and Soil Thermal Physical Parameters

2.1. Project Overview. In this study, a super long subway connecting passage was taken as the engineering background. The center distance of the connecting passage was 42.68 m, and the main body of the passage was located in silty soil and muddy sand. There were hot springs in the strata, resulting in a high ground temperature about 40°C. The connecting passage was reinforced by horizontal freezing and constructed with the mining method. The cross section of connecting passage and the freezing curtain is shown in Figure 1.

The excavation and the construction of the super long connecting passage took a long time, which led to the long freezing time for the freezing project. The connecting passage passed through a subway tunnel with a clear distance of about 7 m. Therefore, in the construction process of connecting passage, the accuracy of the frost heaving control was required to be high. If large frost heaving deformation were to occur, the building would be inclined and cracked, the road or underground pipeline would be damaged, and the safety of the existing tunnel would be endangered, which would in turn cause a serious negative social impact.

2.2. Soil Thermal Physical Parameters. The main thermal physical parameters of each soil layer were obtained through experiments. The experimental results are shown in Table 1.

3. Frost Heaving Tests

3.1. Multifunctional Frost Heaving Testing Machine. The tests were carried out using a WDC-100 multifunctional frost heaving testing machine, which was composed of a loading system, a temperature control system, a moisture compensation system, and a measurement system. This machine could control the applied force, cold temperature, and ambient temperature. The test machine and the sample chamber are shown in Figures 2 and 3.

A cylindrical soil sample with dimensions $\varphi 50 \times 100$ mm is used, and the soil sample was placed in the sample chamber, as shown in Figure 3. There was a set of devices at the top and bottom of the soil sample. A refrigerant circulating pipe and a temperature sensor were arranged inside the device. The cold source was formed by circulating the refrigerant, and the temperature sensor monitored the temperature. A row of evenly distributed temperature measuring holes was set at the soil sample position of the sample cylinder. The distances between the temperature measuring holes and the bottom of the sample were 0.50 cm, 1.75 cm, 3.00 cm, 4.25 cm, 5.50 cm, and 6.75 cm. The temperature acquisition probes extended into the soil through the reserved temperature measuring hole to measure the relationship between the temperature inside the soil and the distance from the cold source.

3.2. Tests and Results Analysis. Single factor controlled frost heaving tests were carried out with the upper load being 0.6 MPa and the moisture content of the soil sample being 26%. The freezing temperatures adopted five levels of −5°C, −10°C, −15°C, −20°C, and −25°C, and the freezing time was 12 h. When considering the influence of the freeze-thaw cycles on the soil, the freezing temperature was −15°C, and the thawing temperature was 15°C. The designed freeze-thaw cycle was 24 h (12 h freezing and 12 h thawing) and the number of freeze-thaw cycles was six.

3.2.1. Temperature Field. The distribution of the soil temperature field for different cold source temperatures is shown in Figure 4, and the distribution of the soil temperature field for the freeze-thaw cycles is shown in Figure 5.

Figure 4 reveals the following:

(1) The entire cooling process could be roughly divided into three stages: the active freezing stage, the attenuation cooling stage, and the stability stage.

(2) In the initial stage of freezing, the temperature of the soil was high and the temperature of the freezing

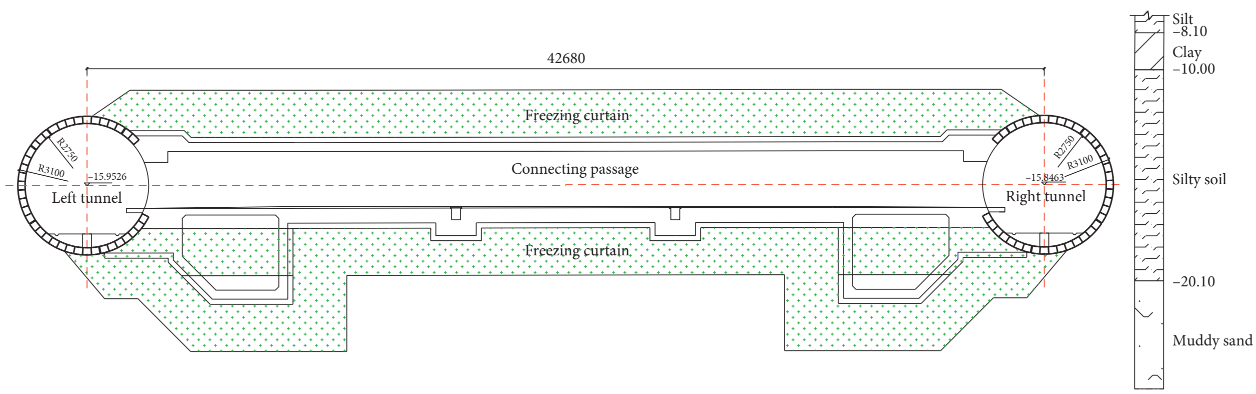

FIGURE 1: Cross section of connecting passage and freezing curtain.

TABLE 1: Thermal physical parameters of soil layer.

Layer	Soil properties	Moisture content (%)	Natural density ($g{\cdot}cm^{-3}$)	Thermal conductivity ($w{\cdot}m^{-1\circ}C^{-1}$) 13°C	Thermal conductivity ($w{\cdot}m^{-1\circ}C^{-1}$) −10°C	Specific heat ($J{\cdot}kg^{-1\circ}C^{-1}$)	Freezing temperature (°C)
1	Silt	55.38	1.98	1.327	1.423	1900	−2.3
2	Clay	24.79	2.13	1.470	1.651	1680	−1.5
3	Silty soil	44.04	2.04	1.286	1.731	1760	−1.8
4	Muddy sand	10.94	2.08	1.271	1.502	1520	−1.1

FIGURE 2: Appearance of the test machine.

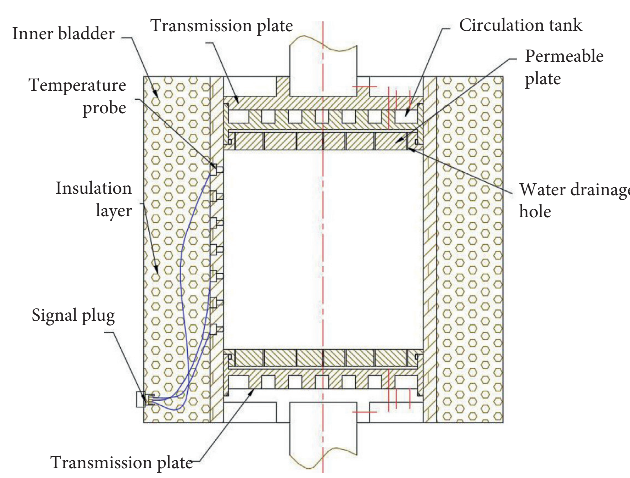

FIGURE 3: Structure of sample chamber.

tube was very low. There was a large temperature difference between the freezing tube and the soil. The temperature gradient was large and the cooling rate of the soil was very fast. The active freezing stage was a stage in which the soil temperature dropped rapidly.

(3) With the decrease of the soil temperature, the temperature gradient between the freezing pipe and the soil decreased and the temperature rate of the soil decreased more. The water in the soil began to freeze and release latent heat, and the soil entered attenuation cooling stage.

(4) As the freezing time went by, the soil temperature continued to decrease. The temperature difference between the freezing pipe and the soil gradually decreased and the heat exchange generally tended to balance. The soil temperature dropped slowly and finally tended to be stable.

(5) The tendencies of the temperature changes at different measuring points were roughly the same. The closer the location was to the cold source, the faster the soil cooling rate was and the lower the stable temperature was. When the temperature of the cold source was −5°C, the final stable temperature of the farthest measuring point (6.75 cm away from the

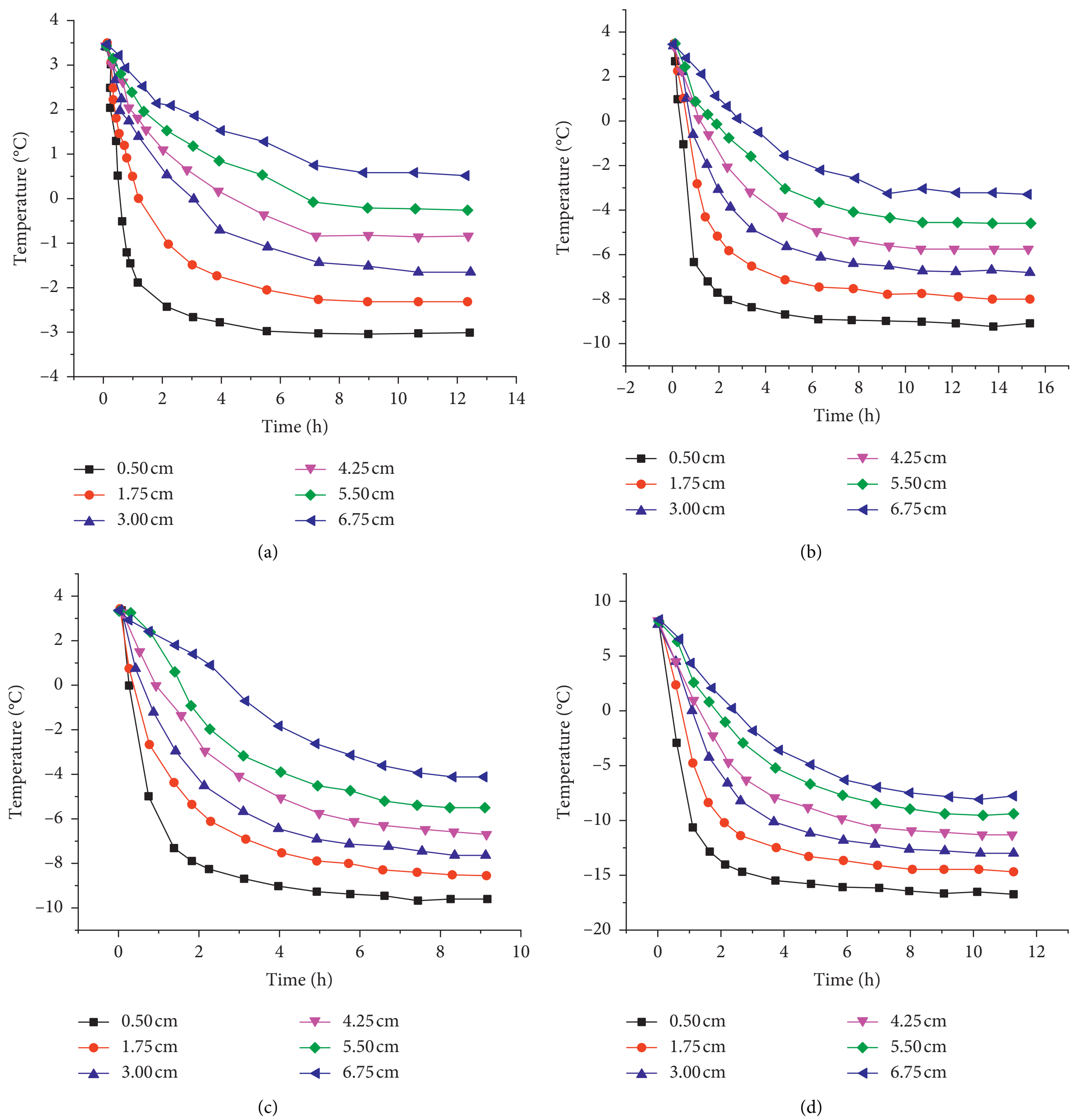

Figure 4: Soil temperature field with different cold source temperatures. (a) −5°C. (b) −10°C. (c) −15°C. (d) −20°C.

cold source) was 0.75°C and the final stable temperature of the measuring points nearest to the cold source (0.5 cm away from the cold source) was −3°C.

(6) The lower the cold source temperature was, the faster the soil temperature change rate was and the lower the final stable temperature was. When the temperatures of the cold source were −5°C, −10°C, −15°C, and −20°C, the final stable temperatures of the farthest measuring point (6.75 cm away from the cold source) were 0.75°C, −3°C, −4°C, and −7.5°C, respectively. The temperature differences between the stable temperatures and the corresponding cold sources were 5.75°C, 7°C, 9°C, and 12.5°C, respectively. The lower the cold source temperature was, the greater the temperature difference was. This showed that the range of frozen soil expansion did not increase linearly with the decrease of the freezing temperature, and there was a limit radius of frozen soil expansion. When the radius was reached, the frozen soil did not expand outward.

In the temporary frozen soil areas, with the seasons and day and night temperature changes, natural frozen soils will produce changes in freeze-thaw cycles. In the process of artificial freezing, due to power failures, freezing pipe fractures, salt water leakages, and other reasons, the freezing process will be interrupted, and the frozen soil will thaw. With measures taken to restore the freezing, the thawed frozen soil will start to freeze again, and the freezing and

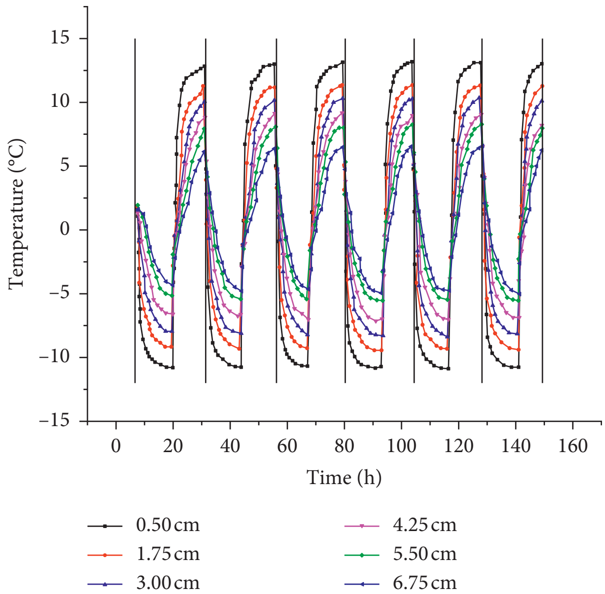

Figure 5: Soil temperature field with freeze-thaw cycles.

thawing processes will also occur. In this experiment, the experimental conditions were closed and undrained, and the amount of soil and water in the test tube did not change. Under freeze-thaw cycles conditions, the soil temperature field changed periodically.

3.2.2. Frost Heaving Rate. When the temperature was −15°C, the relationship between the frost heaving rate and time is shown in Figure 6.

It can be seen from Figure 6 that, during the beginning of freezing, the frost heaving rate was reduced and became a negative value; that is, the phenomenon of "freeze shrinkage" occurred. This phenomenon was caused by the negative pore water pressure in the soil during the beginning of freezing, which reduced the volume of the soil. When the volume reduction caused by the negative pore water pressure was greater than the increase caused by water freezing, the total volume of soil decreased. After the freezing shrinkage reached the critical point, the frost heaving began to occur in the soil. The frost heaving continued to increase and finally tended to be stable. The test results of the soil frost heaving rate for different freezing temperatures are shown in Table 2. The values in Table 2 are the frost heave rates at the stable stage of freezing, that is, the maximum frost heaving rates.

The experimental data were plotted on a scatter plot, and it was judged that the frost heaving rate and the freezing temperature were approximately linearly related according to the image. Therefore, linear fitting was performed to obtain the correlation coefficient R Square = 0.98605, which showed a good fitting effect. The results of the fitting test are shown in Figure 7.

Combining Table 2 and Figure 7, it can be seen that, within the range of the test conditions, the frost heaving rate of the soil became larger as the freezing temperature decreases, which was roughly linear.

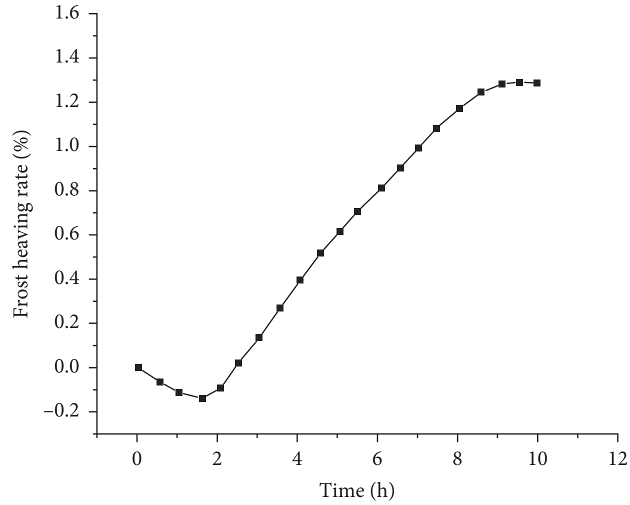

Figure 6: The relationship between frost heaving rate and time.

Table 2: Frost heaving rate for different freezing temperatures.

Temperature (°C)	−5	−10	−15	−20
Frost heaving rate (%)	0.53	0.78	1.22	1.41

Equation	$y = a + b * x$		
Weight	No weighting		
Residual sum of squares	0.00456		
Pearson's r	−0.99508		
Adj. R^2	0.98529		
		Value	Standard erro
B	Intercept	0.23009	0.05831
	Slope	−0.06055	0.00426

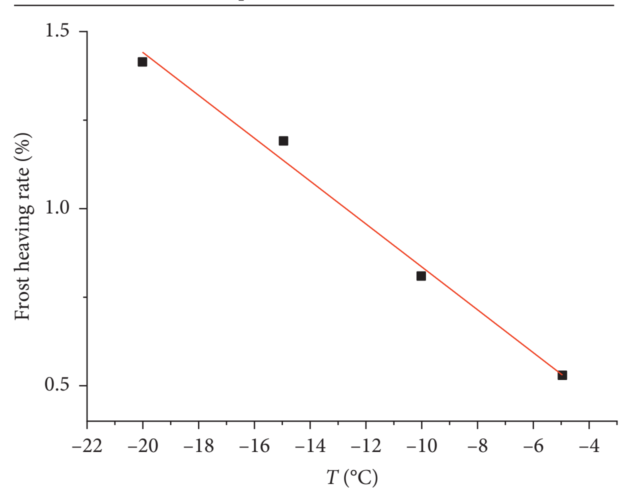

Figure 7: The relationship between the frost heaving rate and the freezing temperature.

3.2.3. Frost Heaving Force. When the temperature was −15°C, the relationship between the frost heaving force and time was as shown in Figure 8.

According to Figure 8, the frost heaving force of the soil gradually increased with the freezing time and finally tended

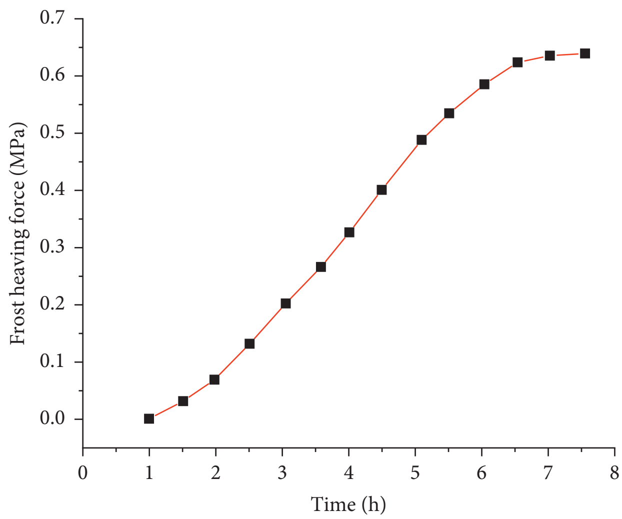

Figure 8: The relationship between the frost heaving force and time.

to be flat. Due to the limitation of experimental instruments, only the compressive stress could be detected. That is, the frost heaving force could be monitored at the stage of frost heaving rate increasing. The frost heaving force in the freezing shrinkage stage could not be monitored, and its value was 0 by default. The test results of the soil frost heaving force for different freezing temperatures are shown in Table 3. The values in Table 3 are the frost heave forces at the stable stage of freezing, that is, the maximum frost heaving forces.

The experimental data were plotted on a scatter plot, and it was judged that the frost heaving force and the freezing temperature were approximately linearly related according to the image. Therefore, a linear fitting was performed to obtain the correlation coefficient R Square = 0.97396, which showed a good fitting effect. The results of the fitting test are shown in Figure 9.

Combining Table 3 and Figure 9, it can be seen that, within the range of the test conditions, the frost heaving force of the soil increased with the decrease of the freezing temperature, which was roughly linear. In the experiment, the maximum frost heaving rate and the maximum frost heaving force of each layer of soil samples at −10°C were as shown in Table 4.

Table 3: Values of frost heaving forces at different temperatures.

Temperature (°C)	−5	−10	−15	−20
Frost heaving force (MPa)	0.37	0.46	0.64	0.74

Equation	$y = a + b * x$		
Weight	No weighting		
Residual sum of squares	0.00154		
Pearson's r	−0.99079		
Adj. R^2	0.9725		
		Value	Standard erro
B	Intercept	0.23266	0.03388
	slope	−0.02561	0.00247

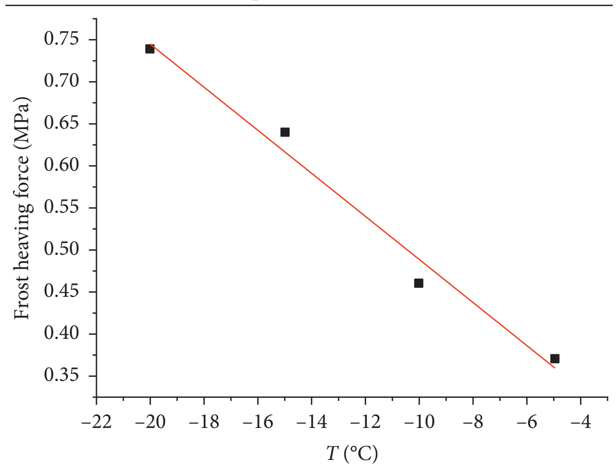

Figure 9: The relationship between the frost heaving force and the freezing temperature.

Table 4: Frost heaving test results.

Layer	Soil properties	Frost heaving rate (%)	Frost heaving force (MPa)
1	Silt	0.92	0.71
2	Clay	0.78	0.46
3	Silty soil	0.76	0.57
4	Muddy sand	0.69	0.15

4. Numerical Simulation Analysis of Thermomechanical Coupling

4.1. Model Parameters. A three-dimensional numerical model was established to simulate the variation law of the formation temperature field and the frost heaving caused by the actual freezing condition. Taking the vertical plane passing through the longitudinal axis of the connecting passage as the symmetry plane, the 1/2 finite element model was established. The material thermal physical parameters of each part are shown in Table 5.

4.2. Model Building. The finite element model was established according to the actual situation of the freezing project. The model of the tunnel and the freezing pipes is shown in Figure 10, and the finite element model after meshing is shown in Figure 11.

4.3. Numerical Simulation Analysis of Temperature Field. A transient thermal calculation was carried out for the development of the soil temperature field in the active freezing period. The distribution cloud charts of the soil temperature field were selected when the freezing times were 15 d, 30 d, 45 d, and 60 d, with 15 d as the interval, as shown in Figure 12.

When freezing, the temperature of the soil around the freezing pipes began to drop rapidly, and the frozen soil cylinder was gradually formed around the freezing pipes. With the increase of the freezing time, the frozen soil cylinder developed outward along the radial direction of the

Table 5: Material thermal physical parameters.

Material	Specific heat capacity C (kJ·kg^{-1}·k^{-1})		Thermal conductivity K (w·m^{-1}·k^{-1})		Enthalpy H (×10^6 J m^{-3})			
	−30~−3°C	0~40°C	−30°C	40°C	−30°C	−3°C	0°C	40°C
Miscellaneous fill	1.30	1.50	1.40	1.10	0	63.8	187.8	269.6
Silt	1.70	1.90	1.49	1.31	0	71.6	415.0	504.7
Clay	1.48	1.68	1.67	1.44	0	72.7	294.0	386.1
Silty soil	1.54	1.76	1.82	1.23	0	67.2	389.8	473.6
Muddy sand	1.18	1.52	1.53	1.24	0	91.3	320.2	432.8
Tunnel segment	0.97		1.28		—			

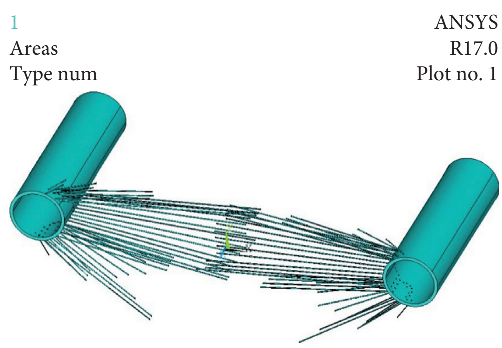

Figure 10: Freezing pipes and tunnel model.

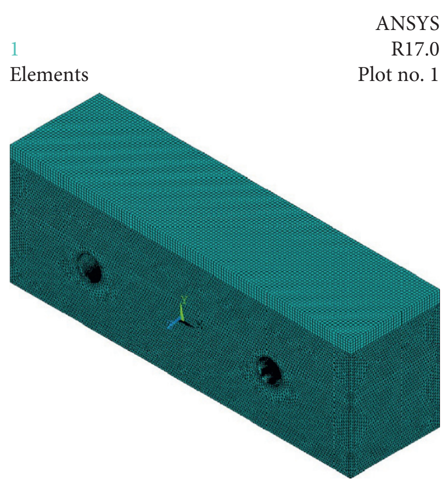

Figure 11: Model meshing.

freezing pipes. After 30 days, most of the adjacent frozen soil had intersected, and areas with the higher temperature gradually decreased with the continuous freezing. When the freezing time reached 60 days, the thickness of the freezing curtain could reach the design requirement of 2.1 m.

4.4. Thermal-Mechanical Coupling Simulation and Analysis. To explore the coupling evolution law of the freezing temperature field and soil displacement field, the thermal-mechanical coupling solution was carried out. The distribution of the soil displacement field under the thermal load is shown in Figure 13.

The frost heaving of the soil around the freezing pipes was caused by freezing, and because of the uneven distribution of the freezing pipes, the overall frost heaving was not uniform. When freezing for 15 days, the larger frost heaving areas were scattered. When freezing for 30 days, the freezing curtain gradually intersected. The frost heaving areas also showed a homogenization phenomenon and gradually gathered and merged. When freezing for 60 days, the frost heaving areas at the top were connected as a whole, showing a phenomenon of the middle parts being large and the two sides being small. Then as the freezing continued, the frost heaving areas were further homogenized and gradually spread from the middle area to both sides, finally becoming steady.

According to the calculation results, the maximum frost heaving of the strata occurred above the middle of the connecting passage. To further analyze the distribution law of the frost heaving at this position, the displacement duration curve of the maximum displacement area was drawn for analysis, as shown in Figure 14. The whole frost heaving process could be roughly divided into two stages. The first was the frost heaving generation stage, during which the frost heaving began to slowly increase. The second stage was the frost heaving development stage, during which the frost heaving began to increase rapidly and reached the maximum value of 193.03 mm in 65 days.

5. Comparative Analysis of Measured Data

5.1. Freezing Temperature Field Measurement. To accurately understand the development law of the freezing curtain in the long connecting passage, temperature measuring points were arranged in the surrounding strata to obtain the temperature field data of the freezing curtain. The layout of the freezing holes and the temperature measuring holes on the left side of the connecting passage are shown in Figure 15.

The temperature measuring points were arranged at 5 m, 12 m, and 19 m of the hole depth to monitor the development of the temperature field at different depth sections. The temperature measuring points were numbered T*i*–*j*, the labels $i = 1–8$ were used according to the different temperature measuring holes, and the labels $j = 1–3$ were used according to different positions of 5 m, 12 m, and 19 m along with the hole depth. The temperature measuring hole T5 was located at the edge of the excavation area, and T7 was located

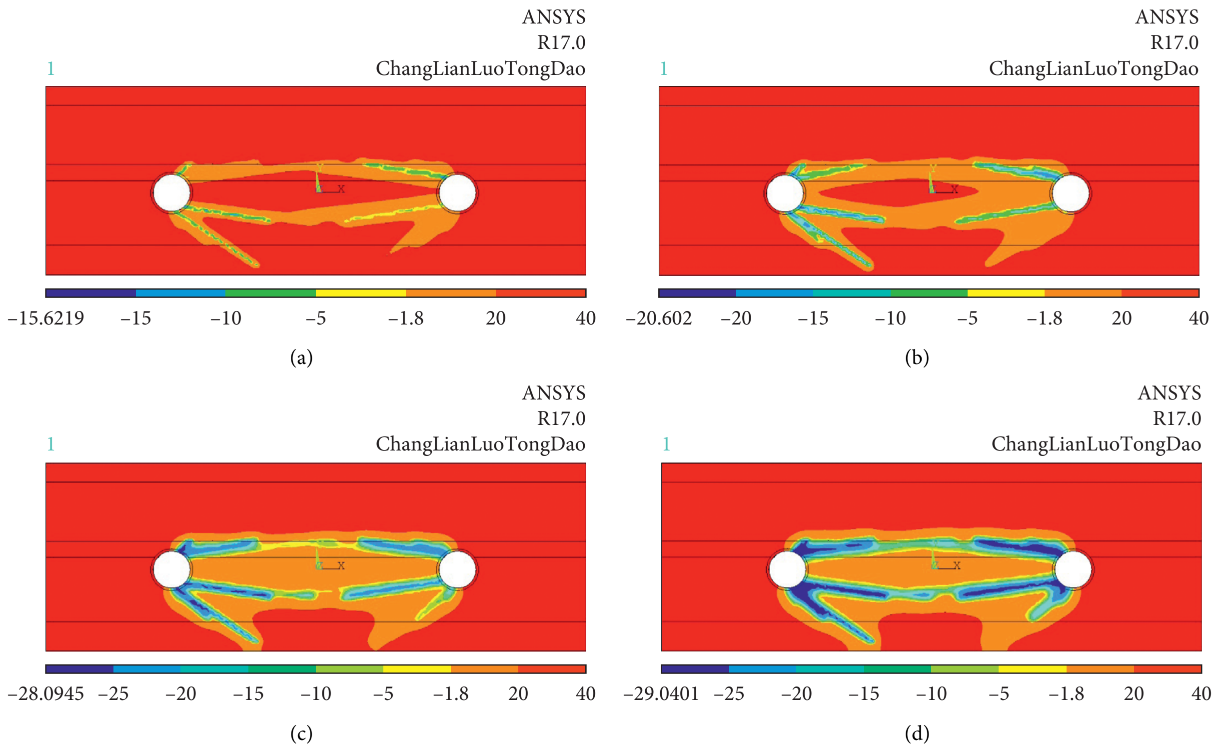

Figure 12: The distribution cloud charts of the freezing temperature fields. (a) 15 d. (b) 30 d. (c) 45 d. (d) 60 d.

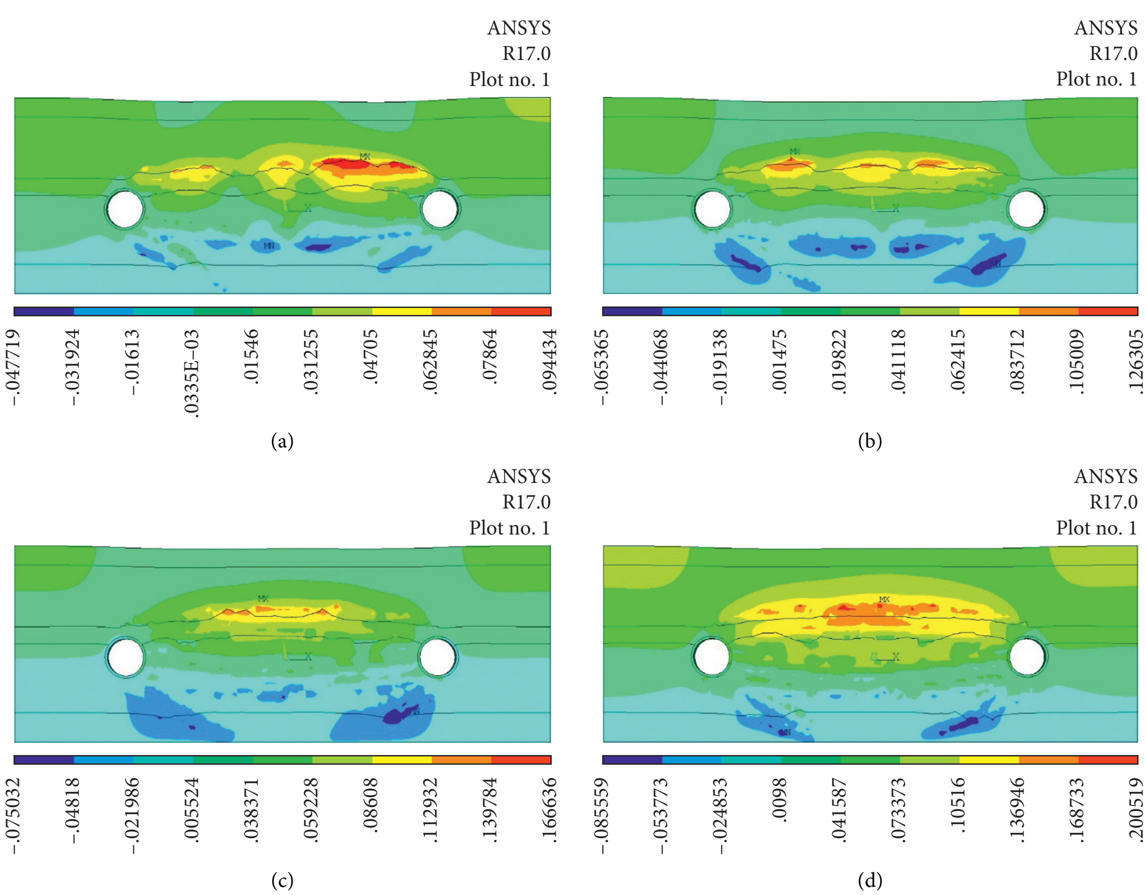

Figure 13: The distribution cloud charts of the displacement field. (a) 15 d. (b) 30 d. (c) 45 d. (d) 60 d.

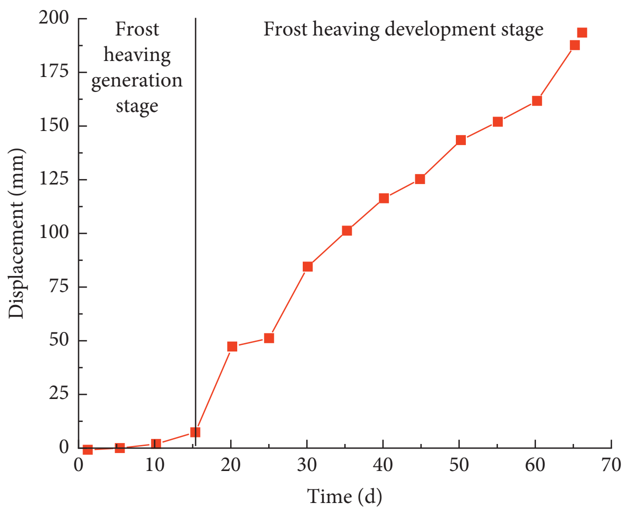

Figure 14: The displacement duration curve.

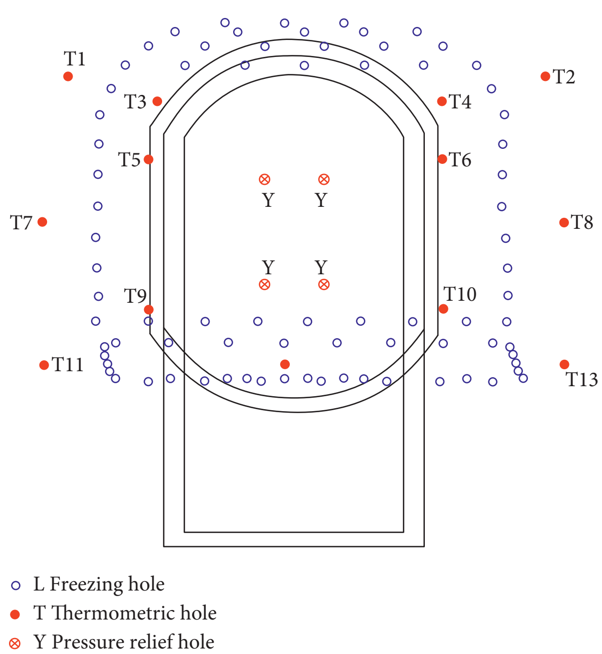

Figure 15: Holes on the left side of the connecting passage.

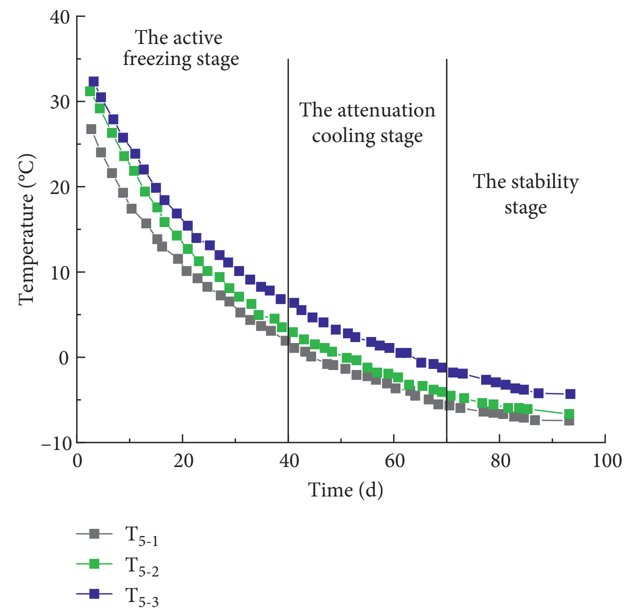

Figure 16: Relationship between temperature and time for T5.

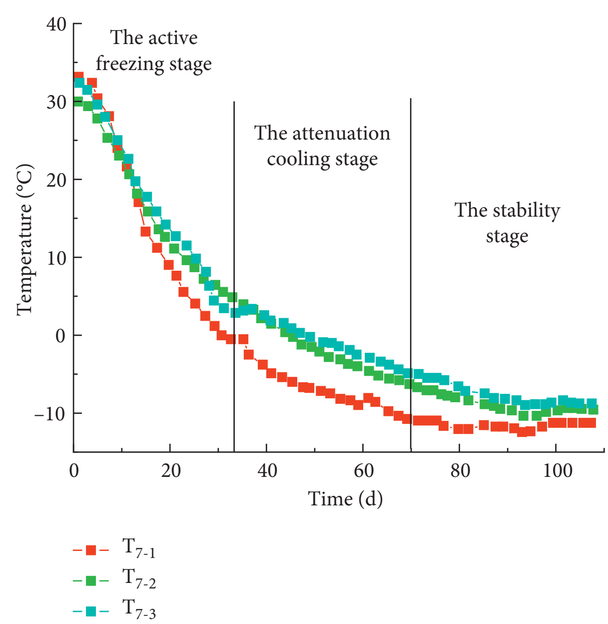

Figure 17: Relationship between temperature and time for T7.

at the edge of the nonexcavation area. The temperature and time relationship curves of the measuring points at different depths are shown in Figures 16 and 17.

The temperature trends for T5 and T7 temperature measuring holes were basically the same, and the entire freezing process could be divided into the active freezing stage, the attenuation cooling stage, and the stability stage. In the active freezing stage, the formation temperature decreased rapidly, lasting for about 40 days. In the attenuation cooling stage, the temperature of the formation was close to 0°C, and the moisture in the soil began to solidify into ice. Due to the effect of the latent heat of the phase change, the temperature slowed down. In the stability stage, the formation temperature dropped to a negative temperature, and the latent heat of the phase change was completed. The soil temperature continues to slow down and finally tended to be stable.

The temperature at the T4-3 measuring point was calculated with finite element software and compared with the measured temperature, as shown in Figure 18.

In the early stage of active freezing, there was a certain difference between the simulated temperature and the measured temperature. The temperature drop curve of the finite element simulation was smoother, but the change of the measured temperature drop curve was more violent. During the late stage of the active freezing period and the maintenance freezing period, the simulated temperature and

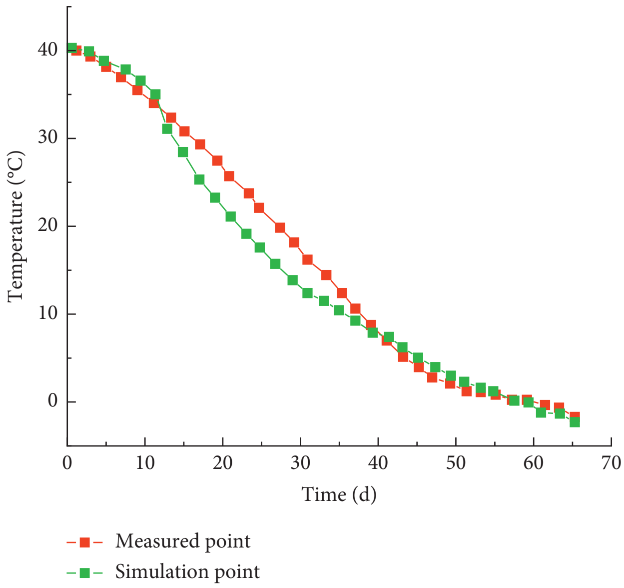

Figure 18: Temperature evaluation at temperature measurement point T4–3.

the measured temperature almost coincided. Therefore, the numerical simulation described above could accurately reflect the variation of the soil temperature field.

5.2. Frost Heaving Measurement. Forty-one monitoring points were arranged on the ground surface within the freezing influence range of the connecting passage to study the frost heaving law of the freezing project. The layout of the monitoring points is shown in Figure 19.

The measuring points DZ5-1–DZ5-7 were located in the middle of the connecting passage, where the frost heaving was more severe. The measuring points DZ5-1–DZ5-4 were selected as the research object to analyze the distribution law of frost heaving during the freezing period. The distances between DZ5-1–DZ5-7 were 3 m, 5 m, and 7 m, respectively. The measured surface deformation values are shown in Figure 20, and the surface frost heaving duration distribution is shown in Figure 21.

The process of surface uplift caused by frost heaving could be divided into a rapid growth stage and a steady growth stage. The rapid growth stage corresponded to the early and late stages of the active freeze period. The stable growth stage corresponded to the maintenance freeze period, during which the soil temperature was basically stable and the frost heaving was also in a relatively stable state.

The numerical model was used to further study the frost heaving law of frozen soil, and the accuracy of the numerical model was evaluated by comparing the model with the field measured data. The numerical calculation was carried out with the corresponding model position of the DZ5-4 measuring point, and the comparative analysis was carried out with the measured value, as shown in Figure 22.

It can be seen from Figure 22 that there was a small deviation in the middle part, and the initial stage and the final stage were relatively consistent. Generally speaking, the

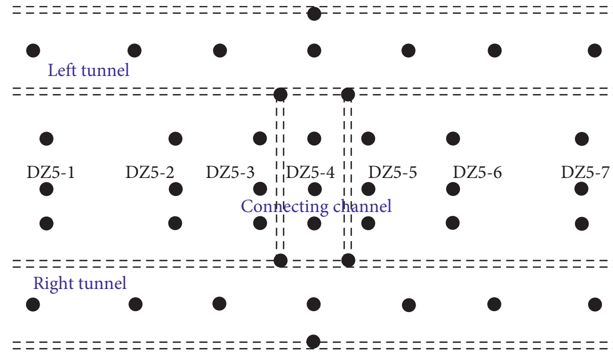

Figure 19: Layout of monitoring points.

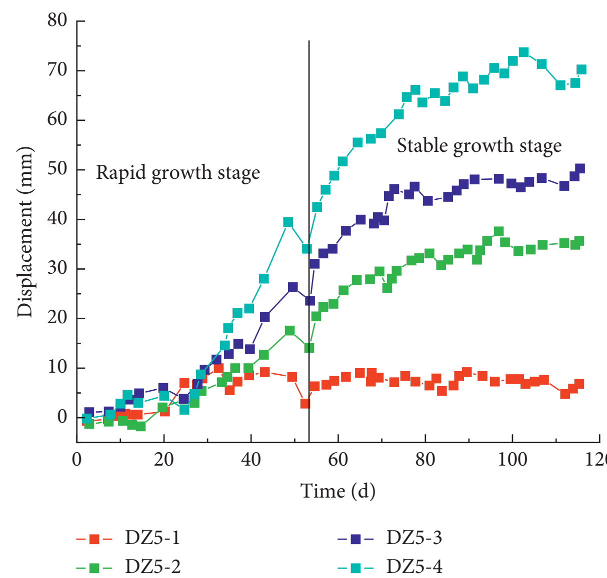

Figure 20: Surface deformation value.

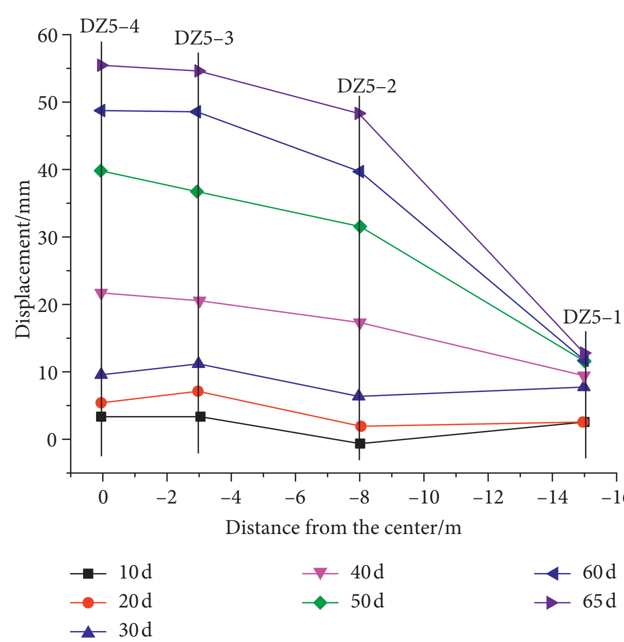

Figure 21: Distribution of frost heaving duration.

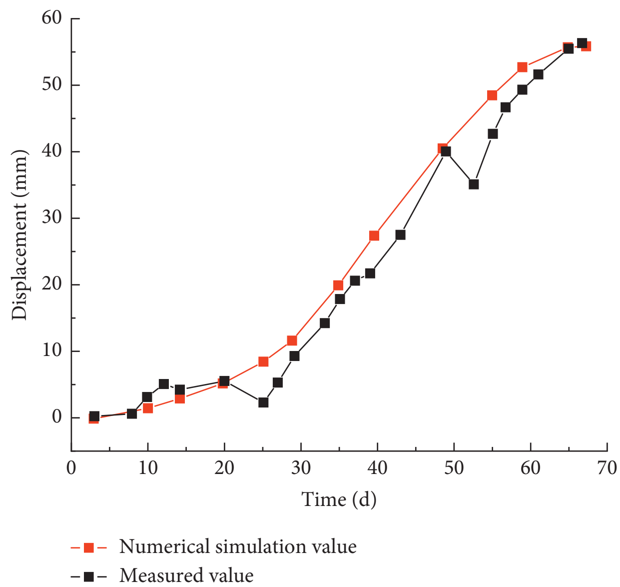

Figure 22: Comparison of calculated and measured values.

final calculation results of the numerical simulation were consistent with the measured data. Therefore, the above numerical simulation could accurately reflect the law of soil frost heaving caused by freezing.

6. Conclusions

The temperature field and the frost heaving characteristics are the keys to the study of the freezing method. The temperature field is the most direct inducement for the formation and development of freezing curtain, and frost heaving can cause structural deformation and damage. In this study, the thermal physical parameters and the frost heaving parameters of soil were obtained through the soil thermal physical tests and frozen soil frost heaving tests. A three-dimensional finite element model was established to simulate the temperature field and frost heaving changes of soil under on-site working conditions, and the model was further compared with the field measured values.

(1) Thermal physical tests and frost heaving tests for frozen soil were carried out to study the temperature field, frost heaving rate, and frost heaving force of soil during frost heaving.

(2) The entire cooling process could be roughly divided into three stages: the active freezing stage, the attenuation cooling stage, and the stability stage. The range of frozen soil expansion did not increase linearly with the decrease of the freezing temperature, and there was a limit radius for the frozen soil expansion. When the radius was reached, frozen soil did not expand outward. For the freeze-thaw cycle, the soil temperature changed periodically.

(3) When the freezing temperatures were −5°C, −10°C, −15°C, and −20°C, the frost heaving rates of soil were 0.53%, 0.95%, 1.28%, and 1.41%, and the frost heaving forces of the soil were 0.37 MPa, 0.46 MPa, 0.59 MPa, and 0.74 MPa, respectively. In the range of test conditions, the frost heaving rate and the frost heaving force of the soil increased with the decrease of the freezing temperature, and the relationship was roughly linear with the temperature.

(4) The development of the formation temperature field could be divided into three periods. In the early stage of active freezing, the formation temperature decreased rapidly. In the late stage of active freezing, the temperature dropped slowly. In the maintenance freezing period, the temperature tended to be stable.

(5) In the finite element model, the calculated temperature value corresponding to the T4-3 measuring point was compared with the measured temperature, and the calculated frost heaving value corresponding to the DZ5-4 measuring point was compared with the measured value, which verified the fact that the numerical calculation could reflect the temperature field change and the frost heaving law of the formation accurately.

Data Availability

The figures and tables data used to support the findings of this study are included within the article.

Conflicts of Interest

The authors declare that they have no conflicts of interest.

Acknowledgments

This study was supported by the National Natural Science Foundation of China (Grant nos. 42061011, 41977236, and 41672278), the Natural Science Foundation of Jiangxi Province (Grant no. 20192ACBL20002), the Doctoral Research Initiation Fund of East China University of Technology (Grant nos. DHBK2019229 and DHBK2019251), and the Science and Technology Project of XPCC (Grant no. 2020AB003). The authors gratefully acknowledge these supports.

References

[1] G. J. Bouyoucos, "Directions for making mechanical analyses of soils by the hydrometer method," *Soil Science*, vol. 42, no. 3, pp. 225–230, 1936.

[2] D. H. Everett, "The thermodynamics of frost damage to porous solids," *Transactions of the Faraday Society*, vol. 57, pp. 1541–1551, 1961.

[3] R. D. Miller, "The porous phase barrier and crystallization," *Separation Science*, vol. 8, no. 5, pp. 521–535, 1973.

[4] R. R. Gilpin, "A model for the prediction of ice lensing and frost heave in soils," *Water Resources Research*, vol. 16, no. 5, pp. 918–930, 1980.

[5] J. M. Konrad and C. Duquennoi, "A model for water transport and ice lensing in freezing soils," *Water Resources Research*, vol. 29, no. 9, 1993.

[6] Y. Wang, T. Sun, H. Yang, J. Lin, and H. Liu, "Experimental investigation on frost heaving force (FHF) evolution in

preflawed rocks exposed to cyclic freeze-thaw conditions," *Geofluids*, vol. 2021, no. 1, pp. 1–12, 2021.

[7] S. Huang, Y. Ye, and X. Cui, "Theoretical and experimental study of the frost heaving characteristics of the saturated sandstone under low temperature," *Cold Regions Science & Technology*, vol. 174, Article ID 103036, 2020.

[8] L. Huang, Y. Sheng, J. Wu, B. He, X. Huang, and X. Zhang, "Experimental study on frost heaving behavior of soil under different loading paths," *Cold Regions Science and Technology*, vol. 169, pp. 102905–102912, 2020.

[9] P. He, M. Xiong, Y. Mu, J. Dong, and X. Na, "Experimental study on frost-heaving force development of Tibetan clay subjected to one-directional freezing in an open system," *Advances in Civil Engineering*, vol. 2021, no. 5, pp. 1–13, 2021.

[10] F. Yue, P. Chou, and G. Yang, "Design and practice of freezing method applied to connected aisle in tunnel under complex conditio," *Chinese Journal of Geotechnical Engineering*, vol. 28, no. 5, pp. 660–663, 2006.

[11] P. He, G. Chen, and Q. Yu, "A couple model of heat, water and stress fields of saturated soil during freezing," *Journal of Glaciology and Geocryology*, vol. 22, no. 2, pp. 135–138, 2000.

[12] C. Xia, Y. Wang, and i. Zheng, "Study of differential frost heave of fractured rock mass," *Rock and Soil Mechanics*, vol. 41, no. 4, pp. 1161–1168, 2020.

[13] B. Wang, C. Rong, and H. Cheng, "Stress analysis of heterogeneous frozen wall considering interaction with surrounding soil," *Journal of China Coal Society*, vol. 42pp. 354–361, z2, 2017.

[14] K. M. Yoshinaka and Y. Neaupanet, "Simulation of a fully coupled thermo–hydro–mechanical system in freezing and thawing rock," *International Journal of Rock Mechanics and Mining Sciences*, vol. 36, no. 5, pp. 563–580, 1999.

[15] K. M. Neaupane and T. Yamabe, "A fully coupled thermo-hydro-mechanical nonlinear model for a frozen medium," *Computers and Geotechnics*, vol. 28, no. 8, pp. 613–637, 2001.

[16] O. B. Andersland and B. Ladanyi, "Frozen ground engineering," *American Society of Civil Engineers*, vol. 384, 2004.

[17] J. Chen, T. Liu, and D. Li, "Study on artificial three - tube freezing model test and freeze program," *Coal Science and Technology*, vol. 45, no. 12, pp. 94–100, 2017.

[18] Y. Jiang, Y. Zhao, and G. Zhou, "Multi–parameter monitoring of frozen soil structure with super–long freezing hole drilling in Guangzhou metro," *Rock and Soil Mechanics*, vol. 31, no. 1, pp. 158–173, 2010.

[19] W. Qi, P. Yang, and M. Jin, "Application and survey analysis of freezing method applied to ultra–long connected aisle in metro tunnel," *Chinese Journal of Underground Space and Engineering*, vol. 6, no. 5, pp. 1065–1071, 2010.

[20] X. Long, G. Cen, and L. Cai, "Hydro–thermal coupling model test and field validation of uneven frost heave of pavement structure," *Journal of Harbin Institute of Technology*, vol. 51, no. 3, pp. 172–178, 2019.

[21] Y. Zhang, Y. Xie, and Y. Li, "A frost heave model based on space–time distribution of temperature field in cold region tunnels," *Rock and Soil Mechanics*, vol. 39, no. 5, pp. 1625–1632, 2018.

[22] D. Li, A. Lu, and Q. Zhang, "Analysis of freezing method for construction of connected aisle in nanjing metro tunnels," *Chinese Journal of Rock Mechanics and Engineering*, vol. 23, no. 2, p. 334, 2004.

[23] J. Hu and P. Yang, "Numerical analysis of temperature field within large–diameter cup–shaped frozen soil wall," *Rock and Soil Mechanics*, vol. 36, no. 2, pp. 523–531, 2015.

[24] H. Cai, Y. Huang, and T. Pang, "Finite element analysis on 3D freezing temperature field in metro connected aisle construction," *Journal of Railway Science and Engineering*, vol. 12, no. 69, pp. 180–187, 2015.

[25] P. Yang and A. Pi, "Study on the effects of large groundwater flow velocity on the formation of frozen wall," *Chinese Journal of Geotechnical Engineering*, vol. 23, no. 2, pp. 167–171, 2001.

[26] D. Li, R. Wang, and P. Hu, "FEM analysis of transient freezing temperature field of frozen multi–wall tube," *Coal Geology & Exploration*, vol. 2, pp. 38–41, 2007.

Hindawi
Advances in Materials Science and Engineering
Volume 2021, Article ID 6627331, 12 pages
https://doi.org/10.1155/2021/6627331

Research Article

Study on Electroosmosis Consolidation of Punctiform Electrode Unit

Xiaoyu Yang, Yongbin Xie, Jianhua Dong, Guosheng Liu, and Yalin Zheng

Western Centre of Disaster Mitigation in Civil Engineering, Ministry of Education, Lanzhou University of Technology, Lanzhou 730050, China

Correspondence should be addressed to Jianhua Dong; djhua512@163.com

Received 5 January 2021; Revised 3 March 2021; Accepted 1 April 2021; Published 12 April 2021

Academic Editor: Hao Zheng

In the electroosmosis method, when the distance between the opposite electrode and the same electrode is equal, the two-dimensional effect of electroosmotic consolidation is significant, and the use of one-dimensional model will overestimate the potential gradient, making the calculated pore pressure value too large. Aiming at this problem, according to the electrode arrangement rule and the minimum composition, a punctiform electrode unit model is proposed, and electroosmotic experiments are carried out on the symmetric and asymmetric unit models. The two-dimensional electroosmotic consolidation governing equation of the punctiform electrode unit is established. The electric potential field of the electrode unit and the finite element form of the electroosmotic consolidation equation are given by the Galerkin method. The PyEcFem finite-element numerical library is developed using Python programming to calculate. The research results show the following: (1) The two-dimensional effect of the potential field distribution of the punctiform electrode unit is significant. The reduction of spacing of the same nature electrode in the symmetrical unit can make the potential distribution close to a uniform electric field. The asymmetry prevents the electric potential field distribution from being reduced to a one-dimensional model. (2) The number of anodes will affect the electroosmosis effect of the soil. The more the anodes, the better the electroosmosis reinforcement effect of the soil, and the distribution of negative excess pore water pressure will be more uniform. (3) In the early stage of electroosmosis, the more the drainage boundaries, the faster the generation of negative pore pressure, but in the middle and late stages of electroosmosis, the potential value becomes the decisive factor, and the amplitude of negative pore water pressure in asymmetric units is higher than that in symmetric units. The potential distribution will not affect the degree of consolidation but will affect the extreme pore water pressure.

1. Introduction

Electroosmosis drainage reinforcement method is a good method to deal with low-permeability soft soil [1]. In 1939, Casagrande [2] applied this method to practical engineering for the first time and achieved success. Since then, it had attracted the attention of many scholars and carried out a large number of experimental studies. These experimental studies mainly focused on the influencing factors of electroosmosis method [3], the characteristics of soil after electroosmosis treatment [4], and how to improve the efficiency of electroosmosis method [5]. On the basis of previous experimental research experience, the subsequent scholars further carried out the theoretical research of electroosmotic consolidation. The theory of electroosmotic consolidation greatly promoted the application of electroosmotic method and deepened people's understanding of electroosmotic method.

One-dimensional electroosmotic consolidation theory was proposed by Esrig [6], which is based on Terzaghi's seepage consolidation principle. Electroosmotic and hydraulic seepage meet the linear superposition principle, and the dissipation law of excess pore water pressure under electroosmotic action is given. Most of the subsequent researches on electroosmotic consolidation theory are based on the classical Esrig theory. Lewis and Humpheson [7] introduced the change of the current and solved the electroosmotic consolidation theory. Wan and Mitchell [8] established the theory of electroosmotic consolidation under surcharge condition and demonstrated the feasibility of electrode reversal, which can effectively reduce the energy consumption of electroosmotic. Shang [9] proposed a two-dimensional theoretical model of vertical electroosmosis under surcharge condition, which can effectively improve the soil reinforcement effect through the combination of surcharge and electroosmosis. Su and Wang [10] extended the one-dimensional electroosmotic consolidation theory to the two-dimensional model based on the idea of partition and initially established the two-dimensional electroosmotic consolidation theory. Li et al. [11] established the electroosmotic consolidation equation in the axisymmetric model and gave the analytical solution, which further developed the consolidation theory of surcharge combined electroosmotic method. Wu et al. [12] based on Biot's theory, the stress of soil under electroosmosis was calculated, and the change of soil properties caused by chemical change was considered in the model. During the electroosmosis drainage process, the soil gradually changed from the initial saturated state to the unsaturated state, so the saturation changed. The electroosmotic consolidation model considering the change of saturation is proposed [13], which makes the calculation results closer to the real situation. On the basis of the above saturation changes, the large deformation theory is introduced to improve the influence of soil properties changes in the process of electroosmotic consolidation by Deng and Zhou [14] and Zhou et al. [15–17]; the change of soil saturation also attracted the attention of Wang et al. [18]. In the two-dimensional model, the vacuum preloading method was introduced into the electroosmotic consolidation model, and the governing equation of this case was given and solved analytically by Wang et al. [19]. Sheng et al. [20] carried out experimental research on the two-dimensional potential distribution of electroosmotic under the action of plastic electrode plate, and the two-dimensional electroosmotic consolidation was calculated through the measured values. The potential attenuation in the process of electroosmosis will lead to the increase of energy consumption, which is discussed by Yang and Dong [21]. These studies improve the theory of electroosmotic consolidation and provide theoretical support for the engineering application of electroosmotic method. However, most of the existing researches on electroosmotic consolidation theory are based on one-dimensional model. Electroosmotic consolidation is largely affected by the electrode arrangement. When the same electrode spacing is equal to that of the opposite electrode, the potential attenuation of soil between the same electrode is more obvious, and the two-dimensional effect is significant. If one-dimensional model is used to describe the electroosmotic consolidation, the deviation caused by this simplification is not obvious at present in essence. The two-dimensional electroosmotic consolidation model based on the idea of partition can only be applied to the electroosmosis with parallel arrangement and cannot be used to calculate the electrode polarity in the case of asymmetry. These problems are still in lack of detailed and in-depth quantitative research. Therefore, it is urgent to establish a two-dimensional electroosmotic consolidation theory which can describe the electrode arrangement.

In this paper, on the basis of previous studies, according to the electrode composition and electrode polarity, the parallel and rectangular electrode arrangement is transformed into a punctiform electrode unit model. Taking the punctiform electrode unit as the research object, the electroosmotic consolidation tests of symmetric unit and asymmetric unit are carried out, and the potential distribution and pore pressure are measured. According to the punctiform electrode unit model, the two-dimensional electroosmotic consolidation equation is established, and the corresponding initial conditions and boundary conditions are given. The governing equation is discretized by Galerkin's method, which expresses the finite element form of governing equation. Python is used to program the numerical calculation library for solving the electroosmotic consolidation of punctiform electrode unit. The two-dimensional potential field and pore pressure field of electroosmosis are calculated. These researches on electroosmotic consolidation of punctiform electrode unit can provide some theoretical support for the engineering application of electroosmotic method.

2. Materials and Methods

2.1. Experimental Materials. In order to study the potential distribution and pore water pressure distribution of electrode unit with different electrode composition, two groups of experiments were carried out. The first model is symmetrical unit, which has two anodes and two cathodes. The second group contains three anodes and one cathode. The length and the width of the model box are all 50 cm, and the height is 25 cm, which is made of plexiglass. There are four electrode rod sockets at the corresponding position at the bottom of the model box, and a 40 cm × 40 cm rectangle is formed between the electrodes (see Figure 1). The metal probe is made of iron wire with a height of about 22 cm, which is used to measure the potential value at a certain point of the soil. Four probes about 1 cm away from the electrodes are used to measure the interface loss voltage in the process of electroosmosis. The rest of the metal probes are rectangular distribution, with vertical and horizontal spacing of 13.33 cm (see Figure 2(a)). The anode is made of iron metal rod with a diameter of 20 mm, the cathode is made of stainless-steel tube with an outer diameter of 20 mm, and the electrode length is 22 cm (see Figure 2(b)). There are drainage holes on the wall of the cathode tube for the discharge of pore water. The water-collecting box is used to collect the water from the cathode, and the quality of the discharged water can be measured in real time through an electronic scale. Micropore water pressure sensors are used to measure pore pressure during electroosmosis, and the maximum range of sensor is from −100 kPa to 100 kPa.

The other devices used include a DC power supply (PS-605D) and a multimeter. The maximum output voltage of the DC power supply was 60 V, and the maximum output

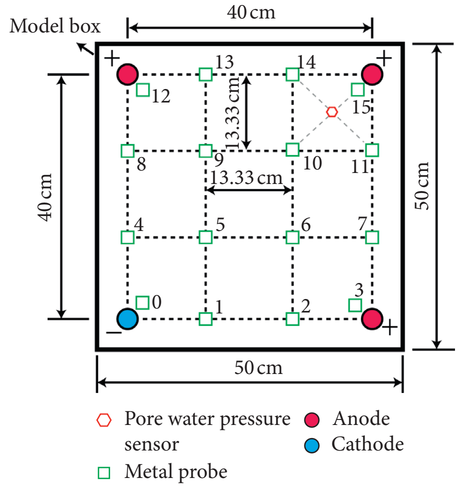

Figure 1: Schematic diagram of electroosmosis test device.

(a) (b) (c)

Figure 2: Electroosmotic consolidation model test. (a) Electroosmosis model box. (b) Metal electrodes. (c) Micropore water pressure sensors.

current was 3 A. The multimeter was used to measure the potential value of the soil.

The soil sample used in the test is remolded silt soil, which is taken from a foundation pit in Lanzhou. The particle size distribution of the soil is shown in Figure 3. The initial moisture content of the soil sample is 29.37%, the filling height of the soil sample in the test is 20 cm, and the soil parameters are shown in Table 1.

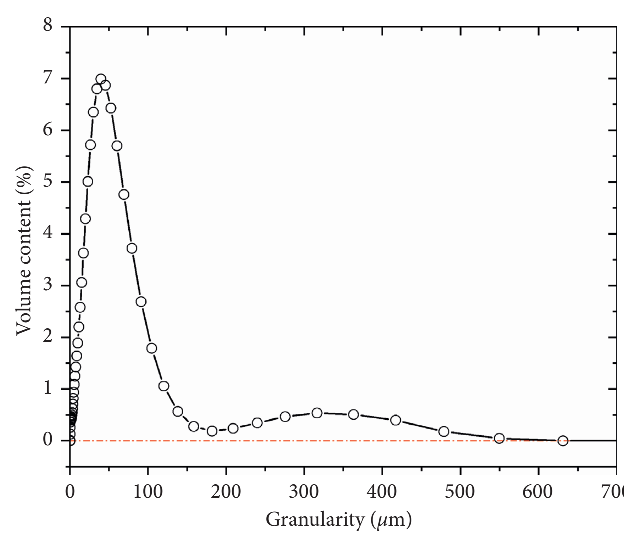

Figure 3: Soil particle size distribution curve.

Table 1: Physical properties of soil samples.

Specific gravity	Liquid limit (%)	Plastic limit (%)	Saturation
2.57	27	17	0.96

2.2. Experimental Methods. The experimental study contains two experimental models, one is the electroosmosis test of the symmetric unit, and the other is the electroosmosis test of the asymmetric unit. In the asymmetric test group, due to the development of soil cracks, the pore pressure sensor became 0 at the 51st hour. Therefore, the electroosmosis duration of the two groups of tests was determined to be 51 hours. Both sets of test power supply voltages are 48 V. Except for the electrode polarity, the other test parameters are the same in the two experimental models.

First of all, the soil sample should be treated. The silt soil was dried and crushed to remodel, and water was added to make the soil saturated. After resting for 48 hours, the average moisture content of the soil sample was about

29.37%, and soil sample saturation was 0.96. The electrode was inserted into the small hole in the model box for fixing, and the electrodes were connected with the DC power supply through the wire. The soil was layered into the model box, and the sample height was 20 cm. The water discharged in the process of electroosmosis flowed out from the cathode and was collected by the water collecting box. The reading interval of drainage quality was two hours, and the measurement is carried out in the daytime, meanwhile. The potential of each metal probe was measured by a multimeter to describe the potential distribution. The pore pressure sensor could continuously record the pore pressure in real time, and the sampling frequency was 1/60 Hz. After the electroosmosis test, the moisture content of soil was measured at each metal probe position.

3. Experiment Results

The amount of pore water discharged during the electroosmosis process can be read through an electronic scale. The soil samples used in the two experiments and the applied voltage are the same. There is only one cathode in the symmetrical unit, and the pore water is discharged at the cathode. In the asymmetric unit, there are two cathodes, and pore water converges at the two cathodes. Figure 4(a) shows the change curve of the quality of discharged water during the electroosmosis process. The drainage rate in the symmetric unit was slightly higher than that in the asymmetric unit before the first 30 hours, but the deviation was smaller. After 30 hours, the drainage rate of the symmetrical unit decreased quickly. After the test, the quality of the discharged water from the asymmetrical unit was slightly higher than that of the symmetrical unit by about 6.9%. During the electroosmosis process, the current generally showed a decreasing trend. However, in the first 8 hours, the currents of the two groups of tests showed an increase (see Figure 4(b)). This phenomenon was caused by the salt content of the soil sample, which was also discovered by other researchers [22]. The current began to decrease after reaching the peak value; at the end of the electroosmosis, the current was lower than the current value at the beginning of the test. The current of the symmetric unit was reduced by 31.8%, and the current of the asymmetric unit was reduced by 44.5%. The drainage effect of asymmetric units is higher than that of symmetric units. The more the anodes, the better the effect of electroosmosis reinforcement. The water content at different positions of the soil after electroosmosis also confirms this conclusion, as shown in Table 2.

A metal probe is placed about 1 cm away from the electrode to measure the interface voltage in the electroosmotic model. Figure 5 is a graph of potential changes at positions 0, 3, 12, and 15 of the metal probes. In the symmetrical unit test, the electric potentials of the two cathodes are relatively consistent, and both attenuate with the progress of electroosmosis, with a decrease of 76.9%. At the probes near the two anodes, the electric potentials also show a decreasing trend, with an average decrease amplitude is 34.3% (see Figure 5(a)). In the asymmetric unit, the distance between the three anodes and the cathode is different, which makes the pore water seepage path different. The anode with a longer distance will have a lower drainage rate than the other two anodes, and the moisture content of the soil will affect the soil. Therefore, the potential at the anode farther away increases with the progress of electroosmosis, and the amplitude is about 16.4%. The other two anode potentials are decreasing, with an average decrease of 40.8% (see Figure 5(b)). There is only one cathode in the asymmetric unit, and its potential value is reduced by 61.4%.

The effective voltage is the voltage that is really applied to the soil. The contact voltage between the electrode and the soil will make the actual electroosmotic voltage to be lower than the power supply voltage. This problem will increase the energy consumption of electroosmosis. The potential values at several metal probes are converted into an effective voltage; that is, the zero-potential-energy surface is selected as the probe at the cathode to obtain the effective voltage change of the electroosmosis test, as shown in Figure 6. The effective voltage in the symmetrical unit continues to decrease, with an average decrease of 25.4% (see Figure 6(a)). The effective voltage decreases faster in the early stage of electroosmosis and changes more slowly in the later stage. In the asymmetric unit, the effective voltage of anode 1 and anode 2 (see Figure 6(b)) showed a downward trend, with an average decrease of 35.8%, while the effective voltage of anode 3, which is farther from the cathode, increased by 44.9%.

The metal probes arranged in the box can obtain the potential distribution of the electrode unit. Figure 7 shows the measured potential distribution of the unit at the beginning of electroosmosis. In the symmetric unit (see Figure 7(a)), the electrodes are arranged symmetrically, so the potential distribution has good symmetry, and the potential gradient changes little near the cathode. In the asymmetric unit (see Figure 7(b)), the reduction of the potential is affected by the electrode arrangement and does not have a symmetrical characteristic. When the distance between the same electrode and the opposite electrode of the punctiform electrode unit is equal, the electric potential distribution of the unit has a strong two-dimensional characteristic, and the electric field distribution is significantly different from a uniform electric field.

Figure 8 shows the measured pore water pressure during the electroosmosis process. The change rate of the pore pressure of the symmetric unit is lower than that of the asymmetric unit. The asymmetric unit contains three anodes, and the drainage rate is faster. The more the anodes, the better the soil electroosmosis effect. The pore pressure of the symmetric unit changes from 1.08 kPa to −17.01 kPa, and the pore pressure of the asymmetric unit changes from 1.465 kPa to −21.53 kPa. With the same electroosmosis conditions and time, the reinforcement effect of asymmetric units is better than that of symmetric units. The more the anodes, the better the electroosmosis drainage effect.

4. Electroosmotic Consolidation Equation and Calculation Method

4.1. Governing Equation. The electroosmosis test of the punctiform electrode unit shows that there is a clear

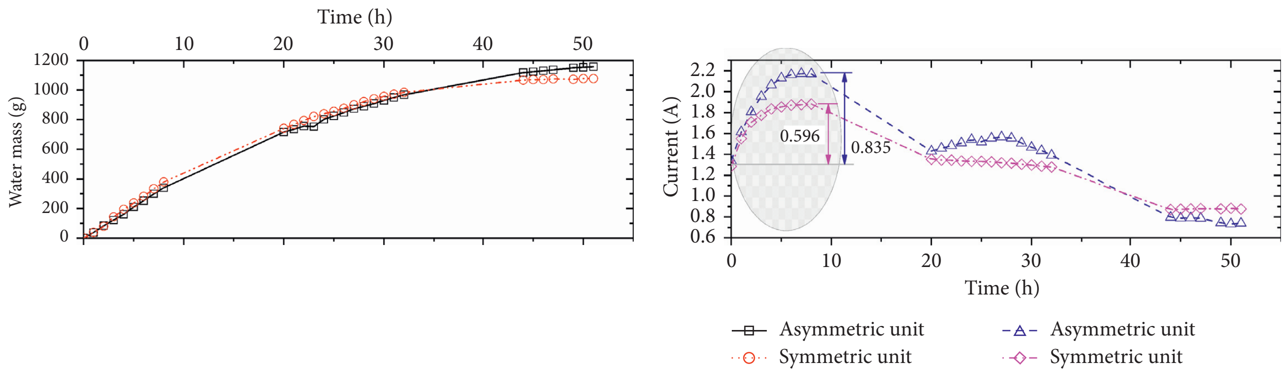

(a) (b)

Figure 4: Test of the actual displacement and current.

Table 2: Soil moisture content on the diagonal of the unit.

Test model	Position 15 (%)	Position 10 (%)	Position 5 (%)	Position 0 (%)
Symmetric unit	19.64	20.65	22.27	26.72
Asymmetric unit	18.42	19.68	21.14	26.39

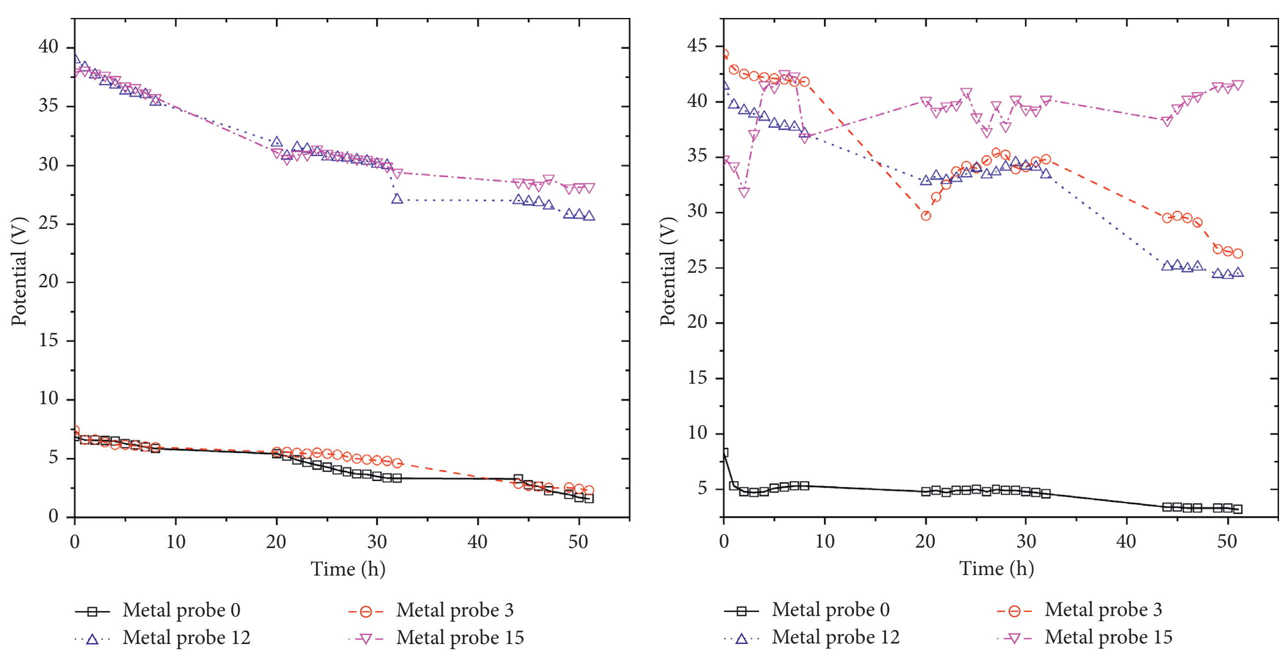

(a) (b)

Figure 5: Electrode potential change curve. (a) Symmetrical unit model. (b) Asymmetrical element model.

difference between the electric potential distribution and the uniform electric field. If the one-dimensional electro-osmotic consolidation theory is used for calculation, the influence of the electric potential distribution on the pore pressure cannot be reflected. Therefore, it does have positive significance to establish the two-dimensional unit theory of electroosmotic consolidation. The model still satisfies the assumptions in the Esrig theory, the soil is considered to be isotropic, the hydraulic seepage meets Darcy's law, and the relationship between the electroosmosis and hydraulic seepage meets the linear superposition principle.

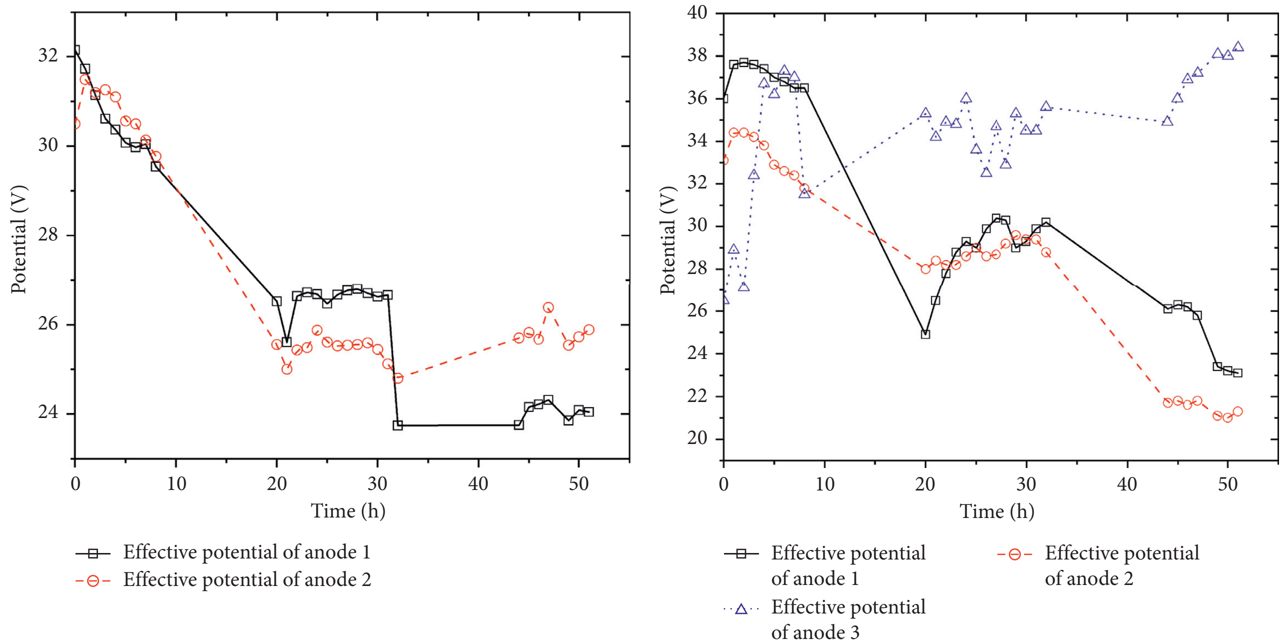

(a)

(b)

Figure 6: Effective potential change curve. (a) The effective potential of the symmetric unit. (b) The effective potential of the asymmetric unit.

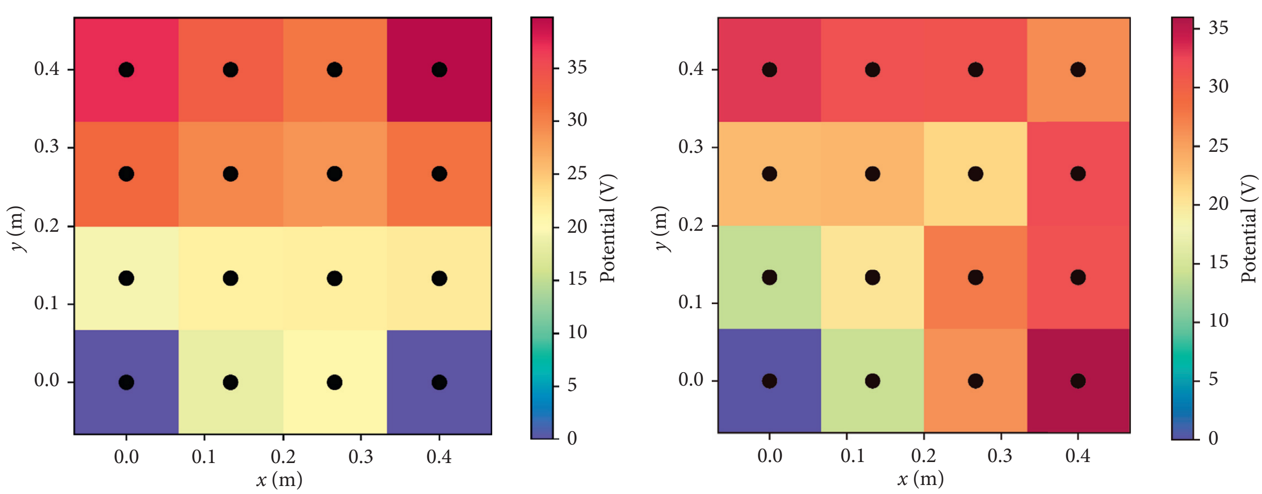

(a)

(b)

Figure 7: Potential distribution of test model. (a) The potential distribution of the symmetric unit. (b) The potential distribution of the asymmetric unit.

The change in soil volume is equal to the volume of pore water flowing out. The outflow of pore water of the microelement body per unit time is shown in the following equation:

$$\Delta Q = \frac{\partial v_x}{\partial x} \mathrm{d}x \cdot (\mathrm{d}y \cdot 1) + \frac{\partial v_y}{\partial y} \mathrm{d}y \cdot (\mathrm{d}x \cdot 1), \quad (1)$$

where ΔQ is the volume of water flowing out per unit time, v_x is the seepage velocity in the x-direction, v_y is the seepage velocity in the y-direction, and $\mathrm{d}x$ and $\mathrm{d}y$ are the lengths of the infinitesimal body in the x- and y-directions, respectively.

The change of soil volume per unit time ΔV is as follows:

$$\Delta V = \frac{\partial \varepsilon_v}{\partial t} (\mathrm{d}x \cdot \mathrm{d}y \cdot 1) = -m_v \frac{\partial u}{\partial t} (\mathrm{d}x \cdot \mathrm{d}y \cdot 1), \quad (2)$$

where ΔV is the change in soil volume per unit time. ε_v is the volumetric strain of the soil. m_v is the volumetric

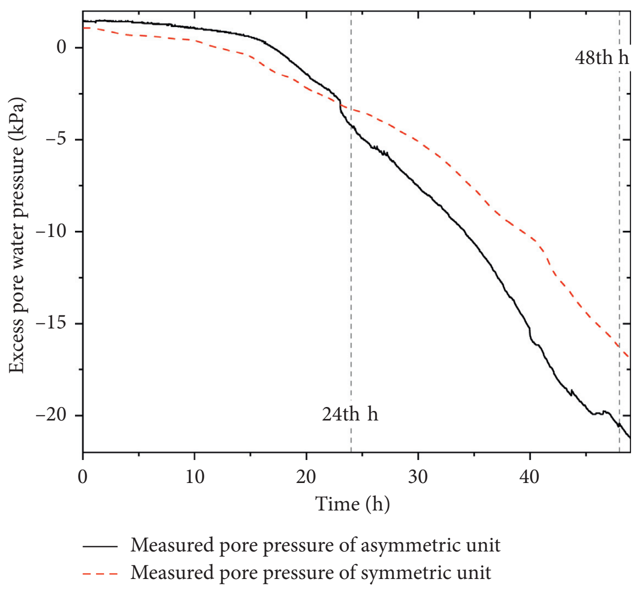

FIGURE 8: Picture of electroosmotic excess pore water pressure.

compressibility of the soil. $u(x, y, t)$ is the pore water pressure function.

According to the principle of water flow continuity, $\Delta V = \Delta Q$, the following equation can be obtained from formulas (1) and (2):

$$\frac{\partial v_x}{\partial x} + \frac{\partial v_y}{\partial y} = -m_v \frac{\partial u}{\partial t}. \tag{3}$$

In the process of electroosmosis, both hydraulic seepage and electroosmosis will cause the flow of pore water. These two flows satisfy the principle of linear superposition. The soil permeability coefficient is equal in two directions, and the electric permeability coefficient is the same in both directions. Equation (4) is as follows:

$$v_x = v_{hx} + v_{ex} = -\left(\frac{k_h}{\gamma_w}\frac{\partial u}{\partial x} + \frac{\partial \phi}{\partial x}\right), \tag{4}$$

where v_x is the velocity of hydraulic seepage in the x-direction, $v_{ex}$is the water flow velocity caused by the electric potential gradient in the x-direction, k_h is the permeability coefficient of soil, k_e is the electric permeability coefficient, and γ_w is the weight of water, and Φ is the potential function.

In the same way, the speed expression in the y-direction can be obtained in the following form:

$$v_y = v_{hy} + v_{ey} = -\left(\frac{k_h}{\gamma_w}\frac{\partial u}{\partial y} + \frac{\partial \phi}{\partial y}\right). \tag{5}$$

Substituting formula (4) and (5) into (3), the two-dimensional electroosmotic consolidation governing equation can be obtained:

$$\frac{\partial^2 u}{\partial x^2} + \frac{\gamma_w k_e}{k_h}\frac{\partial^2 \phi}{\partial x} + \frac{\partial^2 u}{\partial y^2} + \frac{\gamma_w k_e}{k_h}\frac{\partial^2 \phi}{\partial y^2} = \frac{m_v \gamma_w}{k_h}\frac{\partial u}{\partial t}. \tag{6}$$

In order to solve the governing equation, the imaginary $\zeta(x, y, t)$ function is introduced to transform equation (6). The $\zeta(x, y, t)$ expression is shown in the following equation:

$$\zeta(x, y, t) = u(x, y, t) + \frac{\gamma_w k_e}{k_h}\phi(x, y). \tag{7}$$

Combining equation (7) with equation (6), the governing equation of $\zeta(x, y, t)$ can be expressed:

$$C_h\left(\frac{\partial^2 \zeta}{\partial x^2} + \frac{\partial^2 \zeta}{\partial y^2}\right) = \frac{\partial \zeta}{\partial t}, \tag{8}$$

where C_h is the soil consolidation coefficient, $C_h = k_h/m_v\gamma_w$.

Equation (8) is the governing equation for two-dimensional electroosmosis consolidation. This equation is a parabolic partial differential equation. The equation can be solved by combining boundary conditions and initial conditions. After solving $\zeta(x, y, t)$, equation (6) can be used to calculate the pore water pressure distribution $u(x, y, t)$.

4.2. Boundary Conditions and Initial Conditions. The two-dimensional electroosmotic consolidation model of the electrode unit is shown in Figure 9. The origin of the coordinate system is point O, the length in the x-direction is L, and the width in the y-direction is W.

In the punctiform electrode unit, the geometric size of the electrode is much smaller than the size of the unit, so the electrode can be regarded as a point. The opening of the cathode can drain water. At the cathode, the pore water pressure is 0 and the potential value is 0, which meets the Dirichlet condition. The anode is an undrained boundary, and the seepage velocity at the anode is 0, which satisfies the Neumann boundary condition. The points on the boundary other than the electrode position are unconstrained. The boundary conditions of the symmetric unit can be obtained as follows:

$$\zeta(0, 0, t) = u(0, 0, t) + \frac{\gamma_w k_e}{k_h}\Phi(0, 0) = 0, \tag{9a}$$

$$\zeta(L, 0, t) = u(L, 0, t) + \frac{\gamma_w k_e}{k_h}\Phi(L, 0) = 0, \tag{9b}$$

$$\zeta_x(0, W, t) + \zeta_y(0, W, t) = 0, \tag{9c}$$

$$\zeta_x(L, W, t) + \zeta_y(L, W, t) = 0. \tag{9d}$$

The boundary conditions of the asymmetric unit are

$$\zeta(0, 0, t) = u(0, 0, t) + \frac{\gamma_w k_e}{k_h}\Phi(0, 0) = 0, \tag{10a}$$

$$\zeta_x(L, 0, t) + \zeta_y(L, 0, t) = 0, \tag{10b}$$

$$\zeta_x(L, W, t) + \zeta_y(L, W, t) = 0, \tag{10c}$$

$$\zeta_x(0, W, t) + \zeta_y(0, W, t) = 0. \tag{10d}$$

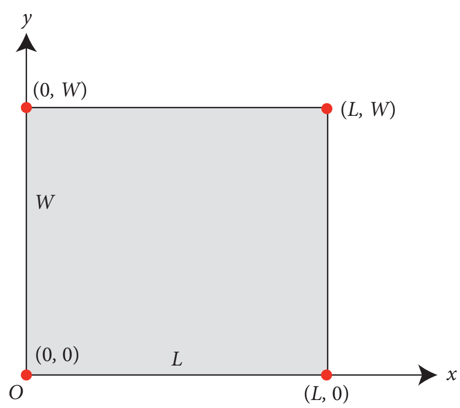

Figure 9: The electrode unit model.

According to formula (7), the initial conditions of the $\zeta(x, y, t)$ equation can be obtained. The initial conditions of both the symmetric unit and the asymmetric unit can be expressed as follows:

$$\zeta(x, y, 0) = u(x, y, 0) + \frac{\gamma_w k_e}{k_h} \Phi(x, y). \tag{11}$$

4.3. The Finite-Element Form. The initial conditions include the electric potential distribution function $\Phi(x, y)$. To solve the two-dimensional electroosmotic consolidation problem, the electric potential field must be calculated first. In one-dimensional electroosmotic consolidation, the electric field is a uniform electric field, and the potential distribution is linearly reduced. But for the punctiform electrode unit, it is necessary to solve the boundary value problem under the action of the point electrode based on the electrostatic field theory. Since the boundary conditions of the potential field and the pore pressure field in the two-dimensional electroosmosis model of the punctiform electrode unit are in the form of discrete points, it is difficult to use analytical solutions. The finite element method is used here for obtaining numerical calculation. For the electric potential field, it satisfies the Laplace equation; see the following equation:

$$\frac{\partial^2 \Phi}{\partial x^2} + \frac{\partial^2 \Phi}{\partial y^2} = 0. \tag{12}$$

The Galerkin method is used to discretize the equation. The finite-element shape is a three-node triangular element, and the corresponding shape function is

$$\Phi(x, y) = \{N_1 \;\; N_2 \;\; N_3\} \cdot \{\varphi_1 \;\; \varphi_2 \;\; \varphi_3\}^T = \{\mathbf{N}\} \cdot \{\boldsymbol{\varphi}\}^T, \tag{13}$$

where $\{\mathbf{N}\}$ is the shape function vector and $\{\varphi\}$ is the potential vector at the node of the element.

The strong formulation of equation (12) is

$$\iint_\Omega \{\mathbf{N}\}^T \cdot \left(\frac{\partial^2 \Phi}{\partial x^2} + \frac{\partial^2 \Phi}{\partial y^2}\right) \mathrm{d}x\mathrm{d}y = 0. \tag{14}$$

Applying Green's formula to equation (12), when it is a homogeneous boundary condition, the weak form corresponding of Laplace equation can be obtained:

$$\iint_\Omega \left(\frac{\partial\{\mathbf{N}\}^T}{\partial x}\frac{\partial \Phi}{\partial x} + \frac{\partial\{\mathbf{N}\}^T}{\partial y}\frac{\partial \Phi}{\partial y}\right) \mathrm{d}x\mathrm{d}y = 0. \tag{15}$$

Combining equations (13) and (15), the finite-element form of the electric potential field governing equation is obtained:

$$\iint_\Omega \left(\frac{\partial\{\mathbf{N}\}^T}{\partial x}\frac{\partial \{\mathbf{N}\}}{\partial x} + \frac{\partial\{\mathbf{N}\}^T}{\partial y}\frac{\partial \{\mathbf{N}\}}{\partial y}\right) \mathrm{d}x\mathrm{d}y \cdot \{\boldsymbol{\varphi}\}^T = 0. \tag{16}$$

The stiffness matrix of the element can be obtained by formula (16), and the total stiffness matrix is obtained through integration. The electric potential boundary condition is the Dirichlet condition, which is introduced into the linear equation system through the Lagrangian penalty function method, so that the electric potential field of the element can be calculated distributed. On the basis of the electric potential field distribution, the initial conditions of the electroosmotic consolidation equation (8) can be determined. The governing equation of the pore water pressure field is an unsteady state equation. First, use the Galerkin method to discretize the spatial items of the equation to obtain the corresponding time i expression:

$$\begin{aligned} &\iint \left(\frac{\partial\{\mathbf{N}\}^T}{\partial x}\frac{\partial \{\mathbf{N}\}}{\partial x} + \frac{\partial\{\mathbf{N}\}^T}{\partial y}\frac{\partial \{\mathbf{N}\}}{\partial y}\right) \mathrm{d}x\mathrm{d}y \cdot \{\mathbf{u}_i\}^T \\ &\quad + \iint \{\mathbf{N}\}^T \cdot \{\mathbf{N}\}\mathrm{d}x\mathrm{d}y \cdot \frac{\mathrm{d}\{\mathbf{u}_i\}^T}{\mathrm{d}t} = 0. \end{aligned} \tag{17}$$

Let $[\mathbf{k}] = \iint ((\partial\{\mathbf{N}\}^T/\partial x)(\partial\{\mathbf{N}\}/\partial x) + (\partial\{\mathbf{N}\}^T/\partial y)(\partial\{\mathbf{N}\}/\partial y))\mathrm{d}x\mathrm{d}y$, $[\mathbf{s}] = \iint \{\mathbf{N}\}^T \cdot \{\mathbf{N}\}\mathrm{d}x\mathrm{d}y$, equation (17) can be expressed as follows:

$$[\mathbf{k}] \cdot \{\mathbf{u}_i\}^T + [\mathbf{s}] \cdot \{\dot{\mathbf{u}}_i\}^T = 0. \tag{18}$$

The backward difference form is used to discretize the time term, which can ensure the convergence of the difference iteration. The time step is Δt:

$$\left(\sum [\mathbf{k}] + \frac{\sum [\mathbf{s}]}{\Delta t}\right) \cdot \{\mathbf{u}_i\}^T = \sum [\mathbf{s}] \cdot \{u_{i-1}\}^T. \tag{19}$$

Using the abovementioned finite-element form, the electric potential governing equation and the electroosmotic consolidation governing equation can be calculated. Here, Python is used to develop a special numerical calculation program for electroosmotic consolidation, which can calculate and solve the electric potential distribution and the pore water pressure.

5. Example Analysis

5.1. Two-Dimensional Effect of Electrode Unit. Consolidation of soil is a slow process. The aforementioned electroosmosis test only took 51 hours, and it is difficult to fully reflect the change of pore pressure during the electroosmosis process.

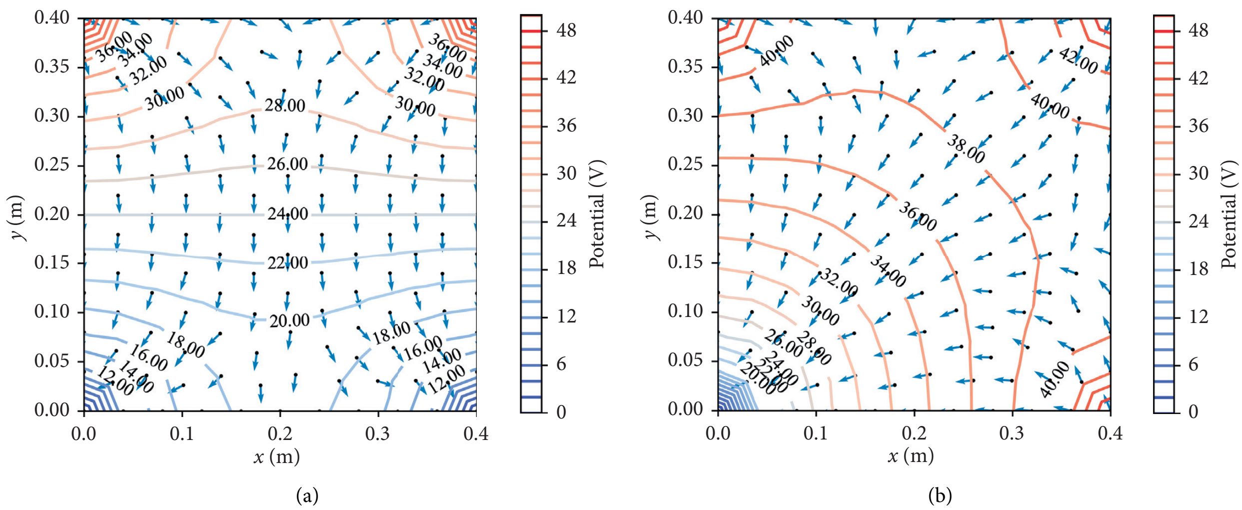

FIGURE 10: Gradient vector illustration of electric potential field. (a) Potential distribution of the symmetrical unit. (b) Potential distribution of the asymmetrical unit.

Therefore, a calculation example is carried out to calculate and analyse the electric potential field and electroosmotic consolidation of the electrode unit. The two-dimensional electroosmosis process must first determine the potential distribution of the unit, and the PyEcFem library is used to calculate this problem. The unit $L = 0.4$ m, $W = 0.4$ m, the applied voltage is 48 V, and the potential distribution of the symmetric unit and the asymmetric unit is obtained, as shown in Figure 10. In the symmetric unit, the numbers of anodes and cathodes are equal, so the potential distribution is symmetrical (see Figure 10(a)). In the case of $W/L = 1$, the potential distribution is significantly different from the uniform electric field, and the potential in the middle of the unit is lower than the potential at the electrode. At this time, if it is still calculated according to the one-dimensional electroosmotic consolidation theory, it will lead to an overestimation of the potential gradient. In the asymmetric unit (see Figure 10(b)), due to the asymmetry of the electrode properties, the potential distribution in this case cannot be simplified to a linear distribution, and the two-dimensional effect of the potential distribution is significant.

In actual engineering, when the distance between the electrodes of the same nature is much smaller than the distance between the electrodes of the opposite, in the case of symmetry, the distribution of the electric potential field is similar to the uniform electric field. In this case, the one-dimensional electroosmotic consolidation model can be used to solve the problem. However, there is a lack of quantitative research. In order to study this problem, the calculations with different spacing ratios (W/L=1, 2, 3, 4, 5) and W remaining unchanged are carried out. The potential distribution is shown in Figure 11. It can be found that as the spacing ratio increases, the potentials' value distribution is getting closer and closer to the uniform electric field. When the electrode pitch ratio is 1, the electric potential has a significant attenuation phenomenon. When the pitch ratio is equal to 5, this phenomenon is basically eliminated.

5.2. Distribution Characteristics of Excess Pore Water Pressure. On the basis of obtaining the electric potential distribution, the calculation of electroosmosis consolidation can be determined. The soil electroosmosis coefficients $k_e = 5 \times 10^{-9} m^2 \cdot (s \cdot V)^{-1}$, $k_h = 2.5 \times 10^{-8}\ \mathrm{ms}^{-1}$, and $C_h = 5 \times 10^{-7}\ \mathrm{m^2 s^{-1}}$; the initial pore water pressure is $u(x, y, 0) = 1.5$ kPa, the total time is 10^8 seconds, and the number of time steps is 10000, so $\Delta t = 10^4$ seconds. Figure 12 shows the pore water pressure distribution of the unit after electroosmosis is completed. There is an obvious difference between the pore pressure distribution of the symmetric unit and the asymmetric unit after electroosmosis. The negative pore pressure in electroosmosis is determined by the potential value. The more the anodes, the larger the negative pore pressure distribution area. The electroosmotic consolidation effect of asymmetric units is better than that of symmetric units.

The electroosmotic consolidation is established on the basis of Terzaghi's seepage consolidation theory. The consolidation speed of the soil is determined by the hydraulic permeability coefficient of the soil. The difference in electric potential distribution will not affect the consolidation speed, as shown in Figure 13(a). The average degree of consolidation curve of the symmetric unit completely coincides with the consolidation curve of the asymmetric unit. This conclusion is consistent with Esrig's theory [6]. The electric potential field mainly affects the pore pressure during the electroosmotic consolidation process. After the electroosmosis is completed, the average excess pore water pressure in the symmetric unit is − 23.962 kPa, while the average excess pore water pressure in the asymmetric unit is 36.068 kPa, as shown in Figure 13(b). The larger the number of anodes, the larger the average potential value of the unit and the stronger the drainage power. In the initial stage of electroosmosis, the symmetric unit contains two cathode drainage boundaries, and the outflow of pore water is higher than that of the asymmetric unit. In the middle and late stages of

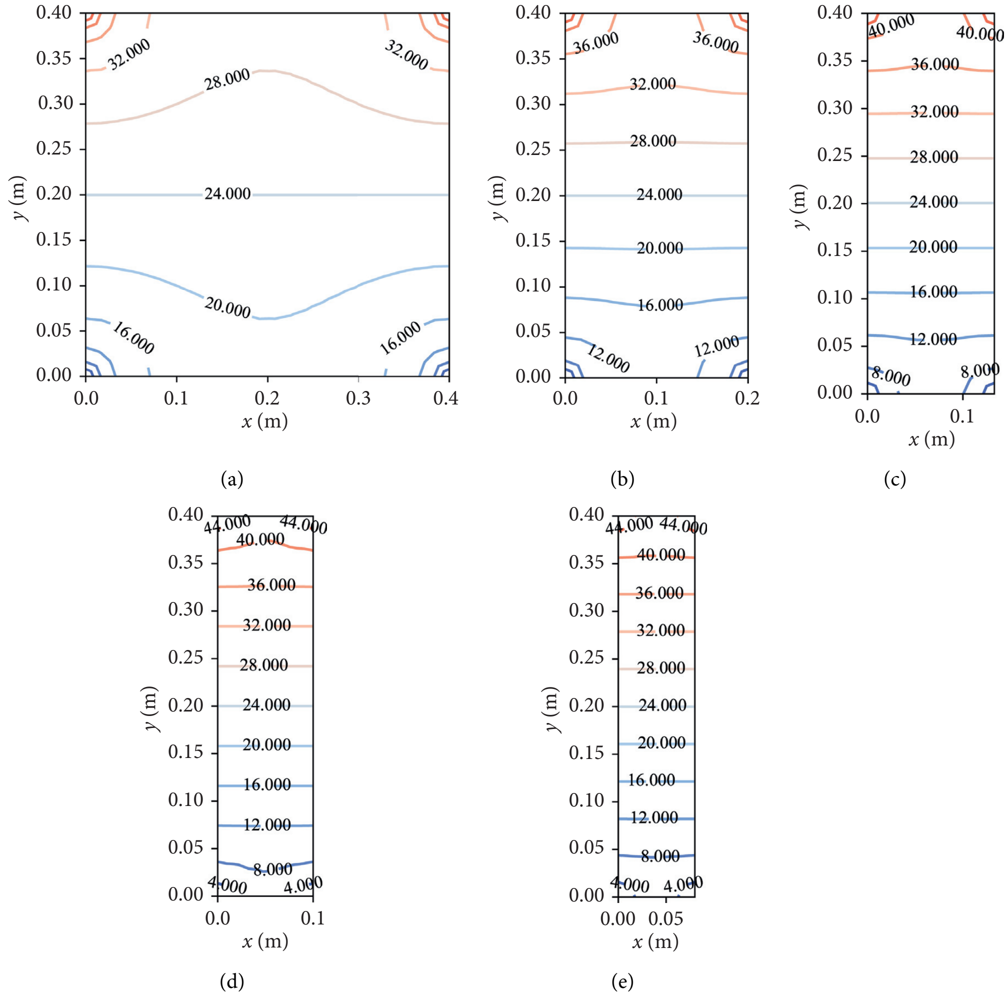

Figure 11: Potential contour plot of symmetric unit. (a) $W = 0.4$ ml $= 0.4$ m. (b) $W = 0.4$ ml $= 0.2$ m. (c) $W = 0.4$ m, $L = 0.133$ m. (d) $W = 0.4$ ml $= 0.1$ m. (e) $W = 0.4$ ml $= 0.08$ m.

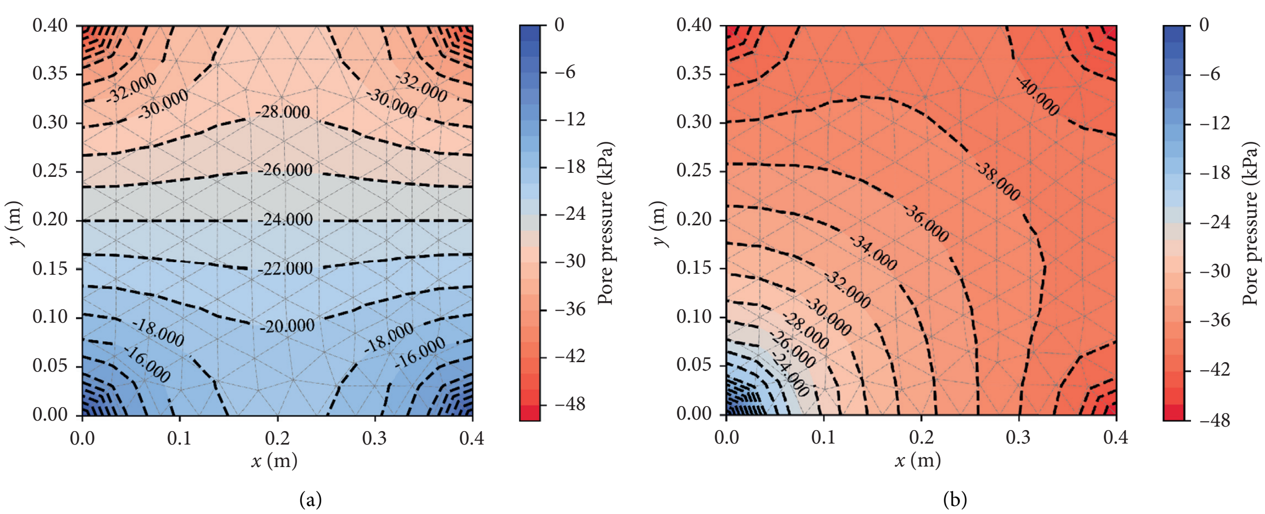

Figure 12: Colormap of excess pore water pressure distribution after electroosmosis. (a) The pore water pressure of the symmetric unit at time 10^8 sec. (b) The pore water pressure of the asymmetric unit at time 10^8 sec.

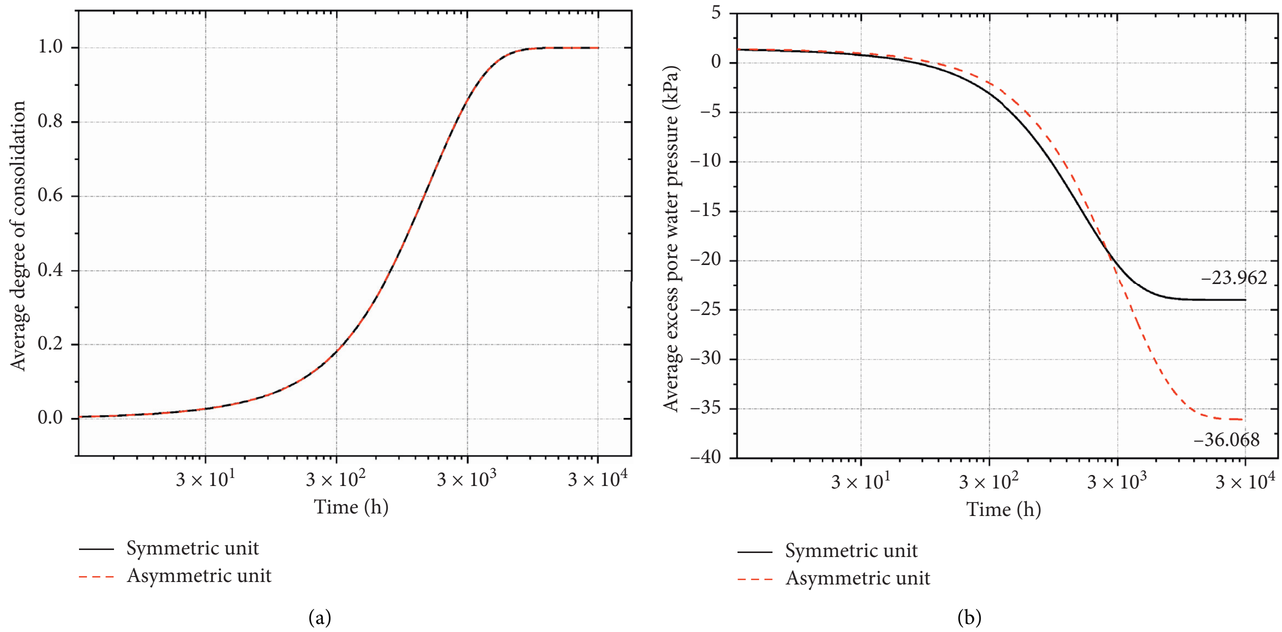

Figure 13: The average degree of consolidation curve and the average excess pore water pressure curve of the unit. (a) The unit average consolidation curve. (b) The curve of excess pore water pressure of unit.

electroosmosis, most of the pore water in the soil has been discharged, the influence of the number of drainage boundaries is reduced, and the driving force of the electric potential gradient becomes the main influence. The pore water pressure change rate of the symmetric unit gradually decreases, while the pore water pressure change rate of the asymmetric unit remains at a relatively high rate. The average excess pore water pressure of the asymmetric unit is 33.56% higher than that of the symmetric unit.

6. Conclusions

This paper focuses on the study of the two-dimensional electroosmotic consolidation characteristics when the electrode spacing is large, and the research object of the punctiform electrode unit is proposed. Electroosmotic consolidation test of the punctiform electrode unit is carried out; in the experiment, the electroosmotic consolidation characteristics of symmetric and asymmetric units and the difference in electric potential field are analyzed. Based on the continuity of water flow and the principle of linear superposition, the governing equation of the two-dimensional electroosmotic consolidation theory is established and the corresponding boundary conditions and initial conditions are given. The Galerkin method is used to discretize the governing equation, and the corresponding PDE numerical calculation module PyEcFem was developed by Python language; at the same time, the numerical solution of the example is carried out. The main conclusions are as follows:

(1) According to the difference of electrode polarity, the electrode unit can be divided into symmetrical unit and asymmetrical unit. The electroosmosis test shows that the drainage of the asymmetric model is higher than that of the symmetric model, but the symmetric model has a faster drainage rate in the initial stage. After the electroosmosis test is over, the water content of the asymmetric unit soil is lower than that of the symmetric unit, and more anodes in the asymmetric unit can promote soil reinforcement.

(2) The potential distribution of the electrode unit has obvious two-dimensional characteristics. In a symmetric unit, as the distance between the same electrodes decreases, the potential distribution tends to be uniform. When the spacing ratio is 5, the potential field is basically close to a uniform electric field.

(3) With the same electroosmotic parameters and power-on time conditions, the electroosmotic reinforcement effect of asymmetric units is better than that of symmetric units. The negative pore pressure distribution in the asymmetric unit is relatively uniform, and the pore water pressure amplitude of the part near the cathode in the symmetric unit is lower than that near the anode. The unevenness of the soil after electroosmosis reinforcement is obvious. The potential distribution will not affect the consolidation rate, but it will affect the extreme value of negative pore water pressure. There are two drainage boundaries in the symmetric unit. In the initial stage of electroosmosis, the change rate of pore pressure is faster than that of the asymmetric unit. In the middle and late stages of electroosmosis, the rate of change of the pore pressure of the symmetric unit decreases more than that of the asymmetric unit. The increase in the number of anodes in electroosmosis consolidation can improve the effect of electroosmosis consolidation.

Data Availability

The data used to support the findings of this study is available from the corresponding author upon request.

Conflicts of Interest

The authors declare that they have no conflicts of interest regarding the publication of this paper.

Acknowledgments

This study was supported by the Natural Science Foundation of China (no. 51778275) and Longyuan Young Innovative and Entrepreneurial Talents (team project no. 2020RCXM120).

References

[1] S. Micic, J. Q. Shang, K. Y. Lo, Y. N. Lee, and S. W. Lee, "Electrokinetic strengthening of a marine sediment using intermittent current," *Canadian Geotechnical Journal*, vol. 38, no. 2, pp. 287–302, 2001.

[2] I. L. Casagrande, "Electro-Osmosis in soils," *Géotechnique*, vol. 1, no. 3, pp. 159–177, 1949.

[3] J. Q. Shang, "Electrokinetic sedimentation: a theoretical and experimental study," *Canadian Geotechnical Journal*, vol. 34, no. 2, pp. 305–314, 1997.

[4] K. Y. Lo, I. I. Inculet, and K. S. Ho, "Electroosmotic strengthing of soft sensitive clays," *Canadian Geotechnical Journal*, vol. 28, no. 1, pp. 62–73, 2011.

[5] L. Bjerrum, J. Moum, and O. Eide, "Application of electro-osmosis to a foundation problem in a Norwegian quick clay," *Géotechnique*, vol. 17, no. 3, pp. 214–235, 1967.

[6] M. I. Esrig, "Pore pressures, consolidation, and electrokinetics," *Journal of the Soil Mechanics and Foundations Division*, vol. 94, no. 4, pp. 899–921, 1968.

[7] R. W. Lewis and C. Humpheson, "Numerical analysis of electro-osmotic flow in soils," *Journal of the Soil Mechanics & Foundations Division*, vol. 99, no. 3, pp. 603–616, 1973.

[8] T.-Y. Wan and J. K. Mitchell, "Electro-osmotic consolidation of soils," *Journal of the Geotechnical Engineering Division*, vol. 102, no. 5, pp. 473–491, 1976.

[9] J. Q. Shang, "Electroosmosis-enhanced preloading consolidation via vertical drains," *Canadian Geotechnical Journal*, vol. 35, no. 3, pp. 491–499, 1998.

[10] J. Q. Su and Z. Wang, "Theory of two-dimensional electro-osmotic consolidation of soils," *Rock and Soil Mechanics*, vol. 25, no. 1, pp. 125–131, 2004.

[11] Y. Li, X. N. Gong, M. M. Lu et al., "Coupling consolidation theory under combined action of load and electro-osmosis," *Chinese Journal of Geotechnical Journal*, vol. 35, no. 2, pp. 388–394, 2013.

[12] H. Wu, W. Wu, and L. Hu, "Numerical model of electro-osmotic consolidation in clay," *Géotechnique*, vol. 62, no. 6, pp. 537–541, 2012.

[13] Y. D. Zhou, A. Deng, and J. Y. Fu, "Modelling electro-osmosis–surcharge preloading combined consolidation of unsaturated soils," *Computers and Geotechnics*, vol. 114, Article ID 103145, 2019.

[14] A. Deng and Y. D. Zhou, "Modeling electroosmosis and surcharge preloading consolidation. II: validation and simulation results," *Journal of Geotechnical and Geoenvironmental Engineering*, vol. 142, no. 4, Article ID 04015094, 2016.

[15] Y. Zhou, A. Deng, and C. Wang, "Finite-difference model for one-dimensional electro-osmotic consolidation," *Computers and Geotechnics*, vol. 54, no. 10, pp. 152–165, 2013.

[16] Y. D. Zhou, A. Deng, and Q. Lu, "A one-dimensional consolidation model considering large strain for unsaturated soil," *Rock and Soil Mechanics*, vol. 39, no. 5, pp. 1675–1681, 2018.

[17] Y. D. Zhou, J. Y. Fu, A. Deng et al., "A nonlinear model for electroomosis-vacuum preloading coupled consolidation," *Chinese Journal of Rock Mechanics and Engineering*, vol. 38, no. 8, pp. 1677–1685, 2019.

[18] L. J. Wang, Y. M. Wang, S. H. Liu et al., "Analytical solution for one-dimensional vertical electro-osmotic drainage under unsaturated conditions," *Computers and Geotechnics*, vol. 105, no. 9, pp. 27–36, 2018.

[19] L. J. Wang, P. H. Huang, S. H. Liu et al., "Analytical solution for nonlinear consolidation of combined electroosmosis-vacuum-surcharge preloading," *Computers and Geotechnics*, vol. 121, no. 2, Article ID 103484, 2020.

[20] Y. Shen, J. T. Feng, Y. H. Ma et al., "Two-dimensional electroosmotic consolidation theory of nonlinear soil voltage distribution characteristics," *Advances in Civil Engineering*, vol. 2019, Article ID 7354873, 10 pages, 2019.

[21] X. Y. Yang and J. H. Dong, "A polymorphic inheritance calculation method of one-dimensional electro-osmotic consolidation considering effective potential attenuation," *Chinese Journal of Rock Mechanics and Engineering*, vol. 39, no. 12, pp. 2530–2539, 2020.

[22] Y. Li and X. N. Gong, "Experimental study on effect of soil salinity on electro-osmotic dewatering in soft clay," *Chinese Journal of Geotechnical Engineering*, vol. 33, no. 8, pp. 1254–1259, 2011.

Hindawi
Advances in Materials Science and Engineering
Volume 2021, Article ID 5548638, 12 pages
https://doi.org/10.1155/2021/5548638

Research Article

A New Mitigation Measure to Counter Thermal Instability of Air-Cooled Embankment in Sandy Permafrost Zones of Tibet Plateau

Minghao Liu, Jing Luo, Liang Zhang, and Xin Ju

State Key Laboratory of Frozen Soil Engineering, Northwest Institute of Eco-Environment and Resources, Chinese Academy of Sciences, Lanzhou 730000, Gansu, China

Correspondence should be addressed to Minghao Liu; liuminghao@lzb.ac.cn

Received 2 February 2021; Revised 13 February 2021; Accepted 24 March 2021; Published 8 April 2021

Academic Editor: Robert Cerný

A crushed-rock revetment (CRR) with high permeability that can be paved on embankment slopes is widely used to cool and protect the subgrade permafrost. In this study, a traditional CRR over warm permafrost was selected to investigate its cooling characteristics based on the ground temperature observed from 2003 to 2014. A new mitigation structure (NMS) was designed to improve the cooling capacity of the CRR and to counter the pore-filling of the rock layer. Numerical simulations were conducted to evaluate the cooling performance and reinforcing capacity of the NMS based on a developed heat and mass transfer model. The results indicate that the traditional CRR can improve the symmetry of the permafrost subgrade and decrease the ground temperature of shallow permafrost. However, the CRR cannot generate strong enough cooling to influence the deep (below 10 m depth) and warm permafrost with a mean annual ground temperature above −1.0°C. The wind-blown sand can further weaken the cooling of the CRR and cause significant permafrost warming and thawing beneath the slopes, posing a severe threat to the long-term safe operation of the embankment. The proposed NMS can produce a significantly superior cooling performance to the CRR. If the CRR is reinforced by the new structure, it can not only effectively cool the underlying warm permafrost but also elevate the permafrost table. The new structure can also protect the rock layer on the slopes from sand-filling. The NMS can be used as an effective method for roadbed design or maintenance over warm permafrost.

1. Introduction

Permafrost is soil or rock with ice that remains at or below 0°C for at least two consecutive years [1, 2]. Land in permafrost zones is permanently frozen to a great depth, with the surface seasonally thawing in the summer [1, 2]. Approximately, 25% of the land area in the Northern Hemisphere is underlain by permafrost stratum [3], which is, however, a type of unstable geological body and highly sensitive to ground temperature changes due to the existence of ground ice [4, 5]. Many critical transportation infrastructures were constructed in the permafrost zones, including the East-Siberian Railway in Russia, the Hudson Bay Railway in Canada, the Alaska Highway in the USA, and the Qinghai-Tibet Railway and Highway in China [6]. Roadway construction in permafrost zones generally disturbs the original ground surface and changes the ground-surface energy balance, leading to the warming and melting of the ice-rich permafrost underneath the embankment and the subsequent uneven thaw settlement [7, 8]. This severely affects the stability and integrity of transportation infrastructures and threatens their long-term safe operation [9]. How to control the ground heat to meet the demand of engineering foundation thermal stability is an important issue in permafrost areas.

The Qinghai-Tibet Plateau (QTP), with an average elevation of over 4000 m, is one of the highest plateaus in the world and contains the largest area of permafrost at high elevation on Earth [10]. Permafrost on the QTP is typically warmer compared with other areas of the northern hemisphere [10, 11] and thus more susceptible to temperature perturbation. Climate warming on the QTP can accelerate permafrost warming and has caused permafrost degradation in recent decades [6, 12]. This leads to the decrease of bearing-capacity of the permafrost foundation and potentially causes the large settlements or failures of the transportations traversed the permafrost areas of the QTP, for example, Qinghai-Tibet Railway, the Qinghai-Tibet Highway, Gongyu Expressway, and so on. Mitigation techniques have been developed based on the active cooling approach to cool the subgrade foundation and to protect the underlying permafrost foundation on the QTP in recent decades [6]. The crushed-rock embankment is a type of air convection embankment by making the best use of cold air energy during cold seasons and has been widely employed in roadbed engineering over permafrost on the QTP [13]. The crushed-rock embankment is constructed using poorly graded rocks with high permeability that can allow air to flow through the rock pores and augment heat extraction from the embankment during winter [12, 14]. It has proven to be an economical and effective technique to cool the permafrost stratum and maintain the foundation stability of embankments [12, 15].

Crushed-rock revetment (CRR), paving the rocks on the side slopes, is one of the typical construction methods of air convection embankment [6, 16]. Although the CRR is prevalent in practical engineering because of its convenient construction and flexible reinforcement, it is facing problems that affect its long-term effective cooling performances. It is particularly concerning that the CRR generates insufficient cooling on the underlying warm permafrost with a mean annual ground temperature above −1.0°C [17, 18]. The limited cooling largely lies in the hot wind that blows into the pore space of the open crushed-rock layer in hot seasons, which can increase heat absorption in the embankment slopes, and is adverse to permafrost stability. The aeolian sands and wreathed rocks frequently occurred on the QTP due to the strong wind and high ultraviolet radiation [19, 20], as is shown in Figure 1, which can block the pore of the rocks and further reduce its convection cooling capacity, aggravating the long-term performance of the CRR. How to optimize it to enhance its cooling performance to counter permafrost degradation and climate warming has become an urgent issue in complex circumstances.

In this study, we firstly investigated the cooling characteristics of a selected CRR embankment in a warm permafrost zone based on the ground temperature observed from 2004 to 2014. Then, a mitigation structure was designed to improve the cooling capacity of the CRR and to counter the sand-filling of the porous rock layer. A coupled heat transfer model was developed and series of numerical simulations were conducted to evaluate the cooling effect and reinforcing performance of the new structure considering climate warming. It is hoped that this study could improve the utilization of cold energy in cold regions and provide guidance for the design and maintenance of embankment traversed warm or thaw-sensitive permafrost zones.

2. Field Observations and Analysis

2.1. Slow Permafrost Warming under the CRR Embankment. As shown in Figure 2, a CRR embankment built in Chuma'er High Plain along the Qinghai-Tibet Railway was selected to analyze its long-term cooling effect and characteristic, based on the observed ground temperature data from 2003 to 2014. Permafrost in this site is typically warm and ice-rich, with a mean annual ground temperature of about −0.9°C. The permafrost table ranges from 2.5 m to 3.0 m. Thus, this region of the monitoring section located is representative of the warm and ice-rich permafrost of the QTP. The thickness of the crushed-rock layer on the sunny and shady slopes of the embankments is 1.6 m and 0.8 m, respectively. Four boreholes with a depth of 16 m were drilled at the two shoulders and the two slope toes of the railway embankment, and one borehole with a depth of 16 m was also drilled in the undisturbed ground as a reference of permafrost thermal status without disturbance, which is 10 m away from the embankment toe. The ground temperatures were measured by thermistors cable with a precision of ±0.02°C, installed in the embankment boreholes. The data was collected manually by a CR3000 data logger two times a month.

Figure 3 shows the ground temperature fields of the CRR embankment in early October of the years 2003, 2005, 2010, and 2014. The 0°C isotherm in the figure is defined as the permafrost table because the maximum seasonal thaw depth usually occurs in October on the QTP. As shown, the permafrost table under the sunny side (left side) of the embankment was slightly deeper than the shady side (right side) and the natural ground in 2003 after the embankment was just constructed. This was mainly due to thermal disturbance caused by embankment construction, while, in 2005, the permafrost table beneath the embankment was elevated obviously, with a magnitude of approximately 2.0 m, revealing the cooling effect of the CRR on the underlying permafrost. Up to 2010, the cooling for the permafrost layer with a depth of −3.0 to −5.0 m continued, which can be confirmed by the elevation of the −0.5°C isotherm under the embankment. The symmetry of the ground temperature field was also improved although the embankment orientation is southeast-northwest direction, which tends to cause different solar radiation on the sunny slope and shady slope of the embankment [21]. It proved that different thickness of the CRR on the two slopes performed satisfactory effects in improving the symmetry of the ground temperature distribution. In 2014, the symmetrical temperature field was maintained and the permafrost table under the embankment was further elevated. These characteristics revealed the good cooling of this structure on the shallow permafrost. However, it should be noted that the deep permafrost experienced a slow warming trend since constructed, as shown by the disappearance of the −1.0°C isotherm.

For further investigation of dynamic variation of permafrost temperatures, Figure 4 was drawn to show time series of permafrost temperatures with depths of 2.0 m, 4.0 m, and 10 m beneath the sunny shoulder of the CRR embankment. The depths were measured from the original ground surface, which represented the shallow and deep permafrost. It can be clearly found that permafrost at the depths of 2.0 m and 4.0 m experienced obvious cooling processes after construction. Particularly after 2008, the temperature amplitude increased, indicating that the heat exchange process during cold seasons increased. In the contrary, the deep permafrost temperature at depth of 11 m

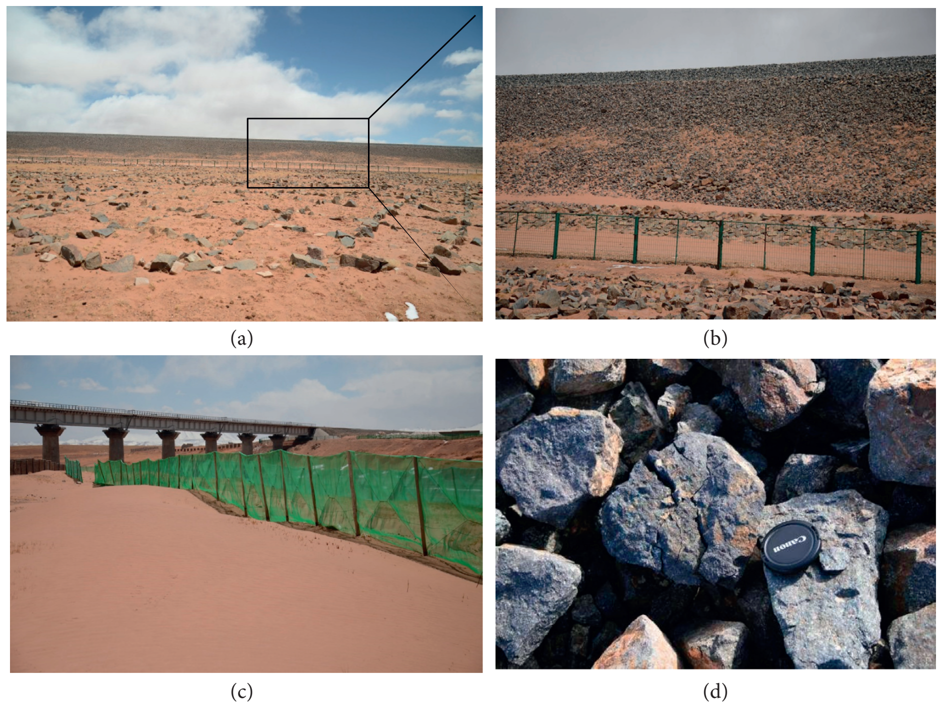

Figure 1: Wind-blown sand and rock-weathering of CRR embankment along the Qinghai-Tibet Railway. (a) Sand-filling of porous rock layer at the Honglianghe section; (b) close-view of sand-filling of the CRR; (c) prevalent sand prevention measure on the QTP; and (d) rock-weathering of the CRR caused by a severe environment.

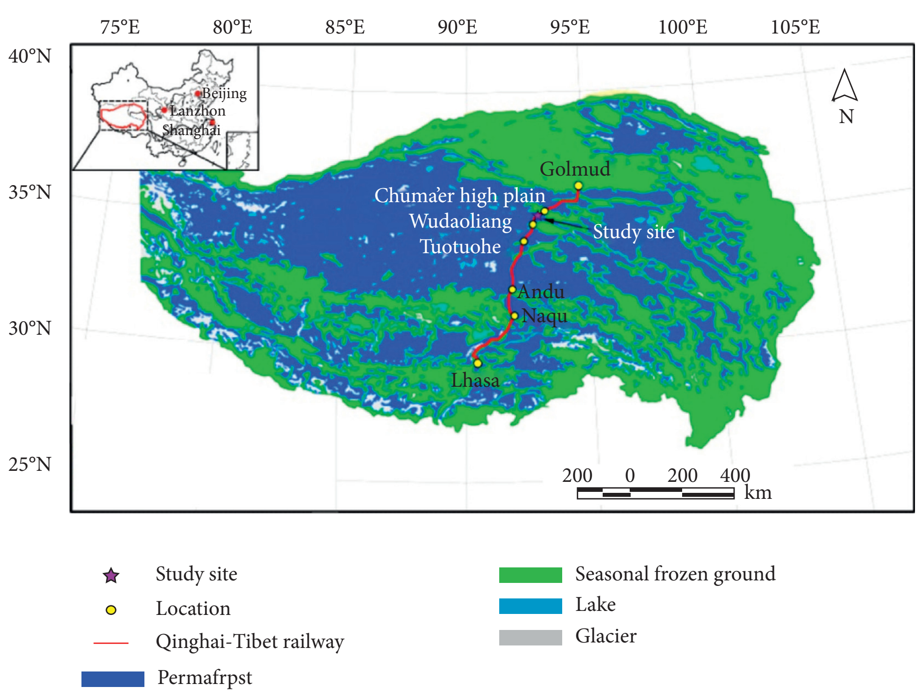

Figure 2: Location of the monitored CRR embankment in the permafrost zone of the QTP. Permafrost data were from the China cold and arid scientific data center (http://westdc.westgis.ac.cn/).

under CRR embankment was rising slowly, with an increase of nearly 0.22°C from 2003 to 2014. Although the warming rate decreased after 2008, the warming trend continued. Thus, it is concluded that the cooling effect of the CRR was relatively limited and could not effectively cool the deeper permafrost.

The long-term monitoring results revealed that the deep permafrost beneath the CRR experienced a significant warming

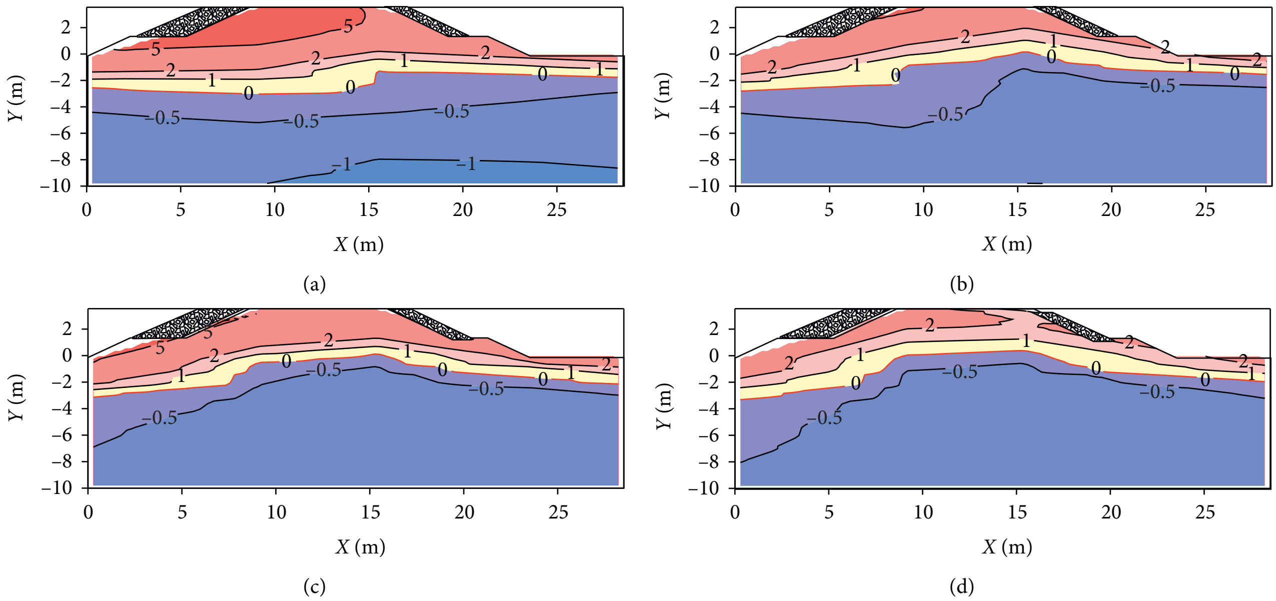

Figure 3: Temperature fields of the monitored CRR embankment on October 1 each year. (a) 2003; (b) 2005; (c) 2010; and (d) 2014.

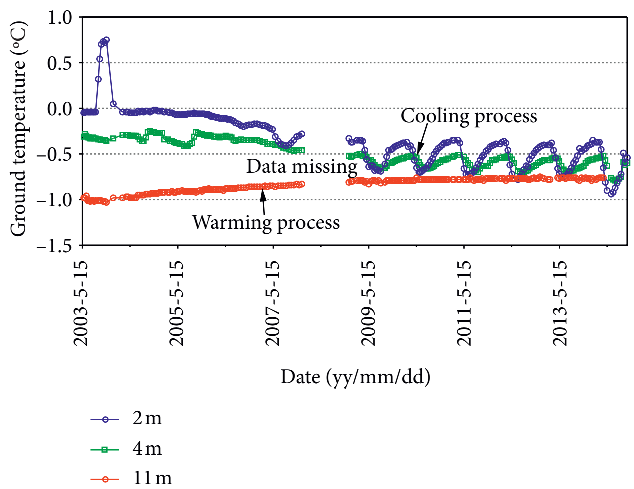

Figure 4: Variations of ground temperatures at depths of 2.0 m, 4.0 m, and 11.0 m beneath the monitored CRR embankment.

process, although the permafrost table beneath the embankment was elevated and the shallow grounds were cooled. The considerable warming of deep permafrost might generate compression deformation, which will reduce the embankment stability and potentially threaten the safe operation [22, 23]. The insufficient and unsatisfied cooling will be challenging the existing CRR to counteract the impact of climate warming in the warm or thaw-sensitive permafrost regions. Thus, how to optimize this structure and propose a new countermeasure is urgent to maintain the long-term thermal stability of embankment over warm permafrost on the QTP.

3. Numerical Modeling

3.1. The New Structure. In this section, a new mitigation measure (NMS) combined a CRR and a slope-warming prevention measure was designed as a countermeasure to improve the cooling capacity and to prevent wind-blown sand. As shown in Figure 5, a soil layer with geotextile was designed to pave on the CRR of the embankment slopes, which aims to prevent the warm wind from entering the rock layer during summer, to remove the solar radiation, and to strengthen convective heat transfer in rock layer during winter. A coupled heat transfer model was developed to evaluate the cooling effects and reinforcing performances of the new structure. Based on the heat and mass transfer theories, the air convection heat transfer in the porous layer and heat conduction with a phase transaction in the soil layers were considered in the model. The heat radiation of the rock layer was not considered in the model. Three sets of simulations were conducted to investigate the geothermal regimes evolution in different scenarios, as shown in Table 1. The geometrical model of the three associated embankments (Figure 6) were referred to the embankment in the Tuotuohe section of the Qinghai-Tibet Railway where the sand-filing damage is widespread.

3.2. Governing Equations

3.2.1. Airflow outside the Porous Rock Layer. The airflow is considered as a turbulent flow at the atmosphere [24]. The air is assumed to be an incompressible fluid with constant physical properties, and the influence of the air temperature on the airflow velocity is negligible. We have the following governing equations for the airflow's turbulent heat transfer process [25]:

Continuity:

$$\frac{\partial v_x}{\partial x} + \frac{\partial v_y}{\partial y} = 0. \tag{1}$$

Momentum:

$$\begin{aligned} \rho \frac{\partial v_x}{\partial t} + \rho \left(\frac{\partial (v_x v_x)}{\partial x} + \frac{\partial (v_y v_x)}{\partial y} \right) &= -\frac{\partial p}{\partial x} + \mu \left(\frac{\partial^2 v_x}{\partial x^2} + \frac{\partial^2 v_x}{\partial y^2} \right), \\ \rho \frac{\partial v_y}{\partial t} + \rho \left(\frac{\partial (v_x v_y)}{\partial x} + \frac{\partial (v_y v_y)}{\partial y} \right) &= -\frac{\partial p}{\partial y} + \mu \left(\frac{\partial^2 v_y}{\partial x^2} + \frac{\partial^2 v_y}{\partial y^2} \right) - \rho_a g. \end{aligned} \tag{2}$$

Energy:

$$\rho_a C_a \frac{\partial T}{\partial t} = \frac{\partial}{\partial x} \left(\lambda_a \frac{\partial T}{\partial x} \right) + \frac{\partial}{\partial y} \left(\lambda_a \frac{\partial T}{\partial y} \right) - \rho_a C_a \left(\frac{\partial (v_x T)}{\partial x} + \frac{\partial (v_y T)}{\partial y} \right), \tag{3}$$

where v_x and v_y are air speed along x- and y-axis; ρ_a is air density; p is air pressure; μ_a is dynamic viscosity, λ_a is air thermal conductivity, and C_a is air specific heat capacity.

3.2.2. Convective Heat Transfer in the Porous Rock Layer. The CRR was considered to be a porous medium in the model. Convection heat transfer of air in the porous layer is a heat and mass transfer process, and it is assumed that only the lacunal air movement is taken into consideration. The governing equations can be expressed as follows [16, 26]:

Continuity:

$$\frac{\partial v_x}{\partial x} + \frac{\partial v_y}{\partial y} = 0. \tag{4}$$

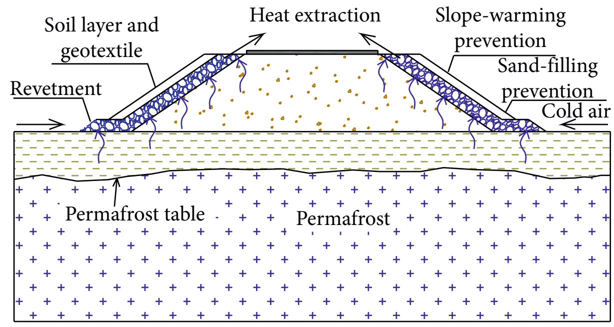

Figure 5: Schematic of the cooling of the proposed NMS.

Momentum:

$$\begin{aligned} \frac{\partial p}{\partial x} &= -\frac{\mu}{k} v_x - \rho_a B |v| v_x, \\ \frac{\partial p}{\partial y} &= -\frac{\mu}{k} v_y - \rho_a B |v| v_y - \rho_\alpha g. \end{aligned} \tag{5}$$

Energy:

$$C^e \frac{\partial x}{\partial t} = \frac{\partial}{\partial x} \left(\lambda^e \frac{\partial T}{\partial x} \right) + \frac{\partial}{\partial y} \left(\lambda^e \frac{\partial T}{\partial y} \right) - \rho_a c_a \frac{\partial}{\partial x} \left(\frac{\partial (v_x T)}{\partial x} + \frac{\partial (v_y T)}{\partial y} \right), \tag{6}$$

where $|v| = \sqrt{v_x^2 + v_y^2}$, B is the inertial drag coefficient, k is the permeability of the porous medium, and Ce and λe are the effective volumetric heat capacity and effective thermal conductivity, respectively.

Air density $\rho \alpha$ can be expressed as a function of the temperature T and the Boussinesq approximation is used to simplify the computation:

$$\rho_\alpha = \rho [1 - \beta (T - T_0)], \tag{7}$$

where T_0 is the corresponding temperature of ρ and β is the thermal expansion coefficient of air.

3.2.3. Conductive Heat Transfer for Soil Layers and Embankment Filling. For soil layers and embankment fillings, the heat transfer process was dominated by the heat conduction, and the phase change process of ice to water needs to be considered when the freeze-thaw processes occur. The heat transfer process can be described as follows [25, 26]:

$$C^e \frac{\partial x}{\partial t} = \frac{\partial}{\partial x} \left(\lambda^e \frac{\partial T}{\partial x} \right) + \frac{\partial}{\partial y} \left(\lambda^e \frac{\partial T}{\partial y} \right). \tag{8}$$

We assume that the phase change of the media occurs in a range of temperatures ($T_p \pm \Delta T$). Based on the sensible heat capacity method [27], C^e and λ^e can be calculated as follows:

Table 1: Description of the designed scenarios with associated cases.

Cases	Designed scenarios description
Case 1	Embankment with the CRR performs a service life of 30 years
Case 2	Embankment with CRR performs for 10 years and then suffers from sand-filling for 20 years
Case 3	Embankment with CRR performs for 10 years and then reinforced with the NMS for 20 years

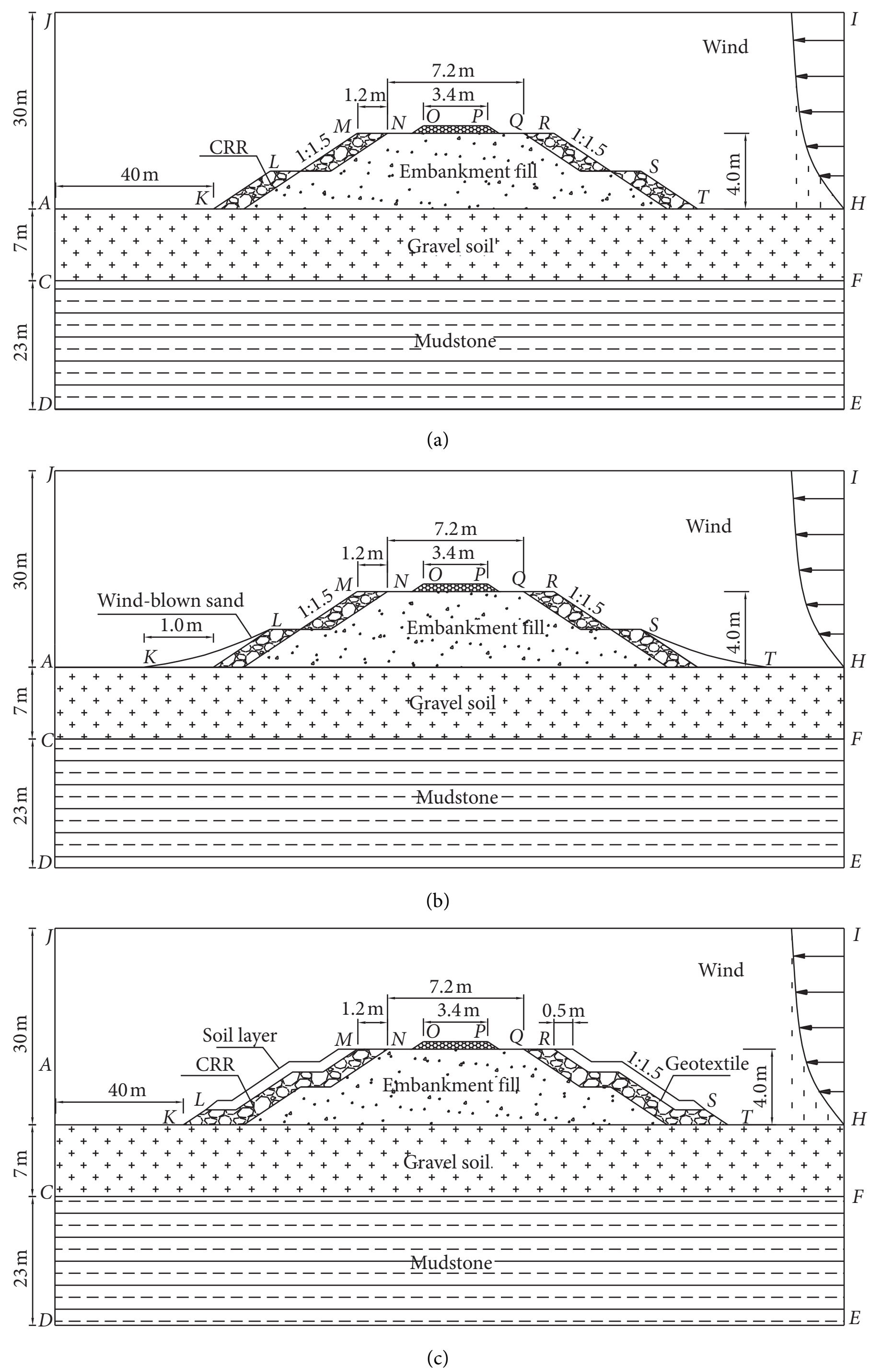

Figure 6: Geometrical model of the three associated embankments in three cases. (a) Case 1; (b) Case 2; and (c) Case 3.

$$C^e = \begin{cases} C_f, & T < (T_p - \Delta T), \\ \dfrac{l}{2\Delta T} + \dfrac{C_f + C_u}{2}, & (T_p - \Delta T) \le T \le (T_p + \Delta T), \lambda^e \\ C_u, & T > (T_p + \Delta T), \end{cases}$$
$$= \begin{cases} \lambda_f, & T < (T_p - \Delta T), \\ \lambda_f + \dfrac{\lambda_u - \lambda_f}{2\Delta T}\left[T - (T_p - \Delta T)\right], & (T_p - \Delta T) \le T \le (T_p + \Delta T), \\ \lambda_u, & T > (T_p + \Delta T), \end{cases} \tag{9}$$

where the subscripts f and u represent the frozen and unfrozen states, respectively; l is the latent heat per unit volume.

3.3. Thermal Parameters and Boundary Conditions. At the elevation of approximately 4500 m on the QTP, the physical parameters for air and crushed-rock layer in the simulations are listed in Table 2. The mean particle size of the CRR is approximately 0.2 m (diameter range from 0.1 to 0.3 m). Thermal parameters needed for the soil layers and embankment fill can be found in Table 3.

To simplify the boundary conditions, the temperature boundaries are employed to the air and ground surfaces. Based on the "adherent layer theory," simplified thermal boundaries are given in equation (10) and Table 4. The geothermal heat flux at the bottom boundaries was assumed to be 0.06 W/m^2. The lateral boundaries were assumed to be adiabatic:

$$T = T_0 + A \sin\left(\frac{2\pi}{8760}t_h + \frac{\pi}{2}\right) + \frac{\Delta T}{365 \times 24}t_h, \tag{10}$$

where T_0 is the annual average value, A is the amplitude, t_h is the time, and ΔT is air temperature rising rate, which is taken as 0.052°C/year on the QTP [26, 30].

The ambient wind affects the convection process in the rock layer. The wind boundary is applied at one side of the model to simulate the prevailing wind direction of north and northwest on the QTP. Based on the observed data for wind on the QTP, wind speed v_h at the height of h in prevailing north direction can be obtained as

$$v_h = \left(4.6 + 1.52 \sin\left(\frac{2\pi}{365 \times 24}t + \frac{3\pi}{2}\right)\right)\left(\frac{h}{10}\right)^{0.16}. \tag{11}$$

3.4. Model Validation. To verify the numerical model, we simulated the thermal regime of a CRR embankment built on Huashixia of the QTP. The simulated and observed temperature profiles at the shady shoulder of the embankment in 2014, one year after construction are shown in Figure 7. It illustrates that the computed temperature curve can fit well with the measured results for the permafrost layer. A large difference between the measurement and simulation was found for the active layer, which mainly results from the simplified boundaries and geological conditions in the model. In general, the numerical model is reasonable for simulating the thermal regime of a crushed-rock embankment in a permafrost region.

4. Numerical Results and Analyses

4.1. Predicted Temperature Fields. Three cases over a 30-year period were simulated. Firstly, the thermal regimes of embankment with CRR when maximum thawing depth reaches in the 5th and 10th years after construction are shown in Figure 8. It can be seen that the temperature field of the CRR embankment is basically symmetrical after construction and the permafrost table under the embankment elevates to near the original ground surface. Such characteristics are similar to the monitored embankment (Figure 3). The CRR begins to show the cooling effect on the permafrost beneath the embankment slopes in the 5th year and beneath the embankment in the 10th year, as indicated by the cold temperature zone of −1.0°C, which gradually expands, as shown in Figure 8. Figure 9 gives thermal regimes of embankment in three cases when maximum thawing depth reaches in the 15th year after construction. The cooling effect of the CRR weakens under the impact of climate warming, as indicated by the shrink of the −1.0°C and −0.8°C isotherms (Figure 9(a)). However, if the rock layer near the toes begins to be filled with sands after the 10th service year (Case 2), the cooling of the CRR will be further weakened, causing obvious warming of the underlying permafrost, as indicated by the rapid shrink of −0.8°C isotherm in Figure 9(b).

In contrast, if the CRR is reinforced by the NMS in the 10th service year, the cooling of the embankment will be improved significantly (Case 3). As shown in Figure 9(c), the colder regions of −1.5°C and even −1.8°C form under the embankment and the permafrost table beneath the embankment slopes is also further elevated obviously after five years' reinforcement. All of these demonstrate the good cooling performance of the new design.

Figure 10 reveals the thermal regimes of embankment in three cases when maximum thawing depth reaches in the 20th year after construction. As shown in Figure 10(a), the disappearance of −1.0°C beneath the embankment indicates that the permafrost temperature obviously increases due to

Table 2: Physical parameters of air and crushed-rock layer [24, 28, 29].

Physical parameters	C (J·m^{-3}·°C^{-1})	λ (W·m^{-1}·°C^{-1})	P (kg·m^{-3})	μ (kg·m^{-1}·s^{-1})	K (m^2)	B (m^{-1})
Air	0.644×10^3	0.02	0.641	1.75×10^{-5}	—	—
Rock layer	1.016×10^6	0.442	—	—	1.39×10^{-5}	211.2

Table 3: Thermal parameters of different media [24, 26, 30].

Thermal parameters	C_{fs} (J·m^{-3}·°C^{-1})	λ_{fs} (W·m^{-1}·°C^{-1})	C_{us} (J·m^{-3}·°C^{-1})	λ_{us} (J·m^{-3}·°C^{-1})	l (J·m^{-3})
Embankment fill	1.913×10^6	1.980	2.232×10^6	1.919	2.01×10^7
Sand	1.465×10^6	0.258	1.465×10^6	0.258	0
Gravel soil	1.863×10^6	2.610	2.401×10^6	1.910	2.32×10^7
Weathered stone	2.122×10^6	1.824	2.413×10^6	1.474	3.81×10^7
Ballast	1.006×10^6	0.346	1.006×10^6	0.346	0

Table 4: Temperature parameters in Equation (10).

Boundaries	T_0 (°C)	A (°C)
Air	−3.8	11.5
Natural ground surfaces	−0.6	12.0
Top surface	0.3	14.0
Crushed-rock surface	1.4	15.2
Embankment slope surfaces	0.8	13.0
Sand surface	0.6	14.0

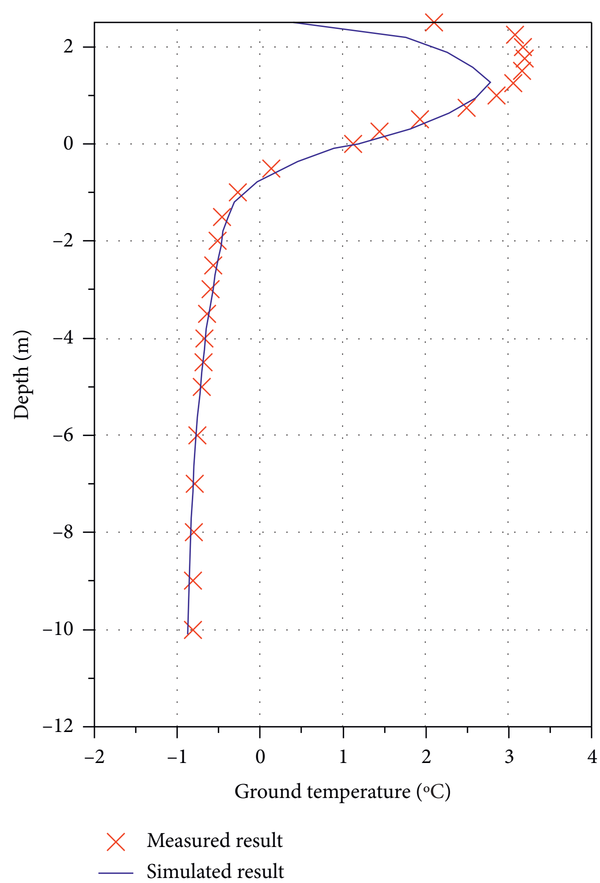

Figure 7: Comparison of the measured and simulated ground temperatures of a CRR embankment on October 15.

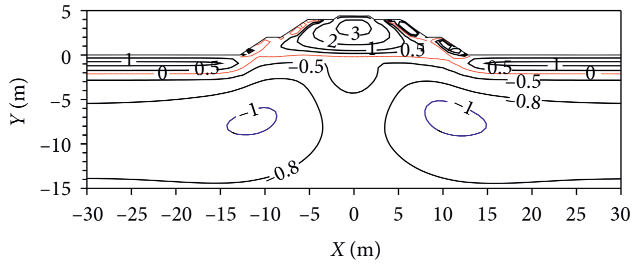

(a)

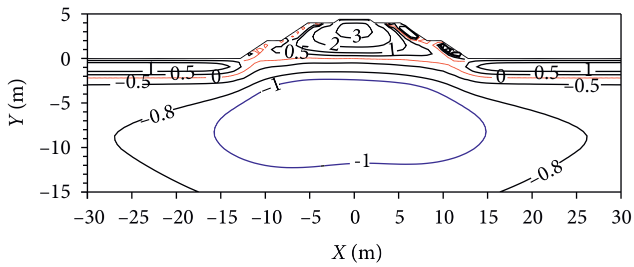

(b)

Figure 8: Thermal regimes of embankment with CRR when maximum thawing depth reaches in the 5th (a) and 10th (b) years after construction.

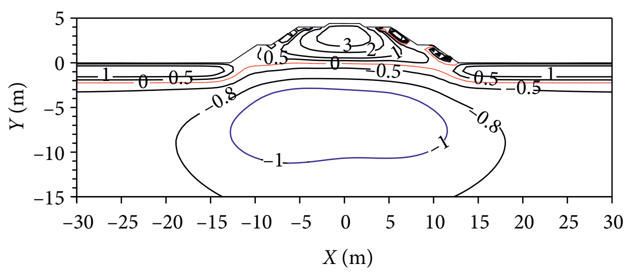

(a)

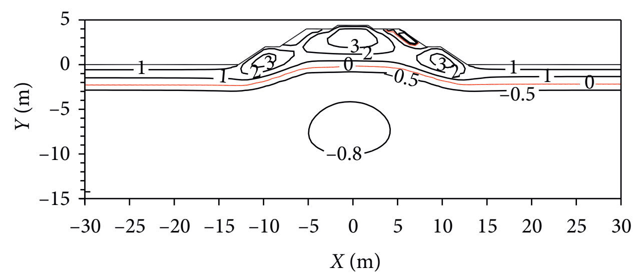

(b)

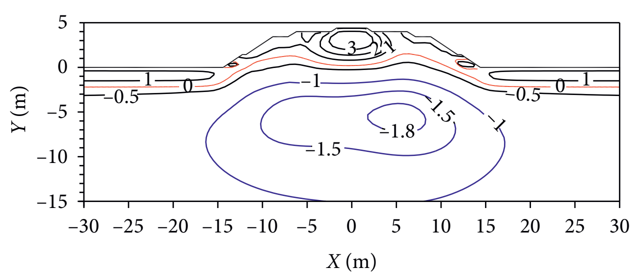

(c)

Figure 9: Thermal regimes of embankment in three cases when maximum thawing depth reaches in the 15th year after construction. (a) CRR embankment; (b) CRR filled with sands; and (c) CRR reinforced with NMS.

the weak cooling of the CRR structure. Warm permafrost (>−1.0°C) is generated beneath the embankment and may cause instability in the embankment because the deformation of the permafrost is promoted by the increase in temperature. For Case 2 (Figure 10(b)), sand-filling seriously affects the convection cooling of the rock layer, leading to severe permafrost warming beneath the embankment, particularly under the embankment slopes, indicated by the downward of −0.5°C while for the embankment reinforced by the NMS (Figure 10(c)), the −1.0°C and −1.5°C isotherms still exist under the embankment, revealing the cold thermal state of the permafrost.

As shown in Figure 11(a), in the 30th year after construction, the permafrost temperature beneath the CRR obviously increases because of climate warming. This implies that the sole CRR cannot produce strong enough cooling for the underlying permafrost to maintain the foundation stability. The sand-filling causes not only the permafrost

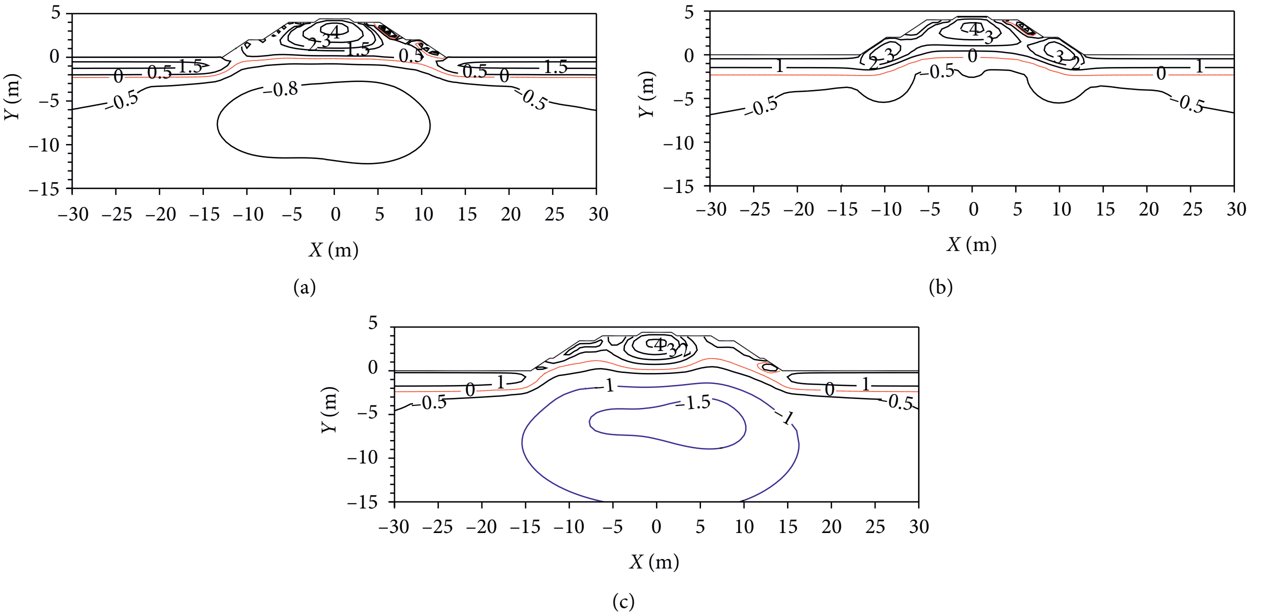

Figure 10: Thermal regimes of embankment in three cases when maximum thawing depth reaches in the 20th year after construction. (a) CRR embankment; (b) CRR filled with sands; and (c) CRR reinforced with NMS.

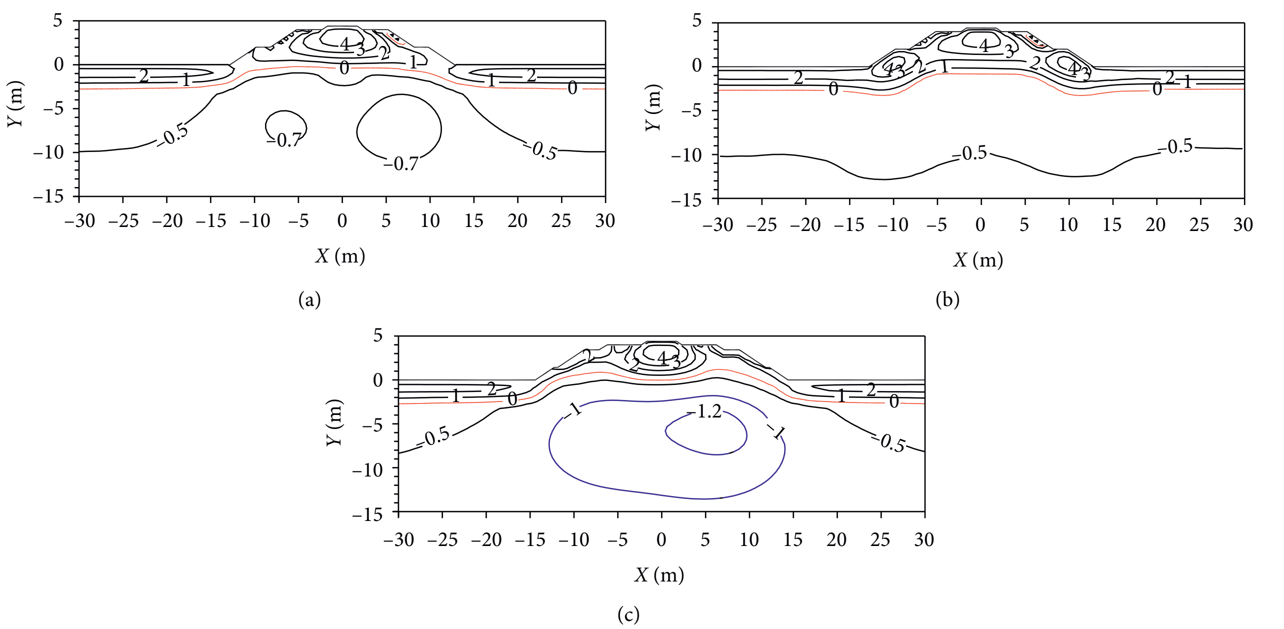

Figure 11: Thermal regimes of embankment in three cases when maximum thawing depth reaches in the 30th year after construction. (a) CRR embankment; (b) CRR filled with sands; and (c) CRR reinforced with NMS.

warming but also the severe permafrost thawing under the slope toes, as indicated by the obvious decline of the permafrost table, as shown in Figure 11(b). Such a process might lead to structure failure of the embankment. The most noticeable characteristic for the new design is the cold zone of −1.0°C, as shown in Figure 11(c), which still covers most regions beneath the embankment to ensure its thermal stability under climate warming. Meanwhile, the permafrost table especially under the embankment slopes rises further into the embankment body, revealing the permafrost aggradation under the effective and sufficient cooling of the NMS.

4.2. Predicted Long-Term Ground Temperature Variations. Figure 12 shows variations of the annual average ground temperatures at a depth of 15 m relative to the original ground surface beneath the centerline of the embankment in

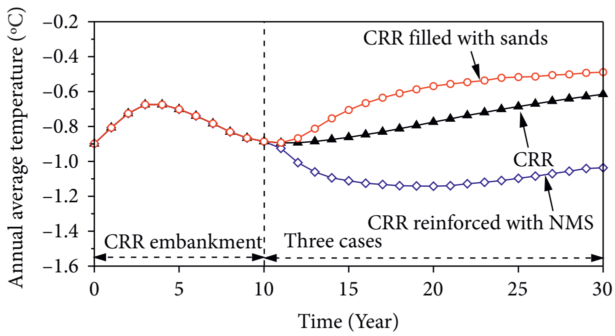

Figure 12: Variations of annual average ground temperatures at 15 m deep underneath the centerline of embankment in three cases during 30 service years.

three cases. It can be found that three stages including thermal disturbance stage, cooling process, and warming process occur in the studied cases. As shown, permafrost at the 15 m depth beneath the CRR experiences a short period of cooling before the 10th year and then experiences a steady warming trend, resulting in nearly 0.3°C temperature rising in the 30th year. The sand-filling can further weaken the convection cooling of the porous rock layer and causes rapid permafrost warming of the foundation. In contrast, the cooling of the NMS can significantly decrease the foundation temperatures and causes obviously decreased temperature than the CRR, which reveals a significant influence on the thermal status of the underlying permafrost of the new structure. Reinforced by the new structure, the permafrost temperature at the depth of 15 m beneath the centerline obviously decreases and is lower than that under the CRR, with a difference of nearly 0.4°C in the service year. It demonstrates the superior cooling effect of the new design and its good reinforced cooling performance.

The new mitigation also plays a role in sand-filling prevention. Although the sand may clog the slope toe and then decrease forced convection cooling, most of the other porous regions exist. Even if the toe is blocked with time, it is not difficult to clean the sand in this small area. A layer of hollow concrete brick with large pore space or a sand-controlling net fence could be arranged close to the slope toe of the new mitigation for further sand prevention.

5. Conclusions

In this study, a traditional CRR embankment over warm permafrost was selected to investigate its cooling characteristics based on the long-term ground temperature observations. An optimized structure was designed to improve the cooling capacity of the CRR and to counter the pore-filling of the rock layer. Numerical simulations were conducted to evaluate the cooling performance and reinforcing capacity of the new structure in sandy permafrost zones based on a developed heat and mass transfer model. The following conclusions can be drawn:

(1) The field results revealed that the traditional CRR could improve the symmetry of the ground temperature distribution, elevate the permafrost table, and decrease the ground temperature of shallow permafrost. However, the cooling capacity of this structure was limited and it could not generate strong enough cooling to influence the deep warm permafrost, causing slow but steady warming of deep permafrost after construction.

(2) The simulated results indicate that the CRR generates an insufficient cooling effect on the warm permafrost and thus cannot maintain the thermal stability of embankment built on warm and thaw-sensitive permafrost under climate warming. The wind-blown sand can further weaken the cooling of the CRR and cause significant permafrost warming and thawing beneath the slopes, posing a severe threat to the long-term safe operation of the embankment.

(3) The NMS can produce a significantly superior cooling performance to the CRR. If the CRR is reinforced by the new structure, it can not only effectively cool the underlying warm permafrost but also elevate the permafrost table. The new structure can also protect the rock layer on the slopes from sand-filling. Therefore, the NMS can be used as an effective method for roadbed design or maintenance over warm permafrost.

Data Availability

The data used to support the findings of this study are included within the article.

Conflicts of Interest

The authors declare that they have no conflicts of interest.

Acknowledgments

This research was supported by the National Key R&D Program of China (Grant no. 2018YFC1505001), the National Natural Science Foundation of China (Grant no. 41701067), the West Light Foundation of Chinese Academy of Sciences (Granted to Dr. Minghao Liu), and the Program of the State Key Laboratory of Frozen Soil Engineering (Grant no. SKLFSE-ZQ-48).

References

[1] R. van Everdingen, *Multi-Language Glossary of Permafrost and Related Ground-Ice Terms*, World Data Center for Glaciology, Boulder, CO, USA, 1998.

[2] Permafrost Subcommittee, *Glossary of Permafrost and Related Ground-Ice Terms*, Associate Committee on Geotechnical Research, National Research Council of Canada, Ottawa, Canada, 1988.

[3] S. Gruber, "Derivation and analysis of a high-resolution estimate of global permafrost zonation," *The Cryosphere*, vol. 6, no. 1, pp. 221–233, 2012.

[4] F. E. Nelson, "Geocryology: enhanced: (un) frozen in time," *Science*, vol. 299, no. 5613, pp. 1673–1675, 2003.

[5] F. E. Nelson, O. A. Anisimov, and N. I. Shiklomanov, "Subsidence risk from thawing permafrost," *Nature*, vol. 410, no. 6831, pp. 889-890, 2001.

[6] G. Cheng, "A roadbed cooling approach for the construction of Qinghai-Tibet railway," *Cold Regions Science and Technology*, vol. 42, no. 2, pp. 169–176, 2005.

[7] M. C. Alfaro, G. A. Ciro, K. J. Thiessen, and T. Ng, "Case study of degrading permafrost beneath a road embankment," *Journal of Cold Regions Engineering*, vol. 23, no. 3, pp. 93–111, 2009.

[8] H.-j. Jin, Q.-h. Yu, S.-l. Wang, and L.-z. Lü, "Changes in permafrost environments along the Qinghai-Tibet engineering corridor induced by anthropogenic activities and climate warming," *Cold Regions Science and Technology*, vol. 53, no. 3, pp. 317–333, 2008.

[9] R. Fortier, A.-M. LeBlanc, and W. Yu, "Impacts of permafrost degradation on a road embankment at Umiujaq in Nunavik (Quebec), Canada," *Canadian Geotechnical Journal*, vol. 48, no. 5, pp. 720–740, 2011.

[10] B. Wang and H. M. French, "Permafrost on the Tibet Plateau, China," *Quaternary Science Reviews*, vol. 14, no. 3, pp. 255–274, 1995.

[11] G. D. Cheng, "Some difference of permafrost on the Qinghai-Tibet Plateau of China and northern Canada," *Journal of Glaciology and Geocryology*, vol. 2, no. 1, pp. 39–42, 1980.

[12] G. Doré, F. Niu, and H. Brooks, "Adaptation methods for transportation infrastructure built on degrading permafrost," *Permafrost and Periglacial Processes*, vol. 27, no. 4, pp. 352–364, 2016.

[13] Q. B. Wu, S. Y. Zhao, W. Ma, Y. Z. Liu, and L. X. Zhang, "Monitoring and analysis of cooling effect of block-stone embankment for Qinghai-Tibet railway," *Chinese Journal of Geotechnical Engineering*, vol. 27, pp. 1386–1390, 2005.

[14] D. J. Goering and P. Kumar, "Winter-time convection in open-graded embankments," *Cold Regions Science and Technology*, vol. 24, no. 1, pp. 57–74, 1996.

[15] Q. B. Wu, H. T. Zhao, Z. Q. Zhang, J. Chen, and Y. Z. Liu, "Long-term role of cooling the underlying permafrost of the crushed rock structure embankment along the Qinghai-Xizang railway," *Permafrost and Periglacial Processes*, vol. 31, no. 4, pp. 172–183, 2019.

[16] Y. M. Lai, M. Y. Zhang, and S. Y. Li, *Theory and Application of Cold Regions Engineering*, Science Press, Beijing, China, 2009.

[17] Y. Mu, W. Ma, Y. Liu, and Z. Sun, "Monitoring investigation on thermal stability of air-convection crushed-rock embankment," *Cold Regions Science and Technology*, vol. 62, pp. 160–172, 2010.

[18] W. Ma, Q. B. Wu, and G. D. Cheng, "Analyses of the temperature fields within an air convective embankment of crushed rock structure along the Qinghai-Tibet railway," *Journal of Glaciology and Geocryology*, vol. 28, no. 4, pp. 586–594, 2006.

[19] L. Chen, W. Yu, F. Han, Y. Lu, and T. Zhang, "Effects of desertification on permafrost environment in Qinghai-Tibetan Plateau," *Journal of Environmental Management*, vol. 262, Article ID 110302, 2020.

[20] Z. J. Lin, F. J. Niu, H. Liu, and J. H. Lu, "Influences of freezing-thawing cycles on physico-mechanical properties of rocks of embankment revetments in permafrost regions," *Rock and Soil Mechanics*, vol. 32, no. 5, pp. 1369–1376, 2011.

[21] M. T. Chai, Y. H. Mu, J. M. Zhang, W. Ma, G. Liu, and J. B. Chen, "Characteristics of asphalt pavement damage in degrading permafrost regions: case study of the Qinghai-Tibet highway, China," *Journal of Cold Regions Engineering*, vol. 32, no. 2, pp. 5–18, 2018.

[22] W. Ma, Y. Mu, Q. Wu, Z. Sun, and Y. Liu, "Characteristics and mechanisms of embankment deformation along the Qinghai-Tibet railway in permafrost regions," *Cold Regions Science and Technology*, vol. 67, no. 3, pp. 178–186, 2011.

[23] J. L. Qi, Y. Sheng, J. M. Zhang, and Z. Wen, "Settlement of embankments in permafrost regions in the Qinghai-Tibet plateau," *Norsk Geografisk Tidsskrift-Norwegian J. Geography*, vol. 61, no. 2, pp. 49–55, 2007.

[24] M. Zhang, Y. Lai, F. Niu, and S. He, "A numerical model of the coupled heat transfer for duct-ventilated embankment under wind action in cold regions and its application," *Cold Regions Science and Technology*, vol. 45, no. 2, pp. 103–113, 2006.

[25] W. Q. Tao, *Numerical Heat Transfer*, Xi'an Jiaotong University Press, Xi'an, China, 2004.

[26] Y. M. Lai, L. X. Zhang, S. J. Zhang, and L. Mi, "Cooling effect of ripped-stone embankments on Qinghai-Tibet railway under climatic warming," *Chinese, Science Bullitin*, vol. 48, no. 6, pp. 598–604, 2003.

[27] L. N. Zhu, "Study of the adherent layer on different types of ground in permafrost regions on the Qinghai-Xizang plateau," *Journal of Glaciology and Geocryology*, vol. 10, no. 1, pp. 8–14, 1988.

[28] M. Zhang, Y. Lai, D. Li, W. Chen, and G. Tong, "Experimental study on ventilation characteristics of a concrete-sphere layer and a crushed-rock layer," *International Journal of Heat and Mass Transfer*, vol. 59, pp. 407–413, 2013.

[29] X. Z. Xu, J. C. Wang, and L. X. Zhang, *Physics of Frozen So*, Science Press, Beijing, China, 2001.

[30] D. H. Qin, Y. H. Ding, and S. W. Wang, "A study of environment change and its impacts in western China," *Frontiers in Earth Science*, vol. 9, no. 2, pp. 321–328, 2002.

Hindawi
Advances in Materials Science and Engineering
Volume 2021, Article ID 5555565, 10 pages
https://doi.org/10.1155/2021/5555565

Research Article

Determining the Thermal Conductivity of Clay during the Freezing Process by Artificial Neural Network

Xiuling Ren [1,2], Yanhui You [1], Qihao Yu [1], Guike Zhang [3], Pan Yue [3] and Mingyang Jin [1,2]

[1] *State Key Laboratory of Frozen Soil Engineering, Northwest Institute of Eco-Environment and Resources, Chinese Academy of Sciences, Lanzhou 730000, Gansu, China*
[2] *University of Chinese Academy of Sciences, Beijing 100049, China*
[3] *Yalong River Hydropower Development Company, Ltd, Chengdu 610065, Sichuan, China*

Correspondence should be addressed to Qihao Yu; yuqh@lzb.ac.cn

Received 27 January 2021; Revised 2 March 2021; Accepted 13 March 2021; Published 27 March 2021

Academic Editor: Xiangtian Xu

Thermal conductivity is an important thermal parameter in engineering design in cold regions. By measuring the thermal conductivity of clay using a transient hot-wire method in the laboratory, the influential factors of the thermal conductivity of soils during the freezing process were analyzed, and a predictive model of thermal conductivity was developed with an artificial neural network (ANN) technology. The results show that the variation of thermal conductivity can be divided into three stages with decreasing temperature, positive temperature stage, transition stage, and negative temperature stage. The thermal conductivity increases sharply in the transition stage. The difference between the thermal conductivity at positive and negative temperature is small when the dry density of the soil specimens is larger than the critical dry density, while the difference is large if the dry density is less than the critical dry density. As the negative temperature decreases, the larger the moisture content of the soil specimens, the larger the increase of thermal conductivity. The effect of initial moisture content on thermal conductivity is more significant than that of dry density and temperature. The change tendency of the thermal conductivity calculated by the established ANN model is basically consistent with that of the laboratory-measured values, indicating that this model can be able to accurately predict the thermal conductivity of the soil specimens in the freezing process.

1. Introduction

The thermal conductivity of soils is an important thermal parameter for modeling the freeze-thaw process of soils and determining the frozen and thawed depth of soils [1]. And the thermal conductivity represents the heat conduction of soils, which will affect the heat transfer process of soils. As we need economic development, more major projects will be built in cold regions, and their thermal stability is crucial for the operation. Therefore, it is very important to study the variation and predictive models of the thermal conductivity of soils during a freezing process.

The thermal conductivity of soils is mainly affected by mineral types, moisture content, dry density, temperature, and grain size [2–11]. A large number of studies have analyzed the variation of the thermal conductivity of soils under the influence of various factors and established the empirical relationship between the thermal conductivity and the impacting factors. The thermal conductivity of soils increases with increasing moisture content [2, 3, 7, 8]. However, the increase of the thermal conductivity of soils in the frozen and thawed status is different, which is mainly caused by the phase transition of water in the frozen state [12]. For a special soil, a power function relationship can be established between the thermal conductivity and the moisture content of soils [13]. The thermal conductivity of soils increases with increasing dry density [2, 7, 14]. The influence of moisture content on thermal conductivity is more significant than that of dry density [15]. The thermal conductivity of soils increases with decreasing temperature [4, 8]. The thermal conductivity of soils in the frozen state is larger than that in the thawed state [4], and the variation of the thermal conductivity with temperature is related to moisture content [4]. Some studies indicated that the porosity and degree of saturation affect the thermal conductivity of sandy soils [16, 17], and the thermal conductivity of sand increases with decreasing porosity and increasing degree of saturation [17]. In addition, soil particle size, structure, and bulk density also affect the thermal conductivity of soils [2, 8, 18]. The thermal conductivity of coarse-grained soils is larger than that of fine-grained soils [2, 8, 18].

Many types of predictive models of thermal conductivity have been proposed, mainly divided into theoretical, empirical, and other models [19]. In terms of theoretical models, Wiener [20] established the series and parallel models of the thermal conductivity based on the heat flow direction and the arrangement of three-phases of porous media. According to Maxwell's equation, Devries [21] assumed that the solid particles of soils were uniformly distributed in the continuous pore fluid and proposed a theoretical model of the thermal conductivity of soils. Johansen [22] proposed a weighted geometric average model to calculate the thermal conductivity of soils. In terms of empirical models, Kersten [4] used a single thermal probe method to test the thermal conductivity of 19 different types of soils by considering the effect of moisture content and dry bulk density and established the empirical equations of the thermal conductivity for silt and clay soils and sandy soils in the frozen and unfrozen state, respectively. Johansen [22] firstly proposed the concept of the normalized thermal conductivity (λ_r), namely, "Kersten's number, Ke," expressed the moisture content and dry density in the Kersten [4] model by a degree of saturation, and normalized the moisture content and dry density. Cote and Konrad [23] proposed a new normalized thermal conductivity model based on the research of Johansen [22]. Chen [17] established the empirical equation of the thermal conductivity based on the porosity and degree of saturation and compared the calculated results with the experimental results and the results in the published literature. And Bi et al. [24] proposed a generalized model for the thermal conductivity of the freezing soils based on frost heave and components of soils.

Artificial neural networks (ANNs) are also widely used in the prediction of thermal parameters [9, 25]. Some researchers used the ANN models to calculate the thermal conductivity [9, 26–28] and thermal diffusivity [29] of soils. He and Huang [26] used the BP neural network model to determine the thermal conductivity of soils by analyzing the relationship between the thermal conductivity and the physical property index of soils and pointed out that the predicted thermal conductivity is close to the measured thermal conductivity values. Based on the ANN technology, Zhang et al. [27] calculated the layered thermal conductivity of the undisturbed soils in the field by taking moisture content and porosity as input layer neurons and the thermal conductivity as the output layer neuron. Zhang et al. [9] established an individual model of the thermal conductivity for different types of soils and a generalized model by considering the influence of soil types via ANN technology, compared the predicted thermal conductivity with the calculated results of three empirical models, and pointed out that the predicted results of the two ANN models are close to the measured thermal conductivity values.

In the published research studies, when calculating the thermal conductivity of soils considering the frozen and thawed status of soils, the influence of the variation of the temperature of the soil in the freezing process on the thermal conductivity model is considered in few studies. Although the ANN models have been successfully used to predict the thermal conductivity of soils, the applicable condition of each predictive model is different, the influence of the variation of negative temperature on the thermal conductivity is less considered in the predictive models, and the ANN technology is seldom used to establish the predictive models of the thermal conductivity of soils during a freezing process. Therefore, the objective of this study is to understand the variation of the thermal conductivity of clay under various impacting factors during a freezing process where the temperature changes from positive to negative and to develop a predictive model of the thermal conductivity of soil during the freezing process by ANN technology. The thermal conductivity of clay is measured in the laboratory, and the effects of initial moisture content, initial dry density, and temperature on the thermal conductivity of soils are analyzed. Based on this, considering the influence of initial moisture content, initial dry density, and temperature on thermal conductivity, a predictive model of the thermal conductivity of soils is developed via ANN technology, which can completely calculate the thermal conductivity of soils when the temperature changes from a positive value to a negative value. And it is validated by comparing the predicted thermal conductivity results with the measured thermal conductivity results.

2. Experimental Materials and Methods

2.1. Experimental Materials. In this study, the clay used for the test was obtained from the Lianghekou region, Sichuan province, China. Figure 1 shows the grain size distribution curve of clay. Figure 2 shows the compaction curve of clay. The maximum dry density is 1.78 g/cm^3. The optimum water content by weight is 17.0%. The basic physical parameters for the soil specimens are listed in Table 1.

In order to study the variation of the thermal conductivity of soils in the compacted and loose status, the thermal conductivity of soils over a wide range of dry densities of about 1.00~1.92 g/cm^3 was tested. The interval within the large dry density was small, and the interval within the low dry density was large; the main purpose is to highlight and analyze the variation of the thermal conductivity of the compacted soils. The temperature decreased step by step from 5°C to −10°C in a freezing process. The soil specimens were divided into 4 groups according to the initial moisture content of different soil specimens, and a total of 192 soil specimens were measured. The specific experimental conditions are shown in Table 2.

2.2. Experimental Methods

2.2.1. Specimen Preparation Process. Firstly, soils were air-dried and crushed, sieved over 2 mm, and the air-dry moisture content of soils was measured by the drying

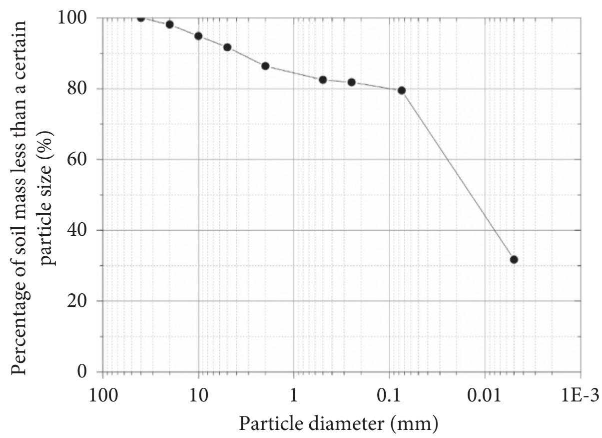

Figure 1: Grain size distribution curve of clay.

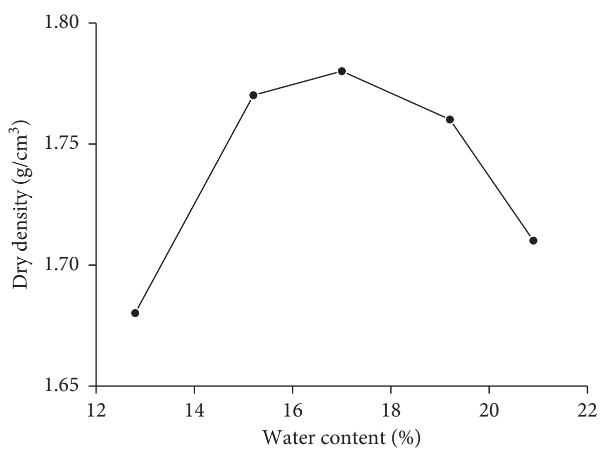

Figure 2: Compaction curve of clay.

Table 1: Basic physical parameters for the soil specimens.

Optimum water content ω_{op} (%)	Maximum dry density $\rho_{d\max}$ (%)	Liquid limit W_L (%)	Plastic limit W_P (%)	Soil specific gravity G_s (g/cm^3)
17.0	1.78	36.9	19.8	2.72

Table 2: Experimental conditions.

Impacting factors	Initial moisture content (%)	Initial dry density (g/cm^3)	Temperature (°C)
Experimental conditions	14	1.92, 1.88, 1.82, 1.73, 1.63, 1.58, 1.44, 1.15	5, 1, −0.5, −1, −5, −10
	16	1.9, 1.86, 1.81, 1.71, 1.62, 1.52, 1.43, 1.14	5, 1, −0.5, −1, −5, −10
	18	1.72, 1.68, 1.62, 1.54, 1.45, 1.36, 1.27, 1.09	5, 1, −0.5, −1, −5, −10
	20	1.69, 1.65, 1.6, 1.51, 1.42, 1.33, 1.24, 1	5, 1, −0.5, −1, −5, −10

method. Secondly, according to the experimental conditions, different amounts of distilled deionized water were added to prepare soil samples with different initial moisture content. Soil samples were stored in a sealed bag for 24 h to make the moisture in the soil samples uniformly distributed. Then, the soils were compacted layer by layer in a cylindrical mold. In order to ensure that the dry density of the upper and lower parts of the soil specimens was basically the same, the soil specimens were compacted from the upper and lower ends. The dry density of the soil specimens was controlled by controlling the height and quality of each layer of the soil specimens. In this way, cylinder soil specimens with different initial moisture content and dry density (Table 2) were obtained with a diameter of 61.8 mm and a height of 50 mm. Finally, the soil specimens were quickly covered with plastic film to keep the moisture content unchanged and were stored for 24 h, so as to ensure that the moisture was uniformly distributed in the soil specimens.

2.2.2. Test Process of Thermal Conductivity. In this study, the thermal conductivity of the soil specimens was measured by a Thermal Properties Analyzer (Anter Quickline-30) (Figure 3), the measuring range is 0.3 ~ 2.0 W/(m·K), and the instrument accuracy is ± 0.0001 W/(m·K). The Thermal Properties Analyzer is mainly based on the transient hot-wire method to determine the thermal conductivity of the soil specimens. Firstly, the temperature of the thermostat (the accuracy is ± 0.01°C) was set to 5°C; when the real-time temperature in the thermostat was the same as the preset temperature, the soil specimens and the instrument probe were placed into the thermostat together. After about 24 h, both the temperature inside the soil specimens and that of the probe were constant at 5°C. Secondly, the probe was placed on the top surface of the soil specimen; after the temperature of the Thermal Properties Analyzer stabilized, the thermal conductivity of the upper end of the soil specimen was measured. Then, the lower end of the soil specimen was put upwards, and the probe was placed to measure the thermal conductivity. The average of the two measured results was taken as the thermal conductivity of the soil specimen. Finally, according to the designed experimental temperature, the temperature of the thermostat was adjusted step by step in a freezing process, and the thermal conductivity of the soil specimens was measured at each temperature in a freezing process in accordance with the previous steps. At each temperature, in order to make the temperature of the soil specimens reach stabilization, the soil specimens were stored in the thermostat for about 6 h before the thermal conductivity was measured. And in the transition process where the temperature changes from positive to negative, the stored time of the soil specimens is about 12 h.

3. Experimental Results and Discussion

The impacting factors of the thermal conductivity of soils mainly include mineral component, moisture content, dry density, temperature, and freeze-thaw cycles [6, 8, 12, 22, 27]. The variation of the thermal conductivity of the soil specimens under the effect of initial moisture content, initial dry density, and temperature will be mainly analyzed in this section. Based on this, the ANN technology is used to develop a predictive model for calculating the thermal conductivity of the soil specimens under the same experimental conditions.

3.1. Variation of the Thermal Conductivity of the Soil Specimens

3.1.1. Influence of Initial Dry Density and Moisture Content on Thermal Conductivity. The variation of the thermal conductivity of the soil specimens with dry density is shown in Figure 4. Under the same initial moisture content of the soil specimens and temperature, the thermal conductivity of the soil specimens increases with increasing dry density, and there is basically a linear change between the two (Figure 4). The main reasons for the increase of the thermal conductivity of the soil specimens with increasing dry density are that, on the one hand, the increase in dry density will increase the content of solid particles inside the soil specimens and the connectivity between soil skeletons and then will increase the heat conduction of the soil specimens. On the other hand, both the pores and porosity of the soil specimens decrease, and the thermal conductivity of the soil skeleton is far larger than that of air (Table 3); then, the thermal conductivity of the soil specimens increases. For a given moisture content, the increase of the thermal conductivity of the soil specimens with dry density is independent of temperature.

In addition, the moisture content of soils is one of the impacting factors of the thermal conductivity of soils. It can be seen from Figure 4 that at the temperature of 5°C and −10°C, the thermal conductivity with the moisture content of 14% at the dry density of 1.44 g/cm^3 is 0.55 W/(m·K) and 0.87 W/(m·K), respectively; and the thermal conductivity with the moisture content of 20% at the dry density of 1.42 g/cm^3 is 1.19 W/(m·K) and 1.48 W/(m·K), respectively. It indicates that the dry density of the soil specimens with the moisture content of 20% and 14% is basically the same, while the thermal conductivity with the moisture content of 20% is larger than that with the moisture content of 14% at positive and negative temperatures. The main reasons for this phenomenon are that, on the one hand, as the moisture content of the soil specimens increases, the pores in the soil specimens will be filled with water, the air in the pores will be expelled, the porosity of the soil specimens will decrease, and the thermal conductivity of water is far larger than that of air. On the other hand, the increase in the moisture content will reduce the space between soil particles and will increase the thermal conduction of soil particles.

3.1.2. Influence of Temperature on Thermal Conductivity. The influence of temperature on the variation of the thermal conductivity of the soil specimens is shown in Figure 5. The results showed that, under the same initial moisture content and dry density, the variation of the thermal conductivity of the soil specimens with temperature can be roughly divided into three stages. In Stage I, positive temperature stage (5~1°C), the thermal conductivity of the soil specimens decreases slightly with decreasing temperature. The main reason for this phenomenon is that, in this stage, the movement of water molecules inside the soil specimens is intense with increasing temperature, which will increase the heat exchange capacity inside the soil specimens. In Stage II, the transition stage from positive to negative temperature (1~−1°C), the thermal conductivity of the soil specimens sharply increases with decreasing temperature. The main reasons for this phenomenon are that, firstly, when the temperature is up to the freezing point within this change range of temperature, the water in the soil specimens will transform into ice, the solid phase of the three-phases system will change from soil skeleton to soil skeleton and ice, the volume of the soil specimens will increase, and the content of unfrozen water, air, and the pores in the soil specimens will decrease. Secondly, the thermal conductivity of ice is about 4 times that of water and far larger than that of air (Table 3). In Stage III, negative temperature stage (−1~−10°C),

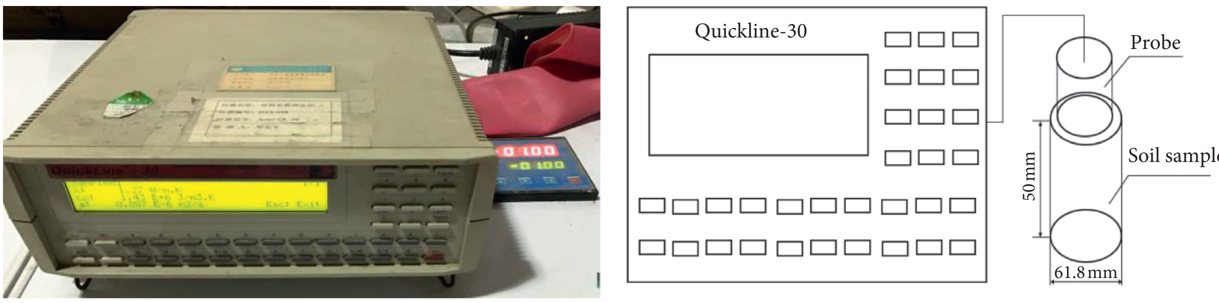

(a) (b)

Figure 3: Experiment apparatus for thermal conductivity. (a) Photograph. (b) Schematic diagram.

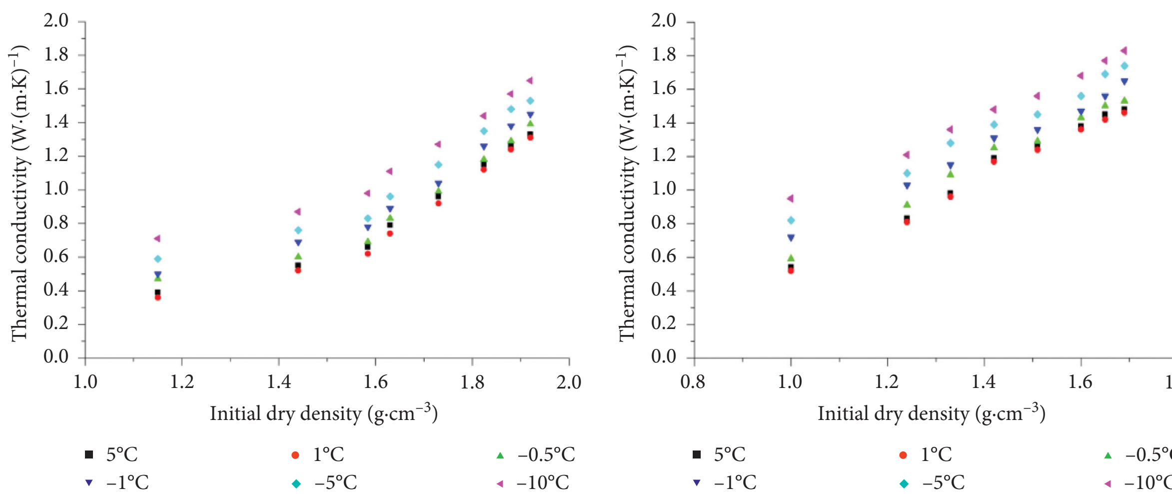

(a) (b)

Figure 4: Variation of the thermal conductivity of the soil specimens with dry density. (a) $w = 14\%$. (b) $w = 20\%$.

Table 3: Thermal conductivity of basic constituents of soils [12].

Basic constituents	Water	Ice	Air	Soil skeleton
Thermal conductivity/(W/(m · K))	0.465	2.21	0.024	1.2 ~ 7.5

as the negative temperature continues to decrease, the thermal conductivity of the soil specimens continues to increase, but the increase is small. This is because although the negative temperature decreases, the limited water in the soil specimens limits the increase of ice.

It can be found from Figure 5 that, for given initial moisture content, the difference between the thermal conductivity of the soil specimens at positive and negative temperatures is related to the dry density. There is a critical dry density; when the dry density is larger than the critical dry density, the difference between the thermal conductivity of the soil specimens at positive and negative temperatures is small, indicating that the thermal conductivity is less affected by temperature. However, when the dry density is less than the critical dry density, the difference between the thermal conductivity of the soil specimens at positive and negative temperatures is large, indicating that the thermal conductivity is greatly affected by temperature. The main reason for the above phenomenon is that the soil specimens with low dry density are loose and with many pores in them; after the water in the soil specimens transforms into ice under the negative temperature condition, the reduction of pores in the soil specimens is more obvious, and the thermal conductivity of ice is much greater than that of air (Table 3).

According to the calculation, the average increment of the thermal conductivity of the soil specimens between the initial moisture content of 20% and 14% is 0.05 W/(m·K); that of the soil specimens between the maximum and minimum initial dry density is 0.024 W/(m·K); that of the soil specimens between the temperature of 5°C and −10°C is 0.021 W/(m·K). It can be seen that, under the influence of different impacting factors, the increase of the thermal conductivity of the soil specimens from large to small is as follows: initial moisture content, initial dry density, and temperature. It indicates that the initial moisture content has the greatest effect on the thermal conductivity, followed by the initial dry density and temperature.

3.2. Development of the ANN Model. In this paper, based on the experimental results, a predictive model of the thermal conductivity of the soil specimens is developed via the ANN technology, and the calculated results are compared with the

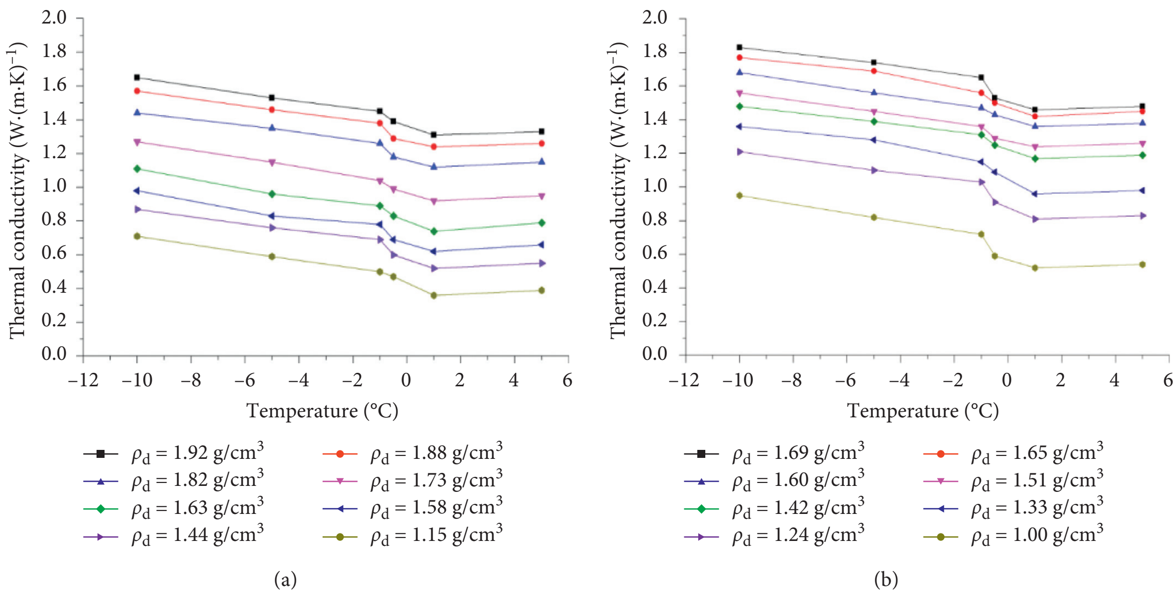

Figure 5: Variation of the thermal conductivity of the soil specimens with temperature. (a)$w = 14\%$. (b)$w = 20\%$.

laboratory-measured results to validate the correctness of the calculated results of the model.

3.2.1. Establishment of the ANN Model. ANN is a multilayer feed-forward neural network, which is composed of an input layer, hidden layer, and output layer, and each layer is composed of different numbers of neurons. In this calculation process, there are 3 neurons in the input layer, including initial moisture content, initial dry density, and temperature of the soil specimens. And there is only one neuron in the output layer, which is the predicted thermal conductivity of the soil specimens. Figure 6 shows the schematic diagram of the structure of the ANN model to calculate the thermal conductivity of the soil specimens. And x, hl, and y denote the neuron of the input layer, hidden layer, and output layer, respectively. Each neuron in the input layer is connected with each neuron in the hidden layer by weights, and each neuron in the hidden layer is connected with the neuron in the output layer by weights.

The ANN uses the Backpropagation algorithm, and the learning process is mainly divided into two stages. The first stage is to input the known learning soil specimens and to calculate the output of each neuron backward from the input layer of the network by setting the structure of the network and the weights and thresholds of the previous iteration; then, the output of each neuron is calculated backward from the input layer of the network. The second stage is to modify the weights and thresholds, to calculate the effect of each weight and threshold on the total error from the output layer, and then to modify each weight and threshold. The two stages are repeated alternately until the convergence is reached.

In addition, the training and test process of multilayer perceptrons (MLPs) are carried out in the ANN toolbox of Matlab 2019. The software is widely used in algorithm development, data analysis, data visualization, and numerical calculation [30].

3.2.2. Parameters Setting. In the general calculation process of the ANN model, the data set is mainly divided into two subsets: the training and validation set. However, it was found that dividing the data set in this way will lead to the model overfitting [31]. And overfitting will prevent the MLPs from properly generalizing the new data in the memory training patterns [32]. Therefore, the data set is divided into three subsets in this calculation process, which are used for training, validation, and testing, respectively, and accounting for 58%, 17%, and 25% of all data. The training data is mainly used to update the weights of the ANN and to establish the most suitable structure of the neural network [25]. The validation data is used to verify the validity of the established model. The testing data is used to determine the thermal conductivity of soils and to validate the accuracy of the model.

The calculated requirements can be met when a network is with one hidden layer [33]; hence, one hidden layer is used in this paper. In addition, the number of neurons in the hidden layer directly affects the performance of the ANN model [27]. Therefore, the number of neurons in the hidden layer is very important for choosing the appropriate structure of the ANN model. The empirical calculation equation for the number of neurons in the hidden layer is [30]

$$n = \sqrt{n_i + n_0} + a, \tag{1}$$

where n is the number of neurons in the hidden layer, n_i is the number of neurons in the input layer, n_0 is the number of neurons in the output layer, and a is a constant in the range of 1~10. Then, the range of n in this calculation is 3~12.

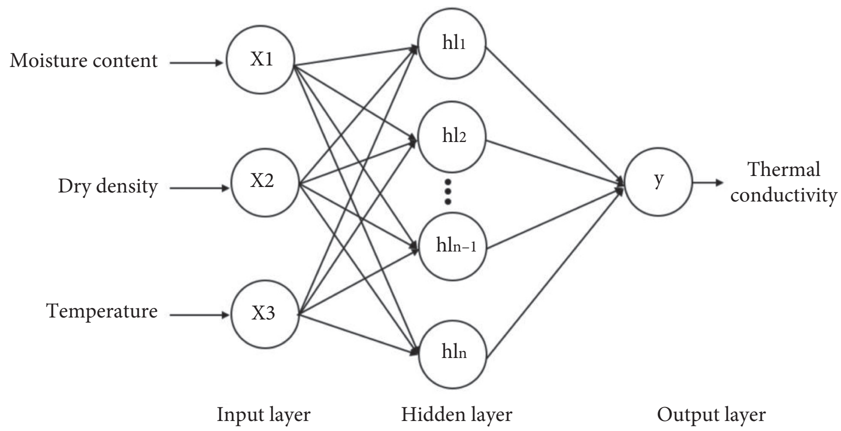

Figure 6: Schematic diagram of the structure of ANN model.

The optimum number of neurons in the hidden layer can be obtained by the following steps: firstly, selecting the number of neurons in the hidden layer to be 3 to train the model, and then, sequentially adding one neuron in the hidden layer for training. When the errors of training, validation, and testing results begin to increase, the training process is terminated. The number of neurons in the hidden layer is considered most appropriate when the errors of training, validation, and testing are small.

We adopt the sigmoid differentiable function as the transfer function of the hidden and output layer of the ANN. Then, the input and output data should be normalized to the range of 0~1, and the calculation equation is

$$x_n = \frac{x_{\max} - x}{x_{\max} - x_{\min}}, \tag{2}$$

where x_n is the normalized data, $x_{\max}$ and $x_{\min}$ are the actual maximum and minimum value, respectively, and x is the actual input and output data.

Table 4 shows the boundary values of the input and output data.

The Levenberg–Marquardt method was used for training the network. The maximum number of network iteration epochs and the expected error goal were selected as 1000 times and 0.0000001, respectively. The learning rate (lr) was selected as 0.01 so as to obtain the most suitable structure of the ANN model.

3.2.3. Model Verification. The comparison between the predicted thermal conductivity of the soil specimens during the training, validation, and testing process of the model with the laboratory-measured thermal conductivity values is shown in Figure 7. The predicted thermal conductivity values during training, validation, and testing are relatively close to the measured thermal conductivity values (Figure 7), indicating that the structure of the established ANN model is reasonable.

In addition, in this study, the correlation coefficient (R^2), square root error (*RMSE*), mean absolute error (*MAE*), and variance (*VAF*) are selected to further validate the accuracy of the calculated results of the established ANN model. The calculation equations are as follows:

$$\begin{aligned} RMSE &= \sqrt{\frac{1}{n}\sum_{i=1}^{n}\left(y_i - y_i'\right)^2}, \\ VAF &= \left[1 - \frac{var\left(y - y'\right)}{var\left(y\right)}\right] \times 100\%, \end{aligned} \tag{3}$$

where n is the number of the soil specimens, y_i is the laboratory-measured thermal conductivity, y_i' is the thermal conductivity calculated by the model, and *var* is an abbreviation of variance. If the values of R^2 and *VAF* are close to 1, *RMSE* and *MAE* are close to 0; it means that the predicted thermal conductivity values of the model are close to the measured thermal conductivity values, and the predicted result is more accurate.

3.2.4. Performance Assessment of the Established Model. The comparison of the thermal conductivity of the soil specimens with the initial moisture content of 16% calculated by the ANN model with the laboratory-measured thermal conductivity is shown in Figure 8. The subscripts m and p of ρ_{dm} and ρ_{dp} denote the measured and predicted values, respectively. Under the same initial moisture content and dry density, the change tendency of the predicted results by the model is basically consistent with that of the measured results with temperature, and the two are relatively close, but the predicted values of the model are slightly larger than the measured values (Figure 8(a)). The correlation coefficient (R^2) between the predicted values of the model and the measured values is high, which is 0.9869 (Figure 8(b)). Table 5 shows the values of R^2, *RMSE, MAE,* and *VAF* of the predicted results of the model compared with the measured results. The values of R^2 and *VAF* are greater than 0.95 and 95%, respectively (Table 5). It indicates that the established ANN model can accurately predict the thermal conductivity of the soil specimens.

The proposed model can be applied to calculate the thermal conductivity of clay in the frozen and unfrozen states and further used to calculate and analyze the variation of the temperature field of soils in cold regions and to estimate the frozen depth of soil.

Table 4: Boundary values of the input and output data.

Data	Variable	Maximum value	Minimum value
Input data	Moisture content (%)	20	14
	Dry density (g/cm^3)	1.92	1
	Temperature (°C)	5	−10
Output data	Thermal conductivity (W/(m · K))	1.83	0.36

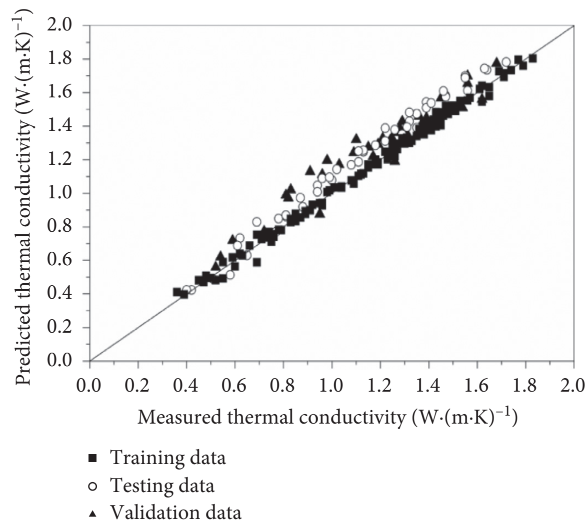

Figure 7: Comparison of the predicted thermal conductivity values of the soil specimens by ANN with the measured thermal conductivity values.

Table 5: Comparison of the parameter values of the predicted thermal conductivity results of the model with the measured thermal conductivity results.

Data sets	R^2	*RMSE* (W/(m · K))	*MAE* (W/(m · K))	*VAF* (%)
Training	0.9974	0.02	0.04	99
Testing	0.9869	0.09	0.1	98
Validation	0.9561	0.11	0.1	95

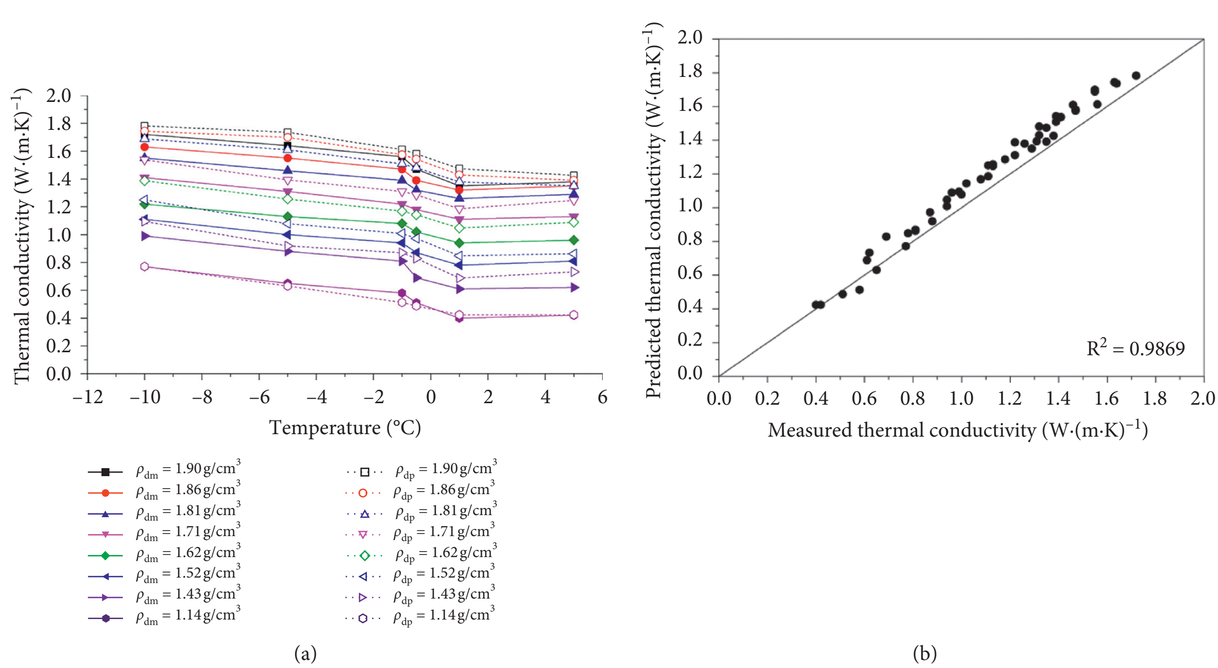

Figure 8: Comparison of the thermal conductivity of the soil specimens with the initial moisture content of 16% predicted by the model with the measured values. (a) Variation curve with temperature. (b) Fitting curve.

4. Conclusions

This paper measures the thermal conductivity of clay under the influence of initial moisture content, initial dry density, and temperature. Then, the variation of the thermal conductivity of the soil specimens during a freezing process where the temperature changes from positive to negative is analyzed, and a predictive model is developed via the ANN technology to calculate the thermal conductivity of the soil specimens under the same experimental conditions. The main conclusions are drawn:

(1) The thermal conductivity of soils is affected by initial moisture content, initial dry density, and temperature, and the initial moisture content plays a dominant role. As the initial moisture content and initial dry density of the soil specimens increase, the thermal conductivity of the soil specimens increases

(2) During different variation stages of temperature, the variation of the thermal conductivity of the soil specimens is different. In the transition stage, the increase of the thermal conductivity is large because water transforms into ice. The variation of the thermal conductivity with temperature is related to the initial moisture content and dry density of the soil specimens. The difference between the thermal conductivity of the soil specimens at positive and negative temperatures is small when the dry density is larger than the critical dry density, while that of the soil specimens is large when the dry density is less than the critical dry density. As the negative temperature decreases, the larger the moisture content, the larger the increase of the thermal conductivity of the soil specimens

(3) The change tendency of the thermal conductivity calculated by the predictive model based on ANN is consistent with that of the laboratory-measured thermal conductivity, and both are close. Both the values of R^2 and *VAF* of the thermal conductivity calculated by the model and the measured thermal conductivity are close to 1, and *RMSE* and *MAE* are lower than 0.11 $W/(m \cdot K)$ and 0.1 $W/(m \cdot K)$, respectively. It indicates that the structure of the established model is reasonable, which can accurately calculate the thermal conductivity of clay.

Data Availability

The data used to support the findings of this study have not been made available because the experimental data involved in the paper are all obtained based on our designed experiments and need to be kept confidential; we are still using the data for further research.

Conflicts of Interest

The authors declare that they have no conflicts of interest.

Acknowledgments

This work was supported by the Second Tibetan Plateau Scientific Expedition and Research (STEP) program (Grant no. 2019QZKK0905), National Natural Science Funds of China (Grant nos. 41801039 and 41772325), and the Science and Technology Project of Yalong River Hydropower Development Company (Grant no. YLLHK-LHA-2019006).

References

[1] T. Ma, T. Tang, X. M. Huang, and H. Wang, “Numerical analysis on thermal regime of wide embankment in permafrost regions of Qinghai–Tibet Plateau,” *Journal of Central South University*, vol. 23, no. 12, pp. 3346–3355, 2016.

[2] N. H. Abu-Hamdeh, A. I. Khdair, and R. C. Reeder, “A comparison of two methods used to evaluate thermal conductivity for some soils,” *International Journal of Heat and Mass Transfer*, vol. 44, no. 5, pp. 1073–1078, 2001.

[3] B. S. Ghuman and R. Lal, “Thermal conductivity, thermal diffusivity, and thermal capacity of some Nigerian soils,” *Soil Science*, vol. 139, no. 1, pp. 74–80, 1985.

[4] M. S. Kersten, *Thermal Properties of Soils, Twin Cities*, University of Minnesota Engineering Experiment Station, University of Minnesota, Minneapolis, MN, USA, 1949.

[5] S. Lu, T. Ren, Y. Gong, and R. Horton, “An improved model for predicting soil thermal conductivity from water content at room temperature,” *Soil Science Society of America Journal*, vol. 71, no. 1, pp. 8–14, 2007.

[6] D. Barry-Macaulay, A. Bouazza, R. M. Singh, B. Wang, and P. G. Ranjith, “Thermal conductivity of soils and rocks from the Melbourne (Australia) region,” *Engineering Geology*, vol. 164, pp. 131–138, 2013.

[7] K. M. Smits, T. Sakaki, A. Limsuwat, and T. H. Illangasekare, “Determination of the thermal conductivity of sands under varying moisture, drainage/wetting, and porosity condition-applications in near-surface soil moisture distribution analysis,” *Hydrology Days*, in *Proceedings AGU Hydrology Days*, pp. 57–65, Fort Collins, CO, USA, 2009.

[8] M. Y. Zhang, J. G. Lu, Y. M. Lai, and X. Y. Zhang, “Variation of the thermal conductivity of a silty clay during a freezing-thawing process,” *International Journal of Heat and Mass Transfer*, vol. 124, pp. 1059–1067, 2018a.

[9] T. Zhang, C. J. Wang, S. Y. Liu, N. Zhang, and T. W. Zhang, “Assessment of soil thermal conduction using artificial neural network models,” *Cold Regions Science and Technology*, vol. 169, Article ID 102907, 2020.

[10] D. W. Liu, D. S. Gu, T. G. Dai, and H. Herbert, “Analysis and calculation of thermal conductivity of rock in deep strata,” *Journal of Central South University of Technology*, vol. 12, no. S1, pp. 114–119, 2005.

[11] X. T. Xu, W. D. Zhang, C. X. Fan, and G. S. Li, “Effects of temperature, dry density and water content on the thermal conductivity of Genhe silty clay,” *Results in Physics*, vol. 16, Article ID 10283, 2020.

[12] X. Z. Xu, J. C. Wang, and L. X. Zhang, *Frozen Soil Physic*, Science Press, Beijing, China, 2010, in Chinese.

[13] Y. Li, M. A. Shao, W. Y. Wang, Q. J. Wang, J. F. Zhang, and J. B. Lai, “Influence of soil textures on the thermal properties,” *Transactions of the CASE*, vol. 19, no. 4, pp. 62–65, 2003, in Chinese.

[14] H. M. Abuel-Naga, D. T. Bergado, A. Bouazza, and M. J. Pender, “Thermal conductivity of soft Bangkok clay from

laboratory and field measurements," *Engineering Geology*, vol. 105, no. 3-4, pp. 211–219, 2009.
[15] L. X. Wang, Q. L. Hu, X. Z. Ling, D. S. Cai, and X. Y. Xu, "Test study on unfrozen water content and thermal parameters of Qinghai-tibet railway frozen silty clay," *Journal of Harbin Institute of Technology*, vol. 39, no. 10, pp. 1660–1663, 2007b, in Chinese.
[16] A. Alrtimi, M. Rouainia, and S. Haigh, "Thermal conductivity of a sandy soil," *Applied Thermal Engineering*, vol. 106, pp. 551–560, 2016.
[17] S. X. Chen, "Thermal conductivity of sands," *Heat and Mass Transfer*, vol. 44, no. 10, pp. 1241–1246, 2008.
[18] O. Nusier and N. Abu-Hamdeh, "Laboratory techniques to evaluate thermal conductivity for some soils," *Heat and Mass Transfer*, vol. 39, no. 2, pp. 119–123, 2003.
[19] Y. Dong, J. S. Mccartney, and N. Lu, "Critical review of thermal conductivity models for unsaturated soils," *Geotechnical and Geological Engineering*, vol. 33, no. 2, pp. 207–221, 2015.
[20] O. Winer, "Abhandl Math-Phys Kl KoniglSachsischenGes," vol. 32, pp. 509, 1912.
[21] D. A. Devries, "Thermal properties of soils," in *Physics of the Plant Environment*, W. R. Van Wijk, Ed., pp. 210–235, John Wiley & Sons, New York, NY, USA, 1963.
[22] O. Johansen, *Thermal Conductivity of Soils*, Trondheim: University of Trondheim, Trondheim, Norway, 1975.
[23] J. Côté and J. M. Konrad, "A generalized thermal conductivity model for soils and construction materials," *Canadian Geotechnical Journal*, vol. 42, no. 2, pp. 443–458, 2005.
[24] J. Bi, M. Y. Zhang, Y. M. Lai et al., "A generalized model for calculating the thermal conductivity of freezing soils based on soil components and frost heave," *Internal Journal of Heat and Mass Transfer*, vol. 150, Article ID 119166, 2020.
[25] Y. Erzin, B. H. Rao, and D. N. Singh, "Artificial neural network models for predicting soil thermal resistivity," *International Journal of Thermal Sciences*, vol. 47, no. 10, pp. 1347–1358, 2008.
[26] F. X. He and Y. Huang, "Solution of thermal conduction coefficient from BP network," *Rock and Soil Mechanics*, vol. 21, no. 1, pp. 84–87, 2000, in Chinese.
[27] Y. Zhang, L. Zhou, Z. Hu et al., "Prediction of layered thermal conductivity using artificial neural network in order to have better design of ground source heat pump system," *Energies*, vol. 11, no. 7, p. 1896, 2018b.
[28] N. Zhang, H. Zou, L. Zhang, A. J. Puppala, S. Liu, and G. Cai, "A unified soil thermal conductivity model based on artificial neural network," *International Journal of Thermal Sciences*, vol. 155, Article ID 106414, 2020.
[29] T. L. Brandon and J. K. Mitchell, "Factors influencing thermal resistivity of sands," *Journal of Geotechnical Engineering*, vol. 115, no. 12, pp. 1683–1698, 1989.
[30] Q. C. Fang, *MATLAB R2016a Neural Network Design and Application: Analysis of 28 Cases*, Tsinghua Publishing Press, Beijing, China, 2018, in Chinese.
[31] J. M. Twomey and A. E. Smith, "Validation and verification," in *Artificial Neural Networks for Civil Engineers: Fundamentals and Applications*, N. Kartam, I. Flood, and J. H. Garret, Eds., pp. 44–64, ASCE, New York, NY, USA, 1997.
[32] M. Banimahd, S. S. Yasrobi, and P. K. P.K. Woodward, "Artificial neural network for stress-strain behavior of sandy soils: knowledge based verification," *Computers and Geotechnics*, vol. 32, no. 5, pp. 377–386, 2005.
[33] K. Hornik, M. Stinchcombe, and H. White, "Multilayer feedforward networks are universal approximators," *Neural Networks*, vol. 2, no. 5, pp. 359–366, 1989.

Hindawi
Advances in Materials Science and Engineering
Volume 2021, Article ID 6670515, 11 pages
https://doi.org/10.1155/2021/6670515

Research Article

Temperature Field Variation Law of Low Exothermic Polymer Grouting Material in Repairing Void Damage of Frozen Soil Subgrade

Bei Zhang[1], **Baolin Wang**[1], **Yanhui Zhong**[1], **Shuangjie Wang**[2], **Xiaolong Li**[1] **and Shilun Wang**[1]

[1]*School of Water Conservancy Engnieering, Zhengzhou University, Zhengzhou 450001, China*
[2]*CCCC First Highway Consultants Co.,Ltd., Xi'an, China*

Correspondence should be addressed to Yanhui Zhong; zhong_yanhui@163.com, Shuangjie Wang; wangshj@ccroad.com.cn, and Xiaolong Li; wennuandeshang@hotmail.com

Received 23 December 2020; Revised 21 January 2021; Accepted 25 February 2021; Published 27 March 2021

Academic Editor: Xiao Dong Zhao

In this study, the self-developed grouting mold was used to study the heat release characteristics of different density polymer grouting material under different temperature conditions. The spatial distribution characteristics of the frozen soil subgrade temperature field under the effect of polymer grouting repair were analyzed. Further, the rules governing the temperature change of a frozen soil subgrade monitoring point under the effect of polymer grouting repair were studied. The heat transfer mechanism of polymer grouting material in frozen soil subgrade was revealed. The results showed that in the void region of the frozen soil subgrade, a discontinuity zone appeared in the temperature field distribution isotherm due to the effect of voids; this zone exhibited a layered radioactive distribution along the two sides of the void area. Furthermore, during the exothermic stage of the curing reaction, the temperature distribution isotherms changed from a layered radioactive distribution to a ring distribution that decreased from the inside to outside. During the natural cooling process, the peripheral temperature of the ring isotherm first decreased and a negative temperature ring-shaped isotherm gradually formed. Finally, the upper boundary of the influence of the heat energy released by the curing reaction on the frozen soil subgrade temperature field was determined to be 30 cm, and the lower boundary was 20 cm.

1. Introduction

Permafrost accounts for 23% of the total land area in the world. At present, numerous highway projects have been built in permafrost regions [1–3]. As a road bearing foundation, frozen soil subgrade contains a large number of ice crystals with different structures. Uneven settlement occurs readily due to freeze-thaw effects and negatively impacts road traffic safety. In recent years, many scholars have studied the laws governing the temperature variation and stability of frozen soil subgrades. Yu et al. [4] studied the heat transfer characteristics of a sand-filled embankment using numerical simulation methods and revealed the rules governing the embankment temperature variations. Based on survey data, Han et al. [5] analyzed the degree of influence of factors such as subgrade height, pavement width, water content, and average annual temperature on the thermal stability of frozen subgrade. Zhang et al. [6, 7] monitored frozen soil subgrade temperatures for up to three years and proposed an empirical model that accounted for factors such as the average temperature, amplitude, and phase difference and analyzed the mechanism of subgrade frost heave development in detail. Liu et al. [8] conducted indoor water migration simulation experiments under freeze-thaw cycling and determined the mechanism of water migration during freezing. Current research supports the conclusion that, in areas of frozen soil, changes in the temperature field will cause frost heaving and thawing damage to the frozen soil subgrade, which is one of the primary causes of embankment instability. Chai et al. [9, 10]

studied the microstructure of soils improved with cement and additives under constant loading and variable temperature conditions to determine how to improve the engineering properties of frozen soil and prevent uneven settlement. Mechanisms to improve frozen soil compressibility and thaw settlement performance were also revealed. Lvanov and Korotkov [11] used granular glass-ceramic foam material as an antifreeze layer and analyzed the principles of frozen soil subgrade temperature changes. Liu et al. [12] used numerical software to establish a model of the frozen soil subgrade of the Qinghai-Tibet Plateau to analyze the rules governing the deformation of the subgrade with and without loading. Zhang and Zhang [13] conducted an experimental study of the characteristics of moisture migration in frozen soil subgrades protected by gravel piles and concluded that gravel piles could effectively prevent the water level from rising, thereby controlling the soil freezing process and improving the bearing capacity of the subgrade. Based on field inspection data, Li et al. [14] analyzed the influence of gravel, ventilation, and the thermal insulation of the embankment on the temperature fields of frozen soil subgrades and revealed the embankment deformation characteristics of three soil layers. Huang et al. [15] used the unascertained measurement theory to establish a model to evaluate frozen soil subgrade stability and analyzed the effects of temperature stability on the subgrade.

In summary, previous research has primarily sought to improve frozen soil subgrade stability by adjusting the heat exchange conditions between the subgrade and the atmosphere, such that the internal temperature field would be in a balanced state. However, the thawed layer thicknesses of frozen soil continue to increase under the combined effects of climate warming and long-term vehicle loading. This can cause void damage due to uneven settlement and deformation of the frozen subgrade. Cement grouting is traditionally the primary method for repairing uneven subgrade settlement. Although the grout can fill loose areas of the subgrade and improve its strength, the material itself is not expansible and cannot raise the subsided pavement. Further, cement grouting requires a long construction period, resulting in traffic impacts due to construction traffic control.

In recent years, due to the expansibility of polymer grouting material, it quickly achieves design strength and can fill subgrade void regions and lift subsided pavement. Therefore, it is widely used to repair the uneven settlement deformation of subgrades. However, the heat energy released by the polymer curing reaction affects the internal temperature field of the frozen soil subgrade. Therefore, in this study, a self-developed grouting mold was used to study the heat release characteristics of polymer grouting material with different densities and different temperatures. Then, according to the engineering practice of nonuniform settlement of frozen soil subgrade, a numerical analysis model was established to study the temperature variation law of polymer grouting material in the process of filling frozen soil void and revealed the heat transfer mechanism of polymer grouting material in frozen soil subgrade. The results could provide theoretical support for the repair of the void damage caused by uneven settlement and the subgrade deformation of frozen soils.

2. Analysis of Void Damage in Field Engineering

Figure 1 shows the uneven settlement of frozen soil subgrade due to void damage. The roads constructed in frozen areas are primarily black asphalt pavement structures, which are more sensitive to the temperature field of the frozen soil subgrade. The black asphalt pavement increases the solar radiation absorption rate, which is converted into heat energy and is transferred downward such that the heat absorbed by the subgrade gradually increases. Further, the closed structure of the asphalt pavement hinders the process of heat dissipation from the subgrade surface, inhibiting the effective release of heat generated inside the subgrade and changing the equilibrium condition of the heat exchange between the frozen subgrade and the atmosphere.

Annually, the total heat absorbed by a frozen subgrade will be higher than the heat released due to the influence of seasonal temperature variations and the thermal conditions previously described. Therefore, the temperature inside the frozen soil subgrade is accumulatively increased, and some ice crystals melt into liquid water, forming a basin-shaped melting area inside the subgrade. Over time, this area gradually expands, and the tensile stress of the soil above it gradually increases. When the tensile stress is greater than the cohesive forces between the soil bodies, voiding damage occurs, leading to a significant reduction in the subgrade bearing capacity. Under the long-term effect of vehicle loads, the upper boundary of the void area simultaneously bears the weight of the soil above it and the compressive effect of vehicle loading, generating tensile stress in the horizontal direction. With the continued increase in tensile stress, longitudinal cracks will gradually appear in frozen soil subgrade, resulting in uneven settlement deformation damage. The continuous effect of the vehicle loads and the influence of rainfall and other atmospheric factors eventually results in slope instability and landslide, as shown in Figure 2.

3. Material and Methods

3.1. Polymer Grouting Material. Polyurethane polymer grouting material is mainly composed of polyisocyanate, polyether polyol, a foaming agent, a catalyst, a foam stabilizer, and various other additives. The exothermic curing reaction primarily consists of gel and foaming reactions [16–18]. The gel curing reaction occurs between the polyisocyanate -NCO groups and the polyol -OH groups; the foaming reaction results from the reaction of the polyisocyanate -NCO groups and H_2O to form CO_2 and urea. The reaction principle is shown in Figures 3 and 4.

3.2. Test Equipment

3.2.1. Grouting System. The vehicle-mounted polymer grouting integrated equipment used in the test mainly includes a pressure-supply device, a grouting pipe, a grouting

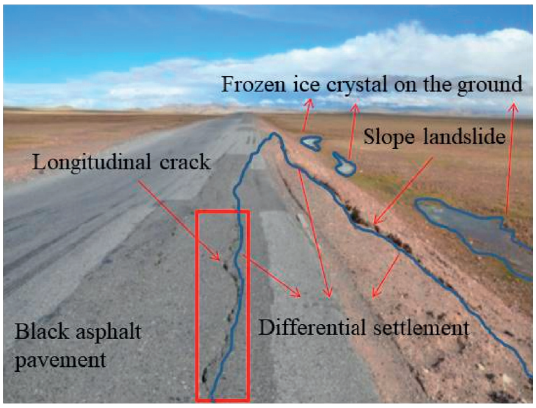

FIGURE 1: Typical damage resulting from a frozen soil subgrade.

gun, and a toolbox for cleaning the grouting equipment regularly. As shown in Figure 5, the self-developed grouting mold is shown in Figure 6. The inner diameter of the mold is 120 mm, the outer diameter is 132 mm, the height is 150 mm, and the thickness of the flange plate is 20 mm.

3.2.2. Data Monitoring Equipment. Figure 7 shows the data monitoring equipment used in the test. Data monitoring equipment includes temperature sensor, temperature collector, and data processing system. The measurement range of the temperature sensor is −200°C~300°C, and the allowable error range is $\pm(0.15 + 0.002|t|)$°C. The data measured by the temperature sensor of the long probe are used to indicate the core temperature of the polymer grouting material, and the data measured by the short probe are used to indicate the surface temperature. The reaction temperature test in the curing stage of the polymer grouting material was carried out under the conditions of −10°C, 0°C, 10°C, 20°C, and 30°C.

3.3. Numerical Analysis

3.3.1. Numerical Model. According to the actual engineering damage profile shown in Figure 1, a typical area of frozen soil subgrade structure with a width of 10 m was selected to study the influence of polymer grouting material on the temperature field of the frozen soil subgrade. The roadway structure consisted of (from top to bottom) a 4 cm AC-13 SBR-modified asphalt upper layer, 5 cm AC-16 unmodified asphalt under layer, 8 cm cement-stabilized macadam base, 18 cm cement-stabilized gravel base, 20 cm graded gravel cushion, and 2.35 m gravelly soil fill. Below the ground surface, there were 1.5 m gravel soil, 2.5 m gravel and clay silt, and 6 m silty clay. In ABAQUS, a numerical model was established by first establishing components of different subgrade structural layers and then performing assembly operations. The resulting two-dimensional numerical analysis model is shown in Figure 8.

3.3.2. Thermodynamic Parameters of Polymer Material. Soil is a three-phase body composed of solid particles, liquid water, and gas. In frozen soil, part of the liquid water in the soil freezes into ice crystals (i.e., transforms into its solid phase) due to the influence of the low-temperature environment. Therefore, frozen soil is a multiphase medium composed of organic matter, solid particles, liquid water, ice, and gas. The gas content of frozen soil is relatively small; by ignoring the influence of gas on the specific heat capacity of the frozen soil, the specific heat capacity of the frozen and thawing soils can be defined according to the following formulas [19–23]:

$$C_f = \frac{C_{df} + (W - W_u)C_i + W_u C_W}{1 + W}, \tag{1}$$

$$C_u = \frac{C_{du} + W C_w}{1 + W}\rho, \tag{2}$$

where C_u and C_f are the specific heat capacities of the melted and frozen soil, respectively; C_{du} and C_{df} are the specific heat capacities of the melting and frozen soil skeletons, respectively; C_i and C_w are the specific heat capacities of ice and water, respectively; W and W_u are the total and unfrozen water contents of the soil, respectively; and ρ is the natural density of the frozen soil. In the temperature field simulation, the asphaltic surface layer material was taken to be a viscoelastic material, and the other layers were linear elastic materials. The road structure layers were assumed to be in complete contact, and the temperature and heat flow changes between the layers were assumed to be continuous and uninterrupted [24,25]. The thermal properties of each layer are shown in Tables 1 and 2.

3.3.3. Boundary Conditions

(1) Solar Radiation Conditions. Solar radiation is the primary source of the earth's light and heat energy and causes the redistribution of the temperature field in a frozen soil subgrade. The daily variation in solar radiation $q(t)$ can be approximated using the following function [26–28]:

$$q(t) = \begin{cases} 0, & 0 \le t < 12 - \dfrac{c}{2}, 12 + \dfrac{c}{2} < t \le 24, \\ q_0 \cos mw(t - 12), & 12 - \dfrac{c}{2} \le t < 12 + \dfrac{c}{2}, \end{cases} \tag{3}$$

where q_o is the maximum radiation at noon, $q_0 = 0.131mQ$, where $m = 12/c$; Q is the total solar radiation in one day, J/m^2; c is the effective light hours, h; and ω is the angular frequency, rad.

Formula (3) is a piecewise function with jump discontinuities. Because the temperature field distribution in the frozen soil subgrade is continuous, Formula (3) can be expanded into a continuous cosine trigonometric form based on the principle of Fourier series correlation [29–32], as shown in Formula (4). In this calculation, the order k can be set as 30 to meet engineering accuracy requirements.

$$q(t) = \frac{a_0}{2} + \sum_{k=1}^{\infty} a_k \cos\frac{k\pi(t - 12)}{12}, \tag{4}$$

where $a_0 = (2q_o/m\pi)$;

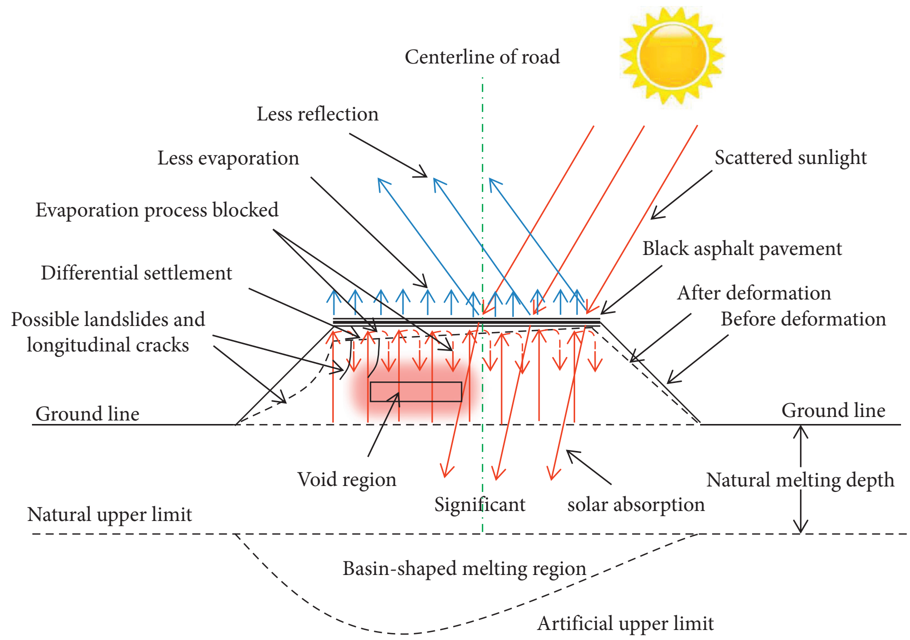

Figure 2: Mechanisms of the formation of uneven frozen soil subgrade settlement.

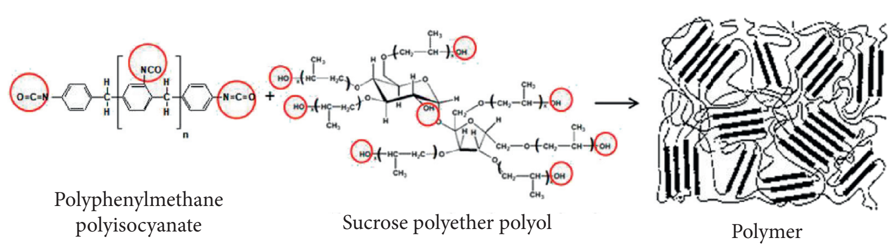

$$\mathrm{RNCO} + \mathrm{R'OH} \rightarrow \mathrm{RNHCOO\,R'} + \text{thermal energy}$$

Figure 3: Principle of gel reaction.

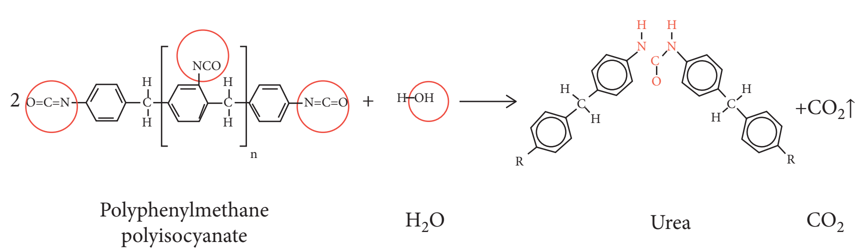

$$2\,\mathrm{RNCO} + \mathrm{H_2O} \rightarrow \mathrm{RNHCONHR} + \mathrm{CO_2} + \text{thermal energy}$$

Figure 4: Principle of foaming reaction.

Figure 5: Vehicle-mounted polymer grouting integrated system.

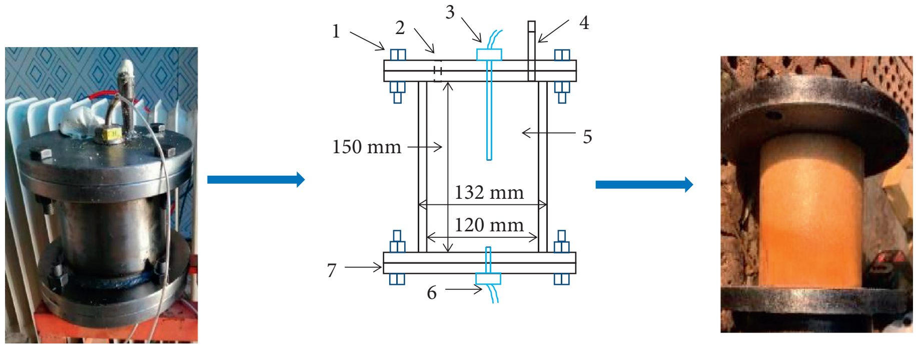

Figure 6: Grouting mold. (1) Bolt; (2) vent hole; (3, 6) temperature sensor; (4) grouting hole; (5) reaction vessel; (7) flange plate.

Figure 7: Data monitoring system.

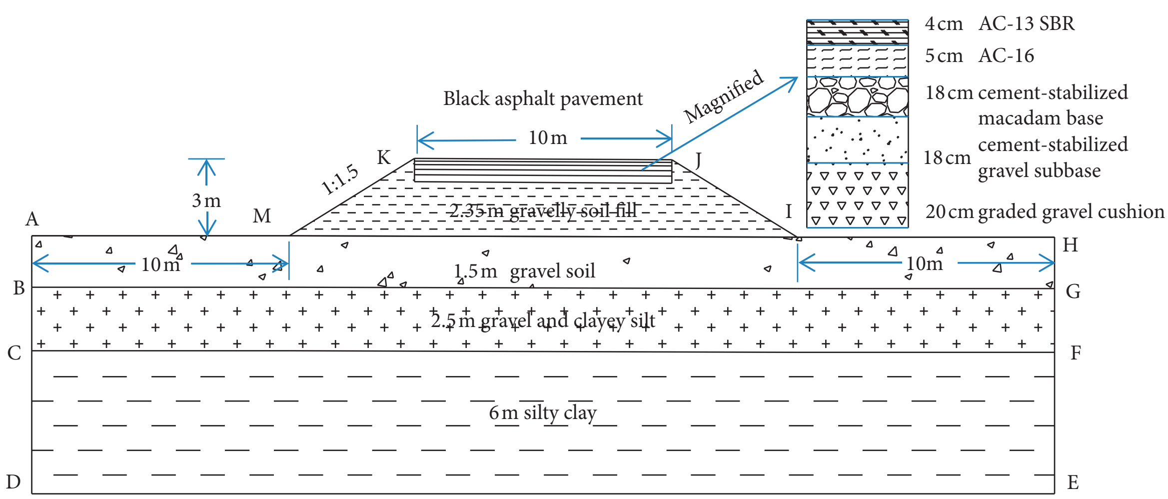

Figure 8: Two-dimensional numerical analysis model.

Table 1: Thermal properties of the subgrade materials.

Parameters	AC-13 SBR-modified asphalt	AC-16 unmodified asphalt	Cement-stabilized macadam	Cement-stabilized gravel	Polymer grouting material
Density ρ (kg/m^3)	2291	2316	2374	2340	250
Specific heat capacity C (J/(kg·°C))	1124	917	1127	1141	1500
Thermal conductivity λ (W/(m·°C))	3.780	4.356	4.572	4.320	0.146

Table 2: Thermal material properties of the foundation.

Parameters	Gravelly soil fill	Gravelly soil	Gravel and clay silt	Silty clay
Density ρ (kg/m^3)	2000	2100	2340	2080
Specific heat capacity of frozen soil C_f (J/(kg·°C))	852	895	983	1200
Specific heat capacity of melted soil C_u (J/(kg·°C))	1020	996	1220	1370
Thermal conductivity of frozen soil λ_f (W/(m·°C))	1.985	2.26	1.32	1.85
Thermal conductivity of melted soil λ_u (W/(m·°C))	1.916	1.98	0.95	1.36

$$a_k = \begin{cases} \dfrac{q_0}{\pi}\dfrac{1}{m+k}\sin(m+k)\dfrac{\pi}{2m}+\dfrac{\pi}{2m}, & k=m, \\[2ex] \dfrac{q_0}{\pi}\dfrac{1}{m+k}\sin(m+k)\dfrac{\pi}{2m}+\dfrac{1}{m-k}\sin(m-k)\dfrac{\pi}{2m}, & k\neq m. \end{cases} \tag{5}$$

(2) Temperature and Convection Heat Exchange Conditions. Under the influence of solar radiation, the atmospheric temperature changes periodically from day to night. In fewer than ten hours, the temperature changes from the daily minimum (approximately 04 : 00–06 : 00) to the daily maximum temperature (approximately 14 : 00), meaning that 14 or more hours are required to change from the highest to the lowest temperature [33]. Therefore, a linear combination of two sine functions is required to simulate the daily temperature change process, as shown in the following formula:

$$T_a = \overline{T}_a + T_m\left[0.96\sin\omega\left(t-t_0\right)+0.14\sin 2\omega\left(t-t_0\right)\right], \tag{6}$$

where $\overline{T}_a$ is the average daily temperature; T_m is the daily temperature change $T_m = (1/2)(T_a^{\max} - T_a^{\min})$; $T_m^{\max}$ and $T_m^{\min}$ are the daily maximum and minimum temperatures, respectively; ω is the angular frequency, $\omega = \pi/12$, rad; and t_0 is the initial time. The time difference was set to be 2 h and $t_0 = 9$ h to represent typical conditions.

Black asphalt pavement is exposed to the environment, and the wind speed affects the heat exchange between the pavement and the atmosphere. The relationship between the heat exchange coefficient h_c and wind speed V_w is linear.

$$h_c = 3.7v_w + 9.4, \tag{7}$$

where h_c is the heat exchange coefficient and V_w is the average daily wind speed, m/s.

(3) Pavement Effective Radiation Conditions. Black asphalt pavement increases the absorption rate of solar radiation [34, 35]. Therefore, the boundary conditions of the effective ground radiation can be defined as

$$q_F = \varepsilon\sigma\left[\left(T_1|_{z=0} - T_z\right)^4 - \left(T_a - T_z\right)^4\right], \tag{8}$$

where q_F is the effective radiation on the ground, W/(m^2·°C); ε is the emissivity (blackness) of the road surface, generally 0.81 for an asphalt road surface; σ is the Stefan–Boltzmann constant (i.e., blackbody radiation constant), $2.014e^{-4}$ J/(m^2·h·K^4); $T_1|_{z=0}$ is the road surface temperature, °C; T_a is the atmospheric temperature, °C; andT_z is the absolute zero, °C, $T_z = -273$°C. Statistical analyses and calculations were performed based on the relevant data obtained for the Qinghai-Tibet Plateau in January. The boundary condition parameters used in this study are shown in Table 3.

Table 3: Boundary condition parameters.

Time	January
Total daily solar radiation (MJ/m^2·d^{-1})	10
Solar radiation absorption rate	0.9
sDaily sunlight (h)	6.38
Daily maximum temperature (°C)	−8.4
Daily minimum temperature (°C)	−23.4
Daily average temperature (°C)	−16.7
Daily average wind speed (m/s)	5.17

4. Results and Analysis

4.1. Law of Temperature Threshold Change. Figure 9 shows the change rule of the center and surface temperature threshold of the polymer grouting material in the mold grouting test. It can be seen from Figure 9 that the center temperature is significantly higher than the surface temperature. The central temperature and surface temperature threshold of polymer grouting materials increase with the increase in density. The increase in the center temperature is larger than that of the surface temperature. In addition, the threshold values of the center temperature and the surface temperature of the polymer grouting materials decrease with the decrease in the ambient temperature.

4.2. Simulation of the Heat Conduction Process. The numerical analysis model shown in Figure 8 was meshed in consideration of the calculation time and accuracy requirements. DC2D3 three-node linear heat transfer triangular elements were used for the slopes on both sides of the subgrade, and DC2D4 four-node linear heat transfer quadrilateral elements were used for the other structural layers. The numerical analysis model after meshing is shown in Figure 10. In the numerical analysis model, the solar radiation boundary conditions were defined using the Load module, by calling the DFLUX subroutine written in the Fortran computer language. The temperature and convection heat exchange boundary conditions were defined using the Interaction module, by calling the FILM subprograms, which were also written in Fortran. The surf radiation module defined the pavement effective radiation boundary conditions.

4.3. Initial Temperature Field. For this study, according to the core sample results obtained on the road, a rectangular void region of 200 × 1 cm was set between the base layer and

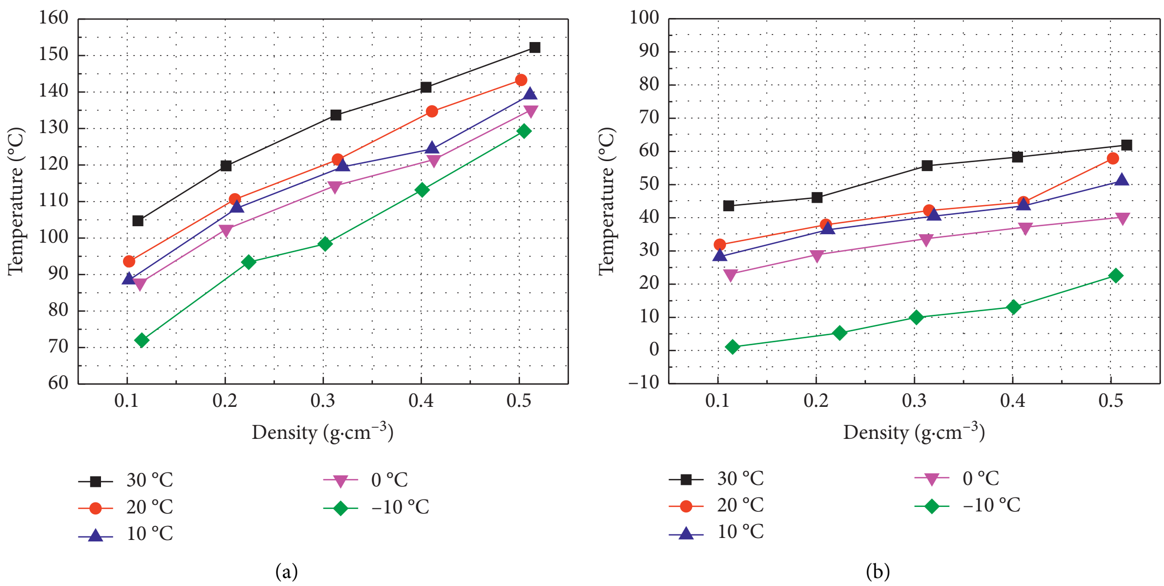

Figure 9: Temperature threshold of polymer grouting material: (a) central temperature and (b) surface temperature.

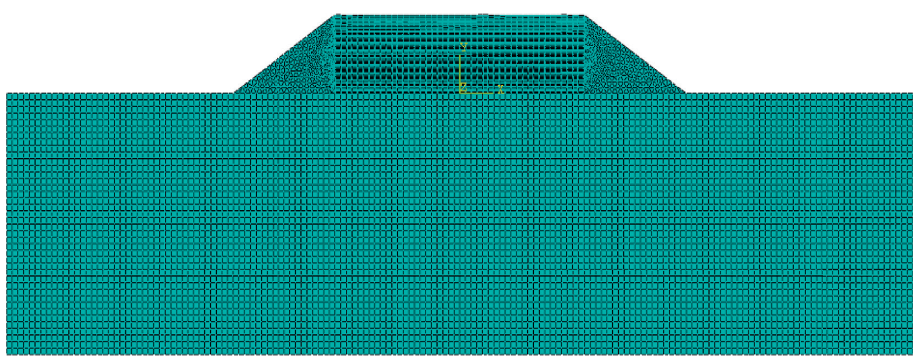

Figure 10: Meshing of the numerical model.

the cushion of the numerical model at a depth of 45 cm from the road surface. In the numerical model, input the thermal property parameters in Tables 1 and 2 into the corresponding structural layer materials. Then, the initial temperature field of subgrade was obtained by steady-state calculation. The initial temperature fields of the frozen soil subgrade models with and without void damage are shown in Figure 11.

Figure 11 shows that the initial temperature field distribution of the two subgrade types had similarities and differences. The minimum temperature of the ground surface of both subgrades was −15°C. As the depth increased, the temperature of the subgrade gradually increased, reaching the maximum temperature of 6°C at 0.5 m below the ground surface. The temperature of the subgrade then decreased gradually with depth, and the entire model had a continuous layered distribution characteristic. In contrast, under the influence of the void effects, the temperature field distribution isotherm displayed a discontinuity zone in the void region of the frozen soil subgrade and presented radioactive distribution characteristics along both sides of the void region. These observations are explained by the void region of the frozen subgrade being full of air. Due to the effect of the freeze-thaw cycle, the humidity of the air was relatively high, and its thermal conductivity was significantly different from that of the surrounding soil. Therefore, the heat conduction process in the void region had a discontinuity, ultimately leading to a discontinuous temperature distribution curve in this area.

4.4. Frozen Soil Subgrade Temperature Field Spatial Distribution Characteristics during Polymer Grouting Repair. Figures 12–14 show the temperature field spatial distribution characteristics under the effect of the polymer grouting repair. Figure 12 shows that the temperature threshold of the polymer grouting material in the void region of the frozen soil subgrade could be as high as 90°C. The curing reaction of the polymer grouting material released heat energy, which caused the temperature of the subgrade near the void region filled by the grout to increase continuously and resulted in the observed ring-shaped

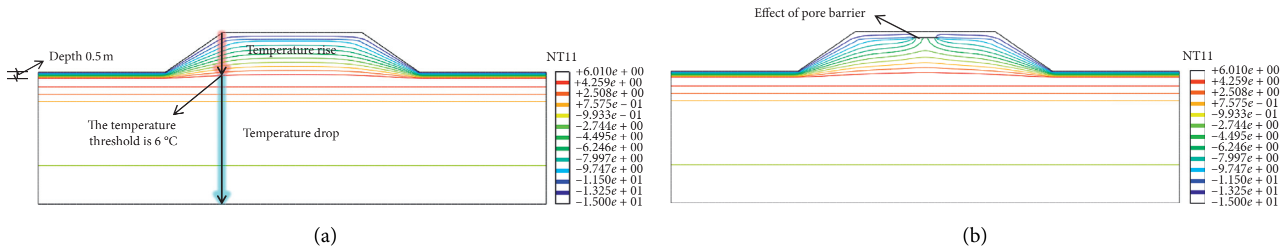

Figure 11: Initial temperature field distribution (a) without void damage and (b) with void damage.

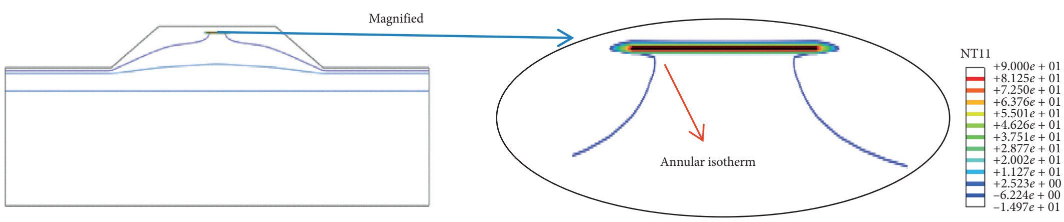

Figure 12: Temperature field distribution characteristics of the polymer grouting material at the maximum central temperature.

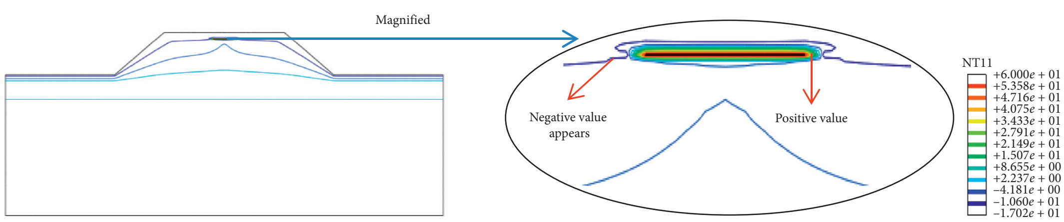

Figure 13: Temperature distribution characteristics of the polymer grouting material when the central temperature decreased to 60°C.

isothermal distribution. The temperature decreased from 81.25°C to 2.52°C from inside to outside the modeled structure. Figure 13 shows that when the central temperature of the polymer grouting material decreased to 60°C, the temperature threshold of the subgrade around the grout-filled void region decreased from 81.25°C to 53.58°C. The temperature of the annular isotherm decreased from 53.58°C to −4.18°C from the inside to the outside, at which time the temperature of the subgrade around the void region was negative, but the ring isotherm remained positive. As shown in Figure 14, when the central temperature of the polymer grouting material decreased to 14°C, the temperature threshold of the subgrade around the grout-filled void region was only 11.75°C, which was 86% lower than the maximum temperature of 81.25°C. The temperature of the annular isotherm decreased from 11.75°C to −9.33°C from inside to outside; concurrently, negative values appeared around the outer ring isotherm, and negative temperature isotherms formed.

Analysis of the spatial distribution characteristics of this temperature field revealed that the temperature of the frozen soil subgrade around the void region increased continuously due to the release of heat energy from the curing reaction. The ice crystals absorbed the heat, melted into liquid water, and absorbed the heat transferred from the polymer grouting material to the surrounding areas. This led to the isotherm around the void region changing from a layered radioactive distribution to a ring distribution that decreased from inside to outside. Locations further from the void region were less affected by the release of heat energy caused by the grout curing. Radioactive isotherms remained around the annular temperature field. The center temperature of the polymer grouting material began to gradually decrease after reaching its maximum due to the effects of the ambient temperature. During this process, the temperature of the outermost layer of the ring-shaped isotherm first began to decrease and then gradually formed a ring-shaped negative temperature isotherm. As the cooling process continued, the range of influence of the thermal energy released by the grout curing on the subgrade temperature field decreased further.

4.5. Time-Varying Temperature Changes in the Monitoring Points of the Frozen Subgrade during Grouting. In the numerical analysis model of frozen soil subgrade, 13 temperature monitoring points with an interval of 2.5 cm were evenly arranged above the center of the void region, and nine temperature monitoring points with an interval of 2.5 cm were evenly arranged below the center of the void region. Figures 15 and 16 show the temperature changes of the monitoring points with time. It can be seen from Figure 15 that the temperatures of the monitoring points located at 0.0 cm, 2.5 cm, 5.0 cm, 7.5 cm, 10.0 cm, 12.5 cm, and 15 cm above the center of the frozen soil subgrade void region were significantly affected by the heat energy released by the

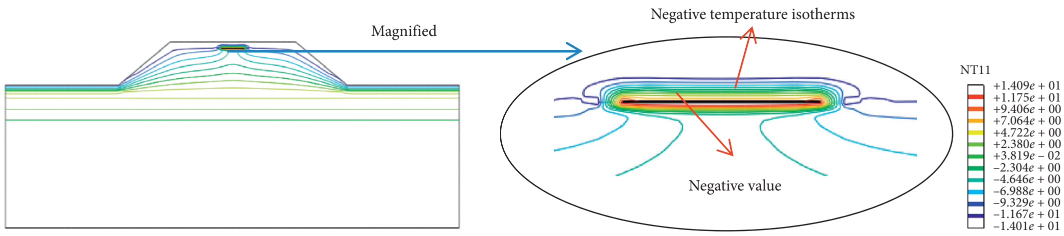

Figure 14: Temperature field distribution characteristics of the polymer grouting material when the central temperature decreased to 14°C.

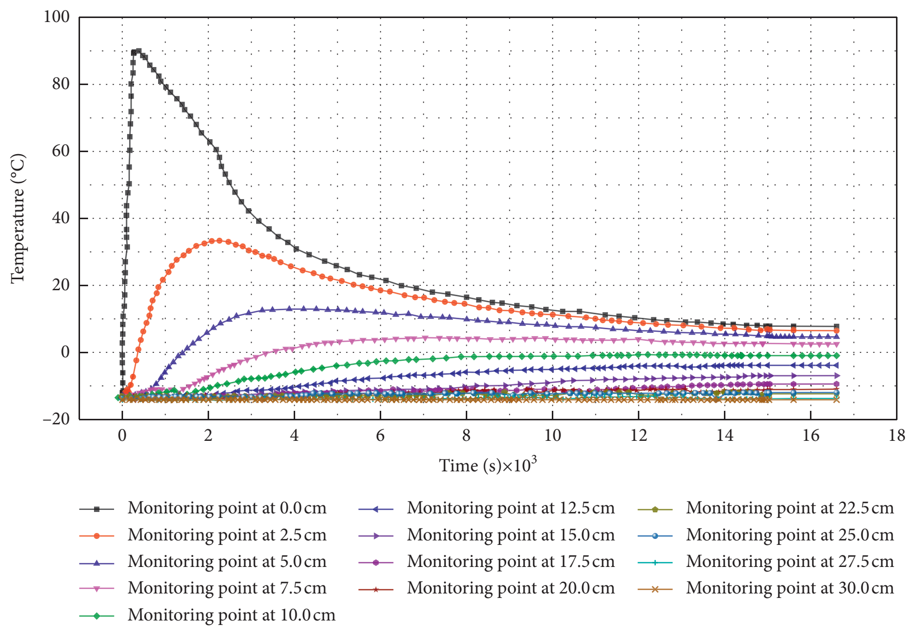

Figure 15: Temperature change over time at the monitoring points above the center of the frozen soil subgrade void region.

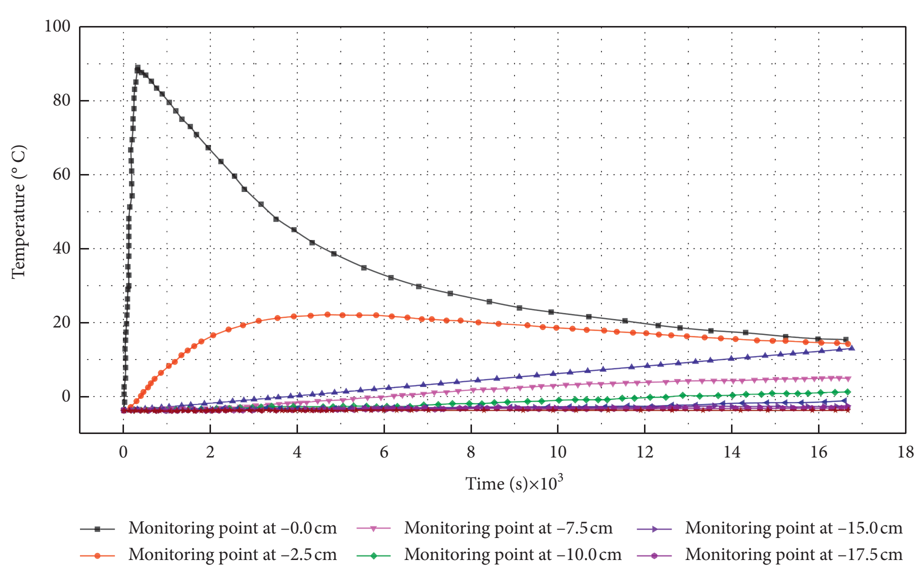

Figure 16: Temperature change over time at the monitoring points below the center of the frozen soil subgrade void region.

polymer grouting material. Among them, the temperature change was the largest at the monitoring point at 0.0 cm, rising to 89.5°C relatively quickly, while the highest temperature at the monitoring point at 2.5 cm was only 32.5°C. The temperature changes of the other six monitoring points were less affected by the heat released by the polymer. Among them, the temperature of the monitoring point at 30 cm was essentially unchanged. Figure 16 shows that the temperatures of the monitoring points located at −0.0 cm, −2.5 cm, −5.0 cm, and −7.5 cm under the center of the void region were substantially impacted by the heat energy released by the polymer grouting material. Among them, the temperature of the monitoring point at 0.0 cm rose rapidly to 89.2°C, while the highest temperature of the monitoring point at −2.5 cm was only 21.5°C. The temperature changes of the other five monitoring points were less affected by the heat released by the polymer, and the temperature of the monitoring point at −20 cm was relatively unchanged.

Comparing Figures 12 and 13 shows that the monitoring points at 0.0 cm and −0.0 cm were located on the critical planes of the upper and lower sides of the void region of the frozen subgrade, respectively. Therefore, the maximum temperature of the two monitoring points was consistent with the temperature threshold of the curing reaction. The temperature threshold of the monitoring point at 2.5 cm was 32.5°C, which is 11°C higher than the 21.5°C observed at −2.5 cm. Comparing the monitoring point temperatures over time reveals that the temperature of the frozen soil subgrade located above the void region changed drastically due to the effect of the heat energy released by the polymer grouting material. The temperature at the monitoring points at 30 cm and −20 cm remained virtually unchanged. Therefore, the upper and lower boundaries of the influence range of the heat release reaction could be considered to be 30 cm and 20 cm, respectively.

5. Conclusions

In this study, firstly, the influence of void damage on the temperature field of frozen soil subgrade was analyzed. Then, the heat transfer characteristics between polymer grouting material polymerization heat release and frozen soil subgrade were studied. Finally, the influence range of polymer grouting material polymerization heat release on the temperature field of frozen soil roadbed was clarified. The conclusions are as follows:

(1) The temperature field inside the frozen soil subgrade had a continuous layered distribution. However, in the void region, the temperature field distribution isotherm was interrupted by a gap, and a discontinuity zone appeared in the void region, revealing the characteristics of the distribution of radioactivity along the two sides of the void region.

(2) During the exothermic curing reaction of the polymer grouting material, the temperature of the frozen soil subgrade around the void region continuously increased due to the release of heat energy. Spatially, the distribution of isotherms changed from a layered radioactive distribution to a ring distribution that decreased from inside to outside. During the natural cooling process, the peripheral temperature of the ring isotherm first decreased and a negative temperature ring isotherm gradually formed.

(3) The temperature of the frozen soil subgrade above the void region was greatly affected by the heat energy released by the polymer grouting material, and the rate of temperature change was greater than for the measurement points below the void region. The upper boundary of the influence range of the thermal energy released by the polymer grouting material on the subgrade temperature field was 30 cm, and the lower boundary was 20 cm.

Data Availability

The data used to support the findings of this study are available from the corresponding author upon request.

Conflicts of Interest

The authors declare that they have no conflicts of interest in this work.

Acknowledgments

The authors acknowledge the support received from the National Key Research and Development Plan (grant no. 2018YFB1600200), National Natural Science Foundation of China (grant nos. 51878622 and 51878624), Major Scientific and Technological Special Project in Henan (grant no. 181100310400), Henan Science Fund for Distinguished Young Scholars (grant no. 202300410354), Program for Science and Technology Innovation Talents in Universities of Henan Province (grant no. 19HASTIT041), Key Research Projects of Higher Education in Henan Province (grant no. 18A580001), and Science and Technology R&D Project (grant no. 2017-ZJKJ-PTJS03).

References

[1] S. J. Wang, Z. Wang, and J. B. Chen, *Expressway Layout and Permafrost Environment Coupling in Permafrost Regions of Qinghai Tibet Plateau*, pp. 2–10, Shanghai Scientific & Technical Publishers, Shanghai, China, 2019.

[2] M. Chai, H. Zhang, J. Zhang, and Z. Zhang, "Effect of cement additives on unconfined compressive strength of warm and ice-rich frozen soil," *Construction and Building Materials*, vol. 149, pp. 861–868, 2017.

[3] H. Li, N. Fang, X. Wang, C. Wu, and Y. Fang, "Evaluation of the coordination of structural layers in the design of asphalt pavement," *Applied Sciences*, vol. 10, no. 9, p. 3178, 2020.

[4] W. B. Yu, H. Da, F. L. Han et al., "Heat transfer characteristics of sand-filled embankment in permafrost regions of Tibetan plateau," *Arabian Journal for Science And Engineering*, vol. 45, no. 5, pp. 3683–3693, 2019.

[5] F. Han, W. Yu, X. Zhang, F. Yu, X. Yi, and D. Hu, "Parameter sensitivity analyses of influence on thermal regime of embankment in Permafrost Regions along the Qinghai-Tibet

Engineering Corridor," *Cold Regions Science and Technology*, vol. 166, p. 102817, 2019.

[6] Y.-Z. Zhang, Y.-L. Du, and B.-C. Sun, "Temperature distribution analysis of high-speed railway roadbed in seasonally frozen regions based on empirical model," *Cold Regions Science And Technology*, vol. 114, pp. 61–72, 2015.

[7] Y. Z. Zhang, Y. L. Du, and B. C. Sun, "Roadbed deformation characteristics of roadbed-bridge transition section for high speed railway in seasonal frozen soil region," *China Railway Science*, vol. 37, no. 1, pp. 39–45, 2016.

[8] L. Q. Liu, X. S. Mao, Q. Wu et al., "Mechanism of groundwater migration in the subgrade in a seasonally frozen soil area," *Journal of Cold Regions Engineering*, vol. 33, no. 4, Article ID 06019001, 2019.

[9] M. Chai and J. Zhang, "Improvement of compressibility and thaw-settlement properties of warm and ice-rich frozen soil with cement and additives," *Materials*, vol. 12, no. 7, p. 1068, 2019.

[10] M. Chai, J. Zhang, W. Ma, Z. Yin, Y. Mu, and H. Zhang, "Thermal influences of stabilization on warm and ice-rich permafrost with cement: field observation and numerical simulation," *Applied Thermal Engineering*, vol. 148, pp. 536–543, 2019.

[11] K. S. Lvanov and E. A. Korotkov, "Investigation of the effect of a layer of granulated foam-glass ceramic on the temperature conditions of frozen soil," *Soil Mechanics and Foundation Engineering*, vol. 54, no. 5, pp. 349–355, 2017.

[12] X. H. Liu, J. Q. Jia, and Y. B. Zhang, "Simulation analysis of the long-term stability for frozen soil roadbed," *Mathematical Problems in Engineering*, vol. 20147 pages, Article ID 605890, 2014.

[13] S. G. Zhang and Z. Zhang, "The experimental research of transverse gravel pile preventing roadbed freezing," in *Proceedings of the 2011 International Conference on Multimedia Technology*, pp. 1300–1302, IEEE, Hangzhou, China, July 2011.

[14] J. Liu, B. Tai, and J. Fang, "Ground temperature and deformation analysis for an expressway embankment in warm permafrost regions of the Tibet plateau," *Permafrost and Periglacial Processes*, vol. 30, no. 3, pp. 208–221, 2019.

[15] C. Huang, Q. Li, S. Wu, and Y. Liu, "Subgrade stability evaluation in permafrost regions based on unascertained measurement model," *Geotechnical and Geological Engineering*, vol. 37, no. 2, pp. 707–719, 2019.

[16] H. Zhang, C. Su, X. Bu, Y. Zhang, Y. Gao, and M. Huang, "Laboratory investigation on the properties of polyurethane/unsaturated polyester resin modified bituminous mixture," *Construction and Building Materials*, vol. 260, p. 119865, 2020.

[17] H. Fang, Y. Su, X. Du, F. Wang, and B. Li, "Experimental and numerical investigation on repairing effect of polymer grouting for settlement of high-speed railway unballasted track," *Applied Sciences*, vol. 9, no. 21, p. 4496, 2019.

[18] S. Saleh, N. Z. M. Yunus, K. Ahmad, and N. Ali, "Improving the strength of weak soil using polyurethane grouts: a review," *Construction and Building Materials*, vol. 202, pp. 738–752, 2019.

[19] R. Jia, Q. Xiong, G. Xu, K. Wang, and S. Liang, "A method for two-dimensional temperature field distribution reconstruction," *Applied Thermal Engineering*, vol. 111, pp. 961–967, 2017.

[20] Q. M. Meng, X. S. Mao, Y. S. Fan et al., "Numerical analysis of the effect of roadside accumulated water on subgrade temperature field in the freezing region," *Applied Mechanics and Materials*, vol. 470, pp. 284–288, 2014.

[21] Q. Yu, K. Fan, Y. You, L. Guo, and C. Yuan, "Comparative analysis of temperature variation characteristics of permafrost roadbeds with different widths," *Cold Regions Science and Technology*, vol. 117, pp. 12–18, 2015.

[22] Y. Zeng, K. Liu, X. Zhou, and L. Fan, "Tunnel temperature fields analysis under the couple effect of convection-conduction in cold regions," *Applied Thermal Engineering*, vol. 120, pp. 378–392, 2017.

[23] M. Mahedi, B. Cetin, and K. S. Cetin, "Freeze-thaw performance of phase change material (PCM) incorporated pavement subgrade soil," *Construction and Building Materials*, vol. 202, pp. 449–464, 2019.

[24] Z. W. Zhu and J. G. Ning, "Numerical analysis on thermal and stress coupling of soil subgrade," *Applied Mechanics and Materials*, vol. 29–32, pp. 107–111, 2010.

[25] Y. Sun, C. Du, H. Gong, Y. Li, and J. Chen, "Effect of temperature field on damage initiation in asphalt pavement: a microstructure-based multiscale finite element method," *Mechanics of Materials*, vol. 144, p. 103367, 2020.

[26] J. Y. Yuan, J. H. Cheng, C. F. Wang et al., "Analysis of heat conduction mechanism on tympanites roadbed," *Advanced Materials Research*, vol. 838, pp. 1286–1290, 2014.

[27] L. Jiang and S. Wang, "Enhancing heat release of asphalt pavement by a gradient heat conduction channel," *Construction and Building Materials*, vol. 230, p. 117018, 2020.

[28] A. Sha, Z. Liu, K. Tang, and P. Li, "Solar heating reflective coating layer (SHRCL) to cool the asphalt pavement surface," *Construction and Building Materials*, vol. 139, pp. 355–364, 2017.

[29] L. Cong, F. Yang, G. Guo, M. Ren, J. Shi, and L. Tan, "The use of polyurethane for asphalt pavement engineering applications: a state-of-the-art review," *Construction and Building Materials*, vol. 225, pp. 1012–1025, 2019.

[30] T. Wang, G. Zhou, J. Wang, and T. Chen, "Statistical characteristics and probabilistic analysis of uncertain settlement of subgrade in permafrost regions," *Cold Regions Science and Technology*, vol. 175, p. 103079, 2020.

[31] H. Liu, F. Niu, and H. Guan, "An engineering evaluation index of thermal asymmetry in subgrade and its optimal design in cold regions," *Cold Regions Science and Technology*, vol. 137, pp. 1–6, 2017.

[32] G. Cheng, Z. Sun, and F. Niu, "Application of the roadbed cooling approach in Qinghai-Tibet railway engineering," *Cold Regions Science and Technology*, vol. 53, no. 3, pp. 241–258, 2008.

[33] G. Cheng, Q. Wu, and W. Ma, "Innovative designs of permafrost roadbed for the Qinghai-Tibet Railway," *Science in China Series E: Technological Sciences*, vol. 52, no. 2, pp. 530–538, 2009.

[34] Z. Zhang, Q. Wu, Y. Liu, Z. Zhang, and G. Wu, "Thermal accumulation mechanism of asphalt pavement in permafrost regions of the Qinghai-Tibet Plateau," *Applied Thermal Engineering*, vol. 129, pp. 345–353, 2018.

[35] Z. Liu, W. Yang, and J. Wei, "Analysis of random temperature field for freeway with wide subgrade in cold regions," *Cold Regions Science and Technology*, vol. 106-107, pp. 22–27, 2014.

Hindawi
Advances in Materials Science and Engineering
Volume 2021, Article ID 5573372, 13 pages
https://doi.org/10.1155/2021/5573372

Research Article

Surface Settlement Analysis Induced by Shield Tunneling Construction in the Loess Region

Caihui Zhu [1,2,3]

[1]State Key Laboratory of Eco-hydraulics in Northwest Arid Region, Xi'an University of Technology, Xi'an, Shaanxi 710048, China
[2]Institute of Geotechnical Engineering, Xi'an University of Technology, 5 South Jinhua Road, Xi'an, Shaanxi 710048, China
[3]Shaanxi Provincial Key Laboratory of Loess Mechanics, Xi'an University of Technology, Xi'an, Shaanxi 710048, China

Correspondence should be addressed to Caihui Zhu; zhucaihui123@163.com

Received 19 January 2021; Revised 8 February 2021; Accepted 27 February 2021; Published 12 March 2021

Academic Editor: Xiangtian Xu

The influence and prediction of shield tunneling construction on surface settlement (SS) and adjacent buildings is a hot topic in underground space engineering. In this work, several analytical methods are utilized to estimate the maximum surface settlement (MSS) and conduct a parametric sensitivity analysis based on Xi'an Metro line 2. The results show that there are mainly nine factors influencing the SS induced by shield tunneling construction in loess strata. The disturbance degree of the surrounding soil during the shield advancing stage has the largest influence on the SS, followed by the seepage of the shield lining segments or falling water levels, which lead to the overlying soil consolidation. After this is the grouting filling effect at the shield tail, followed by the reinforcement effect of the tunnel foundation and the track. The smallest influencing factors on the SS are the shield overexcavation and improper shield attitudes during the construction period. The sensitivity analysis results of the above influencing factors may offer a scientific guidance for the control of shield tunneling construction.

1. Introduction

In the Xi'an loess strata, more than 20 subway lines are under construction or being designed. The subways are constructed with the shield tunneling method, and these subways cross beneath ancient sites, architectural structures, ground fissures, underground pipelines (e.g., water and natural gas), and other buildings. Through long-term investigations of the existing subway lines constructed in loess strata, serious issues with the tunnels and subway stations have been reported, such as the uneven deformation of lining segments, soil strata, and pavements; lining seepage; underground pipeline ruptures; and tilting of buildings and foundations. These issues greatly influence the surface settlement (SS) and the structural integrity of adjacent structures. The SS induced by shield construction can be classified into two categories. In the first category, the SS is caused by the improper control of the shield excavation during the construction period. In the second category, the SS occurs during the postconstruction period because of changes in the mechanical properties of the soil around the tunnel. Controlling and forecasting the SS during shield tunneling are the most important geotechnical engineering problem to be solved. A number of analytic methods have been proposed and widely used to predict the SS in the engineering practice [1–11].

In previous research results, there are many analytical estimation methods to predict the SS induced by tunneling construction. The displacement-controlled boundary around the tunnel opening has usually been expressed as different convergence modes in the reported methods, such as the point source theory [1–3, 12], the complex variable theory [4, 5, 13–16], the stress function elastic theory [6, 7, 17, 18], and the stochastic medium method [8, 9]. Huang and Zeng [10] proposed the uniform convergence model and the analytical solution of the stratum displacement for the double-circle shield tunnel. Based on the elastic solutions of Lame and Kiersch, Liu and Zhang [19] also proposed an analytical solution of the SS caused by tunnel excavation under the condition of plane strain and nonuniform stress field. Lu et al. [20] proposed a unified displacement function of the cross section of a circular shallow tunnel under complex geological and construction conditions. This function is expressed by a Fourier series and can reflect the horizontal and vertical asymmetrical deformation behaviors of the tunnel cross section. Shen and Zhu [21] proposed an analytical method using the virtual image technique and Fourier transform solutions to estimate the ground SS caused by the tail void grouting pressure in shield tunnel construction. Fang et al. [22] reported that a normal probability function can be extended to estimate the SS due to shield tunneling, which can consider various types of shield machines, depths, and diameters. Zhang et al. [11] presented an analytical solution by the complex variable method to predict the soil deformation due to tunneling in clay; this approach considers the linear stiffness influence and the nonuniform convergence boundary condition.

The analytical methods that are described above systematically consider the stratum conditions and the shield construction technologies. However, when predicting the SS in the postconstruction period, it is difficult to consider the variable features of unsaturated-saturated loess strata, such as the underground water level decline, the dissipation of pore water pressure, the creep deformation of the surrounding soil, and the train vibration loading. The water seepage issues and the causes of the uneven settlement of the tunnel in Shanghai Metro lines 1 and 2 have been widely investigated and reported. In addition, the SS that has been induced by the additional load, the underground construction, and fall of the ground water level has also been studied by Shen et al. [23–27]. Ng et al. [28] summarized the settlement measurements of Shanghai Metro line 1 from 1994 to 2007, and the relationship between ground pumping, foundation soil compression, and the tunnel settlement has been reported. Soga et al. [29] studied the tunnel deformation caused by the dissipation of excess pore water pressure of the soil and the aging of grouting materials after lining segments in the London subway. A theory for calculating the SS has been proposed, which considers the interactions between the soil and the lining. Based on dynamic load testing, the critical dynamic stress ratio and the dynamic stress amplitude of saturated loess were proposed by Cui [30]; and the SS caused by the subway vibration loading has been calculated.

In addition, the surface settlement induced by freezing construction is becoming a trending issue in the freeze-thaw zone. Zhou et al. [31] and Shen et al. [23] studied the path-dependent mechanical behaviours of frozen loess based on the experimental investigation. Zheng et al. [32] proposed a practical method to simulate and predict the ground surface deformation during the entire artificial ground freezing construction process. A model test system and numerical method were used by Cai et al. [33] to simulate horizontal ground freezing on the heaving displacement of twin tunnels. Zhou et al. [34] published a segregation potential model to predict the frost heaves during freezing construction.

From the above, valuable results have been reported on analytical methods for the SS induced by underground construction; however, there is still no systematic research to explore the influence degrees of different factors on the SS, which is essential for determining the prioritization of SS control measures. On the basis of summarizing previously reported analytical methods and taking the shield construction of the Xi'an Metro in the loess stratum as the research background, the calculation methods of surface settlement induced by nine factors were proposed, and a parametric sensitivity analysis of the maximum surface settlement (MSS) induced by each individual influence factor was conducted. The resulting sensitivity indexes are sorted in order to provide technical guidance for SS controls during the shield tunneling construction.

2. Estimation of the Maximum Surface Settlement

2.1. Maximum Settlement Estimation of the Tunnel Vault during the Construction Period. Due to the improper control of the shield excavation, the factors inducing the settlement of the tunnel vault mainly include (1) inadequate shield support pressure, (2) insufficient grout filling in the shield tail, (3) insufficient grouting pressure, (4) overexcavation by the shield yawing, and (5) improper shield attitude. The methods to calculate the volume loss of the stratum and the SS generated when the tunnel vault deformation is induced by these factors are summarized in the following.

2.1.1. Tunnel Vault Settlement Induced by Inadequate Shield Support Pressure. During the tunneling of the earth pressure-balanced shield machine, the shield support pressure (P_i) plays a dynamic balancing role on the lateral soil pressure (K_0P_0 or $K_0'P_v' + P_w$) at the excavation surface. When the lateral soil pressure between the shield head and the excavation surface is unbalanced, it inevitably leads to the ground uplift and settlement. When $P_i = K_0P_0$ (see Figure 1(a)), the lateral soil pressure is in an equilibrium state, and little additional stress occurs on the excavation surface. When the shield support pressure is lower than the lateral earth pressure ($P_i<K_0P_0$, see Figure 1(b)), the tunnel vault settlement occurs. When the shield support pressure is higher than the lateral earth pressure ($P_i>K_0P_0$, see Figure 1(c)), the tunnel vault and surface uplift. This principle is illustrated in Figure 1.

In order to determine the tunnel vault settlement induced by an inadequate shield support pressure under undrained conditions, Lee and Rowe [35] proposed a two-dimensional analytical solution by considering the three-dimensional elastic-plastic deformation at the excavation surface. The shield support pressure ratio $\beta = P_i/(K_0'P_v' + P_w)$ is introduced into the above solution, and the tunnel vault settlement (u_{c1}) formula can be written as follows:

$$u_{c1} = \frac{\Omega R\left(K_0'P_V' + P_w - P_i\right)}{2E_u} = \frac{\Omega R(1-\beta)\left(K_0'P_V' + P_w\right)}{2E_u}, \tag{1}$$

where u_{c1} is the tunnel vault settlement and Ω is the horizontal displacement coefficient at the shield excavation surface, which is determined by a 3D numerical simulation

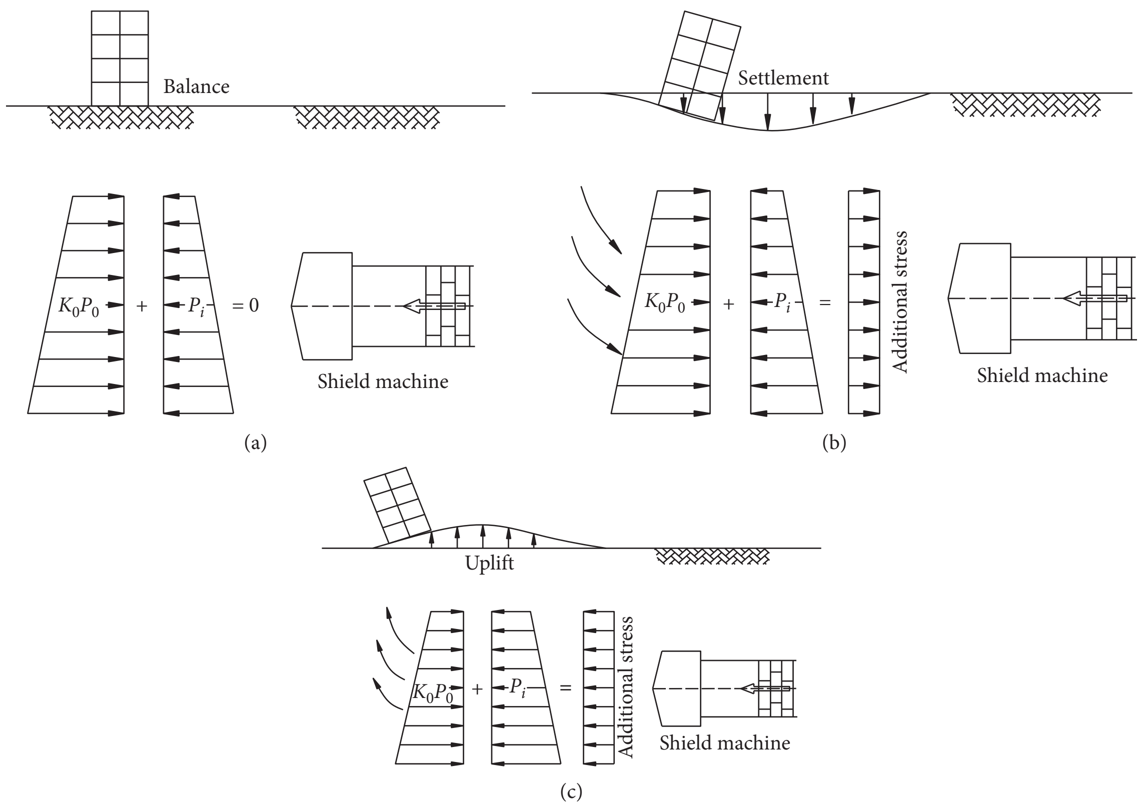

FIGURE 1: Surface movement behavior during the shield machine advancing. (a) $P_i = K_0P_0$. (b) $P_i < K_0P_0$. (c) $P_i > K_0P_0$.

of the shield tunnel excavation. In addition, K_0 is the coefficient of the lateral soil pressure in the tunnel; P_0 is the vertical soil pressure at the tunnel axis (kPa); K_0' is the horizontal lateral pressure coefficient under the undrained condition; P_v' is the vertical effective stress (kPa) at the tunnel axis; P_w is the pore water pressure (kPa) at the tunnel axis; P_i is the support pressure of the shield chamber (kPa); $R = D/2$ is the tunnel excavation radius (m); D is the shield excavation diameter (m); and E_μ represents the undrained elastic modulus of the overlying soil stratum of the tunnel (MPa).

Liu [36] reported that, in reality, drained elastic modulus E_0 is 2.0~5.0 times larger than the compression modulus E_s. He suggested that the relationship between E_0 and E_s could be a function of the initial void ratio (e_0) in the loess stratum:

$$E_0 = \frac{2.718E_s}{e_0}. \tag{2}$$

According to elastic theory, the relationship between the undrained elastic modulus E_u and the partially drained elastic modulus E_0 can be expressed as

$$\frac{E_u}{E_0} = \frac{1+\nu_u}{1+\nu_0}. \tag{3}$$

Therefore, by combining (2) and (3), the undrained elastic modulus can be written as

$$E_u = \frac{2.718E_s\left(1+\nu_u\right)}{\left(1+\nu_0\right)e_0}, \tag{4}$$

where $\nu_u = 0.5$ is the undrained Poisson's ratio and ν_0 is the drained Poisson's ratio. In the loess stratum, ν_0 can be estimated using $\nu_0 = K_0/(1+K_0)$, where K_0 is the coefficient of lateral stress at rest (and is equal to 1.0 under undrained conditions).

Based on the above theory, in shield tunneling construction, the undrained condition means that the soil around the tunnel will not be consolidated and drained during the rapid shield advancing. The soil element is in the uniform compression state, and the coefficient of lateral stress at rest is $K_0 = 1.0$; therefore, the undrained Poisson's ratio $\nu_u = K_0/(1+K_0) = 1/2 = 0.5$.

2.1.2. Tunnel Vault Settlement Induced by Insufficient Grouting at the Shield Tail. During shield tunneling, for controlling the volume loss of the stratum, the grouting at the shield tail can be rapidly filled in the physical gap between the shield shell and the lining $G_p = 2\Delta + \delta$ [35], as illustrated in Figure 2. However, due to the lengthy operation time span, grouting losses can occur during transport, and the grouting volume can shrink and harden. As a result, the grouting cannot fully fill the gap. The soil behind the lining segments collapses, and the tunnel crown settlement occurs.

The settlement of the tunnel crown caused by insufficient grouting at the shield tail is

$$u_{c2} = (1-\omega)G_p, \tag{5}$$

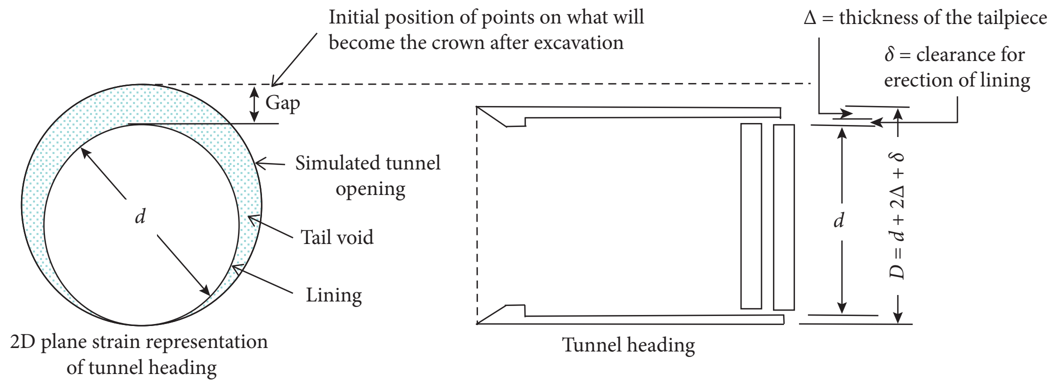

Figure 2: Gap of the shield tail (after Lee and Rowe [35]).

where the parameter G_p is the shield physical gap (mm), d is the outer diameter of the shield segment lining, Δ is the thickness of the shield tail appendages, δ is the lining assembling clearance, and ω is the grouting filling rate. The value of ω is controlled between 0.8 and 1.0; the average value of ω is between 0.90 and 0.95 when the shield control technology is rigorously applied.

2.1.3. Tunnel Vault Settlement Induced by Insufficient Grouting Pressure. As the shield tunnel advances, the synchronous grouting at the shield tail is mainly distributed in the range of 90~180° around the lining arch ring. For a simple analysis, the grouting pressure (P_{il}) at the shield tail is distributed in the "crescent shape" as illustrated in Figure 3. In this way, when the grouting equipment fails or the grouting pressure is not balanced with the initial soil pressure, the soil around the tunnel is inevitably filled into the shield gap, and the volume loss of the stratum occurs. When $P_{il}<P_v$ (see Figure 3(a)), the overlying soil stratum subsides; in contrast, when $P_{il}>P_v$ (see Figure 3(b)), the surface uplifts (i.e., heaves). This principle is illustrated in Figure 3.

Rowe et al. [37] proposed the tunnel vault settlement is caused by an insufficient supporting force. This can be extended to the condition in which the grouting pressure is less than the tunnel vault settlement (u_{c3}). Because the grouting pressure (P_{il}) and the initial soil pressure (P_0) are a pair of unbalanced forces, the grouting pressure ratio $\lambda = P_{il}/P_0$ can be introduced to Rowe's formula to calculate the tunnel vault settlement under different grouting pressure ratios.

$$u_{c3} = \left(\frac{1}{3} \sim \frac{1}{4}\right) \times R\left[1 - \sqrt{\frac{1}{1 + \left(2\left(1 + \nu_u\right)c_u/E_u\right)\left[\exp\left(\left(1 - \lambda\right)P_0 - c_u/2c_u\right)\right]^2}}\right], \tag{6}$$

where E_u, c_u, and ν_u are the undrained elastic modulus (MPa), cohesive strength (kPa), and Poisson's ratio of the overlying strata of the tunnel, respectively. P_0 is the vertical soil pressure of the tunnel axis; P_{il} is the average grouting pressure (kPa) on the tunnel vault; and P_v is the overburden pressure at the tunnel vault. According to the theory of Rowe et al. [37], the values of the coefficients 1/3 and 1/4 in equation (4) are set as follows: when the soil mass at the tunnel crown undergoes elastic deformation, the value is set to 1/3; when the elastic-plastic deformation of the soil mass at the tunnel crown occurs, the value is set to 1/4. The deformation pattern at the tunnel crown is determined by the stability coefficient of the excavation surface N, which has been introduced in Section 2.1.1.

2.1.4. Tunnel Vault Settlement Induced by Overexcavation. As the shield tunnel advances, the heterogeneity of the soil stratum leads to the shield snaking or yawing, causing an overexcavation of the shield. Suppose the radial maximum eccentricity is δ_0, which can be calculated from the measured values of the horizontal eccentricity S_H and vertical eccentricity S_V, and its eccentricity angle is α. Then, the shaded area (S_e) on the tunnel section is the overexcavation area. When the shield tunneling machine is corrected to the design axis, overexcavation inevitably occurs as illustrated in Figure 4. In order to calculate the volume loss of the overburden soil caused by overexcavation, the overexcavation area (S_e) is equivalent to the "crescent" area of the arch. According to the gap parameter principle in Figure 2, the tunnel vault settlement (u_{c4}) caused by the overexcavation can be obtained:

$$u_{c4} = 2\left(\sqrt{2R^2\left(1 - \frac{1}{\pi}\arccos\frac{\kappa L}{2R}\right) + \frac{\kappa L}{2\pi}\sqrt{4R^2 - \kappa^2 L^2}} - R\right), \tag{7}$$

where $\delta_0 = \kappa L$ is the yawing distance of the shield head (mm), κ is the overexcavation rate, $\kappa = 0.0\%–\pm 2.0\%$, and L is the length of the shield tunneling machine (m).

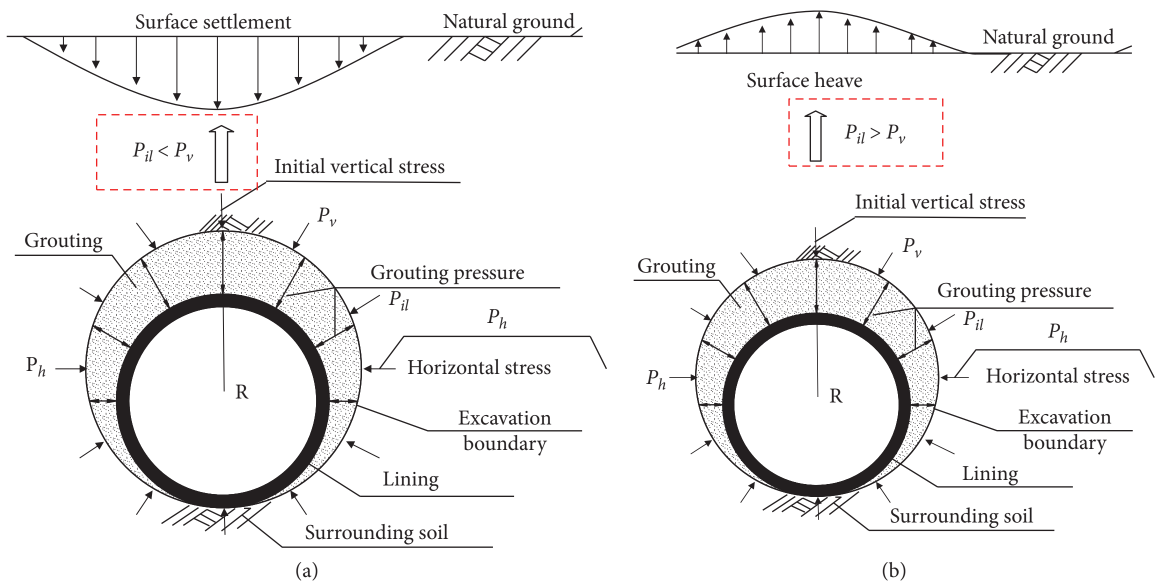

Figure 3: The surface movement during the shield tail grouting: (a) $P_{il} < P_v$ and (b) $P_{il} > P_v$.

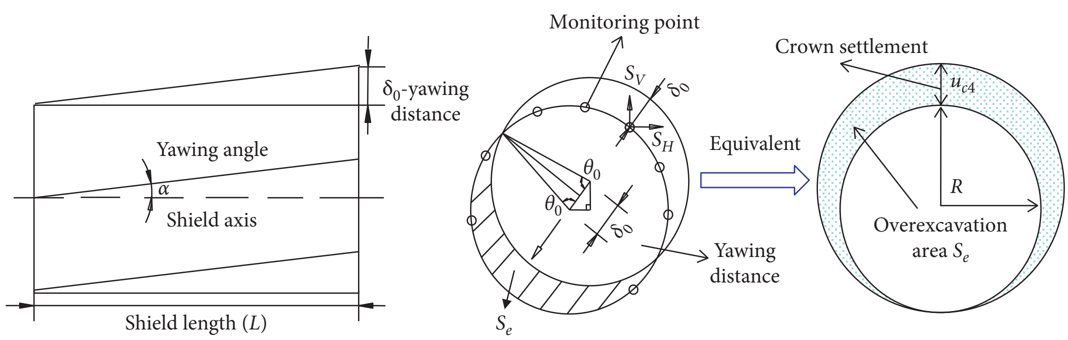

Figure 4: Tunnel vault deformation caused by shield overexcavation.

2.1.5. Tunnel Vault Settlement Induced by Improper Shield Attitude. As the shield tunneling advances, compression deformation occurs at the top or the bottom of the tunnel due to the failure of the tunneling system. The tunnel vault settlement (u_{c5}) caused by the head knocking and lifting of the shield tunneling machine is described as follows:

$$u_{c5} = L\xi, \quad (8)$$

where ξ is the head knocking and lifting slope of the shield tunneling machine deviating from the central axis, generally, the term $\xi = -3.0\%{\sim}+3.0\%$, and L is the length of the shield tunneling machine (m).

2.2. Estimation of the Surface Settlement during the Post-construction Period. The SS caused by the shield tunnel advancing during the construction period can be strictly controlled within the allowed values according to construction experience. However, during the postconstruction period, the geological conditions change over time, which impacts the SS. These dynamic conditions include (1) the recompression of the soil in the loosened circle around the tunnel, (2) the dissipation of excess pore water pressure induced by the shield tunneling advancing, (3) the surrounding soil consolidation due to the failure of the waterproofing behind the lining and the underground water level decline, (4) the foundation settlement caused by the train vibration loading, etc.

2.2.1. Recompression Settlement of the Soil in the Loosened Circle. As the shield advances and cuts, the surrounding soil is disturbed and loosened due to the friction effect between this soil and the shield machine. This can lead to the plastic deformation and instability of the surrounding soil. The radius of the loosened circle is R_0, and the ratio of the loosened circle radius to the shield tunnel excavation radius is defined as $\eta = R_0/R$. Because of the recompression of the loosened soil around the tunnel, the uniform convergence deformation of the tunnel boundary is calculated as follows:

$$\begin{aligned} u_{p1} &= m_v'[\gamma(H - R_0) - P_{il}](R_0 - R) \\ &= m_v'(\eta - 1)R[\gamma(H - \eta R) - P_{il}], \end{aligned} \quad (9)$$

where u_{p1} is the uniform convergence deformation of the loosened soil circle; H is the buried depth of the tunnel axis (m); m_v' is the soil volume compression coefficient of the loosened circle (MPa^{-1}), which is 3~5 times that of undisturbed soil; if considering the secondary grouting or strata pre-reinforcement effect, the volume compression coefficient of the soil m_v' is 0.2~1.0 times that of undisturbed soil; and R_0 is the plastic zone radius of the loosened soil circle (m), which is calculated as follows:

$$R_0 = R\left\{\frac{(1-\sin\varphi)\left[0.5\left(1+K_0\right)P_0-\left(1-K_0\right)P_0+c/\tan\varphi\right]}{P_{il}+c/\tan\varphi}\right\}^{((1-\sin\varphi)/2\sin\varphi)}, \tag{10}$$

where c and φ are the cohesive force (kPa) and the internal friction angle (°) of the soil mass, respectively, K_0 is the lateral pressure coefficient of the soil mass, and P_{il} is the grouting pressure (kPa). If no measured data are available, P_{il} can be taken as the recommendation by Liu [36]:

$$P_{il} = (0.25-0.50)\frac{\gamma R[1+\tan(\pi/4-\varphi/2)]}{\tan\varphi}. \tag{11}$$

Suppose the stratum volume loss (V) due to the recompression of the soil in the loosened circle can be expressed as follows:

$$V = \pi\left[R_0^2-\left(R_0-u_{p1}\right)^2\right]. \tag{12}$$

Then, according to equation (7), the relationship among the total convergence deformations of the tunnel ($2u_{p1}$), the MSS (S_{p1}), and the volume loss (V) is

$$\begin{cases} 2u_{p1} = \dfrac{V}{\sqrt{2\pi}\, i_{z1}}, \\ \\ S_{p1} = \dfrac{V}{\sqrt{2\pi}\, i_1}. \end{cases} \tag{13}$$

The settlement trough width (i_{z1}) caused by soil recompression in the loosened circle during the post-construction period is inconsistent with the surface settlement trough width (i_1) during the construction period. According to experience [38], the relationship between i_{z1} and i_1 can be expressed as $i_{z1} = (1-0.65z_1/H)i_1$, where, $z_1 = H - R_0$. Thus, S_{p1} induced by the recompression of the loosened circle can be written as

$$S_{p1} = 2u_{p1}\left(1-0.65\frac{z}{H}\right) = 2u_{p1}\left[0.35+0.65\frac{R_0}{H}\right]. \tag{14}$$

2.2.2. Consolidation Deformation Caused by the Dissipation of Excess Pore Pressure. As the tunnel advances below the underground water level, when the thrust and friction of the shield tunneling machine and the grouting pressure are not balanced in the initial stress field, the additional load generates. Then, the soil within a certain range around the tunnel exhibits an excess pore pressure. It is assumed that the excess pore pressure at the tunnel crown is P_1, and the excess pore pressure at the ground surface is P_2. The underground water level is d_w below the surface, and the vertical distance between the initial underground water level and the tunnel axis is h_w. According to the measurement, the distribution characteristics of the excess pore pressure around the tunnel are illustrated in the shaded part in Figure 5.

When the shield tunnel passes through the research region, the excess pore pressure gradually dissipates, and the consolidation deformation of the ground surface occurs. It can be calculated as follows [39]:

$$S_{p2} = \frac{(h_w-R)k_y t}{\sqrt{2\pi} i_2}, \tag{15}$$

where S_{p2} is the SS value caused by the excess pore pressure dissipation; k_y is the weighted average of the vertical permeability coefficient (m/d) of the overlying soil layers; i_2 is the settlement trough width; h_w is the depth of the underground water level from the tunnel axis (m); and t is the dissipation time of the excess pore pressure (d). The dissipation time is related to the average excess pore pressure P and the average compression modulus E_s of the soil skeleton as follows:

$$t = \frac{\sqrt{2\pi} kHP}{E_s k_y}. \tag{16}$$

When considering situations in which foundation reinforcement measures are taken, the term E_s can be replaced with the composite foundation formula $E_{sp} = [1+m(n-1)]\alpha E_s$, where m is the replacement rate, n is the pile-soil modulus ratio, and α is the compression modulus ratio between the piles and the soil. According to engineering experience, $E_{sp} \approx 1.5\text{–}6.0E_s$; for saturated loess strata, the average value is $E_{sp} = 4.0E_s$.

When there are no measured data, the average additional pressure (P) at the excavation surface is $P = \pm 20$ kPa. The average excess pore pressure ($P = (P_1+P_2)/2$) in the saturated soil around the tunnel during shield tunnel advancing can also be approximately calculated by Xu [40].

(1) When $N = (K_0'P_v' + P_w - P_i)/c_u > 0$,

$$P = 0.5c_u\left[(N+1+a\sqrt{6}) + a\sqrt{6}\left(\frac{R}{H}\right)^2 \exp(N-1)\right]. \tag{17}$$

(2) When $N = (K_0'P_v' + P_w - P_i)/c_u < 0$,

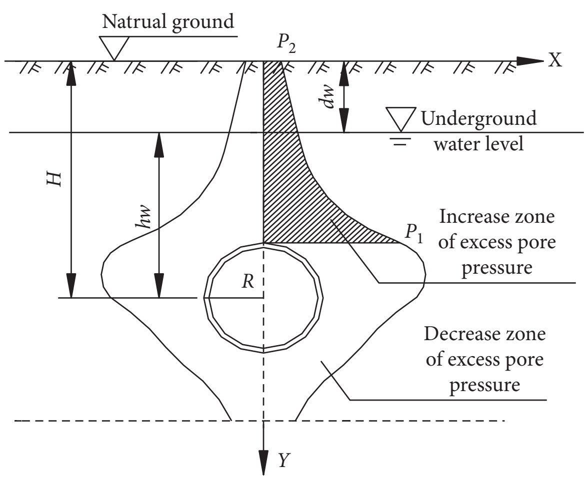

Figure 5: Distribution of excess pore water pressure.

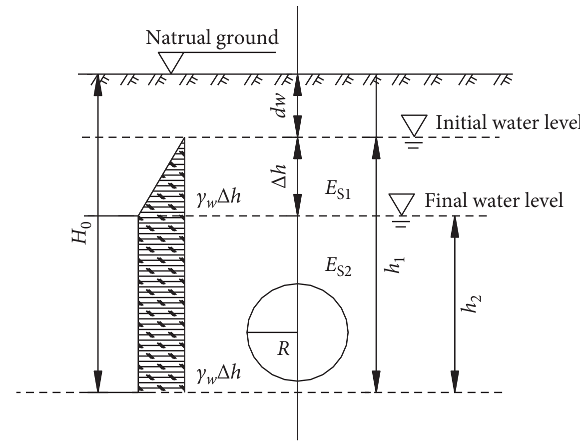

Figure 6: Additional stress caused by the decline of the underground water level.

$$P = 0.5c_u\left[(a\sqrt{6} - N - 1) + a\sqrt{6}\left(\frac{R}{H}\right)^2 \exp(-N-1)\right], \tag{18}$$

where c_u is the undrained shear strength, a is the Henkel coefficient, for saturated loess, $a = 0.12$, and the other parameters have the same physical meaning as for (1). Now, assuming the excess pore pressure ratio $\psi = P/P_0$, the SS caused by the excess pore pressure dissipation is written as

$$S_{p2} = \frac{(h_w - R)P}{E_s} = \frac{(h_w - R)\psi P_0}{E_s}. \tag{19}$$

2.2.3. Consolidation Deformation Caused by the Decline of the Underground Water Level. The underground water level declines when the drainage facilities of the underground structure of the shield tunnel fail, which leads to the long-term consolidation settlement of the ground surface. Suppose that the initial underground water level below the surface is d_w, and H_0 is the reference depth below the surface. The initial water level, the final water level, and the decline of the water level are h_1, h_2, and $\Delta h = h_1 - h_2$, respectively. E_{s1} is the soil compression modulus after consolidation (MPa), and E_{s2} is the compression modulus of the saturated soil (MPa). The water level decline and the effective stress of soil changes are illustrated in Figure 6.

According to Figure 6, based on one-dimensional consolidation theory, the consolidation deformation (S_1) caused by the water level decline within the scope of Δh and the compression deformation (S_2) caused by the increase of the effective stress within the scope of h_2 can be calculated as follows:

$$\begin{cases} S_1 = \dfrac{0.5\gamma_w \Delta h^2}{E_{s1}}, \\[2ex] S_2 = \dfrac{\gamma_w \Delta h\left(H_0 - \Delta h - d_w\right)}{E_{s2}}. \end{cases} \tag{20}$$

Assume that the average densities of loess strata and pore water are $\gamma_l = 19\,\text{kN/m}^3$ and $\gamma_w = 9.8\,\text{kN/m}^3$, respectively, and H_0 is the calculation depth of the additional stress due to the water level decline. According to the theory of soil mechanics, suppose that $\gamma_w \Delta h = 0.2\gamma_l H_0$ and the term H_0 is approximately equal to $3\Delta h$; then, the total consolidation settlement (u_{p3}) at the initial water level caused by the water level decline is

$$u_{p3} = \zeta\gamma_w \Delta h\left[\frac{\Delta h}{2E_{s1}} + \frac{2\Delta h - d_w}{E_{s2}}\right]. \tag{21}$$

When $2\Delta h - d_w \leq 0$, take $2\Delta h - d_w = 0$; when $\Delta h > h_w + R$, take $\Delta h = h_w + R$. If there are no measured values, the term E_{s1} is equal to $1.2E_{s2}$. ζ is the settlement adjustment coefficient, which considers the loess structural and hardening effect after the water loss in the loess; the term $\zeta = 0.3$ is used in the saturated loess area. The decline in the ratio of the water level can be defined as $\theta = \Delta h/h_w$, while equation (21) can be expressed as a function of θ as follows:

$$u_{p3} = \zeta\gamma_w \Delta h\left[\frac{\theta h_w}{2E_{s1}} + \frac{(2\theta + 1)h_w - H}{E_{s2}}\right]. \tag{22}$$

Assume that the stratum volume loss (V) due to the consolidation settlement is equal to $2Ru_{p3}$, while the relationship among the maximum SS (S_{p3}), u_{p3}, and V can be expressed as follows:

$$\begin{cases} u_{p3} = \dfrac{V}{\sqrt{2\pi}\, i_{z3}}, \\[2ex] S_{p3} = \dfrac{V}{\sqrt{2\pi}\, i_3}. \end{cases} \tag{23}$$

According to the theory proposed by Han [38], the relationship between the deep layer settlement trough width (i_{z3}) and the surface settlement trough width (i_3) can be written as $i_{z3} = (1 - 0.65z_3/H)\, i_3$, and the term $z_3 = d_w$. Based on the above principles, the MSS value of S_{p3} caused by consolidation can be obtained as follows:

$$S_{p3} = \frac{i_{z3}}{i_3}u_{p3} = u_{p3}\left(1 - 0.65\frac{d_w}{H}\right). \tag{24}$$

2.2.4. Seismic Surface Settlement Caused by the Train Vibration Loading. During the operational period of the subway, the large and medium pores of saturated loess in the tunnel foundation collapse under the train vibration cyclic loading. This causes a certain fatigue damage and compaction phenomenon of the tunnel foundation, and the settlement of the overlying soil and tunnel occurs. Based on extensive dynamic triaxial cyclic testing of saturated loess strata of the Xi'an subway, Zhang [41] reported that the dynamic stress ratio $R_d = 0.026{\sim}0.192$ when the vibration frequency $f = 2.0$ Hz. In addition, the author reported the following empirical equation that relates the loess residual strain (ε_s^c) and R_d:

$$\varepsilon_s^c = 2cR_d^m\frac{\arctan\left(202.44R_d^m\right)}{\pi}, \tag{25}$$

where $c = 0.333$, $m = 1.259$, and $R_d = 0.5\sigma_d/\sigma_3$; σ_d is the amplitude of the dynamic stress (kPa), and σ_3 is the initial confining pressure of the soil (kPa).

According to the existing empirical analyses, the influence depth of the dynamic stress load (h_d) is reported to as being between 3.0 and 5.0 m beneath the tunnel foundation. In this way, the seismic SS of the saturated loess under the tunnel foundation can be obtained. It should be noted that when the tunnel foundation is unsaturated loess, the seismic deformation does not exist. Based on the theory of stratum volume loss, the volume loss due to seismic deformation (V) is equal to $2Rh_d\varepsilon_s^c$, and the seismic settlement at the tunnel crown can be obtained as follows:

$$u_{p4} = \frac{V}{\sqrt{2\pi}i_{z4}} = \frac{2Rh_d\varepsilon_s^c}{\sqrt{2\pi}i_{z4}} = \frac{0.51cRR_d^m\arctan\left(202.44R_d^m\right)h_d}{i_{z4}}, \tag{26}$$

where i_{z4} is the width of the settlement trough at depth $z_4 = H\text{-}R$; i_4 is the width of the surface settlement trough caused by the seismic settlement. According to the theory proposed by Han [38], $i_{z4} = [1 - 0.65(H\text{-}R)/H)]i_4$. The MSS of S_{p4} caused by the train vibration loading can be written as follows:

$$S_{p4} = \frac{i_{z4}}{i_4}u_{p4} = u_{p4}\left(1 - 0.65\frac{H-R}{H}\right) = u_{p4}\left(0.35 + 0.65\frac{R}{H}\right). \tag{27}$$

2.3. Modified Peck Curve of the Surface Settlement Trough

2.3.1. Surface Settlement Prediction during the Construction Period. It is assumed that the convergence form of tunnel sections is "crescent" shaped, as shown in Figure 2, and the volume loss caused by the convergence of tunnel sections beneath undrained conditions during the shield tunnel construction is equal to that caused by the SS. According to the concept of volume loss [12] and the Peck formula [42], the MSS during the shield construction period under different influencing factors can be estimated. The relationship among S_c, volume loss (V_l), surface settlement trough width (i), shield tunnel excavation radius (R), and tunnel vault settlement (u_c) during the construction period is written as follows:

$$S_c = \frac{V_l\pi R^2}{\sqrt{2\pi}i} = \frac{\pi R^2\left(4u_cR + u_c^2\right)}{4R^2\sqrt{2\pi}i} = \frac{0.313\left(4u_cR + u_c^2\right)}{i}. \tag{28}$$

By taking the aforementioned five influencing factors into consideration, the estimated expressions of the cumulative MSS (S_c) and the cumulative tunnel vault settlement (u_c) during the construction period can be obtained as follows:

$$\begin{cases} S_c = \sum_{j=1}^{5} S_{cj}, \\ u_c = \sum_{j=1}^{5} u_{cj}, \end{cases} \tag{29}$$

where S_{cj} and u_{cj} are the MSS value and the tunnel vault settlement during the construction period, respectively; $j = 1{\sim}5$ is the number of influencing factors; and i is the SS trough width (m). Based on reported experiences, the SS trough width $i = kH$, where k is the coefficient of the SS trough width.

The formula for estimating the SS trough curve (S_{xc}) during the construction period can be obtained by integrating the aforementioned five factors (the five factors are shown in Section 2.1, which are the settlement induced by inadequate shield support pressure, the settlement induced by insufficient grouting at the shield tail, the settlement induced by insufficient grouting pressure, the settlement induced by overexcavation of the shield, and the settlement induced by improper shield attitude, respectively.) as follows:

$$S_{xc} = S_c\left[\frac{-x^2}{2i^2}\right], \tag{30}$$

where x is the horizontal distance between the surface point and the tunnel axis (m).

2.3.2. Surface Settlement Trough Prediction during the Postconstruction Period. Based on Peck's formula [42], the SS during the postconstruction period by considering the above four influencing factors (the four factors are shown in Section 2.2, which are the recompression settlement of the soil in the loosened circle, the consolidation deformation caused by the dissipation of excess pore pressure, the consolidation deformation caused by the decline of the underground water level, and the seismic SS caused by the train vibration loading, respectively) can be obtained as follows:

Table 1: Physical and mechanics parameters of the tunnel's surrounding soils.

Soil types	w (%)	γ_d (kN/m^3)	e_0	c' (kPa)	φ' (°)	c_u (kPa)	K_0'	$K_{20}\times10^{-5}$ (cm/s)	C_v (10^{-3} cm^2/s)	E_s (MPa)	m_v' (MPa^{-1})
Miscellaneous fill	22.5	14.8	0.84	—	—	—	—	—	—	5.6	0.54
Plain fill	23.8–25.8	13.9–14.8	0.86–0.96	—	—	15	0.70	—	—	5.3–6.0	0.5–0.7
New loess	24.6–25.4	14.9–15.5	0.76–0.83	35–36	24.1–26.0	20–24	0.65–0.63	1.2–3.5	1.09–2.16	6.8–7.6	0.39–0.44
Saturated loess	25.5	15.7	0.78	35	22.2	26	—	—	—	6.0	0.50
Ancient soil	22.8–24.9	15.8–16.4	0.66–0.73	40	25.0–26.7	25–26	0.62–0.64	2.92	0.96	5.8–7.2	0.42–0.52
Old loess	22.8–23.9	16.0–16.4	0.66–0.70	32–46	20.1–26.4	22–30	0.60–0.69	0.42–6.1	0.12–2.19	6.9–7.1	0.40–0.42
Silty clay	22.0–22.5	16.4–16.6	0.64–0.66	42–50	27.3–29.3	23–35	0.59–0.61	0.01–1.4	1.06–1.92	7.2–7.8	0.38–0.42

Note: the physical meaning of the parameters is, namely, w: water content, γ_d: dry bulk density, E_s: compression modulus, e_0: pore ratio, c' and φ': index of effective shear strength, m_v': compression coefficient of remorphic loess in the disturbed area, K_0': side pressure coefficient, K_{20}: permeability coefficient, and C_v: consolidation coefficient under nondrainage conditions.

$$S_{xp} = S_{p1}\left[\frac{-x^2}{2i_1^2}\right] + S_{p2}\left[\frac{-x^2}{2i_2^2}\right] + S_{p3}\left[\frac{-x^2}{2i_3^2}\right] + S_{p4}\left[\frac{-x^2}{2i_4^2}\right], \tag{31}$$

where i_1, i_2, i_3, and i_4 are the width of the SS trough under different influencing factors during the postconstruction period.

2.3.3. Total Surface Settlement Trough Prediction. According to the SS characteristics during the construction period and the postconstruction period, the estimating formula for the SS curve with consideration of the above nine influencing factors based on Peck's formula is obtained as follows:

$$\begin{aligned} S_x = S_{xc} + S_{xp} = S_c\left[\frac{-x^2}{2i^2}\right] + S_{p1}\left[\frac{-x^2}{2i_1^2}\right] + S_{p2}\left[\frac{-x^2}{2i_2^2}\right] \\ + S_{p3}\left[\frac{-x^2}{2i_3^2}\right] + S_{p4}\left[\frac{-x^2}{2i_4^2}\right]. \end{aligned} \tag{32}$$

3. Sensitivity Analysis of the MSS Inducement

3.1. Determination of the Influencing Factors. In order to further explore the nine factors (shield support pressure ratio β, grouting filling rate ω, grouting pressure ratio λ, overexcavation rate κ, slope of the shield tunneling machine deviating from the central axis ξ, the ratio of the loosened circle radius η, excess pore pressure ratio ψ, decline in the ratio of the water level θ, and dynamic stress ratio R_d) with respect to their influence degree of the MSS, it is necessary to carry out a single-factor sensitivity analysis. For this study, Xi'an Metro line 2 is taken as the engineering background, and the soil stratum of the tunnel is described as follows: (1) miscellaneous fill (0.5~12.0 m), (2) plain fill (0.0~12.0 m), (3) new loess (0.0~9.0 m), (4) saturated loess (0.0~5.0 m), (5) ancient soil (2.0~5.0 m), (6) old loess (3.0~6.0 m), and (7) silty clay (more than 20 m). The underground water level is 9~12 m below the ground surface, and the tunnel vault is approximately 1~8 m below the underground water level. The shield tunnel crosses the silty clay layer, and above the tunnel crown is the saturated loess. The physical indexes and mechanical parameters of the soil stratum are presented in Table 1 [43].

The tunnel axis of Xi'an Metro line 2 is buried 14~22 m below the ground surface, with an average of $H = 19$ m, the tunnel excavation diameter is $D = 6.2$ m, the length of the shield tunneling machine $L = 8.68$ m, the physical gap of the shield tunneling machine is $G_p = 160$ mm, the control standards for the overexcavation rate are $\kappa = -2.0\%\sim+2.0\%$, and the slope of the shield tunneling machine deviating from the central axis is $\xi = -3.0\%\sim+3.0\%$. According to the engineering experiences of the Xi'an Metro, the variation range of the aforementioned influencing factors and other calculation parameters can be determined; these are presented in Table 2.

3.2. Determination and Analysis of the Sensitivity Index. In order to accurately describe the influence degree of various factors on the MSS, the sensitivity coefficient (M) is introduced. The sensitivity index of a certain factor (F) to the MSS is M_F:

$$M_F = \frac{(\Delta S/S)}{\Delta F/F}, \tag{33}$$

where ΔS is the difference between the MSS of a certain influencing factor and its reference value F, S is the MSS under the reference influencing factor, $\Delta S/S$ is the variation ratio of the MSS, F is the reference value of the influencing factor, ΔF is the variation of the influencing factor F, and $\Delta F/F$ is the variation rate of the influencing factor. When $M_F > 0$, it means that the MSS is positively correlated with the influencing factor F; when $M_F < 0$, it means that the MSS is inversely related to the influencing factor F.

According to formula (33), the sensitivity coefficients of the nine factors mentioned above are defined as follows: M_β, M_ω, M_λ, M_κ, M_ξ, M_η, M_ψ, M_θ, and $M_R d$; these factors can be calculated according to formulas (34) to (42) in Table 3.

Based on equation (32) and Table 2, the calculated MSS and the average sensitivity indexes with different influencing factors are presented in Figure 7. The curves of $\Delta S/S$ and $\Delta F/F$ are illustrated in Figure 8.

From Figures 7 and 8, it can be seen that

Table 2: Numerical analysis schemes for a single factor.

Influencing factors	Parameter's range					Calculate required parameters
β	0.3	0.4	0.5	0.8	0.9	$H = 19$ m, $R = D/2 = 3.1$ m, $G_p = 160$ mm, $i = 8.17$ m
ω	0.8	0.85	0.9	0.95	0.99	$E_{s1} = 6.6$ MPa, $E_{s2} = 5.5$ MPa, $E_u = 25.6$ MPa, $e_0 = 0.76$, $\nu_u = 0.50$, $\nu_0 = 0.39$, $\gamma = 19$ kN/m^3, $K_0' = 0.64$
λ	0.5	0.7	0.9	1.0	1.2	
κ	0.1%	0.5%	1.0%	1.5%	2.0%	$c_u = 20.9$ kPa, $c' = 35.5$ kPa, $\varphi' = 24.4°$
ξ	0.1%	0.8%	1.5%	2.5%	3.0%	$P_0 = \gamma H - P_w = 281$ kPa, $P_w = 80.0$ kPa
η	1.01	1.05	1.1	1.2	1.5	$P_v = \gamma(H - h_w) + \gamma'(h_w - R) = 253.1$ kPa, $K_0'P_v' + P_w = 242$ kPa
ψ	0.02	0.07	0.14	0.21	0.28	$h_w = 8.0$ m, when $\Delta h \le 0.5(H - h_w)$, $\Delta h = 0.5(H - h_w) = 5.5$ m, and $\Delta h \le R + h_w = 11.1$ m
θ	0.69	0.94	1.19	1.31	1.38	
R_d	0.03	0.08	0.a13	0.16	0.2	$h_d = 3$ m

Table 3: Sensitivity indexes of different influencing factors of the MSS.

$M_\beta = (\Delta S_{c1}/S_{c1})/(\Delta\beta/\beta)$	(34)	$M_\eta = (\Delta S_{p1}/S_{p1})/(\Delta\eta/\eta)$	(39)
$M_\omega = (\Delta S_{c2}/S_{c2})/(\Delta\omega/\omega)$	(35)	$M_\psi = (\Delta S_{p2}/S_{p2})/(\Delta\psi/\psi)$	(40)
$M_\lambda = (\Delta S_{c3}/S_{c3})/(\Delta\lambda/\lambda)$	(36)	$M_\theta = (\Delta S_{p3}/S_{p3})/(\Delta\theta/\theta)$	(41)
$M_\kappa = (\Delta S_{c4}/S_{c4})/(\Delta\kappa/\kappa)$	(37)	$M_{Rd} = (\Delta S_{p3}/S_{p3})/(\Delta Rd/Rd)$	(42)
$M_\xi = (\Delta S_{c5}/S_{c5})/(\Delta\xi/\xi)$	(38)		

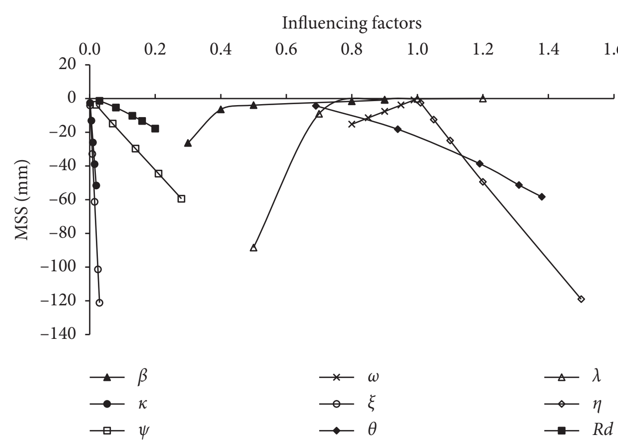

Figure 7: MSS values under different influencing factors.

(1) The MSS tends to decrease with the increase of β, ω, and λ, indicating that the rate of change of these three influencing factors is inversely correlated with the change rate of the SS. Six influence factors (i.e., κ, η, ξ, ψ, θ, and R_d) have positive relationships with the MSS.

(2) From the slope of the relationship curve between the incremental change rate of ($\Delta S/S$) and the incremental change rate of influencing factors ($\Delta F/F$), it shows that, during the construction period, the change of the grouting filling rate (ω) is the most sensitive influence factor to the MSS, followed by the grouting pressure ratio (λ).

(3) During the postconstruction period, the ratio of the loosened circle radius (η) has the most sensitive influence on the MSS, followed by the decline amount ratio of the water level (θ). It can be seen that the grouting effect of the shield tail and the disturbance degree to the surrounding soil during the construction period of shield tunneling have significant influence on the MSS.

(4) Table 3 shows that the average sensitivity index of the nine influencing factors can be ordered from highest to lowest, i.e., $M_\eta = 98.97$, $M_\theta = 11.20$, $M_\omega = 4.00$, $M_{Rd} = 2.14$, $M_\lambda = 1.30$, $M_\beta = 1.15$, $M_\psi = 1.00$, $M_\kappa = 0.99$, and $M_\xi = 0.99$. This order shows that the disturbance degree to the surrounding soil during the shield tunnel advancing has the most significant influence on the MSS. When the declining ratio for the water level is high due to seepage of lining segments, the long-term SS during the post-construction period is also significant. During the construction period of shield tunneling, the grouting filling effect and the control of grouting pressure have great influence on the SS. When the tunnel foundation and track are not reinforced, the SS

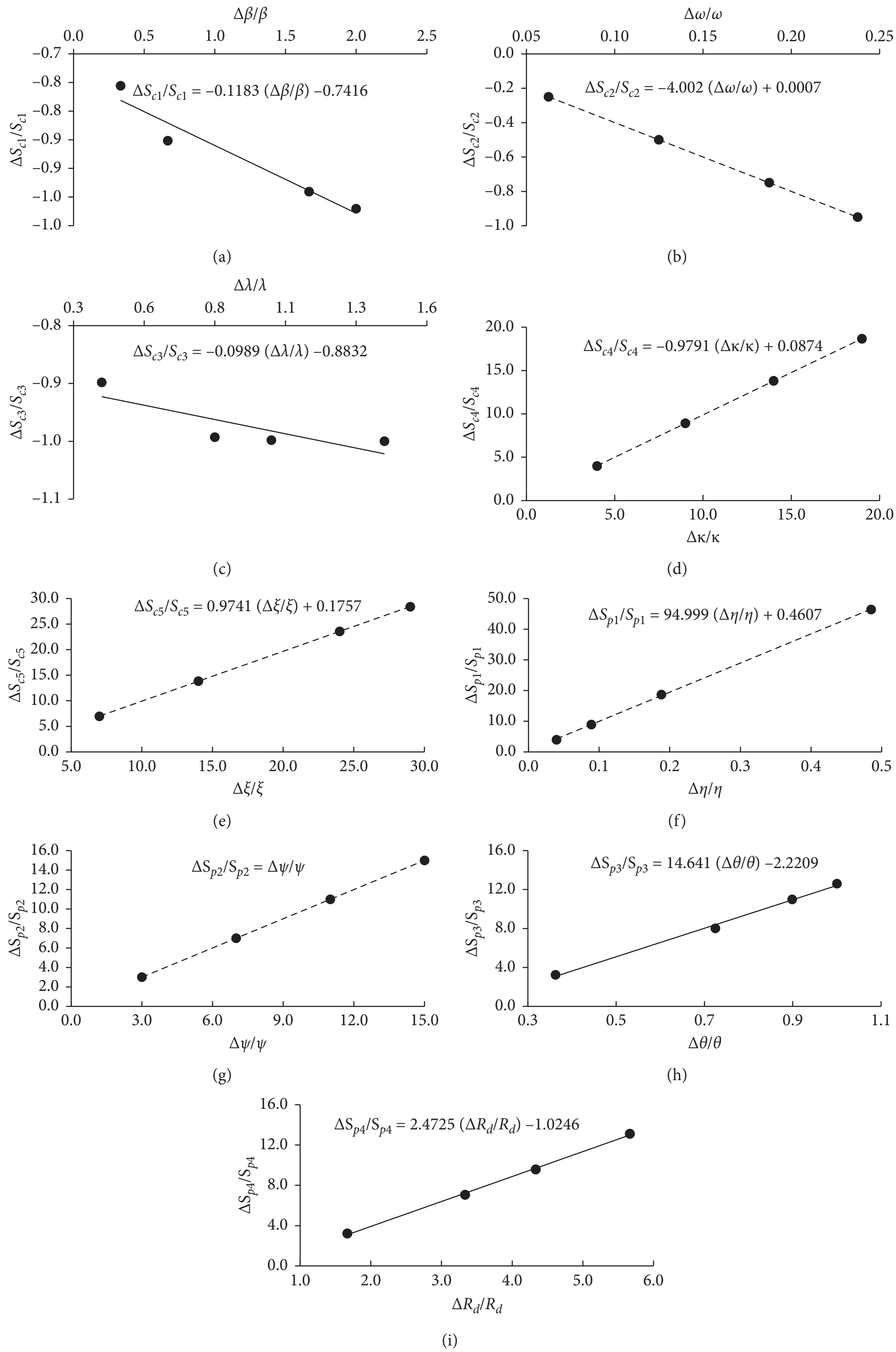

FIGURE 8: Relationship between the MSS ratio and the influencing factor ratios: (a) $\Delta S_{c1}/S_{c1} - \Delta\beta/\beta$, (b) $\Delta S_{c2}/S_{c2} - \Delta\omega/\omega$, (c) $\Delta S_{c3}/S_{c3} - \Delta\lambda/\lambda$, (d) $\Delta S_{c4}/S_{c4} - \Delta\kappa/\kappa$, (e) $\Delta S_{c5}/S_{c5} - \Delta\xi/\xi$, (f) $\Delta S_{p1}/S_{p1} - \Delta\eta/\eta$, (g) $\Delta S_{p2}/S_{p2} - \Delta\psi/\psi$, $\Delta S_{p3}/S_{p3} - \Delta\theta/\theta$, and (i) $S_{p4}/S_{p4} - \Delta R_d/R_d$.

caused by the train vibration loading cannot be ignored. The dissipation of the excess pore water pressure and the adjustment of the shield attitude are all related to the control technology during the construction period of shield tunneling.

4. Conclusion

(1) The SS during the construction period and the postconstruction period induced by the shield tunneling construction mainly includes nine influencing factors: ① inadequate shield support pressure, ② insufficient grouting filling in the shield tail, ③ insufficient grouting pressure, ④ overexcavation by shield yawing, ⑤ improper shield attitude, ⑥ the recompression of the soil in the loosing circle around the tunnel, ⑦ the dissipation of excess pore water pressure induced by the shield tunneling advancing, ⑧ the surrounding soil consolidation due to the failure of waterproofing techniques used behind the lining and the decline in the underground water level, and ⑨ the foundation settlement caused by the train vibration loading.

(2) The average sensitivity index of the above nine influencing factors can be ordered from highest to lowest: $M_\eta = 98.97$ (the ratio of the loosened circle radius η), $M_\theta = 11.20$ (decline in the ratio of the water level θ), $M_\omega = 4.00$ (grouting filling rate ω), $M_{Rd} = 2.14$ (dynamic stress ratio Rd), $M_\lambda = 1.30$ (grouting pressure ratio λ), $M_\beta = 1.15$ (shield support pressure ratio β), $M_\psi = 1.00$ (excess pore pressure ratio ψ), $M_\kappa = 0.99$ (overexcavation rate κ), and $M_\xi = 0.99$ (slope of the shield machine deviating from the central axis ξ). It indicates that the largest influencing factor on surface settlement is the ratio of the loosened circle radius, and the smallest one is the slope of the shield tunneling machine deviating from the central axis.

(3) In summary, the disturbance degree of the surrounding soil during the shield tunnel advancing has the most significant influence on the MSS. The decline of the underground water level has the second largest influence on the SS. The grouting fill effect has the third greatest influence on the SS. The grouting pressure at the shield tail and the shield support pressure at the shield head have the fifth and sixth largest influences on the SS. When the tunnel foundation and the track are not reinforced, the SS caused by the train vibration loading cannot be ignored. The dissipation of the excess pore water pressure, overexcavation rate, and shield machine deviating from the central axis have the seventh, eighth, and ninth influence on the SS.

(4) When the shield tunnels pass through the saturated loess stratum, the disturbance degree on the surrounding soil during shield advancing should be well controlled. The pre-reinforcement measures for the saturated soil within 3~5 m around the tunnel should be taken, and the appropriate antiseepage and vibration reduction measures should be taken for the lining segments and the track, respectively.

Data Availability

No data, models, or code were generated or used during the study.

Conflicts of Interest

The author declares that there are no conflicts of interest.

Acknowledgments

The author would like to extend their gratitude to the National Natural Science Foundation of China (no. 51678484) and the Research Fund of the State Key Laboratory of Eco-hydraulics in Northwest Arid Region, Xi'an University of Technology (2019KJCXTD-12), who funded this research.

References

[1] C. Sagaseta, "Analysis of undraind soil deformation due to ground loss," *Géotechnique*, vol. 37, no. 3, pp. 301–320, 1987.

[2] A. Verruijt and J. R. Booker, "Surface settlements due to deformation of a tunnel in an elastic half plane," *Géotechnique*, vol. 46, no. 4, pp. 753–756, 1996.

[3] N. Loganathan and H. G. Poulos, "Analytical prediction for tunneling-induced ground movements in clays," *Journal of Geotechnical and Geoenvironmental Engineering*, vol. 124, no. 9, pp. 846–856, 1998.

[4] L.-Z. Wang, L.-L. Li, and X.-J. Lv, "Complex variable solutions for tunneling-induced ground movement," *International Journal of Geomechanics*, vol. 9, no. 2, pp. 63–72, 2009.

[5] J. Fu, J. Yang, L. Yan, and S. M. Abbas, "An analytical solution for deforming twin-parallel tunnels in an elastic half plane," *International Journal for Numerical and Analytical Methods in Geomechanics*, vol. 39, no. 5, pp. 524–538, 2015.

[6] A. Abbas, "Drained and undrained response of deep tunnels subjected to far-field shear loading," *Tunnelling and Underground Space Technology*, vol. 25, no. 1, pp. 21–31, 2010.

[7] K. H. Park, "Elastic solution for tunneling-induced ground movements in clays," *International Journal of Geomechanics*, vol. 4, no. 4, pp. 310–318, 2004.

[8] L. Ding, L. Ma, H. Luo, M. Yu, and X. Wu, "Wavelet analysis for tunneling-induced ground settlement based on a stochastic model," *Tunnelling and Underground Space Technology*, vol. 26, no. 5, pp. 619–628, 2011.

[9] X. L. Yu and J. M. Wang, "Ground movement prediction for tunnels using simplified procedure," *Tunnelling and Underground Space Technology*, vol. 26, no. 3, pp. 462–471, 2011.

[10] D. Huang and B. Zeng, "Influence of double-o-tube shield rolling on soil deformation during tunneling," *International Journal of Geomechanics*, vol. 17, no. 11, Article ID 04017105, 2017.

[11] Z. Zhang, M. Huang, X. Xi et al., "Complex variable solutions for soil and liner deformation due to tunneling in clays," *International Journal of Geomechanics*, vol. 18, no. 7, Article ID 04018074, 2018.

[12] C. González and C. Sagaseta, "Patterns of soil deformations around tunnels. Application to the extension of Madrid

Metro," *Computers and Geotechnics*, vol. 28, no. 6-7, pp. 445–468, 2001.

[13] A. Verruijt, "Deformations of an elastic half plane with a circular cavity," *International Journal of Solids and Structures*, vol. 35, no. 21, pp. 2795–2804, 1998.

[14] A. Verruijt and J. R. Booker, "Complex variable analysis of Mindlin's tunnel problem," in *Proceedings of the Booker Memorial Symposium, Developments in Theoretical Geomechanics*, pp. 3–22, Balkema, Rotterdam, Netherlands, 2000.

[15] A. Verruijt and O. E. Strack, "Buoyancy of tunnels in soft soils," *Géotechnique*, vol. 58, no. 6, pp. 513–515, 2008.

[16] J. Fu, J. Yang, H. Klapperich et al., "Analytical prediction of ground movements due to a nonuniform deforming tunnel," *International Journal of Geomechanics*, vol. 16, no. 4, Article ID 04015089, 2016.

[17] W.-I. Chou and A. Bobet, "Predictions of ground deformations in shallow tunnels in clay," *Tunnelling and Underground Space Technology*, vol. 17, no. 1, pp. 3–19, 2002.

[18] K.-H. Park, "Analytical solution for tunnelling-induced ground movement in clays," *Tunnelling and Underground Space Technology*, vol. 20, no. 3, pp. 249–261, 2005.

[19] J. F. Liu and H. Z. Zhang, "Semianalytical solution and parameters sensitivity analysis of shallow shield tunneling-induced ground settlement," *Advances in Materials Science and Engineering*, vol. 2017, Article ID 3748658, 8 pages, 2017.

[20] D. Lu, F. Kong, X. Du, C. Shen, Q. Gong, and P. Li, "A unified displacement function to analytically predict ground deformation of shallow tunnel," *Tunnelling and Underground Space Technology*, vol. 88, pp. 129–143, 2019.

[21] C. Shen and Z. Zhu, "Analytical method for evaluating the ground surface settlement caused by tail void grouting pressure in shield tunnel construction," *Advances in Civil Engineering*, vol. 2018, Article ID 3729143, 10 pages, 2018.

[22] Y.-S. Fang, C.-T. Wu, S.-F. Chen, and C. Liu, "An estimation of subsurface settlement due to shield tunneling," *Tunnelling and Underground Space Technology*, vol. 44, pp. 121–129, 2014.

[23] M. D. Shen, Z. W. Zhou, and S. J. Zhang, "Effect of stress path on mechanical behaviours of frozen subgrade soil," *Road Materials and Pavement Design*, vol. 2021, no. 8, pp. 1–30, 2020.

[24] S.-L. Shen, H.-N. Wu, Y.-J. Cui, and Z.-Y. Yin, "Long-term settlement behaviour of metro tunnels in the soft deposits of Shanghai," *Tunnelling and Underground Space Technology*, vol. 40, no. 1, pp. 309–323, 2014.

[25] Y.-S. Yin, L. Ma, Y.-J. Du, and S.-L. Shen, "Analysis of urbanisation-induced land subsidence in Shanghai," *Natural Hazards*, vol. 63, no. 2, pp. 1255–1267, 2012.

[26] H.-N. Shen, R.-Q. Huang, W.-J. Sun et al., "Leaking behavior of shield tunnels under the Huangpu River of Shanghai with induced hazards," *Natural Hazards*, vol. 70, no. 2, pp. 1115–1132, 2014.

[27] C.-Y. Shen, S.-L. Shen, J. Han, G.-L. Ye, and S. Horpibulsuk, "Hydrogeochemical environment of aquifer groundwater in Shanghai and potential hazards to underground infrastructures," *Natural Hazards*, vol. 78, no. 1, pp. 753–774, 2015.

[28] C. W. W. Ng, G. B. Liu, and Q. Li, "Investigation of the long-term tunnel settlement mechanisms of the first metro line in Shanghai," *Canadian Geotechnical Journal*, vol. 50, no. 6, pp. 674–684, 2013.

[29] K. Soga, R. G. Laver, and Z. Li, "Long-term tunnel behaviour and ground movements after tunnelling in clayey soils," *Underground Space*, vol. 2, no. 3, pp. 149–167, 2017.

[30] G. Q. Cui, *Dynamic Constitutive Model for Saturated Loess and Deformation Analysis for Soil Around Subway Tunnel*Xi'an University of Architecture & Technology, Xi'an, China, 2014.

[31] Z. W. Zhou, W. Ma, S. J. Zhang, Y. H. Mu, and G. Y. Li, "Experimental investigation of the path-dependent strength and deformation behaviours of frozen loess," *Engineering Geology*, vol. 265, Article ID 105449, 2020.

[32] L. Zheng, Y. Gao, Y. Zhou, T. Liu, and S. Tian, "A practical method for predicting ground surface deformation induced by the artificial ground freezing method," *Computers and Geotechnics*, vol. 130, Article ID 103925, 2021.

[33] H. Cai, S. Li, Y. Liang, Z. Yao, and H. Cheng, "Model test and numerical simulation of frost heave during twin-tunnel construction using artificial ground-freezing technique," *Computers and Geotechnics*, vol. 115, Article ID 103155, 2019.

[34] J. Zhou, W. Zhao, Y. Tang et al., "Practical prediction method on frost heave of soft clay in artificial ground freezing with field experiment," *Tunnelling and Underground Space Technology*, vol. 107, Article ID 103647, 2021.

[35] K. M. Lee and R. K. Rowe, "Settlement due to tunneling: Part II -Evaluation of a prediction technique," *Canadian Geotechnical Journal*, vol. 29, no. 5, pp. 941–954, 1992.

[36] Z. D. Liu, *Mechanics and Engineering of Loess*, Shanxi Science and Technique Publishing House, Xi'an, China, 1997.

[37] R. K. Rowe, K. Y. Lo, and G. J. Kack, "A method of estimating SS above tunnels constructed in soft ground," *Canadian Geotechnical Journal*, vol. 20, no. 8, pp. 11–22, 1983.

[38] X. Han, *The Analysis and Prediction of Tunnelling-Induced Building Deformation*, Xi'an University of Technology, Xi'an, China, 2006.

[39] J. Liu and X. Hou, *Shield Tunneling*, China Railway Press, Beijing, China, 1991.

[40] F. Xu, "The analysis of pore water pressure and ground settlement caused by shield tunneling and deep excavation in soft clay," Doctorial thesis, Tongji University, Shanghai, China, 1991.

[41] K. Zhang, *Vibration and Settlement of Loess Due to Subway Moving Loads*, Xi'an University of Architecture & Technology, Xi'an, China, 2011.

[42] R. B. Peck, "Deep excavations and tunneling in soft ground," in *Proceedings of the 7th International Conference on Soil Mechanics and Foundation Engineering*, pp. 225–290, Balkema, Rotterdam, Netherlands, 1969.

[43] C. Zhu and N. Li, "Prediction and analysis of surface settlement due to shield tunneling for Xi'an Metro," *Canadian Geotechnical Journal*, vol. 54, no. 4, pp. 529–546, 2017.

[44] Zhang, *Study on the Laws of Surface Settlement Induced by Shield Construction and Control Technology of Xian Subway Tunnel*Xian University of Science and Technology, Xi'an, China, 2011.

Hindawi
Advances in Materials Science and Engineering
Volume 2021, Article ID 5538059, 10 pages
https://doi.org/10.1155/2021/5538059

Research Article

Numerical Simulation of Effects of River Reconstruction on Flooding: A Case Study of the Ba River, China

Haixiao Jing ,[1] Yongbiao Lang,[2] Xinhong Wang ,[1] Mingyang Yang,[1] and Zongxiao Zhang[1]

[1]*State Key Laboratory of Eco-Hydraulics in Northwest Arid Region of China, Xi'an University of Technology, Xi'an 710048, China*
[2]*Qinghai Research Institute of Investigation & Design of Water Conservancy & Hydropower, Xining 810001, China*

Correspondence should be addressed to Xinhong Wang; wxh@mail.xaut.edu.cn

Received 25 January 2021; Revised 19 February 2021; Accepted 24 February 2021; Published 5 March 2021

Academic Editor: Yanhu Mu

The local reconstruction of river channels may pose obstacles of flood flow, local eddy currents, or high flow velocity which pose potential threats to human life and infrastructures nearby. In the design of such projects, the effects of local reconstruction of the river channel on flooding are often evaluated by the one-dimensional method, which is based on the formula of one-dimensional nonuniform flow. In this study, a two-dimensional hydrodynamic model based on shallow water equations is employed to investigate the impacts of river reconstruction on flooding in the Ba River, China. The finite volume method and an unstructured triangular mesh are used to solve the governing equations numerically. The numerical model is validated by comparison with the results of a physical model of 1 : 120 scale. The backwater effects and impacts of flood flow fields under two flood frequencies are analyzed by comparing the numerical results before and after local reconstruction. The results show that the backwater length under both 10-year and 100-year floods can be reached up to the upstream boundary of the computational domain. However, the maximum water level rises are limited, and the levees in this river channel are safe enough. The flow velocity fields under both floods are changed obviously after local reconstruction in the Ba River. Areas with the potential for scour and deposition of the river bed are also pointed out. The findings of this study are helpful for the evaluation of flood risks of the river.

1. Introduction

River flooding, which is commonly caused by sudden and intense rainfalls or storms in the river's watershed, can cause loss of human lives and serious damage to infrastructures and properties along the river. Furthermore, with the climate change (such as global warming) in recent years, it has been found that extreme rainfalls occur more intensely and therefore result in more serious floods [1, 2]. For river channels through urban areas, hydraulic structures such as weirs and artificial islands are often designed to raise the water level upstream where wetlands or parks are built to improve the scenery nearby. For the design of such hydraulic structures, flooding is treated as one of the most important factors. In addition, the presence of such structures will affect the flooding of the river channel. Therefore, proper evaluation of the impact of river reconstruction on river floods is of great help for the design of river projects and flood risk management of the river channel.

Traditionally, during the design of hydraulic structures, the effects on river flooding are mostly evaluated by the one-dimensional (1D) method which is based on the law of conservation of energy [3, 4]. In this method, the main emphasis is placed on backwater effects. Besides this, the unsteady 1D method based on shallow water equations or Saint-Venant equations is applied widely to evaluate the flood risks of river channels. Forster et al. [5] investigated the flooding and emptying process of a proposed storage area on the Middle Elbe River, where a 1D hydrodynamic model was used for a 20 km reach of the Elbe River and the storage area was modeled by two storage cells each representing one polder basin. Tomasz et al. [6] studied the impact of a bridge on flooding of the Warta River near Wronki in Poland using the 1D HEC-RAS package. Petaccia and Natale [7] developed a 1D numerical model (ORSADEM) and applied it to analyze flood inundation of the Brembo River. Generally, because of their lower computational cost, 1D numerical models have been widely used for the evaluation of river floods. However, for the complex topography of local river channels, such as the curvature and bifurcation, the flow fields are complex and vary in two horizontal coordinates, so the 1D model cannot reproduce the details of the flow fields. Consequently, coupled 1D and 2D models or 2D models were developed and employed to predict flood inundation [8–11].

With the development of the LIDAR technique [12, 13], message passing interface (MPI), and graphic processing unit (GPU) techniques [14–16] in recent years, digital elevation model (DEM) data can be obtained efficiently, and the computational efficiency of 2D models has been improved greatly, promoting the development and application of 2D hydrodynamic models. 1D and 2D unsteady and nonuniform flow modeling of the flood wave routed down river valleys has been presented, including modeling of a channel bifurcation at the confluence and backwater effects [8]. A coupled 1D and 2D hydrodynamic model for flood risk management in urban areas was developed to overcome the drawbacks of each individual modeling approach, and an additional module was used to simulate the rainfall-runoff process in study areas [9]. Using MIKE 21 FM, Wang et al. [10] investigated the effects of bridge piers on river floods in the Jialing River, China. Ahn et al. [17] carried out a numerical simulation to predict the urban inundation area due to extreme rainfall using the Mike21 model. Full-scale fluvial flood modeling over large catchments was carried out using coupled hydrological and hydraulic/hydrodynamic models [11]. By using a multiple modern GPU acceleration technique, more than 2.5 times faster than real time was achieved although it involved 100 million computational cells inside the computational domain. In general, the 2D numerical models are expected to predict the flood flow fields more accurately, which is of great help for the design of hydraulic projects and the management of flood risks.

In this study, the effects of local river reconstruction in the Ba River on flooding are studied by employing a 2D hydrodynamic model. The backwater effects due to the reconstruction of the river channel are analyzed. The velocity fields before and after local reconstruction are also compared and analyzed. The remainder of this study is structured as follows. The study areas and details of the numerical model and validation are presented in Section 2, where the results of a physical model of 1 : 120 scale are used to validate the accuracy of the numerical model developed. In Section 3, backwater effects and flow fields before and after local reconstruction are investigated for two different flood frequencies. According to the flow field results, local scour or deposition of the river channel after reconstruction is also analyzed. Finally, the main conclusions are drawn in Section 4.

2. Materials and Methods

2.1. Study Area. The Ba River, which is one of the main tributaries of the Wei River, originates from the north of the Qinling Mountains, with a total length of 104 km and a total watershed area of 2581 km^2. The upper reach of the Ba River is in the Qinling Mountains, where the terrain is high in the south and low in the north. The average bed slope in the upper reach is about 9%, and floods rise and fall rapidly with a small amount of sediment. The middle and lower reaches of the Ba River have bed slopes of 2.35% and 1.58%, respectively. According to statistics from the Maduwang hydrological station, the maximum flood peak discharge of the Ba River is 2160 m^3/s (August 12, 1953), the multiyear average discharge is 16.8 m^3/s, and the annual total runoff is 529 million m^3. The runoff from July to August is 42.7% that of the whole year, while from December to February of the following year, the runoff is only 6.7% that of the whole year. The annual average sediment concentration is 5.4 kg/m^3, and the annual average sediment load is 2.86 million tons.

The project area is located in the lower reach of the Ba River, which flows through Xi'an city, then into the Wei River, and finally into the Yellow River, as can be seen in Figure 1. The lower reach of the Ba River has a total length of 8.17 km. Three weirs have been built in this reach; these are the 0# weir, 1# weir, and Guangyuntan weir from downstream to upstream. The levees in this reach are designed for 100-year floods with a peak discharge of 3300 m^3/s. With the purpose of building an artificial lake for the 2021 National Games of China, in this project, the reach between Guangyuntan weir and 1# weir, which is about 2.5 km long, is reconstructed by widening the cross section locally and building two artificial islands. With this reconstruction, the water level upstream of the 1# weir will be increased to meet the landscape requirement in this area. However, after local reconstruction, the flood risks in this reach will be changed and must be evaluated carefully. Scientific suggestions or guides must be provided for a better design of this project, which is the purpose of this study.

2.2. Model Description. In this study, a well-documented software MIKE 21 FM, which was developed by the Danish Hydraulic Institute (DHI), was used. The governing equations (in the Cartesian coordinate system) of the model are the two-dimensional shallow water equations, given by

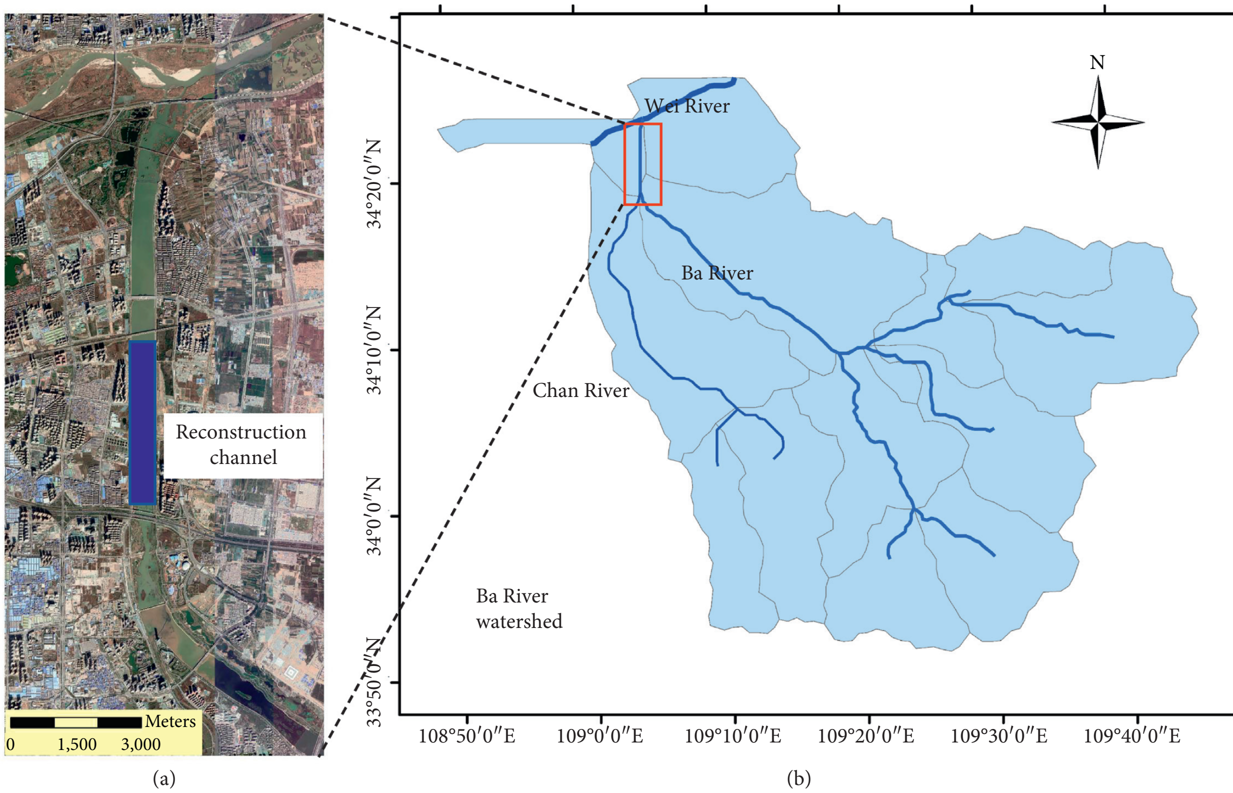

FIGURE 1: Location of the project area: (a) project river channel; (b) watershed of the Ba River.

$$\begin{aligned}
&\frac{\partial h}{\partial t}+\frac{\partial h\overline{u}}{\partial x}+\frac{\partial h\overline{v}}{\partial x}=0,\\
&\frac{\partial h\overline{u}}{\partial t}+\frac{\partial h\overline{u}^2}{\partial x}+\frac{\partial h\overline{uv}}{\partial y}+gh\frac{\partial \zeta}{\partial x}+\frac{g\overline{u}\sqrt{\overline{u}^2+\overline{v}^2}}{C^2}-\frac{1}{\rho}\left[\frac{\partial}{\partial x}\left(h\tau_{xx}\right)+\frac{\partial}{\partial y}\left(h\tau_{xy}\right)\right]=0,\\
&\frac{\partial h\overline{v}}{\partial t}+\frac{\partial h\overline{uv}}{\partial x}+\frac{\partial h\overline{v}^2}{\partial y}+gh\frac{\partial \zeta}{\partial y}+\frac{g\overline{v}\sqrt{\overline{u}^2+\overline{v}^2}}{C^2}-\frac{1}{\rho}\left[\frac{\partial}{\partial x}\left(h\tau_{xy}\right)+\frac{\partial}{\partial y}\left(h\tau_{yy}\right)\right]=0,
\end{aligned} \tag{1}$$

where t is the time; x and y are the horizontal coordinates; h is the total water depth; ζ is the free surface elevation; and $\overline{u}$ and $\overline{v}$ are the depth-averaged velocities in the x and y directions, respectively. g denotes gravitational acceleration; C is the Chezy resistance, which is calculated by the Manning formula. ρ is the water density; and τ_{xx}, τ_{xy}, and τ_{yy} are components of effective shear stress.

The finite volume method was employed to solve the above equations numerically, and a triangular mesh was used. Specifically, the second-order Runge-Kutta method was applied for the time integration. An approximate Riemann solver (Roe's scheme) was used to calculate the fluxes at cell boundaries. A linear gradient reconstruction technique was employed to achieve second-order spatial accuracy. To avoid numerical oscillations, a second-order TVD slope limiter (Van Leer limiter) was used. More details about the numerical method can be found in the MIKE 21 FM manual [18].

To ensure stability during simulation, the time step was adjusted according to the CFL (Courant-Friedrichs-Lewy) number, which is defined as

$$\mathrm{CFL}_{HD}=\left(\sqrt{gh}+|u|\right)\frac{\Delta t}{\Delta x}+\left(\sqrt{gh}+|v|\right)\frac{\Delta t}{\Delta y}, \tag{2}$$

where Δx and Δy are the mesh sizes in the x and y directions, which are approximately the minimum side length of the triangular meshes, and Δt is the time step.

2.3. Numerical Model Setup. The topographies before and after reconstruction of the river channel are presented in Figure 2; these were provided by the Xi'an Water Conservancy Planning Survey and Design Institute, China. For irregular land boundaries, a high-quality unstructured mesh is of great importance to ensuring an accurate numerical simulation. The computational meshes in this study were

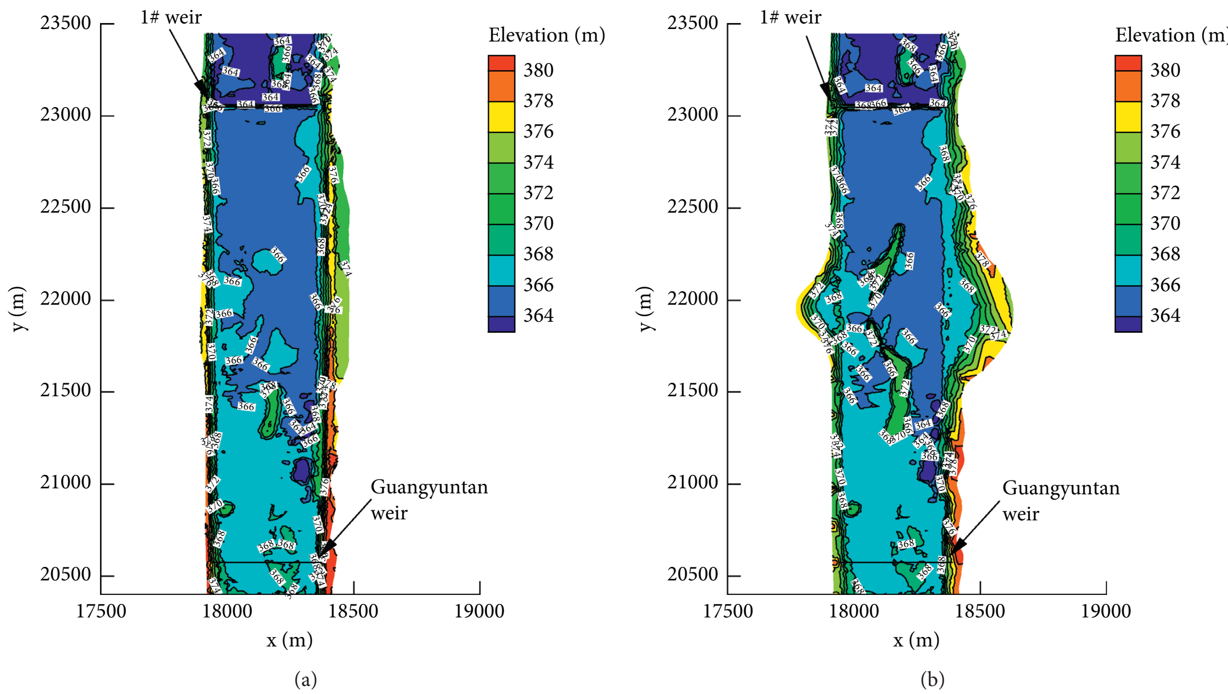

Figure 2: Topographies of the river channel. (a) Before reconstruction. (b) After reconstruction.

generated using the Mesh Generator provided by MIKE software. To ensure the quality of the generated mesh, three parameters, the maximum element area, the smallest allowable angle, and the maximum number of nodes, were provided by Mesh Generator. In this study, we chose the maximum element area as 150 m^2, the smallest allowable angle as 29 degrees, and the maximum number of nodes as 100,000. For the computational domain before reconstruction, there were a total of 17132 elements, while a total of 18411 elements were generated in the mesh of the computational domain after reconstruction. The two sets of meshes before and after local reconstruction were used to investigate the impacts of local reconstruction of the river channel on flooding. Note that the artificial islands, which may be submerged during floods, were identified automatically by the wet and dry boundary method during the simulation.

The Manning coefficient n, which represents the overall resistance of the channel bed, is one of the key parameters for flood simulation. In this study, a constant Manning coefficient ($n = 0.03\ m^{-1/3}s$) was used, which was calibrated by results of a physical model, as detailed in the following section.

Boundary conditions at the upstream and downstream cross sections are also important and have to be specified carefully. In this study, steady-state conditions were taken into account to provide guides for engineering design. Hence, maximum flood discharges were used at the upstream boundary, and constant water levels were used at the downstream boundary. Two scenarios with 10-year and 100-year floods are analyzed in this study. From hydrological analysis, the peak discharges of 10-year and 100-year floods in this river are 1700 m^3/s and 3300 m^3/s, respectively. Water levels at the downstream boundary are affected by several factors such as the topography of the downstream channel and the water level of the Wei River downstream. After careful analysis, the corresponding water levels at downstream boundary are determined to be 369.48 m and 370.55 m for the 10-year and 100-year floods, respectively. Due to the steady-state condition, the initial water levels can be set arbitrarily, and in this study, constant water level the same as the water level at the downstream boundary was used and the initial velocities were set to zeros.

Time step was self-adaptive according to the CFL condition. During computation, the depth at each element was monitored, and the elements were classified as dry, partially dry, or wet. Then, wet and dry interfaces were monitored to identify flooded boundaries.

2.4. Model Validation. Validation of the numerical model was undertaken by comparing it with the results of a 1 : 120 scale physical model of the reconstructed river channel. The physical model was constructed in a laboratory field of Xi'an University of Technology, China. The domain of the physical model was the same as that of the numerical model, ranging from Guangyuntan weir upstream to 1# weir downstream with a length of about 2.6 km, as shown in Figure 3. The physical model was designed according to the gravity similarity criterion. The flood water levels and velocity magnitudes at the locations of 13 cross sections with equal spatial intervals were measured, as shown in Figure 3.

The longitudinal profiles of the sectional average water levels for 10-year and 100-year floods are presented in Figure 4. For 10-year floods, it can be seen that the numerical water level agrees better with experimental data in the

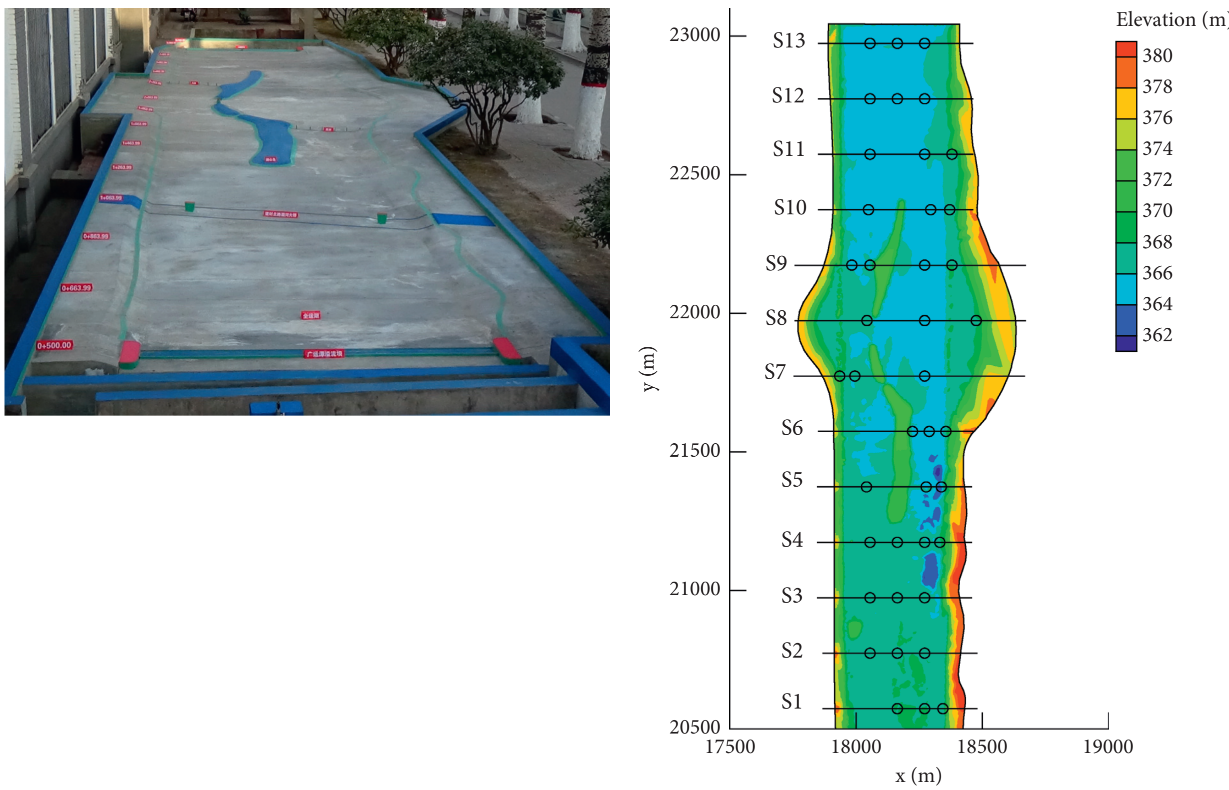

(a) (b)

Figure 3: Physical model and measurement sections and points (circles: measurement points). (a) Picture of the physical model. (b) Measurement sections and points.

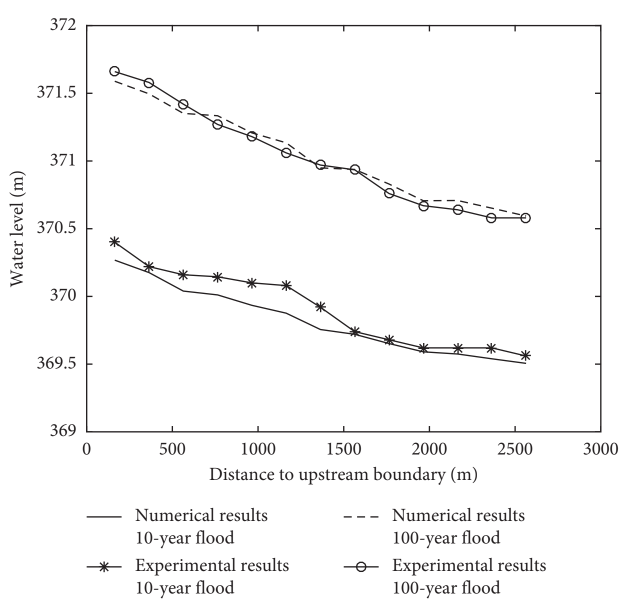

Figure 4: Comparison of longitudinal water level profiles.

downstream channel (distance to upstream boundary 1500 m to 2600 m) than in the upper channel (distance to upstream boundary 0 m to 1500 m), where backwater effects are expected due to the reconstruction of the river channel. The maximum error of the water level was 0.2 m. For 100-year floods, the numerical water level profile fits better with the experimental data for the entire channel, with a maximum error of 0.08 m. In general, the numerical model can well predict the flood water level.

For the flood velocity field, it is noted that the depth-averaged velocities were obtained by the numerical model, while in the physical model, they were approximated by averaging the velocities at two vertical levels of each measurement point. Specifically, due to the small scale used in this study, the maximum water depth in the physical model was about 0.06 m, which corresponds to 7.2 m in the full-scale model. Therefore, at each specific location, two velocities, one at the free surface and another near the bottom, were measured and used to approximate the depth-averaged velocity. The numerical and experimental results of velocity magnitudes at 42 points for a 100-year flood are presented in Figure 5. The dashed line $y = 0.9678x + 0.03086$ denotes a linear fit of the data, which is very close to $y = x$, representing a perfect fit of two datasets. The coefficient of determination R^2, which represents the degree of linear-correlation of variables and ranges between 0 and 1, was found to be 0.8349 (the higher the value, the better the fit). Further, the relative errors were calculated and the results show that there were 26 points with relative errors less than 10%. The maximum error was 18.7% at the left point of section S8; this is probably due to the complex topography near this area. For the 10-year

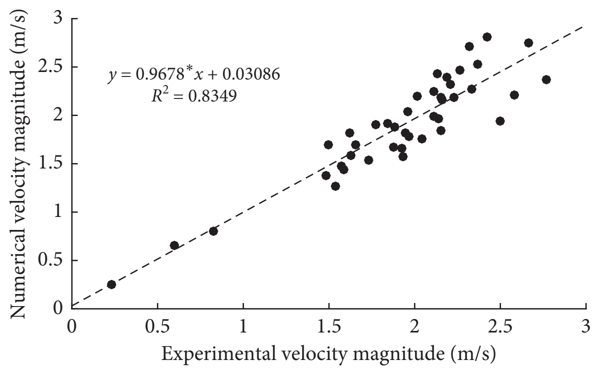

Figure 5: Comparison of flood velocity magnitudes under 100-year floods.

flood, the velocity in the physical model was too small to be measured accurately by pitot tube and will not be used here. Overall, the numerical model developed here was demonstrated to be accurate and appropriate for use in the following analysis.

3. Results and Discussion

The developed numerical model was applied to simulate the flood field before and after river reconstruction for two typical flood frequencies, 10-year and 100-year floods. An analysis of the effects of river reconstruction on the flood flow field was carried out by comparing the results before and after river reconstruction. The effects on both flood water elevations and flow velocity fields are analyzed, and some suggestions are then proposed to guide the project design.

3.1. Backwater Effects. Backwater effects caused by an obstruction in rivers are a common phenomenon which increase flood risk by raising the water level upstream. Comparisons of water surface profiles along the river channel before and after river reconstruction (i.e., at the 13 cross sections) are presented in Figure 6. From the figure, it can be observed that water surface elevations in the upper channel (S1 to S8) rose obviously after local reconstruction, while in the downstream channel (S9 to S13), the flood water surface elevations remained almost unchanged before and after reconstruction under both flood frequencies. The backwater effects were obvious and were mainly due to the construction of the artificial islands (S5 to S10) which blocked flood flow by reducing the river cross sections locally. For the backwater length, it was found that under both flood frequencies the effects of river reconstruction reached up to the upstream boundary (Guangyuntan weir) of the computational domain.

Quantitatively, the maximum water level rises were 0.23 m at section S5 for a 100-year flood and 0.17 m at section S5 for a 10-year flood. The flood water surface slopes were also calculated as 0.036% and 0.041% before and after reconstruction, respectively, for a 100-year flood and 0.03% and 0.032% before and after reconstruction, respectively, for a 10-year flood.

In addition, the levees on both sides of the river were built for 100-year floods. We compared the elevations of the tops of the levees with the computed flood water surface elevations at the 13 sections. The results show that the minimum difference is 5.82 m at section S13 and the maximum difference is 10.11 m at section S1. This demonstrates that the levees for this river channel are safe enough. In general, the effects of local reconstruction on flood water elevation were found to be limited.

It is noted that, for the design of such a project, backwater effects are often evaluated via one-dimensional analysis, in which only cross sections are used. For complex channel sections, the local friction factor has to be determined empirically in the one-dimensional analysis. Besides this, only the cross-sectional average velocities are provided, while it is obvious that the flow field near an artificial island is two dimensional, as reported in the following subsection. Therefore, a two-dimensional method is more appropriate for this type of project.

3.2. Effects on Flow Velocity Fields. The analysis of changes in the velocity field due to local reconstruction of the river channel is also important in engineering. Local high flood velocity can cause erosion of the river bed and threaten the safety of structures, while at locations with lower flood velocity, the deposition of sediments will occur, which can have an adverse impact on structures locally.

Figures 7 and 8 present comparisons of the velocity of flood flow before and after river reconstruction for 10-year and 100-year floods. It can be observed that the flow field through the reconstructed part (S5 to S10) shows obvious changes for both flood frequency conditions. After river reconstruction, the flow between sections S5 and S10 is divided into two parts due to the presence of the artificial islands. For the 10-year flood, the maximum velocity magnitudes between S5 and S10 are about 1.0~1.5 m/s and 1.5~2.0 m/s before and after local reconstruction, respectively. It can also be seen that the maximum velocity is located at the right-hand part of the cross section near S5 and the left-hand part of the cross-section upstream of S10, where the areas of the cross sections are smaller. Lower velocity was found between the two artificial islands and downstream of section S10, which implies that sediment deposition near these areas must be taken into account and special attention must be paid. For the 100-year flood, the maximum velocity magnitudes between S5 and S10 are about 1.5~2.0 m/s and 2.5~3.0 m/s before and after local reconstruction, respectively. The location of maximum velocity is the same as that for the 10-year flood. Also, lower velocity can be seen between the two artificial islands and downstream of section S10, the same as for the 10-year flood.

Figures 9 and 10 present comparisons of the streamlines of flood flow for the 10-year and 100-year floods. It can be seen more clearly that the flood flows are almost uniform before reconstruction under both flood conditions, while after local reconstruction, the streamlines between sections S5 and S10 are obviously changed, which means that the velocity field becomes complex. In addition, the transverse

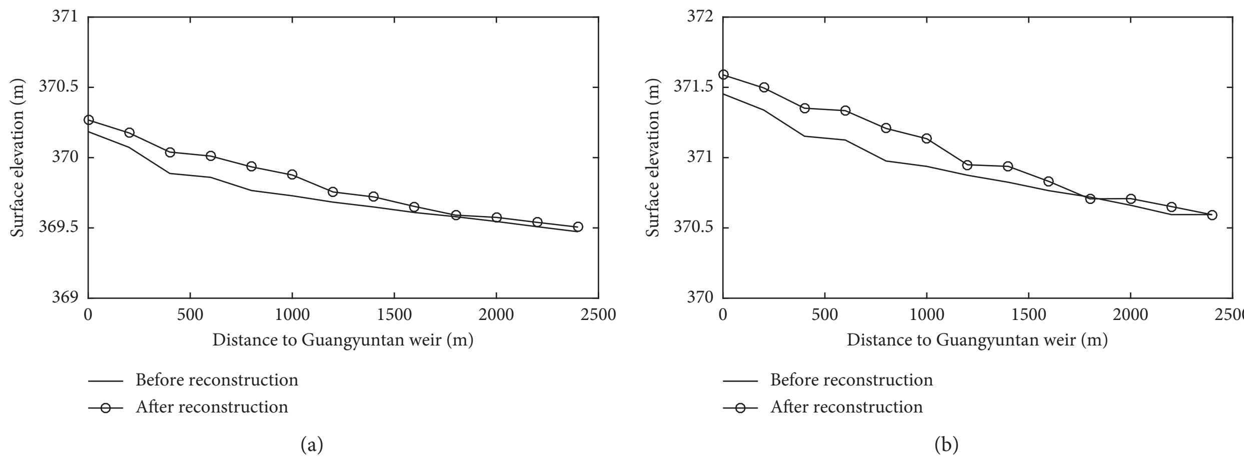

FIGURE 6: Comparisons of flood water surfaces along the river channel before and after river reconstruction. (a) 10-year flood. (b) 100-year flood.

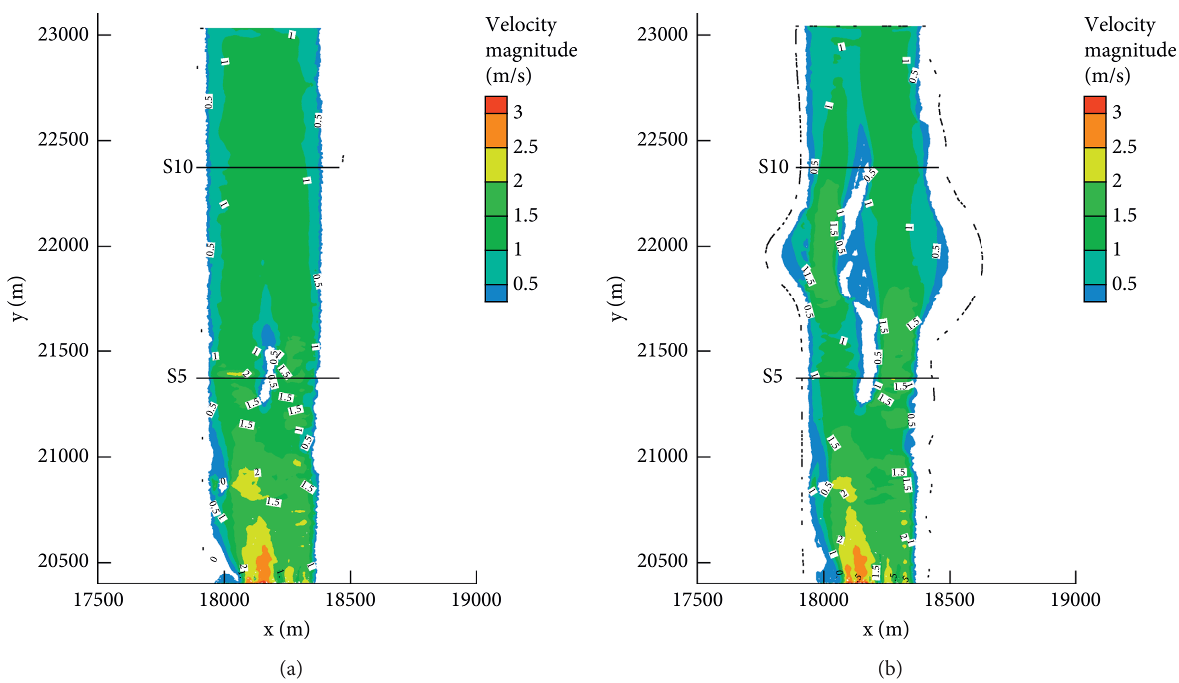

FIGURE 7: Comparisons of the velocity of flood flow before and after river reconstruction for a 10-year flood. (a) Before reconstruction. (b) After reconstruction.

velocity between S5 and S10 was found, and from quantitative analysis, the maximum transverse velocity is approximately 0.5 m/s.

From the flood velocity field above, scour and deposition of the river channel could be qualitatively analyzed. In the design of river engineering, the allowable velocities of the river channel are used empirically to determine the possibility of scour and deposition on the river bed. For coarse sand (diameter greater than 2 mm), the allowable velocity is about 0.5~2.74 m/s, which means that deposition of sand will occur when the velocity is less than 0.5 m/s, while scour will occur with a velocity greater than 2.74 m/s. For fine sediment (diameter smaller than 2 mm), the allowable velocity is about 0.5~1.96 m/s. From the flow velocity magnitude (Figures 7 and 8), sediment deposition will probably occur between the two artificial islands and downstream of section S10 for both 10-year and 100-year floods. The maximum velocity between S5 and S10 for a 10-year flood is about 1.5~2.0 m/s, so the scour of sediment in this condition is limited. However, for the 100-year flood, the maximum velocity between S5 and S10 is 2.5~3.0 m/s, which implies sediment scour in this channel, so special measures must be considered.

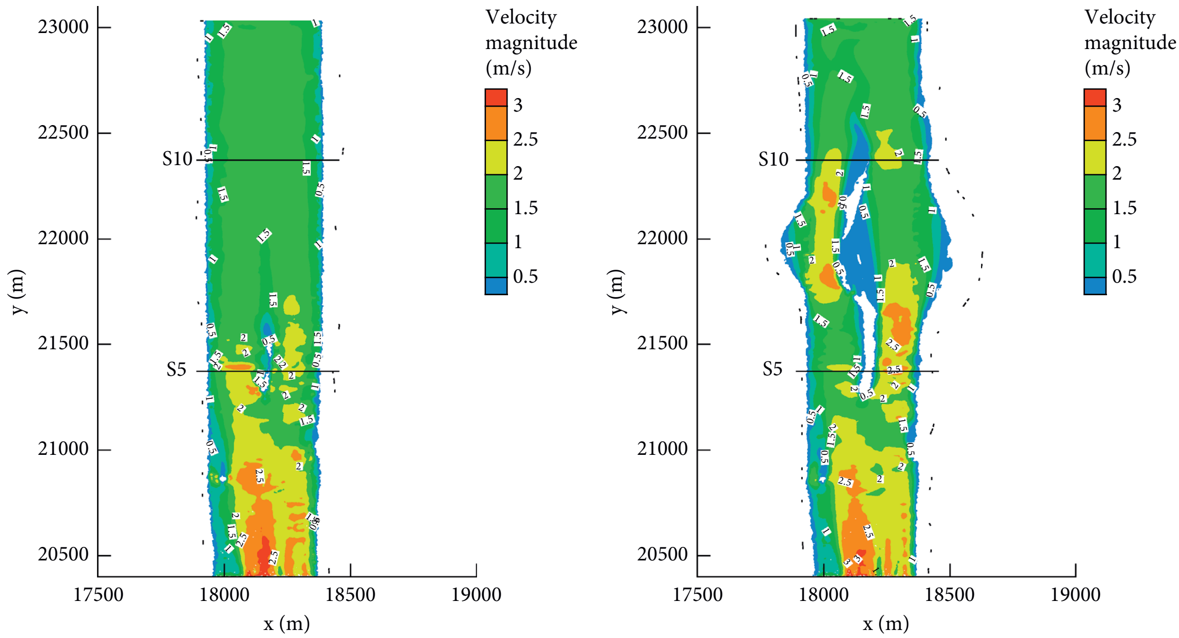

(a) (b)

Figure 8: Comparisons of the velocity of flood flow before and after river reconstruction for a 100-year flood. (a) Before reconstruction. (b) After reconstruction.

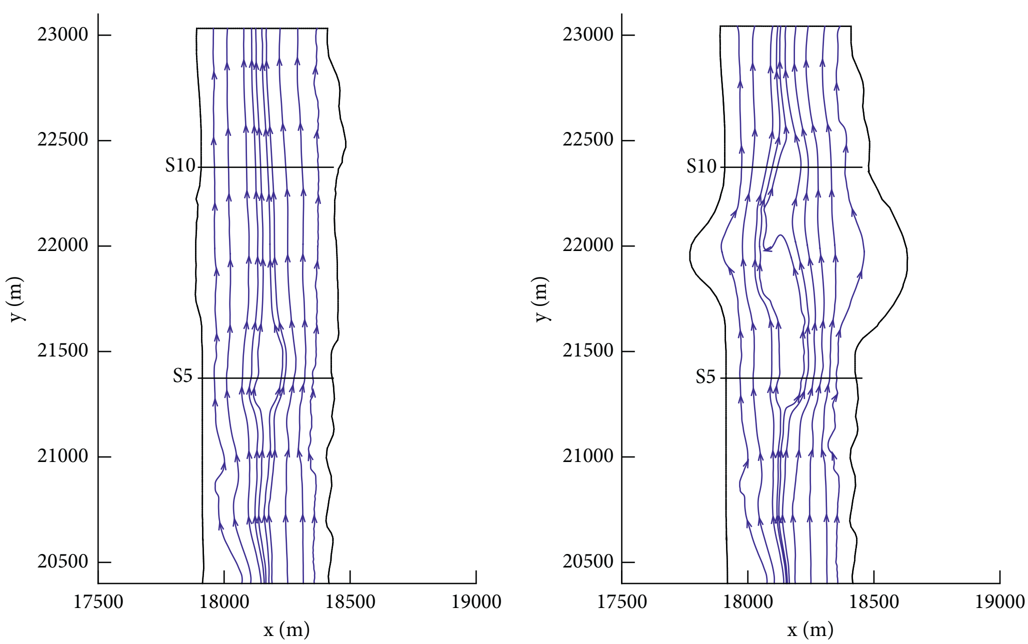

(a) (b)

Figure 9: Comparisons of streamlines before and after river reconstruction for a 10-year flood. (a) Before reconstruction. (b) After reconstruction.

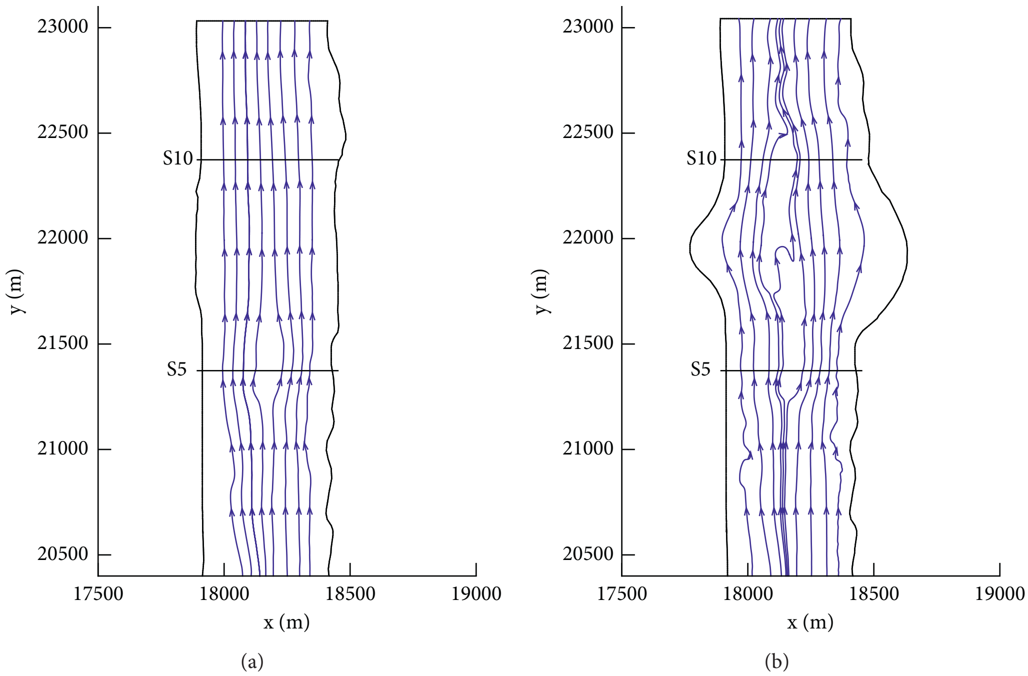

Figure 10: Comparisons of streamlines before and after river reconstruction for a 100-year flood. (a) Before reconstruction. (b) After reconstruction.

4. Conclusions

In order to evaluate the effects of local reconstruction on the flooding of the Ba River in China, a two-dimensional hydrodynamic model was developed, in which the TVD finite volume method was used to solve the 2D shallow water equations. An unstructured triangular mesh was used to treat the natural boundaries more accurately. Numerical models of the river before and after river reconstruction were developed and the model after river reconstruction was validated by comparing it with results obtained from a 1 : 120 scale physical model. Finally, the effects of local reconstruction on the flooding of Ba River under 10-year and 100-year flood conditions were analyzed by comparing the results before and after local reconstruction. Backwater effects and the flow velocity field were analyzed in depth. The main conclusions are as follows.

By comparing the results of the numerical model with those of the physical model, both the free surface elevation and velocity field were found to be well predicted by the 2D model developed herein. Due to the small scale of the physical model, the water depth and velocity in the physical model were small and the magnitude of velocity for some of the domains could not be measured accurately. Hence, a 2D numerical model can be a better method for this type of problem.

Backwater effects due to the local reconstruction were obvious for both 10-year and 100-year floods. The backwater length under both flood frequencies reached up to the upstream boundary (Guangyuntan weir) of the computational domain. The maximum water level rises were 0.23 m at section S5 for a 100-year flood and 0.17 m at section S5 for a 10-year flood. In addition, the levees for this river channel are safe enough. In general, the effects of local reconstruction on flood water elevation in this river channel were limited.

Comparisons of the velocity of flood flow before and after river reconstruction for the 10-year and 100-year floods showed that the flow field through the reconstructed part (S5 to S10) changed obviously for both flood frequency conditions. For both floods, the maximum velocity between S5 and S10 increased after local reconstruction. Further, after local reconstruction, the streamlines between sections S5 and S10 were changed obviously which means that the flood velocity field became complex, and the maximum magnitude of transverse velocity between S5 and S10 was found to be approximately 0.5 m/s. The areas of higher and lower velocities for both floods indicated the possibility of local scour or deposition of sediment. Some measures to address this possibility should be considered near these areas.

Data Availability

All the data used to support the findings of this study are available from the corresponding author upon request.

Conflicts of Interest

The authors declare that they have no conflicts of interest.

Acknowledgments

This research was funded by the National Natural Science Foundation of China (Grant no. 51909211); Natural Science Basic Research Plan in Shaanxi Province of China (Grant no. 2019JQ-744); and Natural Science Foundation of Education Department of Shaanxi Province, China (Grant no. 19JK0591).

References

[1] M. Beniston, "Trends in joint quantiles of temperature and precipitation in Europe since 1901 and projected for 2100," *Geophysical Research Letters*, vol. 36, no. 7, 2009.

[2] K. Davor, A. F. Roger, and B. Michaela, "Flood hazard assessment for extreme flood events," *Natural Hazards*, vol. 84, pp. 1569–1599, 2016.

[3] S. Atabay, K. Haji Amou Assar, M. Hashemi, and M. Dib, "Prediction of the backwater level due to bridge constriction in waterways," *Water and Environment Journal*, vol. 32, no. 1, pp. 94–103, 2018.

[4] K. J. Kaatz and W. P. James, "Analysis of alternatives for computing backwater at bridges," *Journal of Hydraulic Engineering*, vol. 123, no. 9, pp. 784–792, 1997.

[5] S. Förster, C. Chatterjee, and A. Bronstert, "Hydrodynamic simulation of the operational management of a proposed flood emergency storage area at the Middle Elbe River," *River Research and Applications*, vol. 24, no. 7, pp. 900–913, 2008.

[6] D. Tomasz, W. Joanna, and S. Mariusz, "Assessment of the impact of new investments on flood hazard-study case: the bridge on the Warta River near Wronki," *Water*, vol. 7, pp. 5752–5767, 2015.

[7] G. Petaccia and E. Natale, "ORSADEM: a one dimensional water code for flood inundation modelling," *Irrigation and Drainage*, vol. 62, pp. 29–40, 2013.

[8] P. Carling, I. Villanueva, J. Herget, N. Wright, P. Borodavko, and H. Morvan, "Unsteady 1D and 2D hydraulic models with ice dam break for Quaternary megaflood, Altai Mountains, southern Siberia," *Global and Planetary Change*, vol. 70, no. 1-4, pp. 24–34, 2010.

[9] Y. Fan, T. Ao, H. Yu, G. Huang, and X. Li, "A coupled 1D-2D hydrodynamic model for urban flood inundation," *Advances in Meteorology*, vol. 2017, Article ID 2819308, 12 pages, 2017.

[10] W. Wang, K. Zhou, H. Jing, J. Zuo, P. Li, and Z. Li, "Effects of bridge piers on flood hazards: a case study on the Jialing River in China," *Water*, vol. 11, no. 6, p. 1181, 2019.

[11] X. Xia, Q. Liang, and X. Ming, "A full-scale fluvial flood modelling framework based on a high-performance integrated hydrodynamic modelling system (HiPIMS)," *Advances in Water Resources*, vol. 132, Article ID 103392, 2019.

[12] L. Li, M. A. Nearing, M. H. Nichols, V. O. Polyakov, D. Phillip Guertin, and M. L. Cavanaugh, "The effects of DEM interpolation on quantifying soil surface roughness using terrestrial LiDAR," *Soil and Tillage Research*, vol. 198, Article ID 104520, 2020.

[13] M. Yilmaz and M. Uysal, "Comparison of data reduction algorithms for LiDAR-derived digital terrain model generalisation," *Area*, vol. 48, no. 4, pp. 521–532, 2016.

[14] R. Wittmann, H.-J. Bungartz, and P. Neumann, "High performance shallow water kernels for parallel overland flow simulations based on FullSWOF2D," *Computers & Mathematics with Applications*, vol. 74, no. 1, pp. 110–125, 2017.

[15] R. Vacondio, A. Dal Palù, A. Ferrari, P. Mignosa, F. Aureli, and S. Dazzi, "A non-uniform efficient grid type for GPU-parallel Shallow Water Equations models," *Environmental Modelling & Software*, vol. 88, pp. 119–137, 2017.

[16] J. Hou, Y. Kang, C. Hu, Y. Tong, B. Pan, and J. Xia, "A GPU-based numerical model coupling hydrodynamical and morphological processes," *International Journal of Sediment Research*, vol. 35, no. 4, pp. 386–394, 2020.

[17] J. Ahn, Y. Na, and S. W. Park, "Development of two-dimensional inundation modelling process using MIKE21 model," *KSCE Journal of Civil Engineering*, vol. 23, no. 9, pp. 3968–3977, 2019.

[18] MIKE 21, Flow Model FM Hydrodynamic and Transport Module: Scientific Documentation, 2012.

Hindawi
Advances in Materials Science and Engineering
Volume 2021, Article ID 5541181, 16 pages
https://doi.org/10.1155/2021/5541181

Research Article

Effect of Thermal Parameters on Hydration Heat Temperature and Thermal Stress of Mass Concrete

Yuqin Zhao,[1] Gaosheng Li,[1] Caixia Fan,[1] Wentai Pang,[2] and Yongtao Wang[1]

[1]*Institute of Transportation, Inner Mongolia University, Hohhot 010070, China*
[2]*Inner Mongolia Water Resources and Hydropower Survey and Design Institute, Hohhot 010020, China*

Correspondence should be addressed to Yongtao Wang; wyt_827@imu.edu.cn

Received 24 January 2021; Revised 10 February 2021; Accepted 18 February 2021; Published 3 March 2021

Academic Editor: Yanhu Mu

To explore the influence of concrete thermal parameters on the hydration heat temperature and thermal stress of mass concrete, four feature positions of a dam foundation were chosen to analyze the changing process of temperature and stress by varying the thermal parameters, including the thermal conductivity, specific heat, surface heat diffusion coefficient, temperature rise coefficient, solar absorption coefficient, and thermal expansion coefficient. Some conclusions were obtained as follows. Increasing the thermal conductivity and reducing the specific heat and temperature rise coefficient of concrete can effectively reduce the maximum temperature of the central concrete structure. Increasing the solar absorption coefficient, specific heat, and thermal expansion coefficient and reducing the thermal conductivity, surface heat diffusion coefficient, and temperature rise coefficient of concrete can reduce the maximum principal tensile stress in the structure to a certain extent. The maximum principal tensile stress at different positions of the structure has a linear functional relationship with the thermal conductivity, specific heat, and thermal expansion coefficient and has a quadratic function relationship with the surface heat diffusion coefficient, temperature rise coefficient, and solar absorption coefficient. Besides, this study also proposed a series of related anticracking measures. This study was expected to provide a theoretical reference for the design, construction, and cracking disease prevention of mass concrete structures.

1. Introduction

The large hydration heat can be produced in a short time during the casting of mass concrete structure, which leads to the rapid rise of the internal temperature of the mass concrete structure. Especially, the mass concrete structure is also affected by the external environment and the thermal parameters, which is easy to form a large thermal gradient and thermal stress between the core and the surface. As a result, cracks will occur when the thermal stress is larger than the tensile strength of the concrete. Therefore, temperature control is particularly important to the mass concrete [1]. To ensure the integrity and durability of mass concrete structure, the hydration heat temperature, thermal stress distribution, and influencing factors of mass concrete structure in the cold region are analyzed, and taken appropriate temperature control measures are the keys to construction organization design and comprehensive treatment of mass concrete structure diseases.

At present, some researchers have carried out lots of studies to analyze the temperature field, thermal stress, and influencing factors of mass concrete by using the finite element method and monitoring method. Some studies [2–9] found that the results of numerical calculation can accurately predict the distribution of temperature and stress of the structure by comparing with the field monitoring data, and it is feasible to put forward effective temperature control measures for the mass concrete structure according to the finite element simulation results by considering various influencing factors comprehensively at the design stage. So far, the influencing factors such as construction measures, amount and type of concrete material, and pipe cooling parameters have been studied. Reducing concrete casting temperature [10–14], changing casting date [15, 16], layered casting [17–19], and curing concrete [20, 21] can effectively reduce the maximum temperature of the structure. At the same time, changing insulation thickness [22] and types of insulation materials [23] has significant effects on the temperature difference and maximum tensile stress of the structure. The amount and type of concrete raw materials have a significant influence on the internal heat transfer and mechanical properties of concrete. High cement content [24–26] will make the temperature of the structure exceed the specified limit. Low temperature cement [27–29] can reduce the structure temperature and improve the crack resistance of the concrete structure. Additives [30–34] can also effectively reduce the temperature rise of cement hydration heat. The arrangement of cold water pipes is a very effective method to reduce the heat of hydration [35]. Controlling the inlet and outlet temperature of cooling water pipes, the spacing of cooling pipes, and adjusting the convection coefficient [36] between cooling water and concrete are effective measures to control the hydration heat of concrete. Meanwhile, medium-term temperature control and cooling [37] are also very important. Besides, Si et al. [38] also put forward a new idea that the small temperature difference cooling can effectively reduce the temperature gradient and thermal stress. In conclusion, these findings mainly focused on revealing the influence of construction design, amount and type of concrete raw materials, pipe cooling parameters on the hydration temperature, and thermal stress distribution of mass concrete. However, the thermal parameters are also closely related to the thermal-mechanical characteristics of mass concrete structure, such as the thermal conductivity is a factor that directly affects the temperature gradient of the structure. Therefore, it is extremely important to study the influence of concrete thermal parameters on temperature and thermal stress distribution of mass concrete structure for crack control and disease treatment, especially for the mass concrete structure located in the cold region where the temperature changes greatly.

This study relied on Xiwugaigou Roller Compacted Concrete Dam Project in Inner Mongolia, China. A three-dimensional finite element model considering hydration heat release, thermal parameters changing, and actual temperature boundary was built to analyze the maximum temperature, the temperature difference between the core and surface, and maximum principal tensile stress of the mass concrete aiming to study the influence of different values of thermal conductivity, specific heat, surface heat diffusion coefficient, temperature rise coefficient, solar absorption coefficient, and thermal expansion coefficient on the distribution of temperature and thermal stress at the core, surface, 50 mm from the surface, and foot of the concrete foundation. Furthermore, the functional relationship between different thermal parameters and the maximum principal tensile stress at different positions of the structure is determined. Finally, the study also puts forward a series of relevant crack prevention measures. The results will provide a theoretical basis for temperature control and crack prevention of mass concrete structures from the perspective of controlling the thermal properties of concrete materials.

2. Basic Theory

2.1. Heat Conduction Equation. For isotropic solids, the heat conduction equation considering concrete hydration heat is expressed as follows:

$$\frac{\partial T}{\partial \tau} - \frac{\lambda}{c\rho}\nabla^2 T = \frac{\partial \theta(\tau)}{\partial \tau}, \tag{1}$$

where T is the temperature of the concrete, τ is the time, λ is the thermal conductivity, c is the specific heat, ρ is the density of concrete, and $\theta(\tau)$ is the adiabatic temperature rise induced by hydration heat, which is calculated as follows:

$$\theta(\tau) = \theta_0\left(1 - e^{-m\tau}\right), \tag{2}$$

where θ_0 is the adiabatic temperature rise terminal value, and m is the temperature rise coefficient.

2.2. Implicit Expression of Unsteady Temperature Field. Equation (1) becomes a matrix differential equation about the time after spatial discretization by the finite element method. The matrix differential equation is given as follows:

$$[K]\{T\} + [C]\left\{\frac{\partial T}{\partial \tau}\right\} + \{R\} = 0, \tag{3}$$

where $[K]$ is the heat conduction matrix, $[C]$ is the heat capacity matrix, and $\{R\}$ is the thermal load vector. Assume $\tau = \tau_i$ corresponds to $T = T_i$ and $\tau = \tau_{i+1}$ corresponds to $T = T_{i+1}$; then,

$$\begin{gathered}[K]\{T_i\} + [C]\left\{\frac{\partial T}{\partial \tau}\right\}_i + \{R_i\} = 0,\\ [K]\{T_{i+1}\} + [C]\left\{\frac{\partial T}{\partial \tau}\right\}_{i+1} + \{R_{i+1}\} = 0,\end{gathered} \tag{4}$$

ΔT_i can be defined as

$$\Delta T_i = T_{i+1} - T_i = \Delta\tau_i\left(b\left\{\frac{\partial T}{\partial \tau}\right\}_{i+1} + (1-b)\left\{\frac{\partial T}{\partial \tau}\right\}_i\right). \tag{5}$$

Therefore,

$$\left\{\frac{\partial T}{\partial \tau}\right\}_{i+1} = \frac{1}{b\Delta\tau_i}\left[\{T_{i+1}\} - \{T_i\}\right] - \frac{1-b}{b}\left\{\frac{\partial T}{\partial \tau}\right\}_i. \tag{6}$$

Substituting equation (5) in equation (4) obtains

$$[K]\{T_{i+1}\} + [C]\left(\frac{1}{b\Delta\tau_i}\left[\{T_{i+1}\} - \{T_i\}\right] - \frac{1-b}{b}\left\{\frac{\partial T}{\partial \tau}\right\}_i\right) + \{R_{i+1}\} = 0. \tag{7}$$

So equation (4) becomes

$$\left([K] + \frac{1}{b\Delta\tau_i}[C]\right)\{T_{i+1}\} = -\left(\left(\frac{1-b}{b}\right)[K] - \frac{1}{b\Delta\tau_i}[C]\right)\{T_i\} - \frac{1-b}{b}\{R_i\} - \{R_{i+1}\}. \tag{8}$$

The temperature of each node at any time can be obtained by solving the equations. The parameter b is usually taken as 1 in the calculation, which is the backward differential method.

2.3. Finite Element Method for Elastic Creep Thermal Stress of Concrete. Assume that concrete is an elasticity-creep solid. The thermal stress of concrete is calculated by the finite element method without considering the drying shrinkage of concrete [39]. In a three-dimensional space, the strain increment generated in $\Delta\tau_n = \tau_n - \tau_{n-1}$ can be expressed as follows:

$$\{\Delta\varepsilon_n\} = \{\varepsilon(\tau_n)\} - \{\varepsilon(\tau_{n-1})\} = \{\Delta\varepsilon_n^e\} + \{\Delta\varepsilon_n^c\} + \{\Delta\varepsilon_n^T\}, \quad (9)$$

where $\{\Delta\varepsilon_n\}$ is the strain increment, $\{\Delta\varepsilon_n^e\}$ is the elastic strain increment induced by the external force, $\{\Delta\varepsilon_n^c\}$ is the creep strain increment, and $\{\Delta\varepsilon_n^T\}$ is the temperature strain increment. The elastic strain increment is calculated as follows:

$$\{\Delta\varepsilon_n^e\} = \frac{1}{E(\overline{\tau}_n)}[Q]\{\Delta\sigma_n\}, \quad (10)$$

where $\overline{\tau}_n$ is the median age of the concrete, equals to $((\tau_n + \tau_{n-1})/2)$, $E(\overline{\tau}_n)$ is the modulus of elasticity of the concrete at median age, $[Q]$ is a coefficient matrix, and $\{\Delta\sigma_n\}$ is the stress increment. The creep strain increment is calculated as follows:

$$\{\Delta\varepsilon_n^c\} = \{\eta_n\} + C(t, \overline{\tau_n})[Q]\{\Delta\sigma_n\}, \quad (11)$$

where $\{\eta_n\}$ is a matrix related to the creep coefficient, and $C(t_n, \overline{\tau}_n)$ is the specific creep of the concrete at median age.

Then, the relationship between stress increment and strain increment is given as follows:

$$\{\Delta\sigma_n\} = [\overline{D}_n]\left(\{\Delta\varepsilon_n\} - \{\eta_n\} - \{\Delta\varepsilon_n^T\}\right), \quad (12)$$

where $[\overline{D}_n]$ is the stress-strain matrix corresponding to $E(\overline{\tau}_n)$. The unit node force increment can be expressed as follows:

$$\{\Delta F\}^e = \iiint [B]^T\{\Delta\sigma_n\}\mathrm{d}x\mathrm{d}y\mathrm{d}z, \quad (13)$$

where $\{\Delta F\}^e$ is the element nodal force increment, and $[B]^T$ is the transformation matrix of the deformation matrix $[B]$. The above formula can be written as follows:

$$\{\Delta F\}^e = [k]^e\{\Delta\sigma_n\}^e - \iiint [B]^T[\overline{D}_n]\left(\{\eta_n\} + \{\Delta\varepsilon_n^T\}\right)\mathrm{d}x\mathrm{d}y\mathrm{d}z, \quad (14)$$

where $[k]^e$ is the element stiffness matrix. Define

$$[k]^e = \iiint [B]^T[\overline{D}_n][B]\mathrm{d}x\mathrm{d}y\mathrm{d}z, \{\Delta P_n\}_e^c = \iiint [B]^T[\overline{D}_n]\{\eta_n\}\mathrm{d}x\mathrm{d}y\mathrm{d}z, \{\Delta P_n\}_e^T = \iiint [B]^T[\overline{D}_n]\{\Delta\varepsilon_n^T\}\mathrm{d}x\mathrm{d}y\mathrm{d}z, \quad (15)$$

where $\{\Delta P_n\}_e^c$ is the element node load increment by creep, and $\{\Delta P_n\}_e^T$ is the element node load increment by temperature. Therefore, the global balance equation is given as follows:

$$[K]\{\Delta\sigma_n\} = \{\Delta P_n\}^L + \{\Delta P_n\}^C + \{\Delta P_n\}^T, \quad (16)$$

where $[K]$ is the global stiffness matrix, $\{\Delta P_n\}^L$ is the nodal load increment by external loads, $\{\Delta P_n\}^C$ is the node load increment by creep, and $\{\Delta P_n\}^T$ is the node load increment by temperature.

Finally, the stresses of each unit are as follows:

$$\{\sigma_n\} = \sum\{\Delta\sigma_n\}. \quad (17)$$

3. Methods

The Xiwugaigou Reservoir Project, located in Inner Mongolia which is the typical cold region, consists of gravity dam, flood discharge, sand scouring tunnel, and diversion tunnel. According to the difference of materials, it can be divided into foundation section, water retaining section, overflow dam section, flood discharge, sand scouring tunnel section, diversion tunnel section, and joint parts. The maximum dam height is 43.4 m, dam length is 224.0 m, dam crest width is 5.0 m, and the height of the foundation section located in the strong restraining from the area of the dam is 1–3 m. To study the influence of concrete thermal parameters on hydration heat temperature and thermal stress of mass concrete, a three-dimensional finite element model of the dam foundation is established.

3.1. Finite Element Model. The highest foundation dam section with the size of 30 m (length) ∗ 20 m (width) ∗ 3 m (height) is chosen as the study object, which is located on the bedrock foundation, with the size of 40 m (length) ∗ 30 m (width) ∗ 5 m (height). As shown in Figure 1, four feature research points are setup to analyze the changing process of temperature and stress by varying the thermal parameters. Point A is located in the core of the structure, where the maximum temperature occurs. Point B is located 50 mm away from the surface near the boundary area, which is the keypoint to calculate the temperature difference between the core and surface. Point C is located at the surface through which the surface temperature distribution of the structure can be observed directly. And point D is on the foot of the concrete structure which is one of the most prone stress concentration points. The boundary of the concrete foundation and bedrock is divided into 50 mm grids, and others are divided into 1.0 m grids in the model. The finite element model is shown in Figure 2.

3.2. Initial and Boundary Conditions. The initial placing temperature of concrete is taken as the initial temperature of concrete and foundation using the following calculation:

$$T(x, y, z, 0) = T_0(x, y, z) = C(\text{constant}), \quad (18)$$

where T_0 is the initial casting temperature of the concrete taken as 20°C in considering the actual project and construction experience.

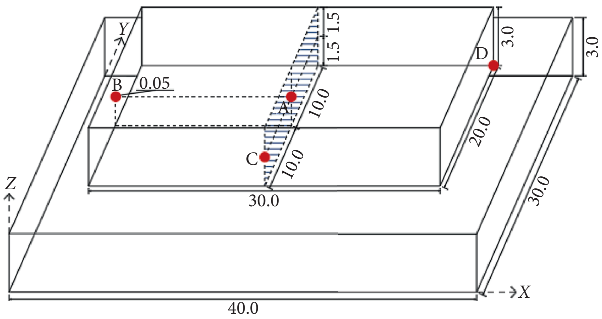

FIGURE 1: Main size and research points of the concrete foundation.

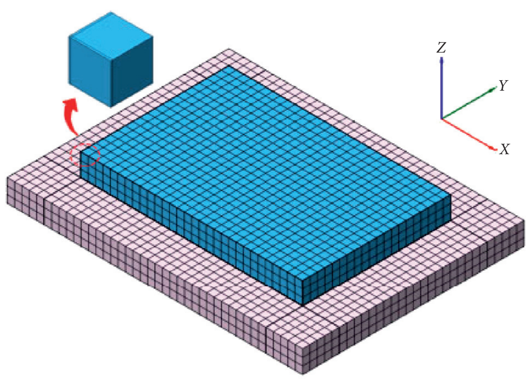

FIGURE 2: Mesh generation of the model.

In the calculation of the stress field, the boundary of the bedrock bottom is set as the fixed displacement constraint, the sides set as the normal displacement constraint, and the other sides of the model are the free surfaces. In the calculation of temperature field, the bottom and side of bedrock are set as the adiabatic boundaries, and the contact surface between bedrock and air and the surface between concrete and air are all set as the third boundary conditions, as shown in the following equation:

$$-\lambda\frac{\partial T}{\partial n} = \beta\left(T - T_a\right), \tag{19}$$

where β is the surface heat diffusion coefficient. T_a is the environment temperature, which is obtained by the monitoring data of the study area, and can be expressed by the following periodic function:

$$T_a = 4.5 + 17.95\,\sin\left(\frac{2\pi}{365}t + \frac{\pi}{25}\right), \tag{20}$$

where t is the time (day), $t = 0$ corresponds to May 1st, $t = 1$ corresponds to May 2nd, and so on. To intuitively see the temperature change of the project site, we present equation (20) in Figure 3. The curve shows that the project site is located in the cold region for negative temperature that occurs in the winter. The red part of the curve is the boundary temperature used in the modeling.

3.3. Parameters Data. The concrete is C20 normal concrete with the density of 2360 kg/m^3, the elastic modulus of 25.5 GPa, and Poisson's ratio of 0.167. The adiabatic

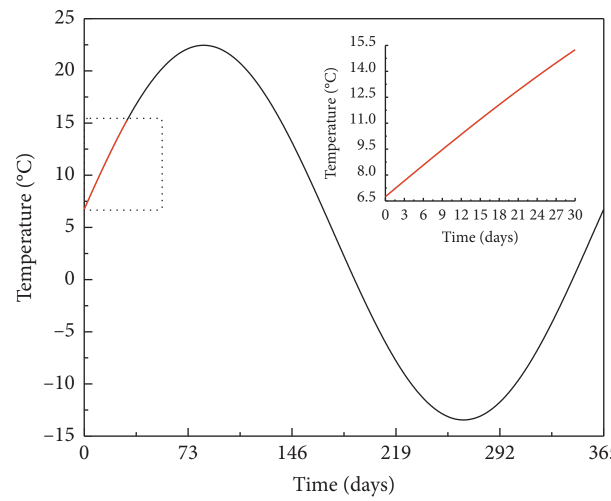

FIGURE 3: Environment temperature change of the project site.

temperature rise of concrete is calculated by equation (2), and the final value of temperature rise is 30°C. The parameters of bedrock are shown in Table 1.

The main parameters influencing the thermal performance of concrete are thermal conductivity, specific heat, temperature rise coefficient, surface heat diffusion coefficient, solar absorption coefficient, and thermal expansion coefficient [40, 41]. These parameters are the basic data for solving the thermal stress caused by the temperature change inside the concrete structure, which mainly depends on the concrete age, aggregate type, cement type, water-cement ratio, unit weight, and temperature. Therefore, thermal parameters are explored as variables in this study. The values of each thermal parameter are shown in Table 2, which cover the possible range in the construction [41, 42].

3.4. Temperature Control Requirements. When the thermal stress exceeds the bearing limit of concrete, the structure will be broken, resulting in thermal cracks. According to the Chinese standard for construction of mass concrete [43], the maximum temperature of the foundation should not exceed 70°C, the temperature difference between the core and surface should not exceed 25°C, and the allowable principal tensile stress of the concrete is 2.45 MPa at the age of 28 days of concrete.

4. Results and Discussion

Based on the concrete foundation model, the influence of each thermal parameter on the maximum temperature, the temperature difference between the core and surface, and maximum principal tensile stress of mass concrete are analyzed by using the control variate method.

4.1. Effect of Thermal Conductivity. Figure 4 shows the relationship of temperature over time with four different thermal conductivities, which are 0.5 W/(m·K), 1.5 W/(m·K), 2.5 W/(m·K), and 3.5 W/(m·K), respectively. As shown in Figure 4, the temperature of point A at the

Table 1: Basic parameters of bedrock.

Material	Density kg/m^3	Elastic modulus GPa	Thermal conductivity W/(m·K)	Specific heat kJ/(kg·°C)	Thermal expansion coefficient $*10^{-6}/°C$	Poisson's ratio
Bedrock	2800	35	2.91	0.72	8.5	0.167

Table 2: Values of various thermal parameters under different conditions.

Conditions	Thermal conductivity λ W/(m·K)	Specific heat c kJ/(kg·°C)	Surface heat diffusion coefficient β $kJ/(m^2·h·°C)$	Temperature rise coefficient m d^{-1}	Solar absorption coefficient r —	Thermal expansion coefficient α $*10^{-6}/°C$
1	0.5~3.5	1	50	0.3	0	10
2	1	0.8~1.2	50	0.3	0	10
3	1	1	18.46~165.13	0.3	0	10
4	1	1	50	0.2~0.4	0	10
5	1	1	50	0.3	0.4~0.8	10
6	1	1	50	0.3	0	8~12

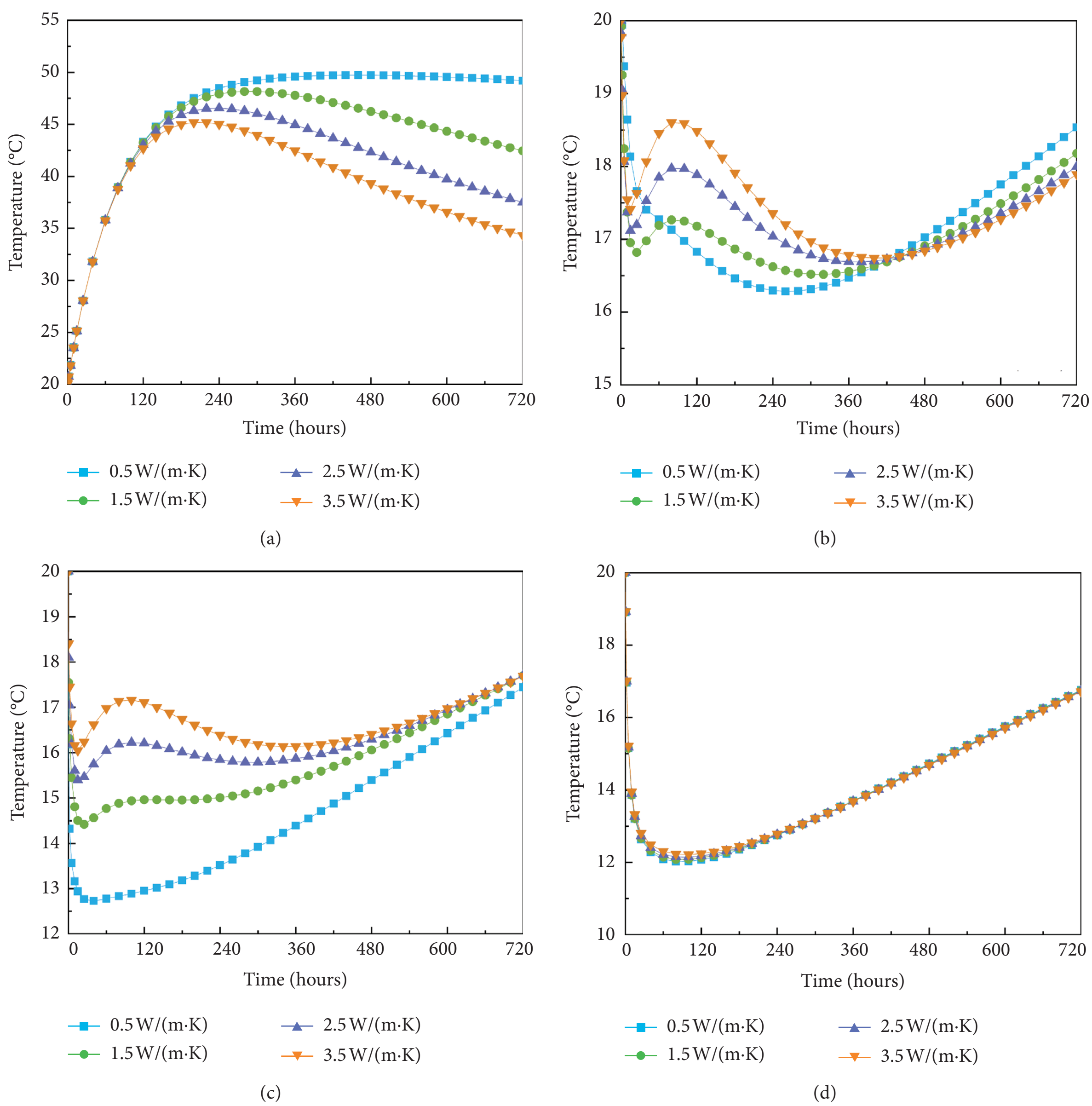

Figure 4: Temperature-time curves with different thermal conductivities. (a) Point A, (b) point B, (c) point C, and (d) point D.

structure core with different thermal conductivities demonstrates a tendency to rise rapidly and then decrease slowly. The maximum temperature of point A is 49.7°C, 48.2°C, 46.6°C, and 45.5°C correspondingly, all appeared at about 240 hours. The temperature of point B located at 50 mm inside the surface demonstrates a twice process of decrease to increase. After 420 hours, the temperature of point B with bigger thermal conductivity is lower than one with a smaller one. The temperature of surface point C demonstrates a similar change process with point B, but with smaller amplitude. However, the temperature of point C in different thermal conductivity changes to the same value that almost equals to the environment temperature. The temperature at point D at the foot of the concrete structure is almost keeping the same change process at different thermal conductivities because it is mainly determined by the environment temperature. At the same time, the temperature difference between the core and surface of the structure is calculated as 33.1°C, 31.6°C, 29.7°C, and 28.0°C, respectively. From the above analysis, it can be found that the hydration heat has the strongest heating effect in the core region of the structure. The heat is mainly released close to the concrete surface. However, increasing the thermal conductivity of concrete has a positive effect on the thermal stability of the construction for reducing the maximum temperature in the core region of the structure and also decreasing the temperature difference between the core and surface of the concrete foundation.

Figure 5 shows the calculated and fitted maximum principal tensile stress at each point with a different thermal conductivity. The principal tensile stress is induced by the action of temperature and self-weight. Due to symmetry, the maximum principal tensile stress of point A is close to zero. Due to the stress relief, the maximum principal tensile stresses at points B and C is all less than allowable principal tensile stress, while the maximum principal tensile stress occurs at point D. Point D is located at the junction of the bedrock, and the structure and the displacement is restrained at the same time; as a result, stress concentration is easy to occur, but it cannot be eliminated in construction. Therefore, more attention should be paid to the maximum principal tensile stress in this region. Moreover, as shown in Figure 4, the maximum principal tensile stress at points A, B, and C decreases, while point D increases with the increase of thermal conductivity. Fitting the maximum principal tensile stress of four points with the thermal conductivity shows a linear relationship with the maximum principal tensile stress of the structure and positive correlation in points A, B, and C while negative correlation in point D. Obviously, the tensile stress of concrete interior can be reduced through increasing the thermal conductivity of concrete, and the situation is just opposite in the junction of the bedrock and the structure. Anyway, the maximum principal tensile stress inside the construction does not exceed the tensile strength of concrete with every thermal conductivity. On the contrary, the maximum principal tensile stress is larger than the tensile strength of concrete when the thermal conductivity is bigger than 1.0 W/(m·K), which can cause structural cracks. The maximum principal tensile stress increases 36.7% when the thermal conductivity changes from 0.5 W/(m·K) to 3.5 W/(m·K). In conclusion, reducing the thermal conductivity of concrete can reduce the risk of structural cracking.

Therefore, suitable thermal conductivity not only ensures the temperature below the standard threshold but also makes sure the stress state under stable. Some research results [44, 45] can be used to realize this target, such as using limestone, lightweight aggregate (expanded shale), recycled, or natural and recycled aggregates to replace basalt, quartzite, siltstone, and other coarse aggregates, adding auxiliary cementitious materials (fly ash and slag) and not too high humidity during casting.

4.2. Effect of Specific Heat. Figure 6 shows the relationship between temperature and time with four different specifics heat which are 0.8 kJ/(kg·°C), 0.9 kJ/(kg·°C), 1.0 kJ/(kg·°C), and 1.1 kJ/(kg·°C), respectively. As shown in Figure 6, the temperature of the four points demonstrates the same change process similar to themselves with different thermal conductivities, as shown in Figure 4. Besides, the temperature rises more with bigger specific heat than that with smaller specific heat. However, the temperature differences with the different specifics heat of the same point are smaller than that with different thermal conductivities, which proposed that thermal conductivity has a greater influence on the temperature than specific heat. The maximum temperature of point A is 48.5°C, 48.8°C, 49.0°C, 49.2°C, and 49.3°C, respectively. The maximum temperature of the first temperature rise at point B is 16.3°C, 16.6°C, 17.0°C, 17.3°C, and 17.6°C, appeared around 80 hours. The maximum temperature of the first temperature rise at point C is 13.7°C, 13.9°C, 14.1°C, 14.3°C, and 14.4°C, also appeared around 80 hours. The temperature at point D is almost keeping the same change process with the environment temperature, basically not affected by specific heat. At the same time, the temperature difference between the core and surface of the structure is calculated as 32.7°C, 32.6°C, 32.5°C, 32.4°C, and 32.3°C, respectively, with each specific heat. Obviously, reducing the specific heat can reduce the maximum temperature inside the structure, but increase the temperature difference between the core and surface of the structure. However, the temperature change is very limited, especially when compared with the change brought about by thermal conductivity.

Figure 7 shows the calculated and fitted maximum principal tensile stress at each point with a different specific heat. The maximum principal tensile stress of point A is close to zero and points B and C are all less than allowable principal tensile stress, and the maximum principal tensile stress occurs at point D for the same reason discussed in Section 4.1. Moreover, as shown in Figure 6, the maximum principal tensile stress at points A, B, and C increases while point D decreases with the increases of specific heat, all change with a linear relationship. Therefore, increasing the specific heat can reduce the maximum principal tensile stress of the construction. The maximum principal tensile stress reduces 6.8% when the specific heat increases from 0.8 kJ/(kg·°C) to 1.1 kJ/(kg·°C).

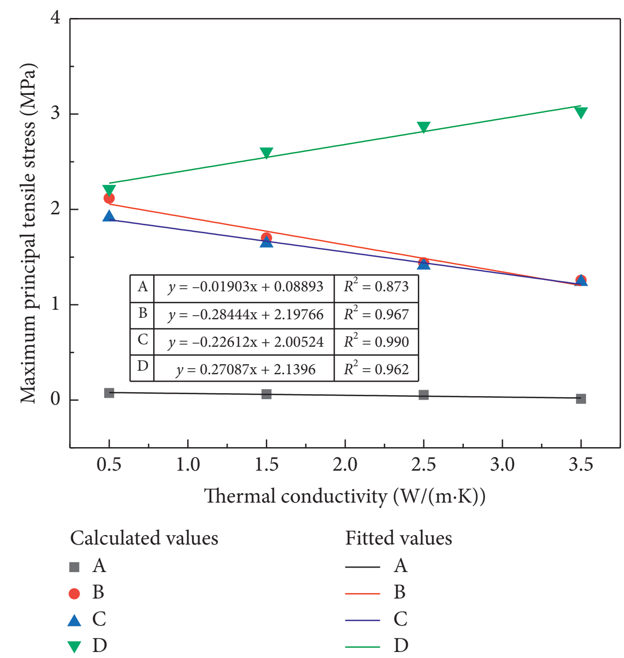

Figure 5: The calculated and fitted maximum principal tensile stress at each point with a different thermal conductivity.

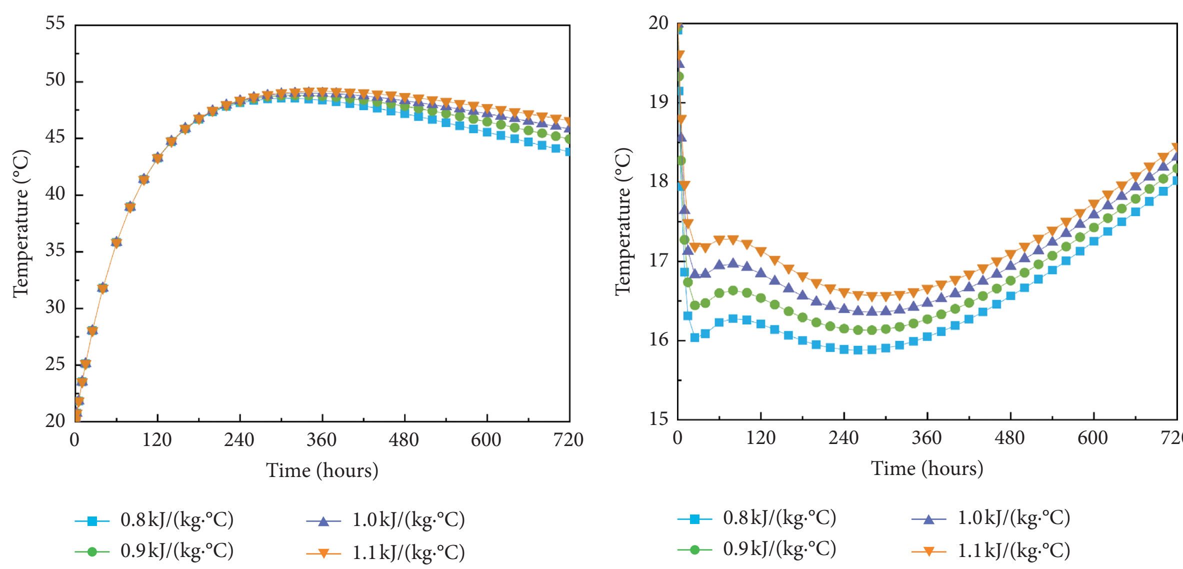

(a) (b)

Figure 6: Continued.

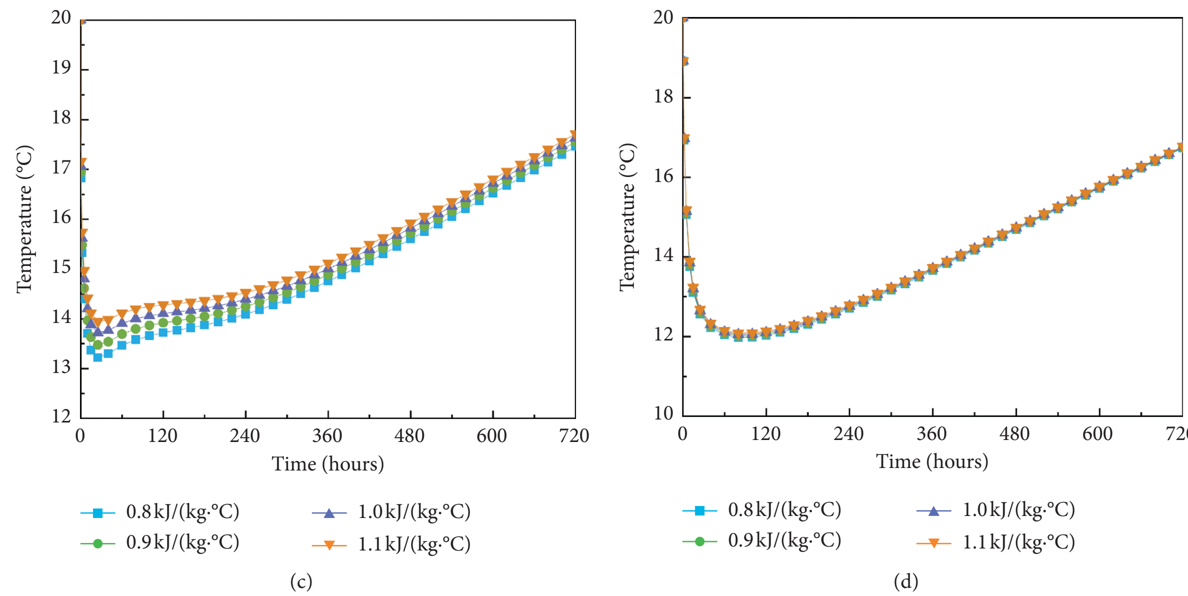

Figure 6: Temperature-time curves with different specifics heat. (a) Point A, (b) point B, (c) point C, and (d) point D.

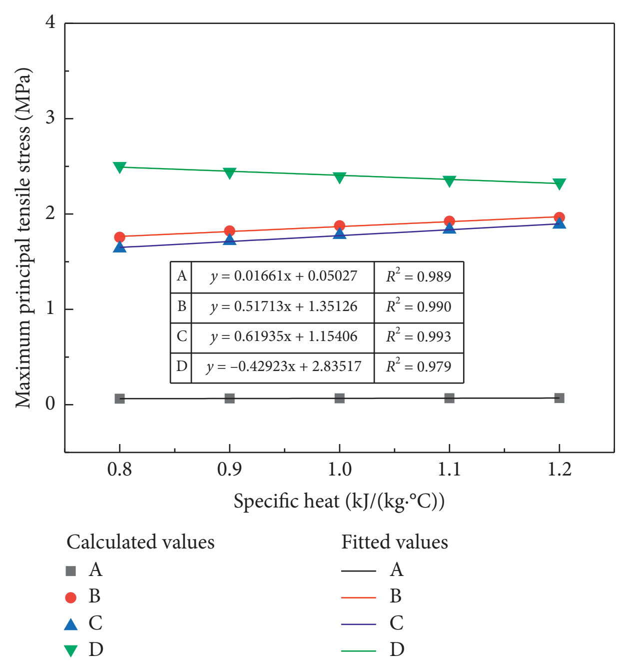

Figure 7: The calculated and fitted maximum principal tensile stress at each point with a different specific heat.

In conclusion, specific heat increase has a positive effect on hydration temperature rise and a negative effect on maximum principal tensile stress. However, the influence of concrete specific heat on the maximum principal tensile stress is greater than that on the maximum temperature. Under the condition that the hydration heat temperature meets the requirements, it enlightens us to control the maximum principal tensile stress to avoid the structure cracking through increasing specific heat methods, such as adding an appropriate amount of fly ash and slag, reasonably reducing the sand ratio, appropriately increasing the content of small stones under the condition of constant coarse aggregate gradation [46].

4.3. Effect of Surface Heat Diffusion Coefficient. Figure 8 shows the relationship between temperature and time with four different surface heat diffusion coefficients which are 18 kJ/(m^2·h·°C), 78 kJ/(m^2·h·°C), 138 kJ/(m^2·h·°C), and 165 kJ/(m^2·h·°C), respectively. It can be seen that the surface heat diffusion coefficient has no obvious influence on the temperature in the central concrete structure, such as point

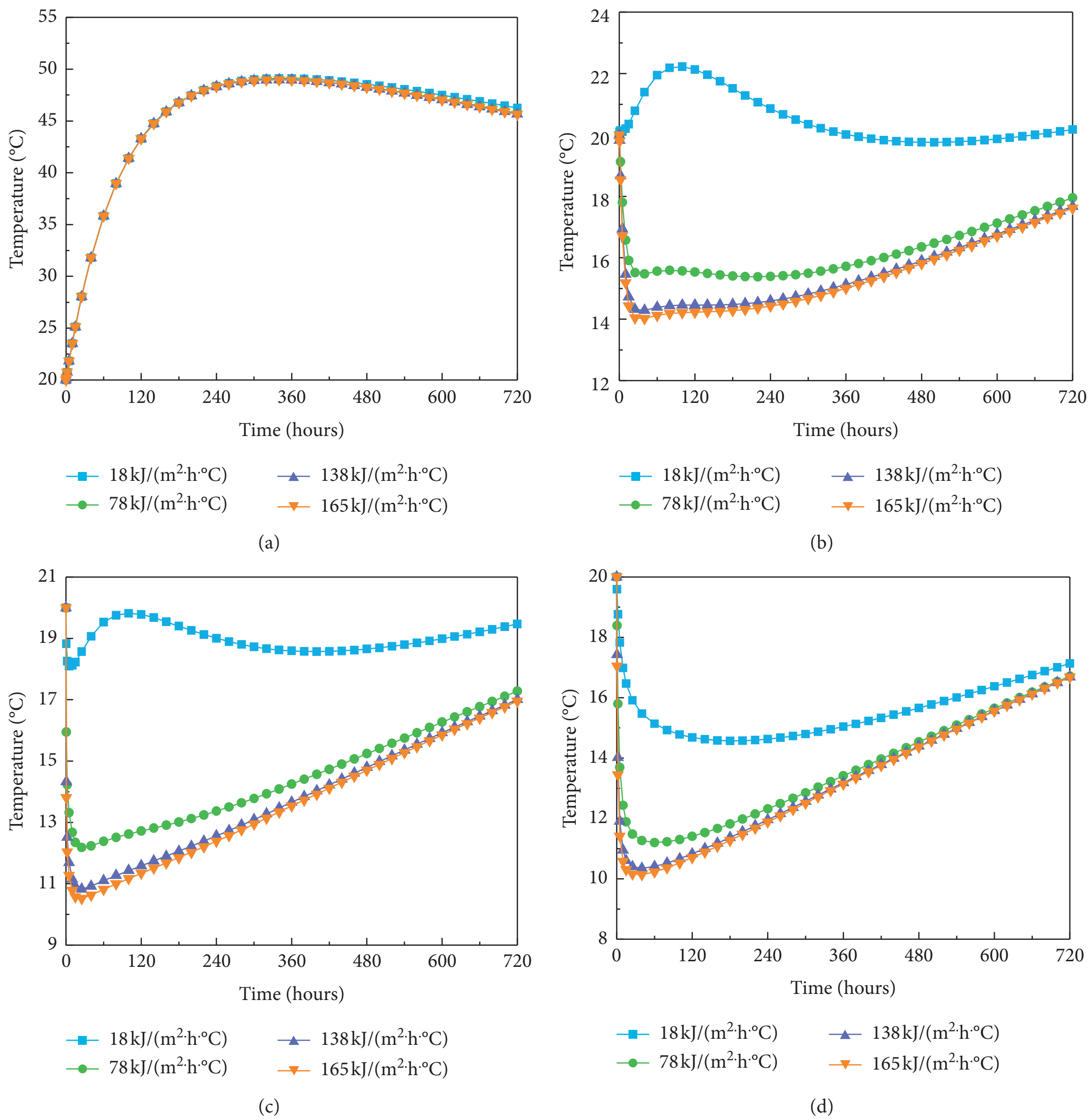

FIGURE 8: Temperature-time curves with different surface heat diffusion coefficients. (a) Point A, (b) point B, (c) point C, and (d) point D.

A. The temperature rise in the central concrete structure is mainly controlled by the thermal conductivity and specific heat. However, the surface heat diffusion coefficient has a more significant impact near the boundary of the structure. As shown in Figure 8, there is an obvious hydration heat temperature rise at points B and C when the surface heat diffusion coefficient equals 18 kJ/(m2·h·°C). The temperature is easily affected by environmental temperature along with the increase of the surface heat diffusion coefficient. The maximum temperature of point A is close to 49.0°C appeared at 340 hours with a different surface heat diffusion coefficient. The temperature difference between the core and surface is 29.0°C, 33.4°C, 34.0°C, and 34.1°C, respectively, with each surface heat diffusion coefficient. Therefore, a bigger surface heat diffusion coefficient contributes to more heat loss in the boundary, but it is not conducive to reduce the temperature difference between the core and surface.

Figure 9 shows the calculated and fitted maximum principal tensile stress at each point with the different surface heat diffusion coefficient. The maximum principal tensile stress of point A is close to zero due to symmetry. The maximum principal tensile stress of points B and C decreases with the surface heat diffusion coefficient increase because that more temperature stress is relieved with a bigger surface heat diffusion coefficient. However, because point D is constrained by the bedrock, the temperature stress cannot be easily relieved with heat loss, so the maximum principal tensile stress shows an increasing trend with the surface heat diffusion coefficient increase. The maximum principal tensile stress at four points all shows a law of quadratic function.

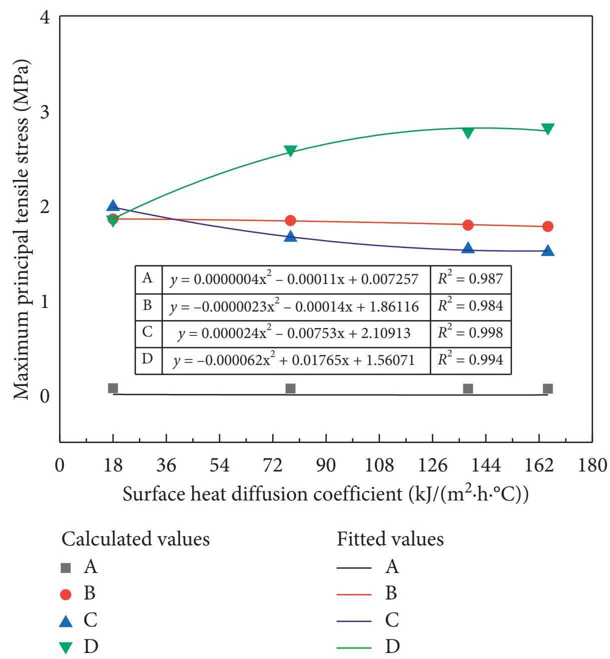

FIGURE 9: The calculated and fitted maximum principal tensile stress at each point with a different surface heat diffusion coefficient.

In conclusion, appropriately reducing the surface heat diffusion coefficient has a positive effect on relieving the maximum principal tensile stress. The maximum principal tensile stress reduces up to 52% when the surface heat diffusion coefficient changes from 165 kJ/(m^2·h·°C) to 8 kJ/(m^2·h·°C). Since the surface heat diffusion coefficient is related to wind speed, surface roughness, and surface thermal resistance condition [47], measures such as surface insulation, adding additives (such as defoamer) can be taken to reduce the surface heat diffusion coefficient and finally reduce the maximum principal tensile stress and prevent the occurrence of structural thermal cracks.

4.4. Effect of Temperature Rise Coefficient. Figure 10 shows the relationship between temperature and time with five different temperature rise coefficients which are 0.20 d^{-1}, 0.25 d^{-1}, 0.30 d^{-1}, 0.35 d^{-1}, and 0.40 d^{-1}, respectively. It can be seen that the temperature rise coefficient has a significant impact on the first hydration heat temperature rise process whether in the core region or near the boundary of the structure, except for the foot point D. The maximum temperature of point A is 48.2°C, 48.7°C, 49.0°C, 49.2°C, and 49.4°C, respectively, appeared at 420 hours, 380 hours, 340 hours, 320 hours, and 280 hours with the corresponding temperature rise coefficient. The temperature difference between the core and surface is 31.3 °C, 32.1°C, 32.6°C, 32.9°C, and 33.2°C, respectively. It is obvious that reducing the temperature rise coefficient can reduce the maximum temperature and also reduce the temperature difference between the core and surface of the structure by changing the rate of temperature rise in the condition of the same hydration heat generated.

Figure 11 shows the calculated and fitted maximum principal tensile stress at each point with a different temperature rise coefficient. The maximum principal tensile stress of four points with a different temperature rise coefficient shows a similar change regulation with that with a different surface heat diffusion coefficient, and the maximum principal tensile stress at four points also shows a law of quadratic function with the temperature rise coefficient. The foot points of the structure, including point D, are also the positions of stress concentration and the maximum principal tensile stress which has exceeded the allowable stress of the concrete if the temperature rise coefficient is greater than 0.30 d^{-1}.

In conclusion, appropriate decrease of the temperature rise coefficient has a positive effect on relieving the maximum principal tensile stress. The maximum principal tensile stress can reduce 18.9% when the temperature rise coefficient changes from 0.40 d^{-1} to 0.20 d^{-1}. Measures such as controlling pouring temperature and reducing the amount of cement [48] can be taken to reduce the temperature rise coefficient and decrease the maximum principal tensile stress in the result.

4.5. Effect of Solar Absorption Coefficient. The thermal parameters analyzed above have not considered the influence of the solar absorption coefficient, which was set to zero. However, studies [42, 49] found that the temperature field of the concrete structure is greatly affected by solar radiation. When calculating the radiant heat of the flat surface of a concrete structure, the annual variation of radiant heat ΔF and the annual average radiant heat $\Delta\overline{T}$ [1] are usually calculated as follows:

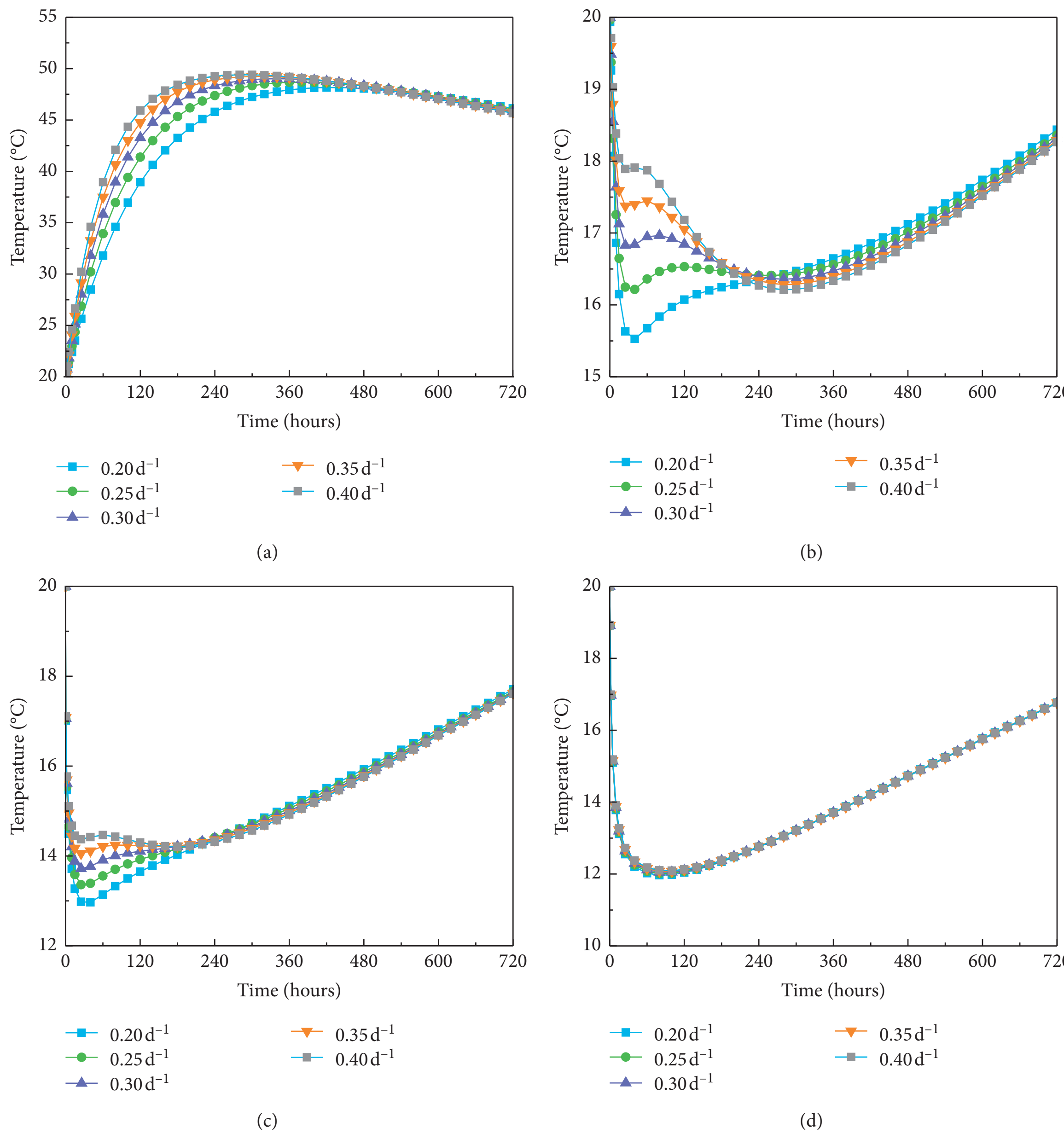

Figure 10: Temperature-time curves with different temperature rise coefficients. (a) Point A, (b) point B, (c) point C, and (d) point D.

$$\Delta F = \frac{A_s}{\beta},$$
$$\Delta \overline{T} = \frac{rS}{\beta}, \tag{21}$$

where A_s is the yearly amplitude of radiant heat, r is the solar absorption coefficient discussed in this section, and S is the solar radiation on cloudy days, which is calculated according to the solar radiation heat S_0 on sunny days. The calculation equation is given as follows:

$$S = S_0 (1 - kn), \tag{22}$$

where k is the coefficient, and n is the cloud cover. In this study, S_0 equals 924.5 kJ/(m^2·h), n equals 0.1, and k equals 0.668.

Figure 12 shows the relationship between temperature and time with six different solar absorption coefficients which are 0, 0.4, 0.5, 0.6, 0.7, and 0.8, respectively. The zero solar absorption coefficient is a contrast study condition. As shown in Figure 12, the solar absorption coefficient has a great impact on the temperature near the boundary of the structure but almost does not influence the core regions. The temperature arises generally linear along with the time at points A, B, and C. Also, the bigger solar absorption coefficient induced the higher temperature rise at these three

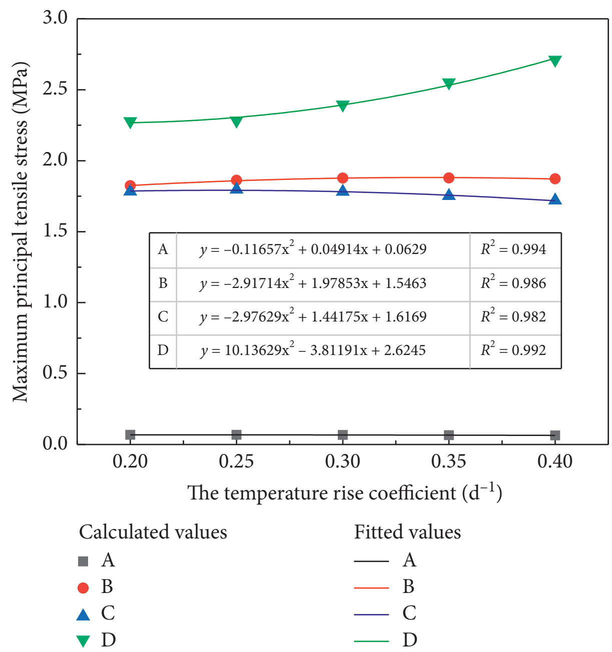

FIGURE 11: The calculated and fitted maximum principal tensile stress at each point with a different thermal temperature rise coefficient.

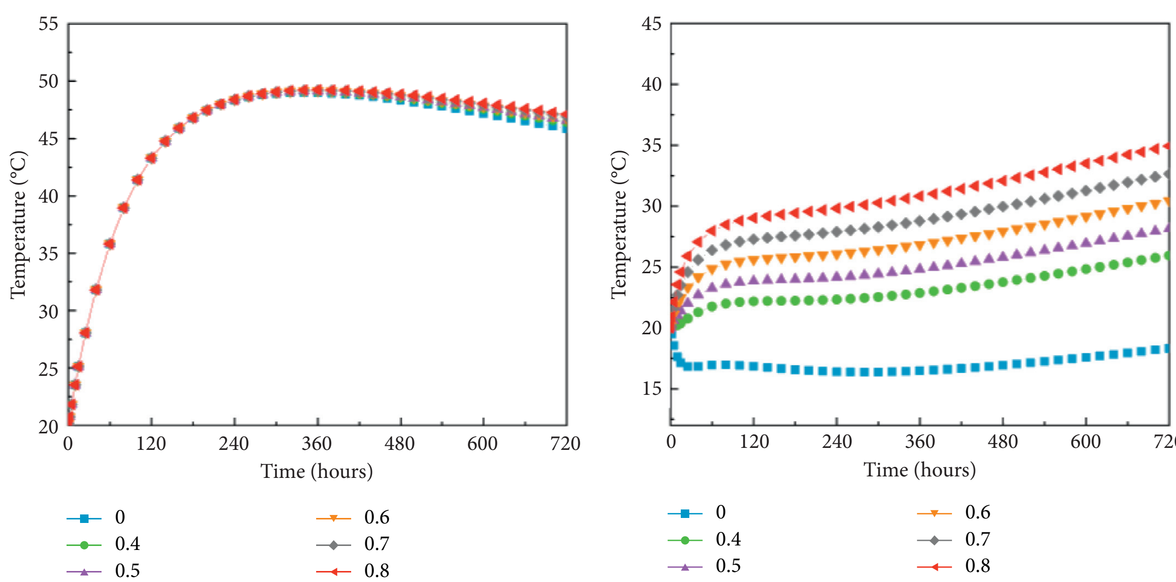

(a) (b)

FIGURE 12: Continued.

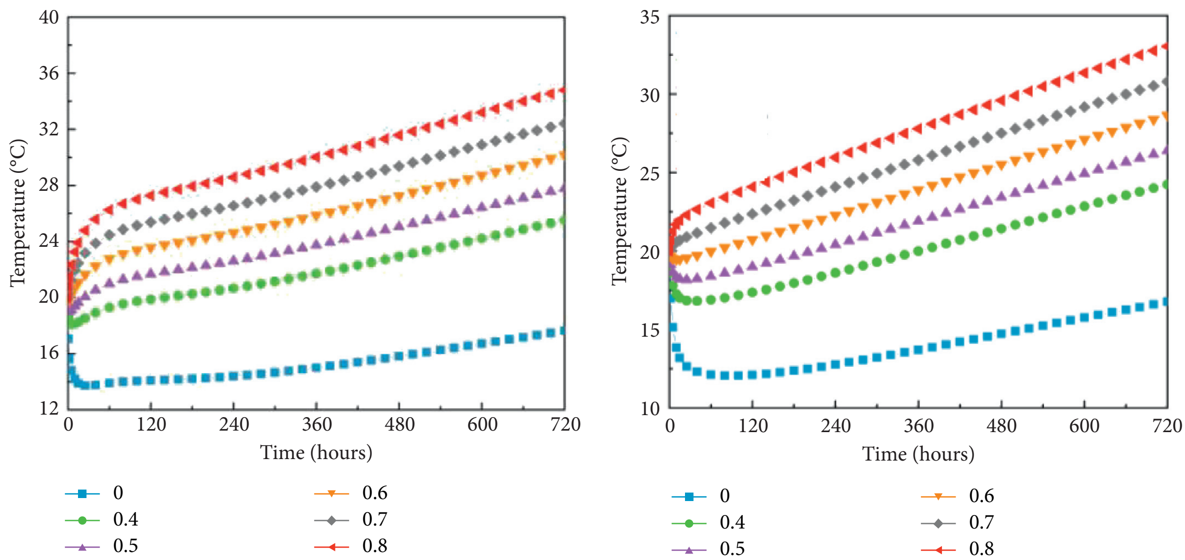

(c) (d)

Figure 12: Temperature-time curves with different solar absorption coefficients. (a) Point A, (b) point B, (c) point C, and (d) point D.

points. The maximum temperature of point A is close to 49.0°C appeared at about 340 hours with the corresponding solar absorption coefficient. The temperature difference between the core and surface is 32.6°C, 26.3°C, 24.3°C, 22.3°C, 20.4°C, and 18.4°C, respectively. It is because that more heat is induced by bigger solar absorption coefficient absorb by the surface and then against the internal heat dissipation. Therefore, it is demonstrated that the temperature difference between the core and surface reduces as the solar absorption coefficient increases.

Figure 13 shows the calculated and fitted maximum principal tensile stress at each point with a different solar absorption coefficient. It can be got that the maximum principal tensile stress of the study points all decrease to a certain degree when the solar absorption coefficient increases. However, in the matter, the maximum principal tensile stress in the structure is no more occurred at point D, but at point C which is located at the surface of the structure. This conclusion just explains the common physical weathering degradation phenomenon of the construction structure. The tensile stress values at all points are less than the allowable tensile stress. Fitting the maximum principal tensile stress with the solar absorption coefficient shows a quadratic function law.

In conclusion, increasing the solar absorption coefficient can reduce the tensile stress of the concrete foundation. The maximum principal tensile stress can reduce 21% when the solar absorption coefficient changes from 0 to 0.8. Because the solar absorption coefficient of the structure surface is related to the surface color [50], measures such as the dark coating of the surface formwork or using dark insulation can play a major role in increasing the surface solar absorption coefficient.

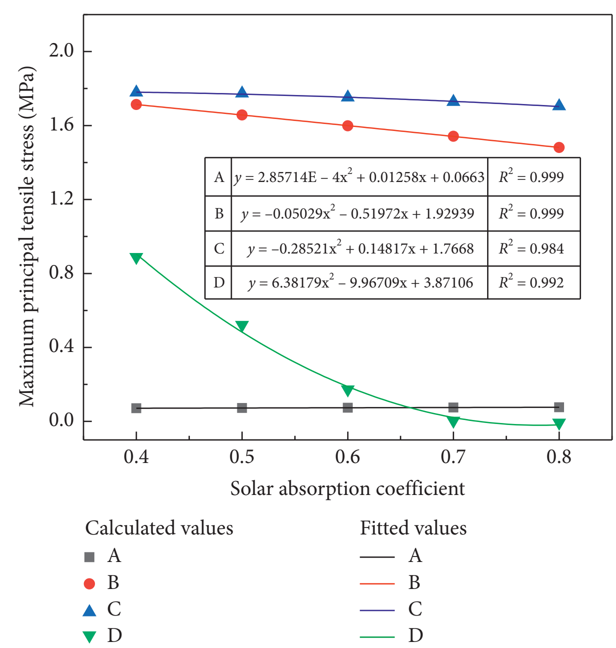

Figure 13: The calculated and fitted maximum principal tensile stress at each point with the different solar absorption coefficient.

4.6. Effect of Thermal Expansion Coefficient. The thermal expansion coefficient is a thermal parameter which not directly impact heat transfer but significantly influences thermal stress. Figure 14 shows the calculated and fitted maximum principal tensile stress at each point with a different thermal expansion coefficient. When the thermal expansion coefficient of concrete changes from $8 * 10^{-6}/°C$ to $12 * 10^{-6}/°C$, the maximum principal tensile stress at

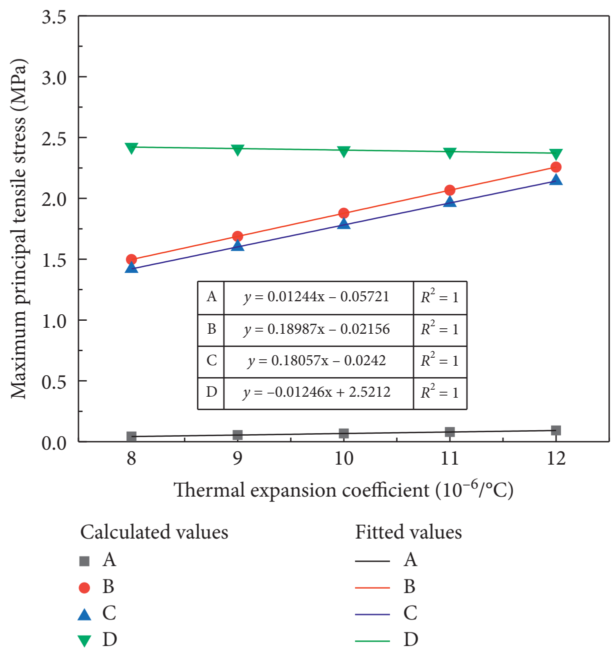

Figure 14: The calculated and fitted maximum principal tensile stress at each point with a different thermal expansion coefficient.

points A, B, and C of the structure increases with the increase of the thermal expansion coefficient while point D decreases. The maximum principal tensile stress of the structure also appears in the foot regions, such as point D. Fitting the maximum principal tensile stress with the thermal expansion coefficient shows a linearly relationship. The main reason is that under unconstrained conditions, the free temperature deformation is given as follows:

$$\begin{aligned} \varepsilon_x = \varepsilon_y = \varepsilon_z = \alpha T, \\ \gamma_{xy} = \gamma_{yz} = \gamma_{zx} = 0, \end{aligned} \quad (23)$$

where α is the thermal expansion coefficient.

Equation (23) shows that the bigger the thermal expansion coefficient, the higher the deformation of the structure and also the higher stress. However, the maximum principal tensile stress at point D shows an opposite change rule because when the thermal expansion coefficient changes from $8 * 10^{-6}$/°C to $12 * 10^{-6}$/°C, the maximum principal tensile stress of points B and C increases almost 50%, and the value has quickly approached point D. This shows that the restraint of the foundation has a certain release by stress increase of the free surface, but it releases little, so the maximum principal tensile stress of the foundation is reduced by only 2%.

5. Conclusions

Aiming to analyze the influence of thermal parameters on the temperature and thermal stress distribution of the foundation, six thermal parameters are chosen and discussed in this study. The main conclusions are listed as follows:

(1) Increasing the thermal conductivity of concrete and reducing the specific heat and temperature rise coefficient can reduce the maximum temperature of the structure. Other thermal parameters have no obvious effect on the maximum temperature.

(2) Increasing the specific heat, solar absorption coefficient, or thermal expansion coefficient has a positive effect on reducing the maximum principal tensile stress, but on the contrary of the effect of the thermal conductivity, surface heat diffusion coefficient, and temperature rise coefficient. Moreover, it is found that fitting the maximum principal tensile stress at different positions of the structure shows a linear function with thermal conductivity, specific heat, and thermal expansion coefficient and a quadratic function with surface heat diffusion coefficient, temperature rise coefficient, and solar absorption coefficient.

(3) Combined with the research results, the following temperature control and crack prevention measures are proposed under the condition of ensuring the concrete strength, such as reducing the amount of cement, increasing the particle size of coarse aggregate, and selecting coarse aggregate with a high thermal expansion coefficient.

Data Availability

The data used to support the findings of this study are available from the corresponding author upon request.

Conflicts of Interest

The authors declare that there are no conflicts of interest.

Acknowledgments

The authors acknowledge the research funding by the National Natural Science Foundation of China (no. 41901070), State Key Laboratory of Frozen Soil Engineering (no. SKLFSE201805), Natural Science Foundation of Inner Mongolia (2017MS0106), and Hydraulic Engineering Science and Technology Project of Inner Mongolia (no. 22200-5176042).

References

[1] B. F. Zhu, *Temperature Stress and Temperature Control of Mass Concrete*, China Water and Power Press, Beijing, China, 2nd edition, 2012.

[2] H. Ding, L. Zhang, P. Zhang, and Q. Zhu, "Thermal and stress analysis of early age concrete for spread footing," *Transactions of Tianjin University*, vol. 21, no. 6, pp. 477–483, 2015.

[3] C. Eloísa, S. Noemí, C. Tiago, and M. L. B. Farinha, "FEA model for the simulation of the hydration process and temperature evolution during the concreting of an arch dam," *Engineering Structures*, vol. 174, pp. 165–177, 2018.

[4] W. C. Liu, W. L. Cao, H. Q. Yan, T. Ye, and J. Wang, "Experimental and numerical studies of controlling thermal

cracks in mass concrete foundation by circulating water," *Applied Sciences*, vol. 6, no. 4, p. 110, 2016.

[5] S. Han, H. Yang, and Y. L. Wang, "Temperature control and numerical analysis for mass concrete pile cap of Haihuang bridge," *IOP Conference Series: Earth and Environmental Science*, vol. 153, no. 5, 2018.

[6] Y. Li, L. Nie, and B. Wang, "A numerical simulation of the temperature cracking propagation process when pouring mass concrete," *Automation in Construction*, vol. 37, pp. 203–210, 2014.

[7] Y. Z. Liu, J. F. Xiang, W. F. Chen et al., "Analysis of the water temperature evolution of long and narrow reservoir from impoundment to first operating period," *Journal of Hydraulic Engineering*, vol. 51, p. 111, 2020.

[8] X. H. He, H. Cheng, and H. X. Qin, "Study on temperature field and construction monitoring of hydration heat of railway cable-stayed bridge pile cap," *Advanced Materials Research*, vol. 243-249, pp. 1589–1596, 2011.

[9] J. Sun and J. Xie, "Simulation analysis of the hydration heat of large diameter CFST arch and its effects on loading age," *Applied Thermal Engineering*, vol. 150, pp. 482–491, 2019.

[10] Y. L. Chen, C. J. Wang, S. Y. Li, and L. J. Chen, "The effect of construction designs on temperature field of a roller compacted concrete dam - a simulation analysis by a finite element method," *Canadian Journal of Civil Engineering*, vol. 30, no. 6, pp. 1153–1156, 2003.

[11] H. W. Zhou, Y. H. Zhou, C. J. Zhao, and Z. Liang, "Optimization of the temperature control scheme for roller compacted concrete dams based on finite element and sensitivity analysis methods," *The Civil Engineering Journal*, vol. 14, no. 3, p. 116, 2016.

[12] M. H. Lee, Y. S. Chae, B. S. Khil, and H. D. Yun, "Influence of casting temperature on the heat of hydration in mass concrete foundation with ternary cements," *Applied Mechanics and Materials*, vol. 525, pp. 478–481, 2014.

[13] Y. Sargam, M. Faytarouni, K. Riding, K. Wang, C. Jharen, and J. Shen, "Predicting thermal performance of a mass concrete foundation: a field monitoring case study," *Case Studies in Construction Materials*, vol. 11, 2019.

[14] X. F. Zhang, S. Y. Li, Y. L. Li, Y. Ge, and H. Li, "Effect of superficial insulation on roller-compacted concrete dams in cold regions," *Advances in Engineering Software*, vol. 42, no. 11, pp. 939–943, 2011.

[15] H. F. Liu, Z. X. Shao, and H. Y. Feng, "Temperature field analysis of hydration heat of mass concrete cap," *Highway*, vol. 7, pp. 176–181, 2017.

[16] L. Han, X. M. Li, and Y. K. Wu, "Thermal stress analysis of concrete gravity dam based on start time," *HongShui River*, vol. 36, no. 5, p. 15, 2017.

[17] Y. C. Wang, Y. Hua, and C. Zhang, "Influence of different temperature control measures on crack resistance of large size concrete structure," *Journal of Highway and Transportation Research and Development*, vol. 36, no. 3, pp. 109–116, 2019.

[18] J. L. Chen, Z. G. Quan, and X. Peng, "Simulation analysis on mass concrete temperature field of lock floor layered pouring," *Journal of Environmental Science and Engineering A*, vol. 9, pp. 476–483, 2016.

[19] Y. N. Yu, W. Zhang, and Y. G. Shen, "Control measures for preventing crack on the surface of mass concrete abutment in early stage," *Journal of Zhejiang University (Engineering Science)*, vol. 44, no. 8, pp. 1621–1628, 2010.

[20] C. H. Zhu, X. T. Li, B. J. Wang, and Y.-J. Xie, "Influence of internal curing on crack resistance and hydration of concrete," *Journal of Building Materials*, vol. 16, no. 2, pp. 221–225, 2013.

[21] W. Z. Jin, L. H. J. Jiang, L. Han, L. Chen, X. Yan, and C. Chen, "Influence of curing temperature on the mechanical properties and microstructure of limestone powder mass concrete," *Structural Concrete*, vol. 22, no. 1, 2020.

[22] C. J. Lin, G. G. Fu, and L. L. Guo, "The experimental study on controlling the hydration heat temperature field of the Zhenyuling bridge pile caps," *Advanced Materials Research*, vol. 594-597, pp. 1509–1515, 2012.

[23] M. X. Zhang, M. C. Li, J. R. Zhang et al., "Experimental study on electrothermal and compaction properties of electrically conductive roller compacted concrete overwintering layer in high RCC dams," *Construction and Building Materials*, vol. 263, p. 111, 2013.

[24] Y. X. Hiu, X. R. Sun, H. Y. Wang et al., "Effect of hydration heat temperature and cracking mechanism of beam end in early stage of T-beam," *Journal of Jilin University (Engineering and Technology Edition)*, vol. 51, no. 3, pp. 1–9, 2020.

[25] G. B. Gao, C. X. Qian, Y. Zhuang, and C. Zhu, "Research on use of phase change materials for reduction of internal temperature rise of mass concrete," *Journal of Hydroelectric Engineering*, vol. 29, no. 1, pp. 197–201, 2010.

[26] L. W. Fu, J. F. Wang, W. P. Cheng, and H.-W. Xiang, "Causes and treatments of quadrate concrete pier's crack," *Journal of Zhejiang University (Engineering Science)*, vol. 44, no. 9, pp. 1738–1745, 2010.

[27] T. Ji, G. J. Ji, and G. X. Chen, "Influence of low-heat Portland cement on properties of dam concrete," *Journal of Hydroelectric Engineering*, vol. 31, no. 4, pp. 207–210, 2012.

[28] J. D. Xin, G. X. Zhang, Y. Liu et al., "Environmental impact and thermal cracking resistance of low heat cement (LHC) and moderate heat cement (MHC) concrete at early ages," *Journal of Building Engineering*, vol. 32, 2020.

[29] Y. Huang, G. Liu, S. Huang, R. Rao, and C. Hu, "Experimental and finite element investigations on the temperature field of a massive bridge pier caused by the hydration heat of concrete," *Construction and Building Materials*, vol. 192, pp. 240–252, 2018.

[30] P. Y Yan, "Mechanism of fly ash's effects during hydration process of composite binder," *Journal of the Chinese Ceramic Society*, vol. 35, no. S1, pp. 167–171, 2007.

[31] C. Wang, C. H. Yang, J. S. Qian, M. Zhong, and S. Zhao, "Behavior and mechanism of pozzolanic reaction heat of fly ash and ground granulated blastfurnace slag at early age," *Journal of the Chinese Ceramic Society*, vol. 40, no. 7, pp. 1050–1058, 2012.

[32] P. Siler, I. Kolarova, J. Kratky, J. Havlica, and J. Brandštetr, "Influence of superplasticizers on the course of Portland cement hydration," *Chemical Papers*, vol. 68, no. 1, pp. 90–97, 2014.

[33] H. Zhao, B. Liao, F. Nian, K. Wang, Y. Guo, and H. Pang, "Investigation of the clay sensitivity and cement hydration process of modified HPEG-type polycarboxylate superplasticizers," *Journal of Applied Polymer Science*, vol. 135, no. 32, p. 46572, 2018.

[34] L. Wang, F. Guo, Y. Lin, H. Yang, and S. W. Tang, "Comparison between the effects of phosphorous slag and fly ash on the C-S-H structure, long-term hydration heat and volume deformation of cement-based materials," *Construction and Building Materials*, vol. 250, p. 118807, 2020.

[35] X. Liu, C. Zhang, X. Chang, W. Zhou, Y. Cheng, and Y. Duan, "Precise simulation analysis of the thermal field in mass concrete with a pipe water cooling system," *Applied Thermal Engineering*, vol. 78, pp. 449–459, 2015.

[36] A. Tasrl and A. Susilawati, "Effect of cooling water temperature and space between cooling pipes of post-cooling system on temperature and thermal stress in mass concrete," *Journal of Building Engineering*, vol. 24, 2019.
[37] G. X. Zhang and Y. Liu, "Temperature control and crack prevention of super-high arch dam," *Journal of Hydraulic Engineering*, vol. 47, no. 3, pp. 382–389, 2016.
[38] Z. Si, D. Yang, L. Z. Huang, S. Li, and Z. Wang, "Effects of small temperature difference cooling on temperature stress of mass concrete," *Chinese Journal of Applied Mechanics*, vol. 35, no. 5, pp. 1146–1151, 2018.
[39] B. F. Zhu, "An implicit method for the stress analysis of concrete structures considering the effect of creep," *Journal of Hydraulic Engineering*, vol. 44, no. 5, pp. 40–46, 1983.
[40] H. W. Sha and T. H. De, "Thermal properties of concrete," *Sichuan Water Power*, vol. 5, no. 3, pp. 71–79, 1986.
[41] L. C. Wang, Z. Chang, and J. W. Bao, "Prediction model for the thermal conductivity of concrete based on its composite structure," *Journal of Hydraulic Engineering*, vol. 48, no. 7, pp. 765–772, 2017.
[42] J. R. Zhang, Y. Q. Zhou, J. P. Lin, and Z. Zhang, "Solar radiation affection on concrete box girder temperature effect," *Journal of Tongji University (Natural Science)*, vol. 36, no. 11, pp. 1479–1484, 2008.
[43] Ministry of Housing and Urban-Rural Development of the People's Republic of China, *GB 50496-2018, Standard for Construction of Mass Concrete, Ministry of Housing and Urban-Rural Development of the People's Republic of China*, China Architecture and Building Press, Beijing, China, 2018.
[44] Y. Sargam, K. Wang, and I. H. Cho, "Machine learning based prediction model for thermal conductivity of concrete," *Journal of Building Engineering*, vol. 34, 2021.
[45] I. Asadi, P. Shafigh, Z. F. B. Abu Hassan, and N. B. Mahyuddin, "Thermal conductivity of concrete: a review," *Journal of Building Engineering*, vol. 20, pp. 81–93, 2018.
[46] Q. Y. Zhang, *Test Research on the Material Property for the Face Slab Concrete of Concrete Face Dam in Cold Regions*, Zhengzhou University, Zhengzhou, China, 2016.
[47] B. F. Zhu, "Critical surface heat release coefficient of concrete blocks," *Water Resources and Hydropower Engineering*, vol. 1, no. 4, pp. 14–19, 1990.
[48] Y. H. Liu, M. Liu, K. X. Liu, and H. W. Wang, "Research and application of single-parameter exponential m value of adiabatic temperature rise of concrete," *Guangdong Building Materials*, vol. 34, no. 2, pp. 9–12, 2018.
[49] Y. Gu, Y. D. Li, and C. R. Yao, "Research of temperature field of concrete box girder under solar radiation," *Journal of Highway and Transportation Research and Development*, vol. 33, no. 2, pp. 46–53, 2016.
[50] K. J. Kontoleon and D. K. Bikas, "The effect of south wall's outdoor absorption coefficient on time lag, decrement factor and temperature variations," *Energy and Buildings*, vol. 39, no. 9, pp. 1011–1018, 2007.

Hindawi
Advances in Materials Science and Engineering
Volume 2021, Article ID 6613114, 12 pages
https://doi.org/10.1155/2021/6613114

Research Article

Long-Term Thermal Regimes of Subgrade under a Drainage Channel in High-Altitudinal Permafrost Environment

Hong Yu,[1,2,3] Hongwu Han,[4] Wei Ma,[2,3] Zekun Ding,[2,3] and Ling Chen[2,3]

[1]*School of Civil Engineering, Lanzhou University of Technology, Lanzhou 730050, China*
[2]*State Key Laboratory of Frozen Soil Engineering, Northwest Institute of Eco-Environment and Resources, Chinese Academy of Sciences, Lanzhou 730000, China*
[3]*University of Chinese Academy of Science, Beijing 100049, China*
[4]*Qinghai Water Resources and Hydropower Engineering Bureau Co. Ltd., Xining 810001, China*

Correspondence should be addressed to Wei Ma; mawei@lzb.ac.cn

Received 4 January 2021; Revised 23 January 2021; Accepted 2 February 2021; Published 12 February 2021

Academic Editor: Ying-hao Huang

In permafrost regions, construction of a channel involves a large amount of excavation activities and changes to surface water body, which can exert great impacts on the thermal regimes of permafrost underlying. In this paper, a coupled mathematical model of heat and moisture transfer was constructed for freeze-thaw soils to investigate the long-term thermal regimes of subgrade beneath a drainage channel built on the Qinghai-Tibet Plateau. Based on the numerical simulations, the thermal regimes of the subgrade both in warm and cold seasons were analyzed within a period of 50 years, as well as the impact of the widths of the channel. The results showed that the channel excavation and flowing water within could lead to a significant underlying permafrost degradation. During the first 30 years, the permafrost beneath the channel mainly experienced a rapid downward degradation. After that, the lateral thermal erosion of the flowing water led to a rapid permafrost degradation beneath the slope of the channel. In cold seasons, the shallow ground beneath the channel would not refreeze due to the flowing water and the thaw bulb actually expanded throughout the year. For the channel with a bottom width of 15 m, the thaw bulb beneath the channel could expand laterally to the natural ground about 10 m far away from the slope shoulder of channel till the 50th year. With different widths, the long-term thermal regimes of the subgrade beneath the channels differed considerably and the maximum difference was at the slope toe of the embankment. With the numerical simulated results, it is recommended that a channel built on permafrost should be wide-and-shallow rather than narrow-and-deep if conditions permit.

1. Introduction

Permafrost is defined as ground (soil or rock including ice) with a temperature at or below 0°C for at least two consecutive years [1, 2]. A quarter of the Northern Hemisphere and 17% of the exposed land surface of earth are underlain by permafrost [3]. The distribution of permafrost on earth can be of altitudinal and latitudinal character [4]. In China, the permafrost area accounts for 22% of the total land area, which is mainly distributed on the Qinghai-Tibet Plateau (QTP), the Northeastern China, and the high mountain areas in the Northwestern China. With an average elevation of more than 4000 m, the QTP has the largest distribution of altitudinal permafrost on earth [5]. Compared with latitudinal permafrost in the Northern America and Siberia, the permafrost on the QTP is characterized with high temperatures and thermal unstable, thus being more sensitive to climatic changes and human activities [6–8].

The QTP is also known as the Asian Water Tower. It is one of the three major distribution areas of lakes in China, and its lake area accounts for more than 50% of the total in China [9, 10]. In the context of global warming, the climate warming and wetting on the QTP was significant during the past decades, which led to significant changes in lake number and area [11–14]. The recent estimations showed that, since the mid-1990s, the area, level, and volume of lakes on the QTP showed a continuous increase [15, 16]. In a study by Liu et al. [17], a rapid expansion since 2000 was observed for lakes in the endorheic basin on the QTP, particularly in the Hoh Xil region with a continuous permafrost distribution. The rapid expansion of lakes could cause flood disasters, which may exert significant threatens to the production and living of local communities, as well as major engineering infrastructures nearby [18–20].

In 2011, the Zonag Lake in the central of the Hoh Xil regions burst suddenly, which was an extreme case of lake evolution on the QTP. After the outburst, a deep and wide gully developed at the breaking point and the flood entered the downstream lakes including the Kusai Lake, Haiding Nor Lake, and Yanhu Lake. At present, the four lakes are already connected together, and the first three ones lost their storage functions, making the Yanhu Lake become a tail-end-lake [21–24]. From 2011 to 2019, the surface area of the Zonag Lake decreased from 269 to 150 km^2, while the surface area of Yanhu Lake increased by almost 3 times from 73 to 209 km^2 [5, 25]. Considering the rapid changes, some researchers conducted predictions and concluded that an overflow would occur to the Yanhu Lake in a minimum of one to two years [21]. At about 10 km downstream the Yanhu Lake, there are the Qinghai-Tibet Railway, Qinghai-Tibet Highway, Qinghai-Tibet Power Transmission Line, Golmud-Lhasa Oil Pipeline, as well as several communication cables. It is well-known that all of them are of great importance for social and economic ties between the Tibet Autonomous Region and the inner China [26–28]. If the Yanhu Lake burst in an uncontrollable condition, these major linear infrastructures would be in danger and even be destroyed by the outburst flood.

To prevent this projected flood disaster, a large-scale drainage project was conducted in 2019 between the potential breaking point of the Yanhu Lake and the Qingshui River at the downstream [9, 29]. When serving as subgrade of man-made infrastructure, the physical and mechanical properties of permafrost are closely related to its thermal regimes [30–33]. Meanwhile, along with seasonal freezing and thawing in the active layer, significant (differential) frost heave and thaw subsidence would occur at the ground surface, which can cause series of damages to structures built upon [34]. Thus, the thermal regime of permafrost is a key variable that determines the bearing capacity and deformation of foundations and the long-term stability and integrity of the structures upon [35–38]. With regard to evolution of permafrost thermal regimes beneath hydraulic structures, the related research studies were scarce as there has been almost no large-scale hydraulic engineering conducted in continuous permafrost regions. In related fields, research studies on thermal interactions between thermokarst lake and underlying permafrost were conducted both in latitudinal and altitudinal permafrost environments. In 1978, a large tundra lake was drained to study the aggradation of permafrost into newly exposed lake-bottom sediments, and the active-layer thickness, snow depth, minimum soil temperatures, near-surface ground ice, soil heave, and permafrost temperatures had been measured for over 20 years [39]. Lin et al. [40] conducted filed observations on water and ground temperatures beneath and around a 2 m deep thermokarst lake on the QTP and found that the mean annual ground temperatures beneath the thermokarst lake were more 5°C higher than those in the surrounding terrain at the same depths. In a study by Niu et al. [41], characteristics of about 250 thermokarst lakes on the QTP were investigated and their influences on permafrost were evaluated based on field measurements in ground temperatures around a lake in the Beiluhe Basin. Through using numerical methods, Wen et al. [42] and Ling and Zhang [43] simulated the temporal and spatial variation of ground temperature and talik thickness beneath an expanding thermokarst lake on the QTP and the Alakan Arctic, respectively. In a study by Wen et al. [42], the lake was assumed to expand linearly with time both in radius and depth, while in a study by Ling and Zhang [43], the lake was assumed to expand linearly with time only in radius. Li et al. [44] conducted a moisture-heat coupled numerical simulation to investigate the permafrost degradation beneath a thermokarst pond with consideration of climate warming. Compared with thermokarst lakes, however, the thermal impact of a drainage channel to underlying permafrost may be more significant and complex due to the excavation of the channel and the running water within the channel. With regard to channels built in cold regions, Li et al. [45] established a moisture-heat-mechanic couple mathematic model and investigated the freeze-thaw influence on the channel using numerical simulations. Considering the effects of the seepage water, Zhang et al. [46, 47] investigated the thermal regimes of the permafrost beneath the dike with various antiseepage measures.

In this paper, the drainage channel of the Yanhu Lake was taken as an example and the thermal interactions among the drainage channel, the drainage water body, and the underlying permafrost subgrade were investigated through field observations and numerical simulations. With the Harlan model and Richard equation, a coupled mathematic model for heat and moisture transfer in freezing-thawing soils was established. Then, a numerical model was constructed based on the engineering geotechnical investigation conducted in the field and the dimensions of the drainage channel. The numerical model was validated with field observations carried out at the drainage channel. Then, the long-term evolution of thermal regimes of permafrost beneath the drainage with three bottom widths was investigated after a validation through using numerical simulations. It is hoped that the results of this study can provide scientific references for predicting and warning of the safe operation of the drainage channel.

2. Mathematical Model and Governing Equations

2.1. Liquid Water Flows. Without considering the effects of water vapor, the equivalent volume of water content θ in freeze-thaw soil based on the law of mass conservation can be expressed as follows:

$$\frac{\partial \theta}{\partial t} = \frac{\partial \theta_u}{\partial t} + \frac{\rho_i}{\rho_w}\frac{\partial \theta_i}{\partial t} = \nabla\left(q_{lh}\right), \tag{1}$$

where θ is the equivalent volume of water content ($m^3 \cdot m^{-3}$); θ_u is the volume of unfrozen water content ($m^3 \cdot m^{-3}$); θ_i is the volume of ice content ($m^3 \cdot m^{-3}$); ρ_i is the density of ice ($kg \cdot m^{-3}$); ρ_w is the density of water ($kg \cdot m^{-3}$); t is the time; and q_{lh} is the liquid water flux density which can represent liquid flows due to a pressure head gradient ($m \cdot s^{-1}$).

The migration of liquid water under potential gradient in frozen soil is similar to that in unfrozen unsaturated soil based on the Harlan model and can be described by Richard equation [48, 49]. Then, it is mainly influenced by the factors including water potential gradient and hydraulic conductivity of soils. The values of water potential gradient and hydraulic conductivity in unfrozen and frozen soils differ considerably, while the regulation of water migration can still be assumed to Darcy's law [50]. Only considering the potential gradient, the flux density of liquid water can be expressed as follows [51, 52]:

$$q_{lh} = -K_{lh}\nabla (h + y), \tag{2}$$

where y is the vertical coordinate (m); h is the pressure head (m); and K_{lh} is the water conductivity coefficient of liquid water under the action of soil-water potential gradient ($m \cdot s^{-1}$). Then, considering the equivalent volume water content θ as a dependent variable, the mass conservation equation of liquid water in unfrozen and frozen soils can be written as follows [53]:

$$\frac{\partial \theta}{\partial t} = \nabla \cdot \left[K_{lh}\nabla (h + y)\right]. \tag{3}$$

The relationship between the amount of water and energy in the soil can be reflected by soil-water characteristic curve (SWCC). Then, SWCC also can represent the relationship between matric, volume water content, and saturation in frozen and unfrozen soils [52]. In this study, the van Genuchten model and Mualem model are adopted to describe the hydraulic properties of unsaturated freeze-thaw soil [53, 54]. The hydraulic properties can be written as follows:

$$h = \frac{-\left(S_e^{1/-m} - 1\right)^{1/n}}{\alpha}, \tag{4}$$

$$S_e = \frac{\theta_l - \theta_r}{\theta_s - \theta_r} = \begin{cases} \dfrac{1}{\left[1 + |\alpha h|^n\right]^m}, & h < 0, \\ 1, & h \geq 0, \end{cases} \tag{5}$$

$$K = \begin{cases} K_s S_e^l \left[1 - \left(1 - S_e^{1/m}\right)^m\right]^2, & h < 0, \\ K_s, & h \geq 0, \end{cases} \tag{6}$$

where S_e is the effective saturation; K_s is the saturation water conductivity coefficient ($m \cdot s^{-1}$); θ_l, θ_s, and θ_r are liquid water content, saturated liquid water content, and residual water content ($m^3 \cdot m^{-3}$); α is the derivative of the soil intake value (m^{-1}); $m = 1 - 1/n$; and n and l are experience parameters, and Mualem suggested that l could be determined as 0.5 [54].

2.2. Heat Transfer. Compared with the heat conduction with phase change of ice to water, the energy released by the heat convection was very small and could be neglected during the heat transfer analysis of freeze-thaw soil [55–57]. Then, the governing equations of heat transfer in freeze-thaw soil can be written as follows [49]:

$$C_m \frac{\partial T}{\partial t} = \frac{\partial}{\partial x}\left(\lambda_m \frac{\partial T}{\partial x}\right) + \frac{\partial}{\partial y}\left(\lambda_m \frac{\partial T}{\partial y}\right), \tag{7}$$

where C_m is the equivalent volume heat capacity and λ_m is the equivalent thermal conductivity. According to the method of sensible heat capacity, equivalent volume heat capacity C_m and equivalent thermal conductivity λ_m in freeze-thaw soils can be written as follows [55, 58]:

$$C_m = \begin{cases} C_f, & T < T_f - \Delta T, \\ \dfrac{C_u + C_f}{2} + \dfrac{L_s}{2\Delta T}, & T_f - \Delta T \leq T \leq T_f + \Delta T, \\ C_u, & T > T_f + \Delta T, \end{cases} \tag{8}$$

$$\lambda_m = \begin{cases} \lambda_f, & T < T_f - \Delta T, \\ \dfrac{\lambda_u - \lambda_f}{2}\left[T - \left(T_m - \Delta T\right)\right] + \lambda_f, & T_f - \Delta T \leq T \leq T_f + \Delta T, \\ \lambda_u, & T > T_f + \Delta T, \end{cases} \tag{9}$$

where $T_f \pm \Delta T$ is the temperature range of phase change; C_u and λ_u are the volume heat capacity and thermal conductivity of unfrozen soil; C_f and λ_f are the volume heat capacity and thermal conductivity of frozen soil; and L_s is the latent heat of phase change in per unit volume. While the temperature ranges of phase change in different soil are difficult to gain, the heat transfer equation adopted in this study is written as follows [49]:

$$C\frac{\partial T}{\partial t} = \frac{\partial}{\partial x}\left(\lambda\frac{\partial T}{\partial x}\right) + \frac{\partial}{\partial y}\left(\lambda\frac{\partial T}{\partial y}\right) + L\frac{\partial \theta_i}{\partial t}\rho_i, \tag{10}$$

where C is the volume heat capacity; λ is the thermal conductivity; and L is the latent heat of freezing of liquid water (approximately 3.34×10^5 J·kg^{-1}).

After soil freezing, not all liquid water can be transferred to solid ice. The rest of liquid water is called as unfrozen water. Then, the unfrozen water content is related to factors including the temperature, pressure, water salinity, mineralogy, soil specific surface area, and soil surface chemistry [59–62]. Based on previous work and related theories, the empirical expression as follows is used to determine the maximum unfrozen water content in the freezing process [49, 50, 52]:

$$\theta_{u\max} = a(T - 273.15)^{-b}, \tag{11}$$

where a and b are parameters related to the soil properties. The volume liquid water content can be determined by temperature and equivalent volume [50, 52]:

$$\theta_l = \begin{cases} \theta, & \text{others,} \\ \theta_{u\max}, & T < T_f \text{ and } \theta > \theta_{u\max}, \end{cases} \tag{12}$$

where T_f is the freezing point of saturated soil (0°C). Previous studies showed that the freezing point of soil is not a fixed value, and the ice grows only when the water content exceeds $\theta_{u\max}$ [63].

3. A Drainage Channel Built in High-Altitude Permafrost Environment

3.1. Study Area and Drainage Channel. In this study, the drainage channel built for Yanhu Lake, in the Hoh Xil region on the QTP, was taken as an example. In the area, the elevation ranges from 4460 to 4500 m a.s.l. The meteorological data were collected from the Wu Daoliang weather station, which is about 70 km far away from the channel. The collected data showed that, in the period from 1965 to 2019, the main annual air temperature ranged from −6.5 to 3.7°C and the main annual precipitation ranged from 136 to 480 mm. Since the 1980s, the climate warming and wetting at the region was significant.

A standard whether station was set up at the channel in 2020. Figure 1 shows the observed air temperatures during the monitoring period from 24 May to 10 November in 2020. In the period, the maximum air temperature reached to 12°C, which appeared in mid-August. Combined with the collected air temperatures from the Wu Daoliang weather station, the air temperature at the projected area can be fitted using a sinusoidal function as follows:

$$T_o = -3.02 + 11.6\sin\left(\frac{2\pi t}{365} + 0.3\right), \tag{13}$$

where t is the time (d).

3.2. Ground Temperature Observation at the Channel. To observe thermal regimes of permafrost subgrade beneath the channel, three ground temperature boreholes including natural ground (NG), slope shoulder (SS), and slope toe (ST) of the channel were drilled after excavation of the channel (Figure 2). The three boreholes were 20 m in depth. Considering the symmetry of the channel, the three boreholes were all arranged at one side of the channel. Within each borehole, 32 ground temperature sensors were installed with a spacing of 0.5 m between 0–10 m depth and of 1 m below 10 m depth. The measurement range of the sensor is from −40 to 40°C, with an accuracy of ±0.05°C. All the sensors were connected to a CR6 data collector, and the observation frequency of ground temperatures was 6 hours.

4. Numerical Simulations and Results Analysis

4.1. Computational Model. Previous studies showed that the boundary error would be less than 10% when the computational domain is 3–5 times of the equivalent diameter of the model [64]. In this study, the computational model was constructed based on the actual dimension of the channel. The depth of the channel was 4.7 m, and the bottom width was set as 25 m. The slope of the channel was released by 1 : 3. At present, the water depth within the channel was determined as 1 m throughout one year based on the field survey. The computation on thermal regimes of subgrade under the channel can be simplified as a 2D unsteady heat transfer problem.

According to the geological survey conducted before the drainage excavation, the soil strata can be simplified as sandy gravel, silty clay, and weathered mudstone from the surface down. The thermal and hydraulic parameters of the three soil layers are listed in Table 1, which were gained based on the borehole drillings and related laboratory tests [34, 49, 50, 52, 65].

4.2. Boundary Conditions. According to the meteorological data from the Wu Daoliang weather station, the long-term air temperatures in the study area showed a linear increase with the rate of 0.33°C/10a. Then, based on the adherent layer theory [62], the upper boundaries of GF and FE were set as temperature boundary:

$$T = -0.502 + 11.6\sin\left(\frac{2\pi t}{365} + 0.3\right) + \frac{0.33t}{3650}, \tag{14}$$

where t is the time (d).

As an alternative to heat budget models, linear correlations between air and water temperatures during open water periods were studied widely in previous studies [66]. Based on the analysis of a stream's heat transport/budget equation, the air temperature shows a good linear relationship with water temperature. The relationship between the water temperature in the lake and the air temperature can be linearly fitted as follows:

$$T_w(t) = A + BT_a(t), \tag{15}$$

where $T_w(t)$ and $T_a(t)$ are the water temperature and the air temperature in the same time scale; A and B are constants; and t is the time (d).

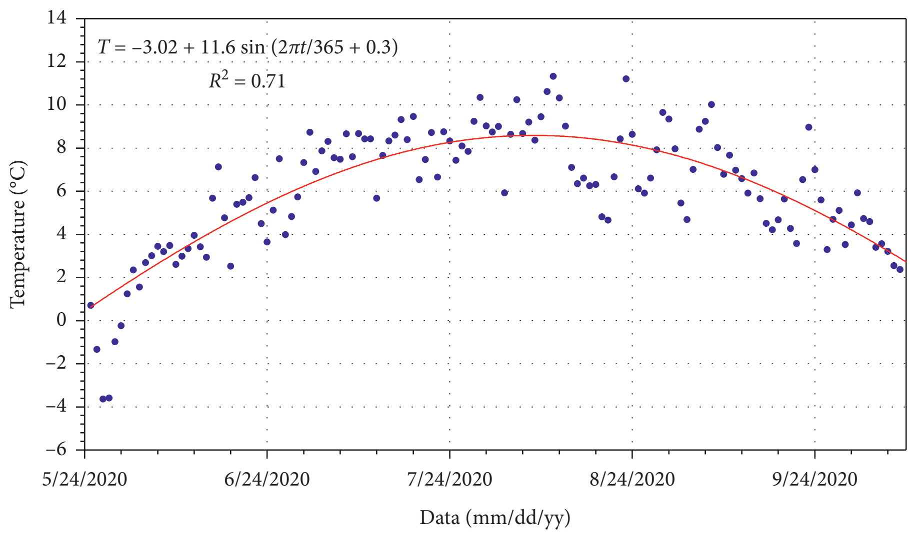

FIGURE 1: Observed air temperatures at the channel from May 24 to November 10, 2020.

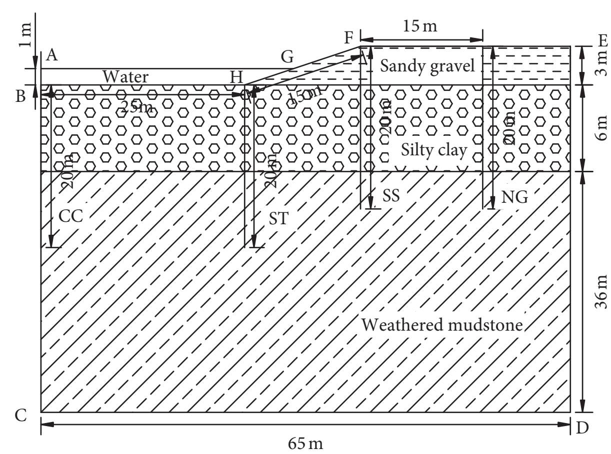

FIGURE 2: Ground temperature boreholes drilled at one side of the channel (unit: m).

TABLE 1: Thermal and hydraulic parameters of the three soil layers.

Parameters	λ_u W·m^{-1} °C^{-1}	λ_f W·m^{-1} °C^{-1}	C_u J·m^{-3}°C^{-1}	C_f J·m^{-3} °C^{-1}	A	B
Sandy gravel	1.91	2.61	2.41×10^6	1.86×10^6	10.67	0.57
Silty clay	1.42	2.12	3.35×10^6	2.54×10^6	6.9	0.47
Mudstone	1.47	1.82	2.09×10^6	1.84×10^6	9.3	0.52
Parameters	α m^{-1}	θ_r	θ_s	K_s m·s^{-1}	P kg·m^{-3}	L_s J·m^{-3}
Sandy gravel	3.28	0.01	0.44	2.4×10^{-7}	1800	2.31×10^7
Silty clay	2.6	0.02	0.35	3.3×10^{-8}	1600	6.51×10^7
Mudstone	2.3	0.02	0.25	1.2×10^{-8}	1700	3.77×10^7

According to the observed water temperatures (equation (15)) in lakes near the study area [40] and the air temperature showed as equation (16), the two constants of A and B in equation (14) used in this study were determined as follows:

$$T_{w1} = 5.96 + 5\sin\left(\frac{2\pi t}{365} - 0.65\right), \tag{16}$$

$$T_{a1} = -4.02 + 11.1\sin\left(\frac{2\pi t}{365} - 8.18\right), \tag{17}$$

where t is the time (d).

Without considering the impacts of artificial heat inputs, ground water inputs, stream shading, and wind sheltering, the values of A and B in equation (14) in the same area have very slight differences [66]. Then, the water temperature in the channel can be written as equation (17). Thus, the boundary BH and BG were set as follows:

$$T_w = 4.72 + 5.21\sin\left(\frac{2\pi t}{365} + 0.3\right) + \frac{0.15t}{3650}, \tag{18}$$

where t is the time (d).

The boundary condition at CD was set as heat flux with the value of 0.03 W/m^2, which was gained from the geothermal gradient within the ground temperature boreholes. The boundary of DE was thermal insulation boundary, and that of BC was the symmetry boundary. With the governing equations and boundary conditions above, the problem was solved numerically using the commercial software of COMSOL Multiphysics. The spatial and temporal discretization of governing equations was carried out by using the finite method. The simulation was conducted over a time period of 50 years before the drainage channel excavation to gain the initial temperature field. After the excavation, the boundary conditions were set as the ones described above.

4.3. Model Validation. A comparison between field observed and numerical simulated ground temperatures at ST on October 15 in the first year after the channel excavation was conducted to validate the numerical model and its parameterization (Figure 3). It can be found that the numerical simulated results agreed with the field observed well within the permafrost layer, including the depth of the permafrost table and the permafrost temperatures below. While in the active layer, there were some slight discrepancies between the numerical simulated and field observed ground temperatures. The discrepancies may relate to the simplification of the soil strata in the numerical simulation and the depth of the temperature sensors installed within the borehole. Overall, the numerical model and its parameterization in this study can be used to simulate the permafrost thermal regimes beneath the channel.

5. Results and Analysis

5.1. Long-Term Permafrost Thermal Regimes beneath the Channel in Warm Seasons. In the permafrost regions on the QTP, the maximum seasonal thaw depth generally occurs in mid-October. In the following analysis, the time point was chose to investigate the long-term permafrost thermal regimes beneath the channel. For brevity, we only took the channel with the width of 15 m as an example.

Figure 4 shows the thermal regimes of subgrade beneath the channel on October 15 within the 50 years after the channel excavation. It can be seen that, due to combined thermal effects of the flowing water and climate warming, the permafrost beneath the channel degraded rapidly with time went on. While in the natural ground far away from the channel, the permafrost degraded slowly due to the climate warming effect. In the 5th year, the maximum seasonal thaw depth at NG, ST, and centerline of the channel (CC) was 2.4, 9.2, and 10.5 m, respectively. A thaw bulb developed beneath the channel due to the thermal effect of flow water. The permafrost temperatures beneath the channel also increased considerably comparing with those beneath the natural ground at the same depths. For example, at the depth of 10 m, the permafrost temperatures under CC and NG were 0.14°C and −0.45°C, respectively, with a difference up to 0.6°C. With increase in the operation time, the thaw bulb beneath the channel expanded rapidly in the vertical direction. In 10th year after the channel excavation, the maximum seasonal thawing depth at CC and ST reached to 16.7 and 14.4 m, respectively. Till the 30th year, the permafrost beneath the channel degraded almost totally within the depth of 30 m. After that, the later thermal erosion of the channel became considerable, and the permafrost beneath the channel slope degraded with the depth of 30 m.

The above results showed that, during the first 30 years of the channel operation, the permafrost beneath the channel experienced a rapid downward degradation because of the significant thermal effect of the flowing water. Along with the rapid downward degradation of permafrost beneath the channel, a large lateral thermal gradient developed beneath the slope of the channel. This significant thermal gradient would cause uneven deformations of the slope and even slumps or collapse because of the temperature dependence of mechanical properties of frozen soils. Thus, how to ensure the slope stability of the channel is a great challenge in permafrost environment.

5.2. Long-Term Permafrost Thermal Regimes beneath the Channel in Cold Seasons. In mid-April, the active layer on the QTP generally refreezes completely. In order to investigate the thermal regimes of subgrade beneath the channel in cold seasons, ground temperature distributions within the subgrade on April 15 within the 50 years after the channel excavation were analyzed in this section.

Figure 5 shows the thermal regimes of subgrade beneath the channel on April 15 within the 50 years after the channel excavation. The shallow ground far away from the slope shoulder of the channel refrozen totally in cold seasons. While, beneath the channel, the thaw bulb beneath the channel did not freeze due to the flowing water. Compared with the last warm season in the same year (Figure 4), the thaw bulb still expanded in the following cold seasons. In the 5th year, the thaw bulb mainly exited vertically beneath the

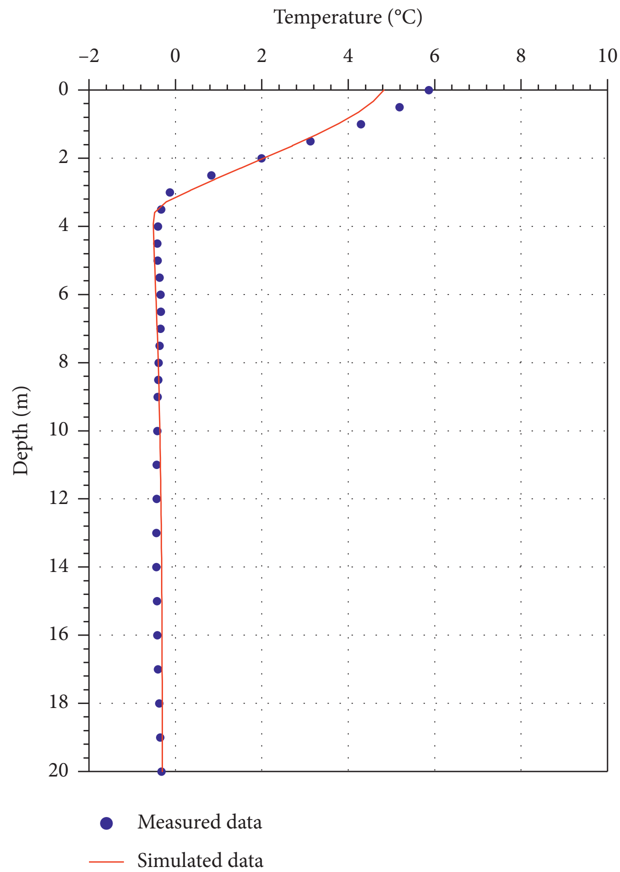

FIGURE 3: Field observed and numerical simulated ground temperatures vs depth at ST on October 15, 1st year after the excavation of the channel.

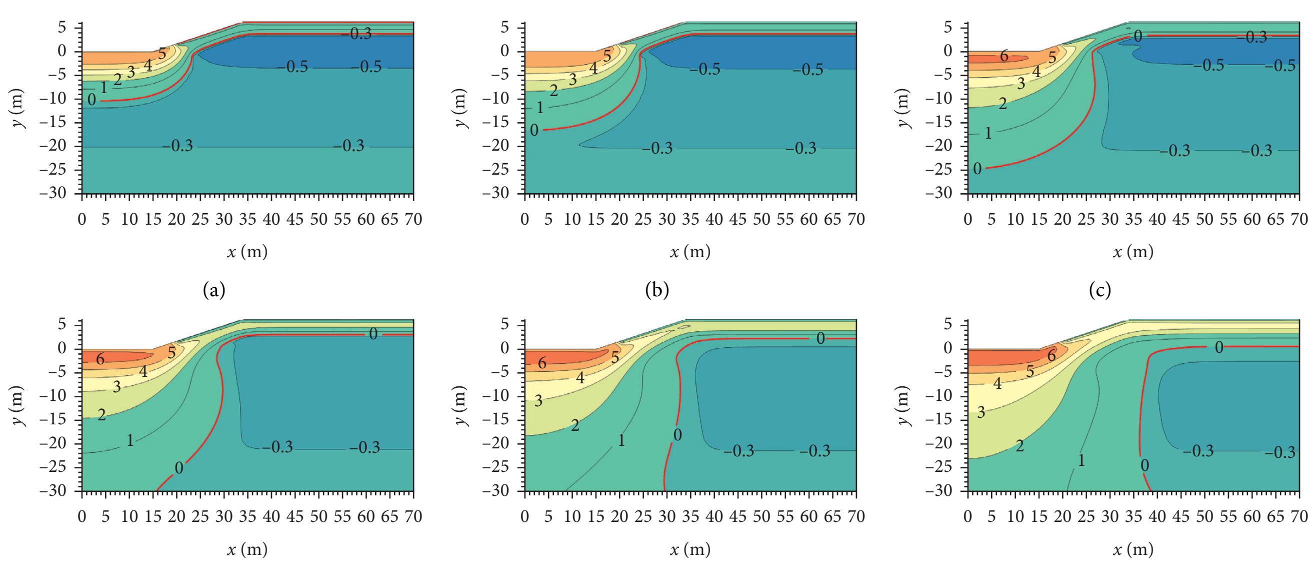

FIGURE 4: Thermal regimes of subgrade beneath the channel on October 15 after 5 (a), 10 (b), 20 (c), 30 (d), 40 (e), and 50 (f) years of the channel excavation (unit:°C).

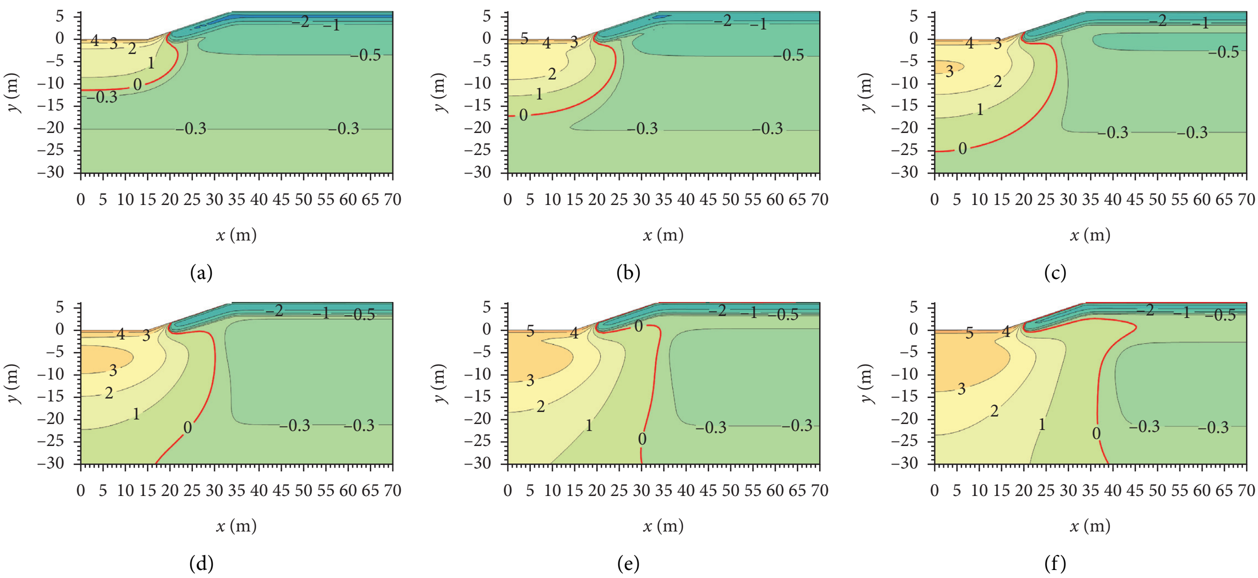

Figure 5: Thermal regimes of subgrade beneath the channel on April 15, after 5 (a), 10 (b), 20 (c), 30 (d), 40 (e), and 50 (f) years of the channel excavation (unit: °C).

bottom of the channel and the water body within the channel. With the time went on, the thaw bulb developed rapidly both in vertical and lateral directions. Special attention should be paid to ground thermal regimes beneath the slope of the channel. The shallow ground on the slope was frozen but the deep ground was thawed in the cold season due to the lateral thermal erosion of the flowing water. Till the 50th year, the thaw bulb in the cold season reached to the natural ground about 10 m far away from the slope shoulder of the channel. This meant that, all the deep ground beneath the slope of the channel was thawed throughout the year.

5.3. Impacts of Channel Width on Long-Term Thermal Regimes of Permafrost Subgrade. The width of the channel is not only related to the slope stability of the channel but also the permafrost degradation beneath the channel. To investigate the impacts of the channel width, a series of numerical simulations with different widths of the channel (15, 25, and 35 m) were carried out in this study. The flow of water was determined as a constant, and then the water depths were different for the channels with different widths. With the channel widths of 15, 25, and 35 m, the water depths were set as 1.53, 1.0, and 0.74 m, respectively.

Figure 6 shows ground temperature profiles at CC, ST, mid-slope (MS), and SS of the channels with the widths of 15, 25, and 35 m on October 15 in the 15th year after the channel excavation. It can be seen that, with different widths of the channel, the long-term thermal regimes of the subgrade differed, but the magnitudes of the difference were different at the four locations. At CC (Figure 6(a)), the ground thermal regimes for the channels with different widths were close to each other. The difference in the maximum thaw depths for the three cases was about 1 m. This means that, with different widths, the thermal erosion from the channels did not differed considerably at this location. While, at ST, the maximum thaw depths for the channels with different widths differed considerably. The smaller the width of the channel was, the grater the maximum thaw depth was at ST (Figure 6(b)). This considerable difference was related to different water depths within the channels with different widths. When the width of the channel increased from 15 to 35 m, the maximum thaw depth at ST decreased from 18.2 to 15.5 m. At MS (Figure 6(c)), the difference in maximum thaw depths for the three cases was also considerable. The wider the channel was, the smaller the maximum thaw depths were. At SS (Figure 6(d)), the ground thermal regimes were also very close to each other with three widths of the channel.

The above results showed that the thermal regimes of subgrade differed considerably for the channels with different widths. The difference mainly existed at slope toe and middle of the slope. While at the centerline and slope shoulder, the ground thermal regimes were very close to each other. For slope stability, the greater thaw depth is

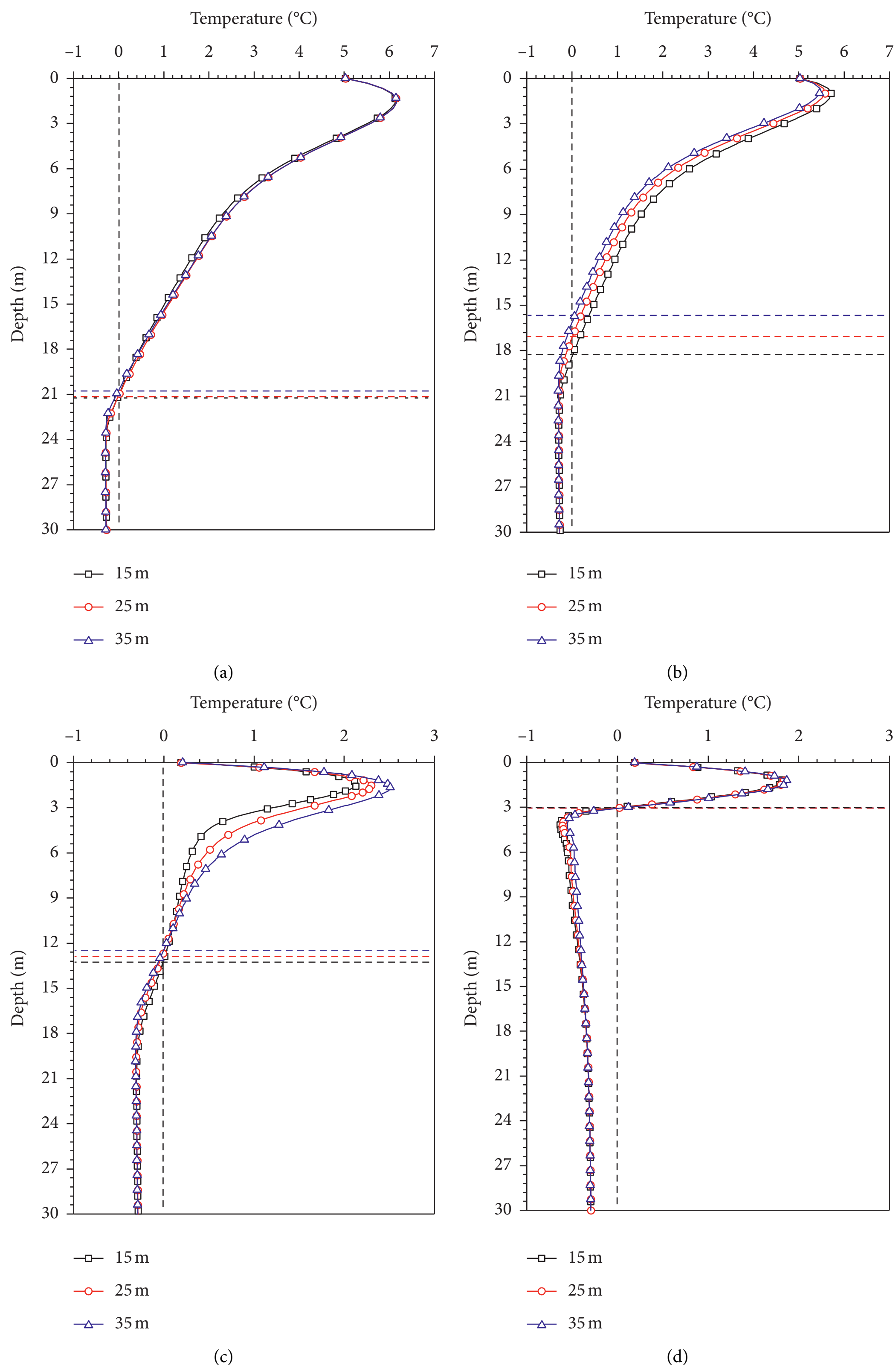

Figure 6: Ground temperature profiles at CC (a), ST (b), MS (c), and SS (d) of the channels with widths of 15, 25, and 35 m on October 15 in the 10^{th} year after the channel excavation.

generally harmful. Thus, it can be concluded that a channel built on permafrost should be wide-and-shallow rather than narrow-and-deep if conditions permit.

6. Conclusions

In permafrost regions, construction of a channel involves a large amount of excavation activities and changes to surface water body, which can exert great impacts on thermal regimes of underlying permafrost. In this paper, a coupled mathematical model of heat and moisture transfer for freeze-thaw soil was constructed to investigate the long-term thermal regimes of subgrade beneath a drainage channel built for an expanding lake on the Qinghai-Tibet Plateau. Using numerical simulations, thermal regimes of the subgrade both in warm and cold seasons were analyzed during a 50-year period, as well as the impact of the channel width. The conclusions were obtained as follows:

(1) In permafrost environment, excavation of the channel and the flowing water within could lead to a significant permafrost degradation. During the first 30 years of the channel operation, the permafrost beneath the channel mainly experienced a rapid downward degradation due to the thermal effect of the flowing water. After that, the lateral thermal erosion of the flowing water caused a rapid permafrost degradation beneath the slope of the channel. With a width of 15 m, the permafrost beneath the channel bottom and slope would degrade totally within a depth of 30 m in a 50-year period.

(2) The ground beneath the channel would not refreeze in cold seasons due to the flowing water within the channel, and the thaw bulb developed throughout a year. During the first 10 years, the thaw bulb mainly existed vertically beneath the channel. After that, the thaw bulb expanded quickly in lateral direction. Till the 50th year after the excavation of the channel, the thaw bulb reached to the natural ground about 25~30 m far away from the centerline of the channel with a width of 15 m.

(3) In permafrost environment, the width of the channel is an important factor. With different widths, the long-term thermal regimes of the subgrade beneath the channels differed considerably. The maximum difference was at the slope toe of the channel. The narrower the channel was, the larger the maximum thaw depth was at the slope toe. Thus, it is recommended that the channels in permafrost environment should be designed as wide-and-shallow rather than narrow-and-deep if conditions permit.

Data Availability

The data used to support the findings of this study are available from the corresponding author upon request.

Conflicts of Interest

The authors declare that they have no conflicts of interest related to this manuscript.

Acknowledgments

This work was supported by the National Natural Science Foundation of China (nos. 41772325 and 41630636).

References

[1] S. Kozarski, L. Marks, and J. Repelewska-Pkalowa, "Multi-language glossary of permafrost and related ground-ice terms," 1998.

[2] Y. H. Mu, G. Y. Li, W. Ma, Z. M. Song, Z. W. Zhou, and W. Fei, "Rapid permafrost thaw induced by heat loss from a buried warm-oil pipeline and a new mitigation measure combining seasonal air-cooled embankment and pipe insulation," *Energy*, vol. 203, Article ID 117919, 2020.

[3] S. Gruber, "Derivation and analysis of a high-resolution estimate of global permafrost zonation," *The Cryosphere*, vol. 5, no. 1, pp. 1547–1582, 2011.

[4] W. Dobinski, "Permafrost," *Earth-Science Reviews*, vol. 108, no. 3-4, pp. 158–169, 2011.

[5] P. Lu, J. Han, Z. Li et al., "Lake outburst accelerated permafrost degradation on Qinghai-Tibet Plateau," *Remote Sensing of Environment*, vol. 249, Article ID 112011, 2020.

[6] H. J. Jun, S. X. Li, G. D. Cheng, S. L. Wang, and X. Li, "Permafrost and climatic change in China," *Global and Planetary Change*, vol. 26, no. 4, pp. 387–404, 2000.

[7] H. J. Jun, Q. H. Yu, S. L. Wang, and L. Z. Lue, "Changes in permafrost environments along the Qinghai-Tibet engi1-neering corridor induced by anthropogenic activities and climate warming," *Cold Regions Science and Technology*, vol. 53, no. 3, pp. 317–333, 2006.

[8] W. Ma, G. D. Cheng, and Q. B. Wu, "Construction on permafrost foundations: lessons learned from the Qinghai-Tibet Railroad," *Cold Regions Science and Technology*, vol. 59, pp. 3–11, 2009.

[9] B. Liang, S. Qi, Z. Y. Li, Y. T. Li, and J. H. Chen, "Dynamic change of Lake area over the Tibetan Plateau and its response to climate change," *Mountain Research*, vol. 36, no. 2, pp. 206–216, 2018.

[10] B. K. Liu, L. Lin, Y. E. Du et al., "Causes of the outburst of Zonag lake in Hoh Xil, Tibetan plateau, and its impact on surrounding environment," *Journal of Geographical Sciences*, vol. 38, no. 2, pp. 305–311, 2016.

[11] J. Du, "Change of temperature in Tibetan plateau from 1961–2000," *Acta Geographica Sinica*, vol. 56, no. 33, pp. 232–239, 2001.

[12] T. Niu, L. Chen, and Z. Zhou, "The characteristics of climate change over the Tibetan Plateau in the last 40 years and the detection of climatic jumps," *Advances in Atmospheric Sciences*, vol. 21, no. 2, pp. 193–203, 2004.

[13] Y. F. Shi, Y. P. Shen, E. Kang et al., "Recent and future climate change in northwest China," *Climate Change*, vol. 80, no. 3-4, pp. 379–393, 2007.

[14] Q. L. You, S. C. Kang, N. Pepin et al., "Climate warming and associated changes in atmospheric circulation in the eastern and central Tibetan Plateau from a homogenized dataset," *Global and Planetary Change*, vol. 72, no. 1-2, pp. 11–24, 2010.

[15] G. Q. Zhang, T. D. Yao, H. J. Xie et al., "Response of Tibetan Plateau lakes to climate change: trends, patterns, and

mechanisms," *Earth-Science Reviews*, vol. 208, Article ID 103269, 2020.

[16] L. Y. Tang, X. F. Duan, F. J. Kong et al., "Influences of climate change on area variation of Qinghai lake on Qinghai-Tibetan plateau since 1980s," *Scientific Reports*, vol. 8, no. 1, p. 7331, 2018.

[17] W. H. Liu, C. W. Xie, L. Zhao et al., "Rapid expansion of lakes in the endorheic basin on the Qinghai-Tibet Plateau since 2000 and its potential drivers," *CATENA*, vol. 197, Article ID 104924, 2021.

[18] G. Zhang, T. Yao, W. Chen et al., "Regional differences of lake evolution across China during 1960s–2015 and its natural and anthropogenic causes," *Remote Sensing of Environment*, vol. 221, pp. 386–404, 2019.

[19] C. Song, B. Huang, K. Richards, L. Ke, and V. Hien Phan, "Accelerated lake expansion on the Tibetan Plateau in the 2000s: induced by glacial melting or other processes?" *Water Resources Research*, vol. 50, no. 4, pp. 3170–3186, 2014.

[20] Y. Lei, K. Yang, B. Wang et al., "Response of inland lake dynamics over the Tibetan Plateau to climate change," *Climatic Change*, vol. 125, no. 2, pp. 281–290, 2014.

[21] W.-h. Liu, C.-w. Xie, L. Zhao et al., "Dynamic changes in lakes in the Hoh Xil region before and after the 2011 outburst of Zonag lake," *Journal of Mountain Science*, vol. 16, no. 5, pp. 1098–1110, 2019.

[22] Y. E. Du, B. K. Liu, W. G. He, S. Q. Duan, F. J. Hou, and Z. L. Wang, "Dynamic change and cause analysis of salt lake area in Hoh Xil on Qinghai-Tibet Plateau during 1976–2017," *Journal of Geographical Sciences*, vol. 40, no. 1, pp. 47–54, 2018.

[23] Q. B. Wu, Y. W. Zhou, and C. J. Tong, *Permafrost Survey and Mapping*, Science Press, Beijing, China, 2018.

[24] Q. Chen, D. P. Wen, X. F. Wen, and S. P. Xie, "Preliminary conception of hydrological monitoring scheme for cocoacili salt lake in Qinghai province," *Yellow River*, vol. 41, no. 11, pp. 7–10, 2019.

[25] X. Yao, M. Sun, P. Gong et al., "Overflow probability of the salt lake in Hoh Xil region," *Journal of Geographical Sciences*, vol. 28, no. 5, pp. 647–655, 2018.

[26] Y. B. Lang, Y. Zheng, W. Jin, Y. H. Mu, and M. T. Chai, "Method of three-dimensional monitoring on permafrost around lake draining project on the Qinghai-Tibet Plateau," *Journal of Yangtze River Scientific Research Institute*, pp. 1–8, 2020.

[27] X. J. Yao, M. P. Sun, P. Gong et al., "Overflow probability of the salt lake in Hoh Xil region," *Journal of Geographical Sciences*, vol. 71, no. 9, pp. 1520–1527, 2016.

[28] C. W. Xie, W. H. Liu, J. C. Wu et al., "Environmental changes caused by the outburst of Zonag Lake and the possible outburst model of Yanhu Lake in the Hoh Xil region," *Journal of Glaciology and Geocryology*, vol. 41, no. 6, pp. 1–16, 2019.

[29] R. H. Ma, G. S. Yang, H. T. Duan et al., "Number, area, and spatial distribution of lakes in China," *Scientia Sinica (Terrae)*, vol. 41, no. 3, pp. 394–401, 2011.

[30] Y. H. Mu, W. Ma, Y. Z. Liu, and Z. Z. Sun, "Monitoring investigation on thermal stability of air-convection crushed-rock embankment," *Cold Regions Science and Technology*, vol. 62, no. 2-3, pp. 160–172, 2010.

[31] Y. Mu, G. Wang, Q. Yu, G. Li, W. Ma, and S. Zhao, "Thermal performance of a combined cooling method of thermosyphons and insulation boards for tower foundation soils along the Qinghai-Tibet power transmission line," *Cold Regions Science and Technology*, vol. 121, pp. 226–236, 2016.

[32] Y. Mu, G. Li, Q. Yu, W. Ma, D. Wang, and F. Wang, "Numerical study of long-term cooling effects of thermosyphons around tower footings in permafrost regions along the Qinghai-Tibet power transmission line," *Cold Regions Science and Technology*, vol. 121, pp. 237–249, 2016.

[33] Y. Mu, W. Ma, G. Li, F. Niu, Y. Liu, and Y. Mao, "Impacts of supra-permafrost water ponding and drainage on a railway embankment in continuous permafrost zone, the interior of the Qinghai-Tibet Plateau," *Cold Regions Science and Technology*, vol. 154, pp. 23–31, 2018.

[34] Z. W. Wu, Y. M. Lai, and E. M. Zang, *Tunnel Engineering in Cold Region*, Ocean Press, Beijing, China, 2003.

[35] Y. M. Lai, M. Y. Zhang, and S. Y. Li, *Theory and Application of Cold Regions Engineering*, Science Press, Beijing, China, 2009.

[36] X. T. Xu, R. Q. Bai, Y. Lai, M. Y. Zhang, and J. G. Run, "Work conjugate stress and strain variables for unsaturated frozen soils," *Journal of Hydrology*, vol. 582, Article ID 124537, 2020.

[37] X. T. Xu, B. X. Wang, C. X. Fan, and W. D. Zhang, "Strength and deformation characteristics of silty clay under frozen and unfrozen states," *Cold Regions Science and Technology*, vol. 172, Article ID 102982, 2020.

[38] X. T. Xu, W. D. Zhang, C. X. Fan, Y. Lai, and J. Wu, "Effect of freeze–thaw cycles on the accumulative deformation of frozen clay under cyclic loading conditions: experimental evidence and theoretical model," *Road Materials and Pavement Design*, vol. 11, 2019.

[39] J. R. Mackay and C. R. Burn, "The first 20 years (1978-1979 to 1998-1999) of ice-wedge growth at the Illisarvik experimental drained lake site, western Arctic coast, Canada," *Canadian Journal of Earth Sciences*, vol. 39, no. 1, pp. 95–111, 2002.

[40] Z. J. Lin, F. J. Niu, J. Luo, M. H. Liu, and G. A. Yin, "Thermal regime at bottom of Thermokarst Lake along Qinghai-Tibet engineering corridor," *Earth Science-Journal of China University of Geosciences*, vol. 40, no. 1, pp. 179–188, 2015.

[41] F. J. Niu, Z. J. Lin, H. Liu, and J. H. Lu, "Characteristics of thermokarst lakes and their influence on permafrost in Qinghai–Tibet Plateau," *Geomorphology*, vol. 132, no. 3-4, pp. 222–233, 2011.

[42] Z. Wen, Z. Yang, Q. Yu et al., "Modeling thermokarst lake expansion on the Qinghai-Tibetan Plateau and its thermal effects by the moving mesh method," *Cold Regions Science and Technology*, vol. 121, pp. 84–92, 2016.

[43] F. Ling and T. Zhang, "Simulating heat source effect of a thermokarst lake in the first 540 years on the Alaskan Arctic using a simple lake expanding model," *Cold Regions Science and Technology*, vol. 160, pp. 176–183, 2019.

[44] S. Li, H. Zhan, Y. Lai, Z. Sun, and W. Pei, "The coupled moisture-heat process of permafrost around a thermokarst pond in Qinghai-Tibet Plateau under global warming," *Journal of Geophysical Research: Earth Surface*, vol. 119, no. 4, pp. 836–853, 2014.

[45] S. Y. Li, Y. M. Lai, M. Y. Zhang, W. S. Pei, C. Zhang, and F. Yu, "Centrifuge and numerical modeling of the frost heave mechanism of a cold-region canal," *Acta Geotechnica*, vol. 14, no. 12, pp. 1113–1128, 2018.

[46] H. Zhang, J. Zhang, E. Wang, Z. Zhang, W. Cao, and P. Zhou, "Thermal and settlement analyses under a riverbank over permafrost," *Computers and Geotechnics*, vol. 91, pp. 48–57, 2017.

[47] H. Zhang, J. Zhang, E. Wang, M. Zhang, Z. Zhang, and M. Chai, "Analysis of thermal regime under riverbank in permafrost region," *Applied Thermal Engineering*, vol. 123, pp. 963–972, 2017.

[48] R. L. Harlan, "Analysis of coupled heat-fluid transport in partially frozen soil," *Water Resources Research*, vol. 9, no. 5, pp. 1314–1323, 1973.

[49] X. Z. Xu, J. C. Wang, and L. X. Zhang, *Physics of Frozen Soil*, Science Press, Beijing, China, 2010.

[50] M. L. Zhang, Z. Wen, K. Xue, L. Z. Chen, and D. S. Li, "A coupled model for liquid water, water vapor and heat transport of saturated-unsaturated soil in cold regions: model formulation and verification," *Environmental Earth Sciences*, vol. 75, no. 8, pp. 1–19, 2016.

[51] K. Hansson, J. Simunek, M. Mizoguchi, L.-C. Lundin, and M. T. van Genuchten, "Water flow and heat transport in frozen soil: numerical solution and freeze-thaw applications," *Vadose Zone Journal*, vol. 3, no. 2, pp. 693–704, 2004.

[52] M. L. Zhang, "The influence of rainfall variations on the thermal-moisture dynamics of the embankment in permafrost regions of the Qinghai-Tibet Plateau," Ph. D. dissertation, University of Chinese Academy of Sciences, Lanzhou, China, 2016.

[53] M. T. van Genuchten, "A closed-form equation for predicting the hydraulic conductivity of unsaturated soils," *Soil Science Society of America Journal*, vol. 44, no. 5, pp. 892–898, 1980.

[54] Y. Mualem, "A new model for predicting the hydraulic conductivity of unsaturated porous media," *Water Resources Research*, vol. 12, no. 3, pp. 513–522, 1976.

[55] Y.-W. Jame and D. I. Norum, "Heat and mass transfer in a freezing unsaturated porous medium," *Water Resources Research*, vol. 16, no. 4, pp. 811–819, 1980.

[56] W. D. An, Z. W. Wu, and W. Ma, *Interaction Among Temperature, Moisture and Stress Field in Frozen Soil*, Lanzhou University Press, Lanzhou, China, 1990.

[57] W. D. An, Z. W. Wu, and W. Ma, *Temperature, Water Stress and Interaction of Frozen Soil*, Lanzhou University press, Lanzhou, China, 1989.

[58] Y. M. Lai, Z. W. Wu, S. J. Zhang, W. B. Yu, and Y. S. Deng, "In-situ observed study for effect of heat preservation in cold regions tunnels," *Journal of the China Railway Society*, vol. 1, pp. 81–86, 2003.

[59] H. B. Dillon and O. B. Andersland, "Predicting unfrozen water contents in frozen soils," *Canadian Geotechnical Journal*, vol. 3, no. 2, pp. 53–60, 1966.

[60] D. M. Anderson and N. R. Morgenstern, "Physics, chemistry, and mechanics of frozen ground: a review," in *Proceedings of the Second International Conference on Permafrost*, pp. 257–288, National Academy of Sciences, Washington, DC, USA, July 1973.

[61] L. U. Arenson and D. C. Sego, "The effect of salinity on the freezing of coarse-grained sands," *Canadian Geotechnical Journal*, vol. 43, no. 3, pp. 325–337, 2006.

[62] M. M. Darrow, S. L. Huang, and S. Akagawa, "Adsorbed cation effects on the frost susceptibility of natural soils," *Cold Regions Science and Technology*, vol. 55, no. 3, pp. 263–277, 2009.

[63] H. P. Hu, S. X. Yang, and Z. D. Lei, "A numerical simulation for heat and moisture transfer during soil freezing," *Journal of Hydraulic Engineering*, vol. 7, pp. 1–8, 1992.

[64] Y. X. Xia and Y. D. Wang, *Mechanical Calculation of Tunnel Structure*, People's Communications Press, Beijing, China, 2001.

[65] J. M. Zhang, "Study on roadbed stability in permafrost regions on Qinghai-Tibetan plateau and classification of permafrost in Highway engineering," Ph. D. Dissertation, University of Chinese Academy of Sciences, Lanzhou, China, 2004.

[66] T. R. Erickson and H. G. Stefan, "Linear air/water temperature correlations for streams during open water periods," *Journal of Hydrologic Engineering*, vol. 5, no. 3, pp. 317–321, 2000.

Hindawi
Advances in Materials Science and Engineering
Volume 2021, Article ID 6687183, 12 pages
https://doi.org/10.1155/2021/6687183

Research Article

Vibration Characteristics of Subway Tunnel Structure in Viscous Soil Medium

Dawei Ren,[1,2] Shengjun Shao,[1] Xiaoshan Cao ,[1] and Yifeng Hu[1]

[1]*School of Civil Engineering and Architecture, Xi'an University of Technology, Xi'an 710048, China*
[2]*School of Sciences, Xi'an University of Technology, Xi'an 710048, China*

Correspondence should be addressed to Xiaoshan Cao; caoxsh@xaut.edu.cn

Received 28 December 2020; Revised 18 January 2021; Accepted 27 January 2021; Published 8 February 2021

Academic Editor: Yanhu Mu

Based on research on subway tunnels in a viscous soil medium, this paper establishes the vibration equation of a tunnel structure by using the theory of moderately thick cylindrical shells and the method of wave propagation. The soil around the tunnel is represented in simplified form as an isotropic viscoelastic medium to obtain the equation of motion of the soil, and the vibration control equation of the tunnel under the influence of viscous soil is obtained by coupling. By numerical calculations, the variation trends in the natural vibration frequency of the tunnel and attenuation affected by soil viscosity under different modes are given. Furthermore, the influences of the tunnel radius, wall thickness, and length on the vibration characteristics of a tunnel structure in viscous soil are discussed. This study will provide a reference for the design of subway vehicles and the antivibration design of subway tunnel structures.

1. Introduction

The influence of environmental vibrations caused by subway train operations is a problem that has attracted much attention, and many researchers have conducted a series of studies on this issue. These studies have mainly involved features such as the track system, tunnel structure, and physical characteristics of the surrounding strata. With the widespread use of shield technology in tunneling, a cylindrical shell structure has become the first choice for urban subway tunneling. The study of the natural vibration characteristics of underground structures, especially the calculation of their natural vibration frequency, is an important part of their dynamic analysis, which provides a theoretical basis for the dynamic calculation of structural design loads. At present, research on such structures mainly focuses on the theory of thin shells [1–4]. However, the thickness diameter ratio of subway tunnel structures is generally greater than 1 : 12, which does not conform to the assumptions of thin-shell theory.

Various studies have been performed to model ground-borne vibrations from underground railways using numerical and analytical methods. Moore and Guan [5] used continuous reflection to study the dynamic response of a tunnel under incident seismic waves, and their results showed that the interaction between soil and the tunnel was significant. Clouteau et al. [6, 7] established a three-dimensional model to calculate the dynamic interaction between a tunnel and soil, simulated the tunnel and soil with a finite element and a boundary element, respectively, and explained how the boundary element effectively simulated the periodic medium. The effectiveness of this method was demonstrated using two tunnels as examples. Forrest and Hunt [2, 3] proposed a pipe-in-pipe model and determined the dynamic response of a tunnel system in three-dimensional elastic soil by considering the tunnel-rock interaction. Gupta et al. [8] compared the pipe-in-pipe model and the periodic finite element-boundary element coupling model and analyzed the dynamic response of a tunnel lining in full space using these two models. Hussein et al. [9] developed a model for analyzing vibrations from railway tunnels in a half-space by using the pipe-in-pipe model. Then, Kuo et al. [10] proposed a pair of parallel-tunnel models in homogeneous full space and calculated the difference between the vertical and horizontal results of the double-tunnel model and the single-tunnel model. Clot et al. [11] extended this model to predict dynamic responses of a double-deck circular tunnel in full space. Parry et al. [12] verified the behavior of the pipelines in a software model of pipeline vibrations to determine ground noise and vibration levels above a construction tunnel. Yang et al. [13] used a centrifuge model experiment and numerical simulations to study the influence of changes in soil parameters with depth on vibrations caused by a tunnel. Via a comparison between experimental results and numerically simulated results, the validity of considering soil as a homogeneous medium in numerical simulations was illustrated.

Both numerical and analytical methods were used in the above studies to simulate the soil mass with a single medium. Therefore, other researchers used model of saturated porous media to simulate soil to increase the accuracy of the models. Senjuntichai et al. [14] studied time-harmonic vertical vibrations of an axisymmetric rigid foundation embedded in a homogeneous poroelastic soil. Kumar et al. [15] analyzed the radial displacement field of the solid phase and fluid phase when the surface of a cylindrical tunnel in saturated porous media was subjected to time-varying loads. Hasheminejad et al. [16, 17] studied the dynamic stress concentration in the area around the porous wall of a cylindrical cavity in an infinite saturated elastic medium under different vibrational modes and considered the dynamic response of the cavity lining and the surrounding soil under a moving load when the lining was not fully in contact with the surrounding saturated soil. Gao et al. [18] improved a 2.5-dimensional finite-element model, and He et al. [19, 20] proposed a 2.5-dimensional coupled finite element-boundary element model to simulate the three-dimensional dynamic interaction between saturated soil and a tunnel. Di et al. [21] presented a 3-dimensional multilayer model of a cylindrical tunnel for investigating train-induced dynamic stress in saturated soils, which considers multiple moving loads and the grouting layer of a shield tunnel. Lu and Jeng [22, 23] studied the dynamic response of fixed infinite cylindrical holes in porous media under axisymmetric ring loading and discussed the analytical determination of the dynamic response of porous media in half-space under moving point loading. On the basis of a fractional derivative model and the theory of saturated porous media, Gao and Wen [24] studied the dynamic characteristics of a viscoelastic soil fractional derivative viscoelastic lining system in the frequency domain under axisymmetric loading and fluid pressure. Yuan et al. [25, 26] determined the pore pressure transfer function of a tunnel in saturated soil, compared the equivalent model of elastic soil with the model of saturated soil, and studied the effect of pore fluids in the soil on the ground vibrations due to a tunnel buried in a layered half-space. In addition, some researchers have paid attention to the effect of the void between the soil and the tunnel interface [27, 28].

The above literature contains in-depth and detailed analyses of the vibrations caused by subway trains from multiple perspectives. However, although they are an essential parameter in vibration propagation, the vibration characteristics of tunnels buried in viscous soil have rarely been reported. In fact, the thickness-diameter ratio of most subway tunnels excavated by shield tunneling machines is greater than $1:12$, and hence it is inappropriate to use thin-shell theory to model a tunnel in most studies. In addition, as a result of the natural complexity of soil, the soil around a tunnel is essentially an unsaturated porous medium. When the coupling between a tunnel and soil is considered, the influence of the soil medium on the natural vibration characteristics of the tunnel structure mainly comprises the influence of the additional mass and additional stiffness. Therefore, in this paper, the theory of moderately thick cylindrical shells is used to build a tunnel model, the Voigt-Kelvin equation is used to describe the constitutive relation of the soil medium, and the dispersion characteristic equation for the vibration characteristics of a tunnel in viscous soil is deduced by coupling of the tunnel and soil.

2. Vibration Equation of Tunnel Structure

The cylindrical coordinate system and a geometric model of the tunnel structure studied in this paper are shown in Figure 1. The tunnel structure is represented by the inner cylinder, and the soil around the tunnel is represented by the outer cylinder. In the figure, L, R, and h represent the length, radius, and wall thickness of the tunnel, respectively; u, v, and w represent the axial, tangential, and radial displacements of the tunnel surface, respectively; x, θ, and r denote the axial, tangential, and radial coordinates of the shell; q_x, q_θ, and q_r represent the external forces on the middle surface of the tunnel structure in the axial, tangential, and radial directions, respectively. On the basis of the theory of moderately thick shells [29], the equations of motion of the displacement components in the tunnel can be established as follows:

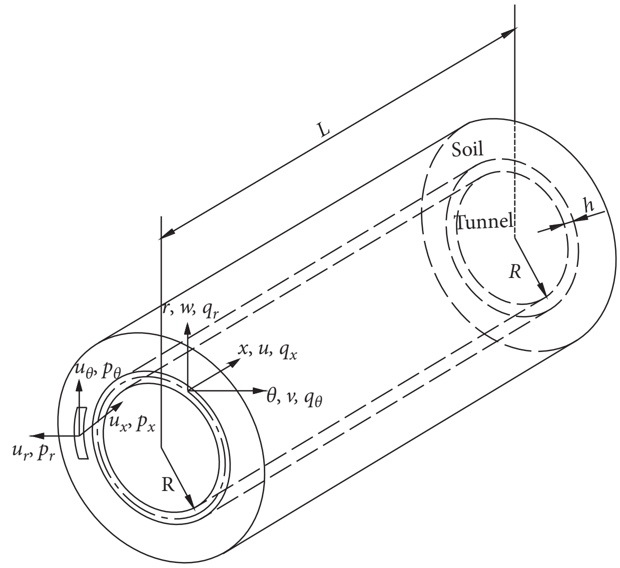

Figure 1: Geometric model of tunnel and soil.

$$\begin{aligned}&\frac{\partial^2 u}{\partial x^2}+\left(\frac{1-\nu}{2R^2}\right)\left(\frac{\partial^2 u}{\partial\theta^2}\right)+\left(\frac{1+\nu}{2R}\right)\left(\frac{\partial^2 v}{\partial x\partial\theta}\right)+\left(\frac{\nu}{R}\right)\left(\frac{\partial w}{\partial x}\right)+\left(\frac{1}{K}\right)q_x\\&\quad+\left(\frac{h^2\varepsilon^{(a)}}{12R}\right)\left(\frac{\partial^2\phi}{\partial x^2}-\left(\frac{1-\nu}{2R^2}\right)\left(\frac{\partial^2\phi}{\partial\theta^2}\right)-\left(\frac{1-\nu}{2R^2}\right)\left(\frac{\partial^2 v}{\partial x\partial\theta}\right)\right)=\left(\frac{\rho J_0}{K}\right)\left(\frac{\partial^2 u}{\partial t^2}\right),\end{aligned}\tag{1a}$$

$$\begin{aligned}&\left(\frac{1+\nu}{2R}\right)\left(\frac{\partial^2 u}{\partial x\partial\theta}\right)+\left(\frac{1-\nu}{2}\right)\left(\frac{\partial^2 v}{\partial x^2}\right)+\left(\frac{1}{R^2}\right)\left(\frac{\partial^2 v}{\partial\theta^2}\right)+\left(\frac{1}{R^2}\right)\left(\frac{\partial w}{\partial\theta}\right)+\left(\frac{q_\theta}{K}\right)\\&\quad+\left(\frac{h^2\varepsilon^{(a)}}{12R}\right)\left(\left(\frac{1-\nu}{2}\right)\left(\frac{\partial^2\varphi}{\partial x^2}\right)-\left(\frac{1}{R^2}\right)\left(\frac{\partial^2\varphi}{\partial\theta^2}\right)\right)+\left(\frac{Gh}{KRk_\tau}\right)\left(\varphi-\left(\frac{v}{R}\right)+\left(\frac{1}{R}\right)\left(\frac{\partial w}{\partial\theta}\right)\right)=\left(\frac{\rho J_0}{K}\right)\left(\frac{\partial^2 v}{\partial t^2}\right),\end{aligned}\tag{1b}$$

$$\begin{aligned}&-\left(\frac{\nu}{R}\right)\left(\frac{\partial u}{\partial x}\right)-\left(\frac{1}{R^2}\right)\left(\frac{\partial v}{\partial\theta}\right)-\left(\frac{1}{R^2}\right)w+\left(\frac{Gh}{KRk_\tau}\right)\left(\frac{\partial}{\partial\theta}\right)\left(\varphi-\frac{v}{R}+\left(\frac{1}{R}\right)\left(\frac{\partial w}{\partial\theta}\right)\right)\\&\quad+\left(\frac{h^2\varepsilon^{(a)}}{12R^3}\right)\left(\frac{\partial\varphi}{\partial\theta}\right)+\left(\frac{Gh}{Kk_\tau}\right)\left(\frac{\partial}{\partial x}\right)\left(\phi+\frac{\partial w}{\partial x}\right)+\frac{q_r}{K}=\left(\frac{\rho J_0}{K}\right)\left(\frac{\partial^2 w}{\partial t^2}\right),\end{aligned}\tag{1c}$$

$$\begin{aligned}&\frac{\partial^2\phi}{\partial x^2}+\left(\frac{1-\nu}{2R^2}\right)\left(\frac{\partial^2\phi}{\partial\theta^2}\right)-\frac{m_x}{D}-\left(\frac{1}{D}\right)\left(\frac{Gh}{k_\tau}\right)\left(\phi+\frac{\partial w}{\partial x}\right)+\left(\frac{1+\nu}{2R}\right)\left(\frac{\partial^2\varphi}{\partial x\partial\theta}\right)\\&\quad+\frac{\varepsilon^{(a)}}{R}\left(\frac{\partial^2 u}{\partial x^2}-\left(\frac{1-\nu}{2R^2}\right)\left(\frac{\partial^2 u}{\partial\theta^2}\right)\right)=\left(\frac{\rho J_2}{D}\right)\left(\frac{\partial^2\phi}{\partial t^2}\right),\end{aligned}\tag{1d}$$

$$\begin{aligned}&\left(\frac{1-\nu}{2}\right)\left(\frac{\partial^2\varphi}{\partial x^2}\right)+\left(\frac{1}{R^2}\right)\left(\frac{\partial^2\varphi}{\partial\theta^2}\right)-\frac{Gh}{Dk_\tau}\left(\varphi-\frac{v}{R}+\left(\frac{1}{R}\right)\left(\frac{\partial w}{\partial\theta}\right)\right)-\frac{m_\theta}{D}+\left(\frac{1+\nu}{2R}\right)\left(\frac{\partial^2\phi}{\partial x\partial\theta}\right)\\&\quad+\frac{\varepsilon^{(a)}}{R}\left(\left(\frac{1-\nu}{2}\right)\left(\frac{\partial^2 v}{\partial x^2}\right)-\left(\frac{1}{R^2}\right)\left(\frac{\partial^2 v}{\partial\theta^2}\right)-\left(\frac{1}{R^2}\right)\left(\frac{\partial w}{\partial\theta}\right)\right)=\left(\frac{\rho J_2}{D}\right)\left(\frac{\partial^2\varphi}{\partial t^2}\right).\end{aligned}\tag{1e}$$

In the above equations, Young's modulus of the shell material is denoted by E, the shear modulus is denoted by G, Poisson's ratio is denoted by ν, and the density of the shell material is denoted by ρ; ϕ and φ represent the rotation of a point in the tunnel structure in the $x-r$ and $x-\theta$ planes, respectively; and m_x and m_θ denote the external forces on the $x-r$ and $x-\theta$ plans, respectively; k_r is the shear factor of the cylindrical shell; and $\varepsilon^{(a)}$ represents this item as an additional term, and t is time, where $k_r=6/5$, $K=Eh/(1-\nu^2)$, $D=Eh^3/12(1-\nu^2)$, $J_0=h$, and $J_2=h^3/12$.

By using the wave propagation method, the solutions related to the displacement, the axial propagation wave number k, and the circumferential mode number n can be obtained as follows:

$$\begin{aligned} u &= U\cos(n\theta)\exp[i(\omega t - kx)],\\ v &= V\sin(n\theta)\exp[i(\omega t - kx)],\\ w &= W\cos(n\theta)\exp[i(\omega t - kx)],\\ \phi &= \Phi\cos(n\theta)\exp[i(\omega t - kx)],\\ \varphi &= \Psi\sin(n\theta)\exp[i(\omega t - kx)], \end{aligned} \tag{2}$$

where U, V, W, Φ, and Ψ are the amplitudes of the displacement of the tunnel structure in the x, θ, and r directions and the $x-r$ and $x-\theta$ planes, respectively, and ω is the frequency. By substituting the form of equation (2) into equations (1a)–(1e), the vibration equation of the tunnel structure based on the theory of moderately thick cylindrical shells can be deduced by omitting the additional terms:

$$[g][l]\overline{U} + [\overline{K}]\mathbf{q} = 0. \tag{3}$$

In equation (3), $[\overline{K}]$ and $[g]$ are diagonal matrices of order 5, $[l]$ is a coefficient matrix of order 5, $\overline{U} = (U, V, W, \Phi, \Psi)^T$, and $\mathbf{q} = (q_x, q_\theta, q_r, m_x, m_\theta)^T$, where the elements of each matrix are as follows:

$$\begin{aligned}
&\overline{K}_{11} = \overline{K}_{22} = \overline{K}_{33} = \frac{1}{K}, \quad \overline{K}_{44} = \overline{K}_{55} = \frac{-1}{D},\\
&g_{11} = \cos(n\theta)\exp[i(\omega t - kx)],\\
&g_{22} = \sin(n\theta)\exp[i(\omega t - kx)],\\
&g_{33} = \cos(n\theta)\exp[i(\omega t - kx)],\\
&g_{44} = \cos(n\theta)\exp[i(\omega t - kx)],\\
&g_{55} = \sin(n\theta)\exp[i(\omega t - kx)],\\
&l_{11} = -k^2 - \frac{1-\nu}{2R^2}n^2 + \frac{\rho J_0}{K}\omega^2, \quad l_{12} = -\frac{1+\nu}{2R}ikn = -l_{21}, \quad l_{13} = -ik\frac{\nu}{R} = -l_{31}, \quad l_{14} = l_{15} = 0,\\
&l_{22} = -\frac{1-\nu}{2}k^2 - \frac{1}{R^2}n^2 - \left(\frac{1}{KR^2}\right)\left(\frac{Gh}{k_\tau}\right) + \frac{\rho J_0}{K}\omega^2, \quad l_{23} = -\frac{1}{R^2}n - \left(\frac{1}{KR^2}\right)\left(\frac{Gh}{k_\tau}\right)n = l_{32}, \quad l_{24} = 0, \quad l_{25} = \left(\frac{1}{KR}\right)\left(\frac{Gh}{k_\tau}\right),\\
&l_{33} = -\frac{1}{R^2} - \left(\frac{1}{KR^2}\right)\left(\frac{Gh}{k_\tau}\right)n^2 - \left(\frac{1}{K}\right)\left(\frac{Gh}{k_\tau}\right)k^2 + \frac{\rho J_0}{K}\omega^2, \quad l_{34} = -\left(\frac{1}{K}\right)\left(\frac{Gh}{k_\tau}\right)ik, \quad l_{35} = \left(\frac{1}{KR}\right)\left(\frac{Gh}{k_\tau}\right)n,\\
&l_{41} = l_{42} = 0, \quad l_{43} = \left(\frac{1}{D}\right)\left(\frac{Gh}{k_\tau}\right)ik, \quad l_{44} = -k^2 - \frac{1-\nu}{2R^2}n^2 - \left(\frac{1}{D}\right)\left(\frac{Gh}{k_\tau}\right) + \frac{\rho J_2}{D}\omega^2, \quad l_{45} = -\frac{1+\nu}{2R}ikn = -l_{54},\\
&l_{51} = 0, \quad l_{52} = \left(\frac{1}{DR}\right)\left(\frac{Gh}{k_\tau}\right), \quad l_{53} = \left(\frac{1}{DR}\right)\left(\frac{Gh}{k_\tau}\right)n, \quad l_{55} = -\frac{1-\nu}{2}k^2 - \frac{1}{R^2}n^2 - \left(\frac{1}{D}\right)\left(\frac{Gh}{k_\tau}\right) + \frac{\rho J_2}{D}\omega^2.
\end{aligned} \tag{4}$$

3. Equation of Motion of Soil

If it is assumed that the soil around a tunnel is a homogeneous and isotropic linearly elastic medium, the equation of displacement for any point within the soil mass can be represented by the following Navier equation of motion [30]:

$$(\lambda + \mu)\nabla\nabla\cdot\overline{\mathbf{u}} + \mu\nabla^2\overline{\mathbf{u}} + \rho_s\mathbf{f} = \rho_s\frac{\partial^2\overline{\mathbf{u}}}{\partial t^2}. \tag{5}$$

In equation (5), $\overline{u} = (u_r, u_\theta, u_x)^T$ is the displacement vector of the soil mass, $\mathbf{f}$ is the vector of body forces, $\lambda = 2\nu_s G_s/(1-\nu_s)$, and $\mu = E_s/2(1+\nu_s)$ are the Lamé constants of the medium (where G_s is the shear modulus, E_s is Young's modulus, and ν_s is Poisson's ratio), ρ_s is the density of the medium, and ∇ is the Hamilton differential operator. In this case, the only body forces acting are those due to gravity; however, because the desired solution relates to vibration about an equilibrium position, these are ignored, and $\mathbf{f}$ is correspondingly set to zero.

If the soil around the tunnel structure is assumed to be a homogeneous and isotropic viscoelastic medium, the constitutive equation is represented by the Voigt-Kelvin equation for viscoelastic materials:

$$s_{ij} = 2\mu e_{ij} + 2\eta\frac{\mathrm{d}e_{ij}}{\mathrm{d}t}, \tag{6}$$

where s_{ij} and e_{ij} represent deviatoric stress and deviatoric strain, respectively, μ is the shear modulus, and η is the coefficient of viscosity. If equation (6) is used to replace the constitutive equation of a linear elastomer $s_{ij} = 2\mu e_{ij}$, the equation of motion of the soil mass can be expressed as

$$(\tilde{\lambda} + \tilde{\mu})\nabla\nabla \cdot \overline{\mathbf{u}} + \tilde{\mu}\nabla^2\overline{\mathbf{u}} + \rho_s f = \rho_s \frac{\partial^2 \overline{\mathbf{u}}}{\partial t^2}. \tag{7}$$

In equation (7), $\tilde{\lambda} = \lambda + \overline{\lambda}(\partial/\partial t)$, $\tilde{\mu} = \mu + \overline{\mu}(\partial/\partial t)$, $\overline{\lambda} = -(2/3)\eta$, $\overline{\mu} = \eta$, and $(\partial/\partial t)$ represents the first partial derivative of the function with respect to time t.

According to the Stokes-Helmholtz vector decomposition theorem, the wave equation (7) can be solved by making use of the scalar potential Π and the vector potential Ω, and hence the displacement vector field can be expressed as follows:

$$\overline{\mathbf{u}} = \nabla\Pi + \nabla \times \mathbf{\Omega}, \tag{8}$$

where Π and Ω satisfy the following wave equations, respectively, in which c_p and c_s are the longitudinal wave velocity and shear wave velocity, respectively, in the soil medium.

$$\nabla^2\Pi = \left(\frac{1}{c_p^2}\right)\left(\frac{\partial^2\Pi}{\partial t^2}\right), \quad \nabla^2\mathbf{\Omega} = \left(\frac{1}{c_s^2}\right)\left(\frac{\partial^2\mathbf{\Omega}}{\partial t^2}\right). \tag{9}$$

The Laplace equation for equation (9) above in a cylindrical coordinate system can be expressed as

$$\begin{aligned}
\nabla^2\Pi &= \left(\frac{1}{r}\right)\left(\frac{\partial\Pi}{\partial r}\right) + \left(\frac{\partial^2\Pi}{\partial r^2}\right) + \left(\frac{1}{r^2}\right)\left(\frac{\partial^2\Pi}{\partial\theta^2}\right) + \frac{\partial^2\Pi}{\partial x^2},\\
\nabla^2\mathbf{\Omega} &= \left(\nabla^2\Omega_r - \frac{\Omega_r}{r^2} - \left(\frac{2}{r^2}\right)\left(\frac{\partial\Omega_\theta}{\partial\theta}\right)\right)\mathbf{e}_r\\
&\quad + \left(\nabla^2\Omega_\theta - \frac{\Omega_\theta}{r^2} + \left(\frac{2}{r^2}\right)\left(\frac{\partial\Omega_r}{\partial\theta}\right)\right)\mathbf{e}_\theta + \nabla^2\Omega_x\mathbf{e}_x,
\end{aligned} \tag{10}$$

where $\mathbf{e}_x$, $\mathbf{e}_\theta$, and $\mathbf{e}_r$ are unit vectors in the principal directions of the cylindrical coordinate system, and Ω_x, Ω_θ, and Ω_r are the components of Ω. Using the decomposition of equation (8), the components of the displacement of the soil medium can be expressed as

$$\begin{aligned}
u_r &= \frac{\partial\Pi}{\partial r} + \left(\frac{1}{r}\right)\left(\frac{\partial\Omega_x}{\partial\theta}\right) - \frac{\partial\Omega_\theta}{\partial x},\\
u_\theta &= \left(\frac{1}{r}\right)\left(\frac{\partial\Pi}{\partial\theta}\right) + \frac{\partial\Omega_r}{\partial x} - \frac{\partial\Omega_x}{\partial r},\\
u_x &= \frac{\partial\Pi}{\partial x} + \left(\frac{1}{r}\right)\left(\frac{\partial(r\Omega_\theta)}{\partial r}\right) - \left(\frac{1}{r}\right)\left(\frac{\partial\Omega_r}{\partial\theta}\right).
\end{aligned} \tag{11}$$

The wave propagation solutions of the wave equation that satisfy equation (9) can be expressed as

$$\begin{aligned}
\Pi &= f(r)\cos(n\theta)\exp[i(\omega t - kx)],\\
\Omega_r &= -ig_r(r)\sin(n\theta)\exp[i(\omega t - kx)],\\
\Omega_\theta &= -ig_\theta(r)\cos(n\theta)\exp[i(\omega t - kx)],\\
\Omega_x &= g_x(r)\sin(n\theta)\exp[i(\omega t - kx)].
\end{aligned} \tag{12}$$

These represent harmonic solutions in the same way as those used in the analysis of the cylindrical shell, but now there are also variations with the radius r, which are governed by the functions f, g_r, g_θ, and g_x, respectively. Here, ω is the frequency in the complex domain, of which the real part is the vibration frequency and the imaginary part is related to attenuation. Substitution of the solutions expressed by equation (12) into equation (9), making use of the definitions expressed by equation (10) and considering each component of the equation in Ω in turn, results in the four following differential equations:

$$\begin{aligned}
&\frac{\mathrm{d}^2 f}{\mathrm{d}r^2} + \left(\frac{1}{r}\right)\left(\frac{\mathrm{d}f}{\mathrm{d}r}\right) - \left[\frac{n^2}{r^2} - \left(\frac{\omega^2}{c_p^2} - k^2\right)\right]f = 0,\\
&\frac{\mathrm{d}^2 g_r}{\mathrm{d}r^2} + \left(\frac{1}{r}\right)\left(\frac{\mathrm{d}g_r}{\mathrm{d}r}\right) + \frac{1}{r^2}\left(-n^2 g_r + 2ng_\theta - g_r\right) - k^2 g_r + \left(\frac{\omega^2}{c_s^2}\right)g_r = 0,\\
&\frac{\mathrm{d}^2 g_\theta}{\mathrm{d}r^2} + \left(\frac{1}{r}\right)\left(\frac{\mathrm{d}g_\theta}{\mathrm{d}r}\right) + \frac{1}{r^2}\left(-n^2 g_\theta + 2ng_r - g_\theta\right) - k^2 g_\theta + \left(\frac{\omega^2}{c_s^2}\right)g_\theta = 0,\\
&\frac{\mathrm{d}^2 g_x}{\mathrm{d}r^2} + \left(\frac{1}{r}\right)\left(\frac{\mathrm{d}g_x}{\mathrm{d}r}\right) - \left[\frac{n^2}{r^2} - \left(\frac{\omega^2}{c_s^2} - k^2\right)\right]g_x = 0.
\end{aligned} \tag{13}$$

According to the property of gauge invariance [31], defining $g_r = -g_\theta$ and substituting into the second and third forms of equation (13) give

$$\frac{\mathrm{d}^2 g_r}{\mathrm{d}r^2} + \left(\frac{1}{r}\right)\left(\frac{\mathrm{d}g_r}{\mathrm{d}r}\right) - \left[\frac{(n+1)^2}{r^2} - \left(\frac{\omega^2}{c_s^2} - k^2\right)\right]g_r = 0. \tag{14}$$

The first and fourth forms of equation (13) are modified Bessel equations of order n, and equation (14) is a modified Bessel equation of order $(n+1)$. From the boundary conditions at an infinite distance, f, g_r, g_θ, and g_x are expressed as

$$\begin{aligned} f(r) &= AW_n(\xi_1 r),\\ g_r(r) &= -g_\theta(r) = BW_{n+1}(\xi_2 r),\\ g_x(r) &= CW_n(\xi_2 r), \end{aligned} \tag{15}$$

where A, B, and C are undetermined constants; W_n and W_{n+1} represent a third class of Bessel functions of orders n and $n+1$, respectively; and $\xi_1 = \sqrt{\omega^2/(c_p^2 - k^2)}$ and $\xi_2 = \sqrt{\omega^2/(c_s^2 - k^2)}$ are the radial components of the longitudinal wave number and the shear wave number in the soil medium, respectively.

By substituting equations (12) and (15) into equation (11), expressions for axial, tangential, and radial displacements can be obtained:

$$\begin{aligned} u_r &= \left[\xi_1 AW_n'(\xi_1 r) - kBW_{n+1}(\xi_2 r) + \frac{n}{r}CW_n(\xi_2 r)\right]\cos(n\theta)\exp[i(\omega t - kx)],\\ u_\theta &= \left[-\frac{n}{r}AW_n(\xi_1 r) - kBW_{n+1}(\xi_2 r) - \xi_2 CW_n'(\xi_2 r)\right]\sin(n\theta)\exp[i(\omega t - kx)],\\ u_x &= \left[-ikAW_n(\xi_1 r) + i\xi_2 BW_{n+1}'(\xi_2 r) + i\frac{n+1}{r}BW_{n+1}(\xi_2 r)\right]\cos(n\theta)\exp[i(\omega t - kx)]. \end{aligned} \tag{16}$$

From the relationship between stress and strain, expressions for stresses σ in the soil medium can be obtained:

$$\begin{aligned} &\begin{pmatrix}\sigma_{rr}\\ \sigma_{r\theta}\\ \sigma_{rx}\end{pmatrix} = \begin{pmatrix}\cos(n\theta) & 0 & 0\\ 0 & \sin(n\theta) & 0\\ 0 & 0 & \cos(n\theta)\end{pmatrix}\begin{pmatrix}d_{11} & d_{12} & d_{13}\\ d_{21} & d_{22} & d_{23}\\ d_{31} & d_{32} & d_{33}\end{pmatrix}\begin{pmatrix}A\\ B\\ C\end{pmatrix}\cdot \exp[i(\omega t - kx)],\\ &d_{11} = (\tilde\lambda + 2\tilde\mu)\xi_1^2 W_n''(\xi_1 r) + \tilde\lambda\frac{\xi_1}{r}W_n'(\xi_1 r) - \tilde\lambda\left(\frac{n^2}{r^2} + k^2\right)W_n(\xi_1 r),\\ &d_{12} = -2\tilde\mu k\xi_2 W_{n+1}'(\xi_2 r),\\ &d_{13} = 2\tilde\mu\left[\frac{n}{r}\xi_2 W_n'(\xi_2 r) - \frac{n}{r^2}W_n(\xi_2 r)\right],\\ &d_{21} = 2\tilde\mu\left[\frac{n}{r^2}W_n(\xi_1 r) - \frac{n}{r}\xi_1 W_n'(\xi_1 r)\right],\\ &d_{22} = \tilde\mu\left[\frac{n+1}{r}kW_{n+1}(\xi_2 r) - k\xi_2 W_{n+1}'(\xi_2 r)\right],\\ &d_{23} = \tilde\mu\left[\frac{1}{r}\xi_2 W_n'(\xi_2 r) - \frac{n^2}{r^2}W_n(\xi_2 r) - \xi_2^2 W_n''(\xi_2 r)\right],\\ &d_{31} = -2ik\tilde\mu\xi_1 W_n'(\xi_1 r),\\ &d_{32} = \tilde\mu\left[\left(ik^2 - i\frac{n+1}{r^2}\right)W_{n+1}(\xi_2 r) + i\xi_2\frac{n+1}{r}W_{n+1}'(\xi_2 r) + i\xi_2^2 W_{n+1}''(\xi_2 r)\right],\\ &d_{33} = -ik\tilde\mu\frac{n}{r}W_n(\xi_2 r). \end{aligned} \tag{17}$$

4. Vibration Control Equation of Tunnel in Viscous Soil

It is assumed that, on the contact surface, the surface displacement of the tunnel structure (cylindrical shell) is equal to that of the soil medium. When $r = R + (h/2)$,

$$\begin{aligned} &U\cos(n\theta)\exp[i(\omega t - kx)] + \Phi\cos(n\theta)\exp[i(\omega t - kx)]\cdot\frac{h}{2} = u_x|_{r=R+(h/2)},\\ &V\sin(n\theta)\exp[i(\omega t - kx)] + \Psi\sin(n\theta)\exp[i(\omega t - kx)]\cdot\frac{h}{2} = u_\theta|_{r=R+(h/2)},\\ &W\cos(n\theta)\exp[i(\omega t - kx)] = u_r|_{r=R+(h/2)}. \end{aligned} \tag{18}$$

By substituting equation (16) into equation (18), the displacement conditions expressed by the matrix for viscoelastic medium can be obtained:

$$\begin{pmatrix} Q_{11} & Q_{12} & Q_{13}\\ Q_{21} & Q_{22} & Q_{23}\\ Q_{31} & Q_{32} & Q_{33}\end{pmatrix}\Bigg|_{r=R+(h/2)} \begin{pmatrix} A\\ B\\ C\end{pmatrix} = \left(U + \frac{h}{2}\Phi \quad V + \frac{h}{2}\Psi \quad W\right)^T, \tag{19}$$

where $Q_{11} = -ikW_n(\xi_1 r)$, $Q_{12} = i\xi_2 W_{n+1}'(\xi_2 r) + i(n+1/r)W_{n+1}(\xi_2 r)$, $Q_{13} = 0$, $Q_{21} = -(n/r)W_n(\xi_1 r)$, $Q_{22} = -kW_{n+1}(\xi_2 r)$, $Q_{23} = -\xi_2 W_n'(\xi_2 r)$, and $Q_{31} = \xi_1 W_n'(\xi_1 r)$, $Q_{32} = -kW_{n+1}(\xi_2 r)$, $Q_{33} = (n/r)W_n(\xi_2 r)$. According to the continuous condition of the force on the contact surface, the force F exerted by the soil medium on the outer surface of the tunnel structure can be determined as follows:

$$\left(F_x \quad F_\theta \quad F_r\right)^T = \left(\sigma_{rx}|_{r=R+(h/2)} \quad \sigma_{r\theta}|_{r=R+(h/2)} \quad \sigma_{rr}|_{r=R+(h/2)}\right)^T. \tag{20}$$

By substituting equation (17) into equation (18), the following continuous conditions can be obtained:

$$\mathbf{F} = \begin{pmatrix} F_x\\ F_\theta\\ F_r\end{pmatrix} = [g']\begin{pmatrix} \alpha_{11} & \alpha_{12} & \alpha_{13}\\ \alpha_{21} & \alpha_{22} & \alpha_{23}\\ \alpha_{31} & \alpha_{32} & \alpha_{33}\end{pmatrix}_{r=R+(h/2)} \begin{pmatrix} A\\ B\\ C\end{pmatrix}, \tag{21}$$

where $\alpha_{11} = -2i\tilde{\mu}k\xi_1 W_n'(\xi_1 r)$, $\alpha_{12} = i\tilde{\mu}\,[(k^2 - (n+1/r^2))W_{n+1}(\xi_2 r) + \xi_2(n+1/r)W_{n+1}'(\xi_2 r) + \xi_2^2 W_{n+1}''(\xi_2 r)]$, $\alpha_{13} = -i\tilde{\mu}k(n/r)W_n(\xi_2 r)$, $\alpha_{21} = 2\tilde{\mu}[(n/r^2)W_n(\xi_1 r) - (n/r)\xi_1 W_n'(\xi_1 r)]$, $\alpha_{22} = \tilde{\mu}[(n+1/r)kW_{n+1}(\xi_2 r) - k\xi_2 W_{n+1}'(\xi_2 r)]$, $\alpha_{23} = \tilde{\mu}[(\xi_2/r)W_n'(\xi_2 r) - (n^2/r^2)W_n(\xi_2 r) - \xi_2^2 W_n''(\xi_2 r)]$, $\alpha_{31} = (\tilde{\lambda} + 2\tilde{\mu})\xi_1^2 W_n''(\xi_1 r) + \tilde{\lambda}(\xi_1/r)W_n'(\xi_1 r) - \tilde{\lambda}((n^2/r^2) + k^2)W_n(\xi_1 r)$, $\alpha_{32} = -2\tilde{\mu}k\xi_2 W_{n+1}'(\xi_2 r)$, $\alpha_{33} = 2\tilde{\mu}[(n/r)\xi_2 W_n'(\xi_2 r) - (n/r^2)W_n(\xi_2 r)]$, and $[g'] = \mathrm{diag}\{g_{11} \; g_{22} \; g_{33}\}$.

Substituting equation (19) into equation (21) gives

$$\mathbf{F} = [g'][\alpha][\beta]\overline{U'}, \tag{22}$$

where $\overline{\mathbf{U}}' = (U + (h/2)\Phi, \; V + (h/2)\Psi, \; W)^T$, $[\alpha] = \begin{pmatrix} \alpha_{11} & \alpha_{12} & \alpha_{13}\\ \alpha_{21} & \alpha_{22} & \alpha_{23}\\ \alpha_{31} & \alpha_{32} & \alpha_{33}\end{pmatrix}\Bigg|_{r=R+(h/2)}$ and $[\beta] = \begin{pmatrix} \beta_{11} & \beta_{12} & \beta_{13}\\ \beta_{21} & \beta_{22} & \beta_{23}\\ \beta_{31} & \beta_{32} & \beta_{33}\end{pmatrix} = \begin{pmatrix} Q_{11} & Q_{12} & Q_{13}\\ Q_{21} & Q_{22} & Q_{23}\\ Q_{31} & Q_{32} & Q_{33}\end{pmatrix}^{-1}\Bigg|_{r=R+(h/2)}$. By extending $\mathbf{F}$, $[g]$, $[\alpha]$, $[\beta]$, and $\overline{U}'$ in equation (22), we can obtain

$$\overline{F} = [g][\overline{\alpha}][\overline{\beta}][\overline{h}]\overline{U}. \tag{23}$$

In equation (23), $\overline{F} = (F_x, F_\theta, F_r, 0, 0)^T$, $\overline{U} = (U, V, W, \Phi, \Psi)^T$, $[\overline{\alpha}]_{5\times5} = \begin{pmatrix} \alpha & 0_{3\times2}\\ 0_{2\times3} & 0_{2\times2}\end{pmatrix}$, $[\overline{\beta}]_{5\times5} = \begin{pmatrix} \beta & 0_{3\times2}\\ 0_{2\times3} & 0_{2\times2}\end{pmatrix}$, $[\overline{h}]_{5\times5} = \begin{pmatrix} I_3 & h_0 I_2\\ 0_{2\times3} & 0_{2\times2}\end{pmatrix}$, I_k is the identity matrix of order k, and $h_0 = (h/2)$.

In accordance with equation (23) for the continuous condition of the force on the contact surface, the force exerted by the soil medium on the surface of the tunnel can be determined by the translation of force:

$$\mathbf{q} = [\overline{h}]^T\overline{F} = [\overline{h}]^T[g][\overline{\alpha}][\overline{h}]\overline{U}. \tag{24}$$

By substituting equation (24) into equation (3), the vibration control equation of a tunnel structure in viscous soil based on the theory of moderately thick shells can be obtained:

$$\left([l] + [\overline{K}][\overline{h}]^T[\overline{\alpha}][\overline{\beta}][\overline{h}]\right)\overline{U} = 0. \tag{25}$$

For the nonzero solution of equation (25), the determinant of its coefficient matrix must be equal to zero, and thus the dispersion characteristic equation for the vibration characteristics of the tunnel can be obtained:

$$\left|[l] + [\overline{K}][\overline{h}]^T[\overline{\alpha}][\overline{\beta}][\overline{h}]\right| = 0. \tag{26}$$

5. Numerical Results

5.1. Boundary Conditions. In this paper, the simplified boundary conditions in the form of solid supports at both ends of the tunnel are selected for calculation. The parameters of the tunnel are selected as follows: $E = 50$ GPa, $\nu = 0.3$, $\rho = 2500\,\text{kg/m}^3$, $h = 0.25$ m, $R = 2.75$ m, $\lambda = 28.8$ GPa, and $\mu = 19.2$ GPa. The parameters of the soil around the tunnel are chosen as follows: $E_s = 400$ MPa, $\nu_s = 0.35$, and $\rho_s = 1960\,\text{kg/m}^3$. The viscosity coefficient of the soil is denoted by η and has units of Pa·s.

In accordance with the simplified treatment of boundary conditions in the case of cylindrical shells in an infinite flow field [1], the boundary conditions at both ends of the tunnel are approximately treated as solid beams in this paper, and it is considered that the wave number for waves propagated in the axial direction is related to the boundary conditions at both ends of the cylindrical shell. The tunnel is represented in simplified form as a cylindrical shell with fixed supports at both ends, and hence $kL = (2m + 1)\pi/2$, where m is the axial mode number. From the wave number k and the circumferential mode number n, the characteristic equation (26) can be used to calculate the frequency of the cylindrical shell under different modes (m, n) in the complex domain. Here, the circular frequency ω is a complex number, of which the real part represents the natural vibration frequency of the tunnel and the imaginary part is related to attenuation. Circular frequency ω and frequency f satisfy $\omega = 2\pi f$, where f is a complex number, $f = f_R + i f_{\text{Im}}$, the real part f_R represents the vibration frequency of the tunnel, and the imaginary part f_{Im} is related to attenuation. To assess the influence of soil viscosity on attenuation at the vibration frequency of the tunnel structure, the attenuation coefficient η^* is introduced and is defined as

$$\eta^* = \exp\left(2\pi \cdot \frac{f_R}{f_{\text{Im}}}\right). \tag{27}$$

5.2. Effect of Soil Viscosity on Frequency of Tunnel Structure. Figure 2 shows the variations in the natural frequency of each mode at different soil viscosities. When $\eta = 0$, the viscous soil around the tunnel becomes isotropic and linearly elastic. With an increase in η, the natural frequencies of the tunnel structure are reduced. The results show that the influence of a viscous soil medium on the vibration characteristics of the tunnel structure is mainly manifested as the influence of additional mass.

Figure 3 shows the variations in the attenuation coefficient η^* of the tunnel for each mode at different soil viscosity. The attenuation coefficient increases significantly with an increase in soil viscosity. This indicates that viscous soil surrounding the tunnel has a strong influence on energy dissipation. In addition, with an increase in soil viscosity, the attenuation coefficient increases to a significantly greater extent for the high-order modes than for the low-order modes, which explains why vibrations at the natural frequency of the tunnel, as shown in Figure 2, are attenuated more significantly in the case of high-order modes at high viscosity.

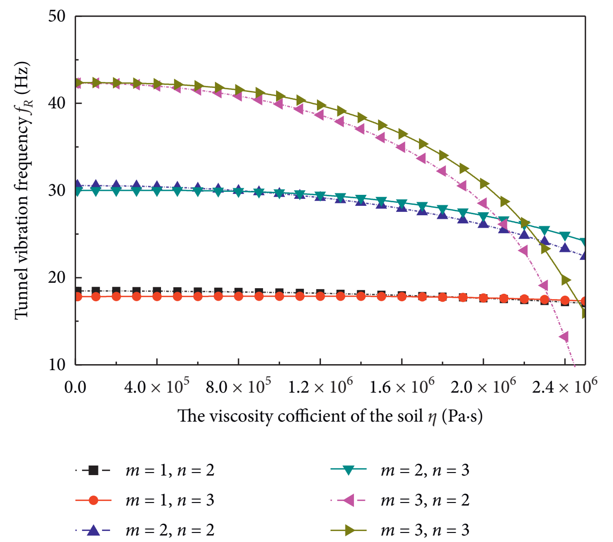

FIGURE 2: Relationship between natural frequency of the tunnel and changes in soil viscosity for different modes.

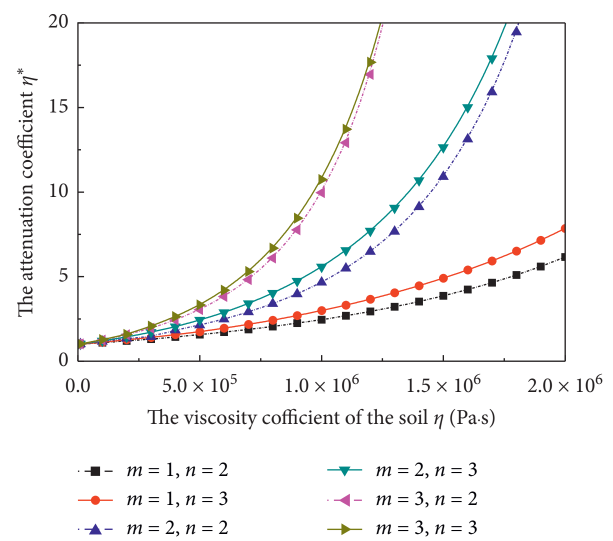

FIGURE 3: Relationship between attenuation coefficient and changes in soil viscosity for different modes.

5.3. Effect of Tunnel Radius on Frequency of Tunnel Structure. In order to analyze the influence of the tunnel radius on the natural vibration frequency of the tunnel structure under the influence of viscous soil, other calculation parameters remain unchanged, while the tunnel radius is varied, and the viscosity coefficient of the soil mass is defined as $\eta = 1.0 \times 10^6$ Pa·s.

As shown in Figure 4, the natural frequency of the tunnel is basically the same at the same axial mode number m for each mode. With an increase in the tunnel radius, the natural frequency of the tunnel for each mode slight increases. Figure 5 shows the attenuation curves for each mode corresponding to Figure 4. At the same axial mode number, the attenuation coefficient for a high circumferential mode number is higher when the tunnel radius is less than 0.3 m. On the whole, it can be seen that the radius has little influence on the natural frequency of the tunnel.

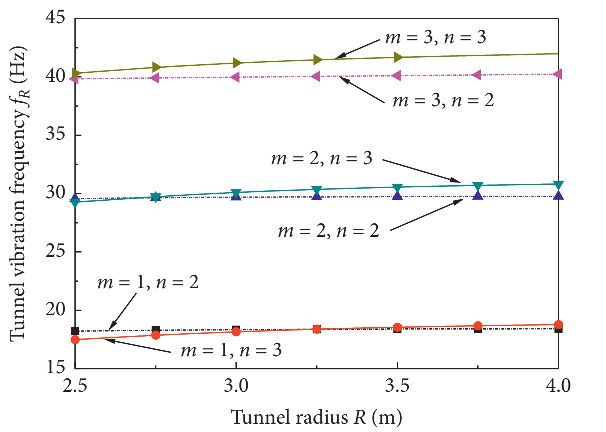

FIGURE 4: Relationship between natural frequency of the tunnel and changes in the tunnel radius change for different modes, where $\eta = 1.0 \times 10^6$ Pa·s.

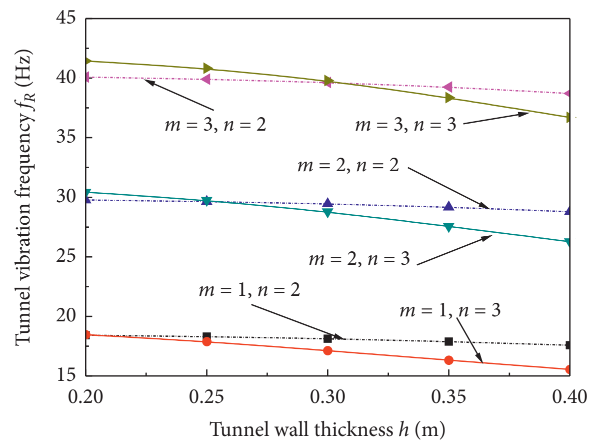

FIGURE 6: Relationship between natural frequency of the tunnel and tunnel wall thickness for different modes, where $\eta = 1.0 \times 10^6$ Pa·s.

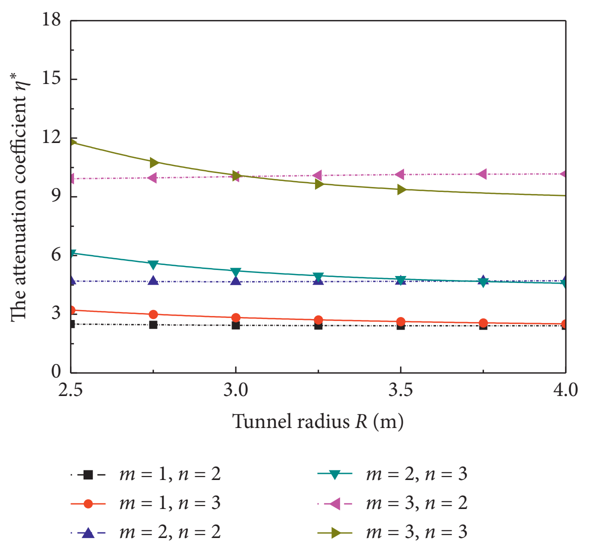

FIGURE 5: Relationship between attenuation and changes in the tunnel radius for different modes, where $\eta = 1.0 \times 10^6$ Pa·s.

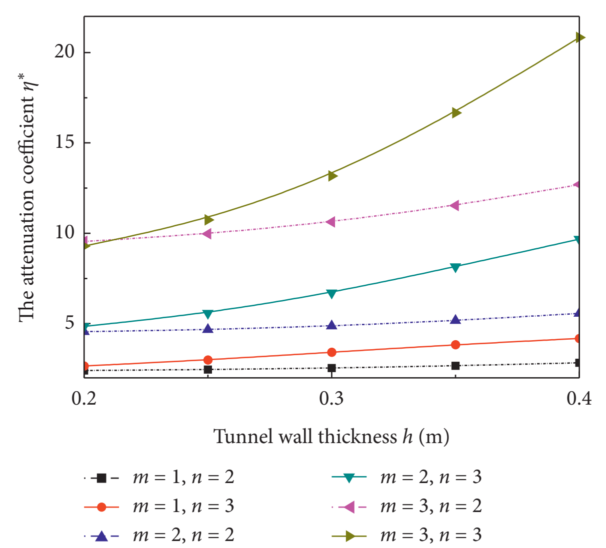

FIGURE 7: Relationship between attenuation and tunnel wall thickness for different modes, where $\eta = 1.0 \times 10^6$ Pa·s.

5.4. Effect of Tunnel Wall Thickness on Frequency of Tunnel Structure. Figure 6 shows the variations in the natural frequency of the tunnel structure at different wall thicknesses. Except for the tunnel wall thickness, the calculation parameters are the same as those given in Section 5.1, and $\eta = 1.0 \times 10^6$ Pa·s. As shown in Figure 6, with an increase in wall thickness, the natural frequency of the tunnel for each mode decreases. All modes with the same axial mode number m have basically the same natural frequency and exhibit the same variation trend. When the tunnel wall thickness is at least 0.3 m, the natural frequency of the tunnel for higher circumferential modes is lower at the same axial mode number. Figure 7 illustrates the variations in attenuation due to the tunnel structure at different wall thicknesses for each mode. The attenuation coefficient increases with an increase in tunnel wall thickness. When the tunnel wall thickness is at least 0.25 m, the attenuation of each mode increases with an increase in tunnel wall thickness, and at the same axial mode number the attenuation coefficient for a high circumferential mode number is higher. This indicates that in a viscous soil medium the influence of an increase in tunnel wall thickness on the natural vibration frequency of the tunnel structure is mainly caused by an increase in the generalized mass of the tunnel.

5.5. Effect of Tunnel Length on Frequency of Tunnel Structure. Figures 8 and 9 show the variations in the natural frequency of the tunnel and attenuation due to the tunnel structure at different tunnel length. Except for the length of the tunnel, the calculation parameters are the same as those given in Section 5.1, and $\eta = 1.0 \times 10^6$ Pa·s. Under the influence of coupling with viscous soil, the natural frequency of the tunnel and attenuation due to the tunnel significantly decrease with an increase in tunnel length, and at the same axial mode number the natural frequency of the tunnel for a high circumferential mode number is lower. As shown in Figure 9, with an increase in tunnel length the attenuation due to the tunnel tends to be constant. This

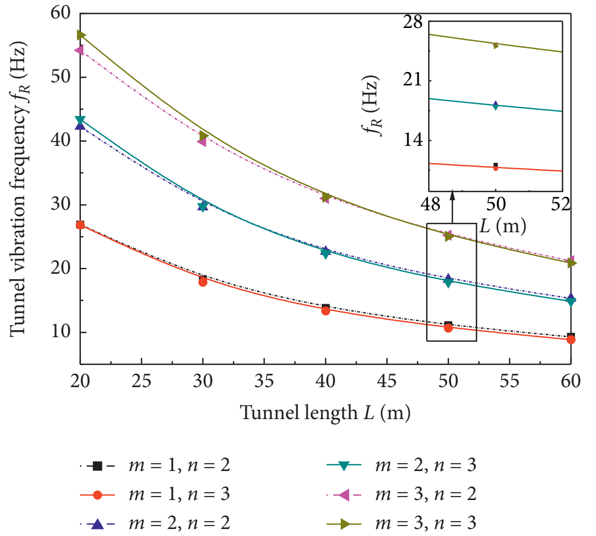

FIGURE 8: Relationship between natural frequency of the tunnel and tunnel length for different modes, where $\eta = 1.0 \times 10^6$ Pa·s.

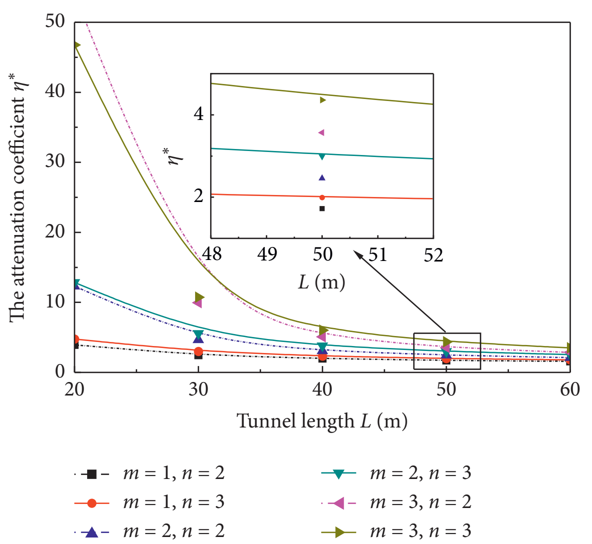

FIGURE 9: Relationship between attenuation and tunnel length for different modes, where $\eta = 1.0 \times 10^6$ Pa·s.

indicates that in a viscous soil medium the effect of an increase in tunnel length on the natural vibration frequency of the tunnel structure is mainly caused by decrease in the generalized stiffness of the structure.

5.6. Effect of Tunnel Depth on Frequency of Tunnel Structure. In this paper, the change of soil modulus is used to measure the buried depth of the tunnel, and the influence of buried depth on vibration frequency of the tunnel is studied. Except for the modulus of soil, the calculation parameters are the same as those given in Section 5.1, and $\eta = 1.0 \times 10^6$ Pa·s. As shown in Figure 10, with an increase in the modulus of soil, the natural frequency of the tunnel for each mode increases. All modes with the same axial mode number m have basically the same natural frequency and exhibit the same variation trend. Figure 11 shows the attenuation curves for each mode

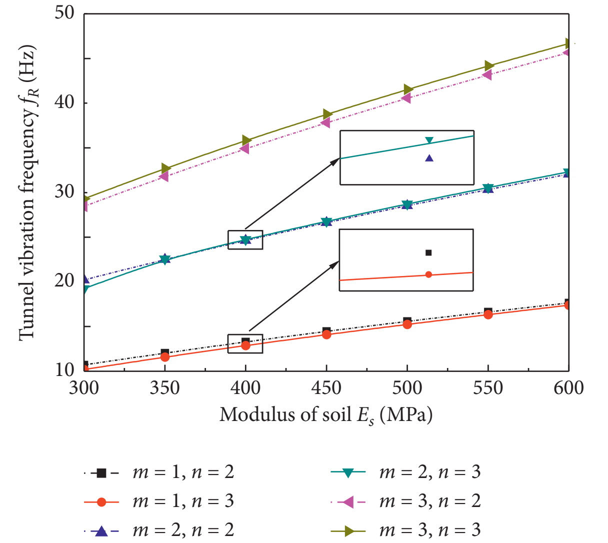

FIGURE 10: Relationship between natural frequency of the tunnel and the modulus of soil, where $\eta = 1.0 \times 10^6$ Pa·s.

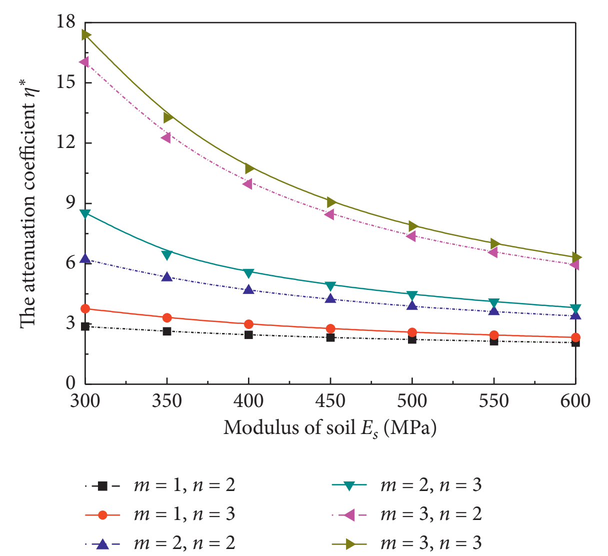

FIGURE 11: Relationship between attenuation and the modulus of soil, where $\eta = 1.0 \times 10^6$ Pa·s.

corresponding to Figure 10. It can be considered that, with the increase of the buried depth of the tunnel, the influence of soil media on the vibration characteristics of the tunnel structure is mainly the influence of additional stiffness.

6. Conclusions

In this paper, the vibration control equation for the coupling of a tunnel and viscous soil is established by using the theory of moderately thick cylindrical shells and the method of wave propagation and representing the soil around the tunnel in simplified form as an isotropic viscoelastic medium. The effect of a viscous soil medium on the natural vibration frequency of the tunnel structure is mainly manifested as the effect of additional mass. For each mode, the natural frequency of the tunnel structure decreases with an increase in the viscosity of the soil around the tunnel, and attenuation increases with an increase in soil viscosity. Higher modes are more sensitive to soil viscosity than are lower modes.

In a viscous soil medium, the natural frequency of the tunnel structure decreases with the increase of tunnel wall thickness, tunnel length, and tunnel buried depth. When the tunnel radius is large, the natural frequency of the tunnel structure slightly increases with an increase in the tunnel radius.

Data Availability

All data, models, and code generated or used during the study appear in the submitted article.

Conflicts of Interest

The authors declare that they have no conflicts of interest.

Acknowledgments

The research described in this paper was financially supported by the National Natural Science Foundation of China (11972285, 11872300, and 11572245) and the Natural Science Foundation of Shaanxi Province (no. 2013JQ1008). This support is gratefully acknowledged.

References

[1] X. M. Zhang, G. R. Liu, and K. Y. Lam, "Coupled vibration analysis of fluid-filled cylindrical shells using the wave propagation approach," *Applied Acoustics*, vol. 62, no. 3, pp. 229–243, 2001.

[2] J. A. Forrest and H. E. M. Hunt, "A three-dimensional tunnel model for calculation of train-induced ground vibration," *Journal of Sound and Vibration*, vol. 294, no. 4-5, pp. 678–705, 2006.

[3] J. A. Forrest and H. E. M. Hunt, "Ground vibration generated by trains in underground tunnels," *Journal of Sound and Vibration*, vol. 294, no. 4-5, pp. 706–736, 2006.

[4] S. Sun, D. Cao, and S. Chu, "Free vibration analysis of thin rotating cylindrical shells using wave propagation approach," *Archive of Applied Mechanics*, vol. 83, no. 4, pp. 521–531, 2013.

[5] I. D. Moore and F. Guan, "Three-dimensional dynamic response of lined tunnels due to incident seismic waves," *Earthquake Engineering & Structural Dynamics*, vol. 25, no. 4, pp. 357–369, 1996.

[6] D. Clouteau, M. Arnst, T. M. Al-Hussaini, and G. Degrande, "Freefield vibrations due to dynamic loading on a tunnel embedded in a stratified medium," *Journal of Sound and Vibration*, vol. 283, no. 1-2, pp. 173–199, 2005.

[7] G. Degrande, D. Clouteau, R. Othman et al., "A numerical model for ground-borne vibrations from underground railway traffic based on a periodic finite element–boundary element formulation," *Journal of Sound and Vibration*, vol. 293, no. 3–5, pp. 645–666, 2006.

[8] S. Gupta, M. F. M. Hussein, G. Degrande, H. E. M. Hunt, and D. Clouteau, "A comparison of two numerical models for the prediction of vibrations from underground railway traffic," *Soil Dynamics and Earthquake Engineering*, vol. 27, no. 7, pp. 608–624, 2007.

[9] M. F. M. Hussein, S. Gupta, H. E. M. Hunt et al., "An efficient model for calculating vibration from a railway tunnel buried in a half-space," in *Proceedings of the 13th International Congress on Sound and Vibration*, Vienna, Austria, June 2006.

[10] K. A. Kuo, H. E. M. Hunt, and M. F. M. Hussein, "The effect of a twin tunnel on the propagation of ground-borne vibration from an underground railway," *Journal of Sound and Vibration*, vol. 330, no. 25, pp. 6203–6222, 2011.

[11] A. Clot, R. Arcos, J. Romeu, and T. Pàmies, "Dynamic response of a double-deck circular tunnel embedded in a full-space," *Tunnelling and Underground Space Technology*, vol. 59, pp. 146–156, 2016.

[12] G. Parry, S. Summers, and D. Yates, "Validation of the pipe in pipe vibration software model to determine ground-borne noise and vibration levels above construction tunnels and the determination of end corrections for different train operating scenarios," *The Journal of the Acoustical Society of America*, vol. 135, no. 4, p. 2288, 2014.

[13] W. Yang, M. F. M. Hussein, and A. M. Marshall, "Centrifuge and numerical modelling of ground-borne vibration from an underground tunnel," *Soil Dynamics and Earthquake Engineering*, vol. 51, pp. 23–34, 2013.

[14] T. Senjuntichai, S. Mani, and R. K. N. D. Rajapakse, "Vertical vibration of an embedded rigid foundation in a poroelastic soil," *Soil Dynamics & Earthquake Engineering*, vol. 26, no. 6-7, pp. 626–636, 2006.

[15] R. Kumar, A. Miglani, and L. Debnath, "Radial displacements of an infinite liquid saturated porous medium with cylindrical cavity," *Computers & Mathematics with Applications*, vol. 37, no. 7, pp. 117–123, 1999.

[16] S. M. Hasheminejad and H. Hosseini, "Dynamic stress concentration near a fluid-filled permeable borehole induced by general modal vibrations of an internal cylindrical radiator," *Soil Dynamics and Earthquake Engineering*, vol. 22, no. 6, pp. 441–458, 2002.

[17] S. M. Hasheminejad and M. Komeili, "Effect of imperfect bonding on axisymmetric elastodynamic response of a lined circular tunnel in poroelastic soil due to a moving ring load," *International Journal of Solids and Structures*, vol. 46, no. 2, pp. 398–411, 2009.

[18] G. Y. Gao, J. F. He, and L. Jia, "Dynamic response induced by running subway in saturated ground," *Journal of Zhejiang University (Engineering Science Edition)*, vol. 44, no. 10, pp. 1925–1930, 2010.

[19] C. He, S. H. Zhou, H. G. Di, and Y. Shan, "A 2.5-D coupled FE–BE model for the dynamic interaction between saturated soil and longitudinally invariant structures," *Computers and Geotechnics*, vol. 82, pp. 211–222, 2017.

[20] S. Zhou, C. He, and H. Di, "Dynamic 2.5-D green's function for a poroelastic half-space," *Engineering Analysis with Boundary Elements*, vol. 67, pp. 96–107, 2016.

[21] H. Di, S. Zhou, C. He, X. Zhang, and Z. Luo, "Three-dimensional multilayer cylindrical tunnel model for calculating train-induced dynamic stress in saturated soils," *Computers and Geotechnics*, vol. 80, pp. 333–345, 2016.

[22] J. F. Lu and D. S. Jeng, "Dynamic analysis of an infinite cylindrical hole in a saturated poroelastic medium," *Archive of Applied Mechanics*, vol. 76, no. 5-6, pp. 263–276, 2006.

[23] J.-F. Lu and D.-S. Jeng, "A half-space saturated poro-elastic medium subjected to a moving point load," *International Journal of Solids and Structures*, vol. 44, no. 2, pp. 573–586, 2007.

[24] H. X. Gao and M. J. Wen, "Frequency responses of a partial sealed tunnel with fractional derivative viscoelastic lining," *Acta Mechanica Solida Sinica*, vol. 33, no. 6, pp. 637–643, 2012.

[25] Z. Yuan, Y. Cai, and Z. Cao, "An analytical model for vibration prediction of a tunnel embedded in a saturated full-space to a harmonic point load," *Soil Dynamics and Earthquake Engineering*, vol. 86, pp. 25–40, 2016.

[26] Z. Yuan, Z. Cao, A. Boström, and Y. Cai, "The influence of pore-fluid in the soil on ground vibrations from a tunnel embedded in a layered half-space," *Journal of Sound and Vibration*, vol. 419, pp. 227–248, 2018.

[27] S. Jones and H. Hunt, "Voids at the tunnel-soil interface for calculation of ground vibration from underground railways," *Journal of Sound and Vibration*, vol. 330, no. 2, pp. 245–270, 2011.

[28] N. Yasuda, K. Tsukada, and T. Asakura, "Elastic solutions for circular tunnel with void behind lining," *Tunnelling and Underground Space Technology*, vol. 70, pp. 274–285, 2017.

[29] Y. Huang, H. R. Huang, F. S. He et al., *The Linear Theory of Elastic Shells*, Science Press, Beijing, China, 2007.

[30] K. F. Graff, *Wave Motion in Elastic Solids*, Oxford University Press, Oxford, UK, 1975.

[31] D. C. Gazis, "Three-dimensional investigation of the propagation of waves in hollow circular cylinders. I. analytical foundation," *The Journal of the Acoustical Society of America*, vol. 31, no. 5, pp. 568–573, 1959.